Neutron Scattering Applications and Techniques

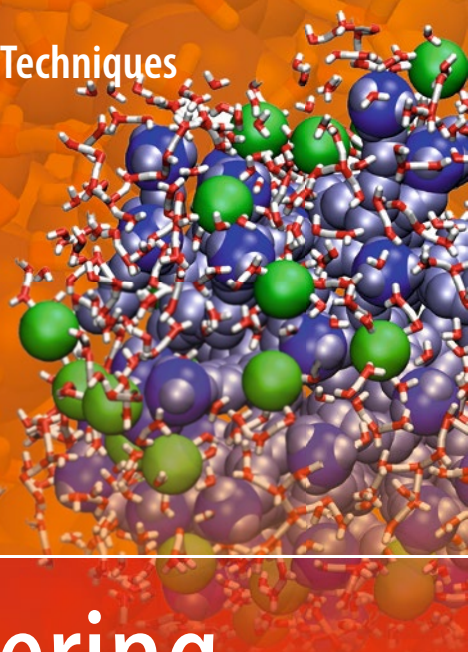

Helmut Fritzsche
Jacques Huot
Daniel Fruchart *Editors*

Neutron Scattering and Other Nuclear Techniques for Hydrogen in Materials

Springer

Neutron Scattering Applications and Techniques

More information about this series at: http://www.springer.com/series/8141

Helmut Fritzsche • Jacques Huot • Daniel Fruchart
Editors

Neutron Scattering and Other Nuclear Techniques for Hydrogen in Materials

Springer

Editors
Helmut Fritzsche
Neutron Scattering Branch
Canadian Nuclear Laboratories
Chalk River, ON, Canada

Jacques Huot
Hydrogen Research Institute
Université du Québec à Trois-Rivières
Trois-Rivières, Québec, Canada

Daniel Fruchart
Institut Néel
Grenoble, France

ISSN 1868-0372 ISSN 1868-0380 (electronic)
Neutron Scattering Applications and Techniques
ISBN 978-3-319-22791-7 ISBN 978-3-319-22792-4 (eBook)
DOI 10.1007/978-3-319-22792-4

Library of Congress Control Number: 2016933246

Printed on acid-free paper

This Springer imprint is published by Springer Nature
The registered company is Springer International Publishing AG Switzerland

Contents

Contributors

Daniel Banks Canadian Neutron Beam Centre, Canadian Nuclear Laboratories, Chalk River, ON, Canada

Hans-Werner Becker RUBION, Central Unit for Ion Beams and Radioisotopes, Ruhr-University Bochum, Bochum, Germany

Pascal Berger Laboratory for the Study of Light Elements (LEEL), NIMBE, CEA, CNRS, Université Paris-Saclay, CEA Saclay, Gif sur Yvette, France

Radovan Černý Laboratoire de Cristallographie, DQMP, Faculté des Sciences, Université de Genève, Genève, Switzerland

Helmut Fritzsche Canadian Nuclear Laboratories, Chalk River, ON, Canada

Michael A. Gharghouri Canadian Nuclear Laboratories, Chalk River, ON, Canada

Axel Griesche Federal Institute for Materials Research and Testing (BAM), Berlin, Germany

Mirco Große Karlsruhe Institute of Technology, Institute for Applied Materials, Karlsruhe, Germany

Bjørn C. Hauback Institute for Energy Technology, Kjeller, Norway

Björgvin Hjörvarrson Department of Physics and Astronomy, Uppsala University, Uppsala, Sweden

Jacques Huot Hydrogen Research Institute, Université du Québec à Trois-Rivières, Trois-Rivières, QC, Canada

Hicham Khodja Laboratory for the Study of Light Elements (LEEL), CEA, Université Paris-Saclay, CEA-SACLAY, NIMBE, Gif sur Yvette, France

Frank Klose Bragg Institute, Australian Nuclear Science and Technology Organisation, Lucas Heights, NSW, Australia
Department of Physics and Materials Science, City University of Hong Kong, Hong Kong SAR, China

Kenneth D. Knudsen Institute for Energy Technology, Kjeller, Norway

Henrik Mauroy Institute for Energy Technology, Kjeller, Norway

Caroline Raepsaet Laboratory for the Study of Light Elements (LEEL), NIMBE, CEA, CNRS, Université Paris-Saclay, CEA-SACLAY, Gif sur Yvette, France

Christine Rehm Bragg Institute, Australian Nuclear Science and Technology Organisation, Lucas Heights, NSW, Australia

Daniel L. Roach Centre for Materials Physics, School of Computing, Science and Engineering, University of Salford, Manchester, UK

Detlef Rogalla RUBION, Central Unit for Ion Beams and Radioisotopes, Ruhr-University Bochum, Bochum, Germany

D. Keith Ross Centre for Materials Physics, School of Computing, Science and Engineering, University of Salford, Manchester, UK

Kouji Sakaki National Institute of Advanced Industrial Science and Technology, Research Institute of Energy Frontier, Hydrogen Industrial Use and Storage Group, Tsukuba, Ibaraki, Japan

Sabrina Sartori Department of Physics, University of Oslo, Oslo, Norway
Centre for Materials Science and Nanotechnology, University of Oslo, Oslo, Norway

Burkhard Schillinger Heinz Maier-Leibnitz Zentrum (FRM II) and Department of Physics E21, Technische Universität München, Garching, Germany

Marina G. Shelyapina Department of Nuclear Physics Research Methods, Faculty of Physics, St. Petersburg State University, Saint Petersburg, Russia

Alexander V. Skripov Institute of Metal Physics, Ural Branch of the Russian Academy of Sciences, Ekatarinburg, Russia

Magnus H. Sørby Institute for Energy Technology, Kjeller, Norway

Zin Tun Canadian Neutron Beam Centre, Canadian Nuclear Laboratories, Chalk River, ON, Canada

Max Wolff Department of Physics and Astronomy, Uppsala University, Uppsala, Sweden

Chapter 1
Introduction

Jacques Huot, Daniel Banks, and Helmut Fritzsche

The interaction of hydrogen with materials is a wide field of research. The simplicity of the hydrogen atom allows us to gain fundamental insights into crystal structures, phase transitions, diffusion, absorption, adsorption, and magnetism in hydrogen-containing metals. These insights could then be used to develop a variety of practical systems for the advancement of our society. One key example is the development of a sustainable and environmentally friendly energy production and distribution systems. Hydrogen is a well-known energy carrier and could be a solution for some of our energy and environmental issues. Hydrogen can be generated from various primary energy sources, especially renewables such as thermal solar, photovoltaic, wind, and hydroelectricity. Hydrogen is the only fuel that can be converted to and from electricity easily, thus making it a potential partner with electricity in the global energy distribution system. As most renewable energy sources are intermittent, using hydrogen to store energy is an elegant and ecological solution. Therefore, hydrogen is expected to be used widely, along with electricity, as a major energy carrier by mid-twenty-first century.

The main drawback of using hydrogen as an energy carrier is its poor volumetric energy density at room temperature and one bar pressure, which is only 1/3000 that

J. Huot (✉)
Hydrogen Research Institute, Université du Québec à Trois-Rivières,
Trois-Rivières, QC, Canada, G9A 5H7
e-mail: Jacques.Huot@uqtr.ca

D. Banks
Canadian Neutron Beam Centre, Canadian Nuclear Laboratories,
Chalk River, ON, Canada, K0J 1J0
e-mail: Daniel.Banks@cnl.ca

H. Fritzsche
Canadian Nuclear Laboratories, Chalk River, ON, Canada
e-mail: Helmut.Fritzsche@cnl.ca

H. Fritzsche et al. (eds.), *Neutron Scattering and Other Nuclear Techniques for Hydrogen in Materials*, Neutron Scattering Applications and Techniques,
DOI 10.1007/978-3-319-22792-4_1

of gasoline. Thus, we need to develop technologies to store and transport hydrogen compactly, effectively and safely if we want to realize the hydrogen economy. Hydrogen can be stored as a gas in high pressure vessels or as a liquid in low temperature tanks but high pressure is hazardous and maintaining cryogenic temperatures consumes energy and is costly. An elegant alternative to gaseous and liquid storage is to use metal hydrides. In a metal hydride, hydrogen is chemically bound to the metal atoms. This enables storing hydrogen more densely than liquid hydrogen under moderate pressure and temperature. The concept of hydrogen storage materials was demonstrated in the late 1960s and R&D started in the 1970s. In addition to hydrogen storage, these metal hydrides are also used for electrodes of Ni-hydrogen batteries which are used in hybrid vehicles. Despite the intensive research on new hydrogen storage materials, further material development is needed in order to obtain a hydrogen storage system that will meet all technical and cost criteria for practical applications.

Nuclear techniques are broadly used to characterize hydrogen-metal systems. This book presents a comprehensive review of various nuclear techniques. Experts in each nuclear technique describe the fundamental aspects of the technique and provide instructive examples in the field of hydrogen-metal interactions.

Chapter 2 is a concise introduction to the neutron and its properties. The goal of this chapter is to provide the beginner with the essential background to comprehend the other neutron related chapters of this book. The basic features of neutrons and how they can be produced and detected are described, followed by a discussion of the interaction of neutrons with matter. The concepts of scattering lengths and cross sections are explained as well as the differences between coherent and incoherent scattering. The chapter ends with a short overview of elastic, inelastic and quasi-elastic neutron scattering.

Neutron powder diffraction is a widely used technique for the fundamental understanding of alloys, particularly those comprising hydrogen. Like X-ray diffraction, neutron diffraction is based on Bragg's law. Both techniques have their own advantages, however, the advantages of using neutrons over X-rays are numerous: neutrons are more penetrating than X-rays thus making it possible to probe the bulk of a material instead of only its surface; the scattering length of neutrons drastically changes from one element to the next one in the periodic table which makes elemental identification easier than when X-rays are used. Moreover, by neutron diffraction one can locate hydrogen atoms (in most cases deuterium is used) in the crystal structure, something that is practically impossible with X-ray diffraction. In Chap. 3, the basic principles of neutron diffraction will be described along with a short introduction to the extensively used Rietveld refinement method. The differences and similarities of the two main sources of neutrons— spallation and nuclear fission—are also discussed. Selected examples on the application of neutron diffraction for the development of metal hydrides are presented.

Total neutron scattering takes advantage of the whole diffraction pattern and not only the Bragg peaks as in conventional analysis, but also takes advantage of the diffuse scattering that originates from local deviations from the perfect crystal structure. In Chap. 4, we will see how total neutron scattering can be used to

determine the shortest distances between the deuterium atoms in a hydride phase. This technique is especially useful for amorphous materials where careful measurement of the diffuse scattering is the only way to extract structural information about the relationship between the metal and hydrogen atoms.

Neutron Reflectometry (NR) is a technique to study structural properties of thin films such as layer thickness, density, and roughness. The advantages of using neutron instead of X-ray reflectometry are numerous: neutrons are more sensitive to light elements, isotope substitution can be easily employed; the high penetration of neutrons enables in-situ hydrogen loading experiments and minimizes beam damage of the sample. As shown in Chap. 5, NR is able to detect hydrogen concentrations of the order of a few atomic percent in layers of nanometer thickness. Therefore, NR can determine an accurate hydrogen concentration profile normal to the surface of a film. It is now well known that structures in the nanometer ranges have different and usually better hydrogen storage properties than their bulk counterparts. Reflectometry allows studying the fundamentals of absorption and desorption in great detail because nanoscale layers can be prepared with well-defined composition and thickness. This enables a distinguishing between, for example, the catalytic surface effect of a cap layer on top of a metal hydride and the catalytic bulk effect of alloying the metal with other elements. Chapter 5 will show examples of this type of investigation for binary and ternary Mg-based alloys.

Small Angle Neutron Scattering (SANS) is an experimental technique that measures elastic neutron scattering at small scattering angles to investigate the structure of various substances at a mesoscopic scale of about 1–100 nm. At this length scale, the hydrogenation thermodynamics and kinetics of metal hydrides can be favourably modified. This field of research has been intensively investigated in recent years. Nanostructures can be produced by a variety of methods such as ball milling, severe plastic deformations, and chemical methods. An especially interesting scheme is nano-confinement of hydrides in porous scaffolds. In principle, this type of material can maintain the benefit of the nanoscale after multiple absorption and desorption steps and thus better conserve their nanoscale based functionality. However, investigating the structure of these materials is difficult using conventional methods. Chapter 6 gives the basic principles of small angle neutron scattering and shows its applications to nano-confined materials for hydrogen storage.

Because of the high penetration of neutrons in materials, they are an ideal probe for imaging objects in order to visualize their internal structures. In the present case, as hydrogen is a strong scatterer of neutrons, this technique is applied to localise hydrogen in a material. By using high resolution CCD cameras, quantitative analysis of neutron radiographs with a spatial resolution of about 20 μm and a hydrogen concentration detection limit of a few parts per million is possible. The combination of short illumination times, down to seconds, and the non-destructive character of neutron imaging enables in-situ investigations of hydrogen absorption, release and redistribution. Chapter 7 explores neutron imaging to study hydrogen permeation in steels and in zirconium alloys. Neutron imaging is also intensively used to probe hydrogen in hydrogen storage materials.

For many neutron scattering techniques, the directionless incoherent scattering of neutrons may be seen as a disadvantage. However, the strong incoherent scattering of hydrogen can be used to accurately determine the presence of small amounts of hydrogen in a material. Chapter 8 gives an introduction to coherent and incoherent neutron scattering and then presents two examples of characterizing small amounts of hydrogen by incoherent neutron scattering. One example is the measurement of hydrogen concentration in nuclear fuels; the other one is the observation of bulk diffusion of hydrogen into a zirconium alloy. This technique is used to study a wide range of phenomena from hydrogen in metal hydrides to hydrogen diffusion.

Other techniques in addition to incoherent scattering that use the large incoherent scattering cross-section of hydrogen are inelastic and quasi-elastic neutron scattering. As the name implies, in quasielastic and inelastic neutron scattering the collision between neutrons and the sample is inelastic, in contrast to neutron diffraction, for example, where the collision is elastic. By knowing the wave vector of the incident and scattered neutron, one can deduce the scattering vector, which will give information about the molecular structure and dynamic of the sample. Inelastic scattering is a form of spectroscopy. Well-known neutron spectrometers are the triple-axis and time of flight instruments. In Chap. 9, the theory of inelastic scattering is described and a few examples related to hydrogen storage are given.

The subject of Chap. 10 is Elastic Recoil Detection Analysis (ERDA). This non-destructive technique provides a depth profiling of light elements in thin layers and in multilayer systems. In ERDA, a high energy (≈ 1 MeV/amu) heavy-ion beam is projected onto a target that has a smaller atomic number than the ion-beam. Analysis of the recoil spectrum enables determination of the depth profile of the sample. ERDA is a good technique to study hydrogen profiling. Typically, its depth resolution is on the order of a few nanometers with a detection limit of a few tenths of a percent. In Chap. 10, after a description of ERDA and its instrumentation, examples of hydrogen detection in four different systems will be given: metals, ceramics, minerals, and thin films.

Nuclear reaction analysis (NRA) is used to obtain the concentration as a function of depth for certain target elements. Basically, a target nucleus is irradiated by a selected projectile nucleus. If the projectile has a certain energy, the target nucleus can undergo a nuclear reaction, during which it will emit characteristic radiation. For example, to obtain the profile of hydrogen distribution the projectile nucleus used is ^{15}N, which has a resonance at 6.4 MeV when colliding with hydrogen. At higher incident energies, ^{15}N projectiles reach the resonance energy in a certain depth due to energy loss in the sample material. Therefore, one can probe the hydrogen profile in a sample by varying the incident energy of the projectile using the energy loss per distance traveled, that is, the stopping power. With this method, absolute concentration of hydrogen and depth profiles in the range up to 2–3 μm with depth resolutions of a few nanometer can be measured. Chapter 11 gives a thorough description of this method illustrated by measurements of hydrogen in hydrogen storage materials, amorphous silicates and hydrogen on crystal surfaces.

Nuclear Magnetic resonance (NMR) is a technique that exploits the magnetic properties of certain atomic nuclei. Hydrogen is the most commonly spin 1/2

nucleus used in NMR investigation. Chapter 12 will show that one can obtain a range of microscopic information from NMR—such as small changes in the environment of hydrogen in a lattice and the hydrogen dynamics. Moreover, using a spin-echo technique the diffusion coefficient can be measured directly.

Positron annihilation spectroscopy (PAS) is a non-destructive technique used to investigate voids and lattice defects associated with open volumes. As the formation of lattice defects is frequently associated with hydrogenation, this technique helps to understand the hydrogenation mechanism in alloys. In Chap. 13, the principles of PAS are explained and some examples on hydrogen storage materials are given.

We hope this book will help experienced as well as new researchers in the field of hydrogen-metal interactions to gain a general knowledge of nuclear techniques and will encourage them to use these techniques to get a better understanding of their materials.

Chapter 2
Neutron Scattering: Introduction

Bjørn C. Hauback and Henrik Mauroy

Abstract Neutron scattering is an important method for characterization of materials. The chapter starts with a presentation of the properties of neutrons and how they are produced. The interaction with matter is the main part of this chapter. The notion of scattering length and cross section are explained as well as the differences between coherent and incoherent scattering. The chapter ends with a short overview of elastic, inelastic and quasi-elastic neutron scattering. The goal of this chapter is to provide to a beginner the essential background for the comprehension of the other neutron related chapters of this book.

Keywords de Broglie relation • Wavelength • Nuclear reactor • Diffraction • Scattering • Isotopes • Hydrogen • Protium • Deuterium • Isotope labelling • Crystalline materials • Cross section • Detector • Spallation source • Charge • Spin • Magnetic dipole moment • Half-life • Wave vector • Thermal neutrons • Nuclear reaction • Fission • Fuel • Moderator • Energy spectrum • Maxwell–Boltzmann distribution • Monochromatic • Monochromator • Scattering angle • Neutron imaging • Proportional counter • Helium-3 • Boron-10 • BF3 • Neutron scintillator • Boron-lined converter • B4C • Scattering length • Scattering center • Nucleus • Nuclear spin • Scattering length density • Scattering cross section • Absorption cross section • Coherent scattering • Incoherent scattering • Phonon • Magnon • Differential cross section • Total scattering cross section • Scattering vector • Q • Pair distribution function • Spin-incoherent • Barn • Magnetic scattering • Elastic scattering • Bragg scattering • Bragg diffraction • Inelastic neutron scattering • Quasielastic neutron scattering • Diffusion

2.1 Introduction

In order to determine where atoms are and what they do in materials we need a probe with a size of the same order of magnitude as the typical distance between atoms, i.e. around 10^{-10} m or 0.1 nm. Historically, the Ångström has been used as a

B.C. Hauback (✉) • H. Mauroy
Institute for Energy Technology, P.O. Box 40, NO-2027 Kjeller, Norway
e-mail: Bjorn.hauback@ife.no; hmauroy@gmail.com

H. Fritzsche et al. (eds.), *Neutron Scattering and Other Nuclear Techniques for Hydrogen in Materials*, Neutron Scattering Applications and Techniques,
DOI 10.1007/978-3-319-22792-4_2

unit with 1 Å = 0.1 nm. The German physicist Wilhelm Röntgen discovered X-rays in 1895 and in the beginning of the twentieth century X-ray diffraction developed rapidly based on X-rays with wavelengths in the range between 0.1 and 0.2 nm. X-ray diffraction turned out to be a great success and was accompanied by electron diffraction in the early 1930s. Electron diffraction utilizes the fact that electrons behave like waves, and can therefore interfere with each other and produce a diffraction pattern. The wavelength of the electron was determined by Louis de Broglie, already in 1924:

$$\lambda = \frac{h}{p} \tag{2.1}$$

where λ is the wavelength, h the Planck constant, and p the momentum carried by the electron. Today this equation is referred to as the de Broglie relation. It is very powerful because it applies to all non-relativistic particles with a mass similar to the mass of atoms. A quite fortunate coincidence is that the mass of the neutron is just right to give it a de Broglie wavelength similar to X-rays used for most scattering studies, i.e. 0.1–0.2 nm. Neutrons were first discovered by James Chadwick in 1932. The first nuclear reactor went critical at Oak Ridge National Laboratory in the USA in late 1943, and the first neutron diffraction experiments were carried out already in 1944. Within a few years it was clear that neutron scattering would be an important tool for characterization of materials, including diffraction, spectroscopy, and imaging. Based on the pioneering work in those days, Clifford Shull and Bertram N. Brockhouse received the Nobel Prize in Physics in 1994. Each of the three scattering techniques, based on neutrons, X-rays, and electrons, respectively, has evolved into an array of different techniques, each specially designed to study particular aspects of crystal structures and dynamics of materials.

X-ray and electron scattering share the same severe shortcoming: they are not very effective to determine atomic positions of light elements, such as hydrogen, carbon, and oxygen in compounds with both light and heavier elements. Furthermore, these probes cannot distinguish between neighboring elements in the periodic table because of almost equal scattering power. Using neutrons the scattering from light and heavier elements are typically comparable (see Fig. 2.1), and thus neutron scattering can give detailed information about both at the same time. Furthermore, neighboring elements in the periodic table can have rather different interactions with neutrons, and in such cases neutron scattering is a unique method. The different scattering by isotopes can also be significant, for example, by hydrogen (protium) and deuterium, and thus isotope labelling can give specific information on the compounds.

The key to understanding neutron scattering is the way neutrons interact with matter. In contrast to X-rays and electrons, which interact with the electrons around a nucleus, the neutron interacts with the nucleus itself. Since the neutrons are neutral they are only deflected when they hit a nucleus. Neutrons are therefore scattered equally well by light elements as the heavier ones. Thus the position of

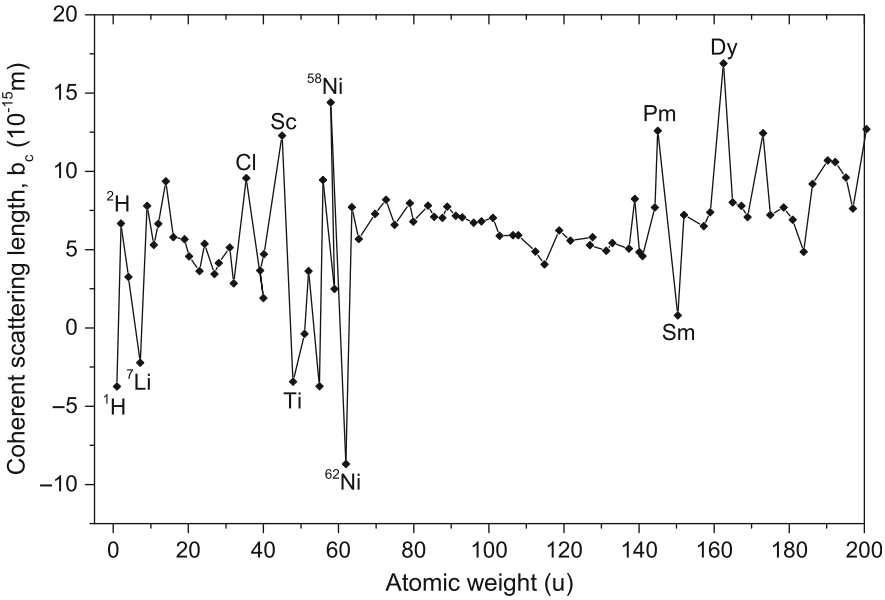

Fig. 2.1 Coherent scattering lengths as a function of atomic weights [3, 4]

hydrogen atoms in crystalline materials can only be accurately determined with neutron scattering.

This brings us over to the second advantage of neutrons: As mentioned earlier neutron scattering has in several cases the ability to distinguish between scattering from neighboring elements in the periodic table. The reason for this is that neutrons are scattered by nuclei, and different types of nuclei have different scattering power. Sometimes they are very different, such as for scandium and titanium (see Fig. 2.1). This effect also applies to isotopes of the same element. ^{1}H (protium) and ^{2}H (deuterium) for example, or ^{58}Ni and ^{62}Ni differ greatly in scattering power (Fig. 2.1).

The fact that neutrons are uncharged means that they can penetrate deeply into matter, in several cases many centimeters and up to meters, before being deflected or absorbed. X-rays from laboratory source setups are nearly not affected by hydrogen atoms, but only a few micrometers of lead is enough to stop them completely, although high-energy X-rays used at synchrotron facilities penetrate more deeply into matter. Neutrons with wavelengths in the range of 0.1–0.2 nm can on the other hand travel through more than 2 m of lead and almost 1 m of aluminium before the intensity is reduced to 50 %. This makes it possible to study samples being kept inside more complicated sample environments than what can easily be used with X-rays. It is therefore possible to measure the bulk properties, for example, in car engines or pipelines. The absence of charge also means that neutrons do not ionize the sample, like X-ray or electron beams, and thus opens up the possibility for studies of fragile specimens such as organic crystals or

invaluable archeological artifacts. It should be added that some elements and isotopes, for example, boron, gadolinium, and cadmium, absorb neutrons strongly, but isotope labelling can reduce the absorption enormously. For example ^{10}B (which accounts for 20 % of natural boron) is a strong neutron absorber while ^{11}B has a very weak absorption, and natural boron is therefore difficult to use in neutron scattering experiments.

The neutron is uncharged because it is composed of one up quark, with a charge of 2/3e, and two down quarks, each with charge −1/3e. Even though the total charge is zero this arrangement leads to a tiny charge distribution that gives rise to a magnetic moment, which in turn makes neutrons interact with the unpaired electrons in magnetic atoms. The possibility to determine magnetic structures on an atomic scale is a unique property of neutron scattering and yet another powerful advantage compared to X-rays.

A final advantage is the similar magnitude of atomic excitations and the kinetic energy of thermal neutrons. By measuring the change in kinetic energy of a neutron when it is scattered inelastically by an atom, information about energy transitions and interatomic forces can be extracted.

It might sound like neutron scattering would render other techniques obsolete, but due to several disadvantages this is not the case. Firstly, the relative ease of penetrating into matter (when there are no neutron-absorbing elements) is a two-edged sword. Not only does it mean that neutrons are weakly scattered, but it makes detection of them tricky. Secondly, the flux of neutrons emanating from a nuclear reactor is low compared to X-ray sources. The ILL (Institut Laue-Langevin) high flux reactor in Grenoble, France, is the most powerful research reactor in the world and has a neutron flux, ϕ, near its core of around $10^{15}\,n\,\mathrm{cm}^{-2}\,\mathrm{s}^{-1}$. For thermal neutrons with velocity $v = 2200$ m/s, this corresponds to a neutron density of $N = \phi/v = 4.5\times10^{15}\,n\,\mathrm{m}^{-3}$. Assuming the same density of gas molecules in air it would produce a pressure of 10^{-7} mbar, which is a quite decent vacuum. To put the 58 MW ILL reactor's flux further into perspective, to obtain a similar flux with photons we would then only need a 1 W light bulb.

Based on the low neutron flux compared to photons, it is paramount that neutrons should be used as efficiently as possible. One obvious way of increasing the neutron flux is to use a neutron beam with a large cross section, and 50–100 cm^2 can easily be achieved. At the same time, however, the sample has to be large in order to make use of all the incoming neutrons. In many cases it is impossible to synthesize huge samples. Therefore, in the last two decades, many different concepts have been developed to increase the neutron flux on the sample, e.g., focusing monochromators and focusing neutron guides, or making better use of the incoming and/or scattered neutrons, e.g., by using a wide wavelength band and using large 2-dimensional detectors. There are about 40 neutron research centers worldwide [1], most of which use a reactor as the neutron source. As the flux is a significant limitation for reactors new powerful spallation sources have recently been constructed in the USA (Spallation Neutron Source, SNS, Oak Ridge National Laboratory) and Japan (J-PARC). Furthermore, a new target station was added to the ISIS facility in the UK. The most ambitious project, the European Spallation

Table 2.1 Basic properties of the neutron and some useful conversions

Mass	$m = 1.67492735 \times 10^{-27}$ kg
Charge	$q_n = 0$
Spin	$s = ½$
Magnetic dipole moment	$\mu_n = -9.6624 \times 10^{-27}$ J · T^{-1}
Mean life time	$\tau = 888 \pm 2$ s
Half-life	$T_{1/2} = 615 \pm 2$ s
Planck constant	$h = 6.62606957 \times 10^{-34}$ J · s
Wave vector (nm^{-1})	$k = 2\pi/\lambda = 2\pi mv/h$
Kinetic energy (meV)	$E = mv^2/2 = k_B T = (hk/2\pi)^2/2\,m$
Thermal neutron velocity (m/s)	$v = \sqrt{(3k_B T/m)}$
Wavelength (nm)	$\lambda = 6.283/k = 395.6/v = 9.045/\sqrt{E} = 3.081/\sqrt{T}$

Source (ESS), is supposed to deliver a neutron beam with a brightness that is 30 times higher than at existing facilities [2]. In many cases, as will be evident in the following chapters, neutrons are complementary to X-rays, and both techniques are needed to solve many problems. Table 2.1 lists some basic properties of the neutron together with some useful conversions.

2.2 Production and Detection of Neutrons

2.2.1 Production of Neutrons

Neutrons can be generated by different nuclear reactions. However for scattering experiments the neutrons have to be produced with such a high rate (~10^{16}–10^{18} neutrons per second), and thus the only possibility is either with nuclear reactors or spallation of heavy elements using high-energy particles. Research reactors usually use uranium as the fuel and produce on average around one extra neutron per fission reaction. Spallation sources operate completely differently. Here protons are accelerated to very high energies (in the range of GeV) and directed at a heavy-metal target, such as tungsten, tantalum, or liquid mercury. The collisions generate around 20–30 neutrons per incoming proton. The produced neutrons are directed to the different instruments with neutron guides.

A common feature to reactors and spallation sources is the production of neutrons with energies in the range of several or even hundreds of MeV. These energies are far too high for use in scattering experiments. Typically the energy needs to be lowered a billion times, to a few tens of meV, in order to get a desired wavelength around the atomic spacing in materials of around 0.1 nm. Neutrons having these low energies are called *thermal neutrons*. Fortunately, lowering the neutron energy is fairly easy to accomplish by passing the neutrons through a *moderating* medium. The neutrons lose their high energy due to the interaction

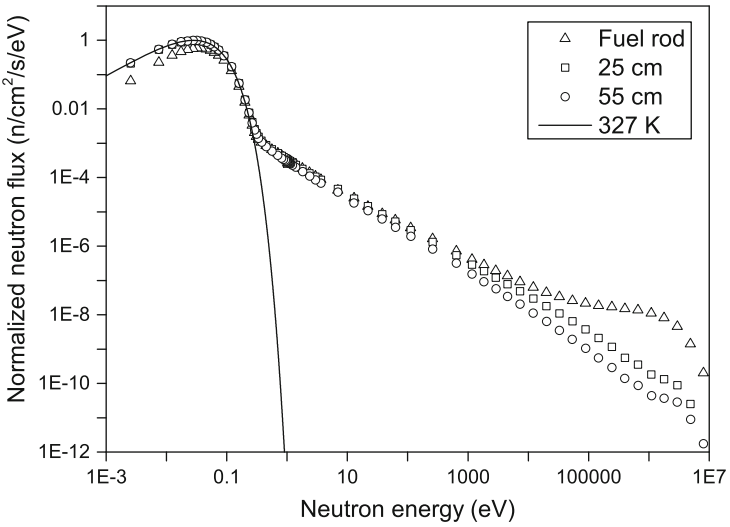

Fig. 2.2 Simulated flux of neutrons (*symbols*) as a function of energy around a uranium oxide fuel rod immersed in heavy water. The flux is calculated for a position close to a fuel rod and at 25 and 55 cm away from the rod, respectively. A Maxwell–Boltzmann distribution at 327 K is superimposed over the data as a *solid line*

with the nuclei of the moderator material and finally reach thermal equilibrium with the moderator. Normal ("light") and heavy water are excellent moderators, and at room temperature will slow neutrons down to around 2200 m/s corresponding to a wavelength of 0.18 nm.

It is important to note that the neutrons emerging from the moderator have a spread in energy, which can be described fairly well with the Maxwell–Boltzmann distribution. The peak of the spectrum is at an energy equal to k_BT, where k_B is the Boltzmann constant and T the absolute temperature. A simulation of the neutron flux around a single uranium oxide fuel rod immersed in heavy water at different distances from the fuel rod at 327 K is shown in Fig. 2.2.

The Maxwell–Boltzmann distribution superimposed as a solid line on the data can only be used to model the flux at low energies because the function does not contain terms that can model the tail observed in the simulated data. The disappearance of the hump at MeV-energies at the end of the tail, when moving from the surface of the fuel rod to 25 cm away, illustrates well how the spectrum is shifted to lower energies when the neutrons are being moderated along their path outwards from the fuel rod. This leads to an increase in the flux of thermal neutrons along the same path since more and more fast neutrons are being moderated, which is illustrated in Fig. 2.3. The shift of the spectrum towards lower energies can also be seen in this figure.

The spectrum can be shifted further to longer or shorter wavelengths by using either a cold or a hot moderator, respectively. A typical cold moderator consists of a container filled with liquid H_2 or D_2 at about 20 K, while a hot moderator is usually a graphite block kept at 2000 K. Table 2.2 lists some typical values for the energy and wavelength of moderated neutrons.

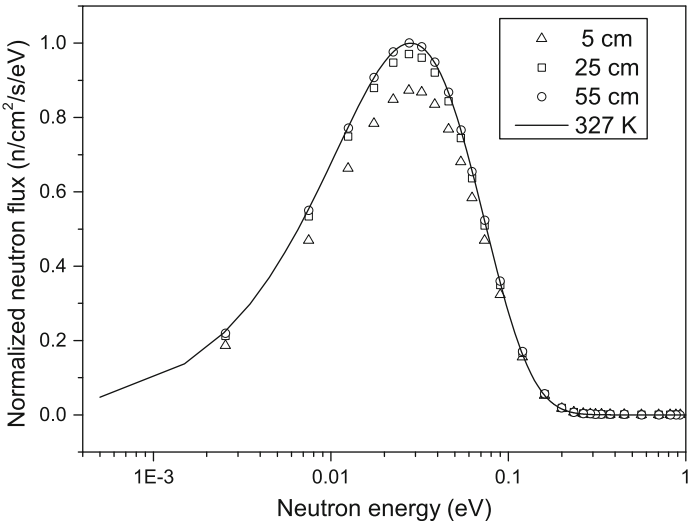

Fig. 2.3 A zoomed in view of Fig. 2.2 showing the neutron flux at thermal energies increases with the distance from the fuel rod. Additional points from a calculation at 5 cm separation from the fuel rod are shown as *triangles*. A Maxwell–Boltzmann distribution at 327 K is superimposed over the data as a *solid line*

Table 2.2 Typical values for neutrons passing through different moderators

Moderator	Energy (meV)	Temperature (K)	Wavelength (nm)
Cold	1–10	20–120	0.3–0.7
Thermal	10–100	120–1000	0.1–0.3
Hot	100–500	1000–6000	0.04–0.1

At reactor sources the neutrons emerge from the moderator as a continuous stream with different energies. This spread in energy is not suited in many scattering experiments where a monochromatic beam of neutrons, i.e. neutrons with a narrow energy band, is required. Such a condition is obtained by placing a single crystal, or several pieces of single crystal material of a highly reflective material, such as pyrolytic graphite, germanium, copper, or silicon, between the neutron source and the sample. This is the so-called monochromator, and it will only transmit neutrons with wavelengths satisfying the Bragg law (see Sect. 2.5.1) in the direction of the sample. The wavelength is determined both by the scattering angle (monochromator take-off angle) and the corresponding set of scattering planes. A velocity selector with a set of choppers can also be used to create a monochromatic beam. Only neutrons with a certain velocity can pass both the first and last chopper blade placed along the direction of the beam. Unfortunately a severe downside to monochromating the beam is that a majority of the neutrons (up to 99 %) are wasted.

The energy spectrum from the source is handled differently at spallation sources. The neutrons are produced in pulses several times per second, thus there is no continuous beam, and a monochromator is not used. Instead, a technique called

Time Of Flight (TOF) is employed. Here neutrons in a wide energy range are utilized by measuring the time it takes for each neutron in the polychromatic beam to travel from the moderator, via the sample, to the detector. As the distance from source to detector is well known, it is possible to determine the neutron velocity, and thus the neutron's energy and wavelength. The fastest neutrons with the shortest wavelength arrive first, while the slowest neutrons are hitting the detector just before the fast neutrons of the next pulse arrive. Instead of measuring a diffraction pattern as a function of scattering angle (as for monochromatic neutrons), the TOF-instrument measures it as a function of time (or wavelength) with a fixed scattering angle. TOF-instruments are not limited to spallation sources. They are frequently being used at reactor sources as well.

A brief introduction to the theory of neutron scattering will be covered later in this chapter, while diffraction techniques in general are covered in Chap. 3.

2.2.2 Detection of Neutrons

Common to all neutron scattering and imaging instruments is the need to detect the neutrons. This is not a trivial task, because the neutron is a particle with low kinetic energy and no charge, and the interaction with matter occurs through very weak nuclear and magnetic forces. The only practical method of detecting a neutron is therefore to produce charged particles in a nuclear reaction involving the neutron and to detect the charged particles instead.

One of the main detection principles is the proportional counter. This is a gas filled tube with a wire, kept at a high positive voltage, placed in the center of the tube. The two traditional gases used to react with neutrons are either ^{3}He or ^{10}B-enriched BF_3 gas, while a mix of several other filler gases such as CH_4, Ar, and CO_2 serve as the ionization medium. The nuclear reactions following absorption of a neutron are:

$$\mathrm{n} + {}^{3}\mathrm{He} \rightarrow {}^{3}\mathrm{H} + \mathrm{p} + 765\ \mathrm{keV} \tag{2.2}$$

for the ^{3}He-capture and

$$\mathrm{n} + {}^{10}\mathrm{B} \rightarrow {}^{4}\mathrm{He}^{+} + {}^{7}\mathrm{Li} + 2310\ \mathrm{keV} \tag{2.3}$$

for the ^{10}B-capture.

Both reactions create charged and highly energetic particles that ionize the gas. This results in a cascade of electrons giving an electric pulse which is detected by the positive wire. The neutron detectors are operated in an energy range where the electric pulse is proportional to the energy of the ionizing particles, meaning that these kinds of detectors allow an efficient discrimination of the smaller pulses obtained from γ-rays, which are almost always present in the background. By using fast electronics it is possible to determine the position of the discharge

along the wire either with the so-called charge or time division methods. These kinds of detectors are so-called position sensitive detectors (PSD) and have a typical spatial resolution of about 1.5 mm. The extreme toxicity of BF_3 makes it challenging to use, and the availability of ^{3}He has significantly been reduced since around 2010, followed by an enormous increase in the price. Thus it has become urgent to develop new efficient neutron detector technologies.

The neutron scintillator is one of the possible replacements for the ^{3}He-detector and has successfully been put in use at several instruments at ISIS and J-PARC. In a scintillator the neutrons are absorbed by ^{6}Li embedded in a conversion material, either a plastic or a glass plate, leading to the following nuclear reaction:

$$\mathrm{n} + {}^6\mathrm{Li} \rightarrow {}^4\mathrm{He} + {}^3\mathrm{H} + 4790\ \mathrm{keV}. \tag{2.4}$$

The charged reaction products have high energy, and excite ZnS that is embedded together with ^{6}Li inside the conversion material. ZnS returns to its ground state with the emission of 470 nm light, which is guided via fiber optics to a photomultiplier where it is transformed into an electric signal. Each absorbed neutron produces around 160,000 photons, making the event easy to detect with modern electronics. Discrimination against γ-rays, which also excite ZnS, is done electronically by analyzing the shape of the electric pulse. Numerous designs of neutron scintillators have been developed. These comprise 2D PSD, semiconductor detectors with ^{6}Li-containing thin films, and ^{6}Li-containing single crystals with the typical compositions Cs_2LiYCl_6 or $LiCaAlF_6$. Neutron imaging, analogous to X-ray imaging, detects neutrons using a two-dimensional CCD-sensor with a ^{6}Li-ZnS scintillator screen mounted on the surface. A light-spot with a diameter of around 50–80 μm appears on the scintillator screen where the neutrons hit. The light from this spot is subsequently detected by the CCD-sensor and fed through a computer. This allows for high resolution imaging of, for example, water transport in the channels of an operating fuel cell, or hydrogen content in the walls of pipelines.

The main drawbacks of the neutron scintillator are limited detection efficiency due to the opaqueness of its own light which limits the thickness of the conversion material, and the limited neutron counting rate as a result of the relatively long afterglow after a neutron capture.

The most recent approach to a replacement technology is the boron-lined converter, which on the other hand displays a high neutron counting rate. The principle is similar to the BF_3-counter, but instead of having ^{10}B supplied in gaseous form, it is provided by a solid micrometer-sized film (e.g., B_4C) covering the inside of the walls of the gas filled cylinder. When a neutron hits the film, and is captured by ^{10}B, the charged reaction products from Eq. 2.3 ionize the filler gas creating the electric pulse. The drawbacks of this design are increased cost and complexity, and lower detection efficiency than with ^{3}He-detectors. However, still the boron-lined converter is proposed to be implemented in the first large-area detectors at the coming spallation source ESS when it comes online in 2022–2023.

2.3 Interaction of Neutrons with Matter

2.3.1 Introduction

From the perspective of a neutron solid matter is quite spacious. This is because the size of the scattering center, the nucleus, is around 100,000 times smaller than the distance between these centers. The interaction with matter is produced by short-range nuclear forces (~10^{-15} m). As a consequence, the non-charged neutron can travel far inside solid matter before being scattered or absorbed by a nucleus. Neutrons interact with matter mainly in three ways: elastic scattering, inelastic scattering, and in absorption processes. The first two are interactions between the neutron and either a nucleus or the magnetic field produced by unpaired electrons. The absorption processes, on the other hand, lead to emission of secondary charged or neutral particles, emission of electromagnetic radiation or fission. Here we will not go into details about absorption interactions, but will mainly focus on the scattering, which is the foundation of most of the neutron characterization techniques. We will describe the different concepts of neutron scattering, followed by a simplistic mathematical derivation of expressions describing neutron scattering. Finally a brief overview of some neutron scattering techniques, relevant to hydrogen containing materials, will be presented.

2.3.2 Scattering Length

Since the nucleus is much smaller than the wavelength of the neutron, the nucleus acts like a point scatterer, i.e. the scattered neutron wave is spread out as a spherical wave (Fig. 2.4). For an incident plane wave $e^{i\mathbf{k}\cdot\mathbf{x}}$, consisting of neutrons travelling

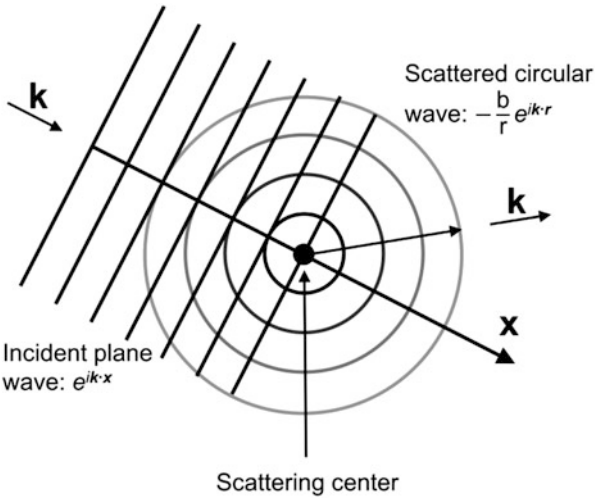

Fig. 2.4 2D representation of a neutron wave with wave function $e^{i\mathbf{k}\cdot\mathbf{x}}$ scattered as spherical wave, $(-b/r)e^{i\mathbf{k}\cdot\mathbf{r}}$, from a fixed nucleus

along **x** with an initial speed $v = |\mathbf{v}|$ and an incoming wave vector **k**, the scattered wave can be expressed as $(-b/r)e^{i\mathbf{k}\cdot\mathbf{r}}$, where the outgoing wave vector **k** is oriented parallel to **r.** **k** and **v** are related by:

$$\frac{h\mathbf{k}}{2\pi} = m\mathbf{v} \tag{2.5}$$

where m and $m\mathbf{v}$ are the mass and momentum of the neutron, respectively. The amplitude of the scattered wave is proportional to the so-called scattering length, b:

$$b = b_c + b_i \tag{2.6}$$

b is a measure of the strength of the neutron–nucleus interaction, measured in fm (10^{-15} m) and varies in an erratic manner throughout the periodic table (Fig. 2.1). It consists of two parts: the coherent scattering length, b_c, which is plotted in Fig. 2.1 as a function of atomic weight, and the incoherent scattering length, b_i, which is discussed later in this chapter. A large absolute value of b means that the neutron is scattered strongly by the nucleus (i.e., on average more of the incoming neutrons are scattered). The neutron scattering length is analogous to the atomic form factor used in X-ray and electron scattering. A positive b means a minus sign in the wave function implying a repulsive interaction between the neutron and the nucleus. Most elements and isotopes have a positive b, but some are negative. A negative b leads to the opposite sign of the scattering amplitude compared to a positive b, equivalent to a 180° phase difference for the outgoing scattered wave. The protium (^{1}H) isotope of hydrogen for example, has a negative scattering length while deuterium (^{2}H) has a positive one. Combinations of positive and negative b-values can also tune the average scattering length of a compound. This is utilized in contrast matching experiments where light and heavy water are mixed in a certain ratio resulting in an averaged scattering length equal to certain parts of a specimen immersed in water. For certain experiments (e.g., small angle neutron scattering or neutron reflectometry) that rely on a scattering length density (SLD) contrast these parts will scatter identically to the surrounding water and be masked away. Contrast matching is explained further in Chaps. 5 and 6.

As shown in Fig. 2.1 some isotopes and neighboring elements display significantly different scattering lengths. For example scandium exists only as one isotope with non-zero spin and has a large positive b_c of 12.1 fm, while titanium consists of several different isotopes with both positive and negative values of b_c, which results in a final combined b_c of −3.37 fm. In several cases the large variations in scattering length between neighboring elements give rise to a significant scattering contrast, while for X-rays and electrons the difference will be too small to be observable.

The strong variations in b arise from the strong dependence on the spin of the nucleus. Isotopes with an even number of both protons and nucleons have nuclear spin I equal to zero and therefore only one scattering length. However those with I different from zero have two different scattering lengths, b_+ or b_-, respectively

(not to be confused with positive and negative values of b), since the spin of the compound nucleus (neutron + nucleus) is either $J = I + ½$ or $J = I - ½$. ^{1}H, for example, has spin ½ and consequently it has two different scattering lengths: $b_+ = 10.81$ fm and $b_- = -47.42$ fm, respectively. ^{12}C, on the other hand, has spin zero and therefore only one scattering length of $b = 6.65$ fm.

The scattering lengths have to be determined experimentally because we do not have an adequate theory of nuclear forces to predict these values from the properties of the nucleus. In practice we are only able to measure one b-value, and thus the separate values of b_+ and b_- must be calculated based on this value. The scattering length of an element will be a mix of the scattering lengths of its different isotopes, just as the scattering length of an isotope is a mix based on the isotope's different nuclear spins.

The sum of scattering lengths in a certain volume of a sample is defined as the SLD, and it is usually denoted by ρ:

$$\rho = \frac{1}{\text{volume}} \sum_j b_j = N \cdot b \tag{2.7}$$

where b_j is the scattering length of atom j and N is the atomic number density ($1/m^3$).

2.3.3 Scattering and Absorption Cross Section

The scattering length gives information about the strength of the interaction between the neutron and the nucleus of the studied compound. The likelihood of such interactions is determined by the effective area of the nucleus as "seen" by a passing neutron. This is called the total cross section, σ_{tot}, and it is simply the sum of the scattering cross section, σ_s, and the absorption cross section, σ_a, for a given nucleus:

$$\sigma_{\text{tot}} = \sigma_s + \sigma_a \tag{2.8}$$

The physical cross section of a heavy nucleus is around 10^{-28} m^2, and the unit one barn is equal to a cross section of 10^{-28} m^2. Because of the direct relationship between the scattering cross section and the scattering length (Eqs. 2.10 and 2.11), the scattering cross section also varies erratically with atomic numbers.

The probability of absorption of a neutron by a nucleus is expressed as the absorption cross section, σ_a, also measured in barn. The speed, or rather the energy, of the incoming neutron is important for the determination of σ_a. The values for the scattering lengths, and the scattering and absorption cross sections, measured for neutrons moving freely at $T = 293$ K, having a kinetic energy of $E = k_B T = 25.3$ meV (corresponding to a speed of $v = 2200$ m/s or a wavelength of $\lambda = 0.1798$ nm), can be found at NIST's webpage [3] or in reference [4].

As a general rule σ_a *decreases* with *increasing* neutron velocity as $1/v$. In addition, the isotopic composition has a substantial influence. Natural boron for instance has $\sigma_a = 768$ barn, which is very large compared to most other elements. However, boron's two isotopes, ^{10}B and ^{11}B, have spectacularly different absorption cross sections of 3835 barn and a miniscule 0.0055 barn, respectively. Even though natural boron only consists of 20 % ^{10}B the final absorption cross section becomes huge. Gadolinium is another spectacular example. σ_a equals a very large 49,700 barn for naturally occurring Gd, composed of a lesser, yet still significant, 85.1 barn for ^{154}Gd, and an astoundingly large 259,000 barn for ^{157}Gd. By using ^{11}B-enrichment neutron scattering experiments on boron compounds are feasible. While neutron scattering on gadolinium compounds seems impossible, it is not as challenging as one might think. Ryan and Cranswick [5], for instance, describe a rather straightforward experimental setup used for neutron diffraction on Gd-containing samples. The reason for these apparently abnormal absorption cross sections for some isotopes is strong resonances between the neutron and the nucleus at certain neutron energies. At these energies other events may be more likely to occur, such as for instance the (n,γ)-reaction, where a neutron is absorbed by the nucleus and a gamma ray plus a secondary neutron is emitted.

2.3.4 Reflection and Refraction

Analogous to reflection of light, neutrons obey Snell's law, and at very small scattering angles they are reflected from surfaces or can be refracted at interfaces between two different media, such as between air and a thin film of some material, or between two different thin films. The critical angle of total reflection is proportional to the square root of the coherent SLD (see Chap. 5, Eq. 5.4). By performing neutron reflectometry experiments (see Chap. 5 for details), it is possible to determine the average SLD profile perpendicular to the surface and estimate the local composition. Layered structures lead to typical interference patterns in the reflectivity curve. By using this effect we can measure the thickness of layers, while the amount of diffuse reflection can give information about the roughness of the surface. Neutron reflectometry is limited to thin films and layers ($<$300 nm) or the regions very close to the surface of a sample. The differences in scattering lengths between neighboring elements of the periodic table and between isotopes, and strong scattering from light elements, such as hydrogen, are important advantages compared to the related X-ray reflectometry method. Chapter 5 presents neutron reflectometry in detail and in particular how it can be utilized to study hydrogen storage materials.

2.4 Coherent and Incoherent Scattering

2.4.1 Coherent and Incoherent Scattering Cross Sections

The coherent and incoherent contributions to the scattering length, b, were introduced earlier. In a similar manner the total scattering cross section, σ_s, is divided into a coherent part, σ_c, and an incoherent part, σ_i:

$$\sigma_s = \sigma_c + \sigma_i, \tag{2.9}$$

In a neutron scattering experiment we are measuring the combined intensity from all waves scattered by all atoms in the sample being exposed to the neutron beam. Consequently, the measured intensities will be determined by the interplay of the different waves with each other, leading to interference effects. Coherent scattering describes interference between waves produced by the scattering of a single neutron with waves coming from all nuclei in the sample. This type of scattering varies strongly with the scattering angle. Examples of coherent processes are so-called Bragg scattering and inelastic scattering by phonons or magnons. The coherent scattering cross section σ_c is given by the square of the average value of b:

$$\sigma_c = 4\pi\left(\sum_j f_j b_j\right)^2 = 4\pi\left(\overline{b}\right)^2 \tag{2.10}$$

where f_j is the relative percentage of a nucleus with a specific scattering length b_j inside the sample.

Incoherent scattering, on the other hand, can be considered as the remaining part of the total scattering when the coherent scattering has been subtracted. The incoherent scattering cross section σ_i is given by:

$$\sigma_i = 4\pi\left(\sum_j f_j b_j^2 - \left(\sum_j f_j b_j\right)^2\right) = 4\pi\left(\overline{b^2} - \left(\overline{b}\right)^2\right) \tag{2.11}$$

In the case of incoherent scattering waves from different nuclei do not interfere with each other, meaning that no structural information can be extracted from this type of scattering. Particle dynamics, however, such as diffusion, is possible to extract because the incoherent scattering gives information about correlations between the positions of the same nucleus at different times. Equation 2.11 is basically telling us that the cause of incoherent scattering is random deviations from the mean scattering length of an element. These variations are resulting from the random distribution of spins ($I \pm ½$) and/or isotopes throughout a sample.

Both the coherent and incoherent cross sections (Eqs. 2.10 and 2.11) depend on the scattering length b, which in turn is dependent on the spin state I of the nucleus.

With b equal for all nuclei in a sample, which is the case for nuclei with zero spin, the incoherent scattering cross section in Eq. 2.11 becomes zero and the scattering is purely coherent. Naturally occurring helium, carbon, and oxygen are very close to mono-isotopic. Because the most abundant isotope of each of these elements has zero spin, the scattering from these naturally occurring elements will therefore almost only scatter coherently.

2.4.2 The Double-Differential Scattering Cross Section

We measure the total scattered intensity, $I(\mathbf{Q},E)$, in a neutron scattering experiment. This is a function of both the scattering vector $\mathbf{Q}$ (Eq. 2.15) and the energy of the scattered neutrons, E. A detector measures $I(\mathbf{Q},E)$ by counting the number of neutrons scattered into an element of solid angle $d\Omega$ in the direction $2\theta,\varphi$ (see Fig. 2.5), having an energy between E and $E + \Delta E$, per the incoming particle flux, Φ. We refer from now on to $I(\mathbf{Q},E)$ as the *double-differential cross section*:

$$I(\mathbf{Q},E) = \frac{d^2\sigma}{d\Omega dE} = \frac{\text{Number of neutrons scattered per second into } d\Omega \text{ in the direction } 2\theta,\varphi, \text{with final energy between E and E} + \Delta\text{E}}{\Phi d\Omega dE} \tag{2.12}$$

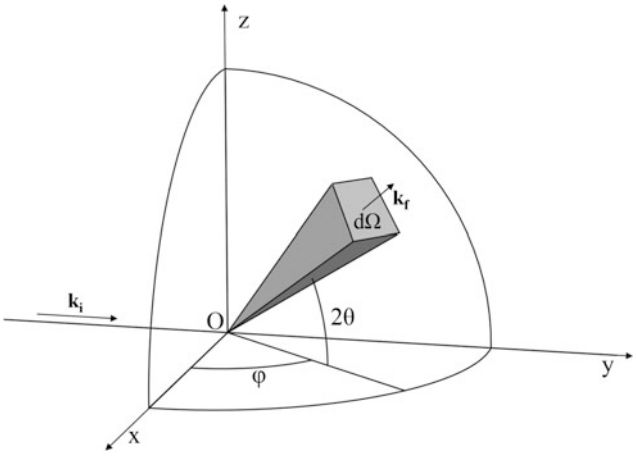

Fig. 2.5 Scattering geometry for a sample mounted at the point O

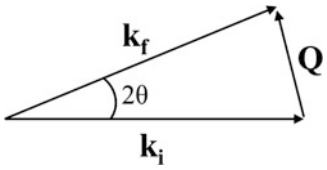

Fig. 2.6 Scattering triangle where $\mathbf{Q} = \mathbf{k_f} - \mathbf{k_i}$ is the difference between the wave vectors of the scattered and incoming neutrons and 2θ the scattering angle

In most cases the detectors measure the whole range of energies, thereby integrating over the energy. Then the measured quantity, called the *differential cross section* is:

$$\frac{d\sigma}{d\Omega} = \int_0^\infty \frac{d^2\sigma}{d\Omega dE} dE. \tag{2.13}$$

The total scattering cross section, σ_s, is defined as:

$$\sigma_s = \int_{\text{All directions}} \left(\frac{d\sigma}{d\Omega}\right) d\Omega. \tag{2.14}$$

The scattering vector $\mathbf{Q}$ is further defined by:

$$\mathbf{Q} = \mathbf{k_f} - \mathbf{k_i} \tag{2.15}$$

where $\mathbf{k_i}$ is the incoming wave vector and $\mathbf{k_f}$ is the scattered wave vector (see Fig. 2.5). When $|\mathbf{k_i}| = |\mathbf{k_f}|$, the scattering is said to be *elastic*. If we consider scattering at an angle 2θ, i.e. axial symmetry, it can be shown by applying a little trigonometry to the scattering triangle in Fig. 2.6 (and using Eqs. 2.1 and 2.5), that $Q = (4\pi/\lambda) \sin\theta$. θ is half the scattering angle and λ the wavelength of the incoming neutrons.

A general expression for the scattered intensity, $I(\mathbf{Q},E)$ in Eq. 2.12, was derived by Van Hove in 1954 [6] and is presented in Eq. 2.16. The actual derivation of this quantum mechanical equation is outside the scope of this book, but is explained in detail in several text books, for example, by Bacon [7], Squires [8], or in Los Alamos Science [9]. Van Hove showed that:

$$I(\mathbf{Q},E) = \frac{1}{2\pi\hbar}\frac{k_f}{k_i}\sum_{j,k} b_j b_k \int_{-\infty}^{\infty} \left\langle e^{i\mathbf{Q}\cdot\mathbf{r}_k(0)} e^{-i\mathbf{Q}\cdot\mathbf{r}_j(t)} \right\rangle e^{-i\omega t} dt \tag{2.16}$$

where the double sum is over *pairs* of atoms labelled j and k, with scattering lengths b_j and b_k, respectively, $\hbar = h/2\pi$ is the reduced Planck constant, and ω is defined by $\hbar\omega = E - E_0$ (i.e., the difference in energy between the initial and final quantum states of the scattering system). The nucleus k is at position $\mathbf{r_k}$ at time zero and the nucleus j is located at position $\mathbf{r_j}$ at time t. The angular brackets denote that we need to perform an average over all thermodynamic states.

Equation 2.16 may seem simple, but since the position vectors $\mathbf{r_j}$ and $\mathbf{r_k}$ are quantum mechanical operators, its evaluation is not straightforward. For instructive purposes we ignore it here and treat the system in a classical manner. Then the double sum on the right side in Eq. 2.16 can be written as:

$$\sum_{j,k} b_j b_k \left\langle e^{i\mathbf{Q}\cdot\mathbf{r}_k(0)} e^{-i\mathbf{Q}\cdot\mathbf{r}_j(t)} \right\rangle = \sum_{j,k} b_j b_k \left\langle e^{i\mathbf{Q}\cdot\left(\mathbf{r}_k(0)-\mathbf{r}_j(t)\right)} \right\rangle$$
$$= \sum_{j,k} b_j b_k \int_{-\infty}^{\infty} \left\langle \delta\left(\mathbf{r} - \left[\mathbf{r}_k(0) - \mathbf{r}_j(t)\right]\right) \right\rangle e^{i\mathbf{Q}\cdot\mathbf{r}} d^3\mathbf{r} \tag{2.17}$$

where $\delta(\mathbf{r})$ is the Dirac delta function which is zero for all position vectors not equal to $\mathbf{r}$. If we now assume an ideal one-isotope sample, all scattering lengths are equal to each other ($b_j = b_k = b$). The scattering lengths can now be moved outside of the summation, and Eq. 2.16 becomes:

$$I(\mathbf{Q}, E) = \frac{nb^2}{2\pi\hbar}\frac{k_f}{k_i} \int_{-\infty}^{\infty}\int_{-\infty}^{\infty} G(\mathbf{r}, t) e^{i\mathbf{Q}\cdot\mathbf{r}} e^{-i\omega t} d^3\mathbf{r} dt \tag{2.18}$$

n is the number of nuclei in the sample and $G(\mathbf{r}, t)$ is the time-dependent *pair distribution function*, which in this classical derivation can be defined as:

$$G(\mathbf{r}, t) = \frac{1}{n}\sum_{j,k} \left\langle \delta\left(\mathbf{r} - \left[\mathbf{r}_k(0) - \mathbf{r}_j(t)\right]\right) \right\rangle. \tag{2.19}$$

$G(\mathbf{r}, t)$ gives the probability to find a nucleus at the origin of a coordinate system at time zero as well as a nucleus at position $\mathbf{r}$ at time t. From Eq. 2.18 we see that the scattered intensity is proportional to the space and time Fourier transforms of $G(\mathbf{r}, t)$. This is a powerful result showing that in theory the crystal structure and its corresponding changes as a function of time is obtained by inverse Fourier transformation of the measured intensity. In reality this is not possible due to the so-called phase problem in crystallography, i.e. the phase information is lost when only the intensity (the scattering amplitude squared) is measured. However during the years several efficient methods to determine crystal structures from scattering data have been developed (see Chap. 3).

Earlier we assumed the sample to be mono-isotopic with just one value of b. In a sample containing more than one isotope, all scattering lengths appearing in Eq. 2.16 are not equal any longer, thus resulting in some important modifications to this equation. If $A_{j,k}$ is an abbreviation for the integral in Eq. 2.16 and we omit the constants, we now get:

$$I(\mathbf{Q}, E) = \frac{\sigma_c}{4\pi}\sum_{j,k} A_{j,k} + \frac{\sigma_i}{4\pi}\sum_{j} A_{j,j} \tag{2.20}$$

$\sigma_c = 4\pi\left(\overline{b}\right)^2$ and $\sigma_i = 4\pi\left(\overline{b^2} - \left(\overline{b}\right)^2\right)$ are the coherent and incoherent cross sections from Sect. 2.4, respectively. The first term in Eq. 2.20 represents the coherent scattering leading to interference effects. From Eqs. 2.16 and 2.20 we see that it depends on the correlation between the positions of different nuclei at different times. On the other hand, the incoherent scattering, represented by the second term in Eq. 2.20, is only dependent on the correlations between the positions of the same nucleus at different times. The incoherent contribution is generally independent of the scattering angle, resulting in a featureless addition to the background that is mostly ignored when performing neutron diffraction experiments. Yet incoherent scattering is very important for studies of diffusion processes using quasielastic neutron scattering.

A classic example of the peculiar nature of incoherent scattering is the big difference between protium and deuterium. Protium is a strong spin-incoherent scatterer because the triplet (total spin moment neutron + nucleus, $J = 1$) and the singlet states ($J = 0$) have very different scattering lengths ($b_+ = 10.81$ fm, $b_- = -47.42$ fm), resulting in $\sigma_i = 80.3$ and $\sigma_c = 1.76$ barn, respectively. Deuterium has only one spin state in its ground state of $I = 1$, and $b_+ = 9.53$ fm and $b_- = 0.97$ fm, and the corresponding values for deuterium are $\sigma_i = 2.05$ and $\sigma_c = 5.59$ barn, respectively. Therefore, naturally occurring hydrogen scatters mostly incoherently leading to a strong and featureless background in the neutron diffraction patterns of hydrogen containing samples. This means if possible deuterided samples should be used for diffraction experiments in order to reduce the incoherent scattering. When performing inelastic or quasielastic neutron scattering, on the other hand, the incoherent scattering is being used for studying diffusion, hence hydrogen is preferred over deuterium due to the much larger incoherent contribution.

By synthesizing compounds where there are specific units or groups of atoms including hydrogen and others with deuterium, the significant difference in scattering is used to mask and enhance specific parts of the compounds. See Chap. 6.

2.4.3 *Magnetic Scattering*

Due to the magnetic moment of neutrons, they interact with unpaired electrons in magnetic materials. This makes neutron scattering a unique method to determine magnetic properties in materials. The magnetic interaction experienced by the neutron is of similar strength as the nuclear interaction, and thus magnetic scattering is of similar intensity as nuclear scattering. In ferromagnetic materials all the magnetic moments are oriented along the same direction. The magnetic unit cell is in this case equal to the crystallographic one, and therefore the magnetic scattering gives additional contribution to the crystalline Bragg peaks only. However, for other kinds of magnetic ordering, for example, antiferromagnetic materials (commensurate or incommensurate with the crystal structure) or magnetic helices, magnetic scattering gives additional peaks in the diffraction patterns. In addition

to determination of the type of magnetic ordering, it is also possible from the data treatment to determine both the direction and sizes of the magnetic moments. Neutrons interact with the unpaired electrons and therefore the scattering is determined by the magnetic form factor which is a function of the scattering angle. Thus the strongest magnetic scattering appears at low angles in the diffraction patterns.

2.5 Elastic, Inelastic, and Quasielastic Neutron Scattering

2.5.1 Elastic Scattering: Bragg Diffraction

Neutron scattering is a multifaceted discipline that has evolved into a vast array of different techniques. The most basic is elastic neutron diffraction, often called Bragg scattering or Bragg diffraction (similar for neutrons and X-rays). These experiments do not require the determination of the energy of the scattered neutrons and from the coherent term in Eq. 2.20 the intensity of the scattered beam as a function of the scattering vector **Q** is given by:

$$I(\mathbf{Q}) = \sum_{j,k} b_j b_k e^{i\mathbf{Q}\cdot(\mathbf{r}_j - \mathbf{r}_k)} = |F(\mathbf{Q})|^2 \tag{2.21}$$

with coherent scattering lengths b_j and b_k, and the *structure factor* $F(\mathbf{Q})$ is defined as:

$$F(\mathbf{Q}) = \sum_j b_j e^{i\mathbf{Q}\cdot\mathbf{r}_j}. \tag{2.22}$$

Crystalline materials are built up of identical entities, called *unit cells*. The unit cell is a parallelepiped spanned by three translation vectors **a**, **b**, and **c** (see Fig. 2.7). The unit cell itself is positioned by a lattice vector $\mathbf{r}_{uvw} = u\mathbf{a} + v\mathbf{b} + w\mathbf{c}$, where u, v, w, are integers. The atomic position for each atom within the unit cell is given by $\mathbf{r}_j$ (see Eq. 2.22), and the overall position of the atom can be expressed as $\mathbf{r}_j = \mathbf{r}_{uvw} + \mathbf{r}_j^{\text{unitcell}}$ (see Fig. 2.7).

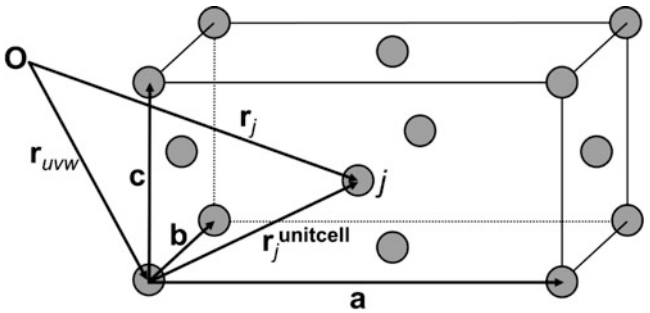

Fig. 2.7 Unit cell of a face-centered orthorhombic lattice with lattice constants **a**, **b**, **c**. $\mathbf{r}_j^{\text{unitcell}}$ is the equilibrium position of atom j in the unit cell

From this expression of $\mathbf{r}_j$ the structure factor in Eq. 2.22 can be expressed as:

$$F_{hkl}(\mathbf{Q}) = \sum_{j}^{n_{\text{unitcell}}} \sum_{u,v,w=-\infty}^{\infty} b_j e^{i\mathbf{Q}\cdot\left(\mathbf{r}_{uvw}+\mathbf{r}_j^{\text{unitcell}}\right)}$$
$$= \sum_{u,v,w=-\infty}^{\infty} e^{i\mathbf{Q}\cdot\mathbf{r}_{uvw}} \sum_{j}^{n_{\text{unitcell}}} b_j e^{i\mathbf{Q}\cdot\mathbf{r}_j^{\text{unitcell}}} \tag{2.23}$$

The first sum is over all unit cells in the crystal, typically assumed to be infinite, and the second sum is over all the n_{unitcell} atoms in the unit cell. The infinite triple sum can be expressed as a sum of δ-functions that describes a lattice, which leads us to the final expression for the structure factor (often named Laue's interference function):

$$F_{hkl}(\mathbf{Q}) = \frac{1}{V} \sum_{j}^{n_{\text{unitcell}}} b_j e^{i\mathbf{Q}\cdot\mathbf{r}_j^{\text{unitcell}}} \sum_{h,k,l=-\infty}^{\infty} \delta(\mathbf{Q} - \mathbf{Q}_{hkl}) \tag{2.24}$$

where $\mathbf{Q}_{hkl} = 2\pi(h\mathbf{a}^* + k\mathbf{b}^* + l\mathbf{c}^*)$, $\mathbf{a}^*$, $\mathbf{b}^*$, and $\mathbf{c}^*$ are the reciprocal vectors of $\mathbf{a}$, $\mathbf{b}$, and $\mathbf{c}$ defined by $\mathbf{a}\cdot\mathbf{a}^* \equiv \mathbf{b}\cdot\mathbf{b}^* \equiv \mathbf{c}\cdot\mathbf{c}^* \equiv 1$ and $\mathbf{a}\cdot\mathbf{b}^* \equiv \mathbf{a}\cdot\mathbf{c}^* \equiv \mathbf{b}\cdot\mathbf{a}^* \equiv \ldots \equiv 0$. h, k, l are integers, while V is the volume of the unit cell. This implies that a crystal with perfect translational symmetry only scatters in certain directions, namely where $\mathbf{Q} = \mathbf{Q}_{hkl}$. The scattering in these directions corresponds to the Bragg scattering. $F_{hkl}(\mathbf{Q})$ is zero everywhere else due to the sum of δ-functions which is zero except for $\mathbf{Q} = \mathbf{Q}_{hkl}$.

The condition for Bragg scattering is visualized in Fig. 2.8 and is usually expressed as the Bragg's law:

$$\lambda = 2d_{hkl}\sin(\theta_{hkl}) \tag{2.25}$$

where λ is the wavelength of the incoming and outgoing neutrons, d_{hkl} is the distance between the family of planes that cut the unit cell vectors **a**, **b,** and **c,** h, k, and l times, respectively, and θ_{hkl} is half the scattering angle between $\mathbf{k}_i$ and $\mathbf{k}_f$ as

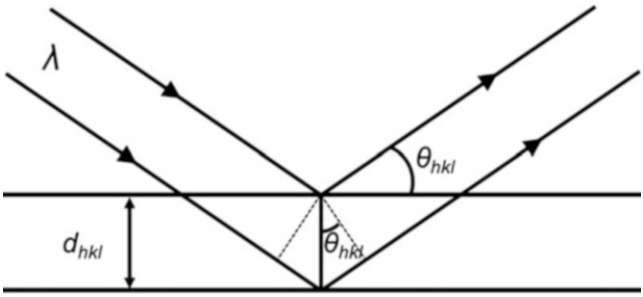

Fig. 2.8 Illustration of Bragg's law. Scattering of neutrons, with wavelength λ, regarded as specular reflection from a set of crystallographic planes shown as *horizontal lines*

seen in Fig. 2.6. The Bragg scattering is often regarded as specular reflections from these planes (Fig. 2.8), hence the scattering in a direction $2\theta_{hkl}$ is called a *Bragg reflection* where *hkl* are the so-called Miller indices for this reflection.

The expression in Eq. 2.24 is only valid for purely stationary atoms. In a real sample thermal energy makes the atoms oscillate about their equilibrium positions and the expression becomes:

$$F_{hkl}(\mathbf{Q}) = \frac{1}{V}\sum_{j}^{n_{\text{unitcell}}} b_j e^{i\mathbf{Q}\cdot\mathbf{r}_j^{\text{unitcell}}} e^{-Q^2\langle u_j^2\rangle/2} \sum_{h,k,l=-\infty}^{\infty} \delta(\mathbf{Q}-\mathbf{Q}_{hkl}) \tag{2.26}$$

where $e^{-Q^2\langle u_j^2\rangle/2}$ is the Debye–Waller factor that is taking into account the thermal vibrations of the atoms, and $\langle u_j^2\rangle$ is the average of the squared displacement of atom *j*. The displacements can also come from static disorder and thus this parameter is designated as an atomic displacement parameter. Since an atom only contributes to the Bragg scattering when it is located at the center of its vibration ellipsoid, the intensity of the Bragg reflection becomes weaker due to the thermal vibrations, and the effect increases for increasing scattering angles. Chapter 3 covers powder neutron diffraction which is one of the major techniques used in studying, for example, hydrogen storage materials.

2.5.2 Inelastic Neutron Scattering: Phonons, Magnons

One of the advantages of using neutrons as a probe when studying condensed matter is that they can be used to measure atomic and molecular vibrations with inelastic coherent scattering, and thereby measuring energy transitions and energy levels in atoms. The term inelastic means that the magnitude of the neutron's wave vector changes as well as the direction during the scattering process, hence the kinetic energy of the scattered neutron is modified. Vibrations of atoms in solid materials are correlated with each other into lattice waves, which are superpositions of waves of different frequencies and wavelengths. These waves are called *phonons*, and have quantized energies of $E = h\nu$, where ν is the frequency of the collective motion of all atoms linked to a given phonon.

Analogous to a phonon, a *magnon* is a quantized energy packet resulting from collective oscillations of the magnetic moments in solid materials. These oscillations are called spin waves. The magnon carries an energy of $E = h\nu$ where ν is the frequency of the spin wave. An excitation of a magnon corresponds to the reversal of one spin ½.

An incoming neutron can interact with a phonon or a magnon, and will either give or take up the quantized energy before being scattered. This process is called inelastic because it involves a change of the kinetic energy of the neutron. Since the energy of a typical phonon or magnon is on the same order as the kinetic energy of the incoming neutrons, the change in energy of the scattered neutron is significant

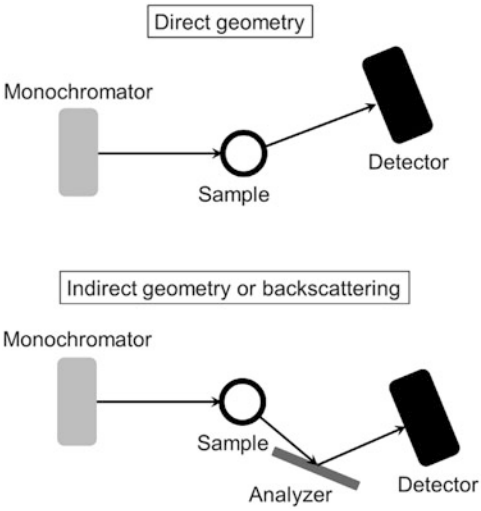

Fig. 2.9 Geometries of inelastic neutron scattering setups

and possible to measure quite accurately. From the change of the neutron energy the phonon and magnon frequencies can be determined. A typical setup (Fig. 2.9) uses either a monochromatic incoming beam, and measures the scattered neutrons with the time of flight method to find the energy transfer (direct geometry), or it measures the scattered neutrons using an analyzer crystal after the sample (indirect geometry). The latter type is commonly referred to as a triple-axis spectrometer. More on this technique can be found in Chap. 9.

2.5.3 Quasielastic Neutron Scattering

As mentioned earlier the incoherent contribution to the scattering in a typical diffraction experiment is handled like a featureless background, which may imply that there is no information obtainable from this. On the contrary, a fair deal of knowledge can be extracted from this signal. In quasielastic neutron scattering (QENS) we can make use of the *incoherent* contribution to the inelastic scattering to measure diffusion processes. Since diffusion in its simplest form is one particle jumping between lattice sites, it makes sense to analyze the incoherent scattering, because it provides the dynamics of individual particles. On the other hand, inelastic *coherent* scattering is due to correlated motions of atoms, e.g., phonons. The big incoherent scattering cross section of hydrogen enables excellent contrast when studying hydrogen diffusion.

Similarly to inelastic scattering, QENS measures energy transitions using similar setups found in Fig. 2.9. The name quasielastic comes from the fact that the measurements are probing events having energy transfers much lower than the incoming energy, with deviations very close to the elastic scattering. Consequently,

the energy has to be measured with high resolution. The energy transitions are generally not quantized, leading to a continuous Lorentzian broadening of the elastic peak (where the energy transfer is zero). More on incoherent neutron scattering and QENS can be found in Chaps. 8 and 9, respectively.

2.6 Summary

Technique	Physical principle	Information provided
Diffraction (Chaps. 3 and 4)	Elastic scattering	Crystal structure on atomic scale: positions of atoms including hydrogen, lattice constants, phase fractions, pair distribution functions
Reflectometry (Chap. 5)	Refraction	Layer thickness and scattering length density profile (e.g., hydrogen profile) with nm resolution and absorption/desorption studies in real time
Small angle neutron scattering (Chap. 6)	Elastic scattering	Structure on a mesoscopic scale (~1–100 nm): macromolecules, porous and biological systems, aggregates of particles in a matrix or scaffolds
Radiography/Neutron imaging (Chap. 7)	Absorption	Structure on a macroscopic level (typical resolution in the order of 50 microns), absorption and desorption studies in real time
Incoherent neutron scattering (Chap. 8)	Incoherent scattering	H_2/D_2 content and absorption/desorption studies in real time
Inelastic scattering (Chap. 9)	Coherent and incoherent inelastic scattering	Dynamic processes: vibrational/rotational states, binding energies
Quasielastic scattering (Chap. 9)	Incoherent inelastic scattering	Dynamic processes: H_2/D_2 diffusion, molecular vibrations and rotations, activation energy

References

1. FRMII, Neutron sources (2015), http://neutronsources.org. Accessed 2 Dec 2015
2. ESS, European Spallation Source (2015), http://europeanspallationsource.se. Accessed 2 Dec 2015
3. NIST, Neutron scattering lengths and cross sections (2015), http://www.ncnr.nist.gov/resources/n-lengths/list.html. Accessed 2 Dec 2015
4. V.F. Sears, Neutron News **3**, 26 (1992)
5. D.H. Ryan, L.M.D. Cranswick, J. Appl. Crystallogr. **41**, 198 (2008)
6. L. Van Hove, Phys. Rev. **95**, 249 (1954)
7. G.E. Bacon, *Neutron Diffraction* (Oxford University Press, Oxford, 1975)
8. G.L. Squires, *Introduction to the Theory of Thermal Neutron Scattering* (Cambridge University Press, Cambridge, 2012)
9. R. Pynn, Los Alamos Science; Neutron Scattering. **19** (1990)

Chapter 3
Neutron Powder Diffraction

Jacques Huot and Radovan Černý

Abstract Neutron powder diffraction is extensively used for the development and fundamental understanding of metal hydrides. In this chapter we will first present the basic principles of neutron diffraction. This will be followed by a discussion about the two main neutron sources used for diffraction experiments: reactors and spallation sources. Analysis of diffraction patterns by Rietveld refinement will be discussed next: we will expose the principle of the method and the significance of various parameters to be refined. The special case of locating the hydrogen using neutron powder diffraction will be discussed in a separate section. The final section is a presentation of a few selected examples of the application of neutron powder diffraction to metal hydrides.

Keywords Borohydride • Coherent scattering length • Constant wavelength (CW) • Crystal structure • Crystallography • Goodness-of-fit • Hydrogen storage • Incoherent scattering length • In-situ • Metal hydride • Magnetic scattering • Null-matrix alloy • Palladium hydride • Peak width • Phase abundance • Powder diffraction • Preferred orientation • Rietveld refinement • Structure factor • Structure solution • Superstructure • Time-of-flight (ToF) • Zircaloy

3.1 Introduction

X-ray powder diffraction (XPD) is a well-known technique that is extensively used in material science and engineering. In the last few decades, the availability of powerful data analysis programs enabled XPD to evaluate a variety of crystal structure parameters. However, the nature of information that can be extracted

J. Huot (✉)
Hydrogen Research Institute, Université du Québec à Trois-Rivières,
3351 des Forges, Trois-Rivières, Canada, G9A 5H7
e-mail: Jacques.huot@uqtr.ca

R. Černý
Laboratoire de Cristallographie, DQMP, Faculté des Sciences,
Université de Genève, Quai Ernest-Ansermet 24, 1211 Genève-4, Switzerland
e-mail: Radovan.Cerny@unige.ch

H. Fritzsche et al. (eds.), *Neutron Scattering and Other Nuclear Techniques for Hydrogen in Materials*, Neutron Scattering Applications and Techniques,
DOI 10.1007/978-3-319-22792-4_3

from XPD patterns is still limited by the fundamental nature of the interaction between the electromagnetic wave and the atoms. In quantum mechanics, a De Broglie wave is associated with any particle. Thus, neutron diffraction is conceptually similar to X-ray diffraction. The main difference between these two radiations is that while X-rays interact primarily with the electron cloud surrounding the atom, neutron scattering is due to the interaction of the atom nuclei with the incident neutron (see Chap. 2). Therefore, neutron powder diffraction (NPD) can provide complementary information not accessible to X-rays. In particular, for hydrogen in metals, neutron diffraction is practically the only technique locating the hydrogen (deuterium) atoms in the lattice. Usually, upon hydrogenation, there will be a reduction of symmetry with an increase of lattice parameters while hydrogen atoms going on specific sites in the crystal structure. However, some metal hydrides keep the same symmetry; this is the case of the well-known metal hydride $LaNi_5$. Let's look at the X-rays and neutron diffraction patterns of this alloy. Figure 3.1 shows the simulated XPD patterns of $LaNi_5$ and its hydride $LaNi_5D_6$. Hydrogen has been replaced by deuterium for reasons that will be explained in Sect. 3.4.5. We see that the relative intensities of the peaks are the same for both patterns. The only major difference is that the pattern of the hydride sample is shifted to the left. This is what we expect for an alloy that experiences an increase of its lattice parameters while keeping the same crystal structure. However, the hydride pattern does not bring information about the localization of the hydrogen (deuterium) atoms in the crystal.

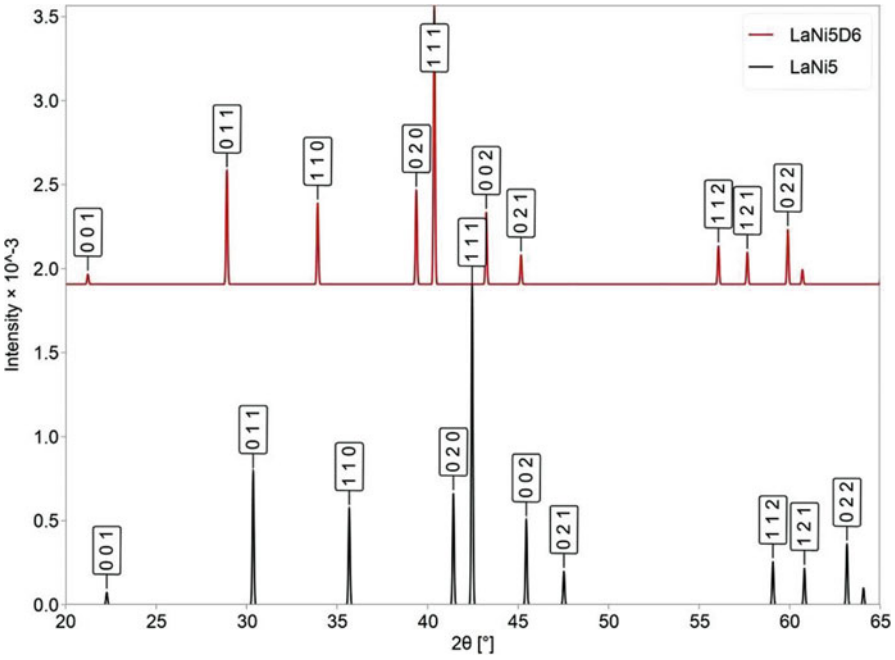

Fig. 3.1 Calculated X-ray powder diffraction patterns of $LaNi_5$ (*bottom*) and $LaNi_5D_6$ (*top*). X-ray wavelength was set at 0.15406 nm

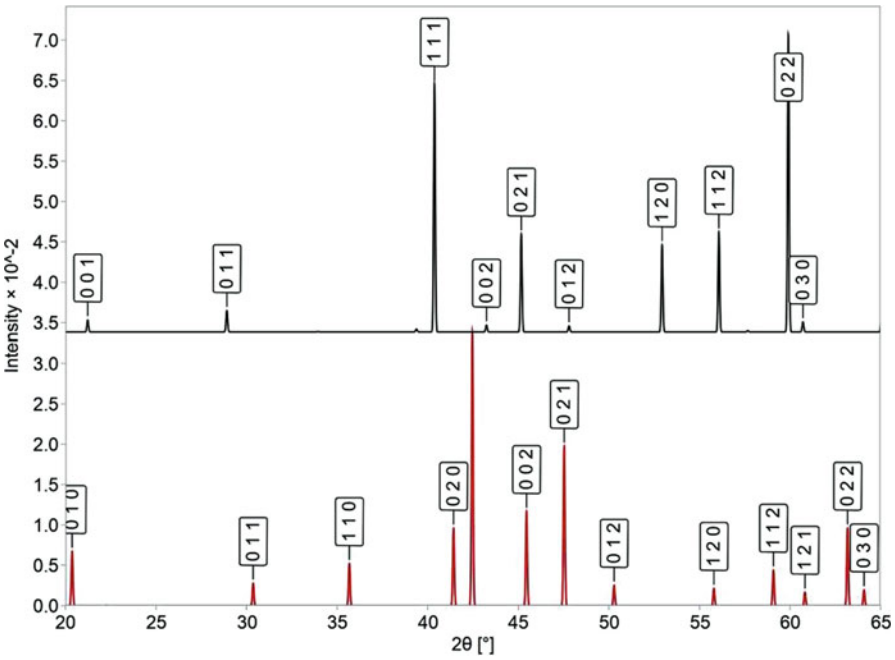

Fig. 3.2 Calculated neutron powder diffraction patterns of $LaNi_5$ (*bottom*) and $LaNi_5D_6$ (*top*). Neutron wavelength was set at 0.15406 nm

Figure 3.2 shows the simulated NPD patterns of $LaNi_5$ and $LaNi_5D_6$. Contrary to Fig. 3.1 here the two patterns are quite different. As the calculation was done for neutrons having the same wavelength as the X-rays of Fig. 3.1, the diffraction peaks are at the same position in the two figures. As for Fig. 3.1, the $LaNi_5D_6$ peaks are shifted to the left compared to the $LaNi_5$ peaks. However, it is clear that the relative intensities are completely different in the two patterns. This is due to the contribution of deuterium atoms to the neutron diffraction.

For the same wavelength neutrons have a much lower energy than X-rays, comparable in energy to the elementary excitations in matter. This means that neutrons can be used to probe not only the static average properties of matter, as for example crystal structure from neutron diffraction, but also dynamic properties of atomic arrangements in the form of phonons (see Chap. 9). As neutrons do not carry electric charges they interact only weakly with matter. Therefore they have large penetration depth and can measure the bulk properties of materials. Weak interaction is also beneficial for in-situ experiments. Usually, in-situ experiments use a bulky sample holder that can sustain high pressures and high temperatures. Neutrons can penetrate these structures and then interact with the sample. In-situ experiments are treated in Chap. 5 of this book. Finally, as neutrons carry a magnetic moment they can be used as a probe for the determination of magnetic properties of matter.

In this chapter we will present the basic principles of NPD and how to analyse it using the Rietveld method. A few selected examples of using NPD for the study of metal hydrides will be presented in sect. 3.6.

3.2 Principles of Powder Diffraction

In this section we will review the main features of powder diffraction with emphasis on neutron techniques. From elementary physics, we know that when a wave is scattered by a point object the outcome is a scattered wave spread in all directions. In this chapter we cover only elastic interactions which mean that the scattered wave has the same wavelength (energy) as the incoming wave. This wave could be an electromagnetic wave as in the case of X-ray diffraction or a De Broglie wave for neutron diffraction.

3.2.1 Crystal Structure

A crystal is defined by a three dimensional periodic repetition of a unit cell. The unit cell is the smallest unit containing the structural and chemical information necessary to uniquely define the crystal. An example of a unit cell is shown in Fig. 2.7.

A complete description of crystallographic symmetry is outside the scope of this chapter. Details can be found in numerous crystallographic textbooks. To describe fully the symmetry of a macroscopic object in three dimensions we need symmetry operations leaving at least one point fixed. These operations may use one or more rotations, reflections, inversions, and rotoinversions. The combination of the symmetry operations of these symmetry elements leads to 32 point groups compatible with the requirement of periodicity. They define 32 crystal classes which are divided between seven crystal systems according to the minimal symmetry (Table 3.1). In three dimensions there are 14 different lattices which describe the periodicity of the crystal. They are called Bravais lattices. The minimal symmetry of crystal systems induces the constraints on relative length of the basic vectors a, b, and c of the three axes x, y, and z defining the unit cell and the three angles α, β, and γ between them. Table 3.1 lists the seven crystal systems and the relationships between axes and angles.

Each Bravais lattice is constructed from the special positions in space that have identical neighbourhood, these are the lattice points. When there is one lattice point at each corner of the unit cell it is called *Primitive* and given the symbol P. However, for any given Bravais lattice the set of primitive vectors is not unique - indeed there are infinitely many nonequivalent choices. If there is an additional lattice point at the centre of the unit cell then it is called *Body Centred* and its symbol is I. When there are lattice points at the corners and at the centre of each face of the unit cell then we have a *Face Centred* Bravais lattice, symbol F. If there are lattice points at

Table 3.1 The seven crystal systems

System	Minimal symmetry	Standard Bravais lattices	Axial lengths and angles
Triclinic	No rotation axis	P	$a, b, c, \alpha, \beta, \gamma$ any
Monoclinic	One twofold rotation (rotoinversion) axis	P, C	a, b, c, β any $\alpha = \gamma = 90°$
Orthorhombic	Three perpendicular twofold rotation (rotoinversion) axes	P, I, C, F	a, b, c any $\alpha = \beta = \gamma = 90°$
Tetragonal	One fourfold rotation (rotoinversion) axis	P, I	$a = b$ $\alpha = \beta = \gamma = 90°$
Trigonal	One threefold rotation (rotoinversion) axis	P P, R	$a = b = c$ $\alpha = \beta = \gamma \neq 90°$ (rhombohedral unit cell) or $a = b$ $\alpha = \beta = 90°, \gamma = 120°$
Hexagonal	One sixfold rotation (rotoinversion) axis	P	$a = b$ $\alpha = \beta = 90°, \gamma = 120°$
Cubic	Four threefold rotation (rotoinversion) axes	P, I, F	$a = b = c$ $\alpha = \beta = \gamma = 90°$

the corners and at the centre of a pair of opposite faces then it is called *Base Centred*, symbol C, if the standard setting is chosen. Otherwise it can be A or B. Finally, the lattice having the rhombohedral unit cell may be better described using hexagonal basic vectors and 3-times larger unit cell with lattice points at the corners and positions (1/3, 2/3, 2/3) and (2/3, 1/3, 1/3). This type of lattice has the symbol R.

A combination of symmetry elements of the 32 point groups with the non-lattice (shorter) translations leads to new symmetry elements: glide planes and screw axes. They combine together with point group symmetry elements into 230 distinct symmetry groups which were found independently by Federov, Barlow, and Schönflies. These are the *space groups*. Not considering aperiodic crystals, any crystal structure can be described in one of these 230 space group. They are listed in the ***International Tables for Crystallography*** which gives for each space group the crystal system, the point group, the general position diagrams, and the symmetry diagram. A good understanding of the ***International Tables for Crystallography*** is essential for a meaningful understanding of diffraction patterns [1].

As we will see later, for diffraction it is important to describe the crystal as built up of families of parallel planes. One such family of parallel planes is called lattice plane and has one interplanar distance d. The way to describe the lattice planes is to use the Miller indices (hkl). To find the Miller indices of a family of parallel planes, first take the intersections of the plane closest to the origin with the x, y, and z axes as fractions of the basis vectors a, b, and c. Second, take the reciprocal values of these intersections and if not integers convert them to integers by multiplying them with their least common denominator. The numbers obtained are the Miller indices

h, k, and l of this family of planes. For example, take a plane that intersects the x axis at 3/4 a, the y axis at 3 b, and the z axis at 1/2 c. The reciprocals are then (4/3, 1/3, 2) which, after multiplication by 3 leads to the Miller indices (416). Planes parallel to an axis intersect this axis at infinity and therefore have a Miller index of zero. Lattice planes could be related to each other by the symmetry operations of the point group, and form a *family* of lattice planes called crystal form which is identified by Miller indices between curly braces $\{hkl\}$. For example, in a cubic system, planes of indices (001), (010), (−100), (00−1), (0−10), and (100) are equivalent and form the $\{100\}$ family. The number of planes in a family $\{hkl\}$ is called multiplicity J_{hkl} of the crystal form $\{hkl\}$. Full explanation of the lattice plane concept can be found in any crystallography textbook.

3.2.2 Neutron Diffraction

In this chapter we cover only the elastic and coherent scattering of neutrons. For more details on neutron scattering, see Chap. 2. The basis of diffraction is Bragg's law:

$$n\lambda = 2d_{hkl} \sin \theta_{hkl} \tag{3.1}$$

where λ is the wavelength of the used radiation, d_{hkl} is the interplanar distance of the lattice plane hkl, and θ_{hkl} is the angle of the lattice plane hkl with respect to the wave vector of the incoming wave (see Eq. 2.25 and Fig. 2.8). Bragg's law is applicable and routinely used for X-rays, electrons, and neutrons. Here, let's just point out important characteristics of the application of Bragg's law for neutron diffraction [2].

(1) Neutrons interact much more weakly with matter than X-rays and electrons. Therefore, even with high neutron flux and large sample volume relatively long counting times used to be necessary. However, modern instruments can acquire good resolution patterns in a short time span. Sample volume of about one cubic centimetre is usually needed in order to have enough scattering.

(2) For X-rays the atomic scattering factor is proportional to the number of electrons. Therefore, it increases monotonically with atomic number and is identical for the isotopes of the same element. This is not the case for the neutron scattering factor as can be seen in Fig. 2.4. This allows the distinction between two neighbouring elements in the periodic table. For example, natural occurring chromium, manganese, and iron have a coherent neutron scattering length b_c of 3.635 fm, −3.73 fm, and 9.45 fm, respectively.

(3) The non-monotonic dependence of b_c on the atomic number has the most important consequences for the localization of hydrogen in crystalline matter. Hydrogen is a strong neutron scatterer while with its one electron, it is nearly invisible for X-rays.

(4) The coherent neutron scattering length b_c does not depend on the scattering angle 2θ. In the case of X-rays, the atomic scattering factor has a $(\sin\theta/\lambda)$

dependence. This means that at high 2θ angle Bragg peaks in X-ray patterns will have lower intensities while for neutrons the Bragg peaks have similar intensities over the whole pattern, depending only on the crystal structure itself. Furthermore, this makes atomic position and displacement parameters much more reliable when using NPD than using XPD.

(5) Another advantage of NPD is that superlattice reflections can be easily seen in the powder pattern [3]. As an example consider the alloy FeCo. From XPD it can be concluded that the structure is cubic but the question remains: is it a body centred cubic (BCC) solid solution where Co and Fe atoms are randomly distributed on the lattice sites or is it a CsCl structure with one type of atom at the centre and the other one at the corners? Figure 3.3 shows the simulated XPD patterns of both structures. It is clear that both patterns are identical and due to low X-ray scattering contrast between Fe and Co it is impossible to distinguish these two structural models by X-ray diffraction.

Let us now look at the calculated patterns for neutron diffraction as shown in Fig. 3.4. Here there is a clear difference between the two patterns and the correct FeCo structural model of CsCl type can be easily identified.

The reason for this discrepancy between X-rays and neutron patterns can be easily seen by looking at the CsCl structure factor using Eq. (2.24). Ignoring the

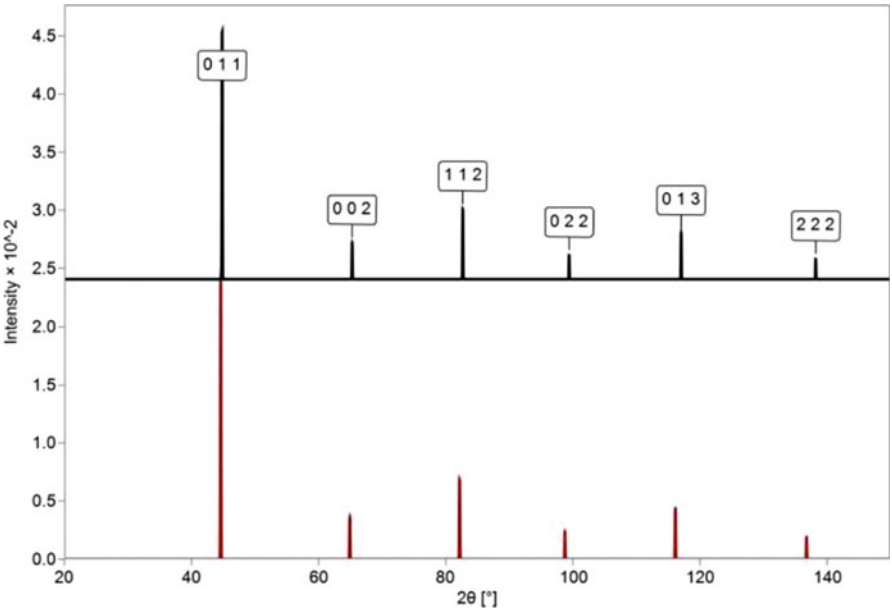

Fig. 3.3 Calculated X-ray powder diffraction patterns of FeCo alloy. *Top pattern* is for a CsCl structure type (space group *Pm*-3*m*), *bottom pattern* is for a body centred cubic structure (space group *Im*-3*m*). Miller indices *hkl* are indicated for each peak. The X-ray wavelength was set at 0.15406 nm

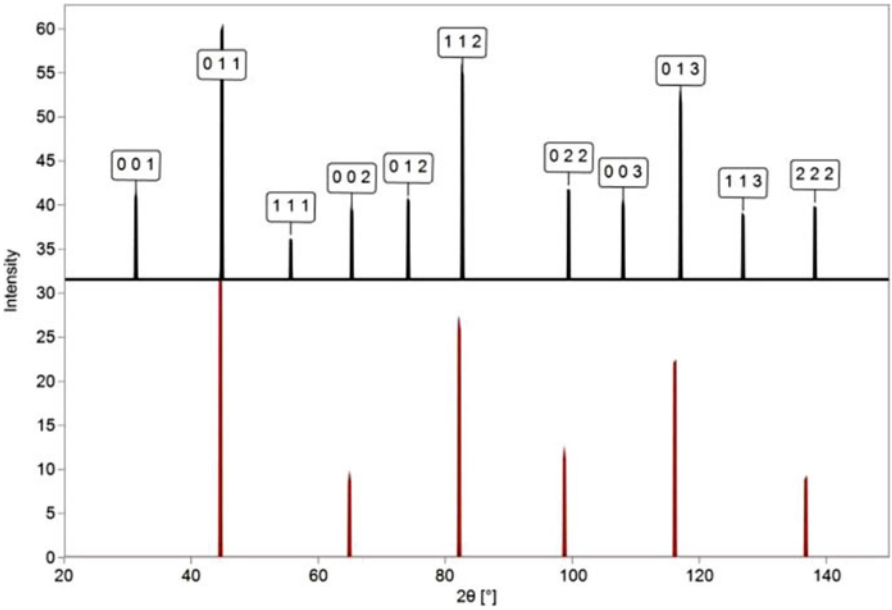

Fig. 3.4 Calculated neutron powder diffraction patterns of FeCo. *Top pattern* is for a CsCl structure type (space group *Pm*-3*m*), *bottom pattern* is for a body centred cubic structure (space group *Im*-3*m*). Miller indices *hkl* are indicated for each peak. Neutron wavelength was set at 0.15406 nm

constant term and the Debye–Waller factors we can write for the structure factor of the CsCl structure type for X-rays:

$$|F_{hkl}|^2 = \left(f_{\mathrm{Fe}} + (-1)^{h+k+l} f_{\mathrm{Co}}\right)^2 \tag{3.2}$$

where f_x is the X-ray atomic scattering factor for atom x. As copper has only one more electron than iron $f_{\mathrm{Co}} \approx f_{\mathrm{Fe}}$ and F_{hkl} is almost zero for $h+k+l$ odd. This is the reason why the peaks with $h+k+l$ odd are essentially absent in the X-ray diffraction patterns. Now let us look on the neutron structure factor. Its expression is:

$$|F_{hkl}|^2 = \left(b_{\mathrm{Fe}} + (-1)^{h+k+l} b_{\mathrm{Co}}\right)^2 \tag{3.3}$$

Here, the scattering length of cobalt and iron are respectively 2.49 fm and 9.45 fm. Thus, even when $h+k+l$ is odd these two terms do not cancel and we get a high intensity of Bragg peaks with $h+k+l$ odd. This is a good example on how neutron diffraction can be used to detect the presence of ordering in a crystal structure.

3.2.3 Magnetic Neutron Scattering on Crystals with Ordered Magnetic Moments

Neutrons have a spin (1/2), and are therefore also scattered by any unpaired electrons on atoms in crystals carrying a magnetic moment. The scattering can be described using a magnetic scattering length, similarly to the nuclear scattering length b describing the nuclear scattering. As the unpaired electrons are located in the outer orbitals of an atom, i.e. within the distances comparable to the wavelength of the neutron radiation, the magnetic scattering length decreases with the scattering angle (more precisely with $\sin\theta/\lambda$) even faster than the X-ray atomic factor f, unlike the nuclear scattering length b which stays constant. As a consequence the information about the magnetic scattering is limited to the low angle (large d-spacing) part of the diffraction pattern contrary to the nuclear scattering. When the magnetic moments have no long-range order (paramagnetic materials), the magnetic scattering may be compared to the nuclear scattering of disordered crystals, i.e. diffuse scattering.

The situation changes when the magnetic moments in the crystals order, i.e. their orientation orders, over a long distance. Different types of ordering exist such as ferromagnetic, antiferromagnetic, and other more complex types of ordering. A periodic magnetic structure is then an equivalent of what we call a crystal (chemical) structure for nuclear scattering. The magnetic lattice is usually not identical to the nuclear lattice, different types of superstructures, commensurate or incommensurate with the nuclear lattice, may appear. The symmetry of the commensurate magnetic structures is described not by one of 230 space groups, but by one of 1651 magnetic (Shubnikov) groups, because one additional parameter appears—orientation of the magnetic moment (up, down). The symmetry of the incommensurate magnetic structures has to be described either by using superspace groups or basis vectors concept.

Determination of magnetic structures from NPD is even more challenging than that of nuclear structures, because more parameters have to be determined (orientation of the magnetic moment), and even less information is observed in the NPD pattern (only low angle part). Hydrogen is an important tool to modify the magnetism of intermetallic compounds and metallic alloys, therefore it is important to present this short note on magnetic scattering. For a complete description of magnetic scattering we refer to dedicated reviews [4].

3.3 Information in a Powder Diffraction Pattern

An experimental powder diffraction pattern contains a lot of different types of information that are important for the material scientists [5]. The positions (values of the Bragg angle θ_{hkl}) of the peaks in the powder pattern contain indirectly information on the crystal lattice through the values of interplanar distances (d_{hkl})

obtained from Bragg's law. The intensities of the peaks contain indirectly information on the positions of the atoms in the unit cell through the values of the structure factors.

It is important to remember that a powder pattern is a one dimensional projection of the three dimensional diffraction pattern obtained on a single crystal. The projection is done on a radial distance from the origin of the reciprocal space, i.e. on $1/d$. The projection results in overlapping of the peaks in the powder pattern, either exact due to the symmetry of the crystal lattice or partial due to the limited resolution of the powder pattern, i.e. due to the width of the peaks.

3.3.1 Phase Identification: Qualitative Phase Analysis

The most obvious information given by a powder diffraction pattern is the phase composition. Each crystalline phase has its own "finger print", i.e. the pattern of positions and intensities of the peaks. This information is used for the so-called phase analysis, i.e. decoding of the observed powder pattern into a mixture of powder patterns of individual phases. The software for doing that is called a "search-match program", and the most used database of known powder patterns is the Powder Diffraction File (PDF) commercialized by the International Centre for Diffraction Data [www.icdd.com]. At least, the main phase should be readily identified because usually the chemical composition and possible phases present are already known. Secondary phases may be harder to recognize for a number of reasons: peaks very small and hard to identify, not enough peaks to have a clear identification, phase coming from an impurity, etc. As most experimenters are more accustomed to X-ray diffraction patterns than neutron ones, phase identification may be a little easier using X-rays instead of neutrons. Most of the data items in the PDF database comes from XPD. For this reason, it is a good practice to measure a X-ray diffraction pattern of the samples before measuring the neutron pattern. However, we have to be aware that some phases may have peaks with a completely different intensity in neutron and X-ray patterns. Thus, a phase may be very easily visible in an X-ray pattern and almost absent in a neutron pattern or vice-versa. Should something unexpected appear in neutron diffraction data, the most recent version of the PDF4+ database is able to search-match neutron intensities against the subset of entries with known crystal structures.

3.3.2 Quantitative Phase Analysis

Once the phases are identified it is possible to obtain quantitative information about their relative abundance. Many techniques have been developed based on the analyses of intensities of individual peaks due to different phases contributing to the pattern, on whole pattern intensity analysis, or Rietveld refinement. More details

can be found in the book by Dinnebier and Billinge [6] or the book by Pecharsky and Zavalij [7]. It should be pointed out that extreme care should be taken when determining and interpreting quantitative composition. Results can be modified by methods of sample preparation, data collection, and analysis. More reliable results are obtained when a known amount of a foreign phase is added to the sample. This known phase will serve as a calibration for phase abundance. However, this technique is not always possible for a number of reasons: mixing the powder with a foreign material is impossible; there are peaks of the foreign phase that overlap with phases to be analysed; the foreign phase could react with the material; etc. The presence of an amorphous phase has also to be taken into account. More details on phase analysis including the amorphous phase content can be found in the proceedings of the excellent powder diffraction school from the series of Erice schools [8].

3.3.3 Peak Width

The shape and width of the peaks in a powder pattern are determined by instrumental effects, i.e. optics of the diffractometer and deviation of the real crystal from an ideal one, such as crystallite size, lattice defects, for example dislocations, described usually by an empirical parameter called microstrain, and stacking faults.

The simplest expression for peak broadening due to crystallite size is the Scherrer formula:

$$\beta_D(2\theta) = \frac{K\lambda}{<D>\ \cos\theta} \tag{3.4}$$

where β_D is the integral breadth of the peak (ratio between peak area and peak maximum) due to crystallite size, λ is the wavelength, $<D>$ is the average crystallite size, θ the Bragg angle, and K is the so-called Scherrer shape factor (usually taken as 0.9). The use of the integral breadth β_D instead of more common Full Width at Half Maximum (FWHM) H in the Scherrer formula makes the resulting crystallite size less dependent on the shape of the peak (rather Lorentzian or rather Gaussian). Peak width dependence on microstrain is given by the equation:

$$\beta_\varepsilon(2\theta) = 4\varepsilon\tan\theta \tag{3.5}$$

where β_ε is the integral breadth of the peak due to microstrain ε. These two expressions could be combined to give the total peak broadening $\beta = \beta_D + \beta_\varepsilon$. This leads to the so-called Williamson–Hall plot.

$$\beta(2\theta)\cos\theta = \frac{K\lambda}{<D>} + 4\varepsilon\sin\theta \tag{3.6}$$

In computing the peak broadening, the instrumental contribution should be subtracted, i.e. the peak profile due to the instrument must be deconvoluted from the observed peak profile. The deconvolution depends on the shape of both profiles. For a simple case when both profiles have the Gaussian shape the subtraction using the FWHM takes the form:

$$H = \sqrt{H^2_{\text{measured}} - H^2_{\text{instrument}}} \tag{3.7}$$

Usually, the instrumental contribution to broadening is evaluated by taking a diffraction pattern of a well-crystallized sample that has negligible size broadening and no microstrain. A common standard used for this purpose is the NIST SRM660 series of LaB_6 standards. SRM660b and the newly released SRM660c were made using the ^{11}B isotope of boron to make them "neutron-friendly". The earlier SRM660 and SRM660a were made with natural boron with the resulting absorption problem that is discussed further in Sect. 3.4.4.

A Williamson–Hall plot should ideally give a straight line whose slope gives the microstrain and intercept the crystallite size. Moreover, such a plot could give an indication of common trends within a family plane. For example, if several $h00$ reflections seem to form a straight line that is above the line of other hkl reflections could mean that the powder crystallites are thinnest in the direction perpendicular to lattice planes $\{h00\}$. Williamson–Hall plots are relatively simple to make and give key crystallographic parameters in a visual manner, and can be used for relative comparison between samples. However, when quantitative results are of importance modern methods such as Whole Pattern Modelling should be preferred [9]. For more details see the books by Dinnebier and Billinge [6], Pecharsky and Zavalij [7], or the proceedings from the Erice school [8].

3.4 Instrumentation

In neutron diffraction experiments, the quality of the measured pattern strongly depends on the counting rate. This means that the first criterion for a neutron source is the flux of available neutrons usually given in neutrons per square centimetres per second (n cm^{-2} s^{-1}). There are presently two main ways to produce neutron for diffraction experiments: nuclear reactors and high energy particle accelerators. Once the neutrons have been produced they have to be "tailored" in order to maximize their interaction with the material. The nature of this preparation will depend on the material's characteristics that are probed. In this section we will briefly review the main sources and preparation techniques for neutrons used for diffraction measurements.

3.4.1 Reactors

In a nuclear reactor, thermal fission of a suitable isotope (usually ^{235}U or ^{239}Pu) takes place with production of neutrons and two fission fragments of unequal masses. For example, fission of ^{235}U produces on average 2.7 fast neutrons. The fission reaction is self-supporting when one of these neutrons causes fission in another ^{235}U atom. This leave, on average, 1.7 neutrons which will be used for diffraction experiment. The energy spectrum of neutron produced by fission is in the MeV range. However, for diffraction experiments neutrons should have wavelength of the order of about 10 nm which correspond to meV energy range. This range of energy corresponds to neutron in thermal equilibrium at room temperature which is why they are called "thermal" neutrons. The thermalization is achieved by using a moderator made of light atoms (usually H_2O or D_2O) and kept at a temperature near 300 K. Some scattering experiments needs neutrons with wavelength considerably different than 10 nm. In these case, a cold source (usually D_2 at $T \approx 20$ K) or a hot source (graphite heated at $T \approx 2000$ K) at inserted into the moderator in order to get neutron with respectively longer and smaller wavelength.

There are a number of research reactors distributed all over the world. The two facilities with highest neutron flux are ILL in France and HFIR in the USA which have fluxes of the order of 10^{15} n cm^{-2} s^{-1}. Other major reactors such as NRU in Canada, FRM-2 in Germany, and OPAL in Australia, have fluxes of the order of a few 10^{14} n cm^{-2} s^{-1}. A list of all nuclear reactors and their websites can be found on the neutronsource.org website [10].

3.4.2 Spallation Sources

Getting higher neutron flux in nuclear reactors is problematic because the power density in the core of high flux fission reactors is limited by the cooling rate of the core (~7 MW l^{-1}). The way to go around this problem and to generate high flux neutrons is to use pulsed spallation sources. In a spallation source intense bursts of neutrons are produced by bombarding heavy atoms target with high energy particles (~1 GeV). The particle is usually a proton which has been accelerated in a synchrotron (linear and cyclotrons are also used). The particle strikes a target made of a heavy metal (depleted uranium, tantalum, mercury, tungsten, etc.) and incorporates within the target atom nucleus. The excited nuclei then cascade down by ejecting neutrons which are absorbed by other nuclei. The final step is the de-excitation of the various target nuclei followed by the emission of numerous lower-energy neutrons. Extremely high neutron flux is generated within each pulse (~10^{19} n cm^{-2} s^{-1}). This sequence of events takes place within 10^{-15} s after the nucleus is hit and about 20 neutrons are produced per incident proton. Therefore, the time distribution of spallation neutrons is determined by the time distribution of the incident high energy proton. For most spallation sources, this pulse frequency is

50 or 60 Hz. As for the reactors, the generated neutrons are slowed down in moderators filled with liquid hydrogen or liquid methane to the energies that are needed for the scattering instruments. The moderator is designed in such a way that the neutrons from an individual pulse are not slowed down too much in order to prevent merging with the next pulse and thus getting a continuum of neutrons. This means that the neutrons will arrive at the experimental station in well-separated pulses. As the pulse travels toward the sample it will spread out because the shorter wavelength neutrons have higher velocities than longer wavelength neutrons. Therefore, the neutron wavelength can be deduced from the arrival time of the neutron. In this way, the entire spectrum of wavelengths could be used for diffraction.

Spallation sources are getting more popular than reactors because of their higher flux and safety issues associated with nuclear reactors. The main spallation sources are ISIS at the Rutherford Appleton Laboratory in United Kingdom, the Spallation Neutron Source (SNS) at Oak Ridge National Laboratory in the USA, the Japan Proton Accelerator Research Complex (J-PARC) in Japan. Usually, spallation sources are operated in pulsed mode. The exception is the Paul Scherrer Institut (PSI) continuous spallation neutron source at the Swiss Spallation Neutron Source in Switzerland. A list of spallation sources in operation and under construction could be found on the neutronsource.org website [10].

3.4.3 Neutron Powder Diffractometer

3.4.3.1 Constant Wavelength (CW) Techniques

Constant wavelength diffractometers are associated with reactor neutron sources. For thermal neutrons (~300 K) the maximum intensity occurs at a wavelength of about 0.1 nm but reasonable intensities are available in the range 0.08–0.2 nm. Figure 3.5 shows a schematic of a constant wavelength neutron powder diffractometer.

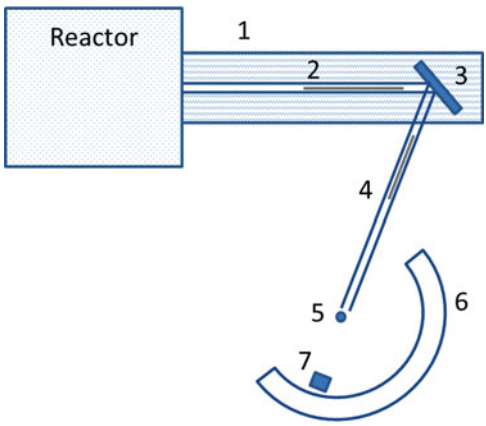

Fig. 3.5 Schematic of a constant wavelength neutron powder diffractometer. (*1*) radiation shielding; (*2*) neutron flight tube and collimator; (*3*) monochromating crystal; (*4*) flight tube and secondary collimator; (*5*) sample; (*6*) detector bank; (*7*) beam stop

Neutrons emerging from the moderator travel through a flight tube where they are collimated before striking a single crystal monochromator. Diffracted neutrons from the monochromator travel through another flight tube with collimator before reaching the sample. Neutrons diffracted by the samples are counted by the detector bank. A beam stop ensure that the direct beam does not reach the detector.

Collimation in the flight tubes is done by absorbing the divergent neutrons. This is done by inserting inside the tube, and parallel to the beam thin metal plates or stretched polymer sheets covered with absorbing paint. These will absorb diverging neutrons. Usually, only in-plane collimation is performed and this could be as good as 5 min of arc. Out-of-plane divergence is often several degrees.

The constant wavelength is selected by the monochromator based on a crystal diffracting only the neutrons of required wavelength. A crystal monochromator is set at a fixed angle with respect to the incoming and outgoing neutron flight tubes. Only neutrons having a wavelength satisfying Bragg's law will enter the outgoing flight tube. The angle between the incident and the reflected beams is called the "take-off angle" of the crystal monochromator. Many materials can be used for monochromators, the most commons are: graphite, copper, silicon, and germanium. A perfect crystal will produce a diffracted beam over a very small range of angles, typically a few minutes of arc. This corresponds to a very small wavelength band ($\Delta\lambda/\lambda \approx 10^{-4}$). However, this means that the neutron flux on the sample will be very low. Therefore, in general, monochromators are plastically deformed in order to create imperfections and increase the wavelength band.

Detection of neutrons is done by a bank of detectors covering a wide range of scattering angles simultaneously. Most detector banks span about 80° in 2θ. Details of detection are given in Sect. 2.2.2.

3.4.3.2 Time-of-Flight Techniques

In order to understand the basic principle of a Time-of-Flight (ToF) diffractometer let us write the Bragg equation in a slightly different way than Eq. 3.1 [11].

$$\lambda_{hkl} = 2d_{hkl} \sin\theta \tag{3.8}$$

We see that if θ is fixed then each interplanar spacing (d_{hkl}) is associated with a particular wavelength (λ_{hkl}). Thus, an incident neutron beam having a wide range of wavelengths can produce many Bragg peaks observed at the same θ angle and associated with a wide array of interplanar spacings. The incident neutrons are selected using bandwidth choppers to produce very short pulses on the sample. The diffracted neutrons are therefore also grouped in pulses propagating at a given angle 2θ toward one of the detectors. The division of the detected neutrons according to their wavelength λ is done by measuring their energy as their ToF between the sample and detector, hence the name of the ToF method. Multiple peaks can therefore be detected at the same position on the detector due to their separation in time.

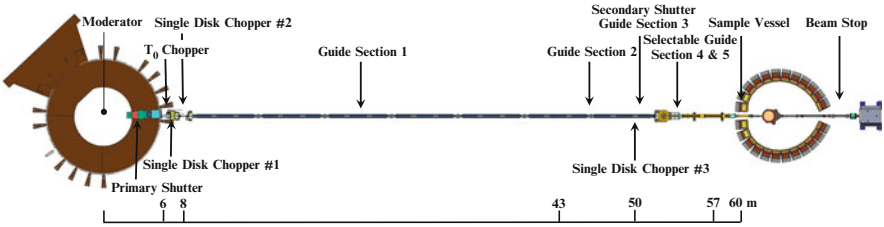

Fig. 3.6 Schematic top view of the high-resolution general purpose powder diffractometer: Powgen

In the first generation ToF powder diffractometers the detectors were grouped into discrete banks around a few selected scattering angles. In order to cover most of the interesting d_{hkl} a broad wavelength range of incident neutrons was necessary. The second generation powder diffractometers expanded the angular coverage both in-plane and azimuthally about the beam, but still maintained the multiple detector bank concept with data reduced effectively to a few scattering angles. The most recent ToF diffractometers rely more on sophisticated data collection and reduction methods analysis rather than the traditional bank-based instrument design. The best example of such a scheme is the POWGEN diffractometer installed at the Spallation Neutron Source (SNS) in Oak Ridge. In this third-generation diffractometer, all detectors data are combined into one histogram (i.e. powder pattern) of high-resolution which makes it a very flexible instrument [12]. Figure 3.6 shows a schematic top view of POWGEN. The long flight path (60 m) is required to achieve high-resolution. Because of the 60 Hz frequency of the source and the long flight path, the instrument has a bandwidth of about 0.1 nm.

The moderator used for POWGEN is a cryogenic poisoned liquid H_2. The straight guide section is a supermirror neutron guide which provides high flux with homogeneous distribution of neutrons on the sample. It also serves to reduce the vertical and horizontal beam dimension. Between the moderator and sample there is a series of choppers. The first chopper (T_0) is used to cut out the very high energy prompt pulse neutrons which otherwise would travel to the instrument and cause increased background levels detrimental to data quality. The following choppers (bandwidth choppers) are used to set the incident wavelength bandwidth and centre by selection of appropriate rotation frequency and phase. The locations of the bandwidth choppers are specifically chosen to prevent frame-overlap; the condition in which fast neutrons from one pulse catch up with slow neutrons from the preceding pulse. The bandwidth choppers could be operated at a slower speed, e.g. 30, 20, or 10 Hz as opposed to the pulse source rate of 60 Hz. In this case, a wider wavelength bandwidth is transported to the sample and consequently diffraction data are collected over a much broader d-spacing range, e.g. 0.06–0.62 nm, in a single measurement. However, operating at a lower frequency involves a trade-off with reduced intensity and resolution.

Table 3.2 Advantages of CW and ToF instruments (from [11])

CW	ToF
Peak shapes are far simpler to model	The whole incident spectrum is utilized
Incident beam spectrum is better characterized	Data are collected to very small d-spacing
Large d-spacings are easily accessible	Very high-resolution is readily attained by using long flight path
Data storage and reduction is simple	Resolution is constant across the whole pattern
Absorption and extinction corrections are relatively straightforward	Complex sample environment is very readily used if 90° detector bank is available
Can fine tune resolution during an experiment	Simpler to intersect a large portion of the Debye–Scherrer cones

The detector angular coverage is $30° < 2\theta < 150°$ which covers an area of 6.9 m^2. High-resolution diffraction data cover d_{hkl} spacing between 0.03 and 1 nm with a resolution of $0.001 < \Delta d/d < 0.016$. The detector modules are based on large ^{6}LiF:ZnS:Ag neutron scintillation screens optically coupled to green enhanced photomultiplier tubes [13].

3.4.3.3 Comparison CW vs. ToF

When considering performing a NPD experiment the user may ask which type of powder diffractometer should be used? There is no simple answer to that question, as there are many aspects to be considered. Each type of instrument has its advantages and disadvantages. Kisi and Howard have compiled a comparison table of the technical advantages of both techniques [11]. This is reprinted in Table 3.2. However, it must be pointed out that most investigations could be performed on either system as long as the experiment is well planned. In practice, the main decisive factor usually turns out to be availability of beam time at a particular neutron source.

3.4.4 Sample

A major advantage of neutrons over X-rays is their high penetration in materials. This enables the utilization of thick sample cells and complex environments (furnaces, electrochemical cells, high pressure cells, etc.). More details about this are given in Sect. 3.7. Disadvantages of neutrons are their weak interaction with the matter, and that neutron sources do not have fluxes as intense as electrons or photon sources. This means that larger samples have to be used. As very few samples are self-supporting solids, some form of sample cell should be used. The geometry and nature of the sample cell should be in accordance with the diffractometer specifications and nature of the sample. A widely used material for sample containers is vanadium. The reason is that it has a very small coherent cross section and thus is

almost "invisible" in the diffraction pattern. The drawback of vanadium is that its mechanical properties do not make it very suitable for high pressure in-situ experiments particularly for hydrogen gas as vanadium absorbs hydrogen and can easily form a hydride. One way to get around this problem is to coat the interior of the cell with copper [14, 15]. Another material that could be used as sample holder is an alloy of composition of 33.44 at.% Zr and 67.56 at.% Ti ($Ti_{2.08}Zr$). This alloy has an average coherent scattering length of zero and thus will not contribute to the diffraction pattern. However, for in-situ experiments involving hydrogen at high pressure and temperature this alloy is not suitable due to hydrogen embrittlement [16]. A way to prevent embrittlement in a sample holder made of $Ti_{2.08}Zr$ is to include a thin-walled AISI316 steel liner [17].

The nature of the sample is also important. The first thing to check is the neutron absorption. As already discussed some elements such as Cd, Gd, and B have extremely large absorption cross sections: even a small amount of these elements in a sample will make it unsuitable for diffraction. As neutron fluxes are small, samples have to be as thick as possible without having too much multiple scattering or absorption. The rule of thumb is to have no more than 10 % of the incident beam scattered [18]. Neutron scattering lengths and absorption change with isotope so sometimes making a sample enriched in a particular isotope can reduce or eliminate the problem. There are a number of websites and software available that will do this calculation. However, one has to remember that, for powder samples, the density in the sample cell is about 0.5–0.67 of the crystallographic density (powder packing).

3.4.5 Materials Containing Hydrogen

It was mentioned in Sect. 2.3.2 that nuclei with even number of protons and neutrons do not contribute to incoherent scattering. Let us take a closer look at hydrogen and its isotope deuterium. The nuclear spin quantum number of hydrogen is ½, thus the neutron–hydrogen system has a triplet state (total spin number = 1) and a singlet state (total spin number = 0). The scattering length of the triplet state and singlet states are respectively 10.85×10^{-12} cm and 17.50×10^{-12} cm. Using these values in Eq. (2.11) gives a very high incoherent scattering cross section (80.3 barn). For deuterium the nuclear spin quantum number is 1 and the incoherent scattering cross section is then 2.05 barn.

Because of the very high incoherent scattering cross section of hydrogen, powder diffraction of hydrogenous materials will have a very high background and be very difficult to analyse. Thus, for diffraction experiments hydrogen is almost always replaced by deuterium. This replacement has essentially no effect on the crystal structure but it may change the thermodynamic properties [19]. The coherent neutron scattering length b_c of hydrogen is −3.74 fm, and that of deuterium is 6.67 fm, i.e. deuterium contributes even more to the diffraction than hydrogen which, on the other hand, has advantage of negative scattering length, i.e. higher scattering contrast to most of metals. Recently it was shown that thanks

to high flux neutron sources providing low statistical noise in the measured powder patterns, hydrogenated samples may be successfully studied [20].

3.5 Rietveld Method

3.5.1 Principle of Rietveld Refinement

There is a wealth of information on Rietveld refinement methods. Here we will expose the basic facts and working knowledge for the beginner. More complete information can be found in the classical book by Young [21], or more recent references [6, 22, 23]. Before the advent of Rietveld refinement the way to analyse a powder diffraction pattern was to fit each individual Bragg peak as, for example, in the Williamson–Hall technique and extract the individual Bragg intensities I_{hkl} which are then analysed in the same way as single crystal data. However, due to low resolution of the diffractometer and also peak overlap in multiphase alloys, many Bragg peaks could not be fully resolved. This could be solved by fitting a number of Gaussians to a group of overlapping peaks. Other more complex peak shape than Gaussian could be used in order to take into account peak asymmetry, sample strain, etc. But no matter what kind of peak shape is used, there are still the problems of partitioning and using a large number of parameters: basically four for each peak even for a simple Gaussian (position, height, width, and background). When the peaks are strongly overlapping these parameters are highly correlated, and the errors in the resulting Bragg intensities become important. Partitioning is a problem with highly or completely overlapping reflections where there is the problem of how much intensity to assign to each reflection. Commonly it is split 50:50 but this may not be accurate.

Rietveld proposed to use the whole pattern and refine the actual structural parameters together with the parameters constraining the peak shape and width between all observed Bragg peaks [24]. In a single dataset Rietveld did not use the integrated intensity of Bragg peaks I_{hkl} but profile intensities y measured at individual points in the powder pattern. The structural parameters, having physical reality, are much less correlated with each other. In addition there are far fewer of them as well as significantly fewer peak profile parameters. Peak positions are determined by at most six lattice parameters (three angles α, β, γ and three axis lengths a, b, c). The peak intensities are determined by the nature and coordinates of the atoms in the unit cell. Peak profiles are described by analytical functions such as Gaussian or Lorentzian functions or a combination of them. Peak widths described by the FWHM can be modelled by a variety of expressions but a simple and effective one has been given by Caglioti et al. [25, 26].

$$H^2(2\theta) = U\tan^2\theta + V\tan\theta + W \tag{3.9}$$

Thus, only three parameters (U, V, W) may be needed to characterize the peak width. The Caglioti formula has been derived from the description of the mosaicity of single crystals used as monochromators for neutron radiation, but it is used empirically also for X-ray sources. The background can be modelled by various functions of the scattering angle 2θ or ToF. Thus, in Rietveld refinement, instead of four parameters for each peak, there are typically only a few tens of physically relevant parameters.

3.5.2 Recording and Calculating Powder Pattern

The goal of a Rietveld refinement is to get a calculated diffraction pattern as close as possible to the one recorded by the diffractometer. Obviously, the most important step in a Rietveld refinement is the recording of the diffraction pattern. One should never rely on Rietveld refinement to extract useful information from a poorly recorded pattern. Desirable characteristics for a sample have been discussed in the preceding section. The more time one spends in the synthesis of a well-crystallized sample, the less time is needed for the analysis of the measured powder pattern. A good practice in choosing the measuring strategy is to consult with the instrument team *before* preparing your sample. They can suggest which type of sample holder will be appropriate for your measurement and indicate the type and size of sample required. Additionally an estimate of the time required will be helpful in preparing a proposal for beamtime.

In recording a pattern some general rule-of-thumb can be used. First, the pattern should include the Bragg peak with the biggest d_{hkl} (or smallest hkl values) corresponding to the crystal structure studied. For a CW diffractometer this is the Bragg peak at the smallest angle 2θ. If this peak is not recorded then it may be quite difficult to correctly identify the crystal structure and Rietveld refinement will be much harder to perform. It is good practice to record first an X-ray pattern of the sample to be studied by neutron diffraction. That way the user can have prior knowledge of the crystal structure and lattice parameters thus making the choice of scanning range for neutron diffraction much easier. Usually, in neutron diffraction the resolution is fixed by the geometry of the apparatus: detector bank for CW diffractometer and wavelength range/position of detector for ToF apparatus.

The second experimental parameter the user has to choose is the recording time. One has to remember that, for CW diffractometer the number of counts in a fixed time is governed by Poisson statistic. Therefore, the standard deviation from the true mean is given by:

$$\sigma = \sqrt{y} \tag{3.10}$$

In principle the intensity in Eq. (3.10) should be the "true" intensity but using the measured intensity, i.e. number of scattered neutrons observed by the detector, is a good approximation. We see that to improve precision by a factor of two means that

intensity has to be quadrupled, meaning that for CW diffractometer recording should be four times longer. This means that increasing precision by "brute force" is usually not practical.

In the preceding derivation we have assumed that the background intensity is small compared to the Bragg peaks' intensities. However, when the background intensity is non-negligible the situation is more complicated. Although the precision of the peak count is still given by Eq. (3.10) the precision of the Bragg intensity is influenced by the precision of the background [27]. Compared to the zero-background case, a Bragg peak with a high background will have a lower absolute precision but the relative precision once the background is subtracted will be higher. Hill and Madsen analysed the effect of counting time on diffraction patterns [28]. They found that reasonable crystal parameters values could be obtained with peaks only 200–500 counts above background. Moreover, they showed that exceeding 2000–5000 counts above background on the strongest Bragg peaks did not improve the quality of the refined crystal structure parameter [29]. Of course, if a minor phase is present, higher counting time may be necessary. The important message is that longer counting time at CW diffractometer not necessarily improve the precision of structural parameters refined by the Rietveld method. On the other hand, high precision of the measured intensities y, i.e. lower statistical noise in the data, is required for ab initio structure solution which starts with indexing of the observed Bragg peaks where often weak peaks must be reliably detected.

3.5.2.1 Calculated Pattern

Let us now look at the calculated pattern. The quantity to be minimized in Rietveld refinement is the residual S_y:

$$S_y = \sum\nolimits_i w_i (y_i - y_{ci})^2 \tag{3.11}$$

where y_i and y_{ci} are respectively the observed and calculated intensities at the ith step. The weight w_i is the inverse of the variance in the determination of y_i.

$$w_i = 1/y_i \tag{3.12}$$

When multiple detectors are employed then the average intensity is used and the weight is given by:

$$w_i = n/y_{i(\mathrm{avg})} \tag{3.13}$$

where n is the number of detectors and $y_{i(\mathrm{avg})}$ is the mean of intensity. The calculated intensity is given by a combination of nonlinear and transcendental analytic or nonanalytic functions [22].

$$y_{ci}(2\theta_i) = \sum^{\text{phases}} \left(S_{\text{ph}} \sum\nolimits_{hkl(\text{phase})} \left(K_{hkl} |F_{hkl}|^2 \Phi_{hkl}(2\theta_i - 2\theta_{hkl}) \right) \right) + b_i \quad (3.14)$$

where the first sum runs over all phases present in the diffraction pattern and the inner sum runs over all *hkl* of each phase. The scale factor S_{ph} is proportional to the weight fraction of each phase and is the basis of the quantitative phase analysis. K_{hkl} is the product of various correction factors and F_{hkl} is the structure factor. The profile function $\Phi_{hkl}(2\theta_i - 2\theta_{hkl})$ normalized to have its integral equal to one represents the contribution of the *hkl* peak to the intensity at point *i*. The background contribution is denoted by the background point b_i. Equations (3.11) and (3.14) are the fundamental equations of the Rietveld method. Without going into any details let us look at the parameters individually.

3.5.2.2 Scale Factor

For a CW neutron diffractometer the scale factor is given by [11]:

$$S_{\text{ph}} = \left(\frac{\Omega_0 \lambda^3 h}{8\pi r} \right) \left(\frac{m}{ZMV_c} \right) \quad (3.15)$$

The first parenthesis is the apparatus contribution: Ω_0 is the incident flux of neutrons (neutrons $\text{m}^{-2}\,\text{s}^{-1}$), λ is the neutron wavelength, *r* is the sample to detector distance, and *h* is the detector height. The second parenthesis is the sample contribution: *m* is the total mass of the phase present in the sample, *Z* is the number of formula units per unit cell, *M* is the mass of one formula unit, and V_c is the unit cell volume. Rietveld refinement will optimize S_{ph} for each individual phase in the whole pattern. From these, one can find the relative abundance of the phases by the relation:

$$w_{\text{ph}x} = \frac{S_{\text{ph}x} Z_{\text{ph}x} M_{\text{ph}x} V_{c\text{ph}x}}{\sum_i S_{\text{ph}i} Z_{\text{ph}i} M_{\text{ph}i} V_{c\text{ph}i}} \quad (3.16)$$

where the subscript ph*x* indicate phase *x* and $w_{\text{ph}x}$ is the relative mass abundance of phase *x*. The sum runs over all crystalline phases present in the diffraction pattern. This equation does not take into account the effect of absorption. As neutrons are highly penetrating this usually does not pose a problem. Any non-crystalline phases are not taken into account in Eq. (3.16).

The correction factor K_{hkl} is the product of various contributions.

$$K_{hkl} = m_{hkl} A_{hkl} L P_{hkl} \quad (3.17)$$

where m_{hkl} is the multiplicity of the reflection *hkl*, A_{hkl} is the absorption correction, *L* the Lorentz factor, and P_{hkl} is a correction for preferred orientation.

3.5.2.3 Multiplicity of the Reflection *hkl*

The multiplicity m_{hkl} of the reflection *hkl* is a number of lattice planes (*hkl*) which are equivalent by the symmetry operations of the Laue group, i.e. the point group symmetry of the diffraction pattern [1]. As they have all the same value of the interplanar distance d_{hkl}, the reflections *hkl* related to these lattice planes will exactly overlap to one Bragg peak in the powder pattern. This is not a problem as they have all the same value of the structure factor amplitude $|F_{hkl}|$. Multiplicity depends on the order of the Laue group and it is related to the multiplicity J_{hkl} of the given crystal form [*hkl*] which is, however, given by the point group of the crystal. As the exact overlap of the reflections in the powder pattern is given by the point group symmetry of the empty lattice, i.e. the highest symmetry in the given crystal system, in some cases also the non-equivalent reflections *hkl* having identical d_{hkl} will overlap to one Bragg peak. The multiplicity varies between 1 and 48. Multiplicity could be useful to identify symmetry change during a phase transformation. For example, if during transformation of a cubic phase the 200 peak splits into 2 peaks with intensity ratio of 2:1 then we could expect that the new phase is tetragonal [11]. On the other hand, if it is the 111 peak that is split with a 3:1 intensity ratio then the new phase will be rhombohedral. Finally, a word of caution: in some cases lattice planes of different *hkl* may have exactly the same Bragg peak position even if they are not equivalent by the Laue group. A good example of this is in the cubic symmetry the 333 and 511 peaks which have the same Bragg angle θ because they have identical interplanar distance d due to the high symmetry of the cubic lattice.

3.5.2.4 Absorption Factor

There may be some confusion in the name and origin of this correction. One has to distinguish between extinction and absorption. If we consider a perfect crystal which is oriented in a Bragg condition then, the diffraction of successive lattice planes will gradually diminish as it penetrates into the crystal. Thus, the whole crystal may not be irradiated. This is called primary extinction [30]. An imperfect crystal has dislocations that actually make the crystal a mosaic of small crystallites thus making primary extinction a small effect. The effect is even smaller in a powder sample. This is then referred to as secondary extinction.

The absorption of the neutrons in the matter by the nuclei–neutrons interaction is the basis of the neutron radiography (Chap. 7). The effect of absorption on the intensity (I) of the neutron beam passing through the matter is given by:

$$I = I_0 \exp(-\mu t) \tag{3.18}$$

where I_0 is the intensity when the beam enters the sample, t is the sample's thickness, and μ is the macroscopic linear absorption coefficient. The absorption coefficient is the addition of several reactions including radiative capture.

It depends on the neutrons velocity (energy), and may considerably vary between different isotopes of a given element. It is usually very low with the exception of several isotopes like ^{10}B, ^{113}Cd, ^{149}Sm, ^{155}Gd, and ^{157}Gd. The linear absorption coefficient of all elements and isotopes is available in tabular form [31, 32]. To a good approximation, absorption is independent of the physical state of the absorber other than its density. Careful selection of the neutron's energy and isotopically pure samples may allow characterization by neutron diffraction of crystal structures in normally high absorbing samples such as europium and samarium hydrides [33]. Usually, the material to be studied contains more than one kind of atom. In that case, it is easier to work with the *mass absorption coefficient* (μ/ρ) where ρ is the solid density. The mass absorption for a phase is then the summation over all elements presents in that phase.

$$\left(\frac{\mu}{\rho}\right)_{\text{phase}} = \sum\nolimits_i w_i \left(\frac{\mu}{\rho}\right)_i \tag{3.19}$$

where w_i is the weight fraction of element i. In a similar way, if the sample has many different crystallographic phases then the mass absorption coefficient is given by:

$$\left(\frac{\mu}{\rho}\right)_{\text{sample}} = \sum\nolimits_j w_j \left(\frac{\mu}{\rho}\right)_j \tag{3.20}$$

where here, the index j runs over all phases present in the sample.

The attenuation effect also depends on the shape of the sample. In powder neutron diffraction the sample holder is usually cylindrical. The correction for this type of geometry has been tabulated [34]. Bowden and Ryan have calculated absorption correction for cylindrical and annular specimens [35]. Contrary to the common belief, they found that the shape of the sample holder has a stronger influence for specimen having higher absorption. They also found that absorption has an effect on the precise determination of peak positions.

Because of the highly penetrating nature of neutrons, absorption correction in neutron diffraction is much less than for X-rays. For most elements the linear absorption μ is less than 1 cm^{-1}, therefore, in CW instruments, for samples of less than a few mm thick absorption can be ignored [18]. Wide d-range of ToF instruments makes them more sensitive to absorption, and should be refined. On the other side, as multiple wavelengths are used with ToF it is possible to refine absorption and displacement parameters at the same time which is impossible with CW instruments. A correction for the sample absorption is commonly found in Rietveld refinement codes and should be used when significant absorption is expected.

3.5.2.5 Displacement Factor

The displacement factor is actually composed of two parts: one is the static displacement of the atoms from the average positions due to disorder; the other one represents the thermal vibrations. Diffraction cannot distinguish these two contributions from the data measured at one temperature.

Let us discuss here thermal displacement, also called the Debye–Waller factor. It represents the oscillation of the atom around its equilibrium position. A full derivation is too lengthy to be given here. More complete discussions are in [2, 11]. Here, we will just quote the expression for the atomic Debye–Waller factor:

$$T = \exp\left[\frac{-B_{\text{iso}} \sin^2\theta}{\lambda^2}\right] \tag{3.21}$$

where B_{iso} is called the atomic temperature factor. This expression is for an isotropic displacement. For example, a site symmetry *m3m* could only accommodate an isotropic displacement. In general the atomic temperature factor is a matrix and the temperature factor could be anisotropic. However, in most cases the quality of the data is not sufficient and to keep a refinement stable we have to assume an isotropic temperature factor. It should be emphasized that in principle a different temperature factor is associated to each atom in the lattice, although this is never achieved in powder diffraction due to insufficient information in a 1D dataset.

3.5.2.6 Lorentz Factor

The Lorentz factor is a continuous function of the scattering angle 2θ, and may be therefore applied to the point intensities y directly or to the Bragg intensities I_{hkl}. The Lorentz factor is in fact due to two geometrical effects. The first one comes from the finite spread of wavelength (λ) in the monochromatized beam and of interplanar spacing (d_{hkl}) in a real crystal. When this is taken into account in Bragg's law it gives some range in 2θ where the crystal diffracts. The width of this range is proportional to $1/\sin 2\theta$. The second effect is coming from the constant length of the receiving slit. As the Bragg peaks form a cone of opening angle 4θ the part of that cone intercepting a straight slit will vary with 2θ. This contribution is proportional to $1/\sin\theta$. The combination of these two effects gives the Lorentz factor for CW powder diffractometer:

$$L(2\theta) = \frac{1}{\sin 2\theta \ \sin\theta} \tag{3.22}$$

This function is illustrated in Fig. 3.7. From this figure we can see that, for structures with large interplanar spacing (i.e. large lattice parameters), the low angle Bragg peaks will most likely have high intensities due to the Lorentz factor.

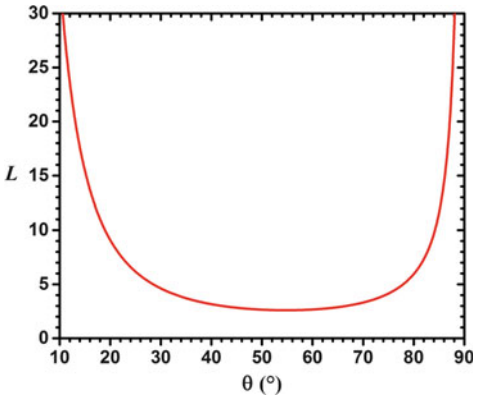

Fig. 3.7 Lorentz L factor for CW powder diffraction

We should mention that for X-ray diffraction the Lorentz factor is usually combined with the effect of X-ray polarization. It is then called the Lorentz-polarization factor and has a different functional form. However, in the present case as neutrons are not polarized upon scattering only the Lorentz factor is needed. The expression of the Lorentz factor for ToF diffractometers is [11]:

$$L_{hkl} = d_{hkl}^4 \sin\theta_{hkl} \tag{3.23}$$

3.5.2.7 Preferred Orientation

Preferred orientation (often called texture) is the deviation from randomness of the distribution of the crystallite orientation in the powder sample, which is one of the basic assumptions of powder diffraction. In general preferred orientation is much less a problem for neutron diffraction than in XPD because of the larger sample and the fact that most of the diffracting crystallites are far from the surface and thus less influenced by the surface geometry. In principle, to get an ideal powder diffraction pattern one has to make sure that all crystallites are randomly oriented in order to have the correct fraction of the specimen volume in the reflecting position for each Bragg peak [7], i.e. reliable relative intensities. Preferred orientation usually occurs when the crystallites shapes are anisotropic (plate-like or needle-like) and results in the introduction of non-random crystallite orientation due to the packing of specimen into the sample holder. For example, plate-like particles will tend to align parallel to each other and to the surface of a flat sample holder. Preferred orientation should not be confused with the situation when there are too few crystallites being irradiated and the powder average is poor [36]. The former isn't fatal to the accurate analysis of a diffraction pattern but the latter is.

Preferred orientation is a major problem in the analysis of a diffraction pattern, especially when the peaks intensities are the basis for structure solution [37]. Although there are ways to model the preferred orientation the best practice is to do all possible efforts to prevent it by proper sample preparation.

In NPD the sample holder is usually cylindrical. In this case the best empirical model describing the distribution of crystallites orientation is one with the axial symmetry where the symmetry axis is along the sample holder cylinder. Integration about this distribution at the scattering angle for each Bragg peak could be expressed by the so-called March–Dollase model [38].

$$P_{hkl} = \left(R^2 \cos^2\alpha + \frac{\sin^2\alpha}{R}\right)^{-3/2} \tag{3.24}$$

where R is an adjustable parameter and α is the angle between the lattice plane hkl and the preferentially oriented lattice plane. This equation applies to plate-like ($R < 1$) and needle-like ($R > 1$) crystallites. For an ideal randomly oriented powder $R = 1$. The advantage of using March–Dollase model is the single refinable parameters. The disadvantage is that it may give an incomplete preferred orientation correction, because the axial symmetry of the orientation distribution, so-called fibre texture, is only an approximation of the real powder distribution in the sample holder. A purely mathematical expression independent of physical model is actually a better way to correct for preferred orientation. In 1965 Roe and Bunge proposed independently to use spherical harmonics to describe preferred orientation [39, 40]. A complete description of this approach is too lengthy to be shown here and we refer the interested reader to a complete derivation given by Popa [41].

3.5.2.8 Structure Factor

The structure factor has been explained in Chap. 2. Here we will just provide a summary. To help the discussion let's write the structure factor in a simpler way, keeping only the form factor and atomic position.

$$F_{hkl} = \sum\nolimits_n b_n \exp[2\pi i(hx_n + ky_n + lz_n)] \tag{3.25}$$

where the sum is over all atoms in the unit cell, and the position of the nth atom is (x_n, y_n, z_n). The important information here is that the atomic distribution is all encoded only in the structure factor and not in the other parameters. Going back to Eq. (3.14) it means that the intensities are dependent on the atomic coordinates.

From the structure factor we can understand the reason for systematic absence of some reflections. As an example take the monoclinic space group $P2_1$ with an atom on a general position (x, y, z). Applying the symmetry operation of the 2_1 axis which is in a standard setting parallel to b axis, there is another atom at position ($-x$, y+½, $-z$). Now, using 3.25 compute the structure factor for Bragg peaks having, for example, $h = l = 0$ we get:

$$F_{0k0} = b\{\exp[2\pi iky] + \exp[2\pi ik(y + ½)]\} \tag{3.26}$$

Rearranging this equation:

$$F_{0k0} = b\exp[2\pi iky]\{1 + \exp[\pi ik]\} \tag{3.27}$$

It is clear that the term between the curly brackets is equal to two when k is even and zero when k is odd. Therefore, lines with Miller indices $0k0$ are absent when k is odd and present when k is even. This is called the reflection condition and is written in the *International Tables for Crystallography* [1] as:

$$0k0 : k = 2n \tag{3.28}$$

Therefore, by observing systematic absences of certain families of peaks one could determine the proper space group.

In closing this discussion we have to briefly mention the so-called "phase problem". From Eq. (3.14) we see that the intensity is a function of the square of the structure factor. As the structure factor is a complex quantity it means that all information on the phase of the structure factor is lost when the intensities, i.e. squares of amplitudes of structure factors are recorded. This makes the determination of the crystal structure of an unknown material from the diffraction, and especially from the powder diffraction pattern a challenging task. In Rietveld refinement the starting atomic positions are already known so the phase problem is not of primary importance in the scope of this chapter.

NPD is mostly used in studying the hydrogen in materials for localizing the hydrogen (deuterium) in the matrix of previously known metal atom positions determined by X-ray diffraction. We will discuss this procedure in Sect. 3.6. A complete treatment of the ab initio structure solution from powder diffraction can be found in standard crystallographic texts [2, 7] or in a dedicated review [42].

3.5.2.9 Profile Function

Peak width has already been discussed in Sect. 3.4. Here we will discuss the shape of individual diffraction peaks in a powder pattern. The line shape should be expressed as a convolution of these three contributions [22].

$$\Phi_{hkl}(2\theta_i - 2\theta_{hkl}) = \mathrm{EP}(2\theta_i) \bigotimes \mathrm{IP}(2\theta_i) \bigotimes \mathrm{MS}(2\theta_i) \tag{3.29}$$

where $\mathrm{EP}(2\theta_i)$ is the emission profile, $\mathrm{IP}(2\theta_i)$ is the instrument contribution, and $\mathrm{MS}(2\theta_i)$ is the sample's microstructure. Over the years a number of profile functions have been used. In its first refinements, Rietveld used Gaussian functions. Later, more sophisticated functions have been proposed, especially the Voigt function (V) which is a convolution of a Gaussian (G) and a Lorentzian (L) functions.

$$V(x) = G(x) \bigotimes L(x) \tag{3.30}$$

where x is given by:

$$x = \frac{2\theta_i - 2\theta_{hkl}}{H_{hkl}} \tag{3.31}$$

and H_{hkl} is the FWHM of the hkl peak. While convolution is the correct operation to combine different contributions to the final shape of the diffraction peak, the Gaussian or Lorentzian functions stay just a mathematical approximation, even if very close to each physical event contributing to the diffraction profile. As the convolution is computationally intensive and difficult when the derivatives of the profile function are needed, as in the case of least-squares refinement, simpler profile functions were proposed. A function that approximates the Voigt function quite well is the so-called Pseudo-Voigt (pV) which is a sum of a Gaussian and a Lorentzian.

$$\mathrm{pV}(x) = (1 - \eta)G(x) + \eta L(x) \tag{3.32}$$

This peak shape could vary from a pure Gaussian ($\eta = 0$) to a pure Lorentzian ($\eta = 1$). It should be mentioned that for a CW diffractometer the peak shape is usually asymmetric as the straight slit is intercepting the diffraction cone [11]. At this time, one way to fit the asymmetry is to divide each peak at the profile maximum into low and high angle parts. Each part is then fitted independently.

For ToF experiments the profile function is usually the one proposed by Von Dreele et al. or a modification of it [38, 43].

$$H(\Delta T) = N[e^{u}\mathrm{erfc}(y) + e^{v}\mathrm{erfc}(z)] \tag{3.33}$$

where ΔT is the difference in ToF between the peak position and the profile point; the terms N, u, v, y, and z are dependent on the profile coefficients. The function $\mathrm{erfc}(x)$ is the complementary error function. The function $H(\Delta T)$ is in fact the convolution of two back-to-back exponentials with a Gaussian [38]. The two exponentials represent the rise and decay of the neutron pulse and are essentially the representation of the particular moderator used. The Gaussian characterizes the scattering angle, flight path, and sample.

A list of profile functions and a more complete discussion about their use can be found in appropriate references [11, 22, 36, 44, 45]. Diverse Rietveld refinement programs may have slightly different peak shape functions incorporated in their software. The selection of the proper peak shape should be done after discussion with the neutron beamline local contact who could run a reference sample for peak shape determination.

3.5.2.10 Background

For a pure crystalline material, the powder diffraction pattern could be modelled by adding individual diffraction peaks corresponding to Bragg reflections to which a background contribution coming from air scattering, incoherent scattering, and thermal diffuse scattering is added [46]. In some old versions of Rietveld refinement the background was manually defined by the user. As this may induce bias, this method should not be used. Many types of functions have been used to describe the background. It is now common practice to use orthogonal Chebyshev polynomials of order 5–10 in combination with an increasing background function [22]. Some caution should be exerted when using higher order polynomials for background because it may partially fit Bragg peaks and thus reduce the quality of the fit. A good procedure is to increase the polynomial order one step at the time and stop when the highest order is no longer statistically significant.

3.5.2.11 Validation of Refined Crystal Structure

As the Rietveld refinement is based on the least-square algorithm, i.e. minimizing the variance (Eq. 3.11) it is natural to use this value to monitor the refinement's progress. From the theory of statistics we know that the expected value of variance is *N*-*P*-*C* where *N* is the number of data points, *P* is the number of fitted parameters, and *C* is the number of constraints. The quality of the fit is then given by the chi-squared (χ^2) or in the present context the goodness-of-fit (GoF) ($=\chi$).

$$\text{GoF} = \sqrt{\chi^2} = \sqrt{\frac{\sum_i w_i (y_i - y_{ci})^2}{N - P + C}} \tag{3.34}$$

In the ideal case, i.e. when the only source of difference between y_i and y_{ci} is the statistical noise, the value of GoF should approach 1. A value less than unity means "over-fitting" and that actually the refinement is just fitting "noise". It means that there are too many refined parameters for the quality of the diffraction pattern.

A number of other agreement factors, more appropriate to ascertain the fit of a powder diffraction pattern, are available. We will briefly introduce and discuss them. More complete explanations are given in [11, 22, 36, 47]. One simple criterion is to measure the agreement between the calculated and observed pattern. This is the profile *R*-factor (R_p) and is given by:

$$R_\text{p} = \frac{\sum_i |y_i - y_{ci}|}{\sum_i y_i} \tag{3.35}$$

The problem with this factor is that it gives more weight to the strong Bragg peaks. The way to solve that problem is to use the weighting factor w_i calculated according to Eq. (3.12), and define the weighted profile R-factor (R_{wp}).

$$R_{\mathrm{wp}} = \sqrt{\frac{\sum_i w_i (y_i - y_{ci})^2}{\sum_i w_i y_i^2}} \tag{3.36}$$

According to the Poisson statistics (Eq. 3.10) the stronger reflections are measured with lower absolute precision, and accordingly have lower weighting factor. We would now like to compare the quality of refinements using different number of parameters, different powder patterns, or different samples. To do this we introduce the expected weighted profile R-factor (R_{exp}).

$$R_{\mathrm{exp}} = \sqrt{\frac{N - P + C}{\sum_i w_i y_i^2}} \tag{3.37}$$

This factor is called expected because $N - P + C$ is actually the expected value of the numerator of the Eq. (3.36). It is easy to see that the GoF is actually the ratio of the observed weighted profile R-factor over the expected weighted profile R-factor.

$$\mathrm{GoF} = \frac{R_{\mathrm{wp}}}{R_{\mathrm{exp}}} \tag{3.38}$$

All the above R-factors are based on the difference between the observed and calculated point intensities as registered in the powder diffraction pattern. They may be calculated including the background contribution to y_i or after having subtracted it. The contribution of the background may be misleading: As the background appears only in the denominator of Eqs. (3.35) and (3.36) (it cancels itself in the numerator), a powder pattern with high background will have artificially low R-factor indicating that we have very well fitted the background, but saying little about how well we have fitted the crystal structure itself. Therefore the background corrected R-factors are the correct indicators of the correct fit of Bragg intensities, which was proposed already by Rietveld himself.

It would be useful to have a R-factor which is similar to single crystal R-factor based on Bragg (integrated) intensities of individual reflections hkl. This is given by the Bragg R-factor (R_{B}).

$$R_{\mathrm{B}} = \frac{\sum_{hkl} |I_{hkl}(\mathrm{obs}) - I_{hkl}(\mathrm{cal})|}{\sum_{hkl} I_{hkl}(\mathrm{obs})} \tag{3.39}$$

where the intensities (I_{hkl}(obs) and I_{hkl}(cal)) are obtained by integrating the profile of each reflection hkl after background subtraction. It is easy to do that for the calculated pattern, but difficult for the measured pattern, because of the peak

overlap. Rietveld has proposed a so-called decomposition formula to obtain the measured integrated intensities I_{hkl}(obs): The observed integrated intensities of reflections overlapping in a cluster are obtained by dividing the total intensity of the cluster according to the ratio of calculated integrated intensities. As a consequence the value of the Bragg R-factor is biased by the actual structural model, and must be therefore used carefully.

In a summary: The good indicator to watch is GoF. If GoF > 1 the structural model or the profile modelling and background should be still improved, but in many cases the value below 2 is already satisfactory. If you have reached 1, you cannot do it better even if the structural model has low precision. Simply the diffraction data are not good enough to increase the precision. Simultaneously one should watch background corrected R_{wp}. Its value will be about twice as big as the value of non-corrected R_{wp}, and can be improved by longer counting times, i.e. by decreasing the statistical noise in the powder pattern. It is difficult to give a target value of R_{wp}. Moreover, as discussed in Sect. 3.5.2, long counting times are not always rewarded by more precise structural parameters [48].

The final comment is about the precision of the refined structural parameters: According to the flow of uncertainties in the least-square algorithm from those of the measured intensities to those of the structural parameters [38] the latter should be multiplied by a single-crystal-like GoF, i.e. calculated using the integrated intensities I_{hkl}(obs) and not the point intensities y_i as done in Eq. (3.33). One integrated intensity I_{hkl}(obs) and not one point intensity y_i is one independent observation determining the structural parameters. Due to already discussed difficulty obtaining the integrated intensities I_{hkl}(obs) we cannot do that and have to use powder-like GoF which was shown to be overestimated, i.e. "too good". Another source of the underestimation of the uncertainties of the refined structural parameters are serial correlations in the observed data, i.e. between individual point intensities in the powder pattern. Several theoretical models were proposed to correct those two handicaps, and good Rietveld programs calculate the correction factors for the uncertainties of the refined structural parameters. Another way to calculate properly the uncertainties of refined structural parameters is bootstrapping [49].

In closing, we should emphasize that even if these numerical factors are of great help and importance in the Rietveld refinement process, a visual inspection of the residual should always be performed. Often, it is the eye of an experienced crystallographer that will give the necessary clue about how good is the refinement and also what is going wrong with it. Furthermore, a check on the fitted parameters values and uncertainties is essential to determine the plausibility of a fit. One has to always make sure that the fitted parameters are consistent with basic crystallographic and chemical principles, and generate a crystal structure which makes a sense from the point of view of interatomic distances, molecular conformation, and coordination polyhedra checked, for example, by bond-valence sums. Related to that and thanks to easier access to solid state density functional theory (DFT) calculations the crystal structures are more and more often validated by the DFT optimization of the structural model obtained from powder diffraction. But DFT,

when applied correctly and exhaustively to the problem, goes beyond the validation of experimental structures. DFT is not only capable of orienting complex groups properly and providing accurate interatomic distances and angles [50], it can in some cases correct features going beyond the local structure [51].

3.5.2.12 Refinement Strategy

Modern Rietveld refinement programs are powerful and can give a solution relatively quickly. We do not advertise here a specific program nor give a list of them. The reason is that new Rietveld programs are appearing regularly and old ones are upgraded or just fade away. Also, different programs may be more suitable for different problems (magnetic structure, peak shape, multiphase compounds, X-rays, ToF neutrons, etc.). The authors' view is that the best program is the one you are familiar with. Unless it is necessary for technical reasons, there is no need to switch from one program to another. The refinement strategy explained below applies to essentially every Rietveld program. However, it is important that the operator use all other chemical, physical, and metallurgical information available in order to get a solution that is meaningful. It should be noted that when n parameters are fitted then effectively the solution is a minimum in an n-dimensional space. When the number of parameters is getting large then it may be easy to fall in local minima and to never find the real solution. It is thus recommended to "turn-on" parameters in a sequence. This is necessary because different parameters have different behaviour. Some parameters are more or less correlated and turning them on at the same time may result in unphysical solution. We present here a standard strategy for the parameters turn-on sequence based on the ones proposed by Young [36], Taylor and Hinczak [23], and by Kisi and Howard [11]. This is a general purpose strategy, variation of this is possible depending on the specific type of pattern, sample, and information to obtain. We assume that the pattern has been collected under the best conditions possible and on a sample of highest possible quality. For CW neutron diffraction an essential step before performing the Rietveld refinement of the sample's diffraction pattern is to establish the neutron wavelength. This is done by recording a diffraction pattern of a reference sample of well-known lattice parameters and subsequently doing a Rietveld refinement keeping the lattice parameters at their literature values and refining the neutron wavelength.

As the name implies, in Rietveld refinement the starting crystal structure should be close enough to the correct one. Almost all Rietveld refinement programs can now import crystal structure directly from files using the Crystallographic Information File (CIF) format. However, before starting the refinement the user should double check the crystallographic information imported because the Rietveld program may use other settings than the one written in the CIF file. Often it is better at this stage to perform a so-called Le Bail or Pawley refinement (for more details, see [4, 14, 27]). These are refinements where the integrated intensities I_{hkl}(cal) are not calculated from a structural model, but are treated as free

parameters either by using the Rietveld decomposition formula (Le Bail) or by the least-square algorithm (Pawley). For a CW diffractometer the first parameter to determine is the 2θ zero offset. For a well-aligned diffractometer the zero offset is known from the beamline scientist, and should not be refined. For a ToF diffractometer the only instrument parameter that should be routinely refined is the parameter called DIFA, all the others (ZERO, DIFC, alpha0, alpha1, beta0, and beta1) are determined by the instrument team.

In the second step, the lattice parameters can be refined along with the background. For multiphase compounds, only the phases that have concentrations more than a few wt.% should have their lattices parameters refined. At this stage it is important to be sure that the lattice parameters are close to the correct ones even if they are not refined. This is imperative because if the lattice parameters are too far from the correct values then the calculated pattern will not overlap the measured one and the refinement will never work. The peak width should also be kept constant and small. The goal is to keep the Bragg peaks sharp in order to centre them on the observed pattern. For the background polynomial it is better to start at a low order at this stage. The number of parameters should be increased stepwise until the parameter of the higher order is zero within its uncertainty. To prevent over fitting, no higher order background parameters should added thereafter. In ToF data it may be necessary to use an alternative background function such as linear or reciprocal interpolation to fit the features that may be visible at very low d-spacings (e.g. diffuse scattering).

The next parameters to refine are the peak widths. It is important to have the Bragg peaks well aligned with the measured peaks. If it is not the case then the refinement may increase the peak widths up to unrealistic values in order to fit the observed peaks. The profile widths parameters are used to evaluate the crystallite size and microstrain. Particular care needs to be taken with nanocrystalline materials where the peaks are inherently broad, or the peaks sometimes may merge into the background if the lattice parameters wander too far. The exact relationship between the fitted parameters and the microstructure depends on the assumed peak shape. A full discussion on how to compute crystallite size and microstrain from peak shape is too lengthy to be given here. The reader should refer to the refinement program's manual and also to specialized references [11, 23, 36, 38, 44, 45, 52].

At this stage the Le Bail or Pawley fit is finished and should correspond to the best agreement between the measured and calculated powder patterns one can obtain. The R_{wp} value obtained here is a "target" value which one should try to approach in the Rietveld refinement, i.e. using a structural model.

At this point one switches to Rietveld refinement, and refines the scale factors of individual phases. If there is some preferred orientation it should be apparent on the residual curve. The Miller indices of preferred orientation are then easily identified and refinement of the corresponding parameters can proceed.

Further fitting can now be performed by refining the atomic parameters (position and site occupancies). The user should be aware of the scattering length of the atoms to be refined and adjust his fitting strategy accordingly. For example, vanadium has a very small scattering length and is essentially "transparent" to

neutrons. Therefore unrealistic site occupancy could be found for vanadium atoms. Similarly, if two atoms have almost identical scattering length then it may be difficult to distinguish them. In this case a simultaneous X-ray and neutron refinement may help.

Once the atomic positions and site occupancies have been refined then the isotropic displacement parameter could be refined. Great caution should be exerted here because this parameter is correlated with the peak intensities and also the displacement parameters have a tendency to be the depository of structure deficiencies. Therefore it is not unusual that displacement parameters have negative values which are unphysical. The displacement parameters also correlate 100 % with the absorption in a CW experiment so the absorption should be determined from the sample density not be refined. Absorption in ToF data can be refined at the same time and should be refined if significant. With data of very good quality anisotropic displacement parameters may be refined for one or more atomic positions. Examination of the GoF-values will tell the user if they have reached the limit of the refinement process. However, inspection of the residual curve should be an integral part of the refinement process. And as already said, at the end of refinement the user should double check all parameters to see if their numerical values are physically and chemically realistic. During refinement the user should use available chemical and physical knowledge to constrain the parameters within realistic values. For example, if a chemical analysis gives the exact proportion of different atoms, then these proportions should be imposed on the refinement as an additional observation using constraints formalism available in the given Rietveld program.

3.6 Localizing Hydrogen by NPD

Powder diffraction is used nearly exclusively for crystal structure characterization of metal hydrides as the hydrogenation of metal alloys results in their pulverization, and the synthesis of lightweight hydrides, like borohydrides, is mostly done by a mechanosynthesis (ball milling) resulting in a fine powder sample [53].

Hydrogen is a weak X-ray scatterer therefore the usual procedure of ab initio structure solution of metal hydrides proceeds in two steps: First the crystal structure of the hydride metal matrix is determined from XPD, and then the hydrogen (deuterium) is localized by NPD. In the case of lightweight hydrides, it may be visible with X-rays, i.e. for $LiBH_4$, the lightest possible borohydride, hydrogen atoms have been located unambiguously by XPD alone [54]. The contribution of hydrogen to the intensity scattered by $LiBH_4$ is 26 % for X-rays compared to 52 % for neutrons [55]. The easy access to X-ray sources makes the XPD the most used diffraction method for the characterization of lightweight hydrides in conjunction with spectroscopic methods like Raman, infrared, and NMR spectroscopy as well as thermal desorption studies [56].

In the two-step structural characterization of metal hydrides first the positions of metal atoms are determined. We will not review this step as it is done by XPD.

Complete reviews can be found in [57] or [58]. The arrangement of metal atoms in metal hydrides usually shows a small deviation from an arrangement with higher symmetry or shorter periodicity which corresponds to the structure of the metal alloy (it does not necessarily exist without hydrogen). This deviation is created by positioning H atoms in the matrix of metal atoms which becomes then only slightly deformed. Because of the small deformation of the metal matrix and the low scattering power of hydrogen for X-rays, the splitting of peaks caused by lowering the symmetry is not very strong and the superstructure peaks are very weak in X-ray patterns; both are clearly visible only in neutron patterns. X-ray patterns with low background are needed to detect the weak superstructure peaks. High angular resolution is necessary in both X-ray and neutron patterns to separate overlapping peaks and to detect the correct symmetry of the structure. The true symmetry can generally be revealed with confidence after successful indexing of the neutron powder pattern in the second step (see the example of $Y(BH_4)_3$).

The hydrogen (deuterium) atoms are then localized in the second step by NPD. As for the ab initio structure solution two methods are possible: Intensity Extraction (IE) based algorithms working in the reciprocal space, (traditionally called Reciprocal Space Methods), and Pattern Modelling (PM) based algorithms working in the direct space (traditionally called Direct Space Methods or Global Optimization Methods), and using the chemical knowledge from that space [42]. For hydrogen localization most of the structure is already known (metal atoms) from XPD. Therefore the procedure is not ab initio. Using IE algorithm the missing hydrogen atoms are localized usually by difference Fourier technique [1] available in all Rietveld programs, i.e. by comparing the nuclear densities calculated from observed amplitudes of structure factors $|F_{hkl}|$ with densities obtained from calculated amplitudes. The phases of structure factors are in both cases the phases calculated from the actual structural model, i.e. without hydrogen atoms, supposing them being already close to the phase of the complete model. The analysis of the differential nuclear density map so obtained may be assisted by analysis of the voids in the metallic matrix available to accept hydrogen atoms. A program TOPOS [59] and geometrical criteria like a minimum radius of 0.40 Å of the atomic site [60], and a minimum H–H distance of 2.1 Å [61] may be used here.

When no reliable integrated intensities I_{hkl} can be extracted from a powder pattern, then the only choice is modelling the pattern as a whole, i.e. a synthetic approach (PM) contrary to the analytical approach (IE). There is no need to extract the integrated intensities, low resolution powder data (~2 Å) are often sufficient, and the methods work with patterns containing broadened, overlapped peaks. Any additional information about the atomic coordination and connectivity leading to lower number of structural parameters to be determined is easily used. Generally the PM methods differ in the algorithm of the global optimization, i.e. algorithm which globally optimizes the structural model to better match the calculated powder pattern to the observed one (diffraction cost function). Algorithms such as Reversed Monte Carlo in Simulated Annealing and Parallel Tempering mode or Genetic algorithms are used. For more information, see [62].

To describe a crystal structure adequately for PM algorithm, it is necessary to take into account the connectivity between the individual building blocks such as coordination polyhedra. This is achieved in the program Fox, the most used PM program among the metal hydride community [63], by applying a dynamic occupancy correction (DOC) which also handles the higher symmetry atomic sites (Wyckoff sites) in the unit cell. It was recognized that DOC is an ideal tool to localize hydrogen in the metallic matrix from NPD. When H atoms are dissolved in the crystal lattice of an intermetallic compound, usually a great number of interstitial sites, typically the tetrahedral holes, can be occupied by hydrogen. These sites are, however, too close one to another to be simultaneously occupied by H atoms. It leads to partially occupied hydrogen sites and an uncertainty in the number of Wyckoff sites occupied by hydrogen. The DOC can easily treat this problem. The starting model for the global optimization in DSM can contain more H atoms than needed for the correct structure. The excess hydrogen atoms are simply merged by DOC.

When hydrogen is covalently bonded in a molecule which is a priori known, like complex anions BH_4^-, NH_2^-, or AlH_4^- in complex hydrides, the hydrogen localization means the localization of the whole molecule, and can be in most cases done by XPD. However, the correct orientation of the molecule, i.e. the coordination mode of the hydrogen atoms is practically inaccessible from XPD, and must be concluded from the vibrational spectroscopy signal, ab initio solid state calculations (DFT) [56] or by using NPD (see the example of $Y(BH_4)_3$).

We present here a few examples of using NPD for a better understanding of metal hydrides. Each case represents a different type of metal hydride as well as a different type of information obtained.

3.6.1 Ti–V–Mn Alloy

An important class of metal hydrides is the transition metals solid solution alloys having a BCC structure. These alloys form hydrides of CaF_2 structure with a ratio of hydrogen atom over metal atoms (H/M) of almost 2 [64]. In this fully hydrided (or dihydrided) structure the metal atoms form an *fcc* sublattice and the hydrogen atoms occupy the tetrahedral (T) sites surrounded by four metal atoms. For a H/M of around 1 (monohydride) the metal sublattice is BCC which is sometimes deformed or distorted. Nakamura et al. were able to shed new light on the monohydride and dihydride structures by studying the composition $Ti_{1.0}V_{1.1}Mn_{0.9}$ using ToF neutron diffraction [65]. Figure 3.8 shows the NPD pattern and Rietveld refinement for a hydrogen content of D/M = ~0.86.

The pattern presented in Fig. 3.8 shows three distinct phases. The main phase (81.1 wt.%) is the monohydride phase which is NaCl type but slightly deformed to tetragonal (space group *I4*/*mmm*). There is a small proportion of dihydride phase (14.1 wt.%) and some $Zr_3V_3OD_x$-type phase (4.8 wt.%). In the monohydride phase, it was established that the deuterium occupies an octahedral site (0, 0, ½) with

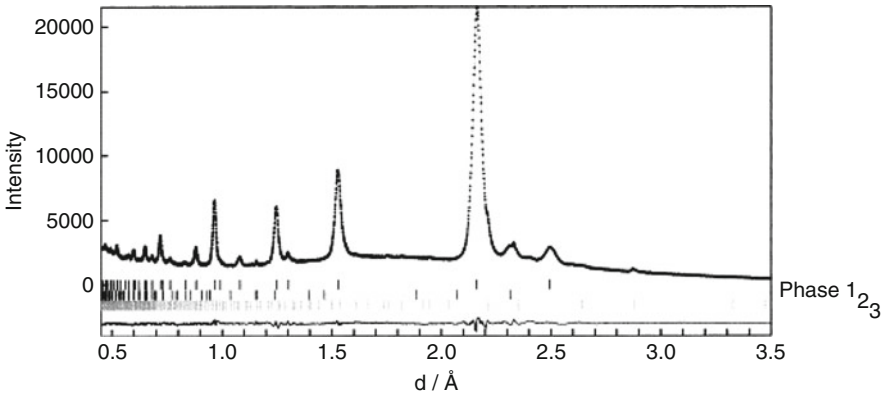

Fig. 3.8 Neutron powder diffraction pattern of the monohydride sample. The *tick marks* below the profile indicate the Bragg peaks positions of the three phases present in the alloy: (*1*) monohydride phase; (*2*) dihydride phase; (*3*) $Zr_3V_3OD_x$-type phase. The *bottom line* shows the difference between the calculated and observed intensities. Reprinted from [65]

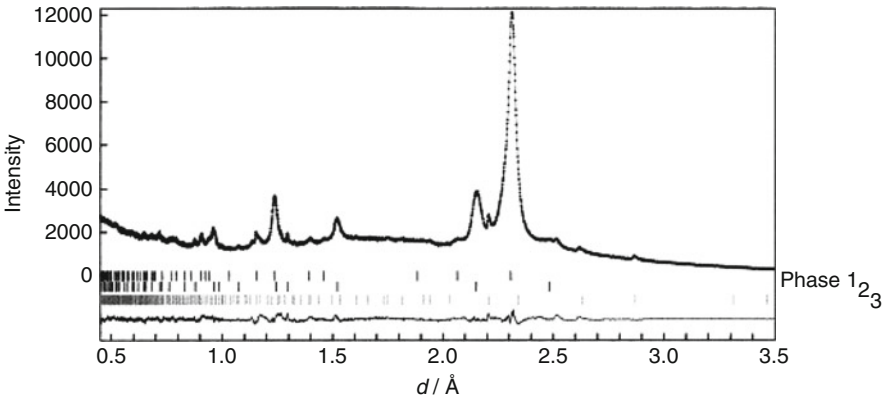

Fig. 3.9 Neutron powder diffraction pattern of the dihydride sample. The *tick marks* below the profile indicate the Bragg peaks positions of the three phases present in the alloy: (*1*) dihydride phase; (*2*) monohydride phase; (*3*) $Zr_3V_3OD_x$-type phase. The *bottom line* shows the difference between the calculated and observed intensities. Reprinted from [65]

occupancy of 0.662. Thus, the composition of the monohydride was established to be $Ti_{1.0}V_{1.1}Mn_{0.9}D_{2.0}$.

Figure 3.9 shows the diffraction pattern and Rietveld refinement for a hydrogen content of D/M = ~1.50. Here, the main phase (82.8 wt.%) is the dihydride. The monohydride and $Zr_3V_3OD_x$-type abundances are respectively 11.6 wt.% and 5.53 wt.%. The dihydride phase is CaF_2 type (space group $Fm\bar{3}m$) as should be the case for BCC alloys. In the dihydride phase the deuterium is on a tetragonal site (¼, ¼, ¼) with occupancy factor of 0.903 which gives a composition of

$Ti_{1.0}V_{1.1}Mn_{0.9}D_{5.4}$. From the atom positions in the lattices, Nakamura et al. were able to determine the deuterium–deuterium distances in the monohydride and dihydride to be 0.267 and 0.216 nm, respectively. The value for the dihydride is close to the minimum H–H distance postulated by Westlake which leads Nakamura to conclude that the dihydride has almost the maximum hydrogen density possible [60].

This investigation is an example of how a new structure, NaCl-type monohydride, was found by neutron diffraction. It also established the type of hydrogen sites and their dimensions.

3.6.2 Ti–V–Cr Alloy

Titanium containing BCC alloys have a large hydrogen capacity and have been intensively studied [66–68]. Upon full hydrogenation, these alloys adopt a *fcc* (Face-Centred Cubic) structure (space group Fm-3m). Alloys of composition Ti–V–Cr present a challenge for neutron diffraction for the following reason: the scattering length of Ti, V, and Cr are respectively −3.438, −0.3824, and +3.635 fm. For a solid solution alloy, these scattering lengths will cancel out, leaving a very small total scattering length. For example, the alloy $Ti_{0.52}V_{0.12}Cr_{0.36}$ has a total scattering length of only −0.5250 fm which is only marginally larger than pure vanadium. Consequently, it is expected that the NPD of $Ti_{0.52}V_{0.12}Cr_{0.36}$ will not show any Bragg's peaks. However, when a small amount of deuterium is absorbed by this alloy the Bragg peaks will appear distinctly. In fact, the pattern is essentially due to the deuterium presence. This will enable a precise localization and quantification of deuterium in the crystal structure. This is clearly seen in Fig. 3.10.

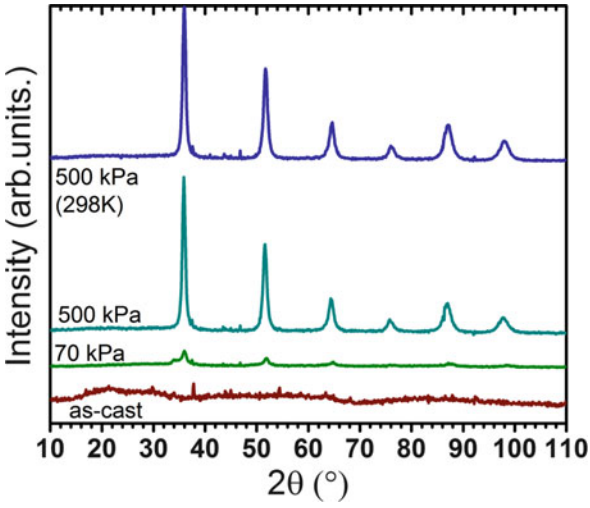

Fig. 3.10 Neutron powder diffraction patterns of $Ti_{0.52}V_{0.12}Cr_{0.36}$ in as-cast state and at various deuterium pressures. All patterns were taken at 473 K unless stated otherwise

Table 3.3 Rietveld refinement parameters of *fcc* phase (space group Fm-3m) for in-situ neutron powder diffraction of $Ti_{0.52}V_{0.12}Cr_{0.36}$ alloy

Pressure (kPa)	Temperature (K)	Lattice parameter (nm)	Crystallite size (nm)	Microstrain (%)	Deuterium occupation factor	Thermal parameter B_{iso} (Å^2)
70	473	0.4289(9)	4.0(6)	–	0.47	3.0
500	473	0.4319(3)	11(2)	0.27(6)	0.97	2.4
500	298	0.4309(2)	13(1)	0.30(2)	1.0	1.9

Deuterium atom is located on 8c site (¼, ¼, ¼)

These diffraction patterns were recorded in-situ on the C2 high-resolution neutron powder diffractometer at the NRU reactor at the Canadian Nuclear Laboratories. The sample holder was a copper-coated vanadium container [15]. After recording the as-cast pattern at 473 K under vacuum, the deuterium pressure was slowly raised and diffraction patterns taken at regular pressure intervals. The pattern recorded at 0.7 bar already shows small Bragg peaks, indicating that the alloy absorbed some deuterium. At 5 bar of pressure the pattern is clearly single-phase *fcc* (Face-Centred Cubic) which means that the alloy was fully deuterided. The temperature was thereafter reduced to 298 K while keeping the deuterium pressure constant. Selected Rietveld refinement parameters of the patterns of Fig. 3.10 are reported in Table 3.3.

The first thing to notice in this table is that the deuterium occupation factor at 500 kPa slightly increases with temperature. At 500 kPa the deuterium site is fully occupied, meaning that the alloy is fully hydrided. Secondly, we see that the thermal parameter also changes. At 473 and under 70 kPa the thermal parameter is slightly bigger than at 500 kPa. This can be explained by the fact that at 70 kPa the deuterium sites are only partially occupied and that, for an occupied site the adjacent sites are empty then, the deuterium atom has more freedom to vibrate on its site. At 500 kPa the thermal parameter slightly decreases when the pattern is taken at 298 K instead of 473 K.

Examination of the crystallite size and microstrain gives us some indication on the hydrogenation mechanism. At 70 kPa the crystallite size is small and there is no microstrain in the structure. When the alloy is fully hydrided the crystallite size had increased by a factor of three and there is now presence of microstrain. These values do not change when the temperature is decreased to 298 K. Therefore, we could expect that the hydrogenation mechanism is more a nucleation and growth phenomena. Finally, the lattice parameter increases with hydrogen content and decreases with temperature as should be expected.

3.6.3 $La_{1.5}Mg_{0.5}Ni_7$ Alloy

The intermetallic compound $LaNi_5$ is a well-known hydrogen storage alloy and has been studied and used since the 1970s. It is representative of the AB_5 hydrides where

A is a hydride-forming element and B is a non-hydride-forming element. $LaNi_5$ can store hydrogen at room temperature under a few bar of hydrogen pressure. It has good hydrogenation/dehydrogenation kinetics and reasonable tolerance to gaseous contaminants. Its main drawbacks are the low reversible hydrogen capacity (~1.28 wt.%) and significant disproportionation upon hydrogen cycling. The crystal structure of $LaNi_5$ and its deuteride has been studied by neutron diffraction by Bowman et al. [69] and Percheron-Guegan [70–72]. It is interesting to note that $LaNi_5$ and $LaNi_5H_6$ both have the same crystal structure (*P6/mmm*). Ono et al. have shown the existence of an intermediate hydride phase corresponding to $LaNi_5H_{\approx 3}$ [73]. Gray et al. have studied the microstructural change during the first hydrogenation and cycling [74, 75]. Thus, crystal structure of $LaNi_5$ and its hydrides are well known. One way to improve the hydrogen storage performances of $LaNi_5$ is by partial substitution of La and/or nickel by other elements. The literature on this is abundant but here we will show one closely related system: La_2Ni_7.

The A_2B_7 alloys are also called superlattice compounds because they are built up by AB_5 and AB_2 slabs alternating along the [001] direction [76]. The hydrides in La–Mg–Ni system have been a subject of numerous studies motivated by the discovery of superior electrochemical properties compared to Mg free compositions [77, 78]. In order to understand the hydrogenation mechanism of these materials it is important to know precisely the atoms positions in the crystal structure. Combined refinement of neutron and synchrotron powder diffractions was undertaken by

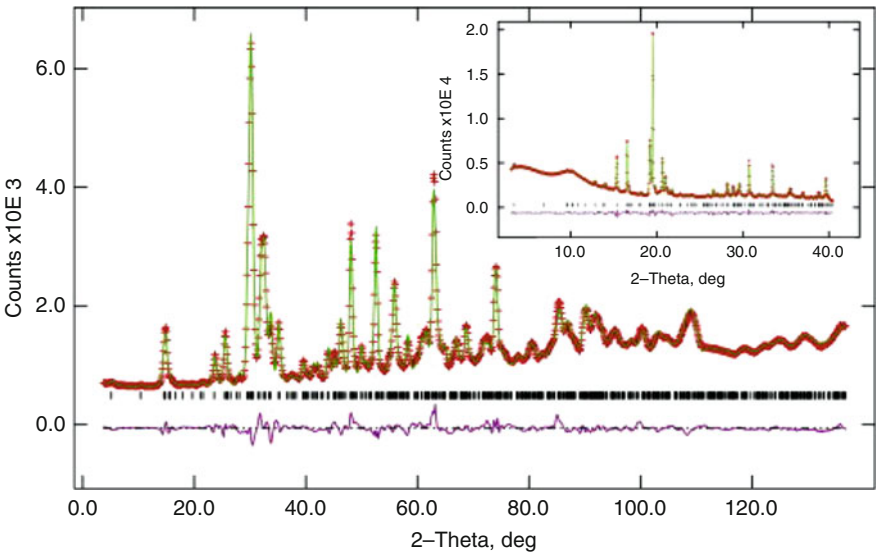

Fig. 3.11 Observed (+), calculated (*upper line*), and difference (*bottom line*) of neutron diffraction pattern of $La_{1.5}Mg_{0.5}Ni_7$ ($\lambda = 0.116$ nm). *Vertical bars* indicate the Bragg peaks positions. *Inset* is the synchrotron X-ray diffraction pattern ($\lambda = 0.07243$ nm). From [79] with permission

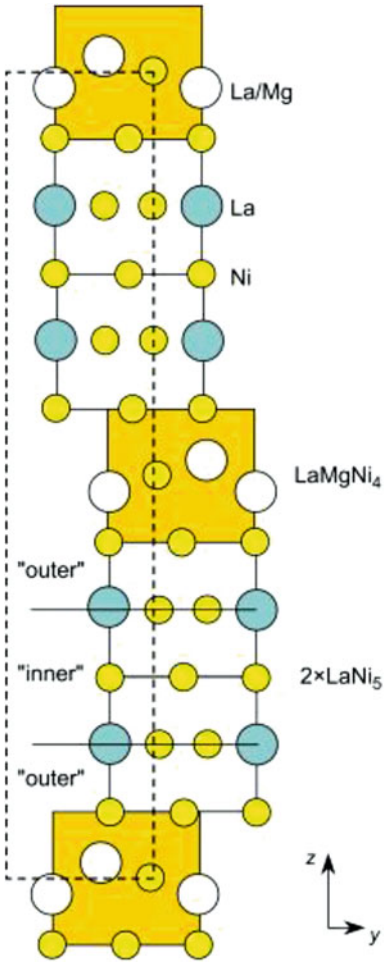

Fig. 3.12 Crystal structure of $La_{1.5}Mg_{0.5}Ni_7$. From [79] with permission

Denys et al. on $La_{1.5}Mg_{0.5}Ni_7$ alloy [79]. Figure 3.11 shows the neutron and X-ray synchrotron patterns along with their respective refinement curves and residues.

The structure of $La_{1.5}Mg_{0.5}Ni_7$ alloy was found to be of $CeNi_7$-type (space group $P6_3/mmc$). La substitution by Mg was only in the AB_2 slabs which then had a composition $LaMgNi_4$. Moreover, these slabs contract because of the smaller atomic radii on magnesium compared to lanthanum. Figure 3.12 shows the crystal structure of $La_{1.5}Mg_{0.5}Ni_7$.

To determine the crystal structure of hydrogenated alloy, Denys et al. performed in-situ and ex-situ diffraction with X-ray and neutron radiations. In Fig. 3.13 we present their ex-situ NPD. Details of the refinement are too lengthy to be shown here. The interested reader should consult the original paper [79]. The main point is that nine deuterium sites were found, distributed in both AB_2 and AB_5 subunits. One deuterium site had occupancy of 0.82, the other eight sites had all occupancies less than 0.5.

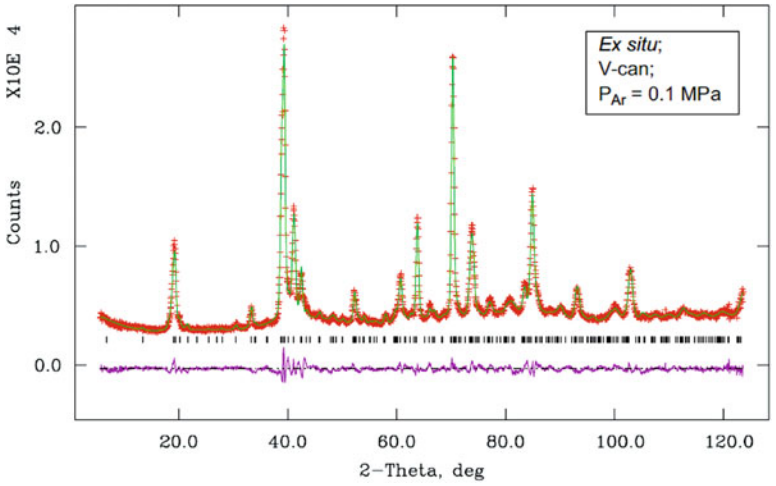

Fig. 3.13 Observed (+), calculated (*upper line*), and difference (*bottom line*) of neutron diffraction pattern of $La_{1.5}Mg_{0.5}Ni_7D_{8.9}$ ($\lambda = 0.1551$ nm). *Vertical bars* indicate the Bragg peaks positions. From [79] with permission

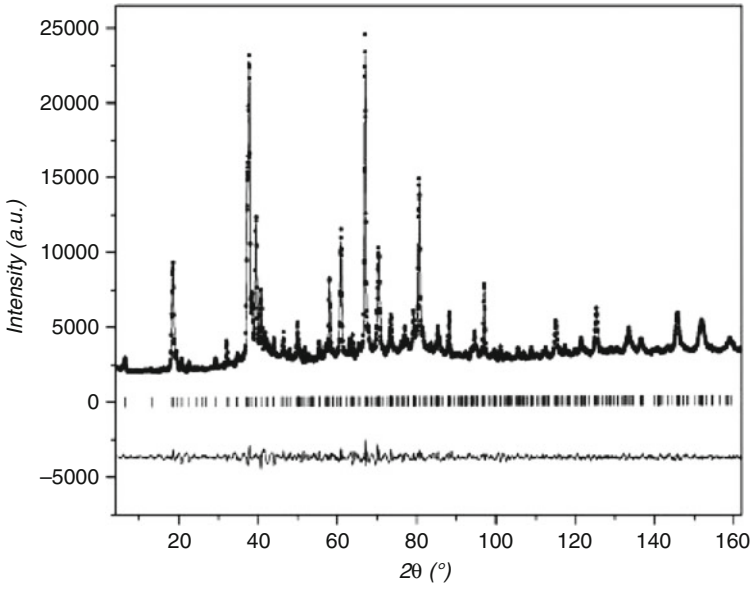

Fig. 3.14 Observed (*points*), calculated (*line*), and difference (*bottom line*) of neutron diffraction pattern of $La_{1.63}Mg_{0.37}Ni_7D_{8.8}$ ($\lambda = 0.1494$ nm). *Vertical bars* indicate the Bragg peaks positions. From [80] with permission

Further work on this type of alloy was published by Guzik et al. who studied the composition $La_{1.63}Mg_{0.37}Ni_7$ [80]. For the alloy they confirm the crystal structure described by Denys et al. However, their conclusion was slightly different for the

hydride $La_{1.63}Mg_{0.37}Ni_7D_{8.8}$. The neutron diffraction pattern is shown in Fig. 3.14. Their refinement indicated that deuterium occupies only five sites reported in the model of Denys et al. while the other four deuterium sites were empty. On the five occupied sites, two of them were fully occupied and the other three had an occupation factor of more than 0.66. The deuterium was evenly distributed on the two types of slabs: the composition was found to be $AB_5D_{4.5}$ and $AB_2D_{4.3}$.

In this example we saw that for complex structures it may be difficult to distinguish between two closely related crystal structures. The main difference between these two investigations is the occupancy number of deuterium atoms. Other independent work is needed in order to confirm one structure or the other.

3.6.4 *Structure of $NaAlD_4$ and $LiAlD_4$*

Complex metal hydrides are salts of general formula $M_xM'_yH_n$, where M is an alkali metal cation or cation complex and M′ is a metal or metalloid. When M and M′ are light atoms (Li, Na, B, Al) the hydrogen capacity by weight is quite high and these compounds could be considered as hydrogen storage materials. However, poor hydrogen absorption/desorption kinetics and lack of reversibility have restricted the research on these hydrides. In 1997 Bogdanovic and Schwickardi showed that hydrogenation of $NaAlH_4$ could be achieved by adding a Ti-based catalyst [81]. This initiated an important effort of the scientific community for the development of dopants for complex hydrides.

Following Bogdanovic and Schwickardi paper, the two most studied complex hydrides have been $NaAlH_4$ and $LiAlH_4$ hydrides. The structure of these two complex hydrides are known through single crystal X-ray diffraction studies [82, 83]. However, neutron diffraction was needed in order to have a good knowledge of the hydrogen position in the lattice and the metal–hydrogen distances. A number of neutron diffraction investigations on doped and undoped $NaAlH_4$ and $LiAlH_4$ have been reported [84–88]. We discuss here the two investigations on undoped hydrides.

The investigation of $LiAlD_4$ structure is an example of simultaneous refinement of X-rays and neutron patterns. Figure 3.15 shows the X-rays and neutron diffraction patterns taken at 295 K. As mentioned in the introduction, the peak relative intensities are totally different in the X-rays and neutron patterns. Moreover, it is easy to see that the high angles peaks have higher relative intensities than their X-rays counterpart.

Simultaneous Rietveld refinement of the two patterns gave atomic positions and thermal parameters for all atoms. It was found that the thermal parameters of deuterium were quite important (B_{iso} between 2.5 and 3.3 $Å^2$) which may be an indication of the low thermal stability of this hydride. The structure is monoclinic (space group $P2_1/c$) with four formula units per unit cell (see Fig. 3.16).

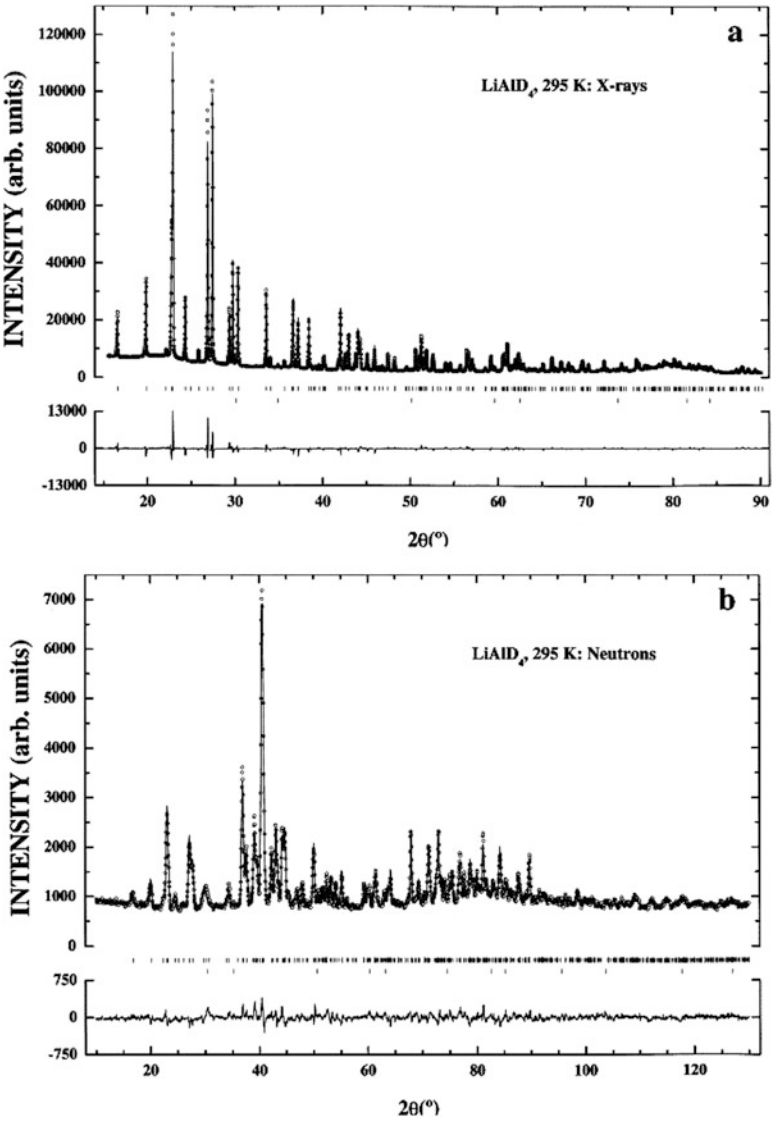

Fig. 3.15 (**a**) X-rays and (**b**) neutron diffraction patterns of $LiAlD_4$. Observed (*points*), calculated (*line*), and difference (*bottom line*) of diffraction patterns ($\lambda =$). *Vertical bars* indicate the Bragg peaks positions. Wavelengths: neutron 0.15546 nm; X-rays 0.15906 nm. From [84] with permission

Each tetrahedra is made of four deuterium atoms with aluminium at the centre (AlD_4). Each lithium atom is bonded to five tetrahedra. The bonding is through one of each tetrahedron. It was established that the AlD_4 tetrahedra were slightly distorted and that this distortion increases with cooling. The Li–D distances ranged

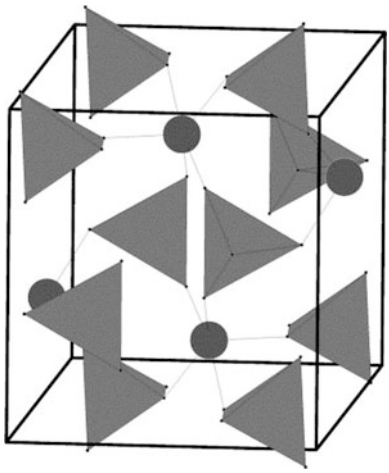

Fig. 3.16 Crystal structure of $LiAlD_4$. AlD_4 tetrahedra are linked via Li atoms. From [84] with permission

from 0.1831 nm to 0.1978 pm. A previous X-ray diffraction experiment found a much broader range of Li–D distances [83]. This may be explained by the inaccuracy of hydrogen position in X-rays patterns. Therefore, we see that accurate atomic position of atoms, and particularly hydrogen, is only possible with neutron diffraction.

The structure of $NaAlH_4$ was determined using single crystal X-ray diffraction to be tetragonal (space group $I4_1/a$) with four formula units per unit cell [82]. However, precise localization of the hydrogen (deuterium) atoms could only be done with neutron diffraction. This work was carried out by Hauback et al. who performed NPD of $NaAlD_4$ at 295 K and 8 K [86]. One of the interests in this work is that despite the fact that the sample contained a significant amount of impurities an excellent structure refinement was possible. Figure 3.17 shows the NPD patterns of synthesized $NaAlD_4$ at 295 K and 8 K. Rietveld refinement gave an abundance of 57 wt.% of $NaAlD_4$ with 29 wt.% of NaF and 14 wt.% of Al.

In Fig. 3.17 a small displacement of Bragg's peaks on cooling is seen, indicating a change in lattice parameters. Also, the peaks relative intensities slightly changed. It was found that the largest shrinking of lattice parameters was along the c axis. As for $LiAlD_4$ the Debye–Waller parameters of deuterium atoms are relatively large, indicating again the relative instability of the compound at room temperature. As expected the Debye–Waller parameters for all atoms diminish when the temperature is reduced. Interestingly, for $LiAlD_4$ the thermal parameters of Li and Al remain identical when the temperature was reduced. For $NaAlD_4$ the effect is different, at 295 K the thermal parameter of Na is bigger than the one for Al but the situation is reversed at 8 K.

Figure 3.18 shows the crystal structure of $NaAlD_4$. As for $LiAlD_4$ the structure consists of isolated $[AlD_4]^{-1}$ tetrahedra connected by Na atoms. Each sodium atom has eight deuterium atoms as its near neighbour, each deuterium being part of a

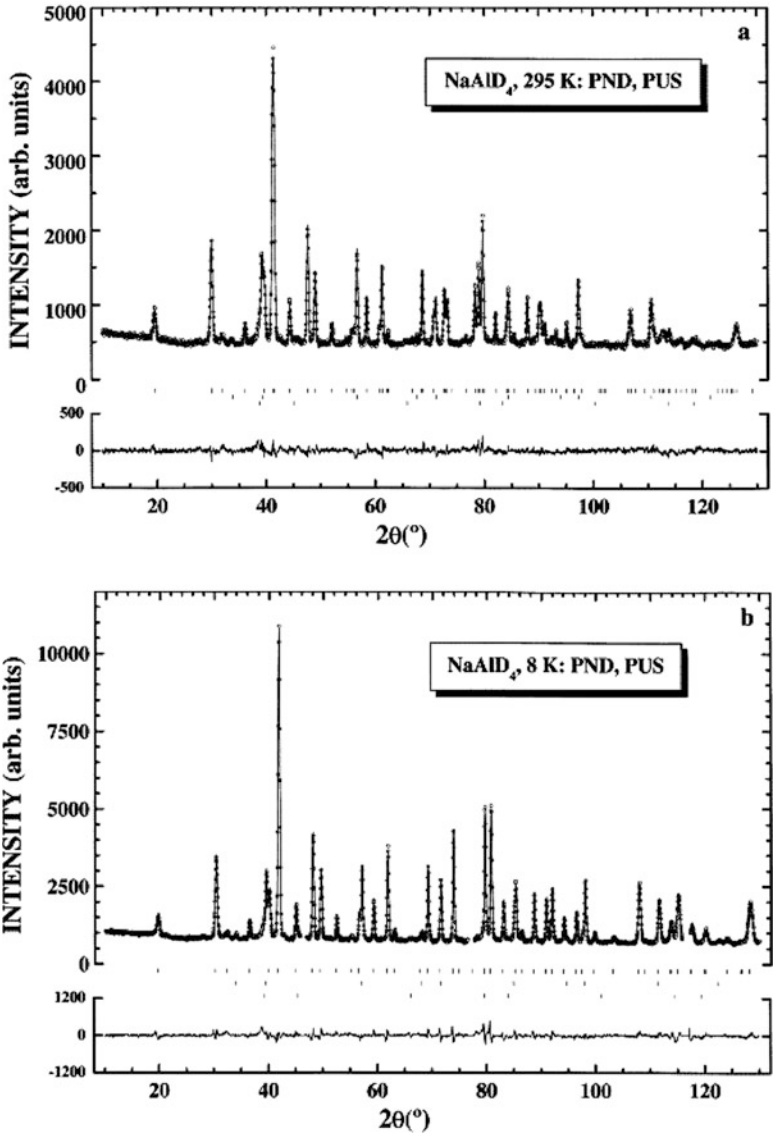

Fig. 3.17 Observed (*points*), calculated (*line*), and difference (*bottom line*) of neutron diffraction pattern of $NaAlD_4$ ($\lambda = 0.15546$ nm). Patterns taken at (**a**) 295 K; (**b**) 8 K. *Vertical bars* indicate the Bragg peaks positions. From [86] with permission

different tetrahedron. The shortest D–D distances are found within the tetrahedron. The Al–D distance is slightly shorter than in $LiAlD_4$. As for $LiAlD_4$, the Al–D distance does not change upon cooling from 295 to 8 K.

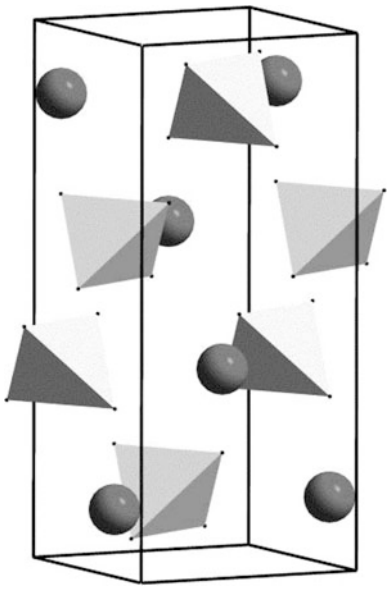

Fig. 3.18 Crystal structure of $NaAlD_4$. AlD_4 tetrahedra are linked via Na atoms. From [86] with permission

3.6.5 β-Yttrium Borohydride $Y(BH_4)_3$: X-rays vs. Neutrons

Yttrium borohydride $Y(BH_4)_3$ is a complex hydride containing the tetrahedral anion BH_4^-. Metal borohydrides have high gravimetric and volumetric capacities of hydrogen, and are therefore of interest for chemical hydrogen storage. Recently high cation mobility was identified in some borohydrides promoting these compounds also as solid state electrolytes for battery application. Yttrium borohydride crystallizes in a room temperature phase α-$Y(BH_4)_3$ (*Pa*-3) which may be compared to the high pressure polymorph of ReO_3, i.e. vertices sharing octahedra. At ~180 °C the α-$Y(BH_4)_3$ transforms to a high temperature polymorph β-$Y(BH_4)_3$. Its crystal structure was studied by XPD [89] and NPD [90]. The XPD data suggested a structure related to the ambient structure of ReO_3, i.e. with undistorted octahedra $Y(BH_4)_6$, lattice parameter *a* and space group *Pm*-3*m* (Fig. 3.19-left). However, the borohydride group BH_4 cannot be ordered in this small cell and stays disordered over two orientations shown in Fig. 3.19-left as thin and thick B–H bonds. The calculated XPD pattern (Fig. 3.20-top) fits perfectly the observed one. Only the NPD has revealed the complete story: The BH_4 groups are perfectly ordered in a cubic cell with twice as big lattice parameter 2*a*, and the space group

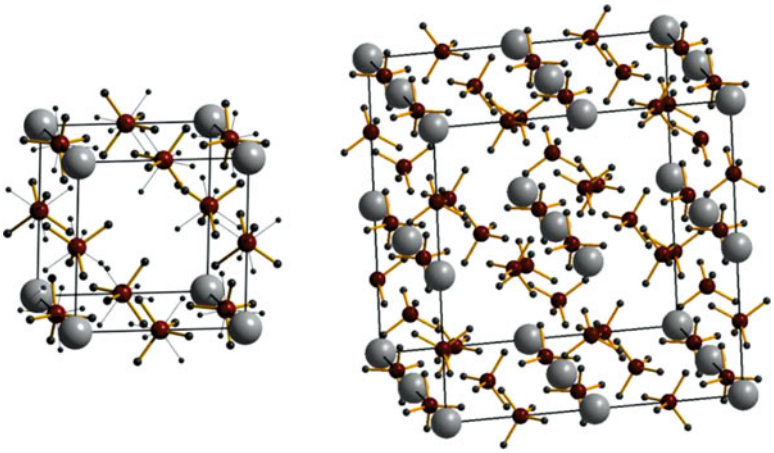

Fig. 3.19 Crystal structure of β-$Y(BH_4)_3$ as seen by: (*left*) XPD [66], (*right*) by NPD [67]. The XPD structure (*Pm*-3*m*) is an average disordered model described in a ½, ½, ½ subcell of the unit cell of the true-ordered NPD structure (*Fm*-3*c*). The borohydride group BH_4 is disordered in the XPD model over two orientations (thin and thick B–H bonds) which become ordered in the NPD model

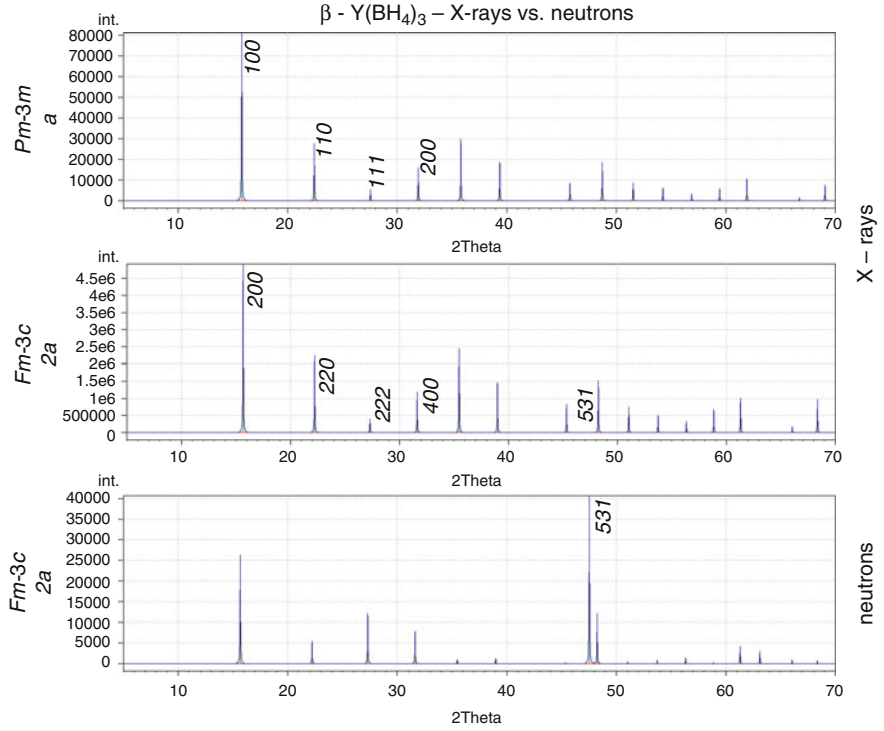

Fig. 3.20 Calculated powder patterns for two structural models of β-$Y(BH_4)_3$: Average disordered model (*Pm*-3*m*) with lattice parameter *a* as seen by XPD (*upper pattern*) and the ordered model (*Fm*-3*c*) with lattice parameter 2*a* as seen by NPD (*lower pattern*), and as calculated for XPD (*middle pattern*). Note that the only difference in the XPD patterns between the disordered and ordered models is the reflection 531 of the ordered model which is practically invisible in XPD patterns, but becomes the strongest peak in the NPD pattern

Fm-3*c*, a minimal supergroup of *Pm*-3*m*. As it can be seen from the calculated XPD with this ordered structural model (Fig. 3.20-middle), there is practically no information about the correct cell in the XPD data. The only superstructure reflection measured in a laboratory XPD data, the reflection 531, is practically invisible, but becomes the strongest peak in the NPD pattern (Fig. 3.20-bottom).

3.6.6 $Mg_6Co_2H_{11}$: Weak Superstructure Induced by Hydrogen

The complex metal hydride $Mg_6Co_2H_{11}$ is a good example of a weak superstructure induced by hydrogen, and nearly invisible in XPD. It is also quite a large structure where the localization of hydrogen (deuterium) by NPD was challenging, and resulted in a description of the hydride as built from CoH_4^{5-} and CoH_5^{4-} complex anions conforming to the 18-electron rule [91]. Its crystal structure (*Pnma*, $a = 8.1120(1)$, $b = 10.0800(1)$, $c = 18.6028(3)$ Å) was solved and refined jointly from one synchrotron (NSLS Brookhaven, $\lambda = 1.6295$ Å) and two neutron powder patterns (ILL Grenoble, $\lambda = 1.5939$ Å and PSI Villigen, $\lambda = 1.7070$ Å). The angular resolution of both neutron experiments was optimized at different 2θ regions, the ILL data were better at high angles and PSI data at low angles. The metal atoms were localized from synchrotron Patterson and Fourier maps of a four times smaller subcell along the *c*-axis, which is the average periodicity of the metal lattice (Fig. 3.21-left). The Mg_2Co intermetallic compound does not exist, but the metal lattice clearly has a tendency to crystallize in the higher symmetry and shorter periodicity of a structure built from ideal co-centred Mg_8 cubes sharing vertices and edges. Only a careful analysis of very weak superstructure peaks in the synchrotron pattern has revealed the true periodicity induced by deuterium atoms, and allowed the refinement of the occupation of 20 proposed D sites (based on minimal interatomic distances) from both neutron patterns. The true periodicity is clearly seen only in the neutron data. See Fig. 3.21-right, where the strongest neutron superstructure reflections are marked as 1 and 2. They are nearly invisible in the synchrotron data where the triplet of strongest superstructure reflections is also marked.

3.7 In-Situ Experiments

In in-situ experiments the evolution of a chemical phenomenon is measured as a function of an external parameter (temperature, pressure, time, etc.) [92]. For example, evolution of the crystal structure of a metal alloy exposed to hydrogen gas pressure and temperature, evolution of the phase composition of a battery

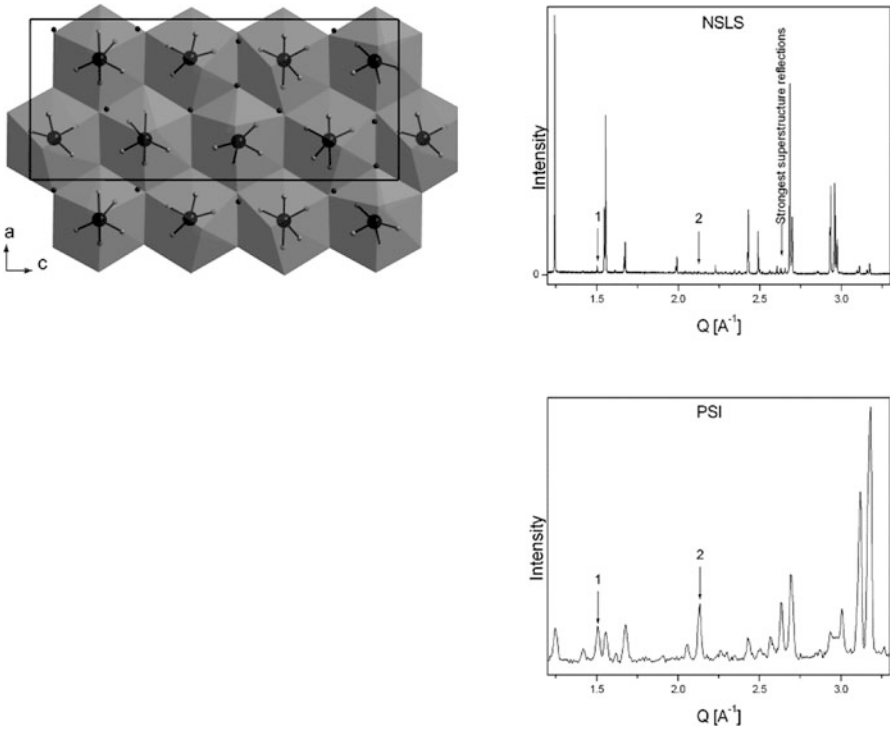

Fig. 3.21 *Left*: One (101) layer of $Mg_6Co_2H_{11}$ structure (Pnma) viewed along the orthorhombic *a*-axis [68]. *Dark grey* (partially transparent) polyhedra are Mg_8 cubes centred with CoH_4 and CoH_5 complexes. Cobalt atoms are represented as the larger and hydrogen atoms as the smaller spheres, the anionic hydrogen in *dark*. *Right*: The four times shorter periodicity of the average structure of metal lattice is visible in low intensity of superstructure reflections in synchrotron pattern (NSLS) compared to the average structure (*Cmcm*) reflections. The true periodicity is clearly seen only in the neutron pattern (PSI), where the strongest neutron superstructure reflections are marked as 1 and 2. They are nearly invisible in the synchrotron data where the triplet of strongest superstructure reflections is also marked. From [86] with permission

electrode when charged or discharged. As we saw in the preceding sections, one of the advantages of neutron radiation is its highly penetrating nature. This is particularly useful for in-situ investigations because the neutron beam has to go through the sample cell and other peripherals (heating elements, pressure cell, etc.) needed for running the experiment. In this section we will briefly discuss about the issues faced in running an in-situ neutron diffraction experiment and show a few specific examples. Further information can be found in recent review papers [92–95].

3.7.1 Cell Design

Obviously, the key in an in-situ experiment is the design of the sample holder and other peripherals. These components have to be able to sustain the experimental conditions while having a minimum impact on the diffraction pattern. In real situations these two characteristics may be contradictories. For example, stainless steel tubing can hold high pressure at elevated temperature but it generates Bragg peaks in the diffraction pattern that could mask sample's peaks. For in-situ experiments done under hydrogen there is the supplementary problem of hydrogen embrittlement thus, only certain type of steel (austenitic) should be used. Bailey et al. have reviewed a number of different alloys and selected Inconel 718 (nickel–chromium–iron–niobium) as the material for their in-situ sample cell [96]. When this type of cell is used for ToF diffractometers, one could select the optimum wall thickness and the required masks for the primary and scattered beams in order to minimize the contribution of the sample holder. Such a procedure is described by Gray et al. who derived an analytical expression taking into account the operation pressure and neutron wavelengths [97]. Gray and Webb [98] also developed a methodology to correct for the attenuation and subtract background due to the sample holder and sample environment.

One way to reduce the intensities of diffraction peaks due to the sample holder is to use an alloy which has a small scattering length while having proper mechanical strength. Vanadium has a small scattering length and is practically transparent to neutrons. Unfortunately, vanadium is also easily hydrided at low temperature and pressure thus making it, in principle, improper as material for a sample cell. One way around this problem is to coat the inside of the cell with a layer of hydrogen impermeable and non-hydriding material such as copper [14, 15]. For example, Flacau et al. made a vanadium can coated with 2 μm of copper that can withstand 15 bar of hydrogen pressure up to 498 K [15].

An elegant approach to minimize the effect of the sample holder on the diffraction pattern is to use the so-called "null-matrix" alloy. The Ti–Zr phase diagram shows a complete miscibility of these two atoms, forming a random substitution solid solutions with hexagonal closed packed structure. The scattering lengths of titanium and zirconium are respectively −3.48 fm and 7.16 fm [31]. This means that an alloy of composition $Ti_{2.08}Zr$ will effectively have a zero scattering length and thus do not exhibit any Bragg peaks [99]. As for any alloy, there is a possibility of hydrogen embrittlement when subjected to hydrogen pressure. This was investigated by Gray and Bailey who found that at low temperature (323 K) the alloy keeps its mechanical integrity even after being exposed to 696 bar of deuterium for 1 month [16]. However, at 373 K embrittlement is fast under high hydrogen pressure (600 bar). Therefore, the use of null-matrix alloy should be restricted to low temperature unless an appropriate liner is incorporated in order to prevent hydrogen diffusion to the null-matrix. For example, a sample holder made of the null-matrix alloy with an internal thin-walled AISI316 liner to prevent hydrogen embrittlement of the $Ti_{2.08}Zr$ has been rated to 1000 bar of D2 at 673 K [17, 100].

Performing in-situ experiments on metal hydride battery electrodes pose the special challenge that, beside the electrode material, the electrode casing and electrolyte will diffract the incident neutron beam thus giving off parasitic peaks and high background. The high background due to the presence of hydrogen in the electrolyte could be reduced by using deuterium. As for the casing, a number of materials have been used: Pyrex [101], silica [102], and the Ti–Zr null-matrix [103]. Recently, a modular coin cell has been developed which enables more flexibility in term of materials to be studied and battery configuration [104].

Many metal hydride systems have been investigated by in-situ techniques. For example, AB_5 alloys [74, 75, 95], titanium-based bcc alloys [105, 106], magnesium-based alloys [17, 107, 108], and TiFe [109].

3.7.2 Palladium

Palladium hydride was the first metal hydride formally identified by Graham in 1866 and is probably the most extensively studied hydride [110]. It also has been the subject of early neutron diffraction experiments by Schull's group who concluded that only octahedral positions are occupied by hydrogen (deuterium) [111]. Since then, numerous neutron diffraction studies have been performed on the palladium–hydrogen system and the general agreement was that hydrogen occupies the octahedral site [112]. However, theoretical calculations indicated that, for deuterium, there is a possibility of stable occupancy in tetrahedral sites [113]. To settle the controversy, McLennan et al. took a theoretical and experimental approach of the Pd-hydrogen system [114]. On the experimental side, they performed in-situ deuteration of palladium using two different instruments: the ToF powder diffraction instrument at ISIS spallation source in UK and the constant wavelength diffractometer at the HIFAR reactor in Australia.

To distinguish between the Octahedral (O) site and Tetrahedral (T) site the authors used the relative intensities of specific Bragg peaks. As the scattering length of deuterium and palladium are respectively 6.674 fm and 5.91 fm, we could, in first approximation, treat them as equal. Palladium has a Cu-type fcc structure. For the stoichiometric hydride PdD, if deuterium occupies the O site then the structure is still fcc but now is NaCl type. Assuming that scattering length of D and Pd are the same it means that, from a neutron diffraction point of view, the unit cell is simple cubic with a halved lattice parameter compared to Pd. Therefore, the (111) Bragg peak of palladium will become practically extinct in PdD. On the other hand, the T sites lie in (200) planes and therefore contribute significantly to the (200) and (220) reflections, but not to (111). Consequently, by recording how the intensities of the (111), (200), and (220) change during deuterium loading one could easily identify which site is occupied by deuterium [114]. From their experimental and theoretical investigation, McLennan et al. found that hydrogen prefers to occupy some of the available tetrahedral sites, particularly in the middle range of concentrations around Pd_8H_4.

3.7.3 Zircaloy-4

A good example of the utility of in-situ experiments is the investigation of corrosion process in Zircaloy-4. Zirconium alloys have higher thermal conductivity, lower linear coefficient of thermal expansion, and smaller thermal neutron cross section than stainless steel. They also resists corrosive attack in most organic and mineral acids, strong alkalis, and some molten salts. Because of all these characteristics, Zircaloys are extensively used in the nuclear industry such as claddings for nuclear fuels used in pressurized water reactors (PWR) and nuclear waste management. To understand the corrosion mechanism under PWR conditions, Lelièvre et al. performed in-situ measurement of Zircaloy-4 [115]. In fact, they used higher temperature (430 °C) than in normal PWR conditions in order to accelerate the corrosion process. As the amount of corroded material was very small, the Bragg peaks associated with zirconia had intensities 10^{-2} to 10^{-3} smaller than the main phase peaks intensities. Despite this, the amount of corroded material estimated was in agreement with electron microscopy observations. By following the change in peaks intensities and positions upon heating and cooling the authors were able to estimate the amount of hydrogen in the $Zr(Cr,Fe)_2$ precipitates.

Acknowledgements The authors would like to thank Dr. Daniel Fruchart (Institut Néel, CNRS), Dr. Pamela Whitfield (Spallation Neutron Source), and Prof. Evan Gray (Griffith University) for useful comments and suggestions.

References

1. International Tables for Crystallography. International Union of Crystallography. Volume A, *Space-group symmetry* (2006). doi:10.1107/97809553602060000100
2. C. Giacovazzo, The diffraction of X-rays by crystals, in *Fundamentals of Crystallography*, ed. by C. Giacovazzo. International Union of Crystallography Texts on Crystallography (Oxford University Press, Oxford, 1992)
3. M.D. Graef, M.E. McHenry, *Structure of Materials* (Cambridge University Press, Cambridge, 2007)
4. T. Chatterji (ed.), *Neutron Scattering from Magnetic Materials* (Elsevier, Amsterdam, 2005)
5. J.S.O. Evans, X-ray and neutron powder diffraction, in *Encyclopedia of Supramolecular Chemistry*, ed. by J.L. Atwood and J.W. Steed (Marcel Dekker, New York, Basel 2004)
6. R.E. Dinnebier, S.J.L. Billinge, *Powder Diffraction: Theory and Practice* (RCS, Cambridge, 2008)
7. V. Pecharsky, P. Zavalij, *Fundamentals of Powder Diffraction and Structural Characterization of Materials*, 2nd edn: 33 Tab (Springer, New York, 2009)
8. U. Kolb, K. Shankland, L. Meshi, A. Avilov, W.I.F. David (eds.), *Uniting Electron Crystallography and Powder Diffraction* (Springer, Dordretch, 2012)
9. P. Scardi, M. Leoni, Whole powder pattern modelling. Acta Crystallogr A **58**, 190–200 (2002)
10. www.neutronsources.org
11. E.H. Kisi, C.J. Howard, *Applications of Neutron Powder Diffraction* (Oxford University Press, Oxford, 2008)

12. O.R.N. Laboratory, *Powgen Experiment*. In. Private communication from A. Huq, Spallation Neutron Source, Oak Ridge National Laboratory
13. A. Huq, J.P. Hodges, O. Gourdon, L. Heroux, Powgen: a third-generation high-resolution high-throughput powder diffraction instrument at the Spallation NeutronSource. Z. Kristallogr. Proc. **1**, 127–135 (2011)
14. K. Iwase, K. Mori, Y. Hishinuma, Y. Hasegawa, S. Iimura, H. Ishikawa, T. Kamoshida, T. Ishigaki, Development of sample holder for in situ neutron measurement of hydrogen absorbing alloy. Int. J. Hydrogen Energy **36**(4), 3062–3066 (2011). doi:10.1016/j.ijhydene.2010.11.044
15. R. Flacau, J. Bolduc, T. Bibienne, J. Huot, H. Fritzsche, Performance of Cu-coated vanadium cans for in situ neutron powder diffraction experiments on hydrogen storage materials. J. Appl. Crystallogr. **45**(5), 902–905 (2012). doi:10.1107/s002188981202938x
16. E.M. Gray, I.F. Bailey, Embrittlement of titanium-zirconium 'null-matrix' alloy by deuterium. J. Neutron Res. **16**(3/4), 127–132 (2008)
17. M.P. Pitt, C.J. Webb, M. Paskevicius, D. Sheptyakov, C.E. Buckley, E.M. Gray, In situ neutron diffraction study of the deuteration of isotopic $Mg^{11}B_2$. J. Phys. Chem. C **115**(45), 22669–22679 (2011). doi:10.1021/jp208355s
18. B.T.M. Willis, C.J. Carlile, *Experimental Neutron Scattering* (OUP, Oxford, 2013)
19. R.H. Wiswall, J.J. Reilly, Inverse hydrogen isotope effects in some metal hydride systems. Inorg. Chem. **11**, 1691 (1972)
20. M.T. Weller, P.F. Henry, V.P. Ting, C.C. Wilson, Crystallography of hydrogen-containing compounds: realizing the potential of neutron powder diffraction. Chem. Commun. **21**, 2973–2989 (2009). doi:10.1039/b821336d
21. R.A. Young, The Rietveld method, in *IUCr Monographs on Crystallography-5*, ed. by R.A. Young (Oxford University Press, Oxford, 1993), p. 298
22. R. Dinnebier, M. Müller, Modern Rietveld refinement, a practical guide, in *Modern Diffraction Methods*, ed. by E.J. Mittemeijer, U. Weizel (Wiley-VCH Verlag GmbH & Co. KGaA, Weinheim, 2012), pp. 27–60
23. J.C. Taylor, I. Hinczak, *Rietveld Made Easy* (Sietronics, Canberra, 2004)
24. H.M. Rietveld, A profile refinement method for nuclear and magnetic structures. J. Appl. Crystallogr. **2**, 65 (1969)
25. G. Caglioti, A. Paoletti, F.P. Ricci, On resolution and luminosity of a neutron diffraction spectrometer for single crystal analysis. Nucl. Instrum. Methods **9**(2), 195–198 (1960). doi:10.1016/0029-554x(60)90101-4
26. G. Caglioti, A. Paoletti, F.P. Ricci, Choice of collimators for a crystal spectrometer for neutron diffraction. Nucl. Instrum. Methods **3**(4), 223–228 (1958). doi:10.1016/0369-643x(58)90029-x
27. H.P. Klug, L.E. Alexander, *X-ray Diffraction Procedures* (Wiley, New York, 1974)
28. R.J. Hill, I.C. Madsen, The effect of profile step counting time on the determination of crystal-structure parameters by X-ray Rietveld analysis. J. Appl. Crystallogr. **17**(OCT), 297–306 (1984). doi:10.1107/s0021889884011547
29. R.J. Hill, I.C. Madsen, Data collection strategies for constant wavelength Rietveld analysis. Powder Diffract. **2**(3), 146 (1987)
30. A. Furrer, J. Mesot, T. Strässle, *Neutron Scattering in Condensed Matter Physics* (World Scientific, Singapore, 2009)
31. V.F. Sears, Neutron scattering lengths and cross sections. Neutron News **3**(3), 26–37 (1992)
32. L. Koester, H. Rauch, E. Seymann, Neutron-scattering lengths – a survey of experimental-data and methods. At. Data Nucl. Data Tables **49**(1), 65–120 (1991). doi:10.1016/0092-640x(91)90012-s
33. H. Kohlmann, Solid-state structures and properties of Europium and Samarium hydrides. Eur. J. Inorg. Chem. **2010**(18), 2582–2593 (2010). doi:10.1002/ejic.201000107
34. D. Schmitt, B. Ouladdiaf, Absorption correction for annular cylindrical samples in powder neutron diffraction. J. Appl. Crystallogr. **31**(4), 620–624 (1998). doi:10.1107/S0021889898002672

35. M. Bowden, M. Ryan, Absorption correction for cylindrical and annular specimens and their containers or supports. J. Appl. Crystallogr. **43**(4), 693–698 (2010). doi:10.1107/S0021889810021114
36. R.A. Young, Introduction to the Rietveld method, in *The Rietveld Method*, ed. by R.A. Young (Oxford University Press, Oxford, 1993)
37. G. Will, *Powder Diffraction: The Rietveld Method and the Two-Stage Method* (Springer, Berlin, Heidelberg, 2006)
38. R.B.V. Dreele, Neutron powder diffraction, in *Modern Powder Diffraction*, ed. by D.L. Bish, J.E. Post. Reviews in Mineralogy, vol 20 (Mineralogical Society of America, Chantilly, 1989)
39. R.J. Roe, Description of crystallite orientation in polycrystalline materials .3. General solution to pole figure inversion. J. Appl. Phys. **36**(6), 2024–2031 (1965). doi:10.1063/1.1714396
40. H.J. Bunge, Zur Darstellung Allgemeiner Texturen. Zeitschrift Fur Metallkunde **56**(12), 872–874 (1965)
41. N.C. Popa, Microstructural properties: texture and macrostress effects, in *Powder Diffraction, Theory and Practice*, ed. by R.E. Dinnebier, S.J.L. Billinge (RSC Publishing, Cambridge, 2008)
42. W.I.F. David, K. Shankland, L.B. McCusker, C. Bärlocher (eds.), *Structure Determination from Powder Diffraction Data* (Oxford University Press, Oxford, 2006)
43. R.B.V. Dreele, J.D. Jorgensen, C.G. Windsor, Rietveld refinement with spallation neutron powder diffraction data. J. Appl. Crystallogr. **15**, 581–589 (1982)
44. E.J. Mittemeijer, U. Welzel, Diffraction line-profile analysis, in *Modern Diffraction Methods* (Wiley-VCH Verlag GmbH & Co. KGaA, Weinheim, 2012), pp. 87–126
45. R.L. Snyder, Analytical profile fitting of X-ray powder diffraction profiles in Rietveld analysis, in *The Rietveld Method. International Union of Crystallography*, ed. by R.A. Young (Oxford Science Publications, Oxford, 1993)
46. J.W. Richardson, Background modeling in Rietveld analysis, in *The Rietveld Method. International Union of Crystallography*, ed. by R.A. Young (Oxford Science Publication, Oxford, 1993)
47. E. Prince, Mathematical aspects of Rietveld refinement, in *The Rietveld Method. International Union of Crystallography*, ed. by R.A. Young (Oxford Science Publications, Oxford, 1993)
48. B.H. Toby, R factors in Rietveld analysis: how good is good enough? Powder Diffract. **21**(1), 67–70 (2006)
49. B. Efron, R. Tibshirani, Bootstrap Methods for standard errors, confidence intervals, and other measures of statistical accuracy. Stat. Sci. **1**(1), 54–75 (1986). doi:10.2307/2245500
50. R. Černý, D.B. Ravnsbaek, P. Schouwink, Y. Filinchuk, N. Penin, J. Teyssier, L. Smrcok, T.R. Jensen, Potassium zinc borohydrides containing triangular $Zn(BH_4)_3^-$ and tetrahedral $Zn(BH_4)_xCl_{4-x}^{2-}$ anions. J. Phys. Chem. C **116**(1), 1563–1571 (2012). doi:10.1021/jp209848r
51. I. Lindemann, R. Domènech Ferrer, L. Dunsch, Y. Filinchuk, R. Černý, H. Hagemann, V. D'Anna, L.M. Lawson Daku, L. Schultz, O. Gutfleisch, Al3Li4(BH4)13: a complex double-cation borohydride with a new structure. Chem. Eur. J. **16**(29), 8707–8712 (2010). doi:10.1002/chem.201000831
52. S.A. Howard, K.D. Preston, Profile fitting of powder diffraction patterns, in *Modern Powder Diffraction*, ed. by D.L. Bish, J.E. Post (Mineralogical Society of America, Chantilly, 1989)
53. D.B. Ravnsbæk, Y. Filinchuk, R. Černý, T.R. Jensen, Powder diffraction methods for studies of borohydride-based energy storage materials. Zeitschrift fur Kristallographie **225**(12), 557–569 (2010)
54. J.-P. Soulié, G. Renaudin, R. Černý, K. Yvon, Lithium boro-hydride LiBH4 I. Crystal structure. J. Alloys Compd. **346**, 200–205 (2002)
55. Y. Filinchuk, D. Chernysov, R. Černý, Lightest borohydride probed by synchrotron X-ray diffraction: experiment calls for a new theoretical revision. J. Phys. Chem. C **112**, 10579–10584 (2008)

56. P. Schouwink, R. Cerný, Complex hydrides – when powder diffraction needs help. CHIMIA Int. J. Chem. **68**(1), 38–44 (2014). doi:10.2533/chimia.2014.38
57. R. Černý, Solving crystal structures of metal and chemical hydrides. Zeitschrift Fur Kristallographie **223**(10), 607–616 (2008). doi:10.1524/zkri.2008.1017
58. R. Černý, Y. Filinchuk, Complex inorganic structures from powder diffraction: case of tetrahydroborates of light metals. Zeitschrift Fur Kristallographie **226**(12), 882–891 (2011). doi:10.1524/zkri.2011.1409
59. V.A. Blatov, A.P. Shevchenko, D.M. Proserpio, Applied topological analysis of crystal structures with the program package ToposPro. Cryst. Growth Des. **14**(7), 3576–3586 (2014). doi:10.1021/cg500498k
60. D.G. Westlake, Hydrides of intermetallic compounds: a review of stabilities, stoichiometries and preferred hydrogen sites. J. Less-Common Met. **91**(1), 1–20 (1983)
61. A.C.Z. Switendick, Phys. Chem. N.F. **117**, 89–112 (1979)
62. R. Černý, V. Favre-Nicolin, Direct space methods of structure determination from powder diffraction: principles, guidelines and perspectives. Zeitschrift Fur Kristallographie **222**(3–4), 105–113 (2007). doi:10.1524/zkri.2007.222.3-4.105
63. V. Favre-Nicolin, R. Černý, FOX, 'free objects for crystallography': a modular approach to ab initio structure determination from powder diffraction. J. Appl. Crystallogr. **35**(6), 734–743 (2002). doi:10.1107/S0021889802015236
64. Y. Fukai, *The Metal-Hydrogen System*, 2nd edn., in Springer Series in Materials Science, vol. 21 (Springer, Berlin, 2005), p. 497
65. Y. Nakamura, K.-I. Oikawa, T. Mamiyama, E. Akiba, Crystal structure of two hydrides formed from a Ti-V-Mn BCC solid solution alloy studied by time-of-flight neutron powder diffraction – a NaCl structure and a CaF_2 structure. J. Alloys Compd. **316**, 284–289 (2001)
66. B. Sakintuna, F. Lamari-Darkrim, M. Hirscher, Metal hydride materials for solid hydrogen storage: a review. Int. J. Hydrogen Energy **32**(9), 1121–1140 (2007)
67. E. Akiba, H. Iba, Hydrogen absorption by Laves phase related BCC solid solution. Intermetallics **6**(6), 461–470 (1998)
68. T. Kabutomori, H. Takeda, Y. Wakisaka, K. Ohnishi, Hydrogen absorption properties of Ti-Cr-A (A = V, Mo or other transition metal) B.C.C. solid solution alloys. J. Alloys Compd. **231**, 528–532 (1995)
69. A.L. Bowman, J.L. Anderson, N.G. Nereson, *Neutron-Diffraction Study of LaNi//5D//7*. (1973), In proceeding: Rare Earth Research, Carefree, Arizona, 30 April 1973 through 3 May 1973. Publisher: AEC, Tech Inf Cent (CONF-730402-P1),Oak Ridge, Tenn. pp. 485–489
70. C. Lartigue, A.L. Bail, A. Percheron-Guegan, A new study of the structure of $LaNi_5D_{6.7}$ using a modified Rietveld method for the refinement of neutron powder diffraction data. J. Less-Common Met. **129**, 65–76 (1987)
71. A. Percheron-Guegan, C. Lartigue, J.C. Achard, P. Germi, F. Tasset, Neutron and X-ray diffraction profile analyses and structure of $LaNi_5$, $LaNi_{5-x}Al_x$ and $LaNi_{5-x}Mn_x$ intermetallics and their hydrides (deuterides). J. Less-Common Met. **74**, 1–12 (1980)
72. C. Lartigue, A. Percheron-Guegan, J.C. Achard, J.L. Soubeyroux, Hydrogen (deuterium) ordering in the β-LaNi5Dx > 5 phases: a neutron diffraction study. J. Less-Common Met. **113** (1), 127–148 (1985)
73. S. Ono, K. Nomura, E. Akiba, H. Uruno, Phase transformations of $LaNi_5$-H_2 system. J. Less-Common Met. **113**, 113–117 (1985)
74. M.P. Pitt, E.M. Gray, E.H. Kisi, B.A. Hunter, Neutron diffraction study of the $LaNi_5$-D system during activation. J. Alloys Compd. **293–295**, 118–123 (1999)
75. M.P. Pitt, E.M. Gray, B.A. Hunter, Evolution of microstructure in the $LaNi_5$-D system during the early absorption-desorption cycles. J. Alloys Compd. **330–332**, 241–245 (2002)
76. E. Parthe, R. Lemaire, Structure block stacking in intermetallic compounds. 1. Rhombohedral-hexagonal Mn+1X5n-1 and monoclinic-hexagonal-trigonal-orthorhombic Mn+1X5n+2 structure series. Acta Crystallogr. Sect. B: Struct. Sci. **31**(JUL15), 1879–1889 (1975). doi:10.1107/s0567740875006413

77. E. Akiba, H. Hayakawa, T. Kohno, Crystal structure of novel La-Mg-Ni hydrogen absorbing alloys. J. Alloys Compd. **408–412**, 280–283 (2006)
78. K. Kadir, T. Sakai, I. Uehara, Synthesis and structure determination of a new series of hydrogen storage alloys; RMg_2Ni_9 (R=La, Ce, Pr, Nd, Sm and Gd) built from Mg_2Ni Laves-type layers alternating with AB_5 layers. J. Alloys Compd. **257**, 115–121 (1997)
79. R.V. Denys, A.B. Riabov, V.A. Yartys, M. Sato, R.G. Delaplane, Mg substitution effect on the hydrogenation behaviour, thermodynamic and structural properties of the La2Ni7-H(D)2 system. J. Solid State Chem. **181**(4), 812–821 (2008)
80. M.N. Guzik, B.C. Hauback, K. Yvon, Hydrogen atom distribution and hydrogen induced site depopulation for the La2−xMgxNi7–H system. J. Solid State Chem. **186**(0), 9–16 (2012). doi:http://dx.doi.org/10.1016/j.jssc.2011.11.026
81. B. Bogdanovic, M. Schwickardi, Ti-doped alkali metal aluminium hydrides as potential novel reversible hydrogen storage materials. J. Alloys Compd. **253–254**, 1–9 (1997)
82. J.W. Lauher, D. Dougherty, P.J. Herley, Sodium tetrahydroaluminate. Acta Crystalogr. **B35**, 1454–1456 (1979)
83. N. Sklar, B. Post, The crystal structure of lithium aluminum hydride. Inorg. Chem. **6**(4), 669–671 (1967)
84. B.C. Hauback, H.W. Brinks, H. Fjellvag, Accurate structure of $LiAlD_4$ studied by combined powder neutron and X-ray diffraction. J. Alloys Compd. **346**, 184–189 (2002)
85. H.W. Brinks, B.C. Hauback, P. Norby, H. Fjellvag, The decomposition of $LiAlD_4$ studied by in-situ X-ray and neutron diffraction. J. Alloys Compd. **351**, 222–227 (2003)
86. B.C. Hauback, H.W. Brinks, C.M. Jensen, K. Murphy, A.J. Maeland, Neutron diffraction structure determination of $NaAlD_4$. J. Alloys Compd. **358**, 142–145 (2003)
87. H.W. Brinks, C.M. Jensen, S.S. Srinivasan, B.C. Hauback, D. Blanchard, K. Murphy, Synchrotron X-ray and neutron diffraction studies of $NaAlH_4$ containing Ti additives. J. Alloys Compd. **376**, 215–221 (2004)
88. V. Ozolins, E.H. Majzoub, T.J. Udovic, Electronic structure and Rietveld refinement parameters of Ti-doped sodium alanates. J. Alloys Compd. **375**, 1–10 (2004)
89. D.B. Ravnsbaek, Y. Filinchuk, R. Černý, M.B. Ley, D. Haase, H.J. Jakobsen, J. Skibsted, T.R. Jensen, Thermal polymorphism and decomposition of $Y(BH_4)_3$. Inorg. Chem. **49**(8), 3801–3809 (2010). doi:10.1021/ic902279k
90. C. Frommen, N. Aliouane, S. Deledda, J.E. Fonneløp, H. Grove, K. Lieutenant, I. Llamas-Jansa, S. Sartori, M.H. Sørby, B.C. Hauback, Crystal structure, polymorphism, and thermal properties of yttrium borohydride $Y(BH_4)_3$. J. Alloys Compd. **496**(1–2), 710–716 (2010)
91. R. Černý, F. Bonhomme, K. Yvon, P. Fischer, P. Zolliker, D.E. Cox, A. Hewat, Hexamagnesium dicobalt undecadeuteride Mg6Co2D11: containing [CoD4]5- and [CoD5]4- complex anions conforming to the 18-electron rule. J. Alloys Compd. **187**(1), 233–241 (1992)
92. M.C. Moron, Dynamic neutron and synchrotron X-ray powder diffraction methods in the study of chemical processes. J. Mater. Chem. **10**(12), 2617–2626 (2000). doi:10.1039/b003604h
93. O. Isnard, A review of in situ and/or time resolved neutron scattering. C. R. Phys. **8**(7–8), 789–805 (2007). doi:http://dx.doi.org/10.1016/j.crhy.2007.10.002
94. T.C. Hansen, H. Kohlmann, Chemical reactions followed by in situ neutron powder diffraction. Zeitschrift für anorganische und allgemeine Chemie **640**(15), 3044–3063 (2014). doi:10.1002/zaac.201400359
95. V.A. Yartys, R.V. Denys, J.P. Maehlen, C.J. Webb, E.M.A. Gray, T. Blach, A.A. Poletaev, J.K. Solberg, O. Isnard, Nanostructured metal hydrides for hydrogen storage studied by in situ synchrotron and neutron diffraction, in *Materials Research Society Symposium Proceedings*, San Francisco, CA; United States, 5 April 2010 through 9 April (2010), pp. 69–79
96. I.F. Bailey, R. Done, J.W. Dreyer, E.M. Gray, A high-temperature high-pressure gas-handling cell for neutron scattering experiments. High Pressure Res. **24**(2), 309–315 (2004). doi:10.1080/08957950410001722028

97. M.P. Pitt, R.I. Smith, E.M. Gray, Time-of-flight neutron powder diffraction with a thick-walled sample cell. J. Appl. Crystallogr. **40**(3), 399–408 (2007). doi:10.1107/s0021889807006668
98. E.M. Gray, C.J. Webb, In-situ diffraction techniques for studying hydrogen storage materials under high hydrogen pressure. Int. J. Hydrogen Energy **37**(13), 10182–10195 (2012). doi:10.1016/j.ijhydene.2012.03.051
99. S.S. Sidhu, L. Heaton, D.D. Zauberis, F.P. Campos, Neutron diffraction study of titanium-zirconium system. J. Appl. Phys. **27**(9), 1040–1042 (1956). doi:10.1063/1.1722538
100. R. Denys, V. Yartys, E. Gray, C. Webb, $LaNi_5$-assisted hydrogenation of $MgNi_2$ in the hybrid structures of $La_{1.09}Mg_{1.91}Ni_9D_{9.5}$ and $La_{0.91}Mg_{2.09}Ni_9D_{9.4}$. Energies **8**(4), 3198–3211 (2015)
101. Ö. Bergström, A.M. Andersson, K. Edström, T. Gustafsson, A neutron diffraction cell for studying lithium-insertion processes in electrode materials. J. Appl. Crystallogr. **31**(5), 823–825 (1998)
102. M. Latroche, Y. Chabre, B. Decamps, A. Percheron-Guégan, D. Noreus, In situ neutron diffraction study of the kinetics of metallic hydride electrodes. J. Alloys Compd. **334**(1–2), 267–276 (2002). doi:10.1016/s0925-8388(01)01799-6
103. M. Bianchini, J.B. Leriche, J.L. Laborier, L. Gendrin, E. Suard, L. Croguennec, C. Masquelier, A new null matrix electrochemical cell for Rietveld refinements of in-situ or operando neutron powder diffraction data. J. Electrochem. Soc. **160**(11), A2176–A2183 (2013). doi:10.1149/2.076311jes
104. J.J. Biendicho, M. Roberts, C. Offer, D. Noréus, E. Widenkvist, R.I. Smith, G. Svensson, K. Edström, S.T. Norberg, S.G. Eriksson, S. Hull, New in-situ neutron diffraction cell for electrode materials. J. Power Sources **248**(0), 900–904 (2014). doi:http://dx.doi.org/10.1016/j.jpowsour.2013.09.141
105. S. Miraglia, D. Fruchart, N. Skryabina, M. Shelyapina, B. Ouladiaf, E.K. Hlil, P. Rango, J. Charbonnier, Hydrogen-induced structural transformation in $TiV_{0.8}Cr_{1.2}$ studied by in situ neutron diffraction. J. Alloys Compd. **442**, 49–54 (2007)
106. Y. Fei, X. Kong, Z. Wu, H. Li, V.K. Peterson, In situ neutron-diffraction study of the Ti38V30Cr14Mn18 structure during hydrogenation. J. Power Sources **241**(0), 355–358 (2013). doi:http://dx.doi.org/10.1016/j.jpowsour.2013.04.118
107. J. Charbonnier, P.D. Rango, D. Fruchart, S. Miraglia, N. Skryabina, J. Huot, B. Hauback, M. Pitt, S. Rivoirard, Structural analysis of activated $Mg(Nb)H_2$. J. Alloys Compd. **404–406**, 541–544 (2005)
108. M. Ponthieu, F. Cuevas, J.F. Fernández, L. Laversenne, F. Porcher, M. Latroche, Structural properties and reversible deuterium loading of MgD 2-TiD2 nanocomposites. J. Phys. Chem. C **117**(37), 18851–18862 (2013). doi:10.1021/jp405803x
109. D. Fruchart, M. Commandré, D. Sauvage, A. Rouault, R. Tellgren, Structural and activation process studies of Fe-Ti like hydride compounds. J. Less-Common Met. **74**, 55–63 (1980)
110. T. Graham, On the absorption and dialytic separation of gases by colloid septa. Phil. Trans. R. Soc. (London) **156**, 399–439 (1866)
111. J.E. Worsham Jr., M.K. Wilkinson, C.G. Shull, Neutron-diffraction observations on the palladium-hydrogen and palladium-deuterium systems. J. Phys. Chem. Solid **3**(3–4), 303–310 (1957)
112. M.P. Pitt, E.M. Gray, Tetrahedral occupancy in the Pd-D system observed by in situ neutron powder diffraction. Europhys. Lett. **64**(3), 344–350 (2003). doi:10.1209/epl/i2003-00187-x
113. C. Elsässer, K.M. Ho, C.T. Chan, M. Fähnle, Vibrational states for hydrogen in palladium. Phys. Rev. B **44**(18), 10377–10380 (1991). doi:10.1103/PhysRevB.44.10377
114. K.G. McLennan, E.M. Gray, J.F. Dobson, Deuterium occupation of tetrahedral sites in palladium. Phys. Rev. B: Condens. Matter Mater. Phys. **78**(1), 014104 (2008). doi:10.1103/PhysRevB.78.014104
115. G. Lelièvre, D. Fruchart, P. Convert, F. Lefèvre-Joud, Characterisation by neutron diffraction in high temperature pressurised water of the surface corrosion and hydrogen embrittlement of Zircaloy-4. J. Alloys Compd. **347**(1–2), 288–294 (2002). doi:10.1016/S0925-8388(02)00775-2

Chapter 4
Total Neutron Scattering

Magnus H. Sørby

Abstract Total neutron scattering is in many ways an extension of neutron powder diffraction (Chapter 3). However, rather then just considering the shape Bragg peaks, the total scattering from the sample is measured and analyzed. This includes the weaker diffuse scattering which contain information about short-range atomic strutural features. This chapter gives an introduction to total neutron scattering theory and instrumentation and gives an overview of total neutron scattering investigations of hydrogen storage materials.

Keywords Total neutron scattering • Hydrogen storage • Total X-ray scattering • Diffuse scattering • Bragg scattering • Neutron powder diffraction • Metal hydrides • Metal deuterides • Complex hydrides • Complex deuterides • Disorder • Short-range order • Spallation source • Data reduction • Pair distribution function • PDF • G(r) • Partial pair distribution function • g(r) • Scattering function • S(Q) • Reverse Monte Carlo modelling • RMCPOW • RMCProfile • DISCUS • Monte Carlo techniques • Structure modelling • Least-square refinement • Switendick criterion • Amorphous materials • Nanocrystalline materials • Vanadium deuteride • Laves phase • FeTi hydride • Metal aluminium amides

4.1 Introduction

The atomic structure is arguably the most fundamental property of a material as it dictates all other properties. Diffraction measurements with X-rays and neutrons (Chap. 3) have over the last century proven enormously successful for determination of the atomic structure of crystalline materials. Such experiments usually only consider the Bragg scattering, i.e. the sharp features in the scattering pattern in the directions given by Bragg's law (Eq. 2.25). The Bragg scattering reveals the long-range order of the atomic structure, represented by the unit cell, which shows the time- and space-averaged positions of the atoms. This averaged picture is often

M.H. Sørby
Institute for Energy Technology, Instituttveien 18, Kjeller NO-2007, Norway
e-mail: magnuss@ife.no

H. Fritzsche et al. (eds.), *Neutron Scattering and Other Nuclear Techniques for Hydrogen in Materials*, Neutron Scattering Applications and Techniques,
DOI 10.1007/978-3-319-22792-4_4

fully adequate to describe and understand crystalline materials, especially when they have a high degree of order. In other cases, the most interesting structural features only extend over length scales of a few interatomic distances. The Bragg scattering does not contain any information about such short-ranged structural features.

Many hydrogen storage materials have substantial disorder in their atomic arrangements. The properties of intermetallic hydrides are for instance tailored by partly substituting some metallic elements by others and the hydrogen atoms may be distributed over partly occupied interstitial sites. Complex hydrides can exhibit orientational disorder of the complex anions [1, 2] and partial substitution of the complex ion for halides [3–5]. Regular diffraction experiments only tell us a part of the story in such cases. From the Bragg scattering we can for instance determine the probability of finding a substituent species on a certain site in the unit cell, but we cannot learn how the presence of a substitute element affects the atomic arrangement in its close proximity.

This chapter presents total neutron scattering as a technique to investigate both long- and short-range structure of materials. As the name implies, this is achieved by not only considering the Bragg scattering but also the *diffuse* scattering which originates from local deviations from the perfect crystal structure. The theory and instrumentation for total scattering measurement as well as the steps for data reduction and analysis are explained. Finally, some examples of total neutron scattering investigations of hydrogen storage materials are highlighted.

4.2 The Total Neutron Scattering Technique

4.2.1 Principles

A material with all atoms at rest in a perfectly periodic pattern extending to infinity in all directions would only give Bragg scattering in a scattering measurement, since there would be complete destructive interference in all directions except those given by Bragg's law. Such materials obviously do not exist. The atomic arrangement in real crystals will always exhibit deviations from the ideal periodicity. These deviations are both dynamic and static, e.g., thermal vibrations, substitutional disorder, vacancies, dislocations, and stacking faults. Any deviation from the perfect infinite periodicity renders the destructive interference between the Bragg peaks imperfect. This gives rise to *diffuse* scattering between and underneath the sharp Bragg peaks, and a corresponding reduction in the Bragg scattering. When only Bragg scattering is analyzed, for instance by Rietveld refinement, the diffuse scattering, along with instrumental contributions, is fitted by a polynomial and simply discarded as "background." A structure model obtained in this manner is of course perfectly periodic and is represented by a unit cell which shows the time- and space-averaged atomic arrangement. The degree of structural disorder can be

inferred from the reduction in the Bragg intensities and is reflected by the Debye–Waller factors and occupancy numbers, which reveal the (isotropic or anisotropic) mean-square displacement of the atoms from the average sites and the degree of occupational disorder (vacancy concentration or substitutional disorder), respectively. However, since the entire atomic arrangement is collapsed into one unit cell, there will be no information about any correlations between the disordered structural features. Information about such correlations is contained in the diffuse scattering and can therefore be revealed by careful measurement of the *total scattering*, i.e. both the Bragg and diffuse scattering. The total scattering is usually represented by the *structure function*, $S(\mathbf{Q})$, given by

$$S(\mathbf{Q}) = \frac{1}{n}\left(\frac{d\sigma(\mathbf{Q})}{d\Omega}\right)_{\text{coherent}} = \frac{1}{n}\sum_{j,k=1}^{n} b_j b_k e^{i\mathbf{Q}\cdot\left(\mathbf{r}_j-\mathbf{r}_k\right)} \tag{4.1}$$

where the summation is over all the n scattering atoms, b_j and b_k are the coherent scattering lengths of atoms j and k, $\mathbf{r}_j$ and $\mathbf{r}_k$ are the positions of atoms j and k (relative to a chosen origin), $\mathbf{Q} = \mathbf{k_f} - \mathbf{k_i}$ is the scattering vector (see also Eqs. 2.12, 2.13, 2.15, and 2.21). $\mathbf{k_i}$ and $\mathbf{k_f}$ have the direction of the incident and scattered beam, respectively. Their magnitudes are treated as equal under the assumption that energy changes in the scattering events are very small compared to the energy of the incident neutrons, the so-called *static approximation* [6], i.e. $|\mathbf{k_f}| \approx |\mathbf{k_i}| = 2\pi/\lambda$ where λ is the incident neutron wavelength. The absolute value of the scattering vector is then $Q = (4\pi\sin\theta)/\lambda$, where θ is half the angle between $\mathbf{k_i}$ and $\mathbf{k_f}$ (Fig. 2.6). $S(\mathbf{Q})$ is obtainable from the experimentally measured scattering, since the differential scattering cross-section, $(\mathrm{d}\sigma(\mathbf{Q})/\mathrm{d}\Omega)_{\text{coherent}}$, is the number of neutrons scattered coherently per second by the sample in the direction $\mathbf{k_f}$ into the solid angle Ω (the solid angle which is reckoned as the point $\mathbf{Q}$ by the detector) divided by the incident flux on the sample. However, since several effects attenuate the beam and only coherent scattering from the sample itself is of interest, corrections must be performed on the measured data to obtain $S(\mathbf{Q})$ (see Sect. 4.2.3). $S(\mathbf{Q})$ is directly related to the atomic arrangement of the scattering material, as it can be Fourier transformed to yield the *pair distribution function* (PDF), $G(\mathbf{r})$. The PDF is the weighted sum of the *partial pair distribution functions*, $g_{u-v}(r)$

$$G(\mathbf{r}) = \sum_{u,v=1}^{s} c_u c_v b_u b_v g_{u-v}(\mathbf{r}) = \int_{-\infty}^{\infty} S(\mathbf{Q}) e^{i\mathbf{Q}\cdot\mathbf{r}} d\mathbf{r} \tag{4.2}$$

where c_u and c_v are the relative atomic concentrations of the species u and v, respectively, and the summation is done over all the s species in the sample. For polycrystalline materials, as well as liquids and glasses, $\mathbf{Q}$ is an isotropic vector so that all the functions above depend only on the magnitude of the scattering vector, $Q = |\mathbf{Q}|$, and not its direction. $g_{u-v}(r)$ is the normalized density of atoms of type v in a spherical shell of thickness dr, at the distance r from an u-atom (averaged over all u-atoms):

$$g_{u-v}(r) = \frac{N_v}{4\pi r^2 \cdot dr \cdot \rho_v} \tag{4.3}$$

where N_v is the number of atoms of type v in the spherical shell. ρ_v is the bulk density of v-atoms so the limiting value of g is 1 when $r \to \infty$. In simple words, $g_{u-v}(r)$ is a function showing the distribution of interatomic distances between the atoms of type u and v. It is important to notice that these are not the distances between the average positions in a crystal lattice, but rather the interatomic distances found in a frozen snap-shot picture of the atomic structure.

The reader should be aware that different formalisms have different definitions of $S(Q)$ and $G(r)$. The functions are often normalized to approach certain limiting values at high-Q and high-r. Although this may seem confusing, it should be kept in mind that the information contained in the functions is independent of the choice of formalism. Different formalisms are discussed in [7].

4.2.2 Instrumentation

There is in principle no difference between a total neutron scattering instrument and a neutron powder diffractometer. Both are used to measure the scattering intensity as a function of Q. However, certain instrument characteristics are necessary to collect total scattering data of high quality. Most notably, the instrument should be able to collect data up to high values of Q. $S(Q)$ should ideally be flat and featureless at the highest Q, allowing for transformation to $G(r)$ without significant truncation ripples. Moreover, high counting rates and low background are important in order to measure the weak diffuse scattering with appropriate statistics. High resolution is less critical for total scattering measurements than for powder diffraction measurements intended for structure determination. The effect of the instrumental broadening of the Bragg peaks is merely a damping of $G(r)$ with increasing r, which can be corrected for during data analysis.

Time-of-flight (TOF) measurements on spallation sources are superior to constant-wavelength measurements at nuclear reactors, especially with respect to the Q-range, for total scattering measurements.

Many instruments have been built primarily for total scattering measurements. Some examples are *GEM* [8], *POLARIS*, *NIMROD* [9], and *SANDALS* at ISIS (UK); *NOVA* at J-Parc (Japan); *NPDF* [10] at LANSCE (USA); *NOMAD* [11] at SNS (USA), and *D4c* [12] at ILL (France).

4.2.3 Data Reduction and Analysis

Raw data from a scattering measurement contain contributions from instrumental background, incoherent scattering, and scattering from the sample container and is attenuated by sample absorption and multiple scattering. In order to obtain $S(Q)$ from the measured data, they must be corrected for all these effects and normalized to the scattering of a standard. The instrumental background must be experimentally measured, since it varies smoothly with Q in much of the same way as the diffuse scattering. Separate measurements are therefore done both for the empty instrument (i.e., nothing mounted in sample position) and for the empty sample container to account for beam attenuation in the sample environment. Finally an isotropic scatterer, for instance a vanadium rod, must be measured for data normalization. Thus three measurements must be performed in addition to the ordinary measurement of the sample. In addition, each data set must be measured for a longer time than in a Bragg scattering measurement to give the required statistics for the weaker diffuse scattering. This high expense in beam time means that there should be good reasons, i.e. suspected interesting short-range structure features, to measure total scattering rather than uncorrected power diffraction data.

As soon as the necessary data sets are collected, there are various computer programs available to perform the data correction. Some freely available alternatives are *PDFgetN* [13] (TOF data), *Gudrun* (TOF and constant-wavelength data), and *CORRECT* (constant-wavelength data). Accurate values for sample density, composition, and thickness must be input to correctly account for absorption and multiple scattering. Detailed treatment of data acquisition and corrections of total neutron scattering data are found in ref. [14].

The next step after corrected and normalized data are obtained is to transform the data into $G(r)$. If the measurement was performed to sufficiently high Q where $S(Q)$ is flat, the transformation can be performed directly according to Eq. 4.2 using software like *PDFgetN* [13] or *Mantid* [15]. If $S(Q)$ still has significant features at $Q_{\max}$, the Fourier transform will introduce truncation ripples in $G(r)$ which make further analysis difficult. In such cases, $G(r)$ may rather be obtained by an inverse method where a hypothetical $G(r)$ defined to a high value of r is refined by a Monte Carlo procedure until its inverse Fourier transform agrees with the experimental $S(Q)$. This procedure is implemented for constant-wavelength and TOF data in the programs MCGR [16, 17] and MCGRtof [18]. Alternatively, further data analysis can be performed directly on $S(Q)$ rather than on $G(r)$ as described later.

There are several possible strategies for analysis of total scattering data. Very basic information can be found by visual inspection of $G(r)$, such as the shortest interatomic distance which corresponds to the position of the first peak. If the first peak is well-separated from the next and is expected to correspond to a single pair correlation, the coordination number can be inferred from the area of the peak. With increasing number of elements in the material, this approach becomes less reliable since $G(r)$ is the sum of all the partial $g(r)s$. For a system with s chemical species, there are $\frac{1}{2}(s(s+1))$ partial PDFs. Thus, computer modelling quickly becomes a necessity for extraction of structural information.

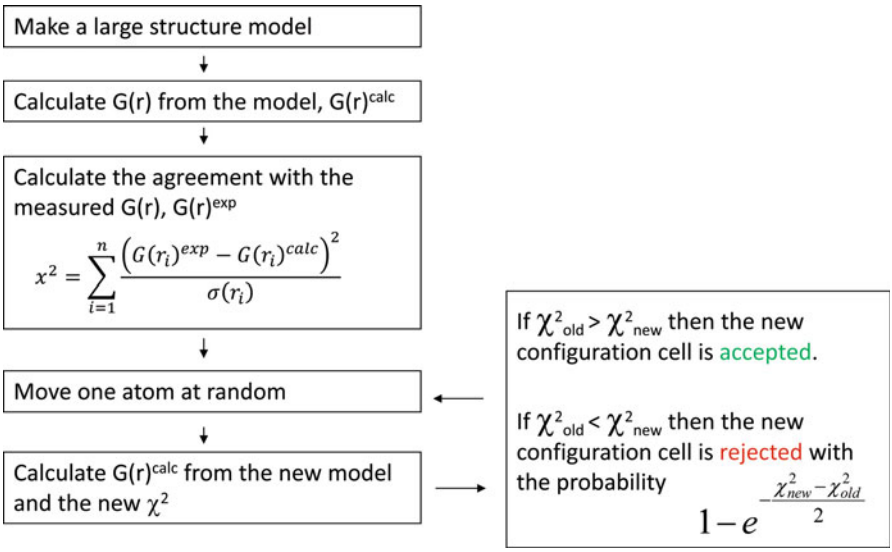

Fig. 4.1 Schematic principle of reverse Monte Carlo modelling

Several modelling strategies exist, and the so-called *Reverse Monte Carlo* (RMC) method is the most versatile and general approach. The RMC method was first described by McGreevy and Pusztai in 1988 [19]. The goal is to create a three-dimensional structure model (i.e., a set of atomic coordinates in a predefined box) that is consistent with the available experimental total scattering data. Such a model will not exhibit the same periodicity as a time-averaged model, but represent a "snap-shot" of the atomic arrangement frozen in time. The principle of the technique is illustrated in Fig. 4.1. The first step is to construct an initial structure model with correct chemical composition and density. If the investigated material is crystalline, the initial structure model will be taken as a large supercell of the crystallographic unit cell. The model must be sufficiently large to give a good statistical representation of the different local atomic configurations in the material. This typically requires several thousand atoms. Random changes are then done to the structure model. Those changes that improve the agreement (given by χ^2, see Fig. 4.1) between the experimental data and the model are accepted. Most of the moves that deteriorate the agreement are rejected, but a small fraction of them are accepted to avoid being trapped in false minima. The process is repeated until there is no further decrease in χ^2, which typically requires millions of attempted moves. The resulting structure model will, in the absence of significant systematic errors, be consistent with the experimental data within the standard deviations. The model will of course not be unique, since every new RMC run will generate a new set of atomic coordinates. However, each of the generated models will show common structural features typical for the investigated material.

The generality of the RMC method is one of its great strengths. It is not limited to crystalline solids [20–22], but can equally well be applied to glasses [23, 24] and

liquids [25–27]. The pioneering work of McGreevy and Pusztai [19] was actually an investigation of the structure of liquid argon. Total scattering data from either X-rays or neutrons or both at the same time can be used. If more than one data set are used, χ^2 is simply replaced by the sum of the individual χ^2 for each data set. The weight of the different χ^2 can be adjusted by scaling the σ factor that denotes the uncertainties in the experimental data points. The method can be extended to any techniques for which an experimental signal can be calculated from a structure model. EXAFS has, for instance, been used in combination with neutron and X-ray total scattering to model the amorphous structure of ion-conducting $(AgI)_x(AgPO_3)_{1-x}$ [28] and the local structure in ferroelectric solid solution $BiFeO_3$-$PbTiO_3$ [29].

Another strength of RMC is that geometrical constraints can be easily incorporated to ensure that the final models are physically sensible. The most important constraints are density and cut-off distances. The density is simply given by the size of the model box and number of different atoms that are put in it and should of course match the bulk density of the material. The cut-off distances define the minimum allowed separation between different types of atoms. Coordination numbers and bond-valence sums are other quantities that can be constrained.

RMC modelling can be performed with several freely available software codes. They are all broadly based on the algorithm in Figure 4.1 but there are some differences in the implementations. *RMCA* is the "original" RMC code written in Fortran. It can handle neutron and/or X-ray total scattering data as $S(Q)$ or $G(r)$ as well as EXAFS data. *RMC++* [30] is based largely on *RMCA*, but the code is completely rewritten and optimized in C++ which is claimed to decrease the calculation times by a factor of three. It also has some possibilities not found in *RMCA*, e.g., to treat known molecular structures as rigid bodies. These codes are most suitable for amorphous and liquid materials since they do not account for the instrumental resolution which is important when sharp features, Bragg peaks, are present in the data.

The most powerful and feature-packed program, *RMCProfile* [31], is developed and continuously improved by a community centered around the instruments *GEM* and POLARIS at ISIS. It can use several different experimental functions simultaneously to increase the correctness of the resulting models at different length scales which makes it suitable for polycrystalline materials. $G(r)$ will usually be one of them, since a properly obtained $G(r)$ from high-quality total scattering data contains detailed information about the short-range order; usually the purpose of a total scattering investigation. However, since $G(r)$ is less sensitive to long-range order, $S(Q)$ can also be included. $S(Q)$ of the model, $S^{\mathrm{calc}}(Q)$, is obtained by Fourier transformation of $G^{\mathrm{calc}}(r)$ calculated from the model. This introduces truncation errors in $S^{\mathrm{calc}}(Q)$ due to the finite size of the model. Thus, the same error must be introduced in experimental $S(Q)$, $S^{\mathrm{exp}}(Q)$, to make the two functions comparable. This is done by convoluting $S^{\mathrm{exp}}(Q)$ with a box function with dimension equal to half the shortest dimension of the model box. This process broadens the features of $S^{\mathrm{exp}}(Q)$ and thereby degrades the information carried by the sharp Bragg peaks. Thus, to effectively use the information about long-range order during modelling,

the Bragg intensities are input to the modelling as a third data set in the form of the unconvoluted scattering profile. The diffuse scattering is fitted with a polynomial and the model's Bragg peak intensities are calculated from the structure factors and broadened with an instrumental resolution function like in a Rietveld refinement. Fitting to $G(r)$, $S(Q)$, and the Bragg peaks simultaneously ensures that the model is consistent with the experimental data on both short and long length scales. Total X-ray scattering data and EXAFS data can also be included in *RMCProfile*.

RMCPOW [32, 33] uses a different strategy to model disorder in crystalline materials. It fits the total scattering data directly at the $S(Q)$ level rather than going through $G(r)$. This is useful for reactor-based data where only moderate Q-ranges are achievable and direct transfer to $G(r)$ is not possible. Crystalline materials give the additional challenge of sharp features in $S(Q)$, i.e. the Bragg peaks, whose width and shape depend on the instrumental resolution. This is solved in *RMCPOW* by telling the program how many crystallographic unit cells the large RMC structure model consists of in each direction. $S(Q)$ is calculated from Eq. 4.1 in discrete points corresponding to the "Bragg peaks" of the large structure model. The subsets of Bragg peaks that are also Bragg peaks for the crystallographic unit cell are broadened by the instrumental resolution function. The remaining "Bragg peaks," which are all "superlattice reflections" of the supercell model, are very closely spaced due to the large size of the model. They are smoothened to model the continuous diffuse scattering. *RMCPOW* can also handle both Bragg and diffuse magnetic neutron scattering. A downside of the RMCPOW approach is that it is computationally much more expensive to calculate the scattering intensity of the model than to calculate $G(r)$ and its Fourier transform.

The software package *DISCUS* [34] can be used to construct complicated models of nanoparticles and bulk disordered materials and simulate their single-crystal diffuse scattering, total scattering, and PDFs. The program includes an RMC module to fit the models to experimental total scattering data.

An alternative to RMC modelling for crystalline materials is so-called real-space Rietveld refinement implemented in the program *PDFfit2* with the graphical user interface *PDFgui* [35]. Much smaller structure models are used, often just one crystallographic unit cell. Effects of correlated or uncorrelated thermal vibrations and partial site occupancies are therefore modelled by refinable parameters rather than being represented directly by the atomic arrangement of the model like in RMC. The model is fitted without any space group symmetry constraints to $G(r)$ by a least-square refinement. The fitting is done in seconds or less and the method is therefore much faster than RMC which requires hours or even days to converge. The increased speed makes "real-space Rietveld refinements" much more suitable to analyze PDFs of multiphase samples, which is in practice very hard with RMC. The method is also suitable for modelling the structure of nanoparticles, since the size and shape of the particles can be described by refinable variables.

More information of RMC modelling can be found in several reviews [36–39]. Total scattering formalism is treated in detail in the books by Nield and Keen [14] and Egami and Billinge [40]. The latter also gives detailed description of "real-space Rietveld refinement."

4.3 Total Neutron Scattering Investigations of Hydrogen Storage Materials

4.3.1 Crystalline Metal Hydrides

The first RMC investigation of metal hydrides was motivated by the wish to experimentally determine the H-H or D-D separation in disordered systems. The "Switendick criterion," which states that hydrogen or deuterium atoms must be separated by at least 2 Å in stable hydrides [41, 42], had been challenged by reports of D-D separations down to 1.6 Å in $RE_3Ni_3In_3D_4$ (RE = La, Ce, and Nd) [43]. This could lead to hydrogen storage materials with greatly increased H densities. H-H distances can be reliably obtained from the Bragg scattering of ordered metal hydrides where all the atomic positions in the unit cell are fully occupied. In disordered metal hydrides, on the other hand, the hydrogen atoms are distributed over some partly occupied sites with no long-range correlation in hydrogen distribution. The partly occupied sites are often separated by much less than 2 Å. Their position and occupancy can be determined by Bragg scattering, but it gives no information about any short-range correlations between the occupancy of different sites. Thus, based on Bragg scattering alone one can only assume that short-range order prevents simultaneous occupation of too closely situated sites.

α-$VD_{0.8}$ was used as the first test compound because it is structurally and compositionally simple. Actually it is quasi-mono-component from a neutron scattering point of view since the coherent scattering from vanadium is close to negligible. Moreover, it is easy to prepare in a pure form as powder or, unlike most other metallic hydrides, as single crystals. The latter point implies that its short-range order was already investigated by single crystal diffuse scattering measurements [44–46].

Neutron powder diffraction and Rietveld refinement reveal the average structure of α-$VD_{0.8}$ where the vanadium atoms form a body-centered cubic (bcc) lattice and deuterium is disorderly distributed mainly over tetrahedral sites and a small fraction (up to 10 % of the D atoms) in octahedral sites [47–49]. The shortest distance between tetrahedral interstices is only 1.1 Å. Tetrahedral and octahedral interstices are separated by only 0.8 Å. Thus, simultaneous occupation of neighboring sites would be a severe violation of the Switendick criterion. However, earlier investigations using total neutron scattering and "short-range order (SRO) parameters" indicate a nearly complete blocking of interstices that are closer than 2 Å from any occupied deuterium site [44–46, 50, 51]. The SRO parameters represent the probability of occupation of different coordination spheres, and were used to make analytical expressions for the diffuse intensity. The parameters could then be refined to fit the calculated diffuse scattering to the observed one. A weakness with this approach is that there is no guarantee that the obtained set of SRO parameters is actually consistent with any possible three-dimensional arrangement

of atoms. Moreover, the method is not very flexible as the complexity of the analytical expression increases rapidly with the complexity of the structure and the number of effects contributing to the diffuse scattering.

Sørby et al. [48] performed reverse Monte Carlo modelling of α-$VD_{0.8}$ based on total scattering neutron data from the instrument SLAD at the former reactor R2 in Studsvik, Sweden. Due to the limited Q-range ($Q_{max} = 10.5$ Å^{-1}) it was not possible to obtain $G(r)$ directly by Fourier transform, and the modelling was performed on $S(Q)$ with the program RMCPOW. Since occupational short-range order of D was believed to be the dominant source of diffuse scattering, the RMC modelling was first performed with all atoms fixed at their ideal crystallographic positions in a $6 \times 6 \times 6$ supercell. Non-scattering reference atoms ("vacancies") were put in all non-occupied interstitial sites and the short-range order was modelled by swap moves between deuterium atoms and vacancies. To account for thermal vibrations, the atomic scattering powers were reduced with a Debye–Waller factor and thermal diffuse scattering corresponding to uncorrelated harmonic atomic oscillations was added to $S^{calc}(Q)$. As opposed to the random starting model, only a minor fraction of the deuterium atoms in the converged model were involved in D-D distances shorter than the Switendick criterion. This fraction was found to have no significant impact on the fit when the modelling was redone with the hard constraint that all D atoms must be separated by 2 Å. Thus it was concluded that the experimental data were consistent with a complete blocking of deuterium atoms within the Switendick radius of any given D atom.

The model was further refined by allowing displacive moves, rather than Debye–Waller factors, to model dynamic and possibly static displacements from the average crystallographic positions. The D-D cut-off was set to 0.7 Å to avoid clustering of D atoms over distances below the resolution of the data. The fit to the experimental data is shown in Fig. 4.2 and the distribution of D-D distances, $g_{D\text{-}D}(r)$, is shown in Fig. 4.3. $g_{D\text{-}D}(r)$ is flat below 2 Å, apart from a very sharp peak at 1.56 Å which was discarded as an artifact due to imperfect data correction. The peak for the first D-D coordination sphere is found at $r = 2.2$ Å, which corresponds to the fourth coordination sphere of tetrahedral interstices. The peak is narrower than expected from uncorrelated thermal vibration. It corresponds to a mean-square displacement of only 0.002 Å^2, which is an order of magnitude lower than that indicated by the displacement factors obtained by Rietveld refinement [48]. Thus, the D atoms appear to vibrate partly in phase.

α-$VD_{0.75}$ transforms to the ordered phase δ-$VD_{0.75}$ below 205 K. The metal lattice is basically the same as in the α-phase, but deuterium is fully ordered with selective occupation of 1/8th of the tetrahedral interstices, lowering the symmetry to orthorhombic. $g_{D\text{-}D}(r)$ for δ-$VD_{0.75}$ was calculated from the crystal structure found in literature and was found to be very similar to that of α-$VD_{0.75}$ up to $r = 3$ Å, which covers the two first coordination spheres. This indicates that the local D-arrangement in the disordered α-phase resembles that of the long-range ordered δ-phase at these short length scales.

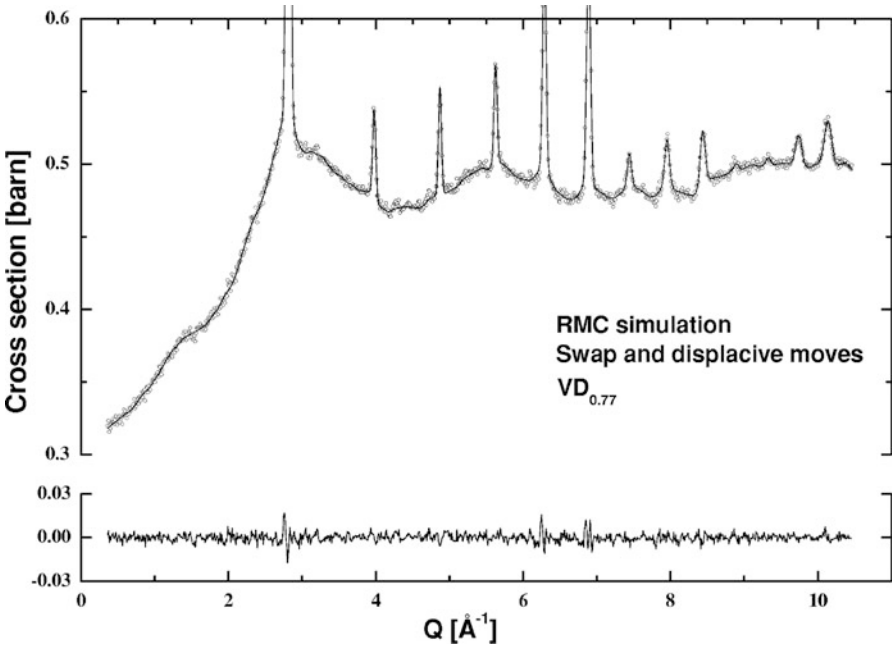

Fig. 4.2 Fit between experimental (*circles*) and calculated (*solid line*) total neutron scattering data for α-$VD_{0.8}$ after RMC modelling. The *y*-axis is cut to better show the fit to the diffuse scattering. Reprinted from [48] with permission

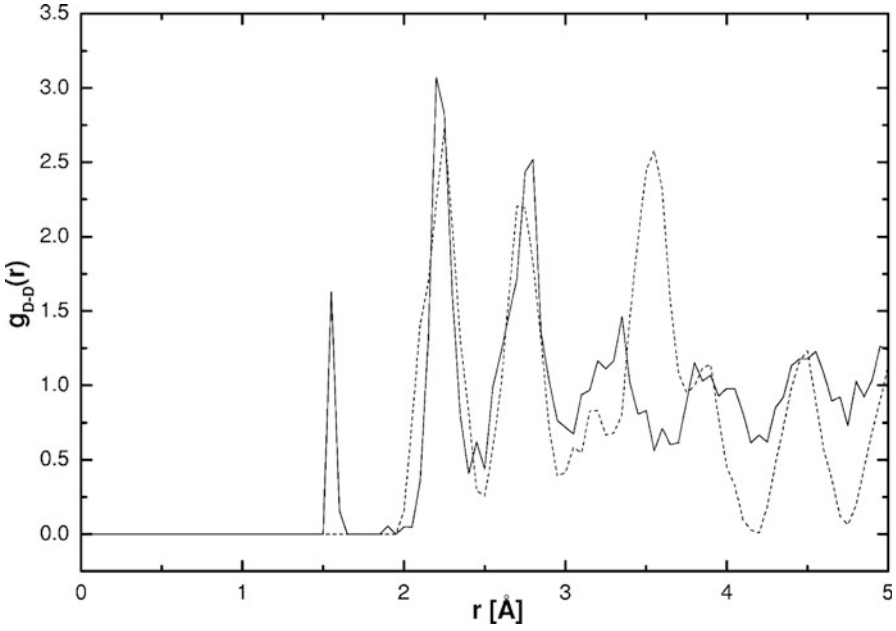

Fig. 4.3 Partial D-D pair distribution function for α-$VD_{0.8}$ (*solid line*) as obtained by RMC. The corresponding function for δ-$VD_{0.8}$ (*dashed line*) is shown for comparison. Reprinted from [48] with permission

Deuterium on octahedral site was omitted for simplicity in the earlier SRO parameter analyses of diffuse scattering from α-$VD_{0.8}$. However, it was easily accounted for in the RMC modelling by allowing jumps from tetrahedral to octahedral sites. In the converged model obtained by site-swapping, 6.6 % of the D atoms were found in octahedral sites in good agreement with the Rietveld refinements. After displacive moves, however, no D atoms were found in the ideal octahedral position but rather distributed around the center of the site. This was ascribed to the high degree of deformation of the octahedra in the bcc structure, which renders the octahedral site 2 + 4 coordinated with 2 distances to V of only 1.58 Å which is much shorter than the V-D distance for the D in the tetrahedral site (1.77 Å). The displacement from the octahedral site toward the unit cell edge ensures more favorable V-D bonding distances. Thus, the octahedral position is in fact never occupied! The same was observed in an RMC investigation of β-$VD_{0.5}$ [52] which is a phase with basically the same V lattice as α-$VD_{0.8}$. Several structure investigations based on Bragg scattering have concluded that most or all deuterium atoms are in octahedral sites [47, 53], but RMC shows that the deuterium atoms are rather distributed around the periphery of the site center.

The work on α-$VD_{0.8}$ was followed up with an investigation of the structurally and compositionally more complicated deuteride $ZrCr_2D_4$ [54]. $ZrCr_2$ is a C15-type Laves phase which forms a disordered deuteride at ambient temperature [55, 56]. Two types of tetrahedra, Zr_2Cr_2 and $ZrCr_3$ are partly occupied. The nearest sites are only 1.2 Å apart, so short-range ordering was expected to prevent such short D-D separations from occurring. RMC modelling with total neutron scattering data was performed in the same manner as with α-$VD_{0.8}$. The swap moves resulted in a model with no D-D distances below 2 Å and a slight under-estimation of the diffuse scattering. Displacive moves resulted in an excellent fit to the experimental data, thus showing that uncorrelated harmonic displacement, as assumed when using only swap moves, is not a good description. Indeed, the width of the first peak in $g_{D\text{-}D}(r)$ is only 60 % of what it would be for uncorrelated thermal vibrations, thus indicating correlated nearest-neighbor vibrations. The $g_{D\text{-}D}(r)$ contains no peak in the 1.5 Å range like α-$VD_{0.8}$, but a very sharp peak is present at 0.7 Å which was the D-D cut-off distance during modelling. This is surely an artifact due to some error in the data, and the influence on the fit was shown to be minor.

The deuterium distribution in $ZrCr_2D_4$ becomes fully ordered around 250 K [56]. Total scattering data were collected for the ordered phase at 150 K. $g_{D\text{-}D}(r)$ was obtained by RMC [54] and is compared with $g_{D\text{-}D}(r)$ for the room temperature disordered phase in Fig. 4.4a and for a random D distribution over the two types of tetrahedral sites in the ratio found by Rietveld refinement in Fig. 4.4b. Except for the strong peak at $r = 1.2$ Å (due to deuterium atoms in nearest-neighbor sites) in the random configuration and spurious peak at 0.7 Å for the disordered structure, the three curves are relatively similar. However, it is clear that the distribution at room temperature is much more similar to the ordered distribution than the random one in the range from 2 to 4 Å which includes the three first coordination spheres. This indicates a local arrangement in the disordered phase that is similar to that of the

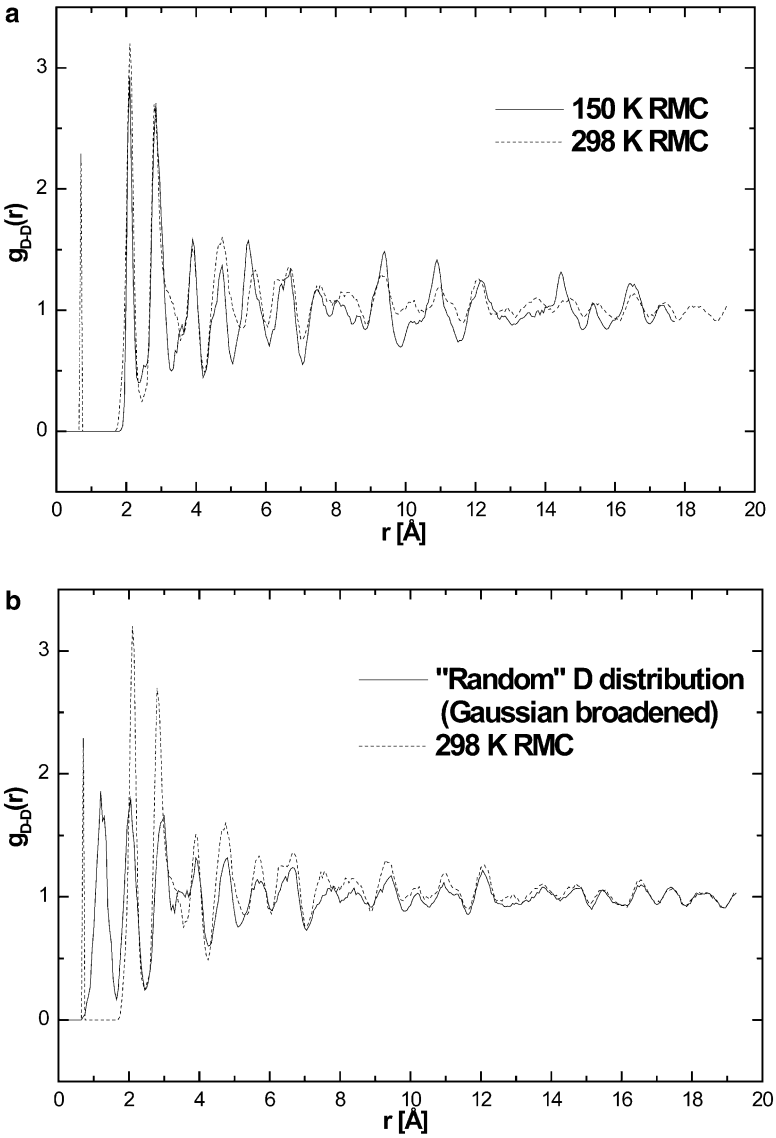

Fig. 4.4 $g_{D\text{-}D}(r)$ from RMC model obtained from total neutron scattering data of disordered $ZrCr_2D_4$ at 298 K (*dotted line*) compared with (**a**) RMC model obtained from total neutron scattering data of ordered $ZrCr_2D_4$ (150 K) and (**b**) model with deuterium randomly distributed in the tetrahedral sites. Reprinted from [54] with for permission

ordered phase at this length scale. With increasing r, the $g_{D\text{-}D}(r)$ for the disordered structure becomes increasingly similar to that of the random model and they become more or less identical above 12 Å. This is therefore taken as the limiting distance for D-D correlations in disordered $ZrCr_2D_4$. It should also be noticed that there is a

slight mismatch in the positions of the first two coordination spheres in the disordered distribution compared to the random distribution (Fig. 4.4b). This indicates some static displacements of the deuterium atoms in the disordered phase. These displacements make the D-D distances in the first two coordination spheres more similar to those found in ordered $ZrCr_2D_4$ as can be seen by the positional match of the same peaks in Fig. 4.4a.

Ropka et al. [57] investigated $YFe_2D_{4.2}$ with TOF total neutron scattering with the GPPD diffractometer at the (now decommissioned) spallation source IPNS, Argonne National Laboratory, USA. $YFe_2D_{4.2}$ is a C15-type Laves phase with disordered deuterium distribution above 338 K, but the deuterium sublattice becomes fully ordered below 332 K. Some structural information could be extracted by simply comparing the PDFs obtained by Fourier transforming the total scattering data obtained for the ordered (290 K) and disordered (350 K) phase (Fig. 4.5). It is clear that the Switendick rule is fulfilled in the disordered phase even though deuterium is distributed over closely spaced Y_2Fe_2 and YFe_3 tetrahedra with no long-range order, according to Rietveld refinements. This can be seen from the lack of any additional peaks below 2 Å in the PDF of the disordered phase compared to the low-temperature phase where deuterium orderly occupies well-separated sites. Moreover, the two PDFs are strikingly similar up to about 8 Å, indicating that SRO in the high-temperature phase extends over that range. The authors especially stress the similarities up to 3.8 Å which correspond to the diameter of the first coordination sphere of tetrahedral sites around Fe. This is taken as support for significant

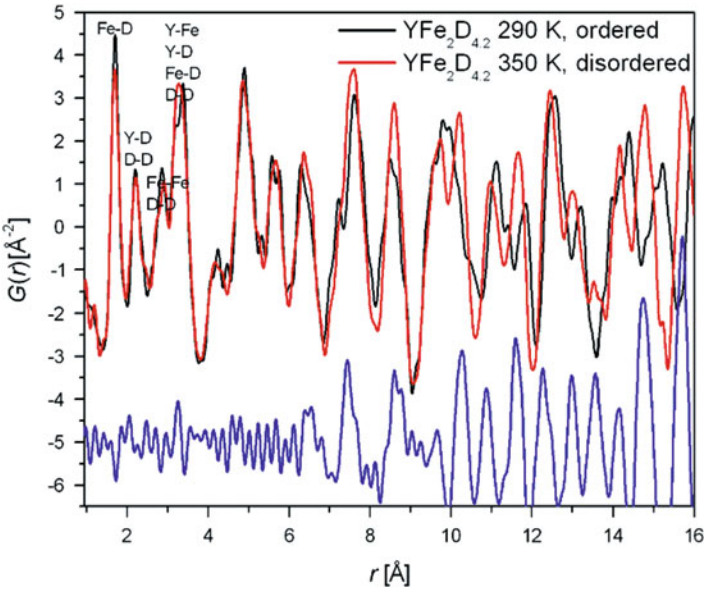

Fig. 4.5 PDFs of $YFe_2D_{4.2}$ from total scattering data collected above (350 K, *red*) and below (290 K, *black*) the order–disorder temperature. The *blue line* is the difference between the two PDFs. Reprinted from [57] with permission

directionality in the Fe-D bonds. RMC modelling with the DISCUS software confirmed strong similarities in the Fe-D coordination, as the RMC models of the disordered phase predominantly contain FeD_4 and FeD_5 polyhedra which are the same coordinations found in the ordered low-temperature phase.

Other crystalline metallic hydrides investigated by total scattering are $Ti_{0.45}Cr_{0.35}Mo_{0.20}D_x$ ($x = 0.6$ and 1.6) [58], deuterated Pd-Au alloys [59] $Mg_{2-x}Pr_xNi_4D_{3.6-4}$ ($x = 0.6$ and 1.0), and the C14 Laves phase $ZrTiNiD_2$ [60].

4.3.2 Amorphous and Nano-sized Metal Hydrides

Hydrogen absorption in metallic glasses (e.g., [61, 62]) and amorphization of crystalline intermetallics upon hydrogenation (e.g., [63, 64]), are well described in the literature. Structural information on the amorphous metal hydride products has, until recently, been very scarce since the scattering is entirely diffuse and therefore classical crystallography is useless.

Suzuki et al. [65] obtained PDFs for amorphous $ZrNiD_x$ with $x = 0$–1.72 from TOF total neutron scattering data collected to $Q = 30$ Å^{-1}. The PDF for the deuterium-free ZrNi glass has the first peak around 2.7 Å which corresponds to Zr-Ni and Ni-Ni separations found in crystalline ZrNi. One new peak appears at 2.1 Å for $ZrNiD_{0.3}$, which was ascribed to Zr-D distances. The area under the peak shows that D is coordinated by 4 Zr atoms at this distance, thus suggesting occupation of Zr_4 tetrahedra in agreement with the D site preference in crystalline ZrNiD. The Zr-D distances are somewhat longer (2.2 Å) in the crystalline phase, which is consistent with higher vibration energies measured with inelastic neutron scattering (INS) for the amorphous $ZrNiD_{0.3}$ and $ZrNiD_{0.48}$ compared to crystalline $ZrNiD_{0.64}$. For amorphous $ZrNiD_{0.58}$ a new peak in the PDF appears at 1.7 Å which corresponds to Ni-D distances. As the Ni-D coordination number increases with increasing D content, there is a corresponding decrease in the Zr-D coordination number, thus keeping the overall metal-D coordination of four. At the highest investigated D content, the average D coordination is 3Zr + 1Ni. From this it was concluded that deuterium has a preference for Zr_3Ni tetrahedra which are also occupied in crystalline $ZrNiD_3$ along with trigonal bipyramidal Zr_3Ni_2 sites. Five-coordinated deuterium does not appear to be common in amorphous ZrNi deuterides.

Several intermetallics undergo amorphization when hydrogenated under certain condition. Itoh et al. [66] obtained PDFs for amorphous (a-)$TbFe_2D_x$ ($x = 2.0$ and 3.0) with total neutron and X-ray scattering. The data were analyzed by fitting the various coordination spheres with Gaussian functions, thus obtaining coordination numbers and interatomic distances. The X-ray PDF, which is completely dominated by metal–metal interactions, showed that the coordination numbers for similar metals, N_{Tb-Tb} and N_{Fe-Fe}, were higher than in crystalline (c-)$TbFe_2D_x$ (~8.5 and 6 vs 6 and 4, respectively), which indicate clustering of similar atoms. From the

neutron PDF, the deuterium atoms were found to be four-coordinated, thus suggesting that they occupy metal tetrahedra in the glass. The amorphous deuteride was expected to contain all five possible kinds of tetrahedra, Tb_4, Tb_3Fe, Tb_2Fe_2, $TbFe_3$, and Fe_4. D has an average coordination close to 3Tb + Fe in a-$TbFe_2D_{3.0}$ but it is suggested that Tb_4, Tb_3Fe, and Tb_2Fe_2 tetrahedra are occupied, since the average coordination depended on the D content. For a-$TbFe_2D_{2.0}$ it was 3.33Tb + 0.62Fe which shows that the Tb-rich tetrahedra are most attractive. This is in good agreement with the high formation enthalpy of Tb hydride.

The site preference for D was later quantified by the first RMC modelling ever performed of an amorphous metal hydride [67]. The X-ray and neutron total scattering data were used simultaneously to create a three-dimensional structure model of a-$TbFe_2D_{3.0}$. It was found that 98 % of the deuterium atoms occupy metal tetrahedra. As expected, the sites with high rare earth (RE) coordination are preferred. About 40 % of the deuterium atoms are located in RE_4 tetrahedra. The distribution of available sites in the amorphous phases was not discussed. The tendency of similar atom clustering is nicely visualized by the RMC model. A 2.5 nm slab of the model is shown in Fig. 4.6. Regions rich in Tb and other regions dominated by Fe are clearly visible. Similar clustering and site preference

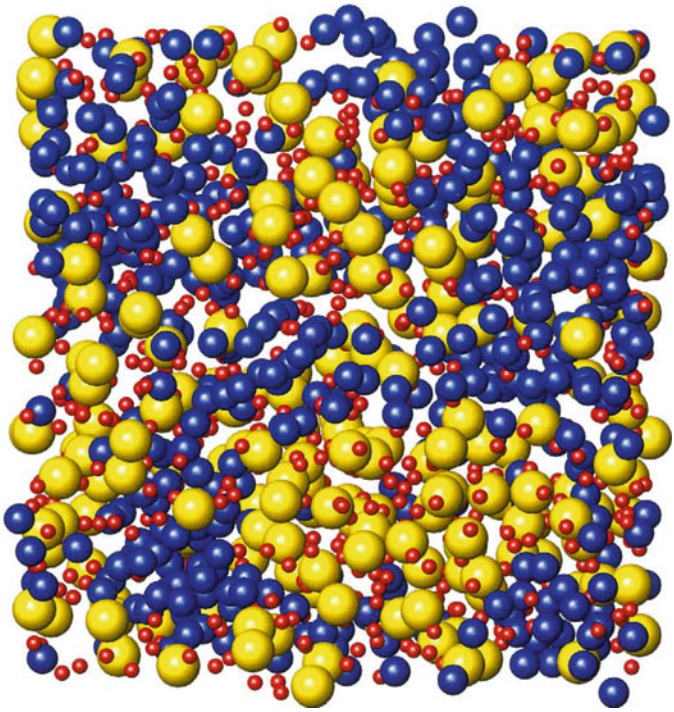

Fig. 4.6 Slice of model of amorphous $TbFe_2D_3$ obtained by RMC modelling from total X-ray and neutron scattering data. *Blue spheres* are Fe, *yellow spheres* are Tb, and *red spheres* are deuterium. The clustering of similar atoms is notable. Reprinted from [67] with permission

were observed for a-$HoFe_2D_{3.0}$ [67]. The amorphous deuteride of the Laves phase $CeFe_2$, a-$CeFe_2D_{3.9}$ is on the other hand markedly different [68]. The tendency of clustering of similar atoms is present but to a lesser extent. The site preference for deuterium is very different with less than 15 % of the deuterium in Ce_4 tetrahedra. Most of the deuterium, about 70 %, is equally divided between Ce_3Fe and Ce_2Fe_2 sites. This is ascribed to the lower availability of the RE_4 tetrahedra due to the lesser extent of clustering. However, the difference in available sites of the various kinds was not quantified.

Titanium and zirconium form a hexagonal close-packed solid solution in all mixing ratios. Due to the negative neutron scattering length of Ti and positive scattering length of Zr, it is possible to make a Zr-Ti solid solution that shows no Bragg scattering of neutrons. This occurs at the composition $Ti_{0.676}Zr_{0.324}$. This solid solution forms an amorphous deuteride, $Ti_{0.676}Zr_{0.324}D_{0.31}$ when mechanically alloyed under deuterium pressure [69]. Despite the "zero-scattering" nature of the metal matrix, there is still information about the metal–metal, metal–D, and D–D correlations in the total neutron scattering data. Metal–metal correlations alone are obtained by total X-ray scattering. Itoh et al. [70] used both data types and RMC to model the structure of $Ti_{0.676}Zr_{0.324}D_{0.31}$. 40 % of the metal atoms in the model have icosahedral or "icosahedral-like" coordination of other metal atoms. Thus the close-packed structure of c-$Ti_{0.676}Zr_{0.324}$ is quite well preserved over short length scales in the amorphous deuteride. 93 % of the D atoms have tetrahedral coordination [71]. About 40 % of the D atoms are in Ti_3Zr sites, and 25 % are in Ti_2Zr_2. The rest is roughly equally divided between Ti_4 and $TiZr_3$ sites while a small fraction of about 1 % is in Zr_4 sites. The distribution of available sites in the amorphous metal matrix is not discussed, but the indicated numbers are in rough agreement with a random occupation of the available sites, if there is neither clustering nor segregation of similar metal atoms.

The classical battery anode material $LaNi_5$ can form a nanocrystalline or amorphous hydride by mechanical milling in H_2 atmosphere [72]. Itoh et al. [23, 73] investigated the amorphous milling product $LaNi_5D_x$ ($x = 1.4$–3.3) by total neutron and X-ray scattering and RMC. Again, a strong preference for tetrahedral coordination around deuterium was found with more than 90 % of the D atoms in such sites. $LaNi_3$ and La_2Ni_2 sites were preferred. Thus, the deuterium sites are markedly different to those in crystalline $LaNi_5D_3$ where most of the D atoms are located in distorted La_2Ni_4 octahedra. The occupation of La_2Ni_2 tetrahedra is, however, common for the crystalline and amorphous state. There is clear evidence of short-range order in the metal lattice. La is grossly overrepresented in the first coordination sphere of Ni where the Ni/La ratio is 2.7, i.e. only about half of the overall Ni/La ratio. Moreover, there are clear common features in many of the coordination polyhedra around Ni. The preferred polyhedron is a trigonal prism with a capping atom on each of the three prism faces. Tetragonal dodecahedra and Archimedean antiprisms, which are obtained by removing or adding, respectively, an atom to the tricapped trigonal prisms, are also common. About 50 % of the Ni atoms have one of these three coordinations. In contrast, there is no specific coordination around La that sticks out as the most common.

$FeTiH_x$ is another "classical" metal hydride which has received attention as a possible hydrogen storage material. Nano-sized $FeTiH_x$ can be obtained by mechanical milling and shows superior sorption kinetics compared to the corresponding bulk material [74, 75]. The PDF obtained by total neutron scattering of nano-sized $FeTiD_{0.97}$ shows several peaks at lower *r*-values than any of the metal–metal distances found in the X-ray PDF [76]. These peaks were ascribed to metal-D distances. Due to the negative neutron scattering length of Ti and positive scattering length of D, the Ti-D distances are easily singled out as negative peaks in neutron PDF. The peaks for Ti-D and Fe-D distances occur at exactly the positions corresponding to M-D distances from crystalline $TiFeD_x$ (2.14 Å and 1.72 Å, respectively) where D occupies Ti_4Fe_2 octahedra. However, the peaks have shoulders which indicate that some of the deuterium atoms have a different environment. This was ascribed to D atoms located in the grain boundaries. Fitting the PDF with Gaussian peaks revealed that the grain boundary deuterium is four-coordinated in a Ti-rich environment. Occupation of mainly Ti_4 and Ti_3Fe tetrahedra was suggested. Moreover, it was estimated that about half of the deuterium atoms were located in the grain boundaries. They appear as shoulders rather than distinct peaks in G(r) because the M-D distribution is broader in the grain boundaries than inside the grains.

Amorphous MgCo alloy can be obtained by ball milling Mg and Co. [77]. TEM investigations with EDS analysis and selected area electron diffraction suggested a homogeneous distribution of Mg and Co with a bcc-like local structure in the alloy. Hydrogenation of the alloys resulted in a mixture of amorphous bcc phase and nanoparticles of Co [78]. Kim et al. [79] investigated amorphous MgCo and its deuteration product $MgCoD_{1.5}$ by total X-ray and neutron scattering; the latter collected at the NPDF instrument at LANCE, USA. The resulting PDFs corresponded poorly to local bcc atomic arrangement. Alternative models were considered, and the best fit to the PDF of the deuteride was obtained by a two-phase model with the phases $MgCo_2$ and Mg_2CoD_5. The domains of atomic arrangements similar to these phases were estimated to be only 10–15 Å. Even though no stable Mg_2Co phase exists, the PDF of the alloy was well fitted by a mixture of $MgCo_2$ and Mg_2Co where the latter has the same metal atom arrangement as Mg_2CoD_5 but without deuterium, thus indicating that such a phase can be stable in a nanostructured state. The hydrogen capacities predicted by the $MgCo_2$-Mg_2CoD_5 model for Mg_xCo_{1-x} agree very well with experimentally determined capacities for $x = 0.2$–0.55.

4.3.3 Complex Hydrides

Metal aluminium amides, $M[Al(NH_2)_4]_n$, contain tetrahedral $Al(NH_2)_4^-$ and may be regarded as alanates where the negatively charged hydrogen atoms are replaced by amide, NH_2^-, anion. Alkali and alkaline earth aluminium amides decompose by

ammonia emission in the attractive temperature range between 50 and 150°C, but composites with LiH rather desorb hydrogen which make them relevant for hydrogen storage [80, 81]. Thermal decomposition of known meal aluminium amides leads to amorphization and the reaction paths are therefore not accessible with regular powder diffraction experiments. Ikeda et al. [82] investigated $LiAl(ND_2)_4$ as-synthesized and at different stages of decomposition with total neutron scattering at the NOVA instrument at J-Parc, Japan. The pristine material was highly crystalline which was evident from the sharp Bragg peaks and low diffuse scattering in $S(Q)$ and strong features in the PDF in the high-r region (Fig. 4.7a). The scattering from a sample decomposed at 400°C was on the other hand entirely diffuse and the PDF is flat above $r \sim 2$ nm due to lack of long-range order (Fig. 4.7c). A sample that was quenched after heated to 160°C showed features intermediate of the two with significant diffuse scattering in addition to weak Bragg peaks from remaining crystalline $LiAl(ND_2)_4$ and only minor oscillations in the PDF above $r \sim 2$ nm (Fig. 4.7b). The low-r regions of the PDFs from the heated samples were compared by the calculated PDFs from several possible decomposition products. It was noticed that the first peak in all PDFs is located at 0.10 nm which corresponds to the N-D distance in amide anion. It was thus concluded that the amorphous decomposition product does not contain imide ions, ND^{2-}, which would give a peak at 0.07 nm due to shorter N-D bonds. They do, however, contain features

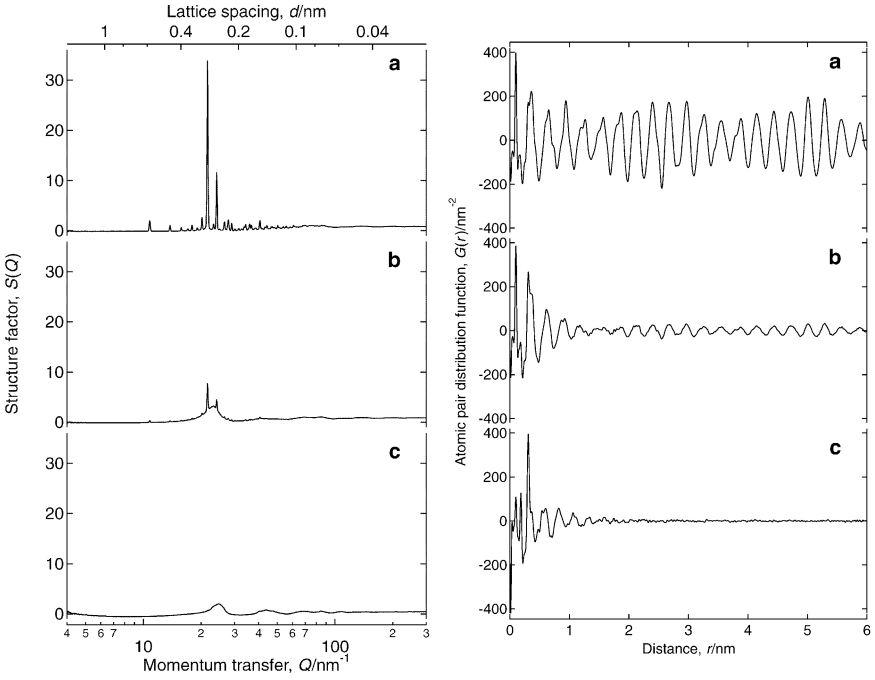

Fig. 4.7 $S(Q)$ (*left*) and PDF (*right*) for $LiAl(ND_2)_4$ (**a**) in pristine state, after heating to (**b**) 160°C, and (**c**) 400°C. Reprinted from [82] with permission

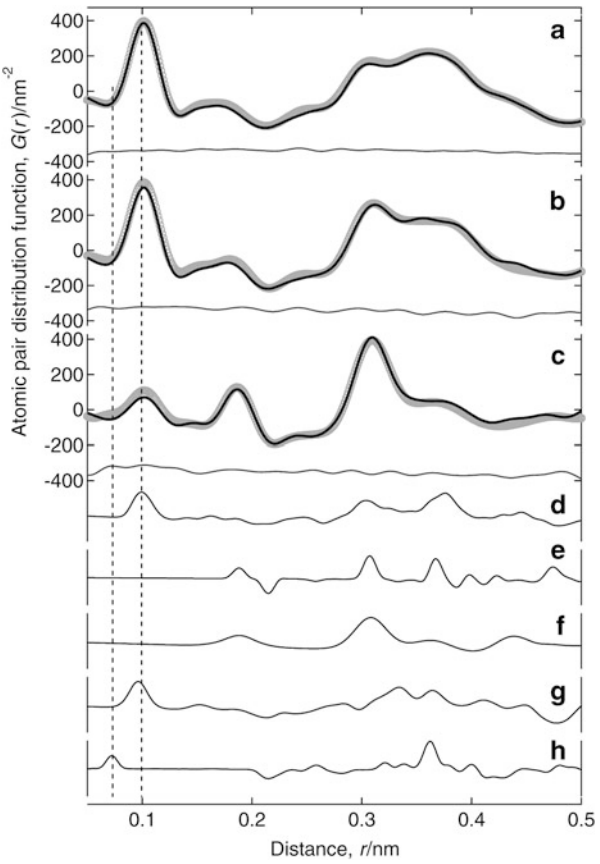

Fig. 4.8 (**a**)–(**c**) The low-*r* region of experimental (*gray circles*) and fitted (*solid line*) PDFs for $LiAl(ND_2)_4$ in (**a**) pristine state and after heating to (**b**) 160°C and (**c**) 400°C. The fitting models are described in the text. (**d**)–(**h**) Calculated PDFs from (**d**) $LiAl(ND_2)_4$, (**e**) Li_3AlN_2, (**f**) AlN, (**g**) $LiND_2$, and (**h**) Li_2ND. The *dashed vertical lines* indicate the typical N-D distance in ND^{2-} (*left*) and ND_2^- (*right*). From [82] with permission

similar to those calculated for Li_3AlN_2 and AlN as well as features from the original $LiAl(ND_2)_4$. The following decomposition reaction was proposed:

$$LiAl(ND_2)_{4(s)} \rightarrow 1/3Li_3AlN_{2(amorphous)} + 2/3AlN_{(amorphous)} + 8/3\ ND_3$$

To check the feasibility of the reaction, the measured PDFs for the heated samples were fitted to the calculated PDFs of Li_3AlN_2 and AlN with fixed 1:2 molar ratio and a refinable amount of remaining $LiAl(ND_2)_4$ with the PDFgui software (Fig. 4.8). The resulting fits are excellent, thus confirming the proposed reaction.

Another example of a total neutron scattering investigation of a complex hydrides is the work by Sato et al. [83]. They studied the evolution of interatomic distances in $LiAlD_4$ with increasing temperature where extracted from PDFs obtained at the instruments NOVA (J-Parc, Japan) and NOMAD (SNS, USA) [83].

4.4 Conclusion

Are the efforts to collect, correct, and normalize total scattering data, perhaps coupled with time-consuming RMC simulations, worthwhile compared to much quicker measurements of raw powder diffraction data and Rietveld refinements? There is no straight answer to this question. For highly crystalline, stoichiometric materials, there is usually not much more to gain from total scattering measurements, although information on correlated or highly anisotropic thermal motion may be inferred. The average picture obtained by Bragg scattering may also be perfectly adequate for more disordered systems. If the question is: "What fraction of the deuterium atoms occupy tetrahedral sites in α-$VD_{0.8}$?", then the information is well contained in the average picture. If we want to know what the shortest distances between the deuterium atoms are in the same phase, the same picture leaves us guessing. For amorphous systems, there is no average picture at all, and careful measurement of the diffuse scattering is the only way to extract structural information from neutron or X-ray scattering. So whether or not it is worth the extra effort, depends entirely on the material under investigation and what one wants to know about it!

References

1. M.P. Balogh, C.Y. Jones, J.F. Herbst, L.G.J. Hector, M. Kundrat, J. Alloys Compd. **420**, 326–336 (2006)
2. K. Ohoyama, Y. Nakamori, S. Orimo, K. Yamada, J. Phys. Soc. Jpn. **74**, 483–487 (2005)
3. M. Matsuo, H. Takamura, H. Maekawa, H.W. Li, S. Orimo, Appl. Phys. Lett. **94** (2009)
4. J.E. Olsen, M.H. Sørby, B.C. Hauback, J. Alloys Compd. **509**, L228–L231 (2011)
5. L.H. Rude, Y. Filinchuk, M.H. Sørby, B.C. Hauback, F. Besenbacher, T.R. Jensen, J. Phys. Chem. C **115**, 7768–7777 (2011)
6. G.L. Squires, *Introduction to the Theory of Thermal Neutron Scattering* (Cambridge University Press, Cambridge, 1978)
7. D.A. Keen, J. Appl. Crystallogr. **34**, 172–177 (2001)
8. A.C. Hannon, Nucl. Instrum. Meth. A **551**, 88–107 (2005)
9. D.T. Bowron, A.K. Soper, K. Jones, S. Ansell, S. Birch, J. Norris, L. Perrott, D. Riedel, N.J. Rhodes, S.R. Wakefield, A. Botti, M.A. Ricci, F. Grazzi, M. Zoppi, Rev. Sci. Instrum. **81** (2010)
10. T. Proffen, T. Egami, S.J.L. Billinge, A.K. Cheetham, D. Louca, J.B. Parise, Appl. Phys. Mater. Sci. Process. **74**, S163–S165 (2002)
11. J. Neuefeind, M. Feygenson, J. Carruth, R. Hoffmann, K.K. Chipley, Nucl. Instrum. Meth. B **287**, 68–75 (2012)
12. H.E. Fischer, G.J. Cuello, P. Palleau, D. Feltin, A.C. Barnes, Y.S. Badyal, J.M. Simonson, Appl. Phys. Mater. Sci. Process. **74**, S160–S162 (2002)
13. P.F. Peterson, M. Gutmann, T. Proffen, S.J.L. Billinge, J. Appl. Crystallogr. **33**, 1192–1192 (2000)
14. V.M. Nield, D.A. Keen, *Diffuse Neutron Scattering from Crystalline Materials*, 1st edn. (Oxford University Press, Oxford, 2001)

15. O. Arnold, J.C. Bilheux, J.M. Borreguero, A. Buts, S.I. Campbell, L. Chapon, M. Doucet, N. Draper, R.F. Leal, M.A. Gigg, V.E. Lynch, A. Markyardsen, D.J. Mikkelson, R.L. Mikkelson, R. Miller, K. Palmen, P. Parker, G. Passos, T.G. Perring, P.F. Peterson, S. Ren, M.A. Reuter, A.T. Sayici, J.W. Taylor, R.J. Taylor, R. Tolchenoy, W. Zhou, J. Zikoysky, Nucl. Instrum. Meth. A **764**, 156–166 (2014)
16. L. Pusztai, R.L. McGreevy, Phys. B **234–236**, 357–358 (1997)
17. P. Zetterström, R.L. McGreevy, Phys. B **276–278**, 187–188 (2000)
18. M.G. Tucker, M.T. Dove, D.A. Keen, J. Appl. Crystallogr. **34**, 780–782 (2001)
19. R.L. McGreevy, L. Pusztai, Mol. Simul. **1**, 359–367 (1988)
20. K. Ohara, Y. Kawakita, L. Pusztai, L. Temleitner, S. Kohara, N. Inoue, S. Takeda, J. Phys. Condens. Matter **22** (2010)
21. M.G. Tucker, D.A. Keen, J.S.O. Evans, M.T. Dove, J. Phys. Condens. Matter **19** (2007)
22. V.M. Nield, D.A. Keen, W. Hayes, R.L. McGreevy, Solid State Ion. **66**, 247–258 (1993)
23. K. Itoh, T. Shoumura, M. Sugiyama, K. Mori, T. Fukunaga, J. Alloys Compd. **474**, 4–8 (2009)
24. J. Swenson, S. Adams, Phys. Rev. Lett. **90**, 155507 (2003)
25. M.A. Howe, Phys. B Condens. Matter **160**, 170–176 (1989)
26. R.Y. Li, J.Y. Qin, T.K. Gu, X.F. Bian, J. Non-Cryst. Solids **354**, 1736–1739 (2008)
27. L. Pusztai, R.L. McGreevy, Phys. Chem. Liq. **24**, 119–125 (1991)
28. J.D. Wicks, R.L. McGreevy, J. Non-Cryst. Solids **192&193**, 23–27 (1995)
29. I. Levin, V. Krayzman, M.G. Tucker, J.C. Woicik, Appl. Phys. Lett. **104**, 4 (2014)
30. G. Evrard, L. Pusztai, J. Phys. Condens. Matter **17**, S1–S13 (2005)
31. M.G. Tucker, D.A. Keen, M.T. Dove, A.L. Goodwin, Q. Hui, J. Phys. Condens. Matter **19** (2007)
32. A. Mellergård, R.L. McGreevy, Chem. Phys. **261**, 267–274 (2000)
33. A. Mellergård, R.L. McGreevy, Mater. Sci. Forum **378–381**, 71–76 (2001)
34. T. Proffen, R.B. Neder, J. Appl. Crystallogr. **30**, 171–175 (1997)
35. C.L. Farrow, P. Juhas, J.W. Liu, D. Bryndin, E.S. Bozin, J. Bloch, T. Proffen, S.J.L. Billinge, J. Phys. Condens. Matter **19** (2007)
36. R.L. McGreevy, J. Non-Cryst. Solids **156–158**, 949–955 (1993)
37. R.L. McGreevy, J. Phys. Condens. Matter **13**, R887–R913 (2001)
38. R.L. McGreevy, P. Zetterström, J. Non-Cryst. Solids **293–295**, 297–303 (2001)
39. R.L. McGreevy, P. Zetterström, Curr. Opin. Solid State Mater. Sci. **7**, 41–47 (2003)
40. T. Egami, S.J.L. Billinge, *Underneath the Bragg Peaks – Structural Analysis of Complex Materials* (Pergamon, Oxford, 2003)
41. A.C. Switendick, Theoretical studies of hydrogen in metals: current status and further projects (Sandia Laboratories, 1978)
42. A.C. Switendick, Z. Phys Chem. Neue Folge **117**, 89–112 (1979)
43. V.A. Yartys, R.V. Denys, B.C. Hauback, H. Fjellvåg, I.I. Bulyk, A.B. Riabov, Y.M. Kalychak, J. Alloys Compd. **330–332**, 132–140 (2002)
44. M. Pionke, W. Schweika, T. Springer, D. Hohlwin, R. Sonntag, Phys. B **213–214**, 567–569 (1995)
45. M. Pionke, W. Schweika, T. Springer, R. Sonntag, D. Hohlwin, Phys. Scr. **T57**, 107–111 (1995)
46. Y. Sugizaki, S. Yamaguchi, J. Alloys Compd. **231**, 126–131 (1995)
47. V.A. Somenkov, I.R. Éntin, A.Y. Chervyakov, S.S. Shil'shtein, A.A. Chertkov, Sov. Phys. Solid State **13**, 2178–2182 (1972)
48. M.H. Sørby, A. Mellergård, R. Delaplane, A. Wannberg, B.C. Hauback, H. Fjellvåg, J. Alloys Compd. **363**, 209–216 (2004)
49. D.G. Westlake, M.H. Mueller, H.W. Knott, J. Appl. Crystallogr. **6**, 206–216 (1973)
50. U. Knell, H. Wipf, G. Lautenschläger, R. Hock, H. Weitzel, R.R. Arons, E. Ressouche, J. Alloys Compd. **231**, 121–125 (1995)
51. U. Knell, H. Wipf, G. Lautenschläger, R. Hock, H. Weitzel, E. Ressouche, J. Phys. Condens. Matter **6**, 1461–1471 (1994)

52. K. Itoh, T. Fukunaga, J. Appl. Phys. **101**, 123528 (2007)
53. H. Asano, M. Hirabayashi, Phys. Status Solidi (a) **15**, 267 (1973)
54. M.H. Sørby, A. Mellergard, B.C. Hauback, H. Fjellvåg, R. Delaplane, J. Alloys Compd. **457**, 225–232 (2008)
55. A.V. Irodova, O.A. Lavrova, G.V. Laskova, L.N. Padurets, Sov. Phys. Solid State **24**, 22–27 (1982)
56. H. Kohlmann, F. Fauth, K. Yvon, J. Alloys Compd. **285**, 204–211 (1999)
57. J. Ropka, R. Cerny, V. Paul-Boncour, J. Solid State Chem. **184**, 2516–2524 (2011)
58. K. Iwase, T. Kamiyama, Y. Nakamura, K. Mori, M. Yonemura, S. Harjo, T. Ishigaki, E. Akiba, Mater. Trans. **47**, 271–274 (2006)
59. D.E. Nanu, M.G. Tucker, W.G. Haije, J.F. Vente, A.J. Bottger, Acta Mater. **58**, 5502–5510 (2010)
60. I. Levin, V. Krayzman, C. Chiu, K.W. Moon, L.A. Bendersky, Acta Mater. **60**, 645–656 (2012)
61. R.C. Bowman, A.J. Maeland, Phys. Rev. B **24**, 2328–2333 (1981)
62. R.J. Furlan, G. Bambakidis, J.S. Cantrell, R.C. Bowman, A.J. Maeland, J. Less-Common Met. **116**, 375–388 (1986)
63. K. Aoki, T. Yamamoto, Y. Satoh, K. Fukamichi, T. Masumoto, Acta Metall. **35**, 2465–2470 (1987)
64. K. Aoki, A. Yanagitani, X.G. Li, T. Masumoto, Mater. Sci. Eng. **97**, 35–38 (1988)
65. K. Suzuki, N. Hayashi, Y. Tomizuka, T. Fukunaga, K. Kai, N. Watanabe, J. Non-Cryst. Solids **61–62**, 637–642 (1984)
66. K. Itoh, K. Kanda, K. Aoki, T. Fukunaga, J. Alloys Compd. **348**, 167–172 (2003)
67. K. Itoh, Y. Miyajima, K. Aoki, T. Fukunaga, J. Alloys Compd. **376**, 9–16 (2004)
68. K. Itoh, K. Aoki, M. Sugiyama, K. Mori, T. Fukunaga, J. Alloys Compd. **446**, 19–22 (2007)
69. T. Fukunaga, K. Itoh, K. Hashi, K. Aoki, Appl. Phys. Mater. Sci. Process. **74**, S957–S959 (2002)
70. K. Itoh, K. Hashi, K. Aoki, K. Mori, M. Sugiyama, T. Fukunaga, J. Alloys Compd. **434**, 180–182 (2007)
71. K. Itoh, K. Hashi, K. Aoki, T. Fukunaga, J. Non-Cryst. Solids **353**, 3049–3052 (2007)
72. H. Fujii, S. Munehiro, K. Fujii, S. Orimo, J. Alloys Compd. **330–332**, 747–751 (2002)
73. K. Itoh, T. Shoumura, K. Mori, M. Sugiyama, T. Fukunaga, J. Non-Cryst. Solids **353**, 1975–1978 (2007)
74. K. Aoki, H. Aoyagi, A. Memezawa, T. Masumoto, J. Alloys Compd. **203**, L7–L9 (1994)
75. H. Aoyagi, K. Aoki, T. Masumoto, J. Alloys Compd. **231**, 804–809 (1995)
76. K. Itoh, H. Sasaki, H.T. Takeshita, K. Mori, T. Fukunaga, J. Alloys Compd. **404–406**, 95–98 (2005)
77. H. Kim, J. Nakamura, H.Y. Shao, Y. Nakamura, E. Akiba, K.W. Chapman, P.J. Chupas, T. Proffen, J. Phys. Chem. C **115**, 7723–7728 (2011)
78. J. Matsuda, H. Shao, Y. Nakamura, E. Akiba, Nanotechnology **20** (2009)
79. H. Kim, J. Nakamura, H.Y. Shao, Y. Nakamura, E. Akiba, K.W. Chapman, P.J. Chupas, T. Proffen, J. Phys. Chem. C **115**, 20335–20341 (2011)
80. T. Ono, K. Shimoda, M. Tsubota, S. Hino, K.-i. Kojima, T. Ichikawa, Y. Kojima, J. Alloys Compd. **506**, 297–301 (2010)
81. J.B. Eymery, L. Truflandier, T. Charpentier, J.N. Chotard, J.M. Tarascon, R. Janot, J. Alloys Compd. **503**, 194–203 (2010)
82. K. Ikeda, T. Otomo, H. Ohshita, N. Kaneko, M. Tsubota, K. Suzuya, F. Fujisaki, T. Ono, T. Yamanaka, K. Shimoda, T. Ichikawa, Y. Kojima, Mater. Trans. **55**, 1129–1133 (2014)
83. T. Sato, K. Tomiyasu, K. Ikeda, T. Otomo, M. Feygenson, J. Neuefeind, K. Yamada, S. Orimo, J. Alloys Compd. **586**, 244–247 (2014)

Chapter 5
Neutron Reflectometry

Helmut Fritzsche, Frank Klose, Christine Rehm, Zin Tun, Max Wolff, and Björgvin Hjörvarsson

Abstract Neutron Reflectometry (NR) is capable to determine the chemical depth profile of thin film samples from the sub-nanometer regime up to about 200 nm thickness. The high sensitivity of neutrons to hydrogen and deuterium enables NR to detect absolute hydrogen concentrations in the at.% range even in nm-thick layers. Therefore, NR is an ideal tool to study in-situ the hydrogen/deuterium absorption and desorption properties of thin films on a nanometer scale—without the need of a calibration sample. After an introduction to the NR technique and required instrumentation, this chapter provides a comprehensive overview of NR applications in various scientific areas, e.g. hydrogen absorption and desorption of Mg-based alloys and thin Nb films, electrochemical measurements on thin Zr and Ti films, and tuning of the oscillating magnetic exchange coupling in Fe/V and Fe/Nb multilayers with hydrogen.

H. Fritzsche (✉)
Canadian Nuclear Laboratories, Chalk River, ON, Canada, K0J 1J0
e-mail: Helmut.Fritzsche@cnl.ca

F. Klose
Bragg Institute, Australian Nuclear Science and Technology Organisation, Lucas Heights, NSW 2234, Australia

Department of Physics and Materials Science, City University of Hong Kong, Hong Kong SAR, China
e-mail: Frank.Klose@ansto.gov.au

C. Rehm
Bragg Institute, Australian Nuclear Science and Technology Organisation, Lucas Heights, NSW 2234, Australia
e-mail: Christine.Rehm@ansto.gov.au

Z. Tun
Canadian Neutron Beam Centre, Canadian Nuclear Laboratories, Chalk River, ON, Canada, K0J 1J0
e-mail: Zin.Tun@cnl.ca

M. Wolff • B. Hjörvarsson
Department of Physics and Astronomy, Uppsala University, 75120 Uppsala, Sweden
e-mail: Max.Wolff@physics.uu.se; Bjorgvin.Hjorvarsson@physics.uu.se

H. Fritzsche et al. (eds.), *Neutron Scattering and Other Nuclear Techniques for Hydrogen in Materials*, Neutron Scattering Applications and Techniques,
DOI 10.1007/978-3-319-22792-4_5

Keywords Antiferromagnetic coupling • Catalyst layer • Critical edge • Deuterium absorption • Electrochemistry • Electro-impedance spectroscopy • Fe/Nb multilayers • Fe/V multilayers • Fresnel's equation • Index of refraction • In-situ hydrogen absorption • Magnetic scattering length • Mg-Al alloy films • Mg-based alloy films • Multilayers • Nb bulk properties • Nb films • Neutron reflectometry • Oscillating magnetic exchange coupling • Polarized neutron reflectometry • RKKY coupling • Scattering length density • Snell's law • Ternary Mg-based alloy films • Thin films • Ti thin films • W/Nb multilayers • Zr thin films

5.1 Introduction

Investigations of surfaces and interfaces have become increasingly important, which has stimulated substantial development within the field of neutron scattering. Combined with the increased degree of perfection in the sample production, the development has opened up new aspects of nanosciences, e.g. through better understanding of the influence of size on obtained properties. Neutron Reflectometry (NR) has played an important role in this context, through the unique information provided by the one-dimensional scattering length density (SLD), which can be obtained by direct fitting of the experimental results. The obtained SLD can provide information about the sample structure along its surface normal, with nanometer resolution.

NR can typically be used to investigate films or layers from the sub-nanometer regime up to about 200 nm thickness. The measured SLD profile can be converted into a chemical profile or gradient which makes NR an invaluable tool to study, e.g. absorption of surfactants at the liquid/solid interface [1], structure of polyelectrolyte multilayers [2], swelling of polymers or membranes during water absorption [3], formation of Langmuir–Blodgett films [1], corrosion [4], expansion of photoactive films during illumination [5], or hydrogen absorption and desorption—to name only a few. X-ray reflectometry (XRR) has about the same Q-resolution as NR and is also used for structural characterization of layered systems. However, there are many examples where NR has a distinct advantage over XRR because the scattering length of neutrons varies randomly from element to element and isotope to isotope, in contrast to X-rays which have a scattering length which scales with the number of electrons.

Especially in the area of hydrogen absorption, NR has a huge advantage over XRR. The changes of the SLD due to hydrogen absorption are nearly undetectable for X-rays, whereas minute changes in hydrogen concentrations are easily detected by NR. For X-rays the scattering length of hydrogen is the smallest of all elements, whereas the neutron scattering length is of the same order of magnitude as for the absorbing material. XRR can therefore not be used to directly determine the hydrogen concentration through the changes in the scattering amplitude. The change in concentration is only obtainable through indirect tracking of the

hydrogen-induced layer expansion in XRR, whereas NR can be used to determine the hydrogen or deuterium concentration directly via the change of the SLD. NR provides therefore unique information, as the lattice expansion and the concentration is accessible through a single measurement. This is very important because the scaling between volume changes and concentration depends on a number of parameters such as site occupancy, clamping to the substrate as well as the ordering of the hydrogen isotopes.

Due to the fact that neutrons carry a magnetic moment, they interact with the sample's magnetization. Therefore, NR can determine the hydrogen depth profile and the magnetic structure of multilayers simultaneously. This unique capability of NR has been used in experiments on Fe/Nb [6] and Fe/V [7] multilayers where the magnetic structure of the Fe layers can be changed through hydrogen uptake of the nonmagnetic Nb or V layers, respectively.

This chapter is organized as follows: in Sect. 5.2 we explain the NR technique, Sect. 5.3 describes the instrumental setup needed to perform NR experiments, in Sect. 5.4 we briefly point out the main differences between bulk samples and thin films, Sects. 5.5 and 5.6 review the hydrogen absorption properties of Mg-based single films, Fe/Nb and W/Nb multilayers, Sect. 5.7 describes the investigation of electrochemical reactions in Zr and Ti films, whereas Sect. 5.8 reviews the change of the magnetic coupling in Fe/Nb and Fe/V multilayers via hydrogen absorption.

5.2 Principles of the Method

Neutrons possess a spin and associated with it is a magnetic moment μ_N interacting with the magnetization of the specimen under investigation. This magnetic interaction is of no relevance for nonmagnetic specimens, whereas for magnetic samples it provides a unique tool to investigate the magnetic structure of the sample under investigation. In Sect. 5.2.1 we will discuss the generic case of unpolarized neutrons used for investigations on nonmagnetic samples and in Sect. 5.2.2 polarized neutrons are discussed for investigations of magnetic samples.

5.2.1 Unpolarized Neutrons

The scattering geometry for a typical reflectometry experiment is shown in Fig. 5.1. An incoming neutron wave hits the surface of a specimen at a grazing angle θ and is partly reflected at an angle θ_r and partly transmitted (refracted) into the specimen at an angle θ_t with respect to the sample surface. For a perfect, mirror-like surface, all the reflected intensity occurs at an angle $\theta_r = \theta$. This is called specular reflectivity. For a very rough or nano-structured surface, so-called off-specular scattering is observed, where intensity is measured at angles $\theta_r \neq \theta$. The intensity of the

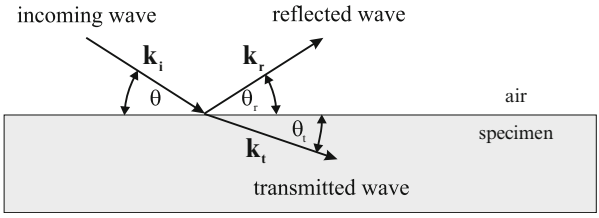

Fig. 5.1 Scattering geometry of a typical reflectometry experiment for samples in air

reflected and transmitted wave can be described with an index of refraction n, identical to classical optics:

$$n = \frac{k_t}{k_i} \tag{5.1}$$

with the wavevector $k_i = 2\pi/\lambda$ in air, the wavevector k_t in the specimen, and the neutron wavelength λ, respectively. The index of refraction can be written as

$$n = \sqrt{1 - \frac{\lambda^2}{\pi} Nb} \tag{5.2}$$

with N being the atomic density and b being the nuclear scattering length. The product Nb is called SLD, which varies randomly from element to element and isotope to isotope. For most materials, the SLD is positive, leading to $n < 1$. The index of refraction describes the interaction of a neutron wave with matter. In contrast to light, this interaction is very weak, the deviation from $n = 1$ (corresponding to no interaction) is typically smaller than 10^{-5}. For example, when using $\lambda = 0.237$ nm and applying Eq. (5.2) to Si, which has an SLD of 207 μm^{-2}, leads to $n = 0.999998$. Snell's law

$$n = \frac{\cos\theta}{\cos\theta_t} \tag{5.3}$$

applies to neutrons as well. For n < 1 Equation (5.3) does not have a solution for small angles as long as $\cos\theta > n$. This phenomenon is called total reflectivity, that is, all the incoming intensity is reflected up to a critical angle θ_c which can be calculated from $\cos\theta_c = n$. Because the deviation of n from 1 is very small and the angles involved are very small, it is possible to expand the square root in Eq. (5.2) and the cosine in Eq. (5.3). This leads to the expression:

$$\theta_c \approx \lambda\sqrt{\frac{Nb}{\pi}} \tag{5.4}$$

with $\theta_c = 0.1^\circ$ for Si, when using neutrons with $\lambda = 0.237$ nm. Total reflectivity is only observed in the medium with the larger n. Therefore, a neutron wave in air

($n \approx 1$) is totally reflected at a Si surface ($n_{Si} < 1$), whereas no total reflection is observed at an air/vanadium interface ($n_V > 1$).

In order to be able to compare reflectivities measured on different instruments, the reflectivity is usually plotted as a function of the scattering vector Q:

$$Q = |\mathbf{k_r} - \mathbf{k_i}| = \frac{4\pi}{\lambda} \sin\theta \tag{5.5}$$

where Q is parallel to the surface normal for the case of specular reflectivity. Figure 5.2 shows the simulated reflectivity curve of a Si wafer with zero roughness, plotted as a function of Q. The reflectivity R is plotted on a logarithmic scale because it drops fast with increasing Q. Total reflectivity is observed up to the critical scattering vector Q_c:

$$Q_c = 4\sqrt{\pi N b} \tag{5.6}$$

For $Q > Q_c$ the reflectivity R is described by Fresnel's equation:

$$R = \left| \frac{\sin\theta - n\sin\theta_t}{\sin\theta + n\sin\theta_t} \right| \tag{5.7}$$

With large Q the reflectivity drops proportional to Q^{-4} (see the dashed line in Fig. 5.2). For samples with many layers Eq. (5.7) has to be applied to all interfaces. Parratt [8] developed a recursion algorithm to solve this mathematical problem.

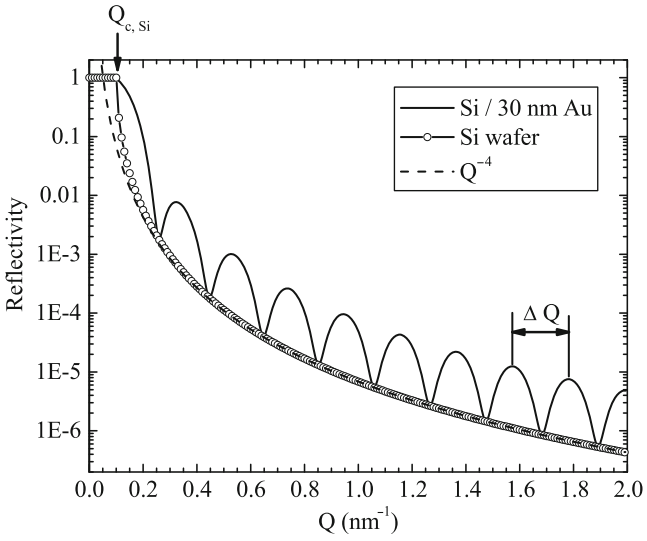

Fig. 5.2 Simulated reflectivity curves of a 30 nm thick Au film on a Si wafer (*solid line*) and a Si wafer (*open circles*) in comparison with the Q^{-4} dependence (*dashed line*). The critical scattering vector of Si is indicated by an *arrow*

Most simulation software packages use either this algorithm or the optical transfer matrix method [9]. Figure 5.2 shows a simulation of a 30 nm thick Au film on a Si wafer. The characteristic oscillations are called Kiessig fringes, named after H. Kiessig [10], who was the first to observe this type of oscillations when performing XRR experiments on Ni. These Kiessig fringes result from the interference of a wave reflected at two interfaces, that is, at the air–film and the film–substrate interface, respectively. The maxima correspond to constructive interference (both waves are in phase), the minima correspond to destructive interference (both waves are out of phase). The amplitudes of the Kiessig fringes depend on the SLD contrast, i.e. the difference of the SLD of the two neighboring media. In Fig. 5.2 the SLD values for Si and Au are 207 and 450 μm^{-2}, respectively, and the larger the SLD contrast, the larger the amplitude in the reflectivity curve. On the other hand, if the SLD of a film is identical to the SLD of the substrate it has been prepared on, this film would be invisible to neutrons. The oscillation period ΔQ (see Fig. 5.2) is proportional to the inverse of the total film thickness d_f and for $Q \gg Q_c$ the following approximation is valid:

$$\Delta Q = \frac{2\pi}{d_f} \tag{5.8}$$

More technical details on NR can be found elsewhere [1, 11–13].

5.2.2 *Polarized Neutrons*

The polarization of neutrons requires special polarizing devices such as supermirrors [14], Heusler monochromators [15], or polarized ^{3}He cells [16]. In a polarized setup (see Fig. 5.3) the majority of the neutron spins (typically more than 96 %) are oriented either parallel (spin-up neutrons) or antiparallel (spin-down neutrons) to the external magnetic field **H**. In the simple case, where the sample's

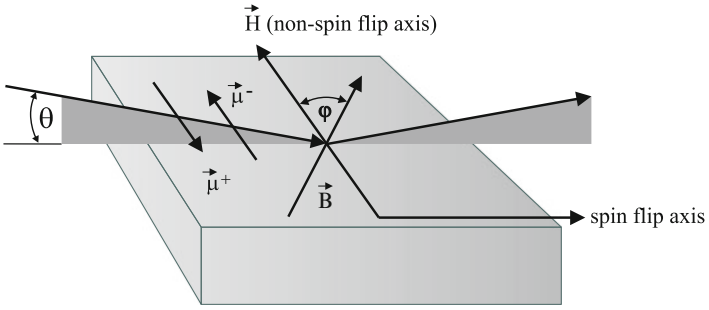

Fig. 5.3 Scattering geometry for polarized neutrons, with the polarization either parallel or antiparallel to the external magnetic field **H**. The sample's magnetization is at an angle φ with respect to **H**

magnetization is parallel to **H**, i.e. $\varphi = 0$, the interaction of the neutron's magnetic moment μ_N with the sample's magnetization can be described by the Zeeman energy:

$$-\mu_N \mathbf{B} = \frac{2\pi\hbar^2}{m} N b_{mag} \tag{5.9}$$

where b_{mag} denotes the magnetic scattering length, with $b_{mag} = 2.695$ fm per μ_B per atom. As can be seen from Eq. (5.9), the magnetic SLD, Nb_{mag}, is sensitive to the relative orientation of μ_N and **B**. Therefore, Eq. (5.2) must be modified accordingly:

$$n = \sqrt{1 - \frac{\lambda^2}{\pi} N\left(b_{nuc} \pm b_{mag}\right)} \tag{5.10}$$

The "+" is used for spin-up neutrons with their spin parallel to **H**, the "−" is used for spin-down neutrons with their spins antiparallel to **H**. It is important to note here that the spin of the neutron is antiparallel to its magnetic moment. Magnetism has been studied very intensely with neutron scattering because the nuclear and magnetic scattering lengths are of the same order of magnitude. For magnetically saturated bulk Ni the nuclear SLD is $Nb_{nuc} = 941\ \mu m^{-2}$ and the magnetic SLD ($B = 0.55\ T$ at room temperature) amounts to $Nb_{mag} = 143\ \mu m^{-2}$. The resulting SLD contrast for spin-up and spin-down neutrons of 1084 and 798 μm^{-2}, respectively, is so large that the corresponding critical scattering vectors Q_c^+ and Q_c^- are well separated. This can be seen in Fig. 5.4 where R^+ and R^-, the simulated

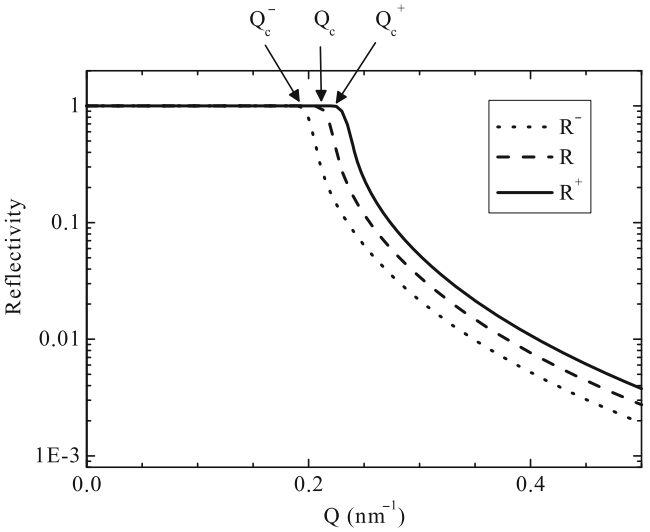

Fig. 5.4 Simulated reflectivity curve for bulk Ni for spin-up neutrons (*solid line*), spin-down neutrons (*dotted line*), and hypothetically nonmagnetic Ni (*dashed line*). The corresponding critical scattering vectors Q_c^+, Q_c^-, and Q_c are clearly separated

reflectivity curves for up and down-neutrons, respectively, are plotted for the case of bulk Ni. For comparison, the reflectivity curve for hypothetically nonmagnetic Ni is included as a dotted line in Fig. 5.4. The information that can be deduced from Fig. 5.4 is the specimen's magnetization. That could have easily been determined by conventional magnetometry as well. However, the big advantage of polarized neutron reflectometry (PNR) is that the substrate does not contribute to the magnetic signal unlike SQUID magnetometry where the signal is typically dominated by the diamagnetism of the substrate. Therefore, PNR has been used very successfully in experiments on ferromagnetic films in the monolayer regime or films with a low magnetization like spin glass systems [17] or diluted magnetic semiconductors [18].

5.2.3 Determination of Hydrogen and Deuterium Content

5.2.3.1 Single Layers

During hydrogen or deuterium absorption the structural properties of an absorbing layer change in a characteristic way as can be seen in Fig. 5.5, where fits to

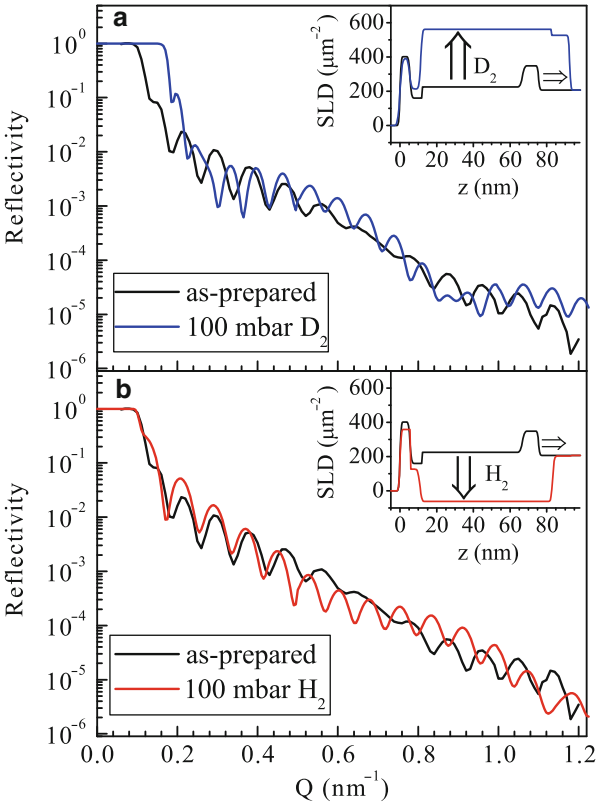

Fig. 5.5 NR curves of a $Mg_{0.8}Cr_{0.1}V_{0.1}$ film prepared on Si/10 nm Ta and capped by a 5 nm Pd/5 nm CrV bilayer after absorption in 100 mbar D_2 (**a**) and 100 mbar H_2 (**b**)

Table 5.1 Fit parameters for the reflectivity curves and SLD profiles shown in Fig. 5.5

	d_{Pd} (nm)	SLD_{Pd} (μm^{-2})	d_{MgCrV} (nm)	SLD_{MgCrV} (μm^{-2})	d_{CrV} (nm)	SLD_{CrV} (μm^{-2})	d_{Ta} (nm)	SLD_{Ta} (μm^{-2})
As-prepared	5.5	402	54.7	225	6.4	161	8.9	349
D-absorbed	5.2	391	71.2	562	6.1	214	10.0	527
H-absorbed	5.5	358	72.3	−62	5.3	126	10.0	202

experimental NR curves of a 55 nm thick $Mg_{0.8}Cr_{0.1}V_{0.1}$ film are shown, which was prepared on a 10 nm Ta buffer layer on a Si substrate and capped with a 5 nm Pd/5 nm CrV bilayer. The identical film, prepared on a Si wafer and cut into two pieces, was used to study the absorption of deuterium (Fig. 5.5a) and hydrogen (Fig. 5.5b). In both cases the Kiessig fringes change in the same way, i.e. ΔQ is decreasing. This is caused by the expansion of the absorbing layer. Due to the positive scattering length of deuterium the SLD of the absorbing layer increases so much that a large shift of Q_c can be observed. In the case of hydrogen no shift of Q_c is observed because when the SLD of the film decreases below the SLD of Si, the Q_c is defined by the bulk Si wafer. More insight can be gained from the corresponding SLD profiles plotted in the insets. A simple 4-layer model was applied to fit the data and the parameters are displayed in Table 5.1. The expansion in thin films is more pronounced than in bulk materials because the films are clamped to the substrate and can only expand in one direction. This leads to an expansion of about 30 % in this Mg-based alloy layer. After having determined the SLD before and after absorption, $(Nb)_M$ and $(Nb)_{M+H}$, as well as the layer thickness before and after absorption, d_M and d_{M+H}, the hydrogen concentration c_H can be determined [19] as follows:

$$c_H = \left(\frac{(Nb)_{M+H}}{(Nb)_M} \cdot \frac{d_{M+H}}{d_M} - 1 \right) \frac{b_M}{b_H} \tag{5.11}$$

In the above equation the hydrogen content is expressed in terms of the ratio of hydrogen to metal atoms. The same equation applies to deuterium absorption and the deuterium concentration c_D. Applying Eq. (5.11) and using the parameters in Table 5.1 results in $c_H = 1.7$ and $c_D = 1.6$, respectively. So, within the error limits, hydrogen and deuterium absorption leads to the same film expansion and hydrogen/deuterium uptake under identical conditions.

5.2.3.2 Multilayers

Multilayers are thin film structures composed of a bilayer that is repeated multiple times. These multilayers are covered with a cap layer (usually Pd) which serves two purposes: avoiding oxidation and facilitating the hydrogen absorption. The SLD profile of such a multilayer, prepared on a MgO substrate and capped with a Pd layer, is displayed in Fig. 5.6, where the black line represents the SLD of a deuterium-free sample and the red line the SLD of a Fe/VD multilayer with a

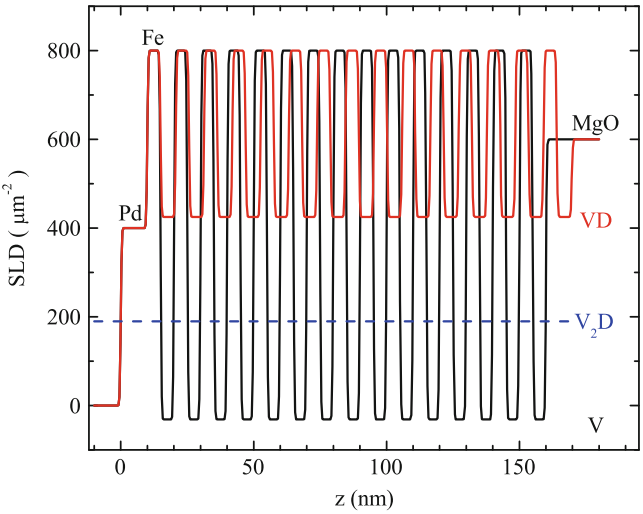

Fig. 5.6 SLD of a [5 nm Fe/5 nm V]$_{15}$ multilayer, prepared on a MgO substrate and capped with a 10 nm Pd catalyst layer, for different deuterium concentrations in the V layer: $c_D = 0$ (*black line*) and $c_D = 1$ (*red line*). The *blue dashed line* represents the SLD of V_2D ($c_D = 0.5$)

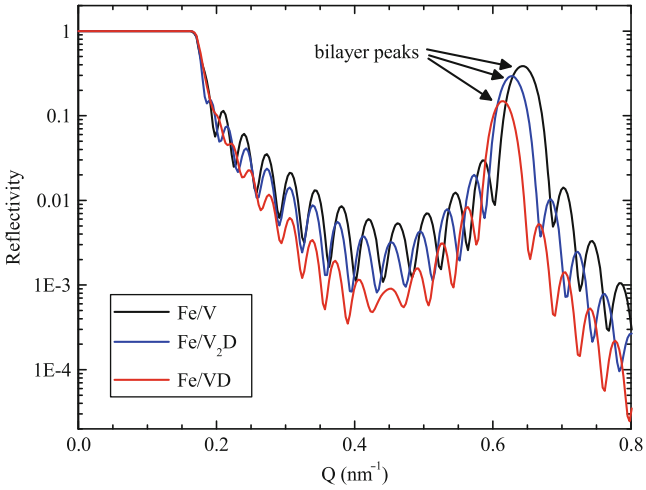

Fig. 5.7 Simulation of NR curves for a [5 nm Fe/5 nm V]$_{15}$ multilayer, prepared on a MgO substrate and capped with a 10 nm Pd catalyst layer, for different deuterium concentrations in the V layer: $c_D = 0$ (*black line*), $c_D = 0.5$ (*blue line*), $c_D = 1$ (*red line*)

deuterium concentration of $c_D = 1$. For comparison, also the SLD for V_2D with $c_D = 0.5$ is indicated with the dashed blue line. Due to the large scattering length of deuterium the SLD of the V layer increases with deuterium content, whereas the SLD of the Fe layer stays unchanged because Fe does not take up any deuterium. Figure 5.7 shows the reflectivity curves of this [Fe/V]$_{15}$ multilayer for different

deuterium concentrations: $c_D = 0$ (black line), $c_D = 0.5$ (blue line), and $c_D = 1$ (red line). In addition to the Kiessig fringes due to the total film thickness (see Sect. 5.2.1), a Bragg peak due to the bilayer periodicity is clearly visible. There are two features that can readily be seen by eye: this bilayer peak is shifted toward smaller Q and its intensity decreases during deuterium absorption. The peak shift is due to the layer expansion during deuterium absorption [20, 21], the decrease in peak intensity is a direct consequence of the increase of the SLD of the V layer because the intensity I of the bilayer peak depends on the SLD contrast of the neighboring Fe and V layers:

$$I \propto \left((Nb)_{\mathrm{Fe}} - (Nb)_{VD_x} \right)^2 \tag{5.12}$$

Therefore, the decrease of the bilayer peak intensity is a measure of the amount of absorbed deuterium.

5.3 Instrumentation

5.3.1 Typical Setup at a Reactor Source

A neutron reflectometer at a reactor source usually has at least the following components: a monochromator along with a wavelength filter to select a well-defined wavelength, two slits to define the beam collimation, a sample goniometer, and a detector. The setup of the D3 reflectometer, located at the NRU research reactor in Chalk River, Canada, is shown in Fig. 5.8. The neutrons coming from the reactor have a broad wavelength distribution. Therefore, a monochromator, for NR mostly pyrolytic graphite (PG), is needed to select a well-defined wavelength λ. As the NRU reactor is not equipped with a cold source, a wavelength of $\lambda = 0.237\,\mathrm{nm}$ is used because a PG filter (F) is very efficient at this specific wavelength reducing the higher order contributions of the monochromator (especially $\lambda/2$ and $\lambda/3$),

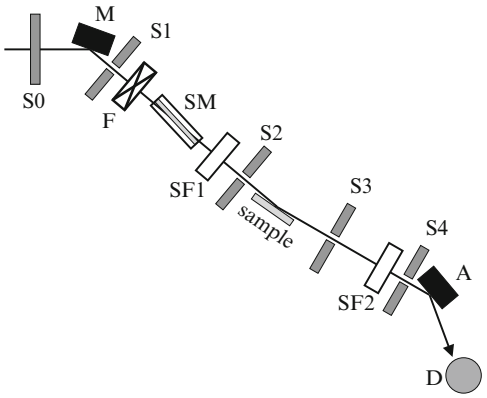

Fig. 5.8 Instrumental setup (*top view*) of the D3 reflectometer at the NRU research reactor in Chalk River, Canada, with the following components: horizontal slits S0, monochromator (M), vertical slits (S1, S2, S3, S4), PG-filter (F), spin-polarizing supermirror (SM), spin flippers (SF1, SF2), spin analyzer (A), and detector (D)

usually by a factor of about 1000. Without filter, the higher order reflections would be observable because the Bragg equation is also satisfied with $n = 2$ and $\lambda/2$ or with $n = 3$ and $\lambda/3$. The collimation of the beam and with it the angular resolution of the instrument is defined by the two vertical slits S1 and S2, whereas the other two vertical slits S3 and S4 help to reduce the background. Slit S0 is a horizontal slit which defines the incoming neutron flux hitting the 30 cm tall PG monochromator. If the experiment requires polarized neutrons, a polarizer is moved into the beam, which consists of a polarizing supermirror (SM) positioned in a magnetic field provided by permanent magnets [14]. The polarizer delivers only spin-down neutrons. If measurements with spin-up neutrons are required, a "spin flipper" [22] (SF1) is needed to convert the spin-down neutrons into spin-up neutrons. Another spin flipper (SF2) is needed in front of the analyzer to determine the spin state of the reflected neutrons because the used spin analyzer (A), a Cu_2MnAl Heusler crystal, reflects predominantly spin-down neutrons [15].

Neutron reflectometers at a cold source usually use a PG monochromator at a wavelength of about $\lambda = 0.46$ nm. The PG filter is then replaced by a Be filter, that reflects all the higher order neutrons with $\lambda < 0.4$ nm out of the beam and instead of a Heusler analyzer an SM or a polarized ^{3}He cell is used as analyzer.

By using chopper systems instead of monochromators [23, 24] a higher neutron flux can be achieved by sacrificing resolution. This is advantageous for the investigation of ultrathin film structures where a lower instrumental resolution can be tolerated.

5.3.2 Typical Setup at a Spallation Source

Reflectometers at short-pulse spallation neutron sources use a large fraction of the emitted wavelength spectrum of the source sequentially to determine the sample reflectivity R as a function of the scattering vector Q. In contrast to monochromatic wavelength reflectometers which probe Q by varying the angle of incidence θ in many fine steps, time-of-flight (TOF) instruments measure $R(Q)$ by varying λ at a fixed scattering angle, i.e. using

$$Q(t) = \frac{4\pi \sin\theta}{\lambda(t)} \tag{5.13}$$

Quantification of λ is achieved by measuring TOF which is the time that a neutron of a particular wavelength needs for traveling from the neutron source to the detector, where $t = 0$ is defined by the moment when the accelerator creates the neutron pulse in the spallation target. The wavelength λ relates to the TOF as:

$$\lambda = \frac{h}{m_n} \cdot \frac{\mathrm{TOF}}{L} \quad \text{or} \quad \lambda\,[\mathrm{nm}] = 395.6 \cdot \frac{\mathrm{TOF[s]}}{L[\mathrm{m}]} \tag{5.14}$$

where $h = 6.626 \times 10^{-34}$ Js is Planck's constant, $m_n = 1.675 \times 10^{-27}$ kg is the neutron mass, and L is the total length of the neutron flight path within the

instrument, i.e. from neutron source/moderator to detector. In order to cover the complete Q range in which measurable reflectivities may be detected, typically data sets at two or more specific angles need to be recorded. In order to determine the true reflectivity R as function of Q, the measured intensities with sample, $I_{\text{sample}}(Q)$, need to be normalized by the beam spectrum without sample, $I_0(Q)$, using the same instrument settings:

$$R(Q) = \frac{I_{\text{sample}}(Q)}{I_0(Q)} \tag{5.15}$$

In order to achieve a convenient resolution function of the data and to allow for convenient data analysis, one often chooses experimental settings such that the relative Q resolution $\Delta Q/Q$ has a constant value of a few percent. In good approximation:

$$\left(\frac{\Delta Q}{Q}\right)^2 = \left(\frac{\Delta\theta}{\theta}\right)^2 + \left(\frac{\Delta\lambda}{\lambda}\right)^2 = \left(\frac{\Delta\theta}{\theta}\right)^2 + \left(\frac{\Delta t}{\text{TOF}}\right)^2 \tag{5.16}$$

where $\Delta\theta$ is the collimation-defined angular spread of the neutron beam hitting the sample at an incident angle of θ. At a short-pulse spallation neutron source like the SNS at Oak Ridge National Laboratory, the intrinsic neutron emission time uncertainty of the neutron source Δt is typically $< 1\,\%$ of the neutron TOF. Therefore, the Q-resolution of a neutron reflectometer at such a source is usually dominated by the angular term. $\Delta\theta/\theta$ is generally set in the range of 1–10 %. Figure 5.9 displays the

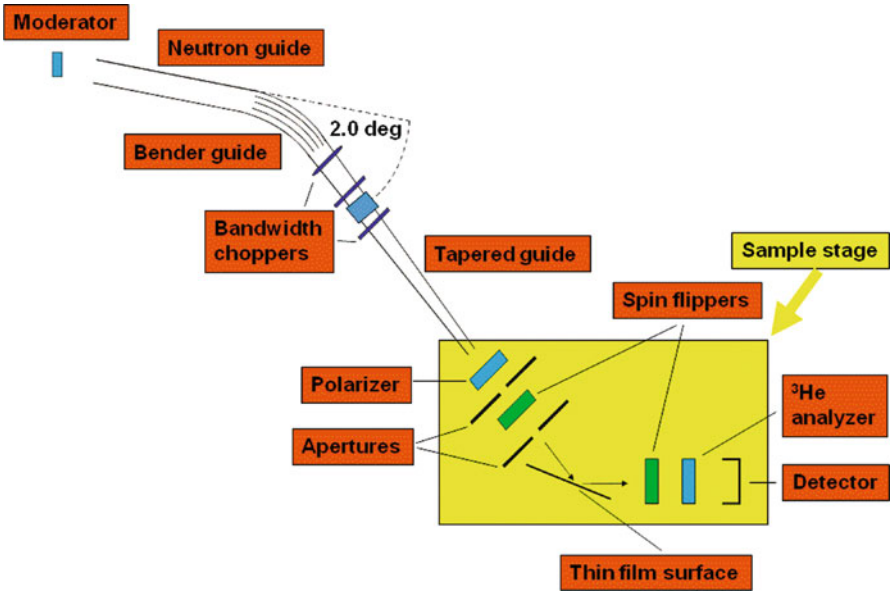

Fig. 5.9 Instrumental setup (*top view*) of the Magnetism Reflectometer at the Spallation Neutron Source in Oak Ridge, USA

experimental setup of the Magnetism Reflectometer (MR) at the SNS. The SNS facility operates at a pulse repetition frequency f of 60 Hz. The MR beamline is attached to a cold liquid hydrogen moderator and uses a neutron guide system. A "bender" guide section is essential for extracting a clean neutron beam for the experiment, because it filters the beam from high-energy gamma and neutron components by avoiding a direct line-of-sight from source to sample. The instrument has a total length of $L \approx 21$ m (source to detector). Since one needs to avoid that fast neutrons from one pulse can catch up with slower neutrons from a succeeding pulse (a process called "frame overlap"), one needs to limit the maximum operational wavelength bandwidth to

$$\Delta\lambda[\text{nm}] = \frac{395.6}{f[\text{Hz}] \cdot L[\text{m}]} = 0.31 \text{ nm} \tag{5.17}$$

This is achieved by a system of three bandwidth limiting choppers. The sample stage of a reflectometer, which typically contains beam optics, sample environment, and detector, is very similar at reactor and spallation neutron sources.

5.3.3 *Sample Environment*

In order to pursue in-situ hydrogen storage research one has to be able to do NR experiments at temperatures of up to about 670 K and hydrogen pressures up to 40 bar. An additional challenge—when working with hydrogen—is to choose only materials for the sample cell that will not be affected by embrittlement. For NR most sample cells are made of Al because it has a low absorption cross section for neutrons and does not readily form a hydride. For temperatures above 670 K stainless steel is the only alternative because the mechanical properties of Al deteriorate quickly with increasing temperature. The disadvantage of steel is the large absorption for neutrons, roughly a factor of 10 higher than for Al. Another disadvantage of steel is the noticeable small angle scattering leading to a smearing of the minima of the Kiessig fringes. A sample cell that has been used on the D3 reflectometer at the NRU reactor in Chalk River can be seen in Fig. 5.10.

5.4 Difference Between Bulk and Thin Film Samples

Due to the important role that surfaces and near-surface layers play in the hydrogen absorption and diffusion process of bulk materials and the fact that in modern technology many materials are used in layered form, much effort has been focused recently on the behavior of hydrogen in nanoscale thin films. In bulk samples the volume expands isotropically during hydrogen absorption and the volume changes linearly with the amount of absorbed hydrogen:

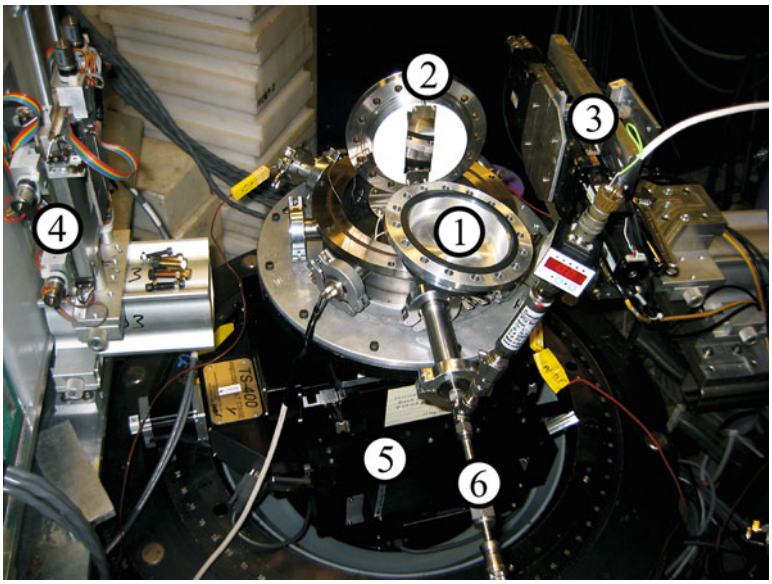

Fig. 5.10 Sample cell used for hydrogen absorption experiments on the D3 reflectometer in Chalk River, Canada. The components are the lid of the sample cell (*1*), the sample (*2*), slit S2 (*3*), slit S3 (*4*), sample goniometer (*5*), and hydrogen gas supply lines (*6*)

$$\frac{\Delta V}{V} = k \cdot c_{\mathrm{H}} \tag{5.18}$$

Thin films, however, are prepared on rigid non-absorbing substrates. Hence, the volume change is highly anisotropic. The films are clamped to the substrate and can only expand along their film normal. Therefore, all the properties that depend on the strain will be different in thin films compared to bulk, e.g. the enthalpy of solution [25]. Usually the shift of Bragg peaks is used in bulk samples to determine the volume change and via Eq. (5.18) the hydrogen concentration. This procedure is no longer valid in thin film structures where the relative change of lattice constants derived from Bragg peaks can deviate from the relative volume change as has been found in Fe/V [20] and Nb films [19]. Recently, it was shown that the hydrogen absorption properties of thin Mg films depend on the cap layer [26]. Mg-alloy forming elements like Pd and Ni increased the plateau pressure by two orders of magnitude. This could be explained with an elastic model where the cap layers lead to a clamping effect during hydrogen absorption.

The interaction of hydrogen with the host film can lead to significant modification of electronic, magnetic, and structural properties [25]. Exciting results have been achieved recently for thin metal films. Among these are Y and La thin films which reversibly switch their optical properties upon hydrogen absorption [27] and Fe/Nb [6] or Fe/V [7] multilayers which reversibly switch their magnetic coupling and magnetoresistivity during hydrogen charging and decharging. For a theoretical

understanding of the remarkable changes of film properties due to hydrogen charging, it is important to know how hydrogen is incorporated into the films, whether structural phase diagrams of the corresponding bulk materials are applicable, and how hydrogen absorption and its kinetics depend on various external parameters such as temperature and hydrogen pressure. Many existing studies have relied solely on X-ray diffraction (XRD). The examples above show how important it is that the hydrogen concentration in films can be determined directly, e.g. with neutron reflectometry.

5.5 Hydrogen Absorption of Mg-Based Thin Films

Magnesium hydride is a very attractive hydrogen storage material for mobile applications because of its high gravimetric storage capacity of 7.6 wt.%. However, slow absorption and desorption kinetics along with its high stability require operating temperatures that are too high for practical applications. Recent efforts have been focused on improving the kinetics by using high energy ball milling to reduce the grain sizes and adding metals or metal oxides as catalysts. In order to better understand the involved processes a characterization at the nanoscale is required. Thin films offer a unique opportunity to study the fundamentals of absorption and desorption in great detail because nanoscale layers can be prepared with well-defined composition and thickness. Using thin films as model systems makes it possible to discriminate, e.g., between the catalytic surface effect of a cap layer on top of a Mg film and the catalytic bulk effect of alloying the Mg film with other elements. This section shows how NR can be used to determine in-situ the hydrogen profile within a thin film system and how this knowledge can be used to better understand the hydrogen absorption properties of Mg-based alloys.

5.5.1 Binary Mg-Al Alloys

5.5.1.1 Mg-Al Alloy Composition

Figure 5.11 shows the reflectivity curve of a 52 nm thick $Mg_{0.7}Al_{0.3}$ thin film in the as-prepared state (a), after hydrogen absorption at 398 K and 40 bar (b), and after desorption at 448 K (c). The film was prepared on a Si wafer and covered by a 10 nm thick Pd cap layer. The open circles represent experimental data, the solid lines represent fits. When looking at the NR curves one can clearly notice the Kiessig fringes caused by the total film thickness. The periodicity changes from the as-prepared (a) to the fully absorbed state (b), i.e. the distance between two maxima is decreasing. This can be easily interpreted as an expansion of the film due to hydrogen uptake. More details can be inferred from the SLD profiles that are plotted as insets in Fig. 5.11 and correspond to the fits shown as solid lines. The film

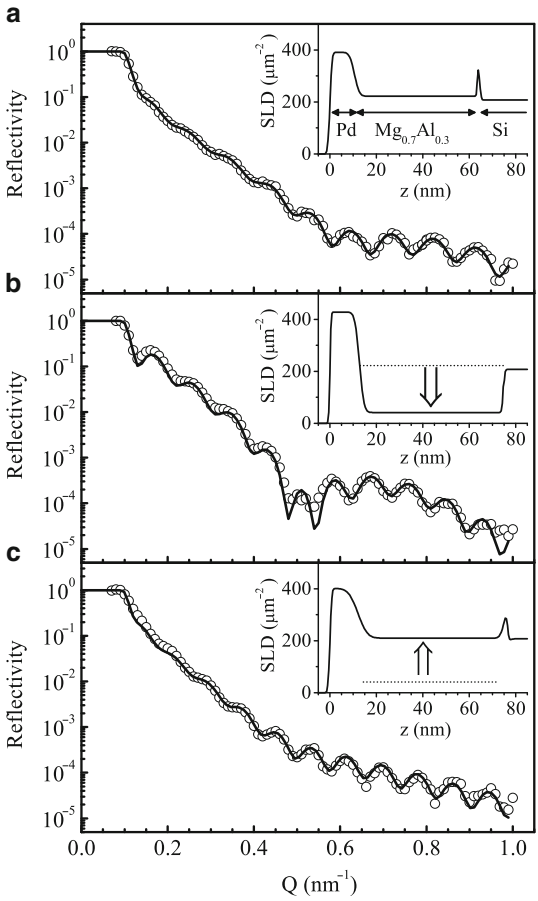

Fig. 5.11 Reflectivity curve of a Pd-covered $Mg_{0.7}Al_{0.3}H_y$ thin film on a Si substrate (**a**) before hydrogen absorption ($y = 0$), measured at 295 K; (**b**) after hydrogen absorption ($y = 1.1$), measured at 295 K; and (**c**) after hydrogen desorption, measured at 448 K ($y = 0$). The *open circles* represent experimental data, the *solid lines* represent fits, and the *insets* show the corresponding SLD profile. The *arrows* in the insets indicate the change of the SLD in the MgAl layer due to hydrogen absorption (**b**) and desorption (**c**)

structure is clearly visible in the SLD profile shown in Fig. 5.11a with a 10 nm thick Pd film (SLD = 402 μm^{-2}), 52 nm thick $Mg_{0.7}Al_{0.3}$ layer (SLD = 220 μm^{-2}), 1 nm SiO_2 layer and the Si wafer (SLD = 207 μm^{-2}). After absorption of hydrogen the SLD profile changes significantly. As indicated by an arrow in the inset of Fig. 5.11b the SLD of the $Mg_{0.7}Al_{0.3}$ layer decreases from 220 μm^{-2} to 42 μm^{-2}. At the same time the thickness of this layer increases from 52 nm to 62 nm. After annealing the film at 448 K the hydrogen can be fully desorbed as can be deduced from the increase of the SLD of the $Mg_{0.7}Al_{0.3}$ layer (see arrow in the inset of Fig. 5.11c). The amount of absorbed hydrogen $c_H = 1.1$ can be calculated using Eq. (5.11). This is close to the theoretical maximum of 1.4, assuming that every Mg atom reacts and forms MgH_2. The slightly reduced hydrogen content is partially due to room temperature desorption because these samples were absorbed ex-situ and then transferred to the neutron instrument.

Various $Mg_{1-x}Al_x$ alloy compositions were investigated [28, 29] and the conclusion was that $Mg_{0.7}Al_{0.3}$ is the optimum composition with regard to hydrogen content and kinetics.

5.5.1.2 The Importance of the Catalyst Layer

It is well known that Pd can easily absorb hydrogen at room temperature and low pressure [30]. Therefore, Pd has been used successfully in thin film research as a cap layer serving as both, a catalyst and a protection against oxidation. However, Pd has the disadvantage that it easily diffuses into Mg [31] at temperatures above 473 K. In order to avoid this interdiffusion a Ta layer was introduced between the Mg-alloy and the Pd layer [32]. This diffusion barrier breaks down for temperatures above 523 K as has been shown recently [33]. Interestingly, this Ta/Pd bilayer also improved the desorption characteristics by decreasing the desorption temperature from 468 K for a single Pd layer to 393 K. Many other bilayer combinations were investigated [34], with Ti/Pd being the one with the most favorable absorption characteristics. With a Ti/Pd catalyst a $Mg_{0.7}Al_{0.3}$ layer can absorb deuterium at room temperature and 100 mbar. The deuterium absorption process of a $Mg_{0.7}Al_{0.3}$ layer capped with a Ti/Pd layer is shown in Fig. 5.12 as a function of deuterium pressure. The 5 nm thick Ti layer can be clearly seen in the SLD profile of the as-prepared film (see Fig. 5.12) because of its large negative value of $-195\,\mu m^{-2}$. Applying a deuterium pressure of $P_D = 1$ mbar at room temperature is already sufficient for the absorption of deuterium into the Ti layer as can be concluded from the increase of the SLD of the Ti layer. The SLDs of the other layers remain unchanged, i.e. no deuterium absorption takes place in any other layer of the film structure. When increasing the pressure to $P_D = 20$ mbar the SLD of the Ti layers increases further due to further deuterium uptake. The SLD of the Pd layer increases as well, whereas the SLD of the $Mg_{0.7}Al_{0.3}$ layer stays constant. At $P_D = 100$ mbar the $Mg_{0.7}Al_{0.3}$ layer is fully absorbed. As a conclusion, the NR experiments successfully revealed a sequential deuterium absorption with the Ti layer being absorbed first before the Pd layer and finally the Mg-alloy.

5.5.2 Ternary Mg-based Alloys

Several ternary Mg-based alloys have been discovered that exhibit fast kinetics at low temperature: Mg-Fe-Ti [35], Mg-Al-Ti [35], Mg-Fe-V [36], Mg-Cr-V [37], and Mg-Fe-Cr [38]. NR experiments have contributed to the understanding why these alloys work so well.

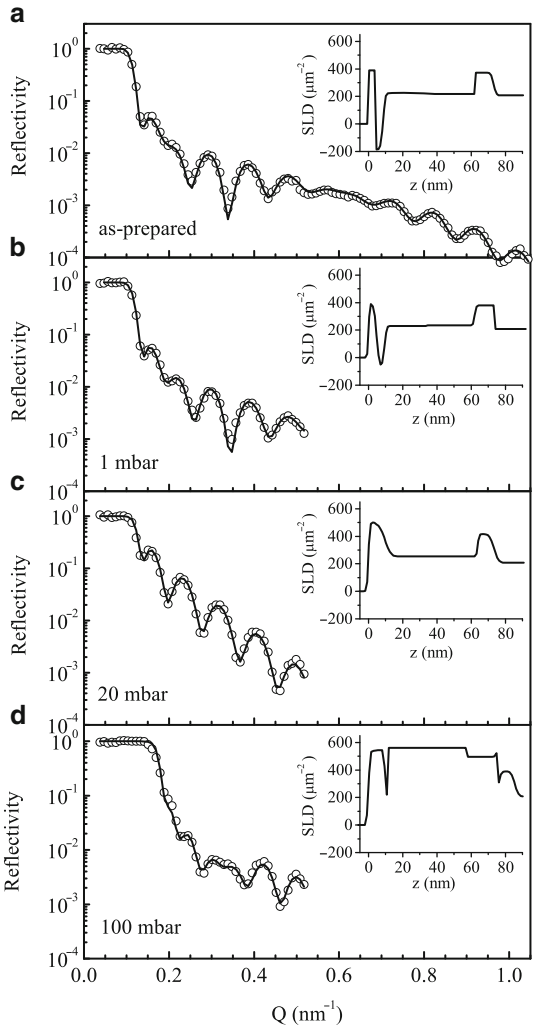

Fig. 5.12 Reflectivity curves of a Si/Ta/$Mg_{0.7}Al_{0.3}$/Ti/Pd film in the as-prepared state (**a**), in 1 mbar D_2 (**b**), 20 mbar D_2 (**c**), and 100 mbar D_2 (**d**)

5.5.2.1 Real-Time Measurements

Figure 5.13 shows a series of reflectivity curves of a 52 nm thick $Mg_{0.8}Fe_{0.1}Cr_{0.1}$ film, prepared on Si/10 nm Ta and capped with a 5 nm Ta/5 nm Pd bilayer, during the exposure to $P_{D_2} = 10$ mbar. Under these conditions the changes are slow enough so that NR can capture the kinetics of the deuterium absorption. The exposure time is indicated in the graph. Most evident is the continuous increase of Q_c during the absorption process as indicated in the graph by the arrow. This increase of Q_c is caused by the increase of the film's SLD [see Eq. (5.6)] due to the large positive scattering length of deuterium. Therefore, by measuring the reflectivity curve close to Q_c it is possible to monitor the deuterium uptake of thin films in-situ in real time.

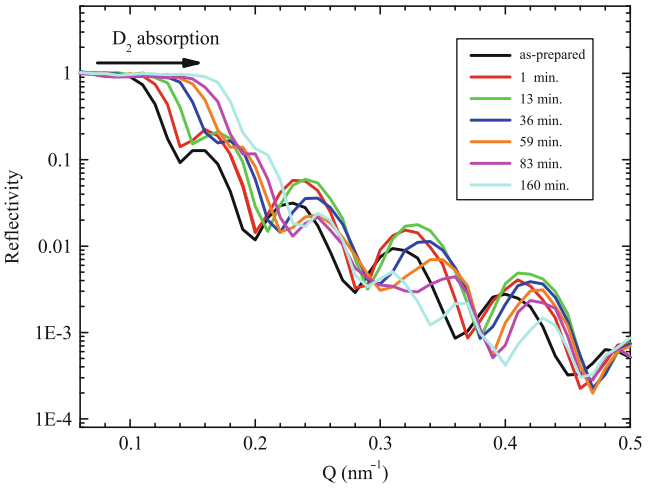

Fig. 5.13 NR curves of a 52 nm thick $Mg_{0.8}Fe_{0.1}Cr_{0.1}$ film, capped with a 5 nm Ta/5 nm Pd bilayer, measured at room temperature and $P_{D_2} = 10$ mbar for different exposure times as indicated

The larger the Q-range the more details about the hydrogen depth profile can be revealed. The Q-range in Fig. 5.13 is large enough to determine whether the film absorbs homogeneously or whether a thin blocking hydride layer forms. It is worthwhile to note that the absorption is instantaneous (in the order of seconds) for $P_{D_2} = 1$ bar.

5.5.2.2 Comparison of Pure Mg to Mg-Cr-V

A comparative in-situ NR study on a 55 nm Mg and a 55 nm $Mg_{0.8}Cr_{0.1}V_{0.1}$ layer helped to understand why these ternary Mg-alloys absorb hydrogen so much faster than pure Mg [37]. Both layers were prepared on Si/10 nm Ta buffer and capped with a 5 nm CrV/5 nm Pd catalyst bilayer. After one hour in $P_{D_2} = 50$ mbar the NR curve of the pure Mg film has noticeably changed (see open circles Fig. 5.14a) due to deuterium absorption. The same is true for the $Mg_{0.8}Cr_{0.1}V_{0.1}$ layer (see open circles in Fig. 5.14b). However, when comparing the NR curves and the corresponding SLD profiles of the two layers (shown in the insets) it is clear that these two films behave very differently. In the alloy layer the deuterium is being absorbed homogeneously throughout the layer whereas in the pure Mg layer a MgD_2 layer has formed close to the interface to the catalyst and no deuterium has been absorbed in the bottom part of the Mg layer. This MgD_2 layer, which had also been observed with nuclear reaction analysis (NRA) [39], blocks the diffusion of the deuterium. In contrast, the Mg-alloy layer absorbs deuterium in the form of a solid solution without forming MgD_2. This can be concluded from the fact that the layer does not expand. After the first desorption the CrV precipitates in small grains

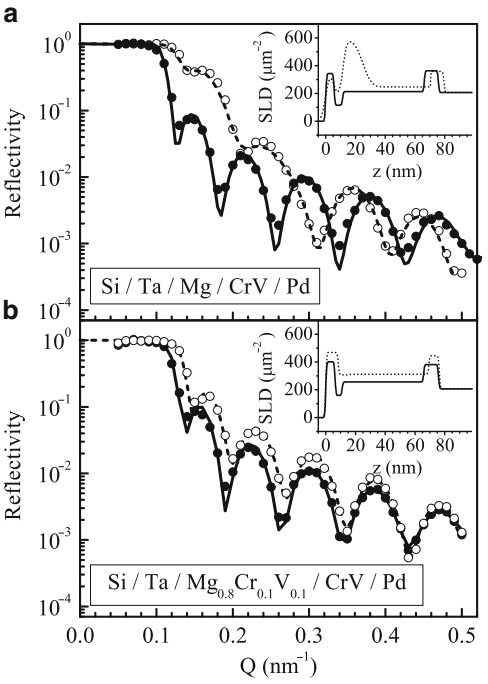

Fig. 5.14 NR curves of a Mg layer (**a**) and a $Mg_{0.8}Cr_{0.1}V_{0.1}$ layer (**b**) in the as-prepared condition (*solid dots*) and in the early phase of the absorption process (*open circles*). The *solid lines* are the fits to the as-prepared samples, the *dashed lines* represent fits in the partially absorbed state

leading to nucleation sites throughout the whole layer and avoiding the formation of a blocking MgD_2 layer. These precipitates have been observed with transmission electron microscopy (TEM) [38].

5.6 Hydrogen Absorption of Polycrystalline and Epitaxial Single-Crystal Nb Films

5.6.1 Nb Bulk Properties

The metal niobium is used as an important ingredient in many specialized engineering materials. While the vast majority of the yearly Nb production is used for manufacturing of high-grade structural steel alloys, there are many other important technical applications of pure or alloyed Nb. Medical implants, linings of chemical plants and jewellery applications, for example, take advantage of niobium's high corrosion resistance. Other applications benefit from its excellent superconducting properties (its superconducting transition temperature of 9.2 K is the highest of all elements). Examples are superconducting coils in magnetic resonance imaging scanners and scientific high-field magnets as well as superconducting radio-frequency (SRF) cavities in particle accelerators.

Niobium shows strong affinity to hydrogen. This can be beneficial in view of hydrogen storage applications but it is also well known that dissolved hydrogen or hydride phases deteriorate chemical stability, mechanical properties ("hydrogen embrittlement" of hydride phases), and superconductivity. For example, niobium hydride is a major contributor to degradation of the quality factor of niobium SRF cavities ("Q-disease") [40]. As Nb hydride phases, which preferentially form on the surfaces of these cavities, have no or poorer superconducting properties, they generate undesirable extra surface resistivity.

Generally, the surface of pure Nb is quite reactive, even at room temperature. Under most conditions, however, Nb will readily form a very thin oxide layer (Nb_2O_5 being the most stable oxide) which is responsible for its chemical stability. But, despite the passivating oxide surface layer, a cold-worked piece of Nb metal manufactured for a real-world application will possess numerous vacancies, dislocations, and grain boundaries, and these can very effectively transport hydrogen from an external source, e.g. from processing materials, to the bulk interior. Even relatively low hydrogen concentrations at levels of 100 at. ppm may substantially deteriorate particular properties, e.g. the ductility of Nb alloy construction materials.

The niobium phase diagram has been studied extensively as a prime example of a metal-hydrogen system [41]. The behavior of H in Nb has close analogies to how real gases behave, including gas–liquid phase transitions. The interstitial solid solution of hydrogen in the host metal is regarded as a textbook example of a "lattice gas" [42].

The equilibrium Nb-H phase diagram was established using pure Nb metal foils or wires which were initially high-temperature vacuum-degassed from hydrogen, which also leads to a re-crystallized metal lattice essentially free of defects such as dislocations and vacancies. Zabel et al. [43] studied the structural thermodynamic phase boundaries by in-situ XRD and charged Nb samples with hydrogen at high temperature in the single phase region and cooled them through the phase boundary below which two distinct lattice parameters, i.e. two structural phases named α (low H concentration) and α' (high H concentration) could be observed simultaneously. In the same work, Zabel et al. also observed a hysteretic behavior when crossing back this phase boundary in a sense that the two distinct phases α and α' continue to exist well above the initial phase transition temperature. This effect depends on the temperature and is increasing when lowering the temperature further below the phase transition temperature. This shows that irreversible stresses created during the $\alpha - \alpha'$ phase separation are responsible for the hysteretic behavior. From this and from other observations, it became clear that the microscopic structure of the hydrogen absorbing Nb, including its vacancy/dislocation densities, strain fields, etc., plays a major role in the hydrogen absorption kinetics, limiting hydrogen concentrations and phase boundary locations. It should be noted that the absorption of hydrogen by niobium lattice vacancies is energetically strongly preferred to absorption into interstitial sites. First-principles calculations of niobium hydride formation showed that a single vacancy can accommodate six hydrogen atoms in the symmetrically equivalent lowest-energy sites and additional hydrogen in the

nearby interstitial sites affected by the strain field: this indicates that a vacancy can serve as a nucleation center for hydride phase formation [40]. The issue of hydrogen absorption and trapping in near-surface layers (< 100 nm) due to strain field effects is extensively discussed in the literature (see references 10–25 in [40]) [44].

5.6.2 *Fe/Nb Multilayers*

In the following, we present insights into the interrelation between hydrogen uptake and structural changes in thin polycrystalline and epitaxial Nb layers, respectively. The main goal of the presented studies was to measure the hydrogen concentration within the Nb layers as a function of an external hydrogen atmosphere and identify related structural changes to the films such as the amount of hydrogen-induced expansion of the Nb atomic lattice spacing and the overall Nb film thickness. The reversibility of the absorption process, particularly after loading to high hydrogen concentrations, was also investigated. Polycrystalline thin Nb layers of variable thickness were prepared by growing Fe/Nb multilayers on oxidized Si substrates [19]. These samples were prepared by ion-beam sputtering at room temperature in an ultrahigh vacuum chamber with a base pressure of $< 5 \times 10^{-9}$ mbar, where the Nb layers grew strongly (110) textured. Epitaxial Nb layers were prepared by growing W/Nb superlattices at elevated temperatures of 200 °C on etched MgO(001) substrates by magnetron sputtering [45, 46]. Both systems were prepared in form of multilayers to optimize the intensity for the scattering experiments discussed below. The Nb thickness was varied over a large range to study the hydrogen absorption process for various interface/film thickness ratios. The nominal compositions of the films were [2.6 nm W (or Fe)/d_{Nb}]$_n$ where d_{Nb} denotes the variable Nb thickness and n the number of bilayer repetitions. Each of the multilayers was capped with a 5.0 nm Pd layer which protects the samples from oxidizing and also facilitates hydrogen uptake by catalytic dissociation of hydrogen molecules which enables them to diffuse much more rapidly into the Nb layers. Table 5.2 summarizes the investigated samples (the stated layer thicknesses are nominal values). The samples, which were never before exposed to hydrogen, were charged from the gas phase within a container suitable for neutron and X-ray scattering experiments initially evacuated to $p < 10^{-5}$ mbar. The hydrogen pressures ranged from 10^{-4} to 900 mbar. Due to a large negative enthalpy of mixing, only the Nb layers of the multilayer absorb hydrogen. After each charging step, the hydrogen concentration was found to be equal in all Nb layers of the stack. We never found

Table 5.2 Nominal layer thicknesses of the investigated multilayers.

Polycrystalline Fe/Nb(110)	Single crystalline W/Nb(100)
[2.6 nm Fe/2 nm Nb]$_{20}$	[2.6 nm W/3 nm Nb]$_{120}$
[2.6 nm Fe/5 nm Nb]$_{10}$	[2.6 nm W/10 nm Nb]$_{100}$
[2.6 nm Fe/10 nm Nb]$_{10}$	
[2.6 nm Fe/100 nm Nb]$_{10}$	

detectable amounts of hydrogen in the W or Fe layers. NR, XRR, and XRD measurements were carried out in-situ at a temperature of 185°C. The reasoning for this temperature is twofold. Firstly, at this elevated temperature the hydrogen absorption is relatively fast. In most cases, it takes only minutes until equilibrium is reached (de-charging requires much longer time, see discussion below). Secondly, the Nb/H bulk phase diagram shows a separation into a hydrogen rich and a hydrogen depleted Nb phase below a critical temperature of 171 °C. The associated specific phase transitions and phase separations are known to result in irreversible stresses and would severely complicate the interpretation of our experimental data. Results of in-situ measurements on Fe/Nb multilayers are shown in Fig. 5.15, where both, the uncharged state (red solid circles) and the state after hydrogen charging at 900 mbar (blue solid circles) are displayed. As can be seen, the effect of hydrogen absorption on the reflectivity spectra is quite dramatic. The charged samples show strongly enhanced chemical Bragg peaks due to the increase in scattering contrast between Nb+H and Fe, and pronounced shifts in the Bragg positions towards smaller Q indicating an expansion of the Nb film thickness. Figure 5.16 shows the experimental data of the film $[2.6\,\text{nm Fe}/100\,\text{nm Nb}]_{10}$ along with fits obtained using the software Parratt32 [47]. Due to the magnetism of the Fe layers and the associated additional contrast mechanism, these experiments were performed with polarized neutrons (see Sect. 5.2.2), i.e. for every pressure one data set with spin-up (solid circles) and one with spin-down neutrons (open circles) was recorded. Due to the magnetism of the Fe layers two clearly different reflectivity curves arise for the two spin states. During the measurements the sample was in a magnetic field of 0.05 T, saturating it magnetically. In all curves a sequence of Bragg peaks is visible reflecting the thickness of one Fe/Nb bilayer. Due to the steep concentration gradient at the Fe/Nb interfaces the reflections are at least recognizable up to the 15th order. Figure 5.17 shows the SLD profiles as calculated from the fits shown in Fig. 5.16. The depth profiles scale for Pd, Fe, and Cr. However, the Nb depth coordinates are reduced by a factor of 10 because of its much larger layer thickness. Figures 5.17a, b represent the SLDs for the measurement at 0 mbar, i.e. in the as-prepared state of the sample, for spin-up (Fe^{+}) and spin-down (Fe^{-}) neutrons, respectively. The measurement with spin-up neutrons is characterized by a strong scattering contrast between the individual Fe and Nb layers, whereas the contrast is much smaller for spin-down neutrons. This explains the low intensities of the Bragg peaks of the corresponding measurement in Fig. 5.16. Figures 5.17c and d represent the SLD profiles after hydrogen charging at 900 mbar.

In contrast to the positive coherent scattering length of Nb ($b_{\text{Nb}} = 7.054$ fm), the coherent scattering length of hydrogen atoms is negative ($b_{\text{H}} = -3.739$ fm). Thus, when hydrogen is absorbed by the Nb layer, the average SLD will be reduced. It follows that the contrast between Fe and Nb increases slightly for the case of spin-up neutrons. For spin-down neutrons (Fig. 5.17d), however, it is significantly increased compared to the non-charged layer (Fig. 5.17b). Hence, at 900 mbar the Bragg peaks for both spin states are more pronounced. The hydrogen-induced Nb layer expansion results in a slight frequency increase of the small-angle oscillations in Fig. 5.16. Furthermore, it is noticeable that the position of the total reflectivity

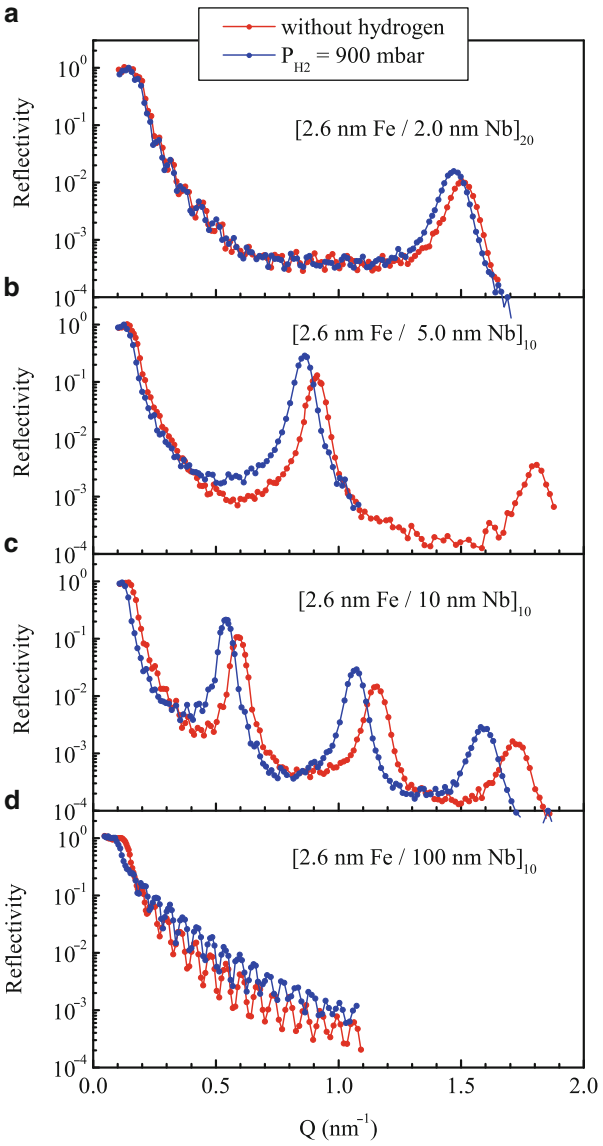

Fig. 5.15 NR curves of Fe/Nb multilayers with various layer thicknesses as indicated, measured in the as-prepared state (*red solid circles*) and at a hydrogen pressure of 900 mbar (*blue solid circles*)

edge Q_c is shifted to a lower Q value after charging at 900 mbar (see dashed line in Fig. 5.16). This is a direct consequence of the hydrogen-induced reduction of the Nb SLD. Since the multilayer consists mainly of Nb, Q_c qualitatively indicates the amount of hydrogen dissolved in the Nb layers. In fact, by measuring Q_c, one can directly determine the SLD of hydrogen-charged Nb (see Sect. 5.2). However, for the exact calculation of the hydrogen concentration c_H one has to take the layer expansion into account [see Eq. (5.11)]. The fit parameters for the four data sets displayed in Fig. 5.16 are listed in Table 5.3.

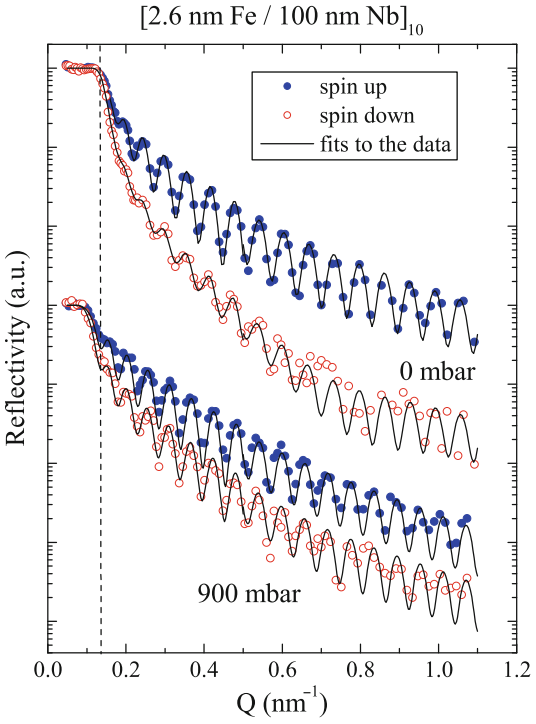

Fig. 5.16 Neutron reflectivity curves of a $[2.6\,\text{nm Fe}/100\,\text{nm Nb}]_{10}$ multilayer in the as-prepared state (0 mbar) and after hydrogen charging at 900 mbar. The *symbols* represent the measured data (*blue solid circles* for spin-up neutrons, *red open circles* for spin-down neutrons). The *solid lines* are fits to the data (see text). The *dashed line* marks the position of the total reflectivity edge at 0 mbar. Reprinted from [19] with permission from the American Physical Society

The hydrogen concentration in the multilayers can be calculated by using the parameters from Table 5.3 and applying Eq. (5.11). This is shown in Fig. 5.18. Obviously, the hydrogen solubility in the Nb films strongly differs from that in bulk Nb and is dependent on the film thickness. The plateau-like pressure region of the curves, at which most of the hydrogen is absorbed, is more than an order of magnitude higher compared to the bulk values.

The hydrogen concentration saturates for layers with large Nb thickness at one hydrogen atom per niobium atom, close to the corresponding value for bulk material. This is surprisingly high in view of the restricted possibility for the in-plane expansion of the Nb lattice. Films with thinner Nb layers ($d_{\text{Nb}} < 5.0\,\text{nm}$) show greatly reduced maximum hydrogen concentrations. It has been emphasized that short-range electron spill over may suppress hydrogen solubility in the vicinity of the interfaces [49] which might explain our data from thin Nb films. Our measurements, however, indicate that long-range mechanical interactions between the hydrogen absorbing Nb layers and adjacent non-absorbing Fe layers are also quite important for the hydrogen uptake process. Only long-range mechanical effects can be responsible for the vastly different plateau pressure positions of the 10 and 100 nm Nb films. In previous literature it has always been assumed that hydrogen absorption in thin films is comparable to the absorption process in largely defect-free bulk metals where the dominant mechanism is hydrogen occupation of interstitial lattice sites in the host metal resulting in lattice expansion. The main

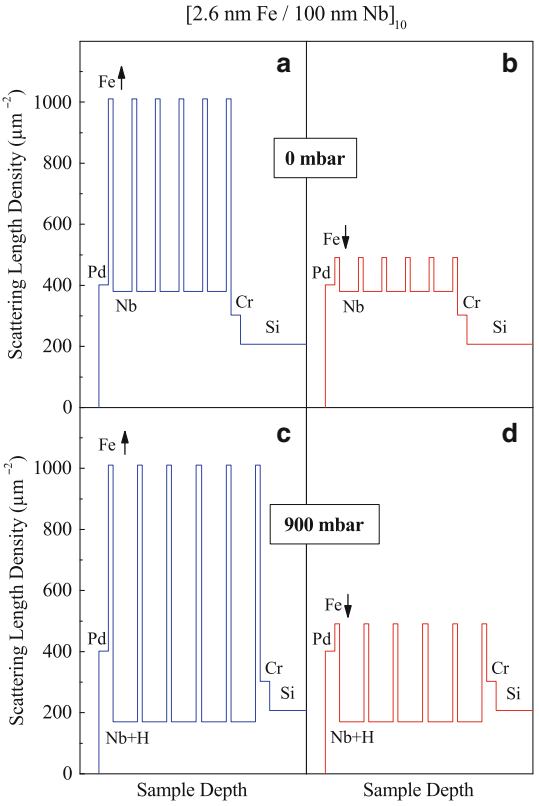

Fig. 5.17 SLD depth profiles for [2.6 nm Fe/100 nm Nb]$_{10}$ in the as-prepared state at 0 mbar for spin-up neutrons (**a**) and spin-down neutrons (**b**), and after charging at 900 mbar for spin-up neutrons (**c**) and spin-down neutrons (**d**). The profiles were constructed by analyzing the data of Fig. 5.16. The Nb depth coordinates are not drawn to scale. Reprinted from [19] with permission from the American Physical Society

Table 5.3 SLD and layer thickness (d_L) for the sample Si/5 nm Cr/[2.6 nm Fe/100 nm Nb]$_{10}$/5 nm Pd as determined from a fit to the data shown in Fig. 5.16

	SLD at 0 mbar (μm^{-2})	SLD at 900 mbar (μm^{-2})	Bulk-SLD (μm^{-2})	d_L at 0 mbar (nm)	d_L at 900 mbar (nm)
Pd	402	402	402	5	5
Nb	380	170	392	93.6	103.5
Fe^+	1010	1030	1300	2.6	2.6
Fe^-	490	570	303	2.6	2.6
Cr	303	303	303	5	5
Si	207	207	207		

difference between thin films and bulk materials with respect to hydrogen-induced structural changes was thought to be the predominantly one-dimensional lattice expansion out of the plane of the films, caused by the adhesion of the film to the substrate, in contrast to the three-dimensional lattice expansion of bulk materials [50]. Our studies of the Nb thin film series reveal a second, unexpected hydrogen absorption mechanism which seems to be of equal importance to the hydrogen absorption on interstitial sites. Analyzing scattering data of the in-situ

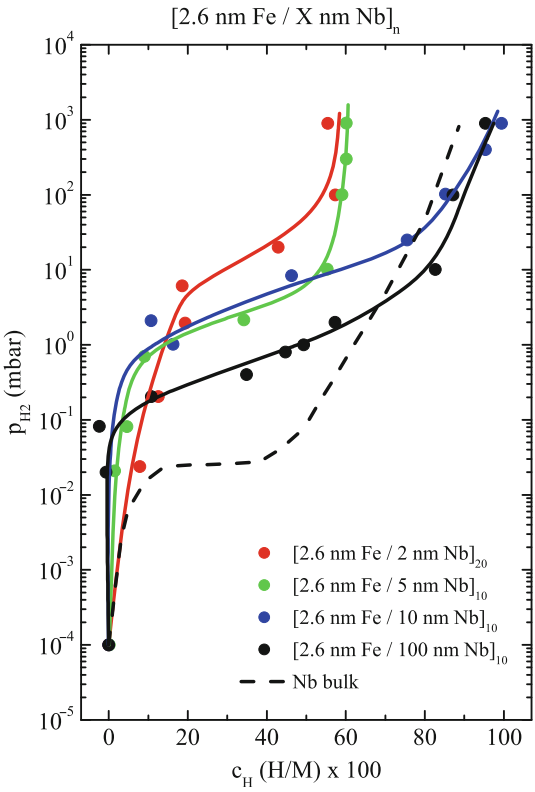

Fig. 5.18 Hydrogen solubility curves of polycrystalline [2.6 nm Fe/d_{Nb}]$_n$ multilayers. Reprinted from [48] with permission from Elsevier

hydrogen loaded multilayers, we found a remarkable result as displayed in Fig. 5.19. There is a vast difference between the hydrogen-induced out-of-plane lattice expansion (determined by in-situ XRD in the high-angle regime) and the expansion of the Nb layer thickness (determined by XRR and NR measurements). For all investigated films, the relative increase at the macroscopic level of the Nb layer thickness is much larger than the relative increase at the microscopic level of the interplanar spacing. The details, however, depend on the actual thickness of the Nb layers. For the thinnest Nb film investigated ($d_{Nb} = 2$ nm), the interplanar lattice spacing increase upon hydrogen loading is very small (< 0.4 %) which indicates low hydrogen solubility at interstitial sites. In contrast, this sample shows a remarkable 7 % increase of its overall film thickness under the same maximum 900 mbar hydrogen pressure. The situation changes as the Nb thickness is increased. The 10 nm and 100 nm Nb film shows ≈ 4.5 % lattice expansion and an unusually high overall film thickness expansion of ≈ 11 %. This clearly demonstrates that, besides the well-known process of absorption at interstitial sites which entails expansion of the atomic lattice planes, there is an additional hydrogen absorption mechanism at work which leads to a large macroscopic swelling of the Nb film.

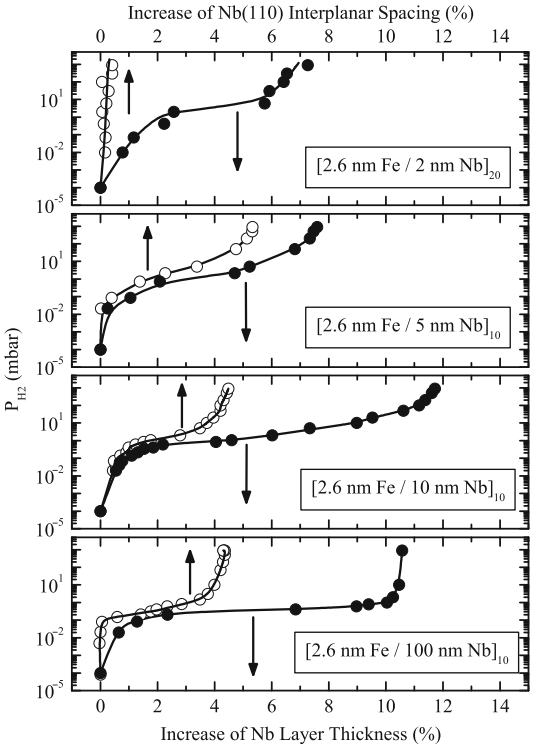

Fig. 5.19 Comparison between hydrogen-induced relative increase of the out-of-plane Nb(110) interplanar spacing (*open circles*) and increase of Nb layer thickness (*solid circles*) in Fe/Nb multilayers for various hydrogen pressures. Reprinted from [51] with permission from Elsevier

The reversibility of repeated hydrogen loading cycles has been studied by conventional X-ray scattering for the case of the [2.6 nm Fe/10 nm Nb]$_{10}$ multilayer. Figure 5.20 shows a comparison of the hydrogen-induced macroscopic Nb layer expansion (measured by NR) and the microscopic expansion of the Nb(110) lattice planes (measured by high-angle X-ray diffraction). The displayed data sets represent changes in the out-of-plane direction, measured during the first three and the sixth charging cycles. Data are presented only for the increasing branches of the cycles. The de-charging branch has been monitored too and was assumed to be completed when constant values for the Nb layer thickness and Nb lattice spacing were approached (typically after 12 h). In the as-prepared state, the Nb layer thickness was determined to be 8.95 nm and increased finally to 10.0 nm when $P_{H2} = 900$ mbar was applied. This corresponds to an enormous relative increase of 11.7 % during the first charging. The removal of the hydrogen gas in the loading chamber resulted in a reduction of the layer thickness to 9.38 nm. The subsequent charging cycles are reversible and show relative thickness increases of only 6.7 %. Note that in all cycles the same maximum thickness of 10.0 nm is reached. The Nb lattice spacing shows just the reverse behavior. In this case the expansion during the first hydrogen loading was small. The lattice spacing $d_{Nb(110)}$ increased only by 4.4 %, from 0.2385 nm to 0.2485 nm. De-charging the film resulted in $d_{Nb(110)} =$ 0. 2320 nm. Note that this value is now considerably closer to the Nb(110) bulk

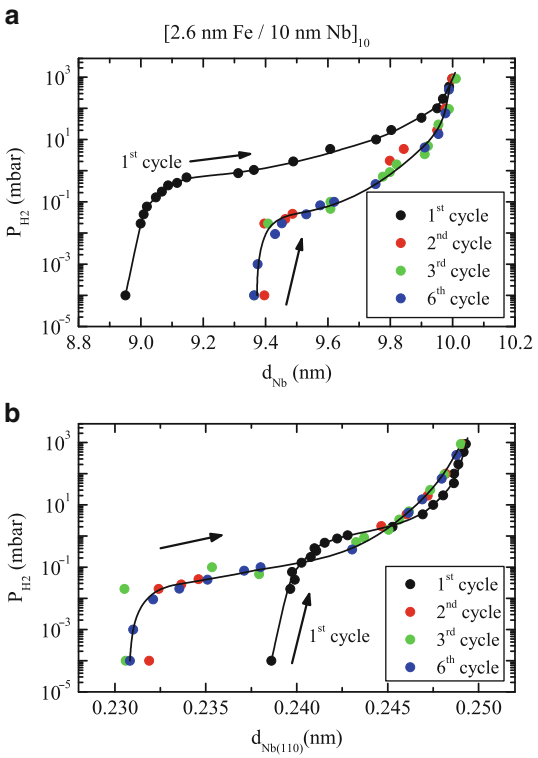

Fig. 5.20 (**a**) Expansion of Nb layer thickness d_{Nb} upon repeated hydrogen charging and decharging, and (**b**) corresponding expansion of Nb(110) lattice planes $d_{Nb(110)}$ in a [2.6 nm Fe/10 nm Nb]$_{10}$ multilayer. Reprinted from [46] with permission from the American Physical Society

value of 0.2333 nm, which demonstrates the effect of hydrogen-induced annealing. The subsequent loadings are again reversible with relative increases of around 7 %. The vast difference between macroscopic and microscopic expansion of Nb during the initial hydrogen loading indicates that a relaxation process takes place which must be a one-time process since in the second and subsequent loading cycles, the relative layer and lattice expansions are almost equal.

5.6.3 W/Nb Multilayers

Experiments on epitaxial W/Nb multilayers exhibit very similar general features [45, 46]. However, the first hydrogen loading of the corresponding W/Nb superlattice shows, compared to the polycrystalline sample, an even more dramatic behavior, since based on our XRD data, the initially well-ordered epitaxial Nb layers break down into much smaller domains. For the epitaxial film, in addition to in-situ studies using NR and XRD, we also employed in-situ extended X-ray absorption fine structure (EXAFS) measurements [45]. From this method one obtains selective information about structural changes occurring perpendicular to

the layer and within the layer by measuring at grazing and normal incidence geometries, respectively. For the (001) oriented epitaxial [2.6 nm W/10 nm Nb]$_{60}$ multilayer, EXAFS allowed one to determine the out-of-plane distance between next-nearest Nb neighbors, as well as the corresponding in-plane values. The experiments confirm the out-of-plane expansion of 6.2 % at 900 mbar obtained by XRD. However, more importantly, they also reveal a small 2.5 % in-plane expansion of the Nb lattice under hydrogen absorption. The in-plane expansion of 2.5 % and the corresponding out-of-plane lattice expansion of 6.2 % result in a total increase in volume of 11.5 %. This amount coincides with the relative increase of the Nb layer thickness expansion of 11.1 % as determined from reflectivity experiments. Hence, one only has to take into account the boundary condition of a fixed in-plane area (i.e., a one-dimensional degree of freedom to expand macroscopically in the out-of-plane direction) in order to explain quantitatively the results shown in Fig. 5.19. This model implies a three-dimensional rearrangement of Nb atoms caused by the massive mechanical lateral strain and its relaxation with increasing hydrogen charging within the Nb layers, especially near the interfaces to the substrate and the unloaded Fe or W layers. As a result, individual Nb atoms are squeezed out of existing lattice planes and start to form additional planes, which finally causes the anomalous large expansion of the layer thickness. Note that the newly created partial lattice planes imply a large amount of additional dislocations. The latter are evidenced by the fact that the out-of-plane X-ray diffraction peaks broaden significantly upon hydrogen absorption. For [2.6 nm W/10 nm Nb]$_{60}$, for example, we find a decrease in coherence length in growth direction from 9.0 nm after preparation to 5.5 nm after hydrogen absorption at 900 mbar. Since lattice imperfections effectively trap hydrogen atoms, the new effect likely also explains the extraordinarily high hydrogen concentrations found in our Nb films and the partial non-reversibility of the hydrogen absorption process itself.

5.6.4 Conclusion

In summary, our combined study of hydrogen absorption in thin Nb films by X-ray, neutron, and synchrotron methods clearly indicate that the commonly accepted model of the hydrogen absorption process in thin films requires a revision. We have investigated repeated hydrogen charging of Nb-containing multilayers and found an anomalously large macroscopic expansion of the Nb layers during the initial loading of the films. In spite of their different structures (polycrystalline in the case of Fe/Nb and epitaxial in the case of W/Nb), the two multilayer systems essentially show the same behavior. This process is explained as a mechanical response of the Nb lattice to the enormous stress that acts on the films during hydrogen uptake. Our results emphasize the importance of geometrical constraints and give new important insights into the hydrogen absorption process in thin films. These findings need to be taken into account in the experimental determination of hydrogen concentration in thin films.

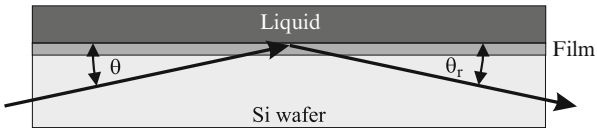

Fig. 5.21 Scattering geometry of a typical reflectometry experiment for samples facing a liquid

5.7 In-Situ Electrochemical Measurements

Neutron Reflectometry is a uniquely powerful tool for studying electrodes and electrochemical reactions. The large penetration of neutrons makes it possible to perform NR measurements in two geometries: in air (see Fig. 5.1) and with the sample facing a liquid (shown in Fig. 5.21). In the liquid geometry the neutron beams (incident and reflected) need to traverse through bulk Si, but the loss of intensity through even a large substrate (100 mm in diameter) is only of the order of 15–20 %. The advantage of this geometry is the free space on the side away from the Si substrate, available for another experiment to be conducted simultaneously with NR. This opportunity has led to combining NR with a number of other techniques. In this article we describe two examples where NR was combined with electro-impedance spectroscopy (EIS). Both examples demonstrate the advantage of probing a single sample by two techniques in-situ. The experimental setup has been described by Tun et al. elsewhere [4].

5.7.1 Zr Thin Films

In this section we describe the anodic oxide growth on a thin Zr film as studied with NR and EIS [52]. The experiment started with NR measurements on the as-prepared thin film to establish the baseline against which all changes are quantified. The next set of measurements were performed with the sample being exposed to a 0.1 mol/L Na_2SO_4 aqueous solution with the cell remaining open-circuit [$E_{OC} = -0.17$ V against saturated calomel electrode (SCE)]. At that stage, compared to the as-prepared sample, the oxide layer showed no change. Significant changes to the oxide layer happened only when an anodic potential was applied in steps of 0.5 V. Figure 5.22 shows anodic growth of the oxide and the thinning of the metal layer. Each NR scan took ≈ 6 h during which the applied potential was held fixed. Since electrochemical reactions take time, it was necessary to give the sample time to come to a steady-state after each potential setting. To check whether the sample had reached its equilibrium state, i.e. whether the NR curve did not change anymore, NR scans were repeated at the same voltage at least twice, and three times at 1.5, 2.0, and 2.5 V_{SCE} settings. To represent the time sequence of the runs, symbols in Fig. 5.22 are encoded as triangles, squares, and solid circles. The triangles correspond to the scan started immediately after setting the potential (first 6 h), the squares to the second scan (6–12 h), and the third scan (12–18 h if carried out) is

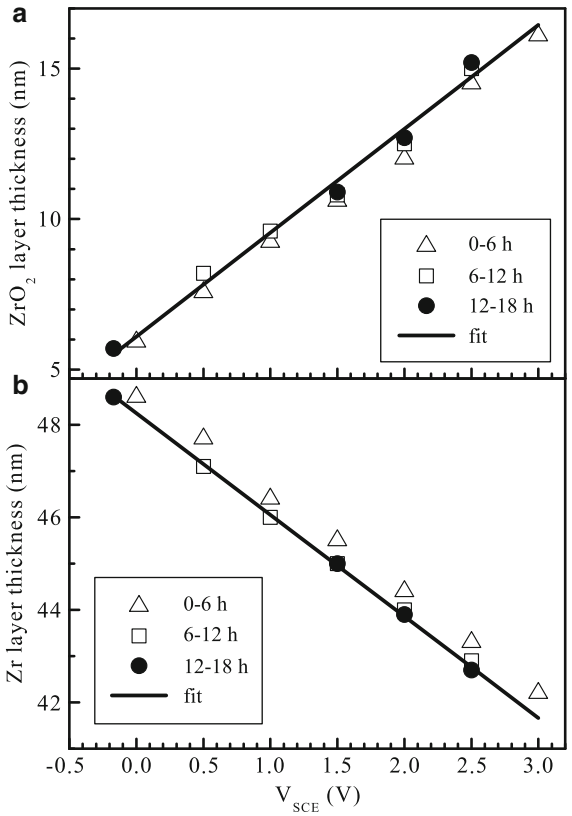

Fig. 5.22 Anodic growth of the ZrO_2 layer (**a**) at the expense of the Zr metal (**b**)

represented by solid circles. A significant difference between the first and second run is not a surprise but the second and third are expected to lie close to each other. The results displayed in Fig. 5.22 meet this expectation but one may question if the squares and circles are close enough. A closer inspection reveals that whenever there are three symbols, the square is always in the middle. This is strong evidence that the small difference between the second and third run is real. Noël et al. [52] concluded that the ionic transport required for forming anodic oxide persists many hours after setting the potential. Furthermore, the authors claim that theirs is "probably the first direct observation of long-time anodic oxide thickening, with the implication that residual current should not always be labeled as electronic or a sign of surface dissolution" [52].

Another important result from Fig. 5.22 is the possibility of least-squares fitting a straight line to all the long-time limit data (circles). This opens up the possibility to determine the anodization ratio [53], i.e. the ratio of the thickness of an anodic oxide film to the applied potential difference required to grow the oxide and maintain its thickness, as well as the Pilling–Bedworth ratio [54], defined as the ratio of the volume occupied by an oxide to the volume of metal consumed in its production. The values for the anodization ratio and the Pilling–Bedworth ratio

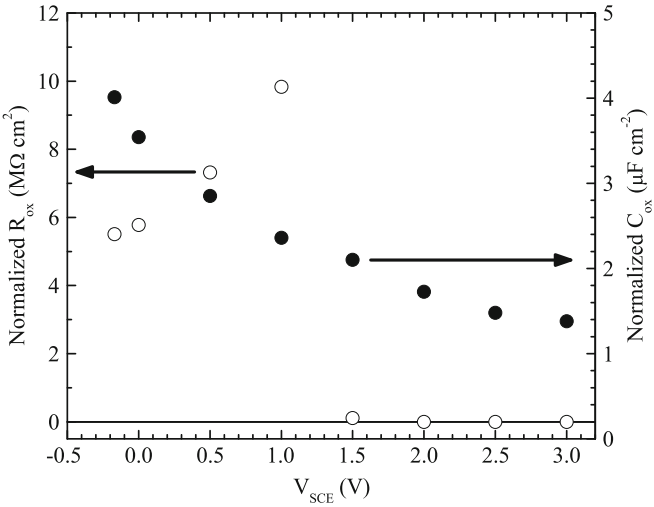

Fig. 5.23 Resistance (*solid circles*) and capacitance (*open circles*) across the oxide layer determined by fitting an equivalent circuit to the EIS data. Note that capacitance is nearly oblivious to the stepwise change at 1.5 V_{SCE}

deduced from these straight lines are in good agreement with the literature values for bulk Zr electrodes. However, there lies a problem: it is well known that bulk Zr electrodes suffer anodic breakdown at ≈ 1 V_{SCE}, and not seeing any sign of discontinuity well before reaching 3 V_{SCE} is a puzzle. For Noël et al. it was very tempting to state that thin films behave differently from bulk electrodes. Preventing them from drawing this "obvious" conclusion was the fact that EIS did detect the anodic breakdown by observing R_{ox}, the (almost DC) resistance of the oxide layer, dropping abruptly between 1 and 1.5 V_{SCE}. This important result is shown in Fig. 5.23.

The layer SLDs yielded additional results. Figure 5.24 shows the decrease of the oxide SLD as the anodization proceeded. Noël et al. concluded that the decrease up to 1 V_{SCE} was purely due to incorporation of OH species in the oxide. Although OH ions have a positive scattering length, its incorporation often leads to lowering of the overall SLD. This has been demonstrated for an anodized Ti film where the presence of H in the TiO_2 layer was independently confirmed by XPS [4]. The abrupt change at 1.5 V_{SCE} is interpreted as time-delayed cracking of the oxide, causing additional decrease of SLD as the cracks were filled with H_2O. The EIS data, which show a sudden drop of resistivity at 1.5 V_{SCE}, are consistent with this interpretation.

A reader may say that EIS measurements are not necessary after all since NR alone, through the variation of oxide SLD, revealed the breakdown at 1.5 V_{SCE}. The counter argument comes from a mystery Noël et al. encountered and remains unsolved to this day: the SLD of the Zr metal layer jumped to a very high value

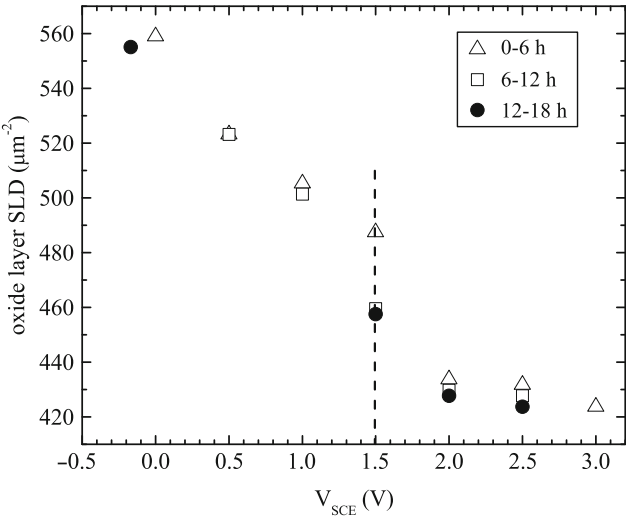

Fig. 5.24 Oxide layer cracking seen as a delayed response of the layer SLD at 1.5 V

(unphysical for chemically pure Zr) when the sample was exposed to the electrolyte and leaving the cell open-circuit. Consequently, Noël et al. treated the SLD values as somewhat unreliable. A single high point in Fig. 5.24 would have been ignored without knowing the EIS data.

5.7.2 Ti Thin Films

In this section we report on the absorption of hydrogen into a Ti thin-film through a passive oxide layer [55]. The experiment started with the characterization of the as-prepared sample in air. Then the sample was exposed to an aqueous electrolyte while initially leaving the cell open-circuit, and finally a potential was applied. The potentials applied were in steps, starting at 0.00 V_{SCE} followed by -0.25, -0.30, -0.40, -0.45, -0.50, -0.55, -0.60, -0.65, and -0.70 V_{SCE}, in that sequence. The first setting, 0.00 V_{SCE}, was so close to the open-circuit potential of the cell that small cell currents were observed both in cathodic and anodic directions during the NR scan. The aqueous solution was prepared with D_2O, not H_2O. Ti is one of the few metals with negative SLD whereas D or D-containing ions have very high positive scattering length. This sign difference makes the ingress of D into Ti, signalled by the increase of the layer SLD, highly "visible" to neutrons. The price paid is that the rise of SLD from the Ti film to the D_2O is so large that the TiO_2 layer is completely hidden in one big sigmoidal step between the metal and the bulk electrolyte. See Fig. 5.25 to fully appreciate this trade-off.

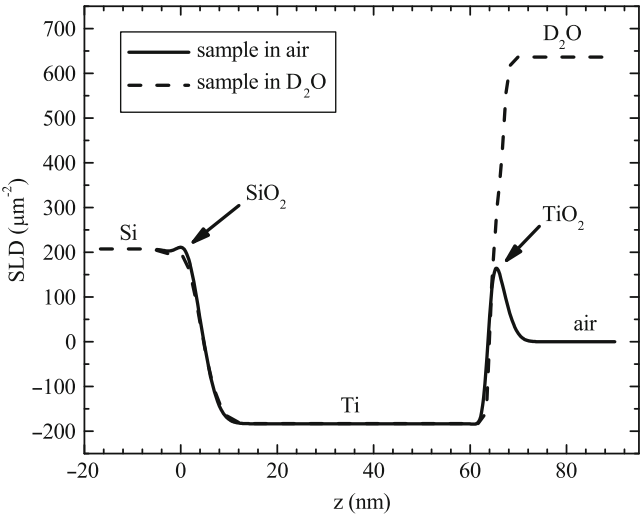

Fig. 5.25 SLD profile in air (*solid line*) and in D_2O (*dashed line*)

Applying increasingly more negative potentials caused changes primarily to the Ti layer: the layer SLD increased monotonically while thickening very slightly beyond $-0.60\ V_{SCE}$. The SLD values plotted in Fig. 5.26 reveal that the cathodic behavior of Ti can be described in terms of four groups of observations (note: when plotting cathodic potentials, the x-axis of the graph starts from the right). These groups are corroborated also by the EIS data [55]. The boundary between group 1 and 2 lies somewhere between -0.3 and $-0.4\,V$, and $-0.6\,V$ is the onset of group 4. Qualitatively different behaviors manifested by a single sample (no arguing of sample-to-sample variation) enabled Vezvaie et al. to reconcile seemingly conflicting literature reports of two key potentials, $-0.37\ V_{SCE}$ [56] and $-0.6\ V_{SCE}$ [57], important in the behavior of a thin-film Ti electrode under cathodic polarization. At the first potential, significant changes in current density, oxide resistivity and capacitance, and the SLD of the Ti were observed. These changes can be attributed to the onset of local oxide conductivity and the underpotential deposition of surface-adsorbed D atoms on the electrode and their entry into the metal through conductive, defective pathways in the oxide. At the second potential, $-0.6\ V_{SCE}$, a marked increase in current density and the D content in the Ti film were observed. This more negative potential is recognized as where the protective oxide becomes ineffective as a barrier by reducing it from the original TiO_2 to TiOOH [57]. It is the threshold for general hydrogen uptake, which leads to significant hydrogen absorption and embrittlement of industrial Ti structures at potentials negative of $-1\ V_{SCE}$. The former potential, $-0.37\ V_{SCE}$, has not previously been generally recognized as a hydrogen ingress threshold in bulk Ti materials, possibly because it does not lead to hydrogen uptake that is sufficient to affect bulk Ti materials.

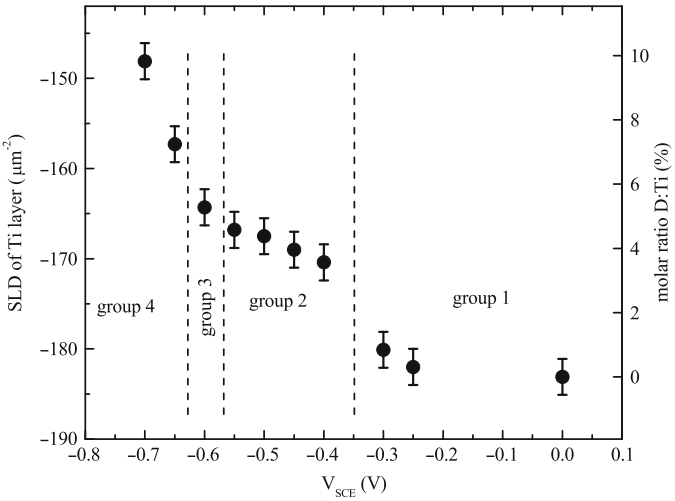

Fig. 5.26 The increase of Ti layer SLD under cathodic potential

5.8 Exchange-Coupled Multilayers

5.8.1 Introduction

Oscillating ferromagnetic (FM)/antiferromagnetic (AFM) exchange coupling in thin film metal structures [58] and the related giant magnetoresistance (GMR) effect [59, 60] have revolutionized the data storage industry in the late 1990s as the GMR effect can be used in field sensors of hard disk drives to read magnetically stored information with unprecedented sensitivity allowing data to be stored in ever smaller magnetic bits. For their discovery of the GMR effect Peter Grünberg and Albert Fert were rewarded the Nobel prize in physics in 2007.

Widely accepted theories for explaining the oscillating magnetic exchange coupling are Ruderman–Kittel–Kasuya–Yosida (RKKY)-like models [61] and models based on quantum interferences in the spacer layer electron system [62]. Both theories conclude that the exchange energy J, which is responsible for the sign of the coupling, oscillates approximately as

$$J \propto \frac{1}{(2\,k_\mathrm{F}\,d_\mathrm{s})^2}\sin\left(2\,k_\mathrm{F}\,d_\mathrm{s}\right) \tag{5.19}$$

where d_s is the thickness of the nonmagnetic spacer layer and k_F the effective (crystallographic orientation dependent) Fermi wave vector of the spacer layer.

For some technical applications it may be highly desirable to actively control the exchange coupling between FM layers, i.e. to be able to tune the strength and the character of this important magnetic interaction. This should be feasible, according

to the above equation, by either changing the spacer layer thickness or by manipulating the relevant Fermi wave vector. While the dependence on d_s has been studied in numerous FM/nonmagnetic thin film combinations, only very few papers exist in the literature dealing with a systematic manipulation of the Fermi wave vector. An example for the change of the Fermi vector is the Fe/V_xCr_{1-x} system in which V and Cr form a solid solution over the entire composition range. It has been shown experimentally and theoretically that by changing the electron concentration of the spacer layer by alloying, the period as well as the amplitude of the coupling energy can be altered [63]. This is, however, a static approach, i.e. the exchange coupling is set by choosing a particular alloy composition.

5.8.2 *Fe/Nb Multilayers*

An intriguing possibility for manipulating the magnetic interaction between exchange coupled FM layers is to introduce hydrogen into a hydrogen-affine spacer layer, thereby changing its electronic properties, including its Fermi wave vector k_F. Hydrogen absorption turned out to continuously and reversibly change the magnetic exchange coupling between iron layers separated by niobium spacer layers within one and the same Fe/Nb multilayer structure [6]. In this study it was demonstrated that hydrogen absorption can result in a complete reversal (i.e., change of sign) of the magnetic coupling. Fe/Nb multilayers were chosen for these experiments because oscillating FM/AFM coupling had been positively identified before [64] and Nb, as the spacer layer, has a high solubility for hydrogen. The tuning of the exchange coupling with hydrogen was also achieved in Fe/La multilayers [65] and Fe/V superlattices [7] which is described in detail in Sect. 5.8.3.

Figure 5.27 shows neutron reflectivity data of the as-prepared (uncharged) Fe/Nb multilayers, each with constant Fe thickness of 2.6 nm but with four different Nb thicknesses (the Nb layers are strongly (110) textured). These different structural (chemical) periodicities result in structural Bragg peaks as indicated in the figure. The samples were measured in their as-prepared state without applying an external magnetic field because, due to the relatively small coupling strength in the Fe/Nb system, even small magnetic fields would possibly have affected the measurements. Therefore, unpolarized neutrons were chosen which made the use of a magnetic guide field unnecessary. The data clearly demonstrate that the magnetic coupling oscillates in sign as function of the Nb thickness as, with increasing Nb layer thickness, an extra half-order peak resulting from coherent AFM coupling of neighboring Fe layers is visible only for $d_{Nb} = 1.5$ nm and $d_{Nb} = 2.4$ nm, but not for $d_{Nb} = 0.8$ nm and $d_{Nb} = 1.8$ nm. In the latter cases, intensity from ferromagnetically coupled Fe layers add to the intensities of the structural Bragg peaks. From analyzing the width of the AFM peak, we find for $d_{Nb} = 1.5$ nm that the AFM coherence in the direction normal to the layers spans over 90–95 % of the total multilayer thickness.

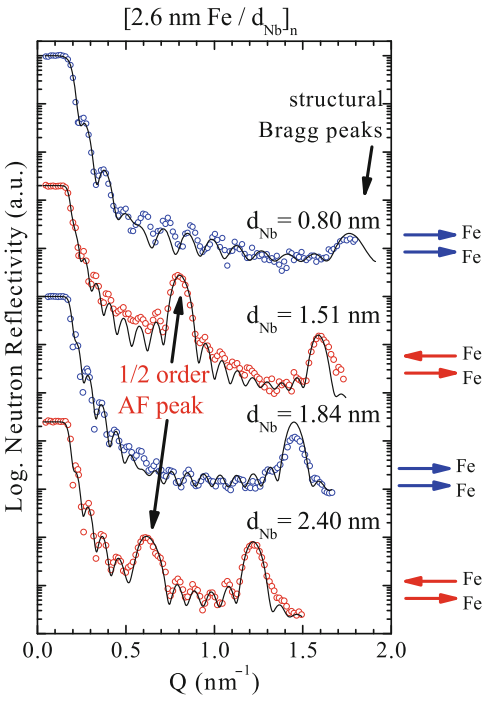

Fig. 5.27 Neutron reflectivity of [2.6 nm Fe/d_{Nb}]$_n$ multilayers measured in the as-prepared state in "zero" external magnetic field. From the intensities of the AFM peaks, maxima of antiparallel coupling of the Fe layers can be inferred at $d_{Nb} = 1.51$ nm and $d_{Nb} = 2.40$ nm, respectively. The *solid lines* are fits to the data

Similarly as in the before presented in-situ hydrogen absorption experiments, the Fe/Nb multilayers were charged with hydrogen from the gas phase in a vacuum chamber around the sample position of the neutron reflectometer at a temperature of 473 K. As before, the hydrogen concentration in the Nb layers is a function of the external hydrogen pressure. This allowed an in-situ observation of changes of the magnetic coupling during the hydrogenation. Figure 5.28 shows the development of the intensity of the AFM half-order peak for the [2.6 nm Fe/1.5 nm Nb]$_{18}$ multilayer upon hydrogen absorption. It can be seen that the AFM peak intensity (and therefore the AFM coupling of the Fe layers) is strongly suppressed with increasing hydrogen content in the Nb layers indicating that FM coupling starts to dominate. At the maximum external hydrogen pressure of 900 mbar, $c_H = 0.25$ is achieved for the sample with $d_{Nb} = 1.5$ nm. The data also show that this effect is completely reversible (although with a strong hysteresis effect) upon lowering the hydrogen concentration in the Nb layers by evacuation of the hydrogen in the loading chamber. The hysteresis in Fig. 5.28 between the charging and de-charging branch is due to a remanence of the magnetic ordering and not to a nonequilibrium hydrogen concentration since the hydrogen uptake (as monitored by in-situ electrical resistivity measurements) is fast and shows no hysteresis. Since the increase of the spacer layer thickness (estimated from the shift of the Fe/Nb bilayer Bragg peak of the 1.5 nm Nb sample) is only approximately 0.05 nm at 900 mbar, i.e., much less than half an oscillation (0.45 nm) of the sinusoidal coupling energy, the expansion

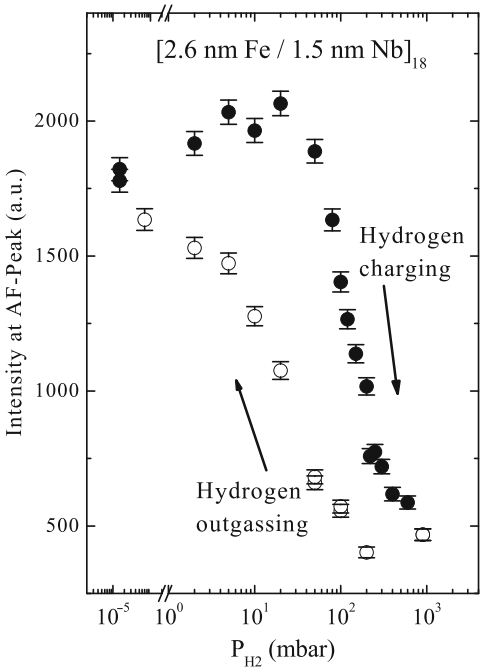

Fig. 5.28 Intensity of the AFM Bragg peak at $Q \approx 0.8\,\mathrm{nm}^{-1}$ of the $[2.6\,\mathrm{nm\ Fe}/1.5\,\mathrm{nm\ Nb}]_{18}$ multilayer as a function of the external hydrogen pressure for the second charging cycle. *Full circles* correspond to increasing, *open circles* to decreasing hydrogen pressure. Note the break in the scale of the abscissa. Reprinted from [6] with permission from the American Physical Society

of the spacer layer cannot be the cause of the sign reversion of the coupling. Therefore, according to the above formula for the exchange energy J, the Fermi wave vector must have been changed, i.e. k_F must have become either larger or smaller. As argued in [6], a decrease of k_F of the Nb spacer layer by approximately 15 % upon hydrogen charging would be able to explain the change from AFM to FM coupling.

Although our interpretation of the experimental results is conceptually simple, Fermi surfaces of transition metals and their change upon hydrogen uptake are complex which makes the detailed understanding far from trivial. Challenged by this, Li and Chou theoretically studied the effect of hydrogen absorption on the magnetic exchange coupling in Fe/Nb multilayers using first-principles electronic structure calculations [66]. In this work the authors systematically studied changes of the electronic band structure, total density of states and Fermi energy/wave vector as a function of hydrogen concentration in NbH_x for $0 \leq x \leq 1$. Their main conclusions are: (a) the Fermi wave vector in Nb(110) can be changed continuously upon hydrogen charging and (b) k_F is reduced compared to that of pure Nb metal at a hydrogen concentration of $c_H = 0.25$, which is in good qualitative agreement with our experimental results and interpretation.

5.8.3 *Fe/V Superlattices*

Fe/V(001) superlattices can be grown with a large structural perfection [20, 67] as illustrated in Fig. 5.29. The resulting samples can be viewed as high quality single crystals, with a close to atomic sharpness of the interfaces. The magnetic properties depend on both, the thickness of the V and the Fe layers, and an oscillatory exchange coupling is observed when changing the thickness of the V layer [68, 69]. The magnetic state of the layers is not uniform, involving reduction of the outermost Fe layers and an induced moment in V, which is antiferromagnetically aligned with respect to the adjacent Fe layers [70]. When hydrogen is absorbed in Fe-V superlattices it is known to reside exclusively in the V layers, with a hydrogen depleted layer in the proximity to the interfaces. The extension of the depleted region varies with hydrogen concentration, from 3 atomic layers at low concentrations to about 1–2 monolayers at intermediate and high concentrations [71]. Significant finite size effects are observed in the absorption [71] of hydrogen in Fe/V superlattices. The biaxial strain state of the V also affects the hydrogen absorption substantially, resulting in a preferred octahedral z-site occupancy, resulting in hydrogen-induced expansion of the V layers [20, 21].

The effect of hydrogen on the interlayer exchange coupling in Fe/V(001) superlattices was performed on samples with V thicknesses around the first AFM resonance [7]. This makes it possible to distinguish between changes in the interlayer distance and changes in the electronic structure, because when the

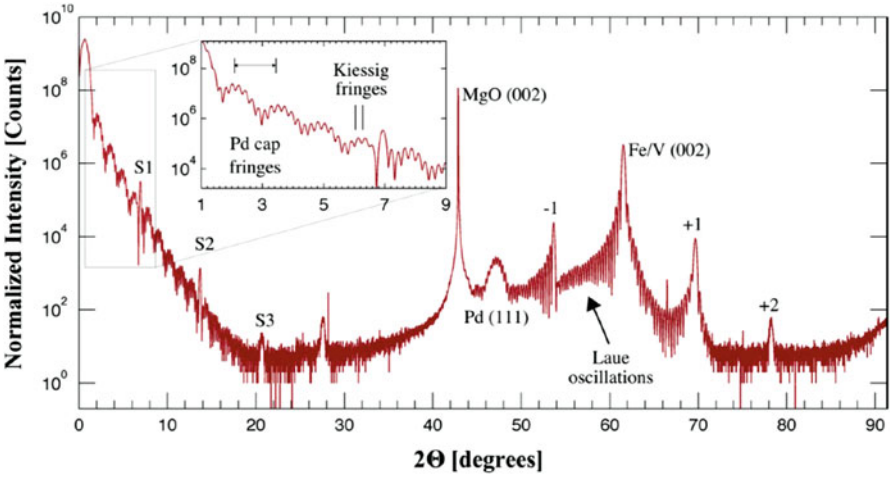

Fig. 5.29 X-ray scattering results from a Fe/V superlattice consisting of 1 monolayer of Fe and 7 monolayers of V. All length scales are observed in the graph, from the Kiessig fringes from the total thickness oscillations to the Bragg peak of the average lattice parameter from the SL. Clear Laue oscillations are also observed between the (002) peak and the diffraction satellites. Reprinted from Pálsson et al. [20] with permission from the American Physical Society

thickness of the V layer is just above the AFM region, the expansion of the layer cannot drive the magnetic state from FM to AFM. A clear transition from FM to AFM state was observed, which proved the importance of the changes in the electronic structure. This was further supported by measurements with V thicknesses at the lower side of the AFM resonance. If the changes in the distance between the Fe layers were the source of the changes in the magnetic state, the AFM coupling should be increased under these conditions. The opposite trend was observed, namely, the weakly coupled AFM aligned Fe layers became ferromagnetically coupled. The changes in the electronic structure were thereby determined to be the main reason for the changes in the interlayer exchange coupling.

The introduction of hydrogen in Fe/V(001) superlattices does not only affect the interlayer coupling, significant changes in the resulting magnetic moment was also observed [72, 73]. These observations were later supported by theoretical calculations [74], emphasizing the influence of interface hybridization on the magnetic properties of extremely thin magnetic layers.

Later, the hydrogen-induced changes in the interlayer coupling were used to affect the magnetic properties of samples, allowing the investigation of the influence of interlayer exchange coupling on the dimensionality of the magnetic phase transitions. These experiments were performed using neutron reflectivity [75] as well as magneto-optical techniques [76]. The results clearly proved not only the effect of interlayer exchange coupling, they also highlighted the effect of boundaries on phase transitions in finite systems. The use of hydrogen to affect the interlayer coupling had thereby taken the step from being a scientific curiosity to become a useful tool to tailor the magnetic properties of nano-magnetic systems. The role of neutron reflectivity in the progress must be considered as essential, as NR experiments provided the proof of the existence of the AFM structures in the first place and later allowed unambiguous determination of the hydrogen induced switching of the magnetic state in both Nb/Fe multilayers and Fe/V superlattices.

References

1. J. Penfold, R.K. Thomas, J. Phys. Condens. Matter **2**, 1369 (1990)
2. G. Decher, Science **277**, 1232 (1997)
3. R. Steitz, V. Leiner, R. Siebrecht, R.v. Klitzing, Colloids Surf. A Physicochem. Eng. Asp. **163**, 63 (2000)
4. Z. Tun, J.J. Noël, D.W. Shoesmith, J. Electrochem. Soc. **146**, 988 (1999)
5. K.G. Yager, O.M. Tanchak, C. Godbout, H. Fritzsche, C.J. Barrett, Macromolecules **39**, 9311 (2006)
6. F. Klose, C. Rehm, D. Nagengast, H. Maletta, A. Weidinger, Phys. Rev. Lett. **78**, 1150 (1997)
7. B. Hjörvarsson, J.A. Dura, P. Isberg, T. Watanabe, T.J. Udovic, G. Andersson, C.F. Majkrzak, Phys. Rev. Lett. **79**, 901 (1997)
8. L.G. Parratt, Phys. Rev. **95**, 359 (1954)
9. C.F. Majkrzak, N.F. Berk, Phys. Rev. B **52**, 10827 (1995)
10. H. Kiessig, Ann. Phys. **402**, 769 (1931)
11. T.P. Russell, Mater. Sci. Rep. **5**, 171 (1990)

12. J.A.C. Bland, Polarized neutron reflection, in *Ultrathin Magnetic Structures I*, ed. by J.A.C. Bland, B. Heinrich (Springer, Berlin, 1994), pp. 305–343
13. H. Fritzsche, Neutron reflectometry, in *Characterization of Materials*, ed. by E.N. Kaufman (Wiley, New York, 2012)
14. T. Krist, C. Pappas, T. Keller, F. Mezei, Physica B **213–214**, 939 (1995)
15. H. Fritzsche, Rev. Sci. Instrum. **76**, 115104 (2005)
16. W.C. Chen, T.R. Gentile, C.B. Fu, S. Watson, G.L. Jones, J.W. McIver, D.R. Rich, J. Phys. Conf. Ser. **294**, 012003 (2011)
17. M. Saoudi, H. Fritzsche, G.J. Nieuwenhuys, M.B.S. Hesselberth, Phys. Rev. Lett. **100**, 057204 (2008)
18. B.J. Kirby, J.A. Borchers, J.J. Rhyne, S.G.E. te Velthuis, A. Hoffmann, K.V. O'Donovan, T. Wojtowicz, X. Liu, W.L. Lim, J.K. Furdyna, Phys. Rev. B **69**, 081307(R) (2004)
19. C. Rehm, H. Fritzsche, H. Maletta, F. Klose, Phys. Rev. B **59**, 3142 (1999)
20. G.K. Pálsson, A.R. Rennie, B. Hjörvarsson, Phys. Rev. B **78**, 104118 (2008)
21. G.K. Pálsson, V. Kapaklis, J.A. Dura, J. Jacob, S. Jayanetti, A.R. Rennie, B. Hjörvarsson, Phys. Rev. B **82**, 245424 (2010)
22. F. Mezei, Z. Phys. A **255**, 146 (1972)
23. T. Saerbeck, F. Klose, A.P. Le Brun, J. Füzi, A. Brule, A. Nelson, S.A. Holt, M. James, Rev. Sci. Instrum. **83**, 081301 (2012)
24. M. James, A. Nelson, S.A. Holt, T. Saerbeck, W.A. Hamilton, F. Klose, Nucl. Inst. Methods Phys. Res. A **632**, 112 (2011)
25. H. Zabel, in *Encyclopedia of Materials: Science and Technology*, ed. by R.W. Cahn, K.H.J. Buschow, M.C. Flemings, B. Ilschner, E.J. Kramer, S. Mahajan, P. Veyssière, 2nd edn. (Elsevier, Oxford, 2001) p. 9246
26. A. Baldi, M. Gonzalez-Silveira, V. Palmisano, B. Dam, R. Griessen, Phys. Rev. Lett. **102**, 226102 (2009)
27. J.N. Huiberts, R. Griessen, J.H. Rector, R.J. Wijngaarden, J.P. Dekker, D.G. de Groot, N.J. Koeman, Nature **380**, 231 (1996)
28. H. Fritzsche, M. Saoudi, J. Haagsma, C. Ophus, E. Luber, C.T. Harrower, D. Mitlin, Appl. Phys. Lett. **92**, 121917 (2008)
29. H. Fritzsche, E. Poirier, J. Haagsma, C. Ophus, E. Luber, C.T. Harrower, D. Mitlin, Can. J. Phys. **88**, 723 (2010)
30. M.A. Pick, J.W. Davenport, M. Strongin, G.J. Dienes, Phys. Rev. Lett. **43**, 286 (1979)
31. H. Fritzsche, M. Saoudi, J. Haagsma, C. Ophus, C.T. Harrower, D. Mitlin, Nucl. Inst. Methods Phys. Res. A **600**, 301 (2009)
32. H. Fritzsche, C. Ophus, C.T. Harrower, E. Luber, D. Mitlin, Appl. Phys. Lett. **94**, 241901 (2009)
33. M. Danaie, H. Fritzsche, P.W. Kalisvaart, X. Tan, D. Mitlin, G.A. Botton, J. Huot, Acta Materialia **90**, 259 (2015)
34. E. Poirier, C.T. Harrower, P. Kalisvaart, A. Bird, A. Teichert, D. Wallacher, N. Grimm, R. Steitz, D. Mitlin, H. Fritzsche, J. Alloys Compd. **509**, 5466 (2011)
35. W.P. Kalisvaart, C.T. Harrower, J. Haagsma, B. Zahiri, E.J. Luber, C. Ophus, E. Poirier, H. Fritzsche, D. Mitlin, Int. J. Hydrog. Energy **35**, 2091 (2010)
36. B. Zahiri, B.S. Amirkhiz, M. Danaie, D. Mitlin, Appl. Phys. Lett. **96**, 013108 (2010)
37. P. Kalisvaart, E. Luber, H. Fritzsche, D. Mitlin, Chem. Commun. **47**, 4294 (2011)
38. H. Fritzsche, W.P. Kalisvaart, B. Zahiri, R. Flacau, D. Mitlin, Int. J. Hydrog. Energy **37**, 3540 (2012)
39. J. Rydén, B. Hjörvarsson, T. Ericsson, E. Karlsson, A. Krozer, B. Kasemo, Z. Phys. Chem. **164**, 1259 (1989)
40. D.C. Ford, L.D. Cooley, D.N. Seidman, Supercond. Sci. Technol. **26**, 095002 (2013)
41. Y. Fukai, *The Metal-Hydrogen System: Basic Bulk Properties*. Springer Series in Materials Science (Springer, Berlin, 2005)
42. H. Zabel, H. Peisl, Acta Met. **28**, 589 (1980)
43. H. Zabel, H. Peisl, Phys. Stat. Sol. A **37**, K67 (1976)

44. A. Romanenko, C.J. Edwardson, P.G. Coleman, P.J. Simpson, Appl. Phys. Lett. **102**, 232601 (2013)
45. F. Klose, C. Rehm, M. Fieber-Erdmann, E. Holub-Krappe, H.J. Bleif, H. Sowers, R. Goyette, L. Tröger, H. Maletta, Physica B **283**, 184 (2000)
46. C. Rehm, H. Maletta, M. Fieber-Erdmann, E. Holub-Krappe, F. Klose, Phys. Rev. B **65**, 113404 (2002)
47. C. Braun, Software Parratt32 developed for BENSC, Hahn-Meitner-Institut, Berlin, Germany, 1999
48. H. Maletta, C. Rehm, F. Klose, M. Fieber-Erdmann, E. Holub-Krappe, J. Magn. Magn. Mater. **240**, 475 (2002)
49. B. Hjörvarsson, J. Rydén, E. Karlsson, J. Birch, J.E. Sundgren, Phys. Rev. B **43**, 6440 (1991)
50. G. Song, M. Geitz, A. Abromeit, H. Zabel, Phys. Rev. B **54**, 14093 (1996)
51. C. Rehm, H. Fritzsche, H. Maletta, F. Klose, Physica B **276–278**, 549 (2000)
52. J.J. Noël, D.W. Shoesmith, Z. Tun, J. Electrochem. Soc. **155**, C444 (2008)
53. R.M. Torresi, O.R. Camera, C.P. De Pauli, M.C. Giordano, Electrochim. Acta **32**, 1291 (1987)
54. N.B. Pilling, R.E. Bedworth, J. Inst. Met. **29**, 529 (1923)
55. M. Vezvaie, J.J. Noël, Z. Tun, D.W. Shoesmith, J. Electrochem. Soc. **160**, C414 (2013)
56. Y. Zeng, J.J. Noël, P.R. Norton, D.W. Shoesmith, J. Electroanalytical Chem. **649**, 277 (2010)
57. T. Ohtsuka, M. Masuda, N. Sato, J. Electrochem. Soc. **134**, 2406 (1987)
58. P. Grünberg, R. Schreiber, Y. Pang, M.B. Brodsky, H. Sowers, Phys. Rev. Lett. **57**, 2442 (1986)
59. M.N. Baibich, J.M. Broto, A. Fert, F.N. Van Dau, F. Petroff, P. Etienne, G. Creuzet, A. Friederich, J. Chazelas, Phys. Rev. Lett. **61**, 2472 (1988)
60. G. Binasch, P. Grünberg, F. Saurenbach, W. Zinn, Phys. Rev. B **39**, 4828 (1989)
61. W. Baltensperger, J.S. Helman, Appl. Phys. Lett. **57**, 2954 (1990)
62. P. Bruno, Europhys. Lett. **23**, 615 (1993)
63. M. van Schilfgaarde, F. Herman, S.S.P. Parkin, J. Kudrnovský, Phys. Rev. Lett. **74**, 4063 (1995)
64. C. Rehm, D. Nagengast, F. Klose, H. Maletta, A. Weidinger, Europhys. Lett. **38**, 61 (1997)
65. W. Lohstroh, F. Leuenberger, W. Felsch, H. Fritzsche, H. Maletta, J. Magn. Magn. Mater. **237**, 77 (2001)
66. C. Li, M.Y. Chou, in *Hydrogen at Surfaces and Interfaces*. Electrochemical Society Proceedings, vol. 2000–16 (2000)
67. P. Isberg, B. Hjörvarsson, R. Wäppling, E.B. Svedberg, L. Hultman, Vacuum **48**, 483 (1997)
68. P. Granberg, P. Isberg, E.B. Svedberg, B. Hjörvarsson, P. Nordblad, R. Wäppling, J. Magn. Magn. Mater. **186**, 154 (1998)
69. M. Ahlberg, E.T. Papaioannou, G. Nowak, B. Hjörvarsson, J. Magn. Magn. Mater. **341**, 142 (2013)
70. M.A. Tomaz, W.J. Antel Jr., W.L. O'Brien, G.R. Harp, J. Phys. Condens. Matter **9**, L179 (1997)
71. G. Andersson, B. Hjörvarsson, P. Isberg, Phys. Rev. B **55**, 1774 (1997)
72. D. Labergerie, K. Westerholt, H. Zabel, B. Hjörvarsson, J. Magn. Magn. Mater. **225**, 373 (2001)
73. A. Remhof, G. Nowak, H. Zabel, M. Björck, M. Pärnaste, B. Hjörvarsson, V. Uzdin, Europhys. Lett. **79**, 37003 (2007)
74. V. Uzdin, D. Labergerie, K. Westerholt, H. Zabel, B. Hjörvarsson, J. Magn. Magn. Mater. **240**, 481 (2002)
75. V. Leiner, K. Westerholt, A.M. Blixt, H. Zabel, B. Hjörvarsson, Phys. Rev. Lett. **91**, 037202 (2003)
76. M. Pärnaste, M. Marcellini, B. Hjörvarsson, J. Phys. Condens. Matter **17**, L477 (2005)

Chapter 6
Small Angle Neutron Scattering

Sabrina Sartori and Kenneth D. Knudsen

Abstract Recent progress on materials for hydrogen storage have pointed out that kinetics and thermodynamics can be modified by nano-confinement of hydrides in porous scaffolds. The investigation of the structural features of these particular systems is challenging with conventional methods, for instance due to the lack of peaks in the diffraction pattern. Small angle neutron scattering is suitable for studying porous systems containing hydrogen and it has been invaluable for the characterisation of the new hydride systems. This chapter presents the basic principles of the technique and gives examples of its application to the field of nano-confined materials for hydrogen storage.

Keywords SANS • Scattering vector • Elastic scattering • Scattering length density • Form factor • Structure factor • Guinier approximation • Porod law • Radius of gyration • Power law • Fractal dimension • Mass fractal • Surface fractal • Coherent scattering • Incoherent scattering • Indirect Fourier transform • Spacial correlation • Isotope labeling • Size distribution • Specific surface area • Beaucage fit • Hydrogen storage • Nano-sized hydrides • Porous scaffold • Infiltration • Borohydrides

6.1 Introduction

Small angle neutron scattering (SANS) is a non-destructive technique well suited to provide information on the size, shape and interaction of nanometer-sized objects. Whereas neutron diffraction is used to study the crystal structure of materials, SANS is a powerful tool to investigate structures larger than just atoms, such as

S. Sartori (✉)
Department of Physics, University of Oslo, Postboks 1048, Blindern, 0316 Oslo, Norway

Centre for Materials Science and Nanotechnology, University of Oslo,
Gaustadalleen 21, 0349 Oslo, Norway
e-mail: sabrina.sartori@fys.uio.no

K.D. Knudsen
Institute for Energy Technology, Instituttveien 18, 2007 Kjeller, Norway
e-mail: kenneth.knudsen@ife.no

H. Fritzsche et al. (eds.), *Neutron Scattering and Other Nuclear Techniques for Hydrogen in Materials*, Neutron Scattering Applications and Techniques,
DOI 10.1007/978-3-319-22792-4_6

macromolecules, porous and biological systems, aggregates of particles in a matrix, and particularly where the difference in scattering characteristics between hydrogen (H) and deuterium (D) can be utilised to highlight domains of specific interest in the compound under investigation. For the same reason SANS can be useful to investigate materials for hydrogen storage. The use of SANS for probing spatial inhomogeneity of the hydrogen concentration in metal hydrides or the lattice strain and dislocation during hydride phase formation, has been reviewed earlier and will not be considered in the present chapter [1]. Small angle neutron scattering has also been used to study the porosity of hydrogen adsorbents and their adsorption capability [1–4]. The purpose of this chapter is to illustrate the theory and the latest applications of SANS in a new field: nano-confined hydrides for hydrogen storage.

6.2 Principles of the Method

6.2.1 Scattering Vector

The scattering vector for a small angle scattering experiment is shown in Fig. 6.1. When an incoming planar neutron wave hits the nucleus of a material, a spherical wave is emitted. The scattering vector $\mathbf{Q}$ equals the difference between the propagation vectors of the scattered and incident radiations.

Scattering can occur with or without exchange of energy between the radiation and the sample. In other words the scattered radiation can have a different wavelength than the incident radiation (inelastic scattering) or it can have the same wavelength (elastic scattering). In the case of elastic scattering, the relation between the absolute values of the scattered and the incident propagation vectors can be expressed by $k_f = k_i = 2\pi/\lambda$, where λ is the wavelength of neutrons.

In a SANS experiment, only elastic scattering is considered and the scattered intensity is plotted as a function of the absolute value of scattering vector Q:

$$Q = |\mathbf{k}_f - \mathbf{k}_i| = \frac{4\pi}{\lambda}\sin\theta \tag{6.1}$$

It follows that the scale observed in a scattering experiment is inversely proportional to the wavelength.

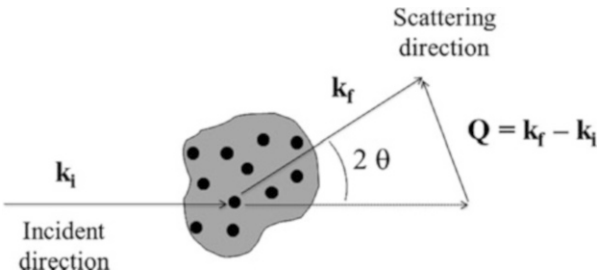

Fig. 6.1 Scattering vector of a SANS experiment at an angle 2θ

6.2.2 Interaction Radiation/Sample

The case of neutrons scattered by one atom can be illustrated as in Fig. 6.2. The incoming plane wave can be expressed as:

$$a(\mathbf{r}) = a_o e^{i\mathbf{k}_i \cdot \mathbf{r}} \tag{6.2}$$

where $e^{i\mathbf{k}_i \cdot \mathbf{r}}$ is the standard exponential notation when disregarding time dependence, and $\mathbf{r}$ is the positional variable. The scattered wave will be spherical, since one atom behaves as a point source.

The equation for the wave scattered by a nucleus at a distance D from the detector and at the origin of the coordinate system is then:

$$a_1^f(\mathbf{D}) = a_o b_1 \frac{e^{i\mathbf{k}_f \cdot \mathbf{D}}}{D} \tag{6.3}$$

where $1/D$ accounts for the wave being spherical and the nuclear scattering length b_1 characterises the interaction of the radiation with the nucleus.

When neutrons are scattered by two nuclei, the scattering produces interference patterns at the detector's position, as illustrated in Fig. 6.3.

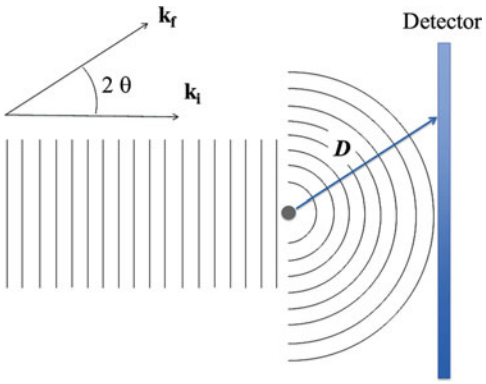

Fig. 6.2 Scattering by one atom

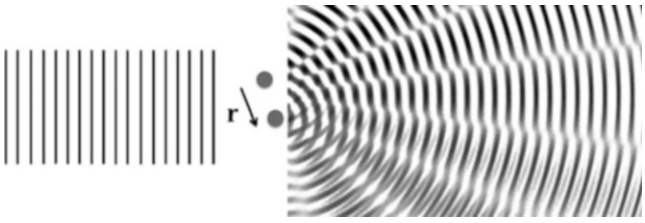

Fig. 6.3 Scattering by two atoms

The wave scattered by the second nucleus will have a difference in path length with respect to the first. This can easily be expressed as $-\frac{\mathbf{Q}}{k}\cdot\mathbf{r}$, where $\mathbf{r}$ is the vector from the first to the second nucleus. To obtain the corresponding phase difference one needs to multiply by k, resulting in a value of $-\mathbf{Q}\cdot\mathbf{r}$ for the phase difference. The distance to the detector (D) does in practice not depend on the nucleus position, since it is much larger than the distance between the nuclei (typically a factor of 10^{10}). The wave scattered by the second nucleus, located at a distance r from the first, can then be expressed as:

$$a_2^f(\mathbf{D}) = a_o b_2 \frac{e^{i\mathbf{k}_f\cdot\mathbf{D}}}{D} e^{-i\mathbf{Q}\cdot\mathbf{r}} \tag{6.4}$$

where b_2 is the scattering length of atom 2, and the phase term $e^{-i\mathbf{Q}\cdot\mathbf{r}}$ accounts for the resulting interference.

If a system is composed of n atoms, as illustrated in Fig. 6.4, the total scattered wave is:

$$a_f(\mathbf{D}) = \frac{a_o}{D} e^{i\mathbf{k}_f\cdot D} \sum_{j=1}^{n} b_j e^{-i\mathbf{Q}\cdot\mathbf{r}_j} \tag{6.5}$$

with the averaged scattered intensity over all possible positions:

$$\langle I_f(\mathbf{D})\rangle = \left\langle a_f(\mathbf{D}) a_f^*(\mathbf{D})\right\rangle = \frac{a_o^2}{D^2}\left\langle \sum_{j=1}^{n} b_j e^{-i\mathbf{Q}\cdot\mathbf{r}_j} \sum_{k=1}^{n} b_k^* e^{i\mathbf{Q}\cdot\mathbf{r}_k}\right\rangle \tag{6.6}$$

The expression can be also written as:

$$\langle I_f(\mathbf{D})\rangle = \frac{a_o^2}{D^2}\left\langle \sum_{j,k=1}^{n} b_j b_k^* e^{-i\mathbf{Q}\cdot\mathbf{r}_{jk}}\right\rangle \equiv \frac{a_o^2}{D^2}\frac{d\sigma}{d\Omega}(\mathbf{Q}) \tag{6.7}$$

where $d\Omega$ is the solid angle element covered by the detector, as illustrated in Fig. 6.5. Thus the scattered intensity will fall off with the square of the distance to the detector, and be proportional to the intensity of the incoming beam, as expected.

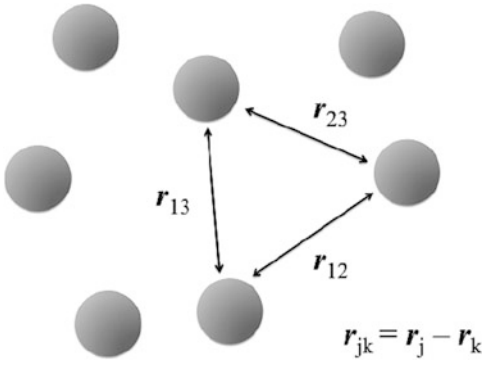

Fig. 6.4 System of n atoms

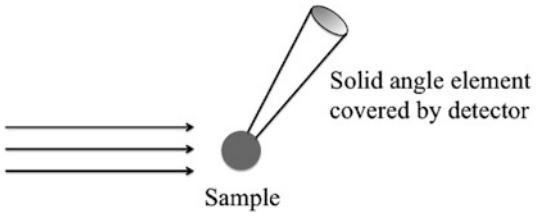

Fig. 6.5 Scattering from a sample into a specific solid angle

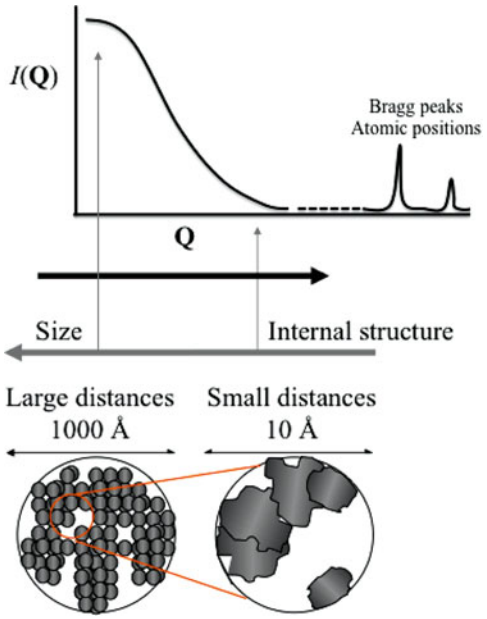

Fig. 6.6 A schematic scattering curve and the relationship between Q and distances in the system under study

The term $\frac{d\sigma}{d\Omega}(\mathbf{Q})$ is called the differential scattering cross section and represents the number of neutrons scattered per second into a solid angle, normalised to the neutron flux of the incident beam and the size of the solid angle. It is expressed in the units of an area, cm^2.

We can also normalise the equation to the unit sample volume V:

$$\frac{d\Sigma}{d\Omega}(\mathbf{Q}) = \frac{1}{V}\frac{d\sigma}{d\Omega} = \frac{1}{V}\sum_{j,k=1}^{n} \langle b_j b_k^* e^{-i\mathbf{Q}\cdot\mathbf{r}_{jk}} \rangle \tag{6.8}$$

This is called the differential scattering cross section per unit sample volume (in cm^{-1}). It is a quantitative representation of the interaction between the radiation and the sample and it contains the information relative to the structure of the sample, independent from the experimental setup.

SANS experiments explore matter in a reciprocal space, giving an inverse relationship between particle size and scattering angle, as illustrated by Fig. 6.6.

Large Q values relate to short distances while small Q values correspond to large distances/objects. Among other things, small angle scattering can be used to obtain information on the average size of pores and how they are distributed. At wider angles, outside the range of SANS, the information would contain the Bragg peaks of the diffraction from atomic or molecular crystal lattices.

6.2.3 Form Factor and Particle Correlation

The scattering of one particle, an assembly of a large number of atoms, produces an interference pattern due to the interaction of the waves scattered by its nuclei. Summing up all the wave amplitudes and taking the square of this sum results in an interference (scattering) pattern at the detector. This pattern changes in a way that is characteristic for the shape of the particle. It is represented mathematically by the so-called "form factor".

Figure 6.7 represents a particle composed by n atoms and embedded in a matrix. We can define a scattering length density of an inhomogeneous particle:

$$\rho(\mathbf{u}) = \sum_j \phi_j(\mathbf{u}) b_j \tag{6.9}$$

where ϕ_j represents the local number density of an atom type in the particle of volume V_p. This scattering length density may vary within the particle, and is thus generally a function of the positional variable $\mathbf{u}$. If the scattering length density of the surrounding matrix is ρ_m, the excess scattering length density becomes:

$$\Delta\rho(\mathbf{u}) = \rho(\mathbf{u}) - \rho_m \tag{6.10}$$

In analogy with Eq. (6.5), a further step is the integration of the scattered wave over all the atoms in the particle with volume V_p (omitting the pre-factors):

$$a_f(\mathbf{Q}) = \int_{V_p} \Delta\rho(\mathbf{u}) e^{-i\mathbf{Q}\cdot\mathbf{u}}\, d\mathbf{u} \tag{6.11}$$

If the system consists of N identical particles with pairwise distances r_j, as shown in Fig. 6.8, the total scattered wave becomes:

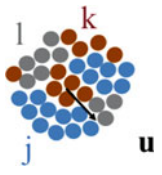

Fig. 6.7 A particle composed by n atoms of different types

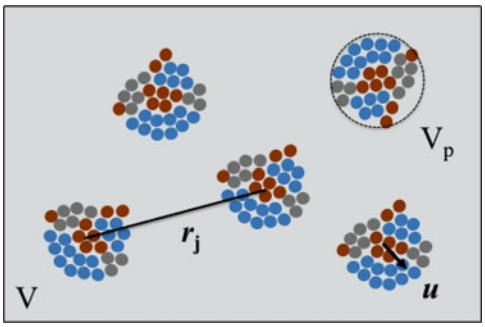

Fig. 6.8 N identical particles in a matrix

$$A_f(\mathbf{Q}) = \sum_{j=1}^{N} a_j^f(\mathbf{Q}) e^{-i\mathbf{Q}\cdot\mathbf{r}_j} \tag{6.12}$$

where $e^{-i\mathbf{Q}\cdot\mathbf{r}_j}$ is the phase term related to the position of the particles.

The resulting scattering from N identical particles interacting in a matrix is:

$$\frac{d\Sigma}{d\Omega}(\mathbf{Q}) \propto \quad \frac{1}{V}\langle A_f(\mathbf{Q}) A_f^*(\mathbf{Q})\rangle \tag{6.13}$$

As pointed out by Guinier et al. [5] it is necessary to consider some assumptions in order to perform the average over orientations indicated in Eq. (6.13). If the scatterers are randomly oriented, then the scattered intensity has spherical symmetry, i.e. $\frac{d\Sigma}{d\Omega}(\mathbf{Q}) = I(\mathbf{Q}) = I(Q)$. Equation (6.13) can then be written as:

$$I(Q) \propto \quad \frac{N}{V}\langle\Delta\rho\rangle^2 V_p^2 P(Q) S(Q) \tag{6.14}$$

where $\langle\Delta\rho\rangle^2$ is the contrast factor (if $\rho = \rho_m$ there is no contrast, therefore no scattering). These assumptions are often satisfied in disordered solids, because the disorder tends to reduce or eliminate correlations between the scatterers. Apart from the concentration $\frac{N}{V}$, the contrast $\Delta\rho$ and the particle volume V_p, the other important parameters in Eq. (6.14) are the form factor $P(Q)$ and the structure factor $S(Q)$. The form factor provides information about size, shape, and internal organisation of *individual* particles. The structure factor provides information about interactions *between* the particles. The separation of $P(Q)$ and $S(Q)$ is formally correct only for spherical particles, but in many cases provides a good approximation also for other systems.

Summing up, these are some of the important points to bear in mind when using small angle scattering:

(1) SANS arises from fluctuations in scattering length density (ρ) in the sample. These fluctuations are caused by heterogeneities in the dimensions of $\sim 10-1000$ Å, for instance particles in a liquid, or pores in a solid

(2) A 3-D structure of heterogeneity, for randomly oriented scatterers, is represented by the 1-D function of $I(Q)$
(3) The spatial resolution of a scattering experiment is $\sim\frac{1}{Q}$
(4) The measured scattered intensity results from the contributions of a form factor (particle size, shape) and a structure factor (inter-particle correlation)

After measuring the intensity scattered by a sample and making the appropriate background correction, the question remains which type of information can be extracted. By grouping the constant terms of Eq. (6.14) into K, it is clear that the scattered intensity is composed of three components

$$I(Q) = KP(Q)S(Q) \tag{6.15}$$

The constant K contains information about the particle contrast, volume, concentration, etc. The value of this constant is particularly important when investigating, for instance, the molecular weight of a particle.

Finally, as commented earlier, the form factor $P(Q)$ is related to the shape and the internal density distribution of the particles. The structure factor $S(Q)$ bears the information of particle-particle interaction. $P(Q)$ approaches 1 for $Q \to 0$, and $S(Q)$ approaches 1 for $Q \to \infty$. For uncorrelated systems $S(Q) = 1$.

The following sections will describe two important approximations in small angle scattering: the Guinier approximation and the Porod law.

6.2.4 Guinier Approximation

The Guinier approximation applies in the case of a dilute system, for sufficiently small Q values and $S(Q) = 1$. This approximation is valid when the system is so diluted that there are no interactions between particles, and at small angles, that is when $QR_G < 1$. R_G is called the "radius of gyration" of an object. The general Guinier approximation [6], valid for any particle shape, can be written as:

$$I(Q) \approx I(0)e^{-\frac{1}{3}Q^2R_G^2} \tag{6.16}$$

The size parameter R_G is model independent, having no information about the shape or the internal structure of the particle. However, R_G can be used to calculate the dimensions of the particle if the shape is already known. For instance, in the case of homogeneous spherical particles, the average radius of such particles can be calculated by the formula $R = \sqrt{\frac{5}{3}}R_G$. Similar arguments can be applied by assuming any other particle shape, where in each case different equations relating R and R_G will be considered.

In a so-called Guinier plot, shown with an example in Fig. 6.9, the logarithm of the intensity is plotted versus Q^2, while R_G is determined by the resulting slope:

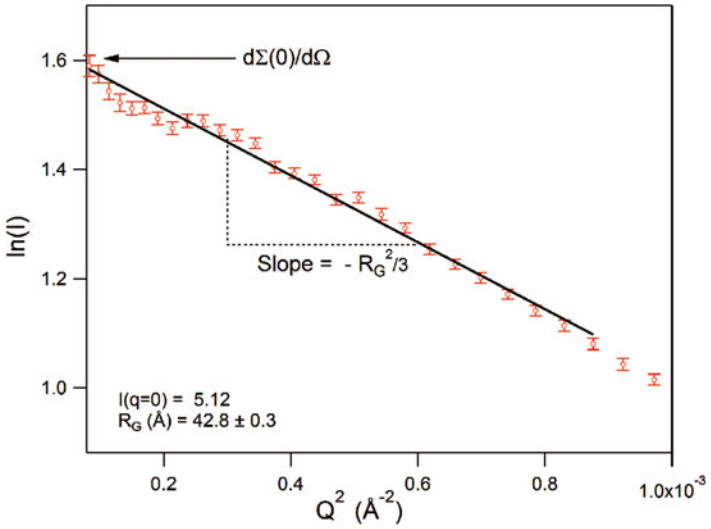

Fig. 6.9 Guinier plot showing how the slope of the regression line can be used to extract the radius of gyration (R_G) and zero-angle intensity. This example is for a particle with R_G equal to 42 Å

$$\ln[I(Q)] = \ln[I(0)] - \frac{R_G^2}{3}Q^2 \tag{6.17}$$

Equation (6.14) can also be used to determine the molecular weight. For instance, for a dilute system of N homogeneous particles in a volume V, with scattering length density ρ_p and volume V_p:

$$I(0) = \frac{N}{V}(\rho_p - \rho_m)^2 V_p^2 \tag{6.18}$$

where ρ_m is the scattering length density of the matrix. A useful way to express Eq. (6.18) is:

$$I(0) = \frac{cM_w}{d^2 N_A}(\rho_p - \rho_m)^2 \tag{6.19}$$

by which it is possible to determine the particle molecular weight M_w from scattering experiments extrapolated to $Q = 0$. Here c is the particle concentration, N_A Avogadro's number, and d the mass density.

6.2.5 *Porod Law*

The Porod law applies for sufficiently large Q, when $QR_G \gg 1$. If the boundary between the scattering objects and the matrix is sharp, the scattered intensity can be written as [7]:

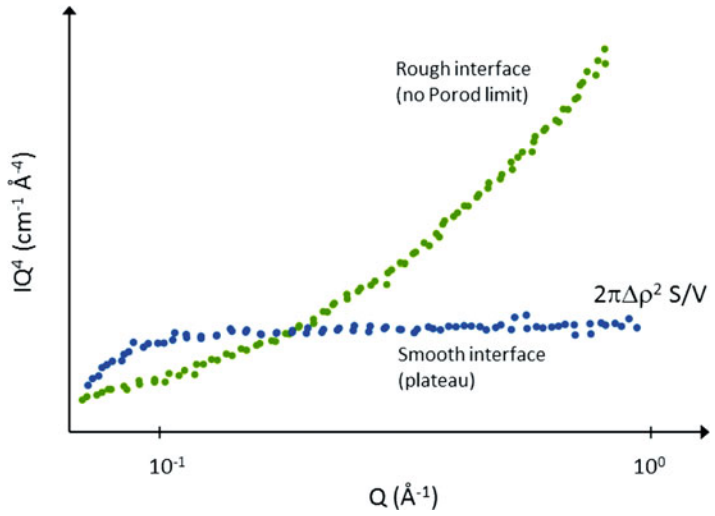

Fig. 6.10 Plot of IQ^4 versus Q for evaluating the specific (internal) surface area of a material

$$I(Q) = \frac{2\pi(\Delta\rho)^2}{Q^4}\frac{S}{V} \tag{6.20}$$

where S is the total area of the interface and $\frac{S}{V}$ is thus the specific surface. From Eq. (6.20) it is clear that the Porod law can be approximated as:

$$I(Q) \sim Q^{-4} \tag{6.21}$$

At large values of Q, the measured intensity gives information on the surfaces of small real-space structures. As will be shown in the case of nano-confined hydrides, it is usual to extract information about the surface of objects from so called Porod plots of IQ^4 versus Q, such as illustrated schematically in Fig. 6.10.

6.2.6 *Particle Shape*

For particles having a well defined shape (e.g. sphere, cylinder, disk) the scattered intensity at intermediate angles provides useful information on their shape [6]. When the particles are spheres:

$$\ln I(Q) \cong \ln I(0) - \frac{R_{G,sphere}^2}{3}Q^2 \tag{6.22}$$

For particles with highly asymmetric shape other expressions are conveniently used. For cylindrical particles:

$$\ln[QI(Q)] \cong A - \frac{R_{G,cylinder}^2}{2}Q^2 \tag{6.23}$$

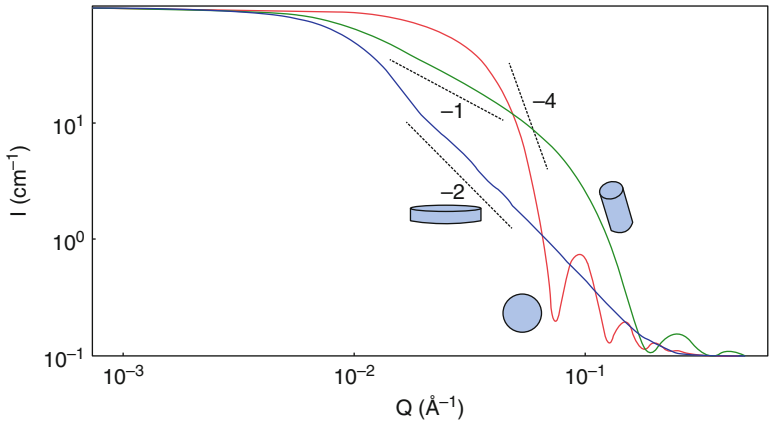

Fig. 6.11 Information domains of the particle form factor illustrated by schematic plots of form factors for different particle shapes: *sphere*, *cylinder*, and *disk*. Characteristic slopes (log-log) for these particle shapes are indicated. The particle dimensions used for these plots are as follows: sphere radius 60 Å, cylinder radius 20 Å and length 400 Å, disk radius 400 Å and thickness 20 Å

For lamellar particles:

$$\ln[Q^2 I(Q)] \cong B - R^2_{G,lamella} Q^2 \tag{6.24}$$

Details about the scattering functions for different particle shapes can be found in most textbooks (e.g. [8]). However, it is important to mention that one seldom deals with monodisperse particles of uniform shape.

The form factor bears information of the characteristic structure of every particle. Schematic plots of form factors for different particle shapes are shown in Fig. 6.11 for log$P(Q)$ plotted versus log(Q). At small angles the features of the form factor is primarily determined by the overall size, while at large angles it is possible to extract information of the surface of an object. The characteristic shape and internal density distribution can be determined by the slope and oscillating features in the middle section of the curve.

By calculating the power law of the form factor at intermediate angles one can roughly classify the particle shapes. In a double logarithmic plot a slope of -1, -2 or -4 indicates cylindrical, disk-like or spherical shape, respectively.

6.2.7 *Fractals*

Fractals are entities which displays self-similarity at every scale, i.e. their structure is independent of the length scale of observation. For a fractal object, the mass measured within a sphere of radius R will change with R according to the relation:

$$M(R) \approx R^D \tag{6.25}$$

where D is the fractal dimension ≤ 3. The scattering law for fractal systems can in general be written as:

$$I(Q) \sim Q^{-\alpha} \tag{6.26}$$

Mathematically, self similarity can be obeyed at all length scales. However, in a typical experiment one distinguishes between individual scatterers (e.g. size R of single particles in an aggregate) and the size ξ of the aggregates. In practice, a fractal behaviour is observed for $\xi^{-1} < Q < R^{-1}$, and the slope α is calculated from the straight line fitting the experimental points in a $\ln I(Q)$-$\ln Q$ plot.

In general, at intermediate Q values the decay of the scattered intensity proportional to $Q^{-\alpha}$ is related to the dimensionality of the structure:

- dense structures with smooth interface for $\alpha = 4$
- mass fractals for $\alpha = D_m$, with $1 < \alpha < 3$
- surface fractal exponents for $3 \leq \alpha \leq 4$, where $\alpha = 6 - D_S$

D_S is called the surface dimension, with values $2 \leq D_S \leq 3$. For a smooth surface $D_S = 2$ and $\alpha = 4$ (Porod law), while for a rough surface D_S and α approach 3.

A schematic overview of the scattering for fractal system is presented in Fig. 6.12.

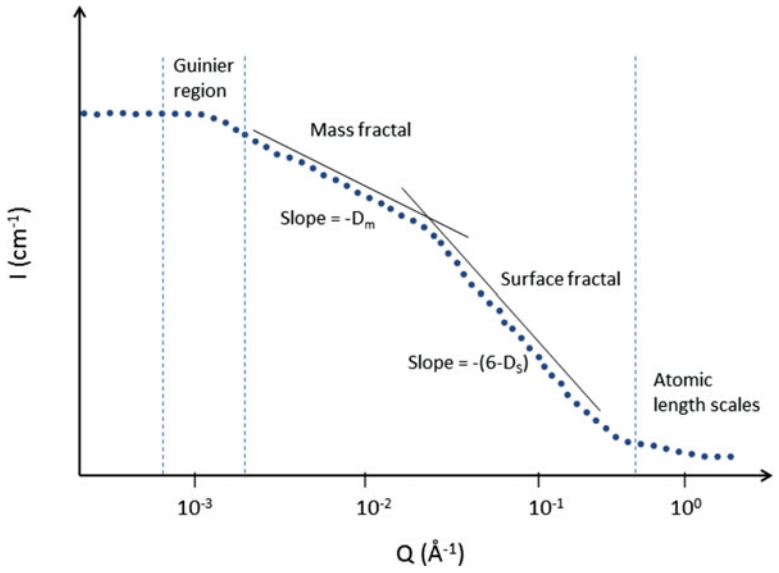

Fig. 6.12 Schematic intensity plot for SANS for fractal-type systems. The scattering at different length scales indicates the Guinier, the mass fractal and the surface fractal regions

6.3 Instrumentation

6.3.1 Typical Setup at a Reactor Source

Aiming for the mesoscopic or colloidal dimensions (tens to several thousand Å), SANS is optimised for the observation of small scattering angles using long wavelength (cold) neutrons. A SANS instrument is typically one of the larger installations found at a neutron facility, and easily recognisable from the spacious evacuated tank housing the SANS detector. A large sample-detector distance is necessary in order to resolve the small scattering angles (down to a few tenths of a degree) corresponding to the lowest Q value that needs to be accessed. The latter is generally below $Q = 0.01$ Å^{-1}, and at some facilities close to 0.001 Å^{-1}.

A typical setup for a pin-hole SANS instrument at a reactor source (Fig. 6.13) usually has at least the following components: a monochromator to achieve a well-defined wavelength, two apertures to define the beam collimation, a sample chamber, and a detector. The monochromator may be a mirror-based setup, but is now often of a velocity selector type. The latter is based on a rotating drum with helically shaped neutron absorbing lamellae, where the rotation speed is used to control the velocity of the neutrons that exit the drum, and thus their wavelength. This will often be in the range 4–10 Å.

The wavelength resolution ($\Delta\lambda/\lambda$) can typically be varied between 10 and 20 %, and may thus be tuned depending on the resolution necessary for the sample in question. In some cases, e.g. for materials with a very low polydispersity index (well below 10 %), it may be advantageous to have even better resolution, and this may be achieved with a mirror-based monochromator or alternatively a time-of-flight (chopper based) setup.

The resolution ($\Delta Q/Q$) in the resulting SANS pattern is a combination of the contribution from the monochromator ($\Delta\lambda/\lambda$), the effective size of a detector element (pixel size), and the geometrical setup defining the beam. A well-designed SANS-instrument achieves a balance between these three contributions, in order to obtain the largest possible flux without compromising to much the resolution $\Delta Q/Q$ of the final SANS pattern. This means that the divergence due to the beam-defining

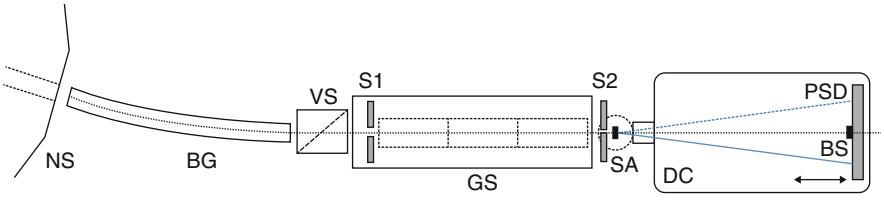

Fig. 6.13 Instrumental setup for a pin-hole SANS instrument at a reactor source. The components are: neutron source (*NS*), neutron beam guide (*BG*), velocity selector (*VS*), entrance aperture (*S1*), guide section (*GS*), sample aperture (*S2*), evacuated detector chamber (*DC*), position sensitive detector (*PSD*), beam stop (*BS*)

apertures should give a contribution to $\Delta Q/Q$ comparable to or smaller than the contribution from the monochromator. Since the sample aperture has a rather fixed position and size, determined by the sample cell geometry, this means in practice that the source aperture is adjusted to achieve the desired geometrical resolution. Moveable guide sections may be used between the source and sample apertures to translate the effective source position closer to or farther from the sample. At a steady neutron source, the optimal source-to-sample distance will generally be equal to the distance between the sample and the detector, which is an additional reason for the large overall lengths of most SANS instruments.

Most modern SANS instruments receive their neutron beam from a so-called cold source, which is a device placed inside the beam channel close to the main neutrons source, containing a material that efficiently slows down the speed of the neutrons. This may be e.g. liquid hydrogen (LH_2), which when maintained at a temperature of 20 K, reduces drastically the speed of an incoming neutron in a multi-collision process. The result is that the Maxwellian distribution of neutron velocities is translated to a significantly lower value. Therefore the wavelength maximum is moved upwards, close to the range that is optimal for SANS, i.e. 4 Å and above. It is of course important that the background not coming from the sample itself is as low as possible. For that reason it is advantageous to avoid a direct line of sight towards the neutron source, so that gamma and fast neutron radiation can be eliminated. This may be achieved by either a curved guide section in front of the monochromator, a neutron bender that deflects neutrons above a given wavelength to a pre-defined angle, or alternatively a mirror-based setup.

The SANS-detector is nowadays always a large two-dimensional (circular or square) detector, usually placed on rails inside the detector chamber, so that it can be translated between a near position (high-Q limit) and far position (low-Q limit). The most common design is that of gas-filled (^{3}He) multi-wire detector with sets of anode and cathode wires (typically 128 $\times$ 128), although solid-state (scintillation-based) detectors are more recent alternatives. In the multi-wire detector, when a neutron interacts with the^{3}He nucleus, the result is the creation of a tritium nucleus (^{3}H) plus a proton with a combined kinetic energy of 765 keV. Due to the high voltage between the anode and cathode planes, this induces a cascade of ionizations, with the final result of a voltage pulse that can be used to locate the incoming neutron both in time and space. For SANS instruments at spallation sources, the general design is similar to that described schematically above. The main difference is that the neutrons hitting the sample cover a broad wavelength band, and thus a certain range in Q, already from the start. In order to catalogue neutrons with different wavelengths, one can then employ time-of-flight techniques which are implemented using synchronised choppers, so that the arrival time of a neutron at the detector can be directly mapped to the wavelength, and thus to a specific Q value. One advantage with such setups is that since a fairly broad Q range can be mapped out with one instrumental setting, in-situ experiments with fast time-dependent phenomena may be more conveniently performed than at a steady neutron source.

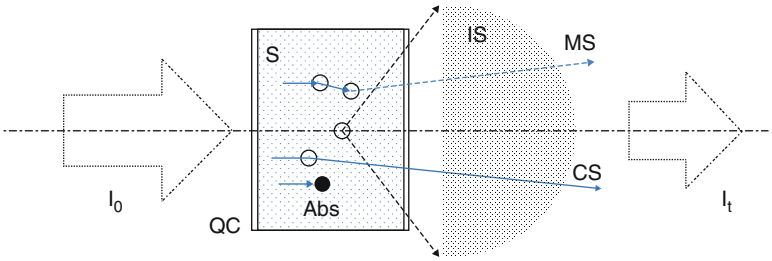

Fig. 6.14 Different processes occurring when the neutron beam hits the sample: Incoming beam (I_o), transmitted beam (I_t), quartz cell (QC), sample (S), absorbed neutron (Abs), coherent scattering (CS), incoherent scattering (IS), multiple scattering (MS)

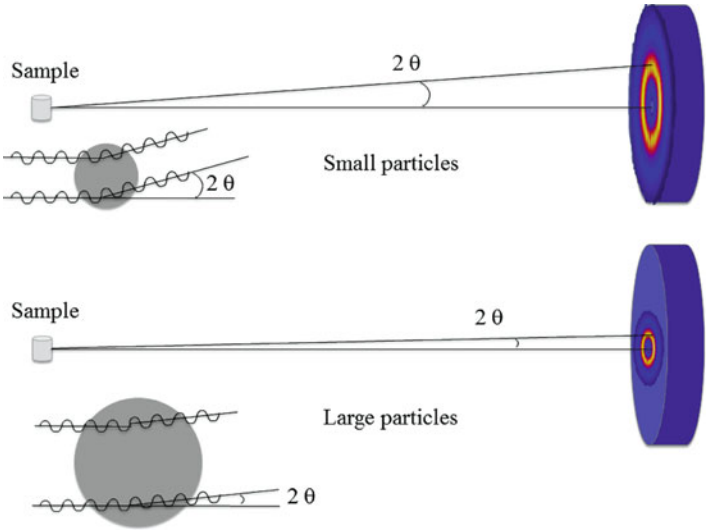

Fig. 6.15 Coherent scattering from two particles of different size

The different processes occurring when the neutron beam interact with the sample are illustrated in Fig. 6.14.

The scattering from two particles of different size will result in a different two-dimensional scattering image on the detector, as shown in Fig. 6.15. The detector is located several meters away from the sample holder and records the intensity of the neutrons scattered through small angles 2θ relative to the incident beam. The scattering profile contains information about the size and shape of the particles, and the example described in Fig. 6.15 shows the constructive interference between the waves scattered by two nuclei within spherical particles. The coherent scattering from the larger sphere occurs into smaller angles and therefore smaller Q.

6.4 Analysis of Data

A sample can be structurally described by performing a Fourier transform of the scattered intensity. However, with this method, some information is lost due to, for instance, isotropic averaging over all orientations. Instead, a more common approach consists in fitting the experimental data with a reasonable model in real space where one assumes the shape of the particles and their interaction potential, calculating the resulting scattering intensity and comparing it to the experimental data in **Q**-space. The process is schematically outlined in Fig. 6.16. The fitting in the reciprocal space should be cautiously considered because often different models can give plausible fitting. For this reason, it is important to stress that a reliable structure will usually be found complementing SANS with the knowledge of the sample composition and the information provided by other techniques.

An alternative approach, useful when little prior information is known about the shape/size of the scattering elements, is given by the indirect Fourier transform (IFT). This is the method employed in several of the studies of nano-scaled hydrides described in the next sections of this chapter. The IFT consists in the extraction of the distance distribution of scattering objects in the sample by employing a trial distribution $p(r)$ as a sum of spline functions in real space within certain limits, transforming this into reciprocal space, comparing with the experimental data, and adjusting the coefficients of the splines until an acceptable fit is achieved:

$$I(Q) = 4\pi \int_0^\infty p(r) \frac{\sin(Qr)}{Qr}\, dr \tag{6.27}$$

Different implementations of this method initially proposed by Glatter [9] can be found, such as the GNOM program [10] and the Global evaluation technique [11].

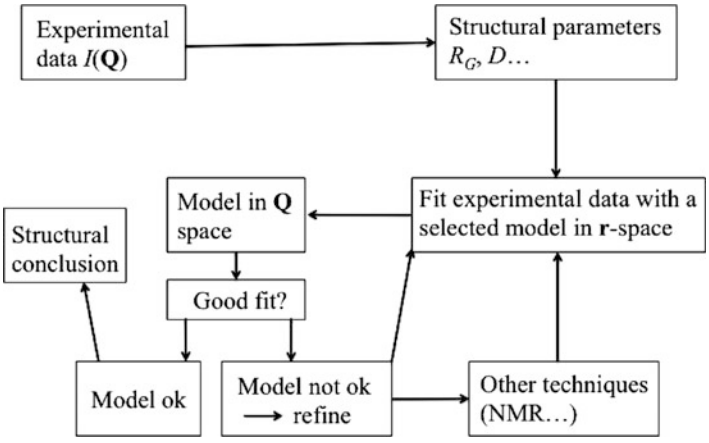

Fig. 6.16 Flow diagram for the analysis of SANS data for a general case

6.4.1 Interacting Particles

The scattered intensity of N randomly oriented identical particles can be expressed by approximating Eq. (6.14) as:

$$I(Q) = N\Delta\rho^2 P(Q)S(Q) \tag{6.28}$$

When the sample is made up of interacting particles, the measured intensity contains information of both the geometry of the particles and their spacial correlations. If $S(Q) = 1$ (uncorrelated particles) the scattered intensity reflects only the size, shape and internal structure of a single particle. For correlated particles, the structure factor $S(Q)$ represents the modification of the intensity due to the spatial correlation of the particles.

The separation of the two contributions, $P(Q)$ and $S(Q)$, can be a problem in small-angle scattering experiments. When a significant interaction between particles is present, as illustrated in Fig. 6.17, it is difficult to extract the characteristic size of the particles (the Guinier range is no longer visible in $I(Q)$), or their organisation (a peak is visible in $I(Q)$ but is displaced with respect to its position in $S(Q)$).

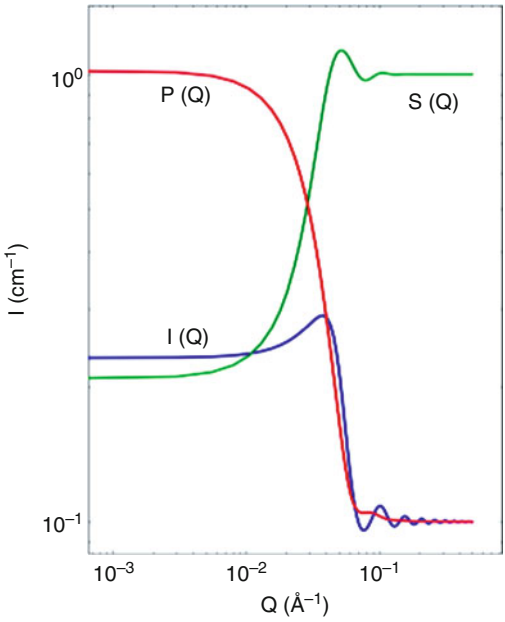

Fig. 6.17 I versus Q for centrosymmetric, correlated particles. Schematic plot of the form factor $P(Q)$, structure factor $S(Q)$, and the overall intensity $I(Q)$ resulting from a combination of $P(Q)$ and $S(Q)$. The plot was made for a spherical particle with a radius of 60 Å, and a hard sphere interaction potential with the same effective radius

To solve this problem, there are three main strategies one can follows for measuring the structure factor:

(1) First, one can measure the intensity scattered by a dilute sample, with $S(Q) = 1$:

$$I_{dil}(Q) = N_{dil}\Delta\rho^2 P(Q) \tag{6.29}$$

After measuring the intensity scattered by the concentrated sample of interest:

$$I_{conc}(Q) = N_{conc}\Delta\rho^2 P(Q)S(Q) \tag{6.30}$$

one can calculate the structure factor by:

$$S(Q) = \frac{I_{conc}(Q)}{I_{dil}(Q)}\frac{N_{dil}}{N_{conc}} \tag{6.31}$$

(2) Another strategy is by isotope labelling only a specific region in each particle, so that $S(Q)$ dominates the scattering while the contrast of the remaining parts will be negligible.
(3) Finally, by proposing a reasonable initial model for the form factor and the structure factor, as discussed in Fig. 6.16. The parameters are corrected until the solution converges.

6.4.2 Contrast Variation and Deuterium Labelling

Real systems in materials science are usually complex, and a simplified "two-phase" description of the structure is rarely adequate. In these systems, the information contained in the scattered intensity concerns the structure as a whole, adding together the contributions of all components. To enhance the structural description of these multicomponent systems, one can highlight a defined component without changing any of the characteristics of the sample. The technique is called *contrast variation*.

In neutron scattering this relies essentially on the use of isotopic substitution. From Eqs. (6.14) and (6.18) we understand that the scattering intensity is proportional to the square of the scattering length density difference between the studied material and the medium, or matrix.

Considering the interaction neutron-nuclei, for the short range strong force, we can use the approximate interaction potential:

$$V(\mathbf{r}) = \frac{2\pi\hbar^2}{m_n} b\delta(\mathbf{r} - \mathbf{R}) \tag{6.32}$$

where b is the scattering length and $\mathbf{R}$ is related to the positions of the nuclei.

b depends on the details of the nuclear structure and varies greatly among elements/isotopes. For a single nucleus the differential cross-section is given by:

$$\frac{d\sigma}{d\Omega} = |b|^2 \tag{6.33}$$

The total cross section is defined as:

$$\sigma = \int \frac{d\sigma}{d\Omega}\, d\Omega = 4\pi b^2 \tag{6.34}$$

and it consists in the effective area presented by a nucleus to an incident neutron. The total scattering cross section can be written as:

$$\sigma_s = \sigma_c + \sigma_i \tag{6.35}$$

where σ_c is the coherent scattering, proportional to b_c^2, and σ_{inc} is the incoherent scattering, giving a diffuse background in the signal proportional to b_i^2. One of the greatest advantages of using neutrons is that each isotope of an element has a different neutron scattering length value, thus they will scatter neutrons differently (though keeping the same physical and chemical properties). Hydrogen and its heavy isotope deuterium, for instance, have scattering lengths of opposite sign, making neutron based techniques very useful to investigate samples containing hydrogen.

In complex systems, by matching ρ_m to ρ for one component of the system, the contribution of that component to the scattering can be eliminated.

Some of the relevant elements for light-weight hydrogen storage materials show large incoherent scattering, as can be seen from the absolute values of the incoherent scattering lengths in the table below. This is especially the case for hydrogen itself (^{1}H), where a substitution with deuterium (^{2}H) reduces drastically the incoherent scattering, and in addition increases the coherent component. As can be seen from the table, when using boron, it is also an advantage to work with pure ^{11}B, and not ^{10}B, where ^{10}B has an abundance of ca 20 % in naturally occurring boron. For Mg and Al the incoherent scattering lengths of the naturally occurring isotopes are intrinsically low, whereas for Li the value is not insignificant, but quite similar for the two isotopes available (^{6}Li and ^{7}Li) (Table 6.1).

Table 6.1 Scattering lengths for some isotopes [12]

Scattering length b [$10^{-15}m$]	^{1}H	^{2}H(D)	^{10}B	^{11}B	^{24}Mg	^{13}Al	^{6}Li	^{7}Li
Coherent b_c	−3.74	6.67	~ -0.2	6.65	5.66	3.45	2.00	−1.89
Incoherent b_i	25.3	4.04	~ -4.7	−1.3	0	0.26	2.22	−2.49

6.4.3 Background Subtraction

Every analysis starts with the quantification and usually also subtraction of the background noise. As mentioned before, in the high-Q limit, the intensity will generally follow a Q^{-4} behaviour. We may then write the measured intensity as:

$$I(Q) = AQ^{-4} + B \tag{6.36}$$

where B is the unknown background contribution. By multiplying Eq. (6.36) by Q^4:

$$I(Q)Q^4 = A + BQ^4 \tag{6.37}$$

The background may then be calculated as the slope of the regression line when plotting IQ^4 versus Q^4, and finally be subtracted from the measured scattered intensity.

6.5 SANS and Porous Media

The SANS technique is highly useful for studying porous materials. The pores act effectively as scattering elements due to the abrupt change in scattering length density (SLD) between the region where there is material and the void, thus giving rise to a scattered intensity proportional to the square of the SLD of the non-void region. Therefore pores in the typical size range for SANS (around 1 to 100 nm) can be effectively studied by this method. The situation is similar when using X-rays as a probe (SAXS), but often the contrast will be intrinsically different with the two methods (see also Sect. 6.7). SANS has the additional advantage that one may play with the contrast in order to, for example, mask out the matrix itself by introducing a liquid or solid having an SLD equal to that of the matrix, thus giving average zero contrast. Along the same lines, if one lets the initially empty pores of the material absorb another phase (infiltration), the change in scattering length density of the filled pores will produce a concurrent change in scattered intensity, therefore being a means of following the absorption of the second phase. The latter effect will be exemplified in the following section. It is important to note that SANS probes all pores within the scattering volume, irrespectively of whether they are internal (closed) pores or whether they have a connection to the matrix surface. This is in contrast to absorption studies with e.g. the BET technique, where only the latter pores are probed. This means that—depending on the specific material in question—one may see quite different values for effective surface areas when employing the two techniques on the same material. It should also be mentioned that SANS may be of use for surface area determinations where adsorption studies are inappropriate due to the interaction of nitrogen with the sample surface [13].

6.6 Nano-Scaled and Infiltrated Hydrides

Small angle scattering is particularly useful when dealing with nano-sized hydrides infiltrated in porous scaffolds. It has been observed that confinement of a complex hydride in microporous and mesoporous scaffolds may enhance the kinetics and lower the desorption temperature of the hydride [14–16]. One explanation of this behaviour can be the reduced diffusion distances. Other reasons may be enhanced interaction with the interface of the walls of the scaffold and structural modifications of the hydride and its products in the nanoscale voids. In this section we will discuss SANS on some selected hydrides: $Mg(^{11}BD_4)_2$, $NaAlD_4$, MgD_2 and $Li^{11}BD_4$-$Mg(^{11}BD_4)_2$.

6.6.1 Infiltrated $Mg(^{11}BD_4)_2$

$Mg(BH_4)_2$ is considered an interesting complex hydride for hydrogen storage applications due to its high theoretical content of 14.9 wt. % hydrogen. One of the main drawbacks is its high decomposition temperature, above 300 °C. Infiltration of this complex hydride has been done in an attempt to improve its performances.

A solution of $Mg(^{11}BD_4)_2$ in diethyl ether was infiltrated into activated carbon (AC1), and pre-treated before use, following a wet incipient impregnation procedure [16]. For this particular case, an amount of 15 wt. % of the infiltrated active material ($Mg(^{11}BD_4)_2$) was carefully chosen to reach but not surpass the maximum loading capacity of the scaffold.

Figure 6.18 shows a comparison between powder X-ray diffraction (PXD) from $Mg(^{11}BD_4)_2$ infiltrated in AC1 and from the bulk powder alone [17]. It is clear that

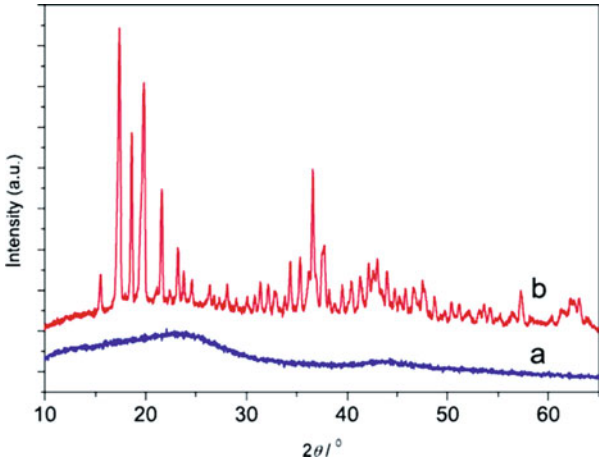

Fig. 6.18 PXD for $Mg(^{11}BD_4)_2$/AC1 (*a*) and for the bulk $Mg(^{11}BD_4)_2$ powder (*b*). Reprinted from [17] by permission of IOP Publishing. All rights reserved

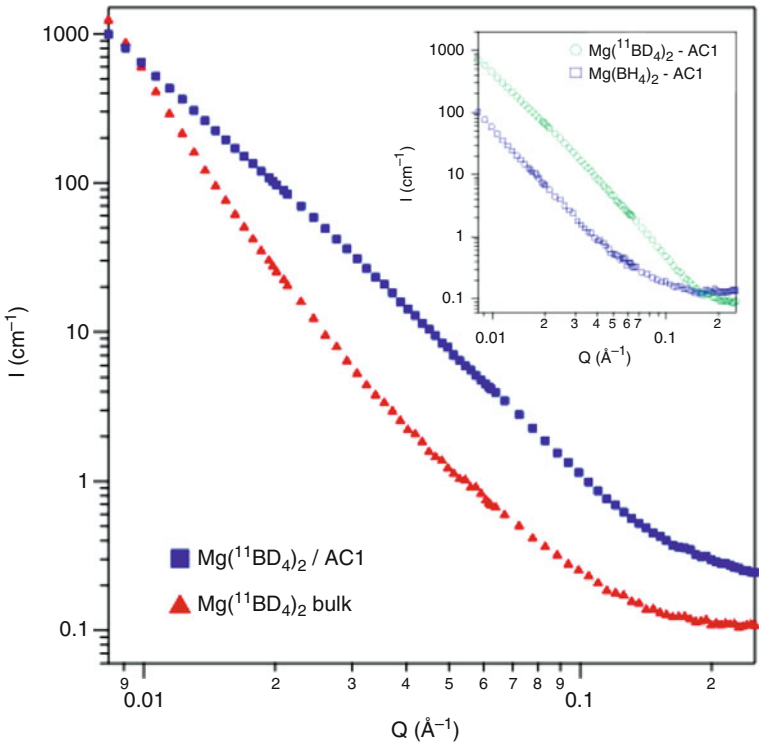

Fig. 6.19 SANS data for Mg(^{11}BD$_4$)$_2$/AC1 and the data from the bulk powder. In the *inset* are shown the reduced SANS data for both the hydrogenated and the Mg-borodeuterate infiltrated samples, where the scattering from the scaffold itself (AC1) has been subtracted. Note that in the *inset* the intensity at high-Q is lower for the deuterated sample due to the reduced incoherent scattering compared to the hydrogen containing sample. Adapted from [17] by permission of IOP Publishing. All rights reserved

the Mg-borodeuterate loses its crystalline character when loaded into the AC1 scaffold (a), thus any distinct particles, if they exist, must be very small in size (nm). The attempts to extract information on the nano-confined systems with other techniques were not conclusive and an interesting discussion was taking place about the features of the system. In this context the use of SANS provided important inputs into understanding the system.

Figure 6.19 shows SANS data for Mg(^{11}BD$_4$)$_2$/AC1 and for the bulk Mg(^{11}BD$_4$)$_2$ powder. Already from visual inspection of the curves one can see that the bulk powder shows a very different scattering behaviour than the infiltrated system. The difference in the pattern for the two curves seems to become significant roughly in the Q range above 0.02 Å^{-1}, or equivalently below a length scale of around 5 nm, indicating that the infiltrated Mg-borohydride has a predominance of small particles compared to the bulk. This observation confirms the data from the PXD measurements presented in Fig. 6.18, that proved the presence of a very different particle size distribution between pure Mg(^{11}BD$_4$)$_2$ and Mg(^{11}BD$_4$)$_2$ /AC1.

The inset of Fig. 6.19 shows SANS data of a hydrogen and deuterium infiltrated samples where the contribution of the AC1 scaffold has been subtracted. In general the scattered intensity from such a two-phase system, including voids, will contain three parts, according to:

$$I(Q) \sim (\rho_{AC} - \rho_{Air})^2 Z_{11} + \left(\rho_{Mg} - \rho_{Air}\right)^2 Z_{22} + (\rho_{AC} - \rho_{Air})\left(\rho_{Mg} - \rho_{Air}\right) Z_{12} \tag{6.38}$$

where Z_{11}, Z_{22} and Z_{12} represent the scattering from the scaffold (AC), from the active material $Mg(^{11}BD_4)_2$ and the interaction scaffold-hydride, respectively, and $\rho_{Air} \sim 0$.

After subtraction of the scaffold scattering (inset of Fig. 6.19), there will still be a certain bias in the Mg-borohydride data due to the remaining cross-correlation term in the interaction between the scaffold and the Mg-borohydride particles, but the data are anyhow useful for a qualitative interpretation.

The inset demonstrates the benefit of using deuterium, as discussed in the theory section. The neutron scattering length density (SLD) for $Mg(^{11}BD_4)_2$ is 7.2×10^{-6} $Å^{-2}$. This is significantly higher in absolute value than for $Mg(^{11}BH_4)_2$, with SLD equal to $-1.54 \times 10^{-6}\,Å^{-2}$. This means that the deuterium-containing sample scatters much stronger due to the enhanced contrast and with an improved signal-to-noise ratio.

One of the first evidences of the effective infiltration of the $Mg(^{11}BD_4)_2$ into AC1 was given by comparing its SANS data with the scattering from the scaffold alone, as shown in Fig. 6.20.

A log-log plot of the curves evidenced a cut-off in the pattern around $Q = 0.025$ $Å^{-1}$. Below this value the infiltrated $Mg(^{11}BD_4)_2$ and the AC1 curves behave similarly (near parallel curves), whereas above this point there is a slope change for the Mg-borodeuterate curve from 2.6 to 2.9. The Q value for this cut-off represents a characteristic length in the system, with $d \sim 1/Q = 4$ nm, where the Mg $(^{11}BD_4)_2$ particles in the system scatter differently than the scaffold itself (AC1). This value confirms the particles dimensions inferred by visual inspection of Fig. 6.19. Some larger particles may also be present, but from PXD measurements this can only account for a small amount since they do not contribute sufficiently to give detectable diffraction peaks. At higher Q values the two curves in Fig. 6.20 approach each other. The value of $\alpha = 2.9$ in the Q range above $Q = 0.025$ $Å^{-1}$ corresponds to a mass fractal dimension D close to the maximum attainable, i.e. $D = 3.0$. This is a sign that the density of the system in the nm range has significantly increased after infiltration with Mg-borohydride. The scaffold alone shows a lower slope, $\alpha = 2.6$, characteristic of a considerably more open system (the porous activated carbon). Thus the absorption of Mg-borohydride is seen to significantly reduce the porosity of the scaffold, in accord with a situation of nm-sized borohydride particles that provide a near complete filling of the smallest pores available in this scaffold.

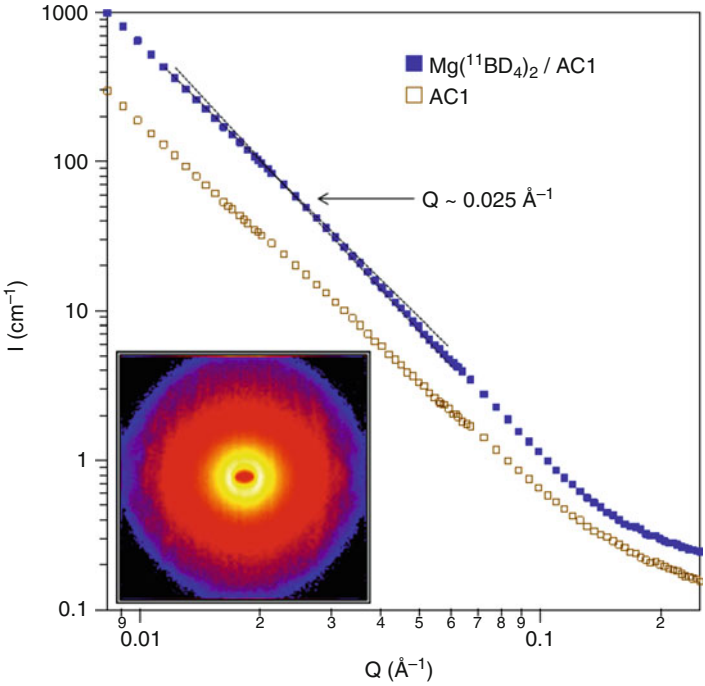

Fig. 6.20 Reduced SANS data for the Mg(^{11}BD$_4$)$_2$ /AC1 compared with the data from the scaffold alone. The *straight lines* follow a different power-law behaviour below and above the cut-off point around $Q = 0.025$ Å^{-1}. The *inset* displays the two-dimensional SANS pattern in the low-Q range ($Q = 0.008 - 0.03$Å^{-1}) for the Mg(^{11}BD$_4$)$_2$ /AC1 sample. Adapted from [17] by permission of IOP Publishing. All rights reserved

6.6.2 *Infiltrated NaAlD$_4$*

Infiltration of NaAlD$_4$ into activated carbon fibers (ACF25) was demonstrated possible following a melt impregnation procedure [18]. The procedure confirmed the possibility to tune the thermodynamic properties of NaAlD$_4$ with the use of a carbon structure host. Also in this case the PXD performed on the nano-composite did not contain useful structural information [19].

Moreover, the specific elements in NaAlD$_4$/ACF25 composite do not produce particularly strong relative contrast with neutrons. In fact, the calculated neutron scattering length densities are 4.9×10^{-6} Å^{-2} and 3.0×10^{-6} Å^{-2} for NaAlD$_4$ and the ACF25 scaffold, respectively. However, the SANS measurements performed on the samples were found useful in describing some features of the NaAlD$_4$/ACF25 composite.

A comparison of SANS curves from the nano-composite, the scaffold alone, and the bulk NaAlD$_4$ highlighted the major difference regarding the bulk material as opposed to the composite [19]: bulk NaAlD$_4$ showed weak scattering at high Q, and

presented relatively more scattering at low and intermediate Q values, indicating that in the bulk the average particle size is significantly larger than in the composite. Furthermore, the curves for the composite and the scaffold followed a similar trend at low Q. However, in the mid/high-Q range, above a Q value of about 0.03 $Å^{-1}$, a significant excess scattering from the composite compared to the scaffold alone demonstrated that upon loading the scaffold with $NaAlD_4$ any changes occur only at the short length scales, well below 10 nm.

The size distribution obtained by means of an indirect Fourier transform of the excess scattering, i.e., of the data obtained by subtracting the scaffold scattering from the composite scattering (although keeping in mind that some cross-correlation terms may not be nulled out upon subtraction) confirmed the small sizes of $NaAlD_4$ particles, well below 40 Å (4 nm), when integrated into the scaffold.

6.6.3 *Infiltrated MgD_2*

MgD_2 was infiltrated in activated carbon fiber (ACF25) [20] and investigated by using SANS [21]. The nano-composite showed improved kinetic and thermodynamic properties [20] but its structural features could not be investigated with conventional methods. Theoretical calculations predicted that changes in the physical and chemical properties appear when the size for the MgH_2 nano-cluster is less than 2.2 nm [21].

In order to identify the particle size and the effective infiltration of the prepared MgD_2/ACF25 composite, SANS performed on the bulk MgD_2 was compared to the composite MgD_2/ACF25 and the scaffold ACF25, as shown in Fig. 6.21. The curves pertaining to MgD_2/ACF25 and to the scaffold alone follow the same trend at low/medium Q (Fig. 6.21), apart from a translation along the y-axis due to the change in total contrast. A clear difference in slope becomes evident at Q values higher than approximately 0.18 $Å^{-1}$, corresponding to particle and pore dimensions of less than a few nm. In this high-Q range, the slope parameter α for the nano-composite has a value of approximately 1.3. This indicates that the particle sizes are so small that the material has a mass fractal behaviour even at the shortest length scale accessible in our experiments (around 1 nm). Figure 6.22 shows the size distribution obtained by means of an indirect Fourier transform of the excess scattering. This curve, with its main peak around 10 Å (1 nm), confirms the small sizes of the MgD_2 particles when they are integrated into the scaffold.

As a rough independent check of the average particle size, a Guinier regression can be performed in the high-Q region (above $Q \approx 0.1$ $Å^{-1}$), where the 'knee' in the composite data is a clear indication of a characteristic size in this size range. The result was a radius of gyration for the MgD_2 particles just below 1 nm (9.7 Å), as shown in the inset of Fig. 6.22.

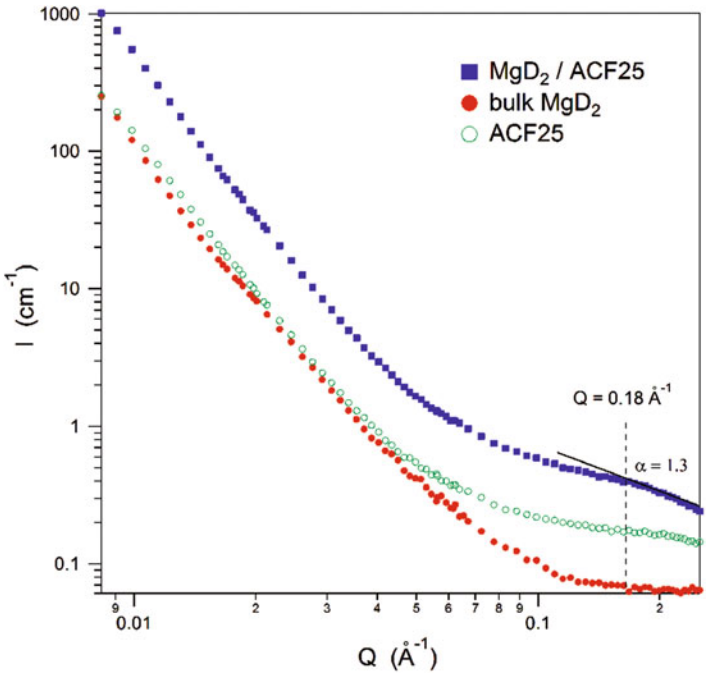

Fig. 6.21 SANS measurements performed at room temperature on ACF25, MgD_2/ACF25, and bulk MgD_2. Adapted with permission from [21]. Copyright 2012 American Chemical Society

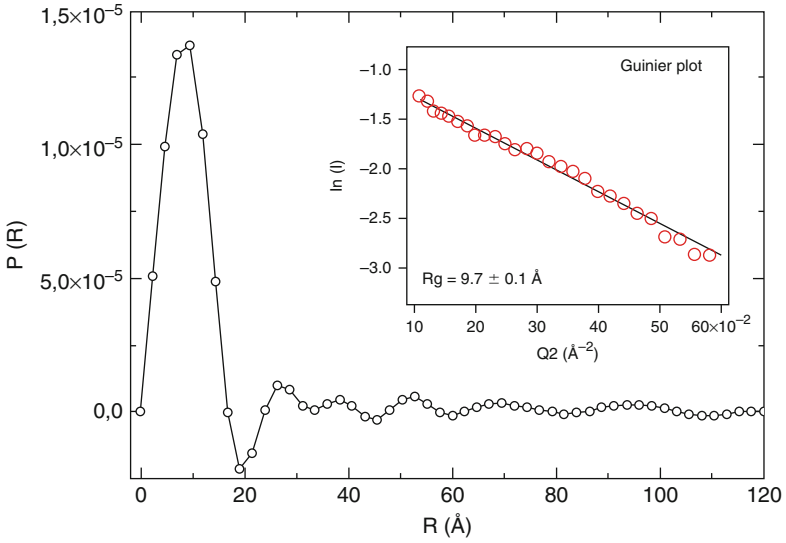

Fig. 6.22 Volume distribution of sizes obtained via indirect Fourier transform of the difference between the composite (MgD_2/ACF25) and scaffold scattering (ACF25). The upper size limit for the transform was 120 Å (12 nm). *Inset*: Guinier plot in the high-Q region ($Q = 0.12 - 0.25$) of the difference between the composite and scaffold scattering. Adapted with permission from [21]. Copyright 2012 American Chemical Society

The SANS data therefore seem to confirm that the nano infiltration of MgD_2 was successful, and that, in line with the theoretical calculations, the very small size measured for the confined MgD_2 is likely to be the reason for the observed destabilisation effect for this system.

6.6.4 $Li^{11}BD_4$-$Mg(^{11}BD_4)_2$

An eutectic mixture of $Li^{11}BD_4$-$Mg(^{11}BD_4)_2$ was synthesised with the isotopically enriched compounds using the method described by Bardaji et al. [22]. The nano-composite sample was prepared by melt infiltration of a 1:1 (molar ratio) composition of $Li^{11}BD_4$-$Mg(^{11}BD_4)_2$ into a carbon scaffold (named IRH33) [23].

To study the particle size, the effective infiltration and the morphological variation of the hydride particles, SANS was performed before and after desorption on both the bulk and the infiltrated sample, Fig. 6.23. The bulk $Li^{11}BD_4$-Mg

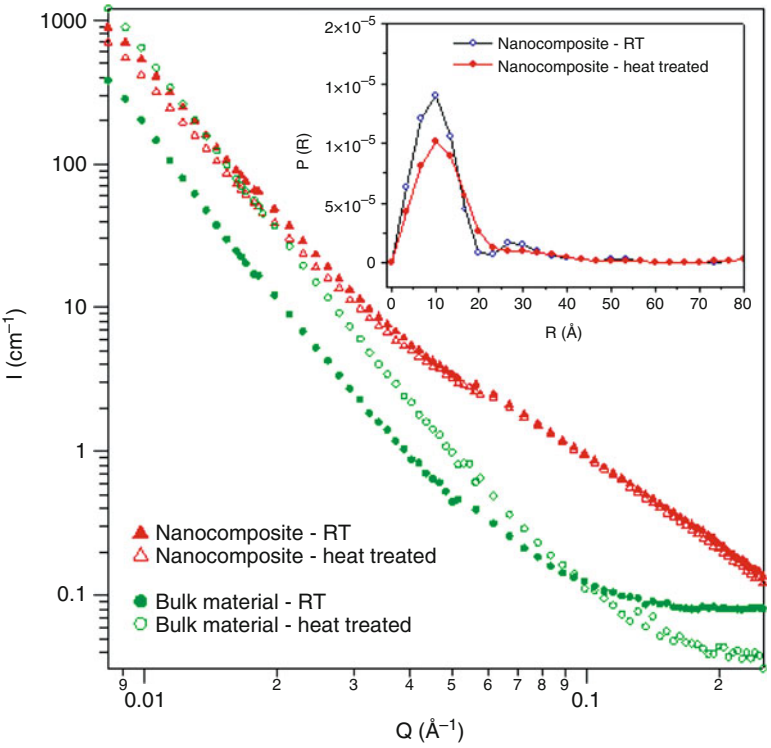

Fig. 6.23 SANS performed on the bulk $Li^{11}BD_4$-$Mg(^{11}BD_4)_2$ and the nano-composite $Li^{11}BD_4$-$Mg(^{11}BD_4)_2$/IRH33 before (*filled symbols*) and after heat treatment under vacuum (*open symbols*) up to 460 °C. *Inset*: Volume distribution calculated with indirect Fourier transform from SANS performed on the nano-composite $Li^{11}BD_4$-$Mg(^{11}BD_4)_2$ /IRH33 before (*filled symbols*) and after (*open symbols*) heat treatment. Adapted from [23] by permission of IOP Publishing. All rights reserved

($^{11}BD_4)_2$ shows large changes before and after heat treatment. Instead, the nano-confined material does not display significant changes, as confirmed by the indirect Fourier transform (Fig. 6.23, inset).

Once infiltrated, the hydrides mixture retains its small size domains during the decomposition, while there is a large variation in the particle size for the bulk under the same conditions. This is likely to ensure an extended interfacial contact between the product phases in the nano-composite, which could facilitate the desorption and justify the lowered decomposition temperature observed experimentally [23].

The Beaucage global scattering model [24, 25] was used to fit the SANS patterns of the scaffold (a) and the nano-composite $Li^{11}BD_4$-Mg($^{11}BD_4)_2$/IRH33 before (b) and after (c) heat treatment, Fig. 6.24.

The scaffold maintains the same features before and after heating, therefore Fig. 6.24 presents only the Beaucage fit before heat treatment (a). The scaffold is characterised by a wide range of pore sizes from 5 to 45 Å, with an average size of 8 Å in the lowest size range (a), and with near smooth pore surfaces ($\alpha = 3.8$). After infiltration (b), the $Li^{11}BD_4$-Mg($^{11}BD_4)_2$/IRH33 composite shows a rougher surface ($\alpha = 3.4$). The resulting particle size, $R_G = 15 \pm 0.5$Å, is slightly larger than the scaffold pore size at these length scales and seems to indicate an apparent expansion of the scaffold after infiltration, as found in other systems [26]. The change in the R_G value could also be due to some hydride particles on the surface of the carbon scaffold, but it is difficult to distinguish between these possibilities. After heat treatment (c), the $Li^{11}BD_4$-Mg($^{11}BD_4)_2$/IRH33 composite exhibit a rougher surface ($\alpha = 3.2$), at the same time seemingly keeping constant the particle size, with a comparable R_G. The mass fractal values, as extracted from the log-log plots at high-Q (not shown here), indicate that the nano-composite becomes slightly more compact after heat treatment (α was found to be 2.0 before heat treatment and 2.2 after). This could account for the very small variation detected in the amount of larger particles after heat treatment, as shown in the inset of Fig. 6.23.

6.7 SANS and SAXS

Small angle X-ray scattering (SAXS) is observed when electron density inhomogeneities of colloidal size exist in the sample. X-rays are attenuated more effectively by heavier atoms, where the scattering originates from the electrons around the nucleus and depends on the number of electrons and the electron distribution. For instance, the signal from Mg will be stronger compared to the carbon because it is a heavier atom, giving a higher scattering contrast. It follows that SANS and SAXS are based on the same theoretical principles, the main difference being the resulting contrast values $\Delta\rho^2$. For this reason neutron scattering and X-ray scattering are used as complimentary techniques.

SANS and SAXS performed at room temperature on bulk Mg($^{11}BD_4)_2$, nano-composite Mg($^{11}BD_4)_2$/AC1, and the scaffold alone are shown in Fig. 6.25. The general trend of the scattering is similar for the two techniques, as expected, because they probe the same structural components but with different contrasts.

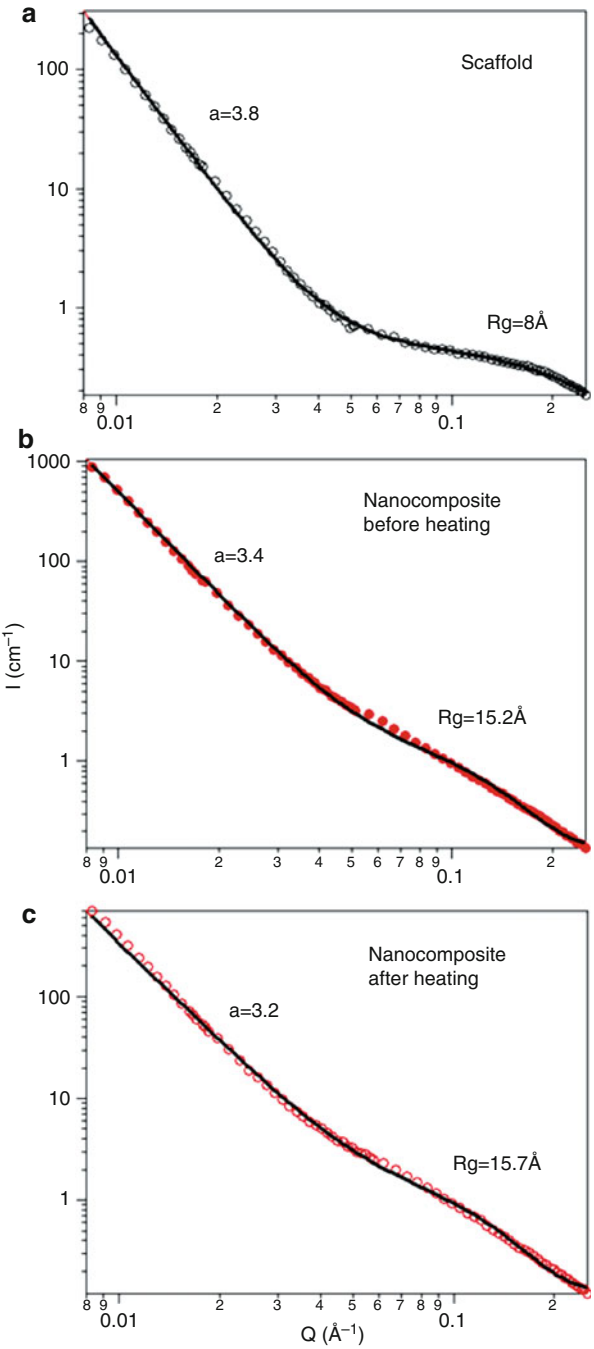

Fig. 6.24 Beaucage fits of SANS data for the scaffold (**a**) and the nano-composite $Li^{11}BD_4$-Mg $(^{11}BD_4)_2$/IRH33 before (**b**) and after (**c**) heat treatment. Adapted from [23] by permission of IOP Publishing. All rights reserved

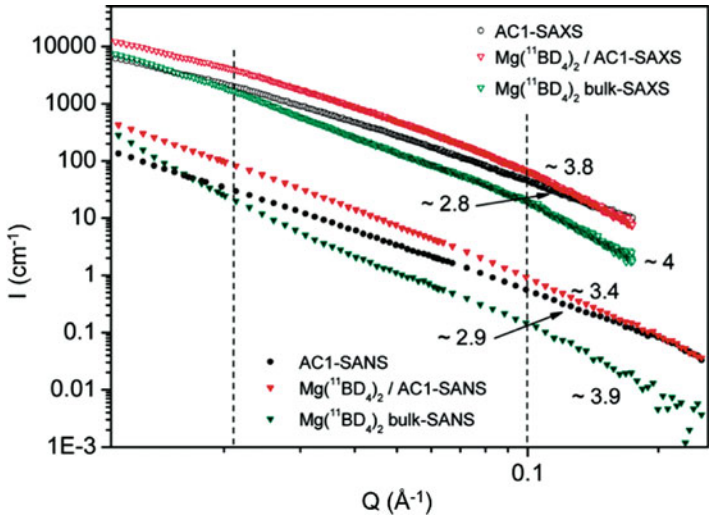

Fig. 6.25 SAXS (*open symbols*) and SANS (*filled symbols*) measurements performed at RT on AC1, $Mg(^{11}BD_4)_2$/AC1, and bulk $Mg(^{11}BD_4)_2$. Reprinted with permission from [26]. - Copyright 2010 American Chemical Society

The relative intensity between the three samples is also the same. For instance, the $Mg(^{11}BD_4)_2$/AC1 sample scatters more than the scaffold alone or the bulk. Furthermore, there is a crossover between the scaffold alone and the bulk just below $0.02\,\text{Å}^{-1}$ in both cases. Below this Q value the bulk sample shows a relatively steep rise of the SANS intensity, indicating a significant amount of large particles, whereas this effect is somewhat less clear with SAXS.

In the middle-Q range, as marked between the two dotted bars of Fig. 6.25 (around $0.02\,\text{Å}^{-1} < Q < 0.1\,\text{Å}^{-1}$), and in the high-$Q$ range (above $0.1\,\text{Å}^{-1}$), the slopes obtained with the two methods agree quite well. As demonstrated from the measured high-Q slopes ($\alpha = 2.8 - 2.9$), the scaffold alone has an open structure even at the smallest length scales. A slope beneath 3.0 in this Q range indicates a mass fractal behaviour, i.e., a system where the individual scatterers are small enough to be present in a large number even at this short scale.

On the other hand, when the scaffold is loaded with magnesium borohydride, the measured slope increases well above 3.0 (i.e., 3.8 for SAXS), showing the conversion to a surface fractal regime, where a majority of the pores have been filled. The value obtained with SANS is slightly smaller ($\alpha = 3.4$). This is ascribed to the different contrast by using SANS for the $Mg(^{11}BD_4)_2$ and AC1 with respect to the surrounding voids. The scattering length densities of $Mg(^{11}BD_4)_2$ and AC1 are $7.2 \times 10^{-6}\,\text{Å}^{-2}$ and ca. $3 \times 10^{-6}\,\text{Å}^{-2}$, respectively, so that the individual features of $Mg(^{11}BD_4)_2$ are enhanced with respect to the scaffold. Instead, with SAXS there is little difference in electron density between the two, thus they are more similar from the scattering point of view.

In addition to the information at room temperature, in the case of materials for hydrogen storage it is particularly interesting to investigate the scattering during

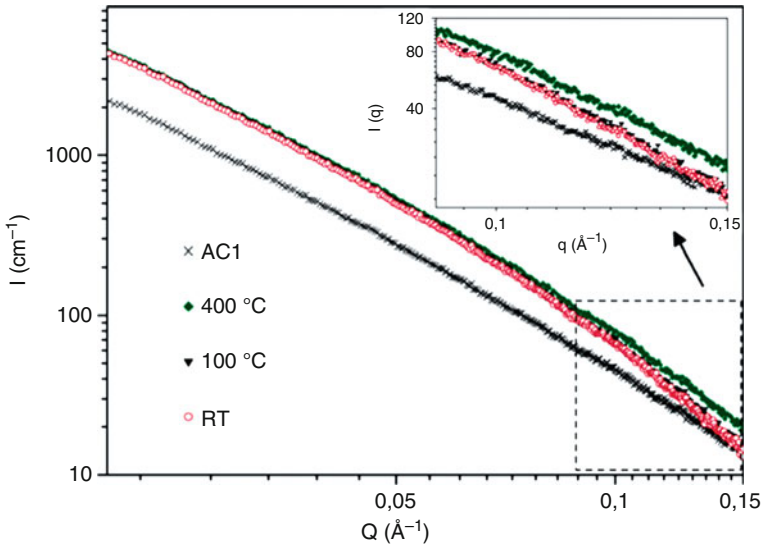

Fig. 6.26 SAXS on AC1 at RT and on Mg($^{11}BD_4$)$_2$/AC1 at RT, 100 °C, and 400 °C. Reprinted with permission from [26]. Copyright 2010 American Chemical Society

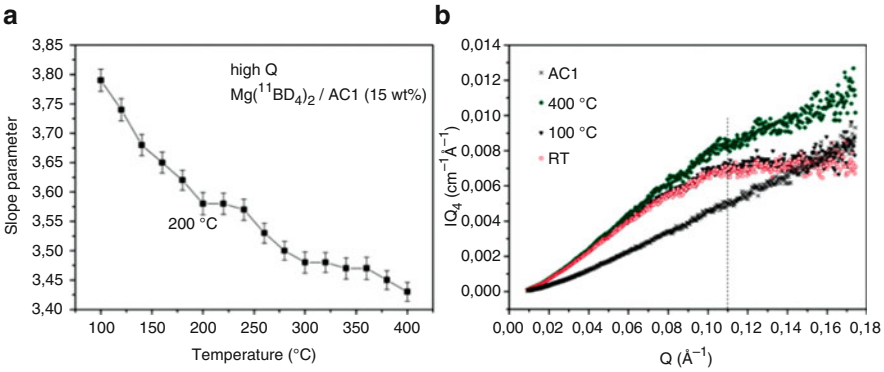

Fig. 6.27 (**a**) Values of slope parameter at high-Q for the in-situ SAXS on Mg($^{11}BD_4$)$_2$/AC1. (**b**) Porod plots of the AC1 scaffold and the Mg($^{11}BD_4$)$_2$/AC1 sample at selected temperatures. Reprinted with permission from [26]. Copyright 2010 American Chemical Society

in situ decomposition. In this particular case, SAXS has been performed on the AC1 scaffold and on the Mg($^{11}BD_4$)$_2$/AC1. Results from selected temperatures are shown in Fig. 6.26. In the low/middle-Q range, the curves follow a trend similar to that of the AC1 alone, and with almost no differences observed as the temperature was increased to 400 °C. This indicates that when infiltrated into the scaffold there is negligible reduction/modification in particle sizes with temperature. The only detectable changes are localised on the surface of the particles, corresponding to the high-Q region, as shown in the inset of Fig. 6.26.

A more detailed study of the change in the slope parameter at high-Q of selected SAXS data is presented in Fig. 6.27a. The decrease in the slope parameter α

from ~ 3.8 to ~ 3.4 suggests that heating makes the particles surface more rough. This change in the characteristics of the surface could be related to the release of hydrogen during heating. As discussed in the theory sections, at high-Q values the scattered intensity generally follows the Porod law. Analogously to what was mentioned for SANS, the constant of proportionality is then a measure of the specific surface in the system. Thus, for SAXS, in the Porod law $I(Q) = K(S/V)(1/Q^4)$, K is a function of the electron density difference between the particles and the surroundings. The plot of IQ^4 as a function of Q for the high-Q limit represents the changes occurring at the materials surface. The specific surface area for the sample in question will be directly proportional to the asymptotic level in the plot. Following this argument, Fig. 6.27b shows Porod plots of the AC1 scaffold as well as the $Mg(^{11}BD_4)_2$/AC1 sample at same selected temperatures considered in Fig. 6.26. For the AC1 scaffold, there is no sign of a plateau at high-Q, confirming that the internal pore surface of the scaffold is rough down to the smallest length scale accessible. Importantly, when the scaffold is loaded with magnesium borohydride, a plateau appears at Q values above $0.10\,\text{Å}^{-1}$, demonstrating a change occurring at the interface. This is a further demonstration that at these small length scales, corresponding to few nanometers, the surface of the pores has been smoothed out due to the presence of the hydride. No changes in specific surface can be observed upon heating from RT to 100 °C. At 400 °C, on the other hand, a significant modification has occurred, with IQ^4 increasing linearly with Q. This shows that the surfaces of the particles have now become rough, resulting in a significantly increased specific surface area with respect to the low-temperature situation. This would be consistent with a change in the surface of the infiltrated particles during the release of hydrogen and the decomposition of the hydride.

Comparison between SANS and SAXS performed on bulk powders of MgH_2 have also been made [27]. These investigations were performed in order to characterise structural changes in MgH_2 systems in relation with reaction kinetics. As shown in Fig. 6.28, it is clear how a different scattering is due to the different sensitivity towards hydrogen for the two methods.

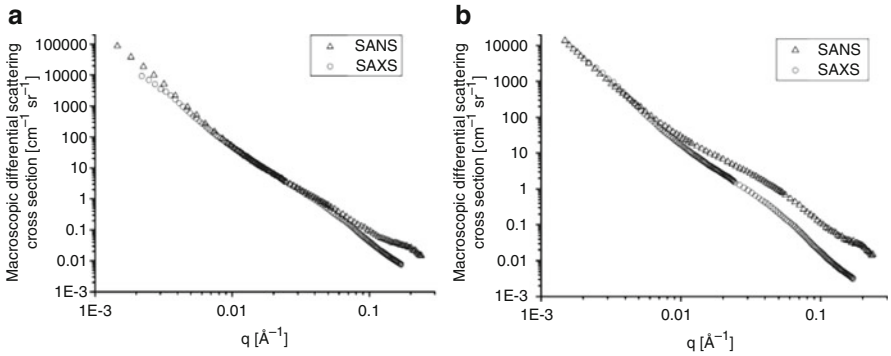

Fig. 6.28 Comparison of SANS and SAXS curves measured at SANS-2 (GeNF) and BW4 (HASYLAB) of MgH_x (**a**) with desorbed hydrogen ('MgH0') and (**b**) fully loaded with hydrogen ('MgH_2'). Reprinted from [27] with permission by IUCr

Acknowledgements Sabrina Sartori is grateful to the Feinberg Foundation Visiting Faculty Program at the Weizmann Institute of Science (Israel) and the University Graduate Center UNIK (Norway), for financial support during the preparation of this chapter.

References

1. D.P. Broom, Hydrogen Storage Materials (Springer, 2011)
2. C.-S. Tsao, Y. Liu, M. Li, Y. Zhang, J.B. Leao, H.-W. Chang, M.-S. Yu, S.-H. Chen, J. Phys. Chem. Lett. **1**, 1569 (2010)
3. C.-S. Tsao, M. Li, Y. Zhang, J.B. Leao, W.-S. Chiang, T.-Y. Chung, Y.-R. Tzeng, M.-S. Yu, S.-H. Chen, J. Phys. Chem. C **114**, 19895 (2010)
4. Z. Mileeva, D.K. Ross, D. Wilkinson, S.M. King, T.A. Ryan, H. Sharrock, Carbon **50**, 5062 (2012)
5. A. Guinier, G. Fournet, C.B. Walker, K.L. Yudowitch, Small-angle scattering of x-rays (Wiley, New York, 1955)
6. O. Glatter, O. Kratky, Small angle x-ray scattering, London: Academic Press (1982)
7. A.J. Allen, J. Am. Ceram. Soc. **88**, 1367 (2005)
8. J.S. Higgins, H.C. Benoit, Polymers and Neutron Scattering, Oxford University Press (1997)
9. O. Glatter, J. Appl. Crystallogr. **10**, 415 (1977)
10. I.D. Svergun, J. Appl. Crystallogr. **25**, 495 (1992)
11. J. Brunner-Popela, O. Glatter, J. Appl. Crystallogr. **30**, 431 (1997)
12. V.F. Sears, Neutron News **3**, 29 (1992)
13. P.J. Branton, P.G. Hall, J. Chem. Soc. Faraday Trans. **91**, 1139 (1995)
14. J.J. Vajo, G.L. Olson, Scr. Mater. **56**, 829 (2007)
15. Y. Zhang, W.S. Zhang, A.Q. Wang, L.X. Suna, M.Q. Fan, H.L. Chu, J.C. Sun, T. Zhang, Int. J. Hydrog. Energy **32**, 3976 (2007)
16. M. Fichtner, Z. Zhao-Karger, J. Hu, A. Roth, P. Weidler, Nanotechnology **20**, 204029 (2009)
17. S. Sartori, K.D. Knudsen, Z. Zhao-Karger, E. Gil Bardaij, M. Fichtner, B.C. Hauback, Nanotechnology **20**, 505702 (2009)
18. W. Lohstroh, A. Roth, H. Hahn, M. Fichtner, Chem. Phys. Chem. **11**, 789 (2010)
19. S. Sartori, K.D. Knudsen, A. Roth, M. Fichtner, B.C. Hauback, Nanosci. Nanotechnol. Lett. **4**, 173 (2012)
20. Z. Zhao-Karger, J. Hu, A. Roth, D. Wang, C. Kubel, W. Lohstroh, M. Fichtner, Chem. Commun. **46**, 8353 (2010)
21. P. Vajeeston, S. Sartori, P. Ravindran, K.D. Knudsen, B. Hauback, H. Fjellvaag, J. Phys. Chem. C **116**, 21139 (2012)
22. E.G. Bardaji, Z. Zhao-Karger, N. Boucharat, A. Nale, M.J. van Setten, W. Lohstroh, E. Roehm, M. Catti, M. Fichtner, J. Phys. Chem. C **115**, 6095 (2011)
23. S. Sartori, K.D. Knudsen, F.S. Hage, R.H. Heyn, E. Gil Bardaij, Z. Zhao-Karger, M. Fichtner, B.C. Hauback, Nanotechnology **23**, 255704 (2012)
24. G. Beaucage, J. Appl. Crystallogr. **28**, 717 (1995)
25. G. Beaucage, H.K. Kammler, S.E. Pratsinis, J. Appl. Crystallogr. **37**, 523 (2004)
26. S. Sartori, K.D. Knudsen, Z. Zhao-Karger, E. Gil Bardaji, J. Muller, M. Fichtner, B.C. Hauback, J. Phys. Chem. C **114**, 18785 (2010)
27. P.K. Pranzas, M. Dornheim, U. Bösenberg, J.R.A. Fernandez, G. Goerigk, S.V. Roth, R. Gehrke, A. Schreyer, J. Appl. Crystallogr. **40**, s383 (2007)

Chapter 7
Neutron Imaging

Axel Griesche, Mirco Große, and Burkhard Schillinger

Abstract Neutron imaging methods are appropriate to investigate hydrogen distributions in several metallic systems. The large total neutron cross section of hydrogen compared to those of elements or isotopes, respectively, in usual structural materials like steels or zirconium alloys allows the detection even of small amounts of hydrogen in such materials. The dependence of the total macroscopic neutron cross section of the sample or component on the hydrogen concentration can be determined experimentally by means of calibration specimens with known hydrogen concentrations. Such a calibration allows for a full quantitative determination of the local hydrogen concentration with a spatial resolution better than 20 μm. Because neutron radiography is fast and non-destructive, in situ investigations of time-dependent processes like hydrogen absorption and release or hydrogen bulk diffusion can be performed. This chapter gives an introduction into the main neutron imaging methods, radiography and tomography, and gives as examples results of neutron imaging investigations of hydrogen in different steels and in zirconium alloys, respectively.

Keywords Neutron imaging • Neutron radiography • Bragg-edge Radiography • Neutron tomography • Hydrogen • Diffusion • Steel • Zirconium alloy

A. Griesche (✉)
Federal Institute for Materials Research and Testing (BAM),
Unter den Eichen 87, 12205 Berlin, Germany
e-mail: axel.griesche@bam.de

M. Große
Karlsruhe Institute of Technology, Institute for Applied Materials,
Postfach 3640, 76021 Karlsruhe, Germany
e-mail: mirco.grosse@kit.edu

B. Schillinger
Heinz Maier-Leibnitz Zentrum (FRM II) and Department of Physics E21, Technische Universität München, James-Franck-Strasse 1, 85748 Garching, Germany
e-mail: burkhard.schillinger@frm2.tum.de

H. Fritzsche et al. (eds.), *Neutron Scattering and Other Nuclear Techniques for Hydrogen in Materials*, Neutron Scattering Applications and Techniques,
DOI 10.1007/978-3-319-22792-4_7

7.1 Introduction

In the last years high-resolution CCD camera systems for the detection of neutrons have been developed and applied for neutron imaging (neutron radiography and neutron tomography). In contrast to formerly used detection systems like films or image plates, they allow exact referencing and with it full quantitative analysis of neutron radiographs in combination with high spatial resolution of the projections.

Neutron imaging methods are particularly appropriate for the investigation of systems containing hydrogen. Hydrogen has a high total neutron cross section, much higher than structural materials like steels or zirconium alloys in which hydrogen uptake can affect the mechanical properties and with it the structural integrity of components. A calibration of the dependence of the neutron attenuation on the hydrogen concentration in the metal allows a fully quantitative analysis of neutron radiographs. The spatial hydrogen distributions can be determined with a resolution better than about 20 μm and an accuracy of up to several parts per million depending on the material system. Neutron tomography offers the possibility of a fully quantitative reconstruction of the 3D hydrogen distribution in a component. The illumination time to obtain a single neutron radiography frame is usually in the range between a couple of seconds and some minutes. Neutron radiography is much faster compared to other methods to investigate hydrogen in materials, and is non-destructive. The combination of these characteristics allows in situ investigations of hydrogen absorption, release, and redistribution.

Neutron imaging methods are widely used to study hydrogen-containing systems. There are many neutron imaging studies concerning, for instance, absorption and desorption of water in construction materials like wood, sandstone or limestone, or in plant roots and leaves. Other studies include the formation and distribution of water in fuel cells, and the distribution of oil in engines. Neutron imaging methods are well suited to investigate hydrogen in metals, too. Studies of hydrogen in steels and in zirconium alloys will be presented in this chapter. Additionally, there are many neutron radiography studies of hydrogen in hydrogen storage materials.

This chapter introduces neutron imaging and describes neutron radiography and tomography experiments which emphasize the resolution of these methods and applications investigating hydrogen in steels and in zirconium alloys.

7.2 Basics of Neutron Imaging

As uncharged particles, free neutrons interact only with the nuclei of other materials, and not with the electron shell. Interaction can occur as absorption by the target nucleus, as incoherent scattering on single nuclei, or coherent scattering processes on lattices, since neutrons, as sub-atomic particles, also possess a de Broglie wavelength. A measure of the probability of the interaction between a nucleus and a neutron is the microscopic cross section σ. The total microscopic neutron cross section σ_{total} is given by

Table 7.1 Microscopic neutron scattering lengths at a wavelength of 0.1798 nm ($E = 25.3$ meV) for hydrogen, iron, and zirconium according to [1]

Element/isotope	σ_c 10^{-24} m^2	σ_i 10^{-24} m^2	σ_a 10^{-24} m^2	σ_{tot} 10^{-24} m^2
H	1.757	80.26	0.333	82.02
^{1}H	1.758	80.27	0.333	82.03
^{2}H	5.59	2.05	0.0005	7.64
^{3}H	2.89	0.14	0	3.03
Fe	11.22	0.4	2.56	14.18
^{54}Fe	2.2	0	2.25	4.45
^{56}Fe	12.42	0	2.59	15.01
^{57}Fe	0.66	0.3	2.48	3.47
^{58}Fe	28	0	1.28	29.28
Zr	6.44	0.02	0.185	6.645
^{90}Zr	5.1	0	0.011	5.111
^{91}Zr	9.5	0.15	1.17	10.82
^{92}Zr	6.9	0	0.22	7.12
^{94}Zr	8.4	0	0.05	8.45
^{96}Zr	3.8	0	0.02	3.82

$$\sigma_{\text{tot}} = \sigma_a + \sigma_i + \sigma_c \tag{7.1}$$

where σ_a is the absorption cross section and σ_i and σ_c the incoherent and coherent scattering cross section, respectively. Examples of the microscopic cross sections for the isotopes of hydrogen, iron, and zirconium are given in Table 7.1.

For the case that the elastic scattering is low compared to the sum of absorption and inelastic scattering or if the nuclei are in solution the so-called total macroscopic neutron cross section Σ_{tot} is given by:

$$\Sigma_{\text{tot}} = \sum_i N_i \ \sigma_{\text{tot}_i} \tag{7.2}$$

where i is the index of the isotope and N_i the number density of the isotope.

For high-energy fission neutrons with energies of 1–2 MeV, the interaction is mostly incoherent scattering, dependent on the mass of the target nuclei. For neutrons thermalized in the reactor moderator, the wavelengths are in the range of 0.18 nm (25 meV). For cold neutrons thermalized in liquid-hydrogen vessels, also called "cold sources," the wavelengths range from 0.3 to beyond 1.2 nm (9 meV to less than 0.6 meV, respectively), which is well in the range of interatomic spacings in materials.

The probability for neutron absorption in a nucleus is inversely proportional to the square root of its kinetic energy, so this probability also rises with increasing wavelength. The absorption probability also depends on the inner structure of the nucleus. As a result, there may be huge differences in neutron absorption and scattering between isotopes of the same element. Figure 7.1 shows the mass attenuation coefficient for X-rays, gamma rays, fast and thermal neutrons versus the elements of the periodic table [2].

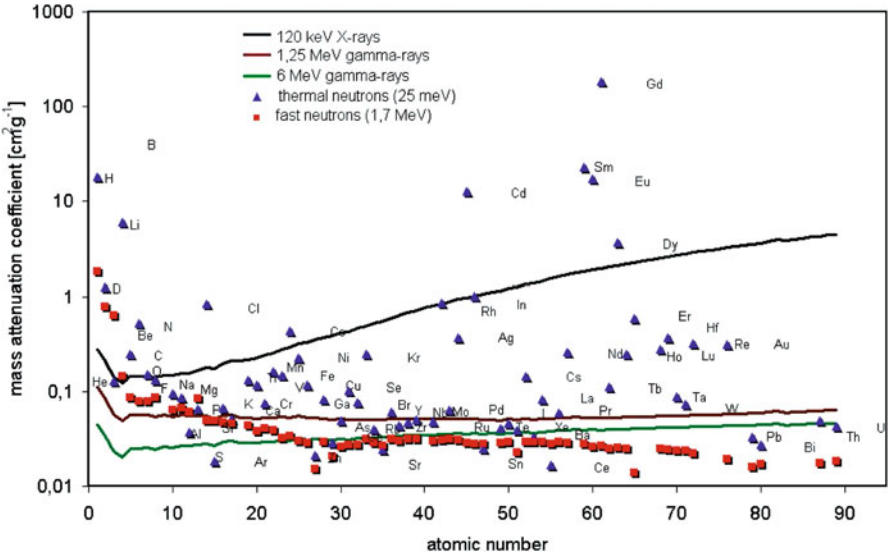

Fig. 7.1 The mass attenuation coefficient for X-rays, gamma rays, fast and thermal neutrons versus the elements of the periodic system [2]

The attenuation for X-rays and gamma rays at energies above the absorption edges of the element increases monotonically with the number of electrons in the shell of the elements. Likewise, the attenuation for fast fission neutrons follows a pattern, decreasing with the mass difference between neutrons and target nuclei. But the behavior of thermal neutrons does not follow an obvious pattern. The attenuation for neutrons is much lower than for X-rays for most metals widely used as structural materials, although two heavy metals, namely Cd and Gd, and the light elements H, Li, and B strongly attenuate neutrons.

The most advantageous property of neutron radiography is the high penetration power of thermal neutrons in metals combined with high sensitivity for hydrogen allowing, for example, detection of oil through the metal walls of a combustion engine.

If a neutron beam passes matter, its intensity is attenuated as follows:

$$I = I_0 \ \exp(-\Sigma_{\text{tot}} \ s) \tag{7.3}$$

with I and I_0 the intensity behind and before the sample, respectively, with length s through a material with total macroscopic neutron cross section Σ_{tot}. I_0 represents the intensity without sample. If the sample is mounted in the beam, the neutron beam has to pass through the sample, and the path length through air is reduced by the sample thickness:

$$I = I_0 \ \exp\left[-\left(\Sigma_{\text{tot}}^{\text{sample}} - \Sigma_{\text{tot}}^{\text{air}}\right) s^{\text{sample}}\right] \tag{7.4}$$

Typically, $\Sigma_{\text{tot}}^{\text{air}}$ is much smaller than $\Sigma_{\text{tot}}^{\text{sample}}$ and a background noise I_B has to be taken into account caused, for instance, by electronic noise of the system or by gamma radiation of the source or activated components. The total neutron cross section can be determined by

$$\Sigma_{\text{tot}}^{\text{sample}} = \frac{-\ln\left(\frac{I-I_B}{I_0-I_B}\right)}{s} \tag{7.5}$$

7.3 Neutron Radiography Experiments

Neutron radiography has been around since the first nuclear research reactors became available in the 1950s and 1960s, but the early installations were of limited usability.

Neutrons generated by the fission reaction in research reactors were moderated to thermal energies in the order of 30 meV, and exited the reactor vessel through an aluminum window and a consecutive flight tube. Compared to an X-ray tube, intensities are low, and the necessary aperture is very large which leads to high divergency of the emitted beam and thus low resolution images.

Figure 7.2 shows a sketch of the radiography facility of the 250 kW Mark TRIGA reactor at the Atominstitut Vienna [3] - a rather large conical flight tube with a short length between the aperture and the sample and detector, and a lift for

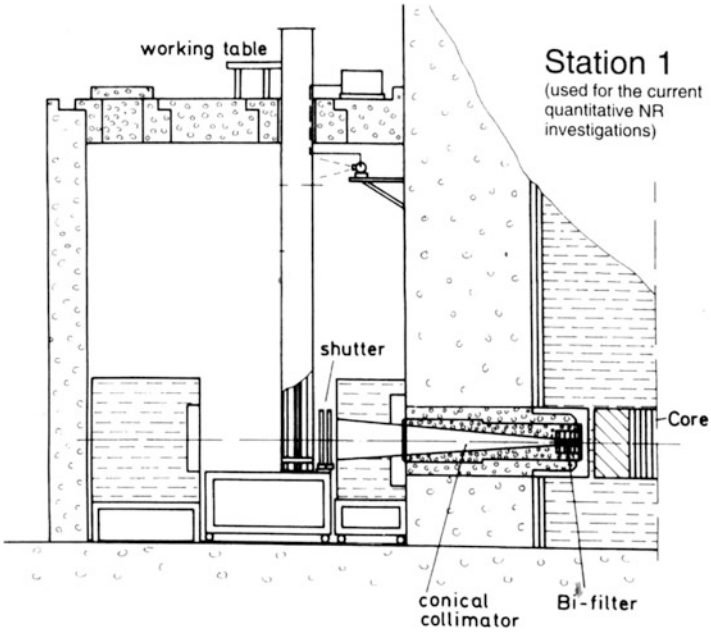

Fig. 7.2 Cross section of the radiography facility of the 250 kW Mark TRIGA reactor at the Atominstitut Vienna [3]

the sample and for film cassettes. As a detection system, film cassettes were used, where conventional the film was blackened either by light emitted from a neutron scintillation screen, or by conversion electrons emitted by a gadolinium converter foil. The sensitivity of the film was low, its response was non-linear, and exposures could hardly be repeated under identical conditions, so film neutron radiography had limited use.

7.3.1 Digital Radiography

A major leap happened with the advent of CCD cameras and personal computers that were powerful enough to perform digital image processing on large amounts of data. The combination of the new scientific cooled CCD cameras for long-time exposures and existing neutron scintillation screens allowed for building very sensitive neutron detectors that delivered digital, quantitative, and repeatable information.

From experiments at different neutron beamlines [4], it became clear that bad image quality was also caused by limited collimation. The newly gained sensitivity of the CCD detectors allowed sacrificing some intensity to increase beam quality, and optimizing future imaging facilities.

7.3.2 Beam Geometry: A Pinhole Camera

Compared to the focus of an X-ray tube, the aperture of a neutron radiography facility is rather large, and acts as a virtual area source (Fig. 7.3). The shadow of the sample is projected onto the detector by neutrons coming across the distance L from the aperture with diameter D. Their flight paths are not parallel but depend on their origin within the aperture cross section. Each point of the sample is projected to the detector in distances l_1 and thus smeared onto a circle of diameter d_1.

Image quality increases with larger L, but smaller D and l_1, so the aperture should be as small as possible and as far away as possible, which of course decreases the available intensity, while the sample should be placed as close as possible to the detector. The ratio of the aperture-to-sample distance vs. the aperture

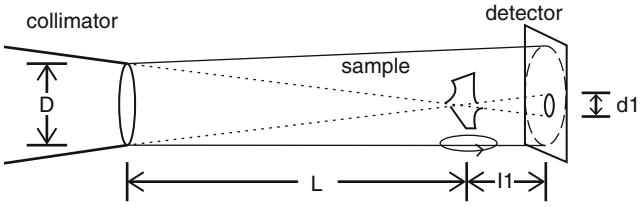

Fig. 7.3 Projection of a sample [5]

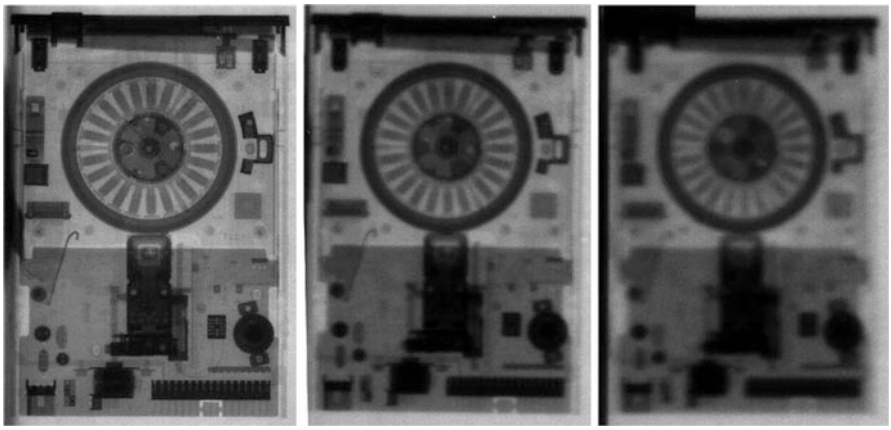

Fig. 7.4 (**a–c**) Floppy drive at $L/D = 71$ in 0, 10, and 20 cm distance to the detector [4]

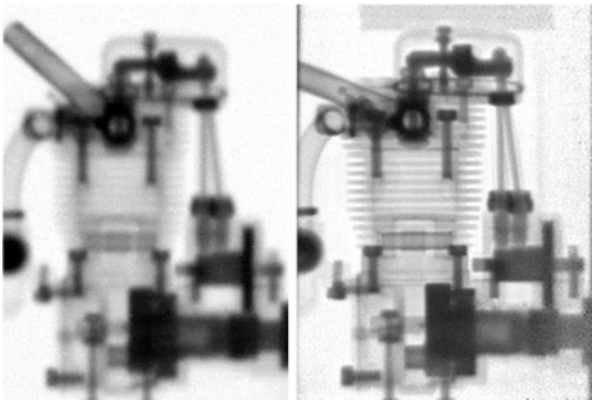

Fig. 7.5 (**a, b**) Toy engine at $L/D = 71$ and $L/D = 320$ [4]

diameter, L/D, is defined as the resolution parameter of an imaging installation, or simply the L/D ratio. Figure 7.4a shows the neutron radiography of a floppy drive in direct contact ($l_1 = 0$) with the detector at a facility with $L/D = 71$, Fig. 7.4b shows the same, only in distance of $l_1 = 10$ cm - which would be required to be able to rotate the sample for computed tomography.

For high quality measurements, collimation ratios beginning at $L/D = 300$ should be considered (Fig. 7.5).

Various kinds of resolutions are relevant for neutron imaging experiment:

- R_l - the lateral resolution (minimum discernible size or separation of features)
- R_c - the contrast resolution (minimal distinguishable difference in the neutron transmission)
- R_t - the time resolution (minimal time to detect a neutron radiograph in the quality needed)
- R_λ - the wavelength resolution (for wavelength dispersive radiography)

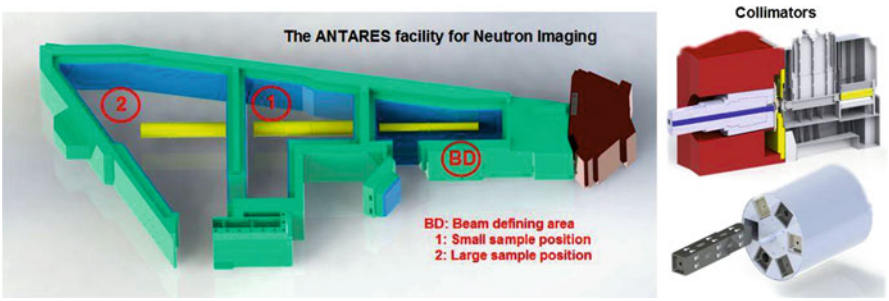

Fig. 7.6 ANTARES uses a separate shutter and a collimator selector drum [6]

These different kinds of resolution are not independent. For a source with given neutron flux, one kind of resolution can only be improved by decreasing at least one of the others. The contrast resolution can be estimated by

$$R_c = \frac{\sqrt{N - N_b}}{N + N_b} \tag{7.6}$$

N and N_b are the numbers of "real" (non-amplified) total and background counts detected, respectively. For $N \gg N_b$ it can be roughly estimated by $R_c \approx 1/\sqrt{N}$.

High lateral resolution comes at a cost because intensity is proportional to D^2/L^2. Different facilities can only be compared at equal L/D ratios. ANTARES at the FRM II reactor of Technische Universität München offers collimation ratios between 140 and 7100 that are achieved with six different collimators and two different sample positions (Fig. 7.6).

7.3.3 *Hardware Limit of the Resolution*

As uncharged particles, thermal neutrons can only be detected via a nuclear reaction. For scattering instruments, gas counters with Helium-3 and BF_3 gas are employed that either have no spatial resolution (counting tubes) or limited resolution (multiwire chambers with $\geq$1 mm spacing). For neutron imaging instruments, the most common detector is a camera-scintillation screen combination, either zinc sulfide combined with lithium fluoride (ZnS + LiF) or gadolinium oxysulfide (Gd_2SO_3). The reaction $^6Li(n,\alpha)^3H$ produces 4.7 MeV of kinetic energy in the reaction products, which have to be stopped in the scintillation screen, causing multiple scintillation. In a 100 µm thick ZnS + LiF screen, the average range of the reaction products is on the order of 50 µm, causing a light spot (including dispersion) of about 80 µm size for one detected neutron, with roughly 177,000 photons.

In a Gd_2SO_3 screen, which is also commonly used as X-ray detector, an absorbed neutron generates a conversion electron of 187 keV plus a gamma cascade up to

8 MeV. Scintillation is mostly done by the conversion electron, which has a range similar to the particles in the ZnS screen. The spatial resolution is thus limited by the size of the light spot that is generated by one detected neutron.

Strategies to overcome this limitation include thinned screens (in the order of 5–20 μm) and fast semiconductor detectors that detect single neutron events and calculate the center of the generated light or charge spot in real time [7].

The currently most intense neutron imaging facility ANTARES delivers a very high flux of 1×10^8 n/cm^{2}s at $L/D = 400$. With a thinned screen, the detection efficiency may be 10 %, so on a 10 μm × 10 μm pixel, only 10 neutrons are detected per second. The detection of hydrogen requires the statistics of several thousands of neutrons, which causes long exposure times, especially when computed tomography is required (see below).

7.3.4 Computed Tomography

The combination of projections of the sample taken at different angles allows a three-dimensional (3D) reconstruction of the spatial material distribution. The value of the voxel (basic volume element determining the resolution) corresponds with the total macroscopic neutron cross section. 3D quantitative imaging requires rotation of the sample and recording of multiple angular views. From these, the inner distribution of the attenuation coefficient within the sample can be reconstructed. A detailed description can be found in [8].

The mathematically exact case requires $\pi/2$ times as many angular projections as the detector has pixels in one line (or better, as pixels are required to record the sample). In reality, there are many other factors decreasing the image quality, so the best possible resolution is usually achieved with half that number, or less. Still, for the ideal case, a 1024×1024 pixel detector would require 1570 projections, causing long exposure times. Measurements with less than 400 images are usually not sufficient if high resolution is required. To be more exact, the required number of projections is determined by the maximum width (in pixels) of the sample projected on the detector, not the total detector width.

Several computer programs for the 3D sample reconstruction from the neutron tomography measurements are available. For the analysis and visualization of the 3D data, special programs have to be applied, too.

Examples for results of neutron tomography investigations will be given in Figures 7.13, 7.14, 7.20, and 7.26. The examples represent reconstructed 3D hydrogen distributions in steels or zirconium alloys, respectively.

7.3.5 Other Imaging Methods

Many other neutron imaging methods have been developed in the recent few years. They go beyond the scope of this book and are only briefly mentioned for completeness.

7.3.5.1 Stroboscopic Neutron Imaging

Even the most intense neutron sources do not deliver sufficient flux to allow for continuous short-time imaging in the millisecond range. But repetitive motion (e.g., a running engine) can be imaged by recording many identical time windows within consecutive cycles of the motion. An image intensifier is used as a fast shutter for a cooled CCD camera. The CCD camera records multiple exposures on its chip which are read out as one after sufficient accumulation of intensity. The same technique may be used to perform energy-dependent measurements on a pulsed time-of-flight source.

7.3.5.2 Bragg-Edge Neutron Imaging

In transmission radiography, attenuation may be caused by absorption or by scattering, which also removes neutrons from the direct beam. Coherent scattering on crystal lattices happens when the neutron wavelength is smaller or equal to the lattice plane spacing. If the wavelength is longer, coherent scattering is no longer possible, and the transmission increases steeply. This is the so-called Bragg edge. It depends on the crystal structure and allows for the discrimination of different structures in one energy scan. If stress and strain are present in the lattice, it becomes distorted, and the location of the Bragg edge shifts. High-resolution energy scans with neutrons even allow for the detection of stress and strain in a transmission image. Bragg edges typically exist in the region between 0.3 and 0.45 nm, which requires a cold neutron spectrum to examine.

7.3.5.3 Magnetic and Depolarization Measurement

As magnetic particles with a spin, neutrons can be polarized by supermirrors, Heusler crystals or He-3 cells (see chapter 5.2.2), and then analyzed after transmission through a magnetic sample. The rotation of the polarization allows for the measurement of magnetic fields. Depolarization of the beam shows magnetic domains and structures.

7.3.5.4 Linear Phase Contrast and Dark Field Imaging

A linear phase grating creates a coherent wave front that creates an interference pattern after a phase shift grating. An analyzer grating allows the detection of pure phase shift in an otherwise non-absorbing sample, or only scattered neutrons in dark field mode.

7.3.6 High-Resolution Neutron Imaging Facilities Worldwide

At the time of writing, less than a dozen high-resolution neutron imaging facilities exist worldwide which offer access for external users. Details to these facilities are available at their instrument web pages.

- ANTARES (Cold spectrum) at Heinz Maier-Leibnitz Zentrum (FRM II) of Technische Universität München, Germany
- CONRAD (Cold spectrum) at Helmholtz-Zentrum Berlin, Germany
- NEUTRA (Thermal spectrum) and ICON (Cold spectrum) at Paul Scherrer Institut, Switzerland
- NIF (Cold spectrum) at NIST Center for Neutron Research, USA
- DINGO (Thermal spectrum) at ANSTO, Australia
- RADEN (Cold spectrum, time-of-flight) at J-PARC, Japan
- MNRC, McClellan Nuclear Radiation Center (Thermal spectrum), USA

Other high-resolution neutron imaging facilities exist which do not offer or offer only limited access to external users. An example is the radiography facility at LLB Saclay (France). Additionally, the following high-resolution imaging facilities are under construction:

- SANRAD (Thermal spectrum) at NECSA, South Africa
- IMAT (Cold spectrum, time-of-flight) at ISIS, United Kingdom

Future projects:

- ODIN (Cold spectrum, time-of-flight) at ESS, Sweden
- VENUS (Cold spectrum, time-of-flight) at SNS, USA
- N.N. CARR (Cold spectrum and thermal spectrum) at CARR, China

Additionally, several low or medium resolution imaging facilities are in operation, for instance, in Brazil, Canada, Hungary, Poland, Indonesia, or South Korea. Other neutron sources offer the possibility of neutron radiography without having a beamline dedicated for imaging requests like high L/D or large, homogeneous illuminated neutron beam cross sections.

7.4 Investigation of Hydrogen in Steel and Iron

The phenomenon of hydrogen embrittlement (HE) is often accompanied by hydrogen-assisted cracking (HAC), when internal stresses are present [9, 10]. HE takes place if atomic hydrogen is generated, e.g., due to corrosion processes or during the process of arc welding, and if the hydrogen diffuses faster into the material than it recombines at the surface to H_2. The atomic hydrogen can even form metal hydrides in the base material as in Ti, which can cause HE. In any case, the lattice will be distorted, which blocks slip planes, yielding a brittle material with no or only weak ductility. Further, the atomic hydrogen can recombine at inner surfaces to form molecular hydrogen, which produces additional internal loads or even separation of the material, forming a pore [11]. In the case that such a material or component, respectively, experiences sufficiently high tensile loads, a delayed brittle fracture may occur, often referred to as cold cracking in welding. Here, the time delay is determined by the interaction of the stress field with the atomic hydrogen. Figure 7.7 shows a typical cold crack in a weldment.

In order to understand all aspects of the hydrogen embrittlement mechanism and to be able to predict the lifetime of a steel component in a corrosive environment, the knowledge of the hydrogen transport and trapping phenomena is important. The hydrogen transport and trapping phenomena play an important role in the HAC process because hydrogen can initiate cracks and can foster the crack propagation due to embrittlement [13].

There are several techniques available to investigate the hydrogen transport and the hydrogen trapping behavior in metallic materials. For instance, the permeation technique [14] allows measuring effective hydrogen diffusion coefficients as characteristic quantity for the transport behavior. Another example is the carrier gas hot extraction (CGHE) technique that measures the quantity of released hydrogen as a function of temperature [15]. This allows determining the type of sites in the

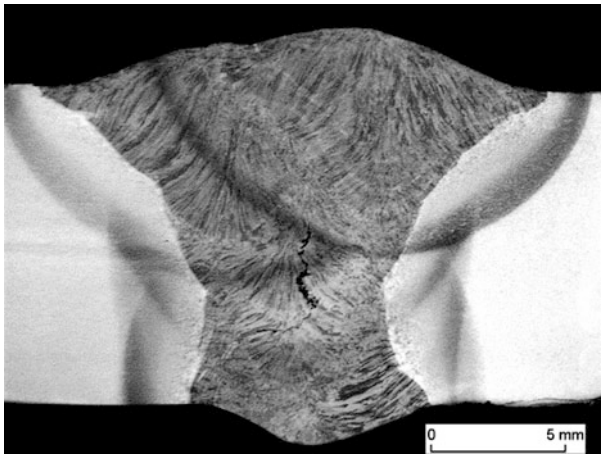

Fig. 7.7 Light microscopic image of a polished section of a multi-pass weldment in a high-strength steel. Hydrogen-induced cold cracks are clearly visible in the weld metal [12]

material where the atomic hydrogen was located, e.g., at dislocations or grain boundaries. All of these techniques are destructive and require a sample preparation. Further, the information is gained ex situ combined with a limited spatial and/or temporal resolution.

The advantage of neutron imaging techniques is the visualization and measurement of a certain element or isotope distribution, respectively, which is difficult or laborious to achieve with other techniques. Neutron radiography provides a new insight into bulk material, e.g. in iron and steels, due to the selective nature of interaction of neutrons with matter. In this chapter, two examples are given to highlight the power of neutron radiography in visualizing hydrogen distributions. Another example to show the power of the in situ neutron radiography technique compared to the CGHE technique is given in [16].

Importantly, the accuracy of quantitative neutron transmission imaging can be substantially decreased if highly scattering isotopes, like ^{1}H, are present in the sample. There are several solutions to overcome this potential problem. Either the experiments are performed at a large distance (>2 cm) between sample and detector or one applies numerical corrections to the images. The first solution yields a decrease of the spatial resolution due to the limited beam divergence and the second solution needs a priori information about the sample. A third solution is the use of a collimator placed between sample and detector [17]. The collimator removes the scattered neutrons from the transmitted beam without image distortions. In the experiments presented below, the sample–detector distance was always several centimeters at minimum.

For the sake of completeness, it should be mentioned that other nuclear characterization techniques have also been used to study hydrogen transport and to measure hydrogen distributions in iron and steels. Hanada used tritium autoradiography (TARG) to measure hydrogen around imperfections in tempered martensitic steel [18] and Katano used TARG to measure hydrogen distributions at inner interfaces in Cr-Mo high-strength steels [19]. Garet applied TARG to visualize tritium located at non-metallic inclusions in low alloy steels [20]. Although concentrations as small as 0.1 wt.ppm could be detected, the time resolution was in the order of some 10 min.

The following chapters present some examples in which simple neutron transmission radiography has been used to measure hydrogen diffusion and hydrogen distributions in iron and steels. In all experiments, a simple pinhole camera setup has been used.

7.4.1 In Situ Diffusion Measurements

As an example, the process of measuring a diffusion coefficient of hydrogen within a duplex stainless steel is described. Such Cr-Ni-Mo steel consists of a ferritic and an austenitic phase with a volume fraction of approximately 50 % of each phase. Both crystallographic phases differ largely in their hydrogen solubility and in their

hydrogen diffusion coefficient. Neutron radiography experiments [21, 22] have been performed in order to measure an overall effective hydrogen diffusion coefficient. This hydrogen transport process is called effusion and includes, besides the volume diffusion towards the surface, desorption of hydrogen gas from the surface into the surrounding atmosphere.

Small coupons with the dimensions $45 \times 5 \times 2$ mm^3 were cut from rolled plates and the surfaces were cleaned and polished. The hydrogen was introduced by electrochemical charging for 48 h in a 0.1 M H_2SO_4 solution. An amount of 0.25 g/L $NaAsO_2$ served as surface recombination inhibitor to increase the rate of inward diffusing atomic hydrogen. The current density at the cathode, i.e., at the coupons, was 10 mA/cm^2. The coupons were stored in liquid nitrogen to prevent hydrogen losses due to effusion of the highly mobile hydrogen. The coupons were mounted in an infrared furnace just before the measurement at the neutron imaging facility ANTARES of the research neutron source Heinz Maier-Leibnitz (FRM II) in Garching, Germany. Hydrogen-charged and hydrogen-free coupons were each packed in stacks of five in order to obtain a reasonable image contrast between the charged sample stack and the uncharged sample stack as reference (see Fig. 7.8).

The image acquisition parameters are given in Table 7.2.

The coupons were placed in a neutron-transparent infrared radiation furnace that allows measurement at elevated temperatures in order to determine the temperature dependence of the diffusion coefficient. The temperature was kept constant after rapid heating for the rest of the experiment. Hydrogen desorption during heating could not be avoided but the heating phase was very short compared to the

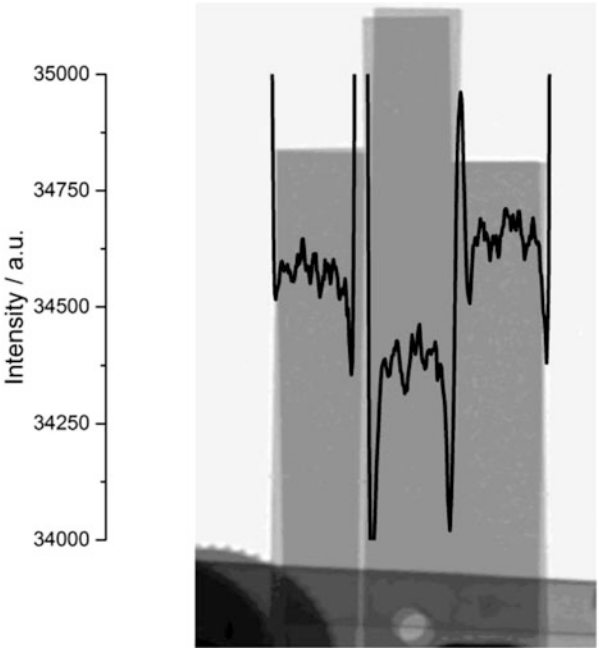

Fig. 7.8 Neutron transmission image and corresponding intensity profile of duplex stainless steel (EN 1.4462) coupons with hydrogen (*middle*) and without hydrogen (*left* and *right*)

Table 7.2 Experimental parameter of the radiography setup

Aperture L/D	260
Neutron flux	2.2×10^8 cm^{-2} s^{-1}
CCD camera	Andor DW436N-BV, 16-bit, 2k × 2k pixel
Scintillator	Cu and Ag doped ^{6}LiF + ZnS
Effective pixel size	70 µm
Distance sample–detector	80 mm
Exposure time	20 s

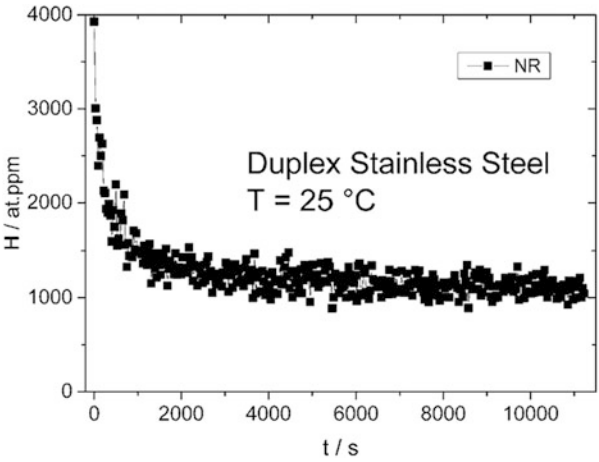

Fig. 7.9 Hydrogen concentration $c_H(t)$ as a function of time t at room temperature measured with neutron radiography (NR). The line is a guide-to-the-eye

isothermal phase and thus we neglected the loss of hydrogen during heating. The transmission images were recorded continuously during the isothermal heating phase. Later, the image quality was enhanced by standard correction procedures taking into account, for example, the dark current and electronic offset of the camera (dark field di) and the characteristics of the neutron beam (open beam ob): Corrected Image = (Original Image − di)/(ob − di). The quantitative analysis of the transmission images and the conversion of gray values into concentration units were done by an ImageJ script. Therefore, a mean gray value of a larger area was read out for each set of coupons (both the hydrogenous I_{sample} and the non-hydrogenous $I_{\text{reference}}$). Normalizing I_{sample} to $I_{\text{reference}}$ for each image yields $I(t)$ that can be converted into $c_H(t)$ with help of standards of known composition [23]. Figure 7.9 presents the result of such a hydrogen effusion experiment at room temperature and Fig. 7.10 presents a result from an experiment at 350 °C.

The hydrogen effusion takes place within about 5000 s. Then the hydrogen concentration remains more or less constant. The effused hydrogen stems mainly from the ferritic phase because the hydrogen diffusion coefficient of pure α-iron is known to be orders of magnitudes higher than the hydrogen diffusion coefficient in austenite. The hydrogen solubility in both phases behaves contrarily. The ferritic phase has only a very limited solubility for hydrogen whereas the austenitic phase

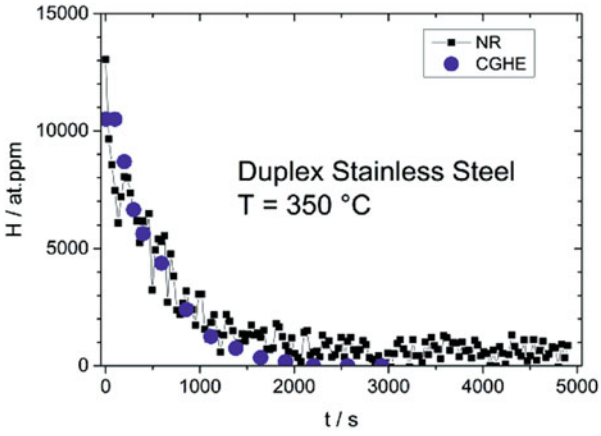

Fig. 7.10 Hydrogen concentration $c_H(t)$ as a function of time t at $T = 350$ °C measured with neutron radiography (NR) and carrier gas hot extraction (CGHE). The line is a guide-to-the-eye

can store much more hydrogen. Thus the remaining hydrogen with a concentration of 1000 at.ppm can be assigned to the austenitic phase and effuses at room temperature only very slowly.

The measured hydrogen flux out of the sample is not only determined by the phase-specific diffusion coefficients but also by the shape and spatial distribution of both phases. The relationship between the geometry and the phase-dependent diffusive hydrogen flux, the so-called tortuosity, is nicely described by Olden et al. [23].

The hydrogen effusion experiment at 350 °C started with a higher initial hydrogen concentration than that shown in Fig. 7.9, but shows the same trend of the curve. Here, the quickly diffusing hydrogen leaves the ferritic phase already in approximately 3000 s due to the higher temperature compared to the experiment presented in Fig. 7.9. Again, the austenitic phase still contains approximately 1000 at.ppm hydrogen. Figure 7.10 also shows the result of a CGHE experiment carried out with the same temperature-time-profile. Qualitatively, the decay of $c_H(t)$ of both measurements is very similar, which would yield a very similar effective diffusion coefficient. The base-line that is reached asymptotically by the decay of $c_H(t)$ is different. Whereas the neutron radiography experiment clearly measures the hydrogen in the sample, the CGHE measures only the hydrogen that is desorbed from the sample surface and transported by the carrier gas to the sensor.

7.4.2 In Situ Measurements of Hydrogen Distributions

The uptake of hydrogen in iron and steel consists of several steps [24]. The adsorption of hydrogen molecules at the surface is followed by the dissociation in atoms or ions, respectively, and the subsequent diffusion in the bulk. The diffusion rate of hydrogen through the surface can be limited by each of these steps. Limiting

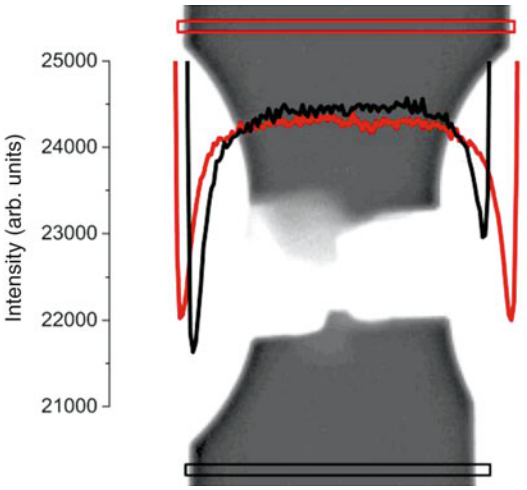

Fig. 7.11 Neutron transmission image of a part of an electrochemically hydrogen-charged tensile sample of lean duplex steel (EN 1.4162) after rupture. The *red* and *black lines* correspond to the intensity profiles measured in the respective rectangles. A 1 mm thick region at the right side of the lower sample part was cut off just before taking the image

the diffusion rate causes a certain concentration profile underneath the surface and with that the change of mechanical properties, including the ductility (local hydrogen embrittlement). Figure 7.11 shows an experiment in which we could measure such hydrogen concentration profiles below the surface. The edges of the tensile sample show black regions where obviously hydrogen is enriched (see symmetric red curve in Fig. 7.11). In order to prove that the observed black regions at the edges are not an artifact due to neutron reflection at the parallel surface (the sample thickness in the neutron flight direction is 5 mm), the right side of the lower sample part has been carefully cut off. The asymmetric intensity profile (see black curve in Fig. 7.11) shows clearly that hydrogen-enriched material was removed.

The massive uptake of hydrogen can cause another type of material damage called blistering. The nucleation and growth of hydrogen blisters in iron and steels has been investigated theoretically and experimentally in various studies (e.g., [25, 26]). The results show that atomic hydrogen can induce superabundant vacancies. In these vacancies and at other inner surfaces of the material, hydrogen atoms recombine to hydrogen molecules. This can yield micro cavities or pores, respectively. The pressure in the cavities or pores increases and cracks will be initiated when the stress induced by the hydrogen gas pressure is up to the cohesive strength of the material. Growing cracks directly below the surface can lift the material and blisters form at the surface that can often be seen by eye. For illustration, Fig. 7.12 shows a metallographic cross section of an iron sample with a blister.

The use of neutron imaging reveals here a new insight into the blistering mechanism [27]. Figure 7.13 shows an image of a neutron tomography reconstruction of a blistered iron sample. The tomography has been performed at the CONRAD instrument of the BER II research reactor at the Helmholtz-Zentrum Berlin in Germany. The parameters of the neutron tomography are given in Table 7.3.

The reconstruction of the radiographic projections directly visualizes the hydrogen distribution (see Fig. 7.13). Such images can be taken only if the hydrogen in

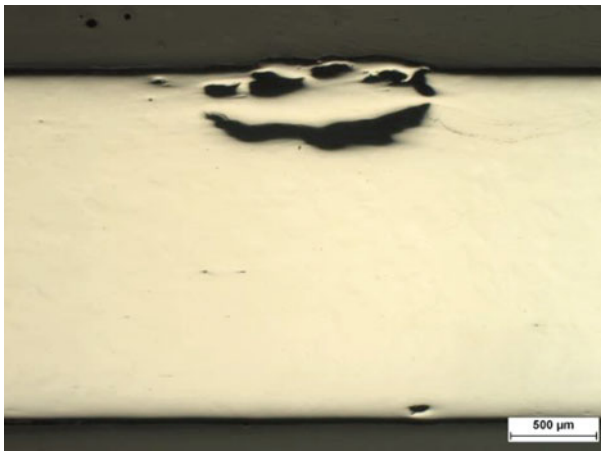

Fig. 7.12 Light microscopic image of a metallographic cross section of a blister. The sample material is technical iron (ARMCO™)

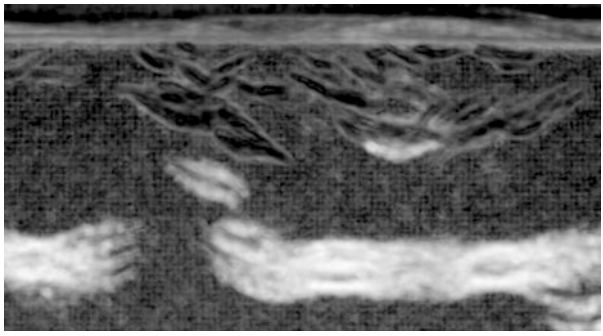

Fig. 7.13 Neutron tomography image taken from a 3D reconstruction of a blistered iron (ARMCO™) sample. Underneath the sample surface various cracks (*black*) are visible. Cracks further away from the surface are filled with hydrogen (*white*)

Table 7.3 Experimental parameter of the neutron tomography

Aperture L/D	500
Neutron flux	2×10^8 cm^{-2} s^{-1}
CCD camera	Andor DW436N-BV, 16-bit; 2k × 2k pixel
Scintillator	10 µm Gd_2O_2S
Effective pixel size	6.4 µm
Distance sample–detector	40 mm
Exposure time	80 s
Spatial resolution in reconstruction	20–30 µm

the sample is immobile because a neutron tomography usually lasts a couple of hours. This is the case for the molecular hydrogen that is trapped in closed cracks. The cracks that have a connection to the sample surface contain no hydrogen anymore. A detailed analysis of this experimental finding is given in [28].

The 3D reconstruction of a model of the sample contains not only the information about the hydrogen distribution but also the information about regions with no

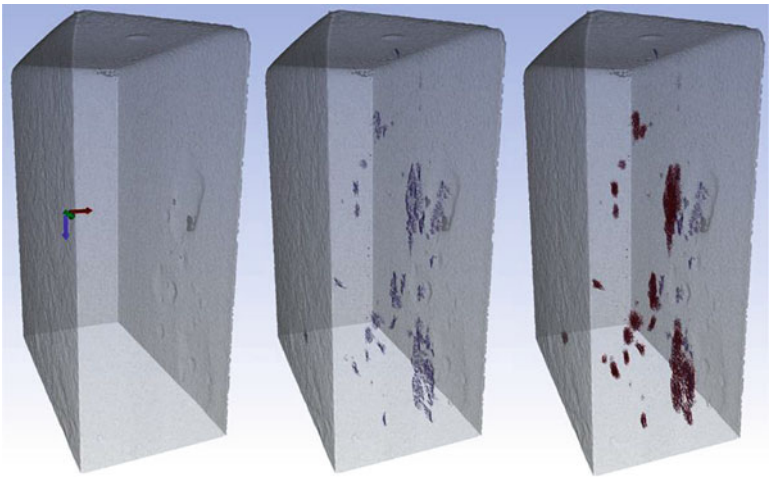

Fig. 7.14 Inclined view on the reconstructed 3D model of a part of a hydrogen-charged technical iron sample. The rendered surface with blisters is shown *left*. The crack distribution (*blue*) in the interior is presented in the *middle* and the additional hydrogen distribution (*red*) to the *right*. Most of the cracks are filled with hydrogen except some of the cracks underneath blisters. The sample depth is 5 mm

attenuation of the neutron intensity. Thus, the 3D model of a blistered iron sample can show the distribution of the blister on the sample surface, of the cracks in the volume and of the hydrogen (see Fig. 7.14).

7.5 Investigations of Hydrogen in Zirconium Alloys

7.5.1 Introduction

Hydrogen uptake by zirconium, its concentration, distribution and precipitation are of high safety relevance in nuclear technologies. Zirconium alloys are widely used in generation II and III reactors. Pressurized water reactors (PWRs) as well as boiling water reactors (BWR) use fuel cladding tubes made of zirconium alloys. In CANDU® reactors, the pressure tubes are made of Zr-2.5 % Nb. In Western European PWRs, the guide tube of the control rods is made from Zirconium alloys, too.

Zirconium alloys react with water during corrosion under operation conditions or with steam under transient accident conditions at high temperatures, respectively. The simplified reaction can be described as follows:

$$Zr + 2\,H_2O = ZrO_2 + 4H \tag{7.7}$$

An additional source of free hydrogen is radiolysis of water.

The hydrogen produced can recombine to H_2 molecules which are released to the environment or can be absorbed by the remaining metallic zirconium. This absorbed hydrogen results in a degradation of the mechanical properties, for instance, in embrittlement and reduction of the thermo-shock stability. The injection of a large amount of water into the damaged reactor core is the main measure to cool it down to terminate a nuclear accident. If the thermo-shock stability of the fuel cladding is insufficient, fragmentation of the fuel rod can occur, accompanied by fission product release and fuel relocation.

A couple of methods are applied to investigate the hydrogen–zirconium system. Most of them are destructive. Zirconium hydrides in cladding tubes have a length of 10–20 μm and a thickness on the order of 1 μm. They can be investigated metallographically. The integral amount of hydrogen in a sample can be determined by means of hot extraction. The sample is molten and the released hydrogen is measured. Other methods are, for instance, Transmission Electron Microscopy (TEM), X-ray diffraction (XRD), Cold Neutron Prompt Gamma Activation Analysis (CNPGAA [29]), or Elastic Recoil Detection Analysis ([30] and see chapter 10).

Neutron imaging methods are applied by several research groups to study hydrogen in zirconium alloys at different depth of analyses [31–38].

In this section, the application of neutron imaging methods is described and examples for the applications are given.

7.5.2 *Ex Situ and In Situ Investigations of the Hydrogen Uptake During Steam Oxidation of Zirconium Alloys*

Hydrogen has about one order of magnitude higher total microscopic neutron cross section than zirconium (see Table 7.1). As a consequence, the contrast between hydrided and hydrogen-free zirconium base alloys is high and even small hydrogen concentrations in zirconium alloys can be detected. The correlation between the total macroscopic neutron cross section and the hydrogen concentration has to be determined in order to measure the hydrogen concentration in zirconium alloys quantitatively by means of neutron imaging methods.

This correlation can be calculated if the following parameters are well known: The spectrum of the neutron source, the neutron wavelength dependence of the detection efficiency of the camera system, and the neutron wavelength dependence of the microscopic total neutron cross section of hydrogen. Whereas the neutron spectrum and the detector efficiency are instrumental parameters and can be determined separately, the total neutron cross section depends on the neutron wavelength as shown in Fig. 7.15 [39], on the bonding state of hydrogen in the material, and on the temperature.

If these parameters are not sufficiently known, the dependence of the total macroscopic neutron cross section on the hydrogen can be calibrated by means of samples with known hydrogen concentration. As an example, the calibration of this

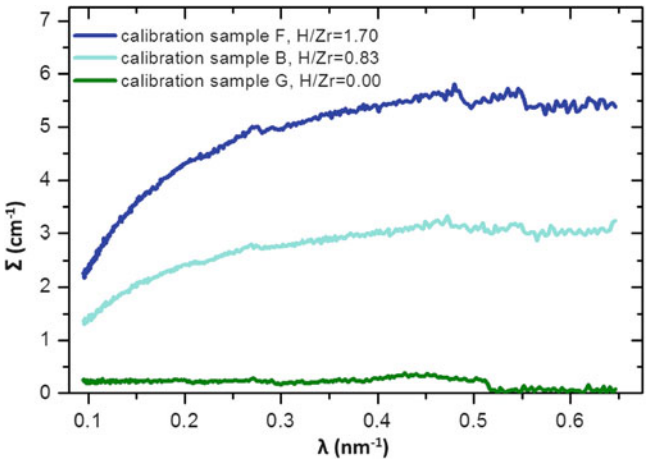

Fig. 7.15 Dependence of the total macroscopic neutron cross section of Zircaloy-4 specimens with different hydrogen concentration on the neutron wavelength measured at ENGIN-X, ISIS, UK [39]

correlation for the quantitative analysis of hydrogen in zirconium-based nuclear fuel cladding tubes will be described in the following paragraphs.

In order to produce calibration specimens, segments of as-received cladding tubes were annealed in a very clean Ar/H_2 atmosphere at various temperatures and hydrogen partial pressures. The dependence of the ratio between the number densities of hydrogen and zirconium $c_H = N_H/N_{Zr}$ in the metallic zirconium on temperature and hydrogen partial pressure in the gaseous environment is given according to Sieverts' law by:

$$c_H = \frac{N_H}{N_{Zr}} = \exp\left(\frac{\Delta S}{R} - \frac{\Delta H}{RT}\right) \cdot \sqrt{P_{H_2}} \tag{7.8}$$

R is the universal gas constant (7.314 J mol^{-1} K^{-1}) and P_{H_2} the hydrogen partial pressure in Pa.

The values of the enthalpy ΔS and in the entropy ΔH were determined for temperatures between 800 and 1500 °C in [40]. However, the amount of hydrogen absorbed can also be determined experimentally by measurement of the mass gain during annealing or by the reduction of the total gas pressure if the annealing is performed in an autoclave in stagnant atmosphere. A set of such calibration specimens was produced and applied for the calibration of the dependence of Σ_{total} on N_H/N_{Zr}. Figure 7.16 shows the neutron radiographs of the tube-shaped calibration specimens applied. Obviously, the neutron attenuation increases with increasing hydrogen concentration.

The horizontal intensity distribution of the specimen with $N_H/N_{Zr} = 0.99$ is given in Fig. 7.17. It is typical for tube-shaped specimen. The neutron path length through

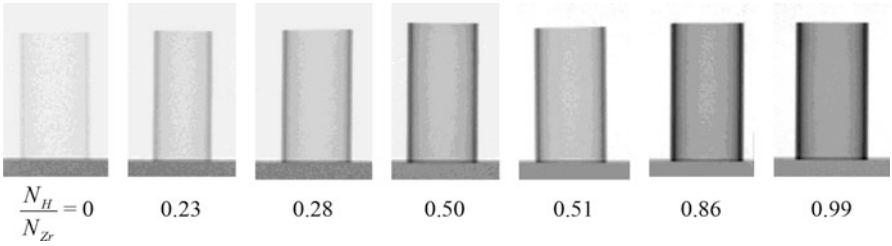

Fig. 7.16 Neutron radiographs of the calibration specimens taken at the CONRAD facility, Helmholtz-Zentrum Berlin, Germany

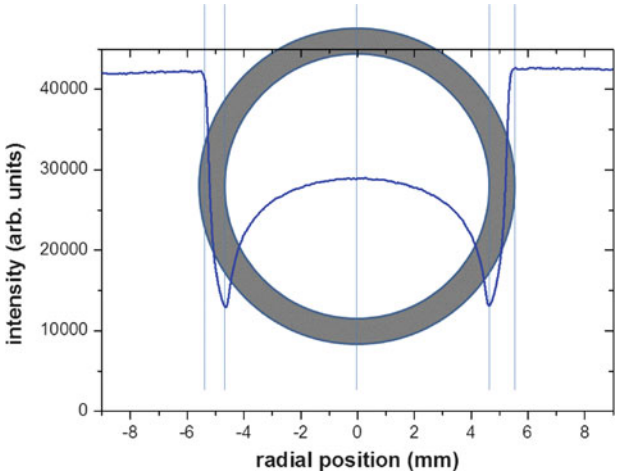

Fig. 7.17 Horizontal intensity distribution typical for tube-shaped specimens measured for the sample with $N_H/N_{Zr} = 0.99$

the tube wall s depends on the radial position x, as the scheme of the specimen cross section in Fig. 7.2 shows. The thin vertical lines illustrate the neutron path at the outer and inner surface and at the middle position of the tube. On the basis that the tube segment is oriented vertically and perpendicular to the neutron beam, s can be described by:

$$s = \Re\left(\sqrt{d_o^2 - (x - x_0)^2} \; - \; \sqrt{d_i^2 - (x - x_0)^2}\right) \tag{7.9}$$

$\Re$ is the real part of the complex term, x_0 is the middle position of the sample, and d_o and d_i the outer and inner diameter of the tube, respectively. On this basis, the intensity distribution can be fitted. However, such a fit is very sensitive to the correct alignment of the specimen. Less sensitive to the alignment is the intensity in the middle of the tube. Here, s equals twice the wall thickness in good approximation.

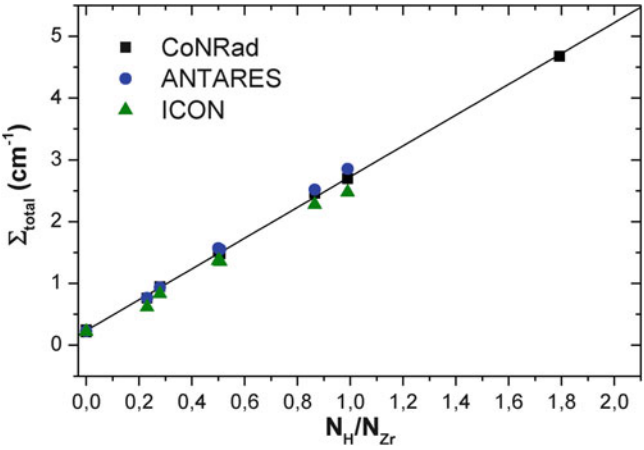

Fig. 7.18 Calibration of the dependence of the total macroscopic neutron cross section Σ_{total} on the number density ratio between hydrogen and zirconium N_H/N_{Zr} measured ex situ at the facilities ANTARES (FRM-II TU München, Germany), CONRAD (Helmholtz-Zentrum Berlin, Germany), and ICON (SINQ, PSI Villigen, Switzerland)

Figure 7.18 gives the calibration curve measured at ANTARES (FRM-2, TU München, Germany), CONRAD (Helmholtz Centre Berlin, Germany), and ICON (SINQ, Paul Scherrer Institut Villigen, Switzerland). Even the differences between the measurements at the different facilities are small; the calibration measurements should be done during each beam time to exclude effects of different neutron spectrum and detector setup. Further details about the ex situ calibration and about the influence of the neutron spectrum and detection system are given in [36].

A similar procedure was followed to calibrate the effect of the oxide layer formed at the sample's surface. Specimens were oxidized in Ar/O_2 atmosphere and the measured total macroscopic neutron cross sections were correlated with the oxide layer thickness measured metallographically after the neutron radiography experiments. Even though the effect of the oxide layer is much smaller than the effect of the hydrogen absorption; the attenuation by the oxide layer has to be corrected for a quantitative analysis.

For in situ investigations at temperatures above 700 °C such prefabricated calibration specimens cannot be applied because the hydrogen would be released to the gas atmosphere according to Eq. 7.8. Therefore, the cladding tube segments have to be hydrogen loaded in situ, too [41]. Figure 7.19 gives an example measured at the ICON facility (SINQ, PSI Villigen, Switzerland). Hydrogen partial pressures of 3.85, 7.41, and 13.79 kPa, respectively, were applied for each temperature. The number density ratio N_H/N_{Zr} was calculated according to Eq. 7.8 with the values determined in [40]. From the scattering of the calibration data, it can be derived that the accuracy of the quantitative hydrogen determination in the cladding tubes is about 50 wt.ppm for ex situ measurements and about 30 wt.ppm for in situ experiments, respectively. The reason for the higher accuracy in the in situ

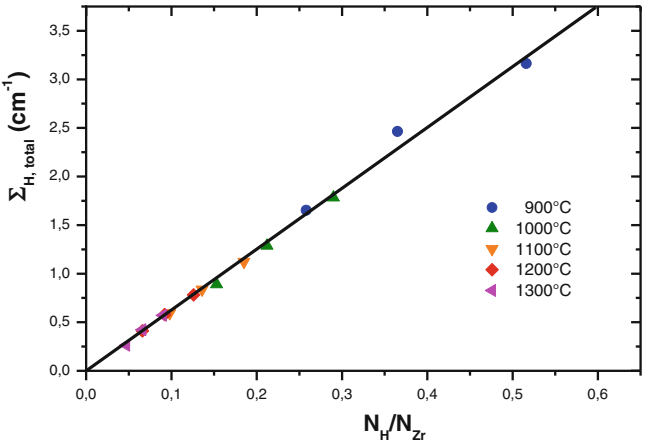

Fig. 7.19 Calibration of the dependence of the total macroscopic neutron cross section Σ_{total} on the number density ratio between hydrogen and zirconium N_H/N_{Zr} measured in situ at the ICON facility at various temperatures and hydrogen partial pressures [41]

experiment than in the ex situ measurements is the ability to use the initial state of the sample as reference, whereas in ex situ measurements an additional specimen has to be used for the hydrogen-free state. Further information about the in situ calibration at temperatures between 900 and 1300 °C are given in [41, 42].

In the tomography analysis, the so-called CT value is calculated for each volume element called "the voxel." This CT value corresponds to the attenuation coefficient or, in terms of neutron physics, to the total macroscopic neutron cross section. The set of calibration specimens was used to verify the quantitative reconstruction [43]. Figure 7.20 gives a horizontal slice of the reconstructed data of the calibration specimen assembly. The results are satisfying at least for the specimens with a H/Zr number density ratio of about 0.5 and below. For the nearly completely hydrided sample with a number density ratio of about 1.8, the CT number was determined too low.

Taking into account that in some projections the neutron path length through the tube wall is much higher than the wall thickness, multiple scattering and beam hardening (the change between the initial neutron spectrum and the spectrum behind the sample due to stronger attenuation of neutrons with larger wavelength) can be the reason for the discrepancy in the exact value of the hydrogen concentration and with it in the exact total macroscopic neutron cross section.

Neutron radiography was applied to investigate the hydrogen uptake during steam oxidation of various commonly used cladding materials in the temperature range between 600 and 1400 °C [44]. Figure 7.21 gives an example of the hydrogen concentration in various cladding alloys after isothermal oxidation in steam at temperatures between 600 and 1100 °C. The oxidation times are different for the different temperatures but are the same for all materials. The oxidation times were chosen to reach comparable oxide layer thicknesses at all temperatures. Whereas

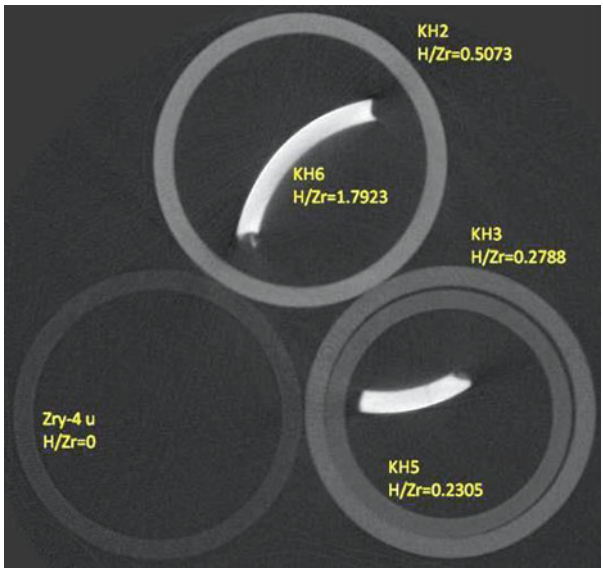

Fig. 7.20 Horizontal slice of the 3D reconstruction of the calibration specimen assembly

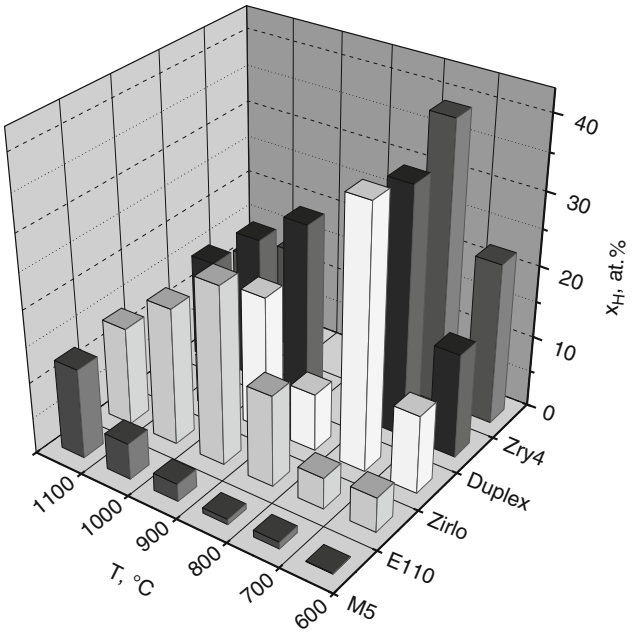

Fig. 7.21 Hydrogen concentrations in various commonly used cladding alloys after isothermal oxidation in steam

for the Zr-1.0 % Nb alloy M5® the concentration of absorbed hydrogen increases monotonically with increasing temperature, the other materials show local maxima and minima in the temperature dependence of hydrogen uptake.

The reason for this is the so-called breakaway effect. At about 1000 °C, a phase transition between monoclinic (low temperature) and tetragonal (high temperature) structure occurs in the zirconium oxide. However, the oxide starts to grow in tetragonal structure even at temperatures below 1000 °C. At the beginning of the reaction, the oxide growth starts with sub-stoichiometric composition. The oxide grains are small and coherence stresses to the metallic zirconium are formed. These three effects decrease the tetragonal–monoclinic phase transition temperature.

When the oxide layer reaches a certain thickness, a martensitic transformation to the monoclinic structure occurs. The consequence of the crack structure formed by this phase transformation is the so-called hydrogen pump effect: Steam penetrates into open cracks in the oxide layer and reaches the oxide/metal interface. Here the steam reacts and free hydrogen becomes enriched in the crack. According to Eq. 7.8 a higher hydrogen partial pressure results in higher hydrogen absorption. This reduces the total gas pressure in the crack. New steam is sucked into the crack and the described process starts again. In [45], a detailed description of the process is given. The appearance of the crack structure and the temperature range, in which the breakaway effect occurs, differ for the various zirconium-based cladding materials, explaining the different temperature dependence of the alloys.

The effect can clearly be observed in in situ neutron radiography experiments as well [42]. Figure 7.22 shows radiographs of an in situ steam oxidation experiment at 1000 °C using a Zry-4 specimen. The images are referenced to the initial state and thus, only the hydrogen is visible in the images. The corresponding development of the hydrogen concentration is given in Fig. 7.23. At first, a rapid hydrogen uptake occurs within seconds to a concentration of about 200 wt.ppm. In the next 1800 s the concentration keeps more or less constant. Then the crack structure in the oxide is formed and the hydrogen concentration increases to a maximal value of about 1400 wt.ppm. Though not presented in images of Fig. 7.22, later, the hydrogen concentration decreases because the metallic zirconium is consumed by the oxidation. The completely oxidized specimen does not contain a significant amount of hydrogen as shown in Fig. 7.23.

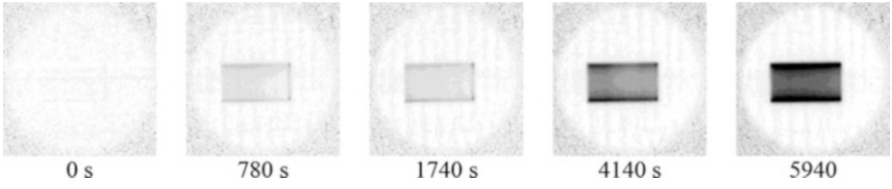

Fig. 7.22 In situ neutron radiographs of a Zry-4 specimen oxidized in steam at 1000 °C

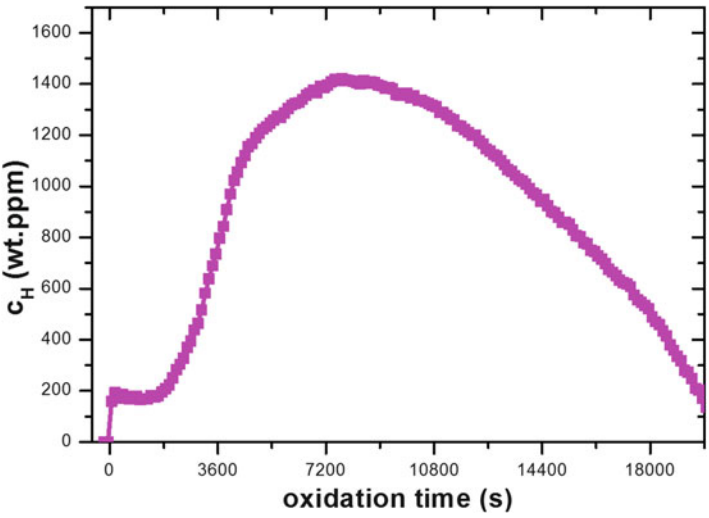

Fig. 7.23 Development of the hydrogen concentration in the Zry-4 sample oxidized at 1000 °C in steam

7.5.3 Inspection of Samples from Large-Scale Accident Simulation Tests

In the framework of the QUENCH program at the Karlsruhe Institute of Technology, design basis loss of coolant accidents (LOCAs) and beyond design basis severe accidents were simulated experimentally at fuel rod bundle scale. In the framework of the post-test examinations, neutron imaging was applied to analyze the hydrogen uptake of the claddings.

In the subprogram QUENCH-ACM (ACM = advanced cladding materials), different fuel rod bundle simulators with the various cladding alloys used in Europe and the USA were tested with the same temperature scenario [46]. Corner rods were withdrawn during and after the tests, allowing the analysis of the material behavior in different accident stages. These corner rods were used to determine the hydrogen uptake of the claddings during the various stages. Figure 7.24 compares the axial hydrogen distribution determined for the different materials. The Russian cladding tube material E110, a Zr-1.0 % Nb alloy produced at a process different to M5®, shows a more than five times higher hydrogen uptake than in the other alloys. The reason is the much higher susceptibility for breakaway (see Sect. 7.5.1) than the other materials investigated [47]. These results led to changing of the production process for the material. First results obtained for the new E110g alloy are promising. The breakaway susceptibility is strongly reduced.

In another subprogram called QUENCH-LOCA, the hydrogen uptake during design basis LOCAs is simulated [48]. The coolability of the reactor core during such an accident has to be proved. According to the international regulation rules,

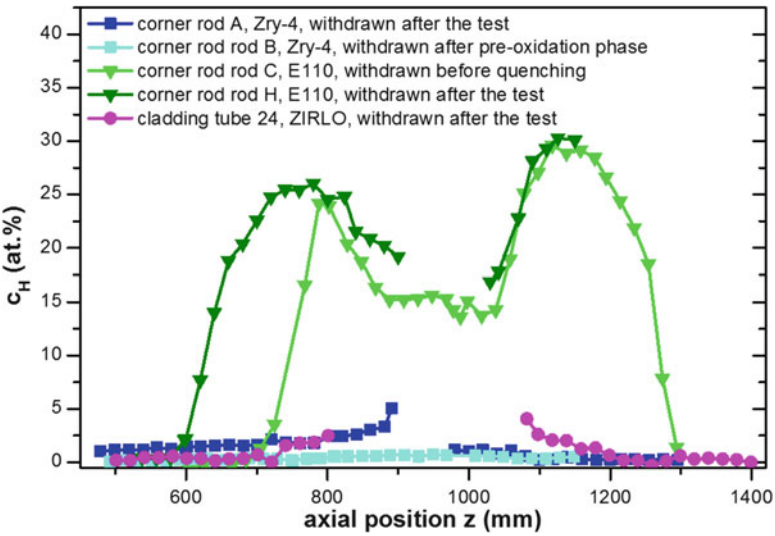

Fig. 7.24 Axial distribution of the hydrogen concentration in different cladding materials after similar accident scenarios

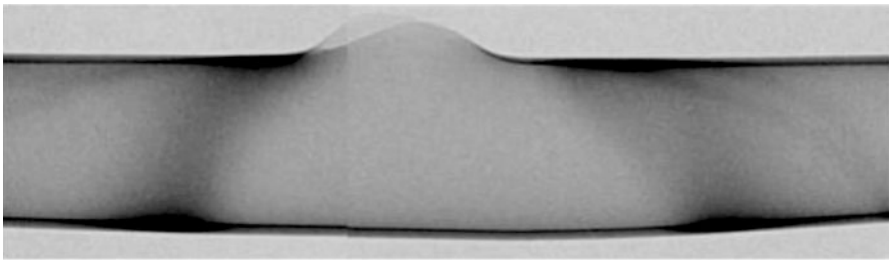

Fig. 7.25 Neutron radiograph of the burst region of the cladding tube #01 of the QUENCH-L0 test. The darker hydrogen-enriched areas are clearly visible

the coolability is given if the temperatures do not exceed 1200 °C and the oxidation degree of the cladding is limited. The second requirement is quantified by the so-called equivalent cladding reacted (ECR) criteria. The international rules postulate that ECR has to be below 17 %. Below this ECR the remaining cladding ductility keeps high enough to endure the thermo-shock during emergency water quenching. Actual results have shown that the hydrogen uptake reduces the cladding ductility as well, and the regulations will be changed in respect to this fact.

In order to prove the coolability of reactor cores during LOCA relevant for German nuclear power reactors, it was simulated in the QUENCH facility. After the test, the claddings were investigated by means of neutron imaging [49]. As an example, Fig. 7.25 shows the neutron radiograph of a cladding applied in the QUENCH-L0 test. The dark hydrogen-enriched areas are clearly visible. During LOCA, the inner pressure results in a plastic deformation of the cladding tube

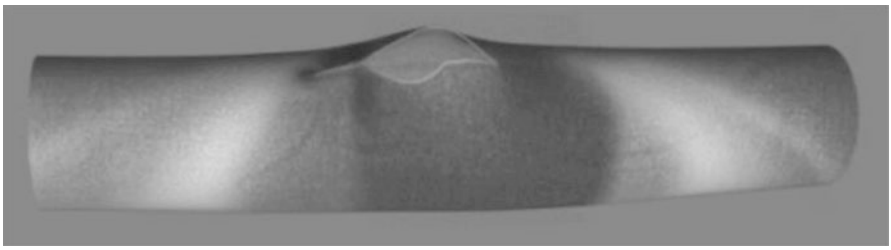

Fig. 7.26 3D reconstruction of the hydrogen distribution in the cladding tube #01 of the QUENCH-L0 test. The brighter the position, the higher the hydrogen concentration

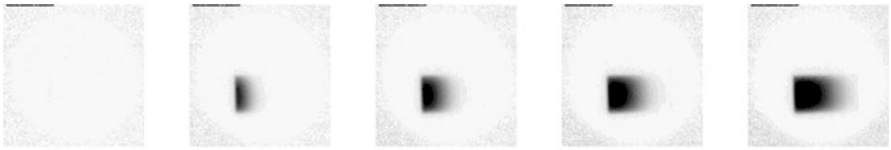

Fig. 7.27 Image sequence of the hydrogen diffusion into Zry-4 at 1173 K, measured at ICON

(ballooning), which is connected with a reduction of the tube wall thickness. Together with the fact that front and back side of the sample are projected, it is not possible to obtain quantitative results from one radiograph alone. Therefore, neutron tomography has to be applied quantitatively to determine the hydrogen distribution in the cladding.

Figure 7.26 shows a 3D reconstruction of this tube region. The gray value corresponds to the total macroscopic neutron cross section. It means that hydrogen-enriched areas are brighter than the sample regions without hydrogen. Using the calibration between total macroscopic cross section and hydrogen concentration, the 3D hydrogen distribution can be determined fully quantitatively.

7.5.4 In Situ Investigations of the Hydrogen Diffusion in Zircaloy-4

The hydrogen diffusion in the cubic high temperature phase of Zircaloy-4 was investigated at temperatures between 900 and 1300 °C by means of in situ neutron radiography [50]. For the experiments, solid cylinders made of Zircaloy-4 were oxidized. The oxide layer prevents the hydrogen uptake. At one base plane, the oxide layer was removed by mechanical grinding and polishing. Only through this plane can hydrogen penetrate into the sample. The in situ experiments were performed in Ar/H_2 atmospheres. Figure 7.27 gives some examples of the

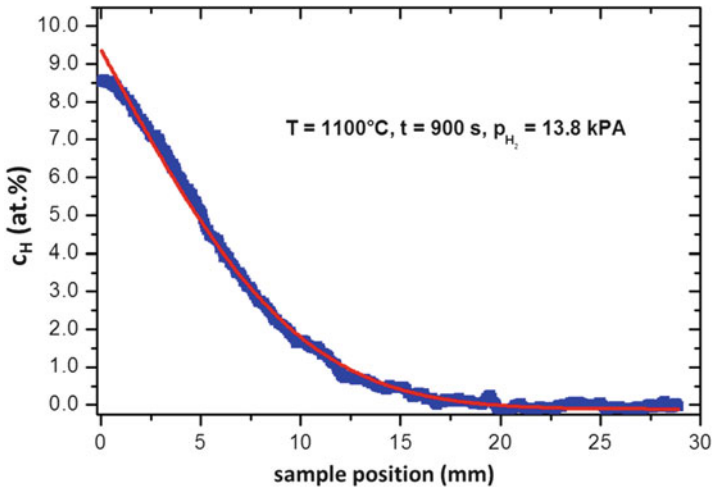

Fig. 7.28 Axial distribution of the hydrogen concentration in the solid Zircaloy-4 cylinder after 900 s at 1100 °C

radiographs of the cylinders referred to the initial state. The propagation of the hydrogen penetration into the material is clearly visible. The axial dependence of the neutron transmission of the total macroscopic neutron cross section and of the hydrogen concentration can be determined from the axial changes of the pixel counts for all of the images. An example is given in Fig. 7.27.

The data can be fitted by the analytical diffusion equation for a semi-infinite system with constant concentration at one side ($c(x=0)=c_0=\text{constant}$) and ($c(x=\infty)=0$) (Fig. 7.28):

$$c(x,t) = c_0\left(1 - \text{erf}\left(\frac{x}{2\sqrt{Dt}}\right)\right) \tag{7.10}$$

c is the hydrogen concentration, x the distance to the surface where the hydrogen penetrates, D the diffusion coefficient, and t the time. From the Arrhenius-plot of the fitted diffusion coefficient given in Fig. 7.29 the temperature correlation including the activation energy of the hydrogen diffusion in Zircaloy-4 can be calculated. The following correlation was determined:

$$D_\text{H} = 0.023\,\frac{\text{cm}^2}{\text{s}}\exp\left(\frac{48.3\frac{\text{kJ}}{\text{mol K}}}{RT}\right) \tag{7.11}$$

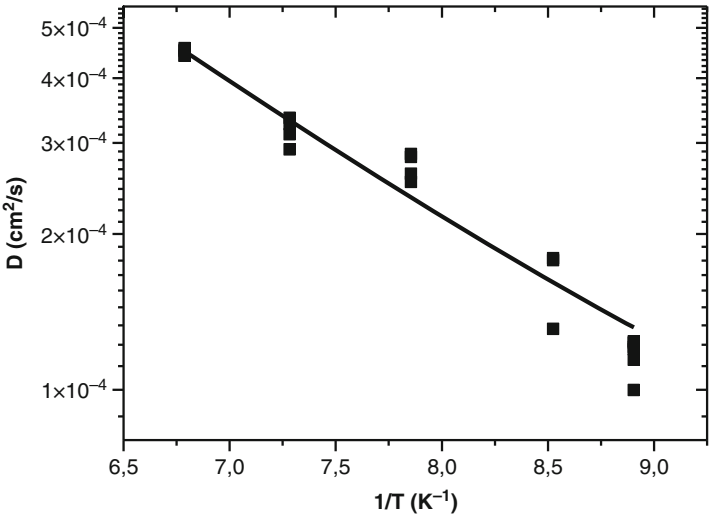

Fig. 7.29 Temperature dependence of the hydrogen diffusion coefficient in Zircaloy-4

References

1. V.F. Sears, Neutron News **3**, 26 (1992)
2. T. Bücherl, Ch. Lierse von Gostomski, Radiography and Tomography Using Fission Neutrons at FRM-II, World Conf. Non-Destructive Testing, 2004
3. S. Körner, B. Schillinger, P. Vontobel, H. Rauch, Neutron Tomography on a Low Power research reactor, World Conf. Nondest. Testing, Roma, 2000
4. B. Schillinger, Improved Radiography and 3D Tomography Due to Better Beam Geometry, 6th World Conf. Neutron Radiography, Osaka, 1999
5. B. Schillinger, Design and Simulation of Neutron optical Devices Plus Flight Tube for Neutron Radiography, 7th World Conf. Neutron Radiography, Roma, 2002
6. B. Schillinger, D. Bausenwein, P. Böni, M. Schulz, T. Reimann, P. Schmakat, The new Imaging Beam Line ANTARES, Internal Review Heinz Maier-Leibnitz Zentrum (FRM II), 2014
7. A.S. Tremsin, M. Lerche, B. Schillinger, W.B. Feller, Nucl. Inst. Methods Phys. Res. A **748**, 46 (2014)
8. A.C. Kak, M. Slaney, *Principles of Computerized Tomographic Imaging*, IEEE Press, New York, (1988)
9. H.G. Nelson, in *Treatise on Materials Science and Technology*, ed. by C.L. Briant, S.K. Banerji, vol. 25 (Academic, New York, 1983), p. 275
10. H.K. Birnbaum, I.M. Robertson, P. Sofronis, in *Multiscale Phenomena in Plasticity: From Experiments to Phenomenology, Modelling and Materials Engineering*, ed. by J. Lépinoux, D. Mazière, V. Pontikis, G. Saada, vol. 367 (Springer, Netherlands, 2000), p. 367
11. J.B. Condon, T. Schober, J. Nucl. Mater. **207**, 1 (1993)
12. P. Wongpanya, *Effects of Heat Treatment Procedures on the Cold Cracking Behaviour of High Strength Steel Welds*, vol. 36 (PhD thesis, BAM, Berlin, 2008), ISBN 978-3-9812072-7-9
13. S.P. Lynch, *in Proceedings of Hydrogen Effects on Material Behavior and Corrosion Deformation Interactions*, Moran, 2003, ed. by N.R. Moody, A.W. Thompson, R.E. Ricker, G.S. Was, R.H. Jones

14. W. Raczynski, in *Corrosion of Metals and Hydrogen-related Phenomena: Selected Topics*, vol. 59, ed. by J. Flis (Elsevier, 1991), p. 267
15. Y.D. Park, I.S. Maroef, D.L. Olson, Weld J. **81**, 27 (2002)
16. A. Griesche, E. Solórzano, K. Beyer, T. Kannengiesser, Int. J. Hydrog. Energy **38**, 14725 (2013)
17. A.S. Tremsin, N. Kardjilov, M. Dawson, M. Strobl, I. Manke, J.B. McPhate, Nucl. Inst. Methods Phys. Res. A **651**, 145 (2011)
18. H. Hanada, T. Otsuka, H. Nakashima, S. Sasaki, M. Hayakawa, M. Sugisaki, Scr. Mater. **53**, 1279 (2005)
19. G. Katano, K. Ueyama, M. Mori, J. Mater. Sci. **36**, 2277 (2001)
20. M. Garet, A.M. Brass, C. Haut, F. Guttierez-Solana, Corros. Sci. **40**, 1073 (1998)
21. K. Beyer, T. Kannengiesser, A. Griesche, B. Schillinger, J. Mater. Sci. **46**, 5171 (2011)
22. K. Beyer, T. Kannengiesser, A. Griesche, B. Schillinger, Nucl. Inst. Methods Phys. Res. A **651**, 211 (2011)
23. V. Olden, C. Thaulow, R. Johnsen, Mater. Des. **29**, 1934 (2008)
24. A. Borgschulte, R. Gremaud, R. Griessen, Phys. Rev. B **78**, 094106 (2008)
25. X.C. Ren, Q.J. Zhou, W.Y. Chu, J.X. Li, Y.J. Su, L.J. Qiao, Chin. Sci. Bull. **52**, 2000 (2007)
26. D.P. Escobar, C. Minambres, L. Duprez, K. Verbeken, M. Verhaege, Corros. Sci. **53**, 3166 (2011)
27. A. Griesche, E. Dabah, N. Kardjilov, A. Hilger, I. Manke, T. Kannengiesser, Int. J. Mater. Res. **105**, 640 (2014)
28. A. Griesche, E. Dabah, T. Kannengiesser, N. Kardjilov, A. Hilger, I. Manke, Acta Mater. **78**, 14 (2014)
29. A. Couet, A.T. Motta, R.J. Comstock, R.L. Paul, J. Nucl. Mater. **425**, 211 (2012)
30. C. Raepsaet, P. Bossis, D. Hamon, J. Bechade, J. Brachet, Nucl. Inst. Methods Phys. Res. B **266**, 2424 (2008)
31. F. Gröschel, P. Schleuniger, A. Hermann, E. Lehmann, Nucl. Inst. Methods Phys. Res. A **424**, 215 (1999)
32. R. Yasuda, M. Matsubayashi, M. Nakata, K. Harada, J. Nucl. Mater. **302**, 156 (2002)
33. E. Lehmann, P. Vontobel, A. Hermann, Nucl. Inst. Methods Phys. Res. A **515**, 745 (2003)
34. E. Lehmann, P. Vontobel, N. Kardjilov, Appl. Radiat. Isot. **61**, 503 (2004)
35. E. Svab, G. Meszaros, Z. Somogyvari, M. Balasko, F. Körösi, Appl. Radiat. Isot. **61**, 471 (2004)
36. M. Große, E. Lehmann, P. Vontobel, M. Steinbrück, Nucl. Inst. Methods Phys. Res. A **566**, 739 (2006)
37. A. Agrawal, Y. Kashyap, P.S. Sarkar, A.N. Behra, M. Shukla, R.N. Singh, A. Sinha, J.K. Chakravartty, J. Nucl. Mater. **421**, 47 (2012)
38. Z. Wang, U. Garbe, H. Li, R. Harrison, A. Kaestner, E. Lehmann, Metall. Mater. Trans. B (2014). doi:10.1007/s11663-013-9866-0
39. M. Große, M. Steinbrück, A. Kaestner, Nucl. Inst. Methods Phys. Res. A **651**, 315 (2011)
40. M. Steinbrück, J. Nucl. Mater. **334**, 58 (2004)
41. M. Große, M. van den Berg, C. Goulet, E. Lehmann, B. Schillinger, Nucl. Inst. Methods Phys. Res. A **651**, 253 (2011)
42. M. Große, J. ASTM Int. **8**, 575 (2011)
43. M.K. Große, J. Stuckert, M. Steinbrück, A.P. Kaestner, S. Hartmann, Phys. Procedia **43**, 294 (2013)
44. M. Steinbrück, N. Ver, M. Große, Oxid. Met. **76**, 215 (2011)
45. M. Grosse, High-temperature oxidation in nuclear reactor systems, in *Nuclear Corrosion Science and Engineering*, ed. by D. Feron, C.E.A. Saclay, vol. 22 (Woodhead Publishing Series in Energy, France, 2012)
46. M. Große, M. Steinbrück, J. Stuckert, A. Kastner, B. Schillinger, J. Mater. Sci. **47**, 6505 (2012)
47. M. Große, G. Kühne, M. Steinbrück, E. Lehmann, P. Vontobel, J. Stuckert, J. Phys. Condens. Matter **20**, 104263 (2008)

48. J. Stuckert, M. Große, C. Rössger, M. Klimenkov, M. Steinbrück, M. Walter, Nucl. Eng. Des. **255**, 185 (2013)
49. M. Große, J. Stuckert, M. Steinbrück, A. Kaestner, J. Nucl. Mater. **420**, 575 (2012)
50. M. Große, M. van den Berg, C. Goulet, A. Kaestner, J. Phys. Conf. Ser. **340**, 012106 (2012)

Source of Further Information

IAEA TECDOC on "Characterization and Testing of Materials of Relevance to Nuclear Energy Sector Using Neutron Beams"; in preparation by the IAEA, Vienna, 2014
L. Josic, E. Lehmann, A. Kaestner, Nucl. Inst. Methods Phys. Res. A **651**, 166 (2011)
J.R. Santisteban, M.A. Vicente-Alvarez, P. Vizcaino, A.D. Banchik, S.C. Vogel, A.S. Tremsin, J.V. Vallerga, J.B. McPhate, E. Lehmann, W. Kockelmann, J. Nucl. Mater. **425**, 218 (2012)
M. Große, M. Steinbrück, E. Lehmann, P. Vontobel, Oxid. Met. **70**, 149 (2008)
S.C. Vogel, ISRN Mater. Sci. **2013**, 1 (2010)
http://www.ncnr.nist.gov/resources/n-lengths/
Proceedings of the World Congresses on Neutron Radiology
Proceedings of the Intern. Techn. Meetings on Neutron Radiography
Proceedings of the NEUWAVE Meetings
www.frm2.tum.de
www.psi.ch
www.nist.gov
http://www.helmholtz-berlin.de/quellen/ber/index_en.html

Chapter 8
Incoherent Neutron Scattering

Michael A. Gharghouri

Abstract Hydrogen scatters neutrons strongly and incoherently, which makes neutrons very sensitive to the presence of hydrogen in materials (Squires, *Introduction to the Theory of Thermal Neutron Scattering*, 3rd edn. Cambridge University Press, New York, 2012). This strong incoherent scattering removes neutrons from a transmitted beam, so that hydrogen-rich regions appear as dark spots in neutron radiographs. The scattered neutrons are spread into all directions and appear as a contribution to the background in neutron diffraction patterns, often viewed as a nuisance. In this chapter, we first provide a brief introduction to coherent and incoherent neutron scattering. We then present two examples in which incoherent neutron scattering reveals knowledge of practical value. In the first example, we describe an experiment to determine the smallest change in hydrogen concentration that can be detected in nuclear fuels (~10 wt. ppm) by incoherent neutron scattering. Hydrogenous materials such as water and organic lubricants are often used in the processing of fuels for nuclear reactors, and residual lubricants trapped in the fabricated fuels can lead to complications in fuel performance. Neutron scattering is very sensitive to the presence of hydrogen in bulk specimens, and hence of water or hydrogen-rich organic lubricants. Furthermore, since neutron scattering is non-destructive and simple to apply, it is an ideal technique for quantifying hydrogen-bearing contaminants in fuels for the purpose of quality assurance. A brief description of the uncertainties associated with a typical neutron counting experiment is provided. Though the experiment deals with nuclear fuels, the method is straightforward and easily applicable to other materials. In the second example, we describe an in situ experiment in which both coherent and incoherent neutron scattering are used to study the bulk diffusion of hydrogen into a zirconium alloy in order to accurately determine the solubility limit of hydrogen. In CANDU® nuclear power reactors, pressurized heavy water coolant flows over fuel bundles in pressure tubes made of Zr–2.5Nb alloy. Over time, deuterium accumulates in the zirconium alloy, resulting in the precipitation of hydrides which can lead to various types of failure, such as Delayed Hydride Cracking (Puls, *The Effect of Hydrogen and Hydrides on the Integrity of Zirconium*

M.A. Gharghouri (✉)
Canadian Nuclear Laboratories, Chalk River, ON, Canada, K0J 1J0
e-mail: michael.gharghouri@cnl.ca

H. Fritzsche et al. (eds.), *Neutron Scattering and Other Nuclear Techniques for Hydrogen in Materials*, Neutron Scattering Applications and Techniques,
DOI 10.1007/978-3-319-22792-4_8

Alloy Components: Delayed Hydride Cracking. Springer, New York, 2012). Accurate quantitative knowledge of the deuterium (hydrogen) concentration at which hydrides start to form is thus critical to inform regulations limiting the acceptable residence time of pressure tubes in power reactors. Again, though the experiment deals with a specific alloy, the technique is straightforward to apply and is applicable to a wide range of materials.

Keywords Background • CANDU® • Coherent neutron scattering • Counting Statistics • Diffraction pattern • Incoherent neutron scattering • Nuclear fuel • Zr-2.5Nb alloy • H-Zr phase diagram • Zr alloy

8.1 Introduction

Hydrogen scatters neutrons strongly and incoherently, which makes neutrons very sensitive to the presence of hydrogen in materials [1]. This strong incoherent scattering removes neutrons from a transmitted beam, so that hydrogen-rich regions appear as dark spots in neutron radiographs. The scattered neutrons are spread into all directions and appear as a contribution to the background in neutron diffraction patterns, often viewed as a nuisance. In this chapter, we first provide a brief introduction to coherent and incoherent neutron scattering. We then present two examples in which incoherent neutron scattering reveals knowledge of practical value. In the first example, we describe an experiment to determine the smallest change in hydrogen concentration that can be detected in nuclear fuels by incoherent neutron scattering. Though the experiment deals with nuclear fuels, the method is straightforward and easily applicable to other materials. In the second example, we describe an in situ experiment in which both coherent and incoherent neutron scattering are used to study the bulk diffusion of hydrogen into a zirconium alloy in order to accurately determine the solubility limit of hydrogen. Again, though the experiment deals with a specific alloy, the technique is straightforward to apply and is applicable to a wide range of materials.

8.2 Coherent and Incoherent Scattering

Consider a two-dimensional periodic array of atoms as shown in Fig. 8.1. Because neutrons lack any electrical charge, they pass through the material unaffected by Coulomb interactions with electron clouds, but interact with the atomic nuclei through the short-range strong nuclear force [1]. In discussing the interaction of neutrons with matter, it is thus appropriate to think of crystalline matter comprising a simple periodic array of nuclei, as shown in Fig. 8.2. The weak interaction between neutrons and electrons also accounts for the high penetration of neutrons into many materials. Effectively, for neutrons, matter is mostly composed of empty space.

Consider a neutron, represented by a plane wave, impinging on a periodic array of nuclei. The presence of a nucleus perturbs the plane wave, either attracting or

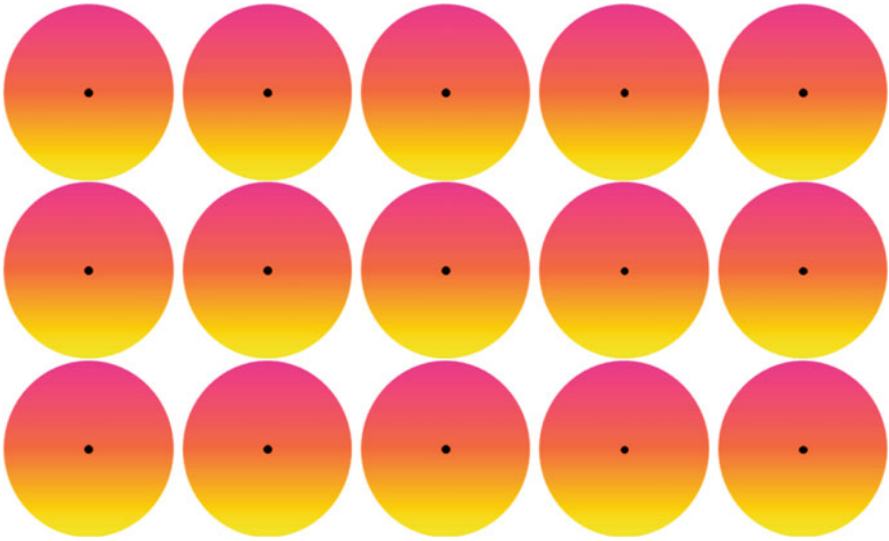

Fig. 8.1 Two-dimensional periodic array of atoms, with the nuclei and associated electron clouds represented by the *small black dots* and *larger orange concentric circles*, respectively

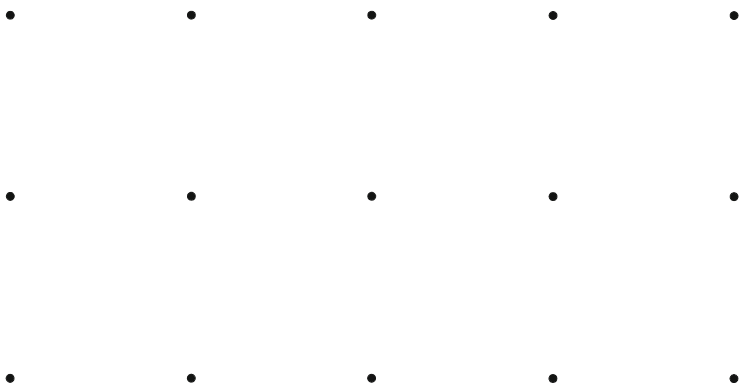

Fig. 8.2 Two-dimensional periodic array of atomic nuclei in solid matter, where the distance between nuclei is about 100,000 times as large as the nuclear radius

repelling the neutron slightly, so that, effectively, the nucleus becomes the point source of a spherical wave with the same wavelength as the incident neutron, but phase-shifted ahead or behind by an amount that depends on the sign and magnitude of the force between the neutron and the nucleus. This process is illustrated in Fig. 8.3. Each nucleus is the point source of a spherical wave, and the array of points creates a family of spherical waves that superpose.

In *coherent scattering*, the phase-shift between the incident plane wave and the scattered spherical wave is fixed and is the same for every nucleus. As a result, for periodic arrays of nuclei such as crystals, coherent scattering is reinforced in

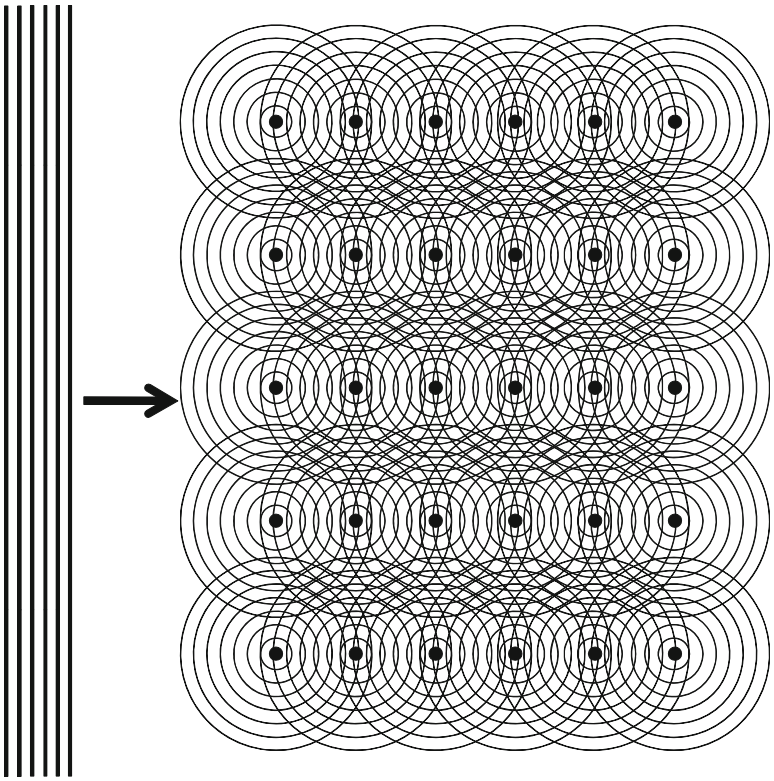

Fig. 8.3 Two-dimensional schematic illustration of a neutron, represented by a plane wave, impinging on a periodic array of atomic nuclei, each nucleus perturbing the wave front and serving as a point source of a spherical wave

specific directions. This constructive interference between waves emanating from the nuclei in a crystal is illustrated in Fig. 8.4, in which the direction at which the neutron scattering signal is detected is given by the scattering angle 2θ ($=90^\circ$ in this case). Constructive interference results in high-amplitude scattered waves at specific scattering angles. In other words, any given neutron has a high probability of being scattered at specific scattering angles which are related to characteristic distances in the crystal lattice. This directional reinforcement gives rise to neutron diffraction peaks.

In *incoherent scattering*, the phase-shift between the incident plane wave and the scattered spherical wave for each nucleus is random. As in coherent scattering, each nucleus is the point source of a spherical wave, and the array of point sources creates a family of spherical waves that superpose. However, the lack of a phase relationship between the incident wave and the scattered waves precludes the possibility of constructive interference. Instead, the intensity due to incoherent scattering appears as a diffuse signal, neutrons being scattered in all directions rather than in specific directions as diffraction peaks.

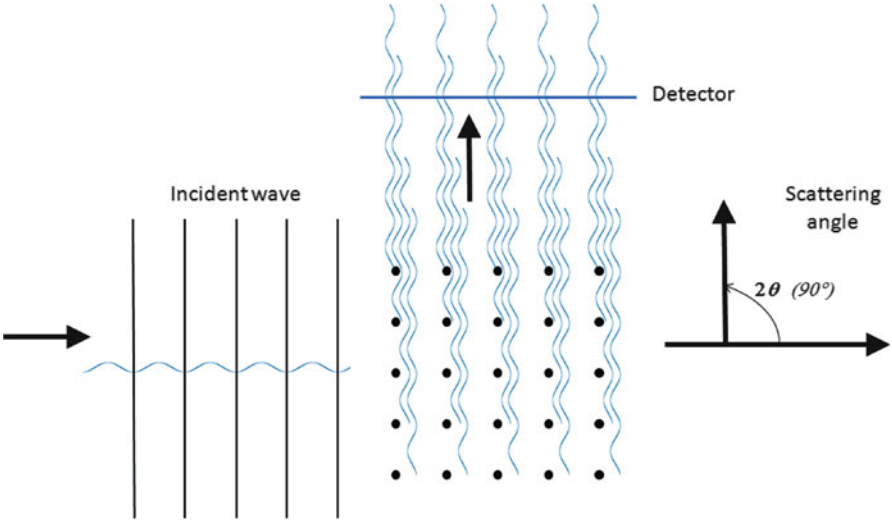

Fig. 8.4 Schematic illustration of a neutron, represented by a plane wave, impinging on a periodic array of atomic nuclei, giving rise to constructive interference at a scattering angle 2θ ($=90^\circ$ in this case)

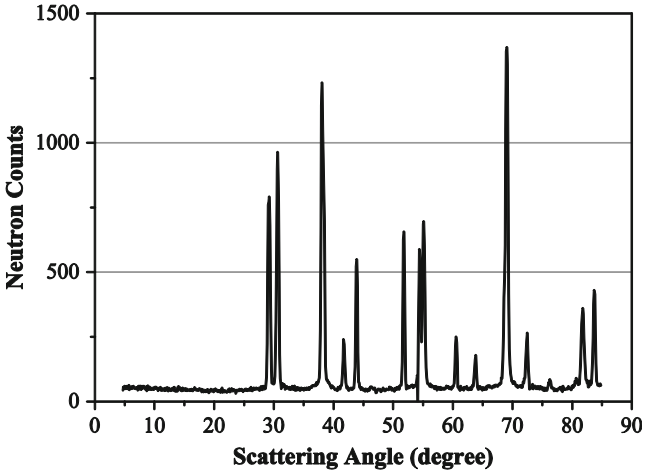

Fig. 8.5 A typical neutron diffraction pattern

In a neutron diffraction experiment, a detector is scanned across a range of scattering angle, and the neutron signal (count) is recorded as a function of the scattering angle, giving rise to a neutron diffraction pattern. The diffraction pattern consists of a set of peaks at scattering angles for which constructive interference conditions are satisfied for coherently scattered neutrons, superposed on a background comprised of several components (Fig. 8.5). The background intensity

arises from neutrons that are incoherently scattered from the atomic nuclei in the sample, from non-uniformity of atoms or isotopes in the crystal lattice of the specimen, from neutrons that enter the detector from locations other than the specimen, or from noise in the detector.

In addition to coherent and incoherent scattering, *absorption* of thermal neutrons occurs when a neutron impinging on a nucleus is captured by the nucleus, forming an isotope that decays to the ground state by the emission of radiation such as gamma or beta rays. In this case, the absorbed neutron is removed from the incident neutron beam and does not contribute to the diffraction pattern.

Each neutron interacting with a nucleus can undergo coherent scattering, incoherent scattering, or absorption. The probability of each type of interaction is expressed by a numerical quantity, called a cross-section [1, 2]. The larger the cross-section, the more likely the corresponding type of interaction. Thus, for example, the absorption cross section represents the effective area that a nucleus presents to the incoming neutron that might lead to absorption.

Since hydrogen is a very strong incoherent scatterer of neutrons, every hydrogen atom in a sample, whether incorporated in a solid phase (solid solution, hydride), in a liquid, or in a gas pocket, contributes strongly to the incoherent component of the neutron spectrum, often dominating the other components of background intensity in a diffraction pattern. The incoherent scattering from a hydrogen-containing sample scales directly with the total amount of hydrogen in the sample. Table 8.1 includes scattering and absorption cross sections for a selection of elements. In the table, ^{1}H refers to the hydrogen isotope having one proton and no neutrons in the nucleus, while ^{2}H refers to the hydrogen isotope having one proton and one neutron in the nucleus. ^{1}H is by far the most common isotope of hydrogen, and is thus generally referred to simply as hydrogen, while ^{2}H is referred to as deuterium. The table shows that the incoherent scattering cross-section of ^{1}H is 2–3 orders of magnitude higher than those of typical structural metals Zr, Fe, and Al. Of the metals, Ti is one of strongest incoherent neutron scatterers, but its incoherent scattering cross section is still about 30 times smaller than that of ^{1}H.

Table 8.1 Scattering and absorption cross sections for a selection of elements (1 barn $= 10^{-28}$ m^2) [2]

Element	Coherent scattering cross section(barn)	Incoherent scattering cross section(barn)	Absorption cross section(barn)
^{1}H (hydrogen)	1.7583	80.27	0.3326
^{2}H (deuterium)	5.592	2.05	0.000519
^{233}U	12.8	0.1	574.7
Zr	6.44	0.02	0.185
Fe	11.22	0.4	2.56
Al	1.495	0.0082	0.231
Ti	1.485	2.87	6.09

8.3 Sensitivity of Incoherent Neutron Scattering to Hydrogen in Nuclear Fuels

Hydrogenous materials such as water and organic lubricants are often used in the processing of fuels for nuclear reactors. Residual lubricants trapped in the fabricated fuels can lead to complications in fuel performance.

Since the incoherent scattering of neutrons by hydrogen nuclei is very strong and neutrons are very penetrating, neutron scattering is very sensitive to the presence of hydrogen in bulk specimens, and hence of water or hydrogen-rich organic lubricants. Furthermore, since neutron scattering is non-destructive and simple to apply, it is an ideal technique for quantifying hydrogen-bearing contaminants in fuels for the purpose of quality assurance.

A simple way to determine how the incoherent neutron scattering signal changes as a function of hydrogen concentration is to add known quantities of hydrogen in steps and measure the increased intensity of the background in a diffraction pattern. In this section, we describe experiments in which known quantities of distilled water were added to a known quantity of fuel powder in steps, and the background intensity was measured after each controlled water addition. Since the only change in the sample between measurements is the quantity of water, the change in background intensity of a diffraction pattern can be entirely attributed to the increase in incoherent neutron scattering from the hydrogen in the samples after each controlled water addition.

The samples consisted of nuclear fuel powders loaded into aluminium alloy cans fitted with microlitre syringes (commonly used for chromatography) containing distilled water. A schematic of the assembly is shown in Fig. 8.6.

The neutron scattering measurements were carried out on the L3 diffractometer of the Canadian Neutron Beam Centre, located in the NRU reactor, Canadian Nuclear Laboratories. The (113) reflection of a germanium mosaic single crystal was used to obtain neutrons with a nominal wavelength of 0.237 nm. The 32-channel detector on this instrument spans a range of approximately 2.5° in scattering angle.

A schematic plan view of the experimental setup is shown in Fig. 8.7. The cross-sections of the incident and scattered beams were defined by cadmium masks. The intersection of the incident and scattered beams defines the gauge volume, which is fixed in space. The gauge volume was large enough to fully contain the fuel powder, as shown in the figure. The scattering vector, $\boldsymbol{Q}$, is the bisector of the incident and scattered beams.

Prior to impinging on the sample, the incident neutrons pass through a low-efficiency monitor detector (Fig. 8.7), which provides a measure of the number of neutrons interacting with the sample, referred to henceforth as the monitor value (*DBMon*). Each measurement continues until the target monitor value is reached. By normalizing each neutron scattering measurement to the monitor value, meaningful comparisons between measurements can be made which are not affected by fluctuations in neutron flux related to, for example, variations in reactor power.

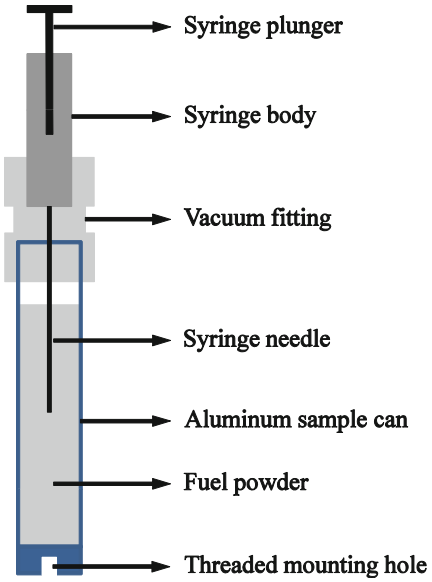

Fig. 8.6 Schematic of sample can/syringe assembly

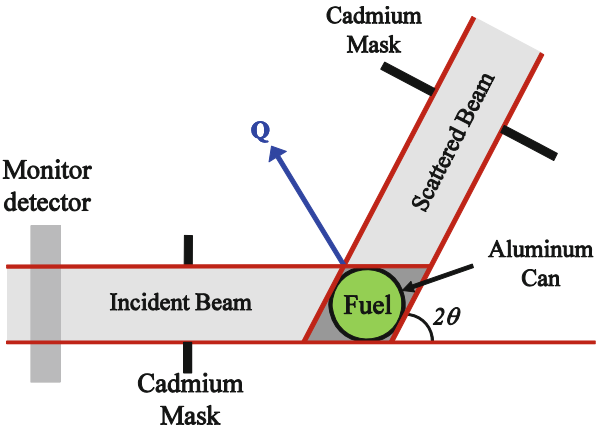

Fig. 8.7 Schematic plan view of experimental setup

To ensure that the cans were properly centred within the gauge volume, the aluminium {111} diffraction peak ($2\theta = 60.9°$) was used to scan the can across the gauge volume. All measurements were performed with the cans in the vertical orientation. A height of approximately 45–50 mm was sampled. A photograph of the experimental setup is shown in Fig. 8.8.

Intensity measurements of the diffraction-pattern background were performed at a nominal scattering angle of $2\theta = 10°$, at which no diffraction peak occurred. An example of a typical profile of neutron counts across the 32-channel detector is shown in Fig. 8.9. Counts were accumulated over the range of scattering angle covered by the shaded rectangle ($2\theta \sim 10° \pm 0.6°$). This range excluded those

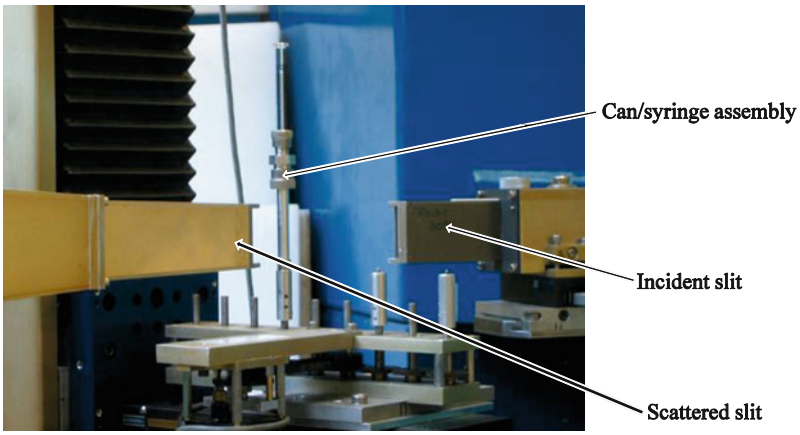

Fig. 8.8 Experimental setup at the L3 diffractometer

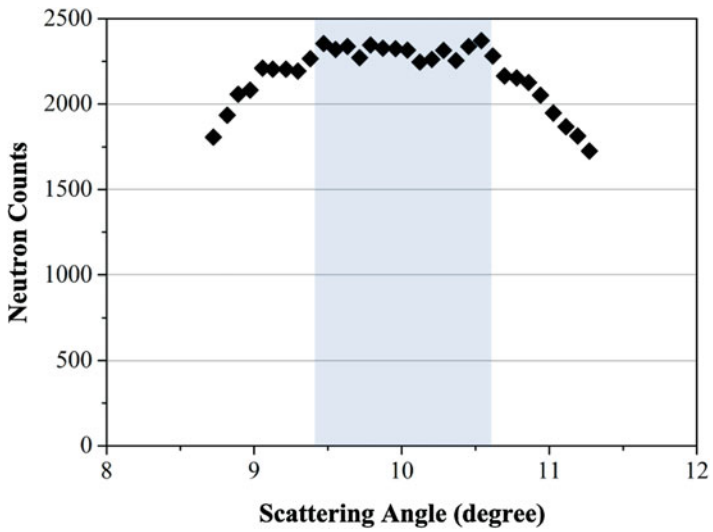

Fig. 8.9 Example profile of neutron counts across the 32-channel detector at a nominal scattering angle $2\theta = 10^{\circ}$

channels of the detector for which the counts fall off due to the neutron beam being partially blocked by the collimating elements.

The background intensity as a function of the change in hydrogen concentration is plotted in Fig. 8.10. The counting time was approximately 30 min per acquisition. The counts were normalized by the monitor value (*DBMon*) then scaled by an arbitrary factor of 1000 for comparison. The data show a linear correlation between the change in background intensity and the corresponding change in hydrogen concentration, determined by dividing the mass of hydrogen added by the mass

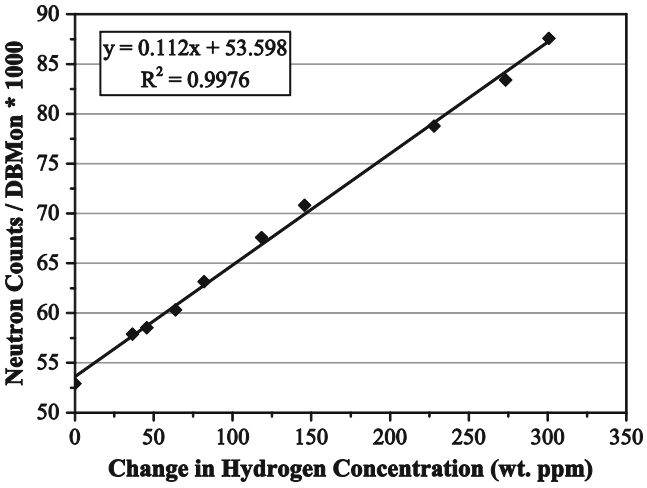

Fig. 8.10 Normalized and scaled background intensity as a function of the change in hydrogen concentration

of fuel powder. The best-fit line is also shown in Fig. 8.10, along with the corresponding equation and correlation coefficient.

As a neutron travels through a sample, it interacts with the nuclei, each nucleus becoming a new source of spherical waves as described in the introduction to this chapter. Similarly, as a scattered wave travels through the sample, it can be re-scattered. Such re-scattering of a scattered wave is referred to as multiple scattering. If the material is composed of strong scatterers in high concentration, the likelihood of multiple scattering is high, which could influence the resulting diffraction pattern. In the case of the fuel powders used here, the only very strong scatterer is hydrogen. The low hydrogen loading in the present experiments ensures that multiple scattering and absorption from hydrogen do not significantly influence the background signal, leading to the linear relationship in Fig. 8.10.

The smallest change in hydrogen concentration which can be measured in these experimental conditions can be estimated by determining the smallest change in neutron intensity that can be measured and comparing this value with the slope of the best-fit line in Fig. 8.10.

Neutron scattering is a stochastic process. The probability p that a neutron will interact with a nucleus is very low ($p \ll 1$) and constant. Furthermore, the neutron flux on a sample is typically on the order of 10^6 n/cm^2/s, so the number of neutrons impinging on a sample during a typical measurement is very large. A neutron experiment can thus be considered a stochastic process characterized by a low probability p and high number of trials N. The Poisson distribution (Eq. 8.1), which describes the probability $P(n)$ that an event characterized by a probability p independently occurs n times in N trials, where $p \ll 1$ and $n \ll N$, is thus well suited to neutron scattering experiments.

$$P(n) = \frac{\lambda^n e^{-\lambda}}{n!} \tag{8.1}$$

In Eq. (8.1), $\lambda = Np$ is the mean value for n. For the Poisson distribution, the standard deviation σ is equal to the square root of λ. In a neutron scattering experiment, the best estimate of the mean for a given count is the count itself; thus, taking the standard deviation as a measure of the uncertainty in any given measurement, the uncertainty is the square root of the measurement itself.

Consider two measured counts c_1 and c_2 corresponding to a sample with two different hydrogen contents. Based on the considerations above, the uncertainties in c_1 and c_2 are $\sigma_{c_1} = \sqrt{c_1}$ and $\sigma_{c_2} = \sqrt{c_2}$, respectively. The corresponding normalized and scaled intensities and their uncertainties are then obtained as follows:

$$\begin{aligned} I_1 &= \frac{c_1}{DBMon} \times 1000 \qquad \sigma_{I_1} = \frac{\sigma_{c_1}}{DBMon} \times 1000 = \frac{\sqrt{c_1}}{DBMon} \times 1000 \\ I_2 &= \frac{c_2}{DBMon} \times 1000 \qquad \sigma_{I_2} = \frac{\sigma_{c_2}}{DBMon} \times 1000 = \frac{\sqrt{c_2}}{DBMon} \times 1000 \end{aligned} \tag{8.2}$$

From Eq. (8.2), the uncertainties in the intensities I_1 and I_2 depend on the counts c_1 and c_2, which in turn depend on the amount of hydrogen present, since the incoherent scattering from hydrogen contributes significantly to the neutron count.

The highest normalized and scaled count was ~88 (Fig. 8.10). We therefore use this value as the basis for the calculations, with $DBMon = 160 \times 10^3$.

For small changes in hydrogen concentration $I_1 \approx I_2$ and $\sigma_{I_1} \approx \sigma_{I_2}$. Taking $I_1 = I_2 = 88$ and $\sigma_{I_1} = \sigma_{I_2} = 0.74$, the uncertainty in the difference between I_1 and I_2 is given by:

$$\sigma_{I_1 - I_2} = \sqrt{\sigma_{I_1}^2 + \sigma_{I_2}^2} = 1.05 \tag{8.3}$$

Dividing this value by the slope of the best-fit line in Fig. 8.10 yields a minimum detectable change in the concentration of hydrogen of ~10 wt. ppm (1.05/0.11). This value for the sensitivity of the measurement corresponds to a single 30-min measurement at each hydrogen concentration.

A significantly higher sensitivity can be obtained by increasing the acquisition time (higher *DBMon*), since the relative uncertainty in a count decreases with increasing count, i.e., $\sqrt{c}/c$ decreases as c increases. For example, under the conditions used for the current measurements, counting twice as long per point reduces the uncertainty σ_I by a factor of $\sqrt{2}$, i.e., $\sigma_{I_1} = \sigma_{I_2} = {}^{0.74}/_{\sqrt{2}} = 0.52$. As a result, $\sigma_{I_1 - I_2} = 0.74$, giving an improved sensitivity of ~7 wt. ppm. The sensitivity of the method would continue to increase with increasing counting time, but with a diminishing effectiveness for the increase of measurement time.

The sensitivity of the method could also be improved by increasing the sample size as a given change in hydrogen concentration in a large sample would require a proportionately larger addition of hydrogen than would a small sample. Assuming the matrix material contributes little to the incoherent scattering signal, the change in the incoherent scattering signal would thus be stronger for the larger sample, thereby increasing the sensitivity of the measurement. There are practical limits to improvements that can be obtained by increasing the sample size—neutron penetration is not infinite. In addition, the relative uncertainty associated with a neutron count improves with a diminishing effectiveness for the increase of measurement time.

If the host material is also a strong incoherent scatterer, it will contribute significantly to the intensity of the background in a diffraction pattern. Though the contribution of the host material in a sample will not change with increasing hydrogen concentration, changes in the signal from the incoherent scattering of hydrogen will be proportionately weaker as they are superposed on an already strong background.

Finally, the instrument configuration is a very important factor—the inherent background signal from, e.g., gaps in the shielding surrounding the detector should be minimized.

8.4 Determining the Solubility Limit of Hydrogen in Metallic Materials [3]

In CANDU® nuclear power reactors, pressurized heavy water coolant flows over fuel bundles in pressure tubes made of Zr–2.5Nb alloy. Over time, deuterium accumulates in the zirconium alloy, resulting in the precipitation of hydrides which can lead to various types of failure, such as Delayed Hydride Cracking [4]. Accurate quantitative knowledge of the deuterium (hydrogen) concentration at which hydrides start to form (the terminal solid solubility), and how this concentration varies with temperature, is thus critical to inform regulations limiting the acceptable residence time of pressure tubes in power reactors.

The binary H–Zr phase diagram, which gives the compositions and relative quantities of the phases in equilibrium at a given temperature and overall composition (at atmospheric pressure), is shown in Fig. 8.11. The region labelled α on the right corresponds to the range of compositions and temperatures at which the system at equilibrium consists of a single phase interstitial solid solution of hydrogen atoms in a hexagonal-close-packed zirconium matrix. The region labelled δ on the left corresponds to the range of compositions and temperatures at which the system at equilibrium consists of a single phase δ-hydride with a nominal composition of $ZrH_{1.6}$ (the actual composition varies). The white area labelled $\alpha + \delta$ corresponds to the compositions and temperatures at which the system at equilibrium consists of a two-phase mixture of α solid solution and δ-hydride. The

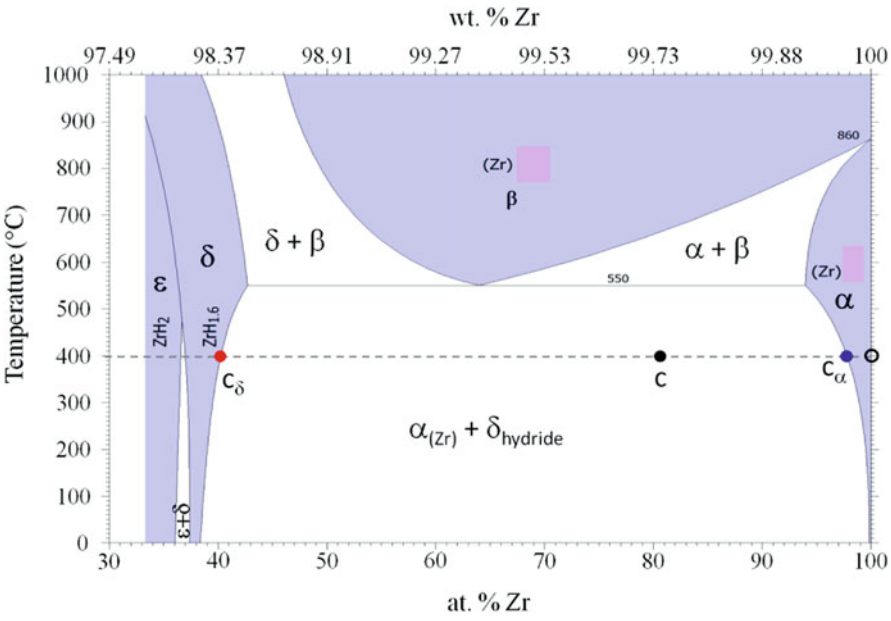

Fig. 8.11 Binary H–Zr phase diagram [5]

terminal solid solubility (TSS) is the boundary between the single phase α and two-phase α + δ regions.

Consider a sample of pure zirconium, initially containing no hydrogen, at a temperature of 400 °C, represented by the open circle at the intersection of the isotherm at 400 °C (dotted grey line) and the right vertical axis (pure Zr) in Fig. 8.11. As hydrogen diffuses into the zirconium metal at constant temperature, the alloy composition moves to the left along the isotherm from the open circle to the black dot at overall composition c. To the right of the blue dot, only α solid solution is present. To the left of the blue dot, δ-hydride precipitates are present in equilibrium with the α solid solution. For the entire range of compositions at 400 °C within the α + δ two-phase region, the compositions of the α solid solution and δ-hydride phases are c_α and c_δ, respectively. Additionally, the weight fraction of δ is given by the Lever Rule (all concentrations expressed as wt.% Zr):

$$\text{Weight fraction hydride} = \frac{c - c_\alpha}{c_\delta - c} \tag{8.4}$$

Equation 8.4 shows that, for compositions in the two-phase region, the weight fraction of hydride is proportional to the overall hydrogen concentration c, since c_α and c_δ do not change.

Neutron scattering constitutes a unique means to study hydrogen solubility and hydride precipitation in metals at constant temperature because:

1. Coherent neutron scattering gives rise to characteristic hydride diffraction peaks, whose integrated intensities vary in proportion to the total mass of hydride present.
2. As hydrogen enters the metal, the rising intensity of the background of the diffraction pattern, due to incoherent scattering from hydrogen, provides an accurate measurement of the total hydrogen concentration in the metal.

By performing measurements at a series of temperatures, the solubility as a function of temperature can be obtained, from which the TSS line in the phase diagram can be plotted.

In this work, a specimen of Zr–2.5Nb pressure-tube material was mounted in a vacuum furnace. The furnace was first carefully evacuated. A low pressure (2 mbar) of hydrogen gas was then introduced. The specimen temperature was held constant. Over time, hydrogen diffused into the sample, at a rate controlled by the thickness of a nickel coating deposited on the surface of the specimen and by the gas pressure. The rate of ingress was slow enough to prevent the formation of a hydride surface scale—scanning electron microscopy at the end of the experiment revealed that the hydrides formed homogeneously throughout the specimen. Neutron diffraction data were acquired at discrete time intervals on a 32-channel detector spanning ~2.5° in scattering angle. The neutron wavelength was $\lambda = 0.237$ nm. The experiments were performed on the E3 spectrometer of the Canadian Neutron Beam Centre, located in the NRU reactor, Canadian Nuclear Laboratories.

The specimen was first heated to the target temperature of 250 °C. The first diffraction pattern acquired at the target temperature is shown in Fig. 8.12. The diffraction peaks at scattering angles of ~51°, 51.7°, and 52.4° occur because the $\lambda/2$ and $\lambda/3$ components of the incident neutron beam were not filtered out for this experiment. The tail of a strong peak is also visible at the left edge of Fig. 8.12.

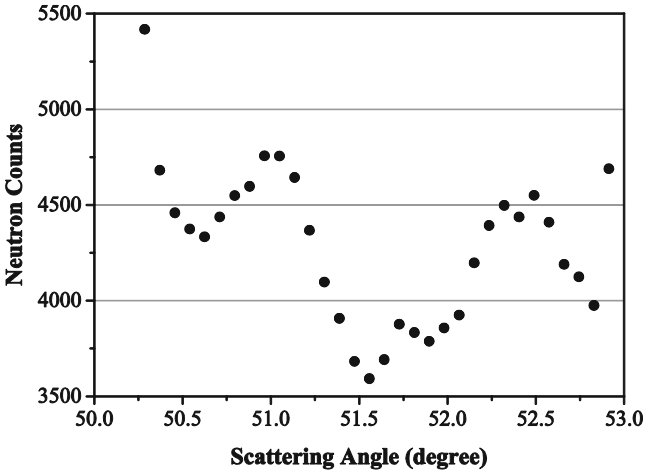

Fig. 8.12 Initial diffraction pattern acquired at 250°C

The phase, wavelength, and indices corresponding to each diffraction peak in Fig. 8.12 are shown in Table 8.2.

Since all of the peaks in the initial diffraction pattern in Fig. 8.12 correspond to the α- and β-Zr matrix phases, whose texture and phase fractions do not evolve significantly during the experiment, this pattern constitutes an unchanging background which can be subtracted, channel by channel, from all subsequent diffraction patterns, with appropriate normalization.

The resulting background-corrected diffraction patterns for selected times after the onset of hydrogen ingress are shown in Fig. 8.13. At early times, the signal increases uniformly over the entire range of scattering angle. All of the intensity arises from incoherent scattering from hydrogen, scaling in proportion to the amount of hydrogen in the specimen. Eventually, when the hydrogen concentration exceeds the solubility limit, the {111} peak of the δ-zirconium hydride appears and grows with time. The incoherent signal beside the diffraction peak also continues to grow as the amount of hydrogen increases. The evolution of the diffraction pattern with time is shown in the three-dimensional colour map and the colour contour plot in Fig. 8.14.

Table 8.2 Indexed diffraction peaks from the initial diffraction pattern

Nominal scattering angle (°)	Phase	Wavelength	Indices
50.0	α-Zr	λ	$10\bar{1}0$
51.0	α-Zr	$\lambda/2$	$2\bar{1}\,\bar{1}2$
51.7	α-Zr	$\lambda/3$	$3\bar{1}\bar{2}3$
52.4	β-Zr	$\lambda/3$	$10\bar{1}0$

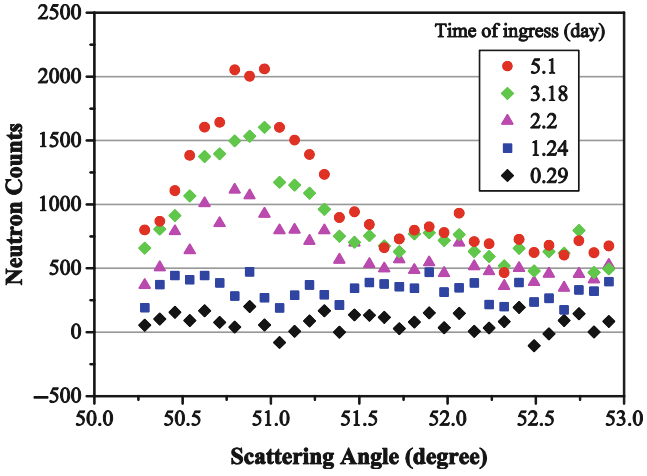

Fig. 8.13 Selected diffraction patterns, with initial background subtracted

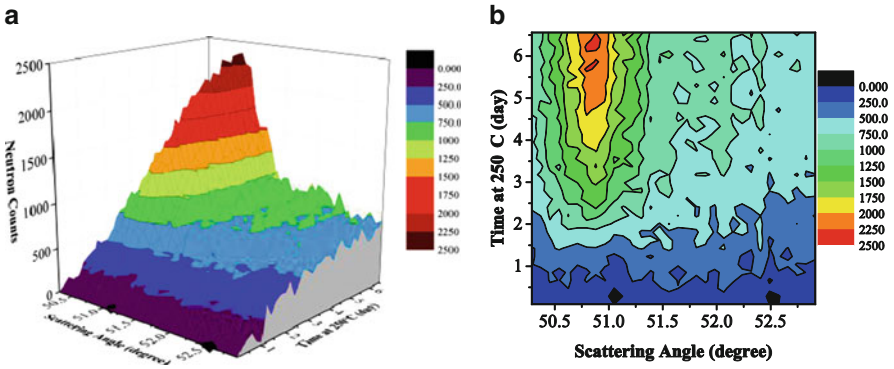

Fig. 8.14 (**a**) Three-dimensional colour surface map and (**b**) colour contour plot of background-corrected neutron data

Fig. 8.15 Colour contour plot of background-corrected neutron data showing the tail and peak sections for analysis

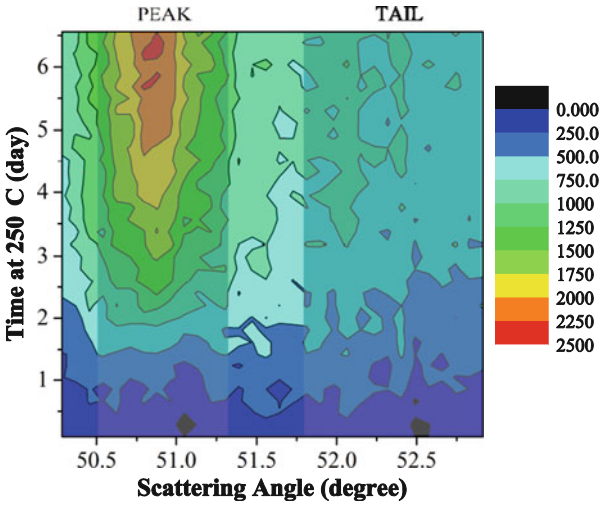

In Fig. 8.15, two sections of the contour plot are highlighted—the left-hand (peak) and right-hand (tail) sections.

The intensity in the tail section is due entirely to incoherent scattering from hydrogen, while the intensity in the peak section is due to contributions from incoherent scattering of hydrogen, and also from diffraction from the hydride phase. For each channel in the detector, the difference in intensity between the tail and peak sections in Fig. 8.15 is thus due solely to the additional contributions from diffraction in the peak section. It is not possible to determine how much of the incoherent signal is from hydrogen incorporated in the hydride or dissolved in the matrix unless the phase fraction of the hydride is known.

Since changes in the incoherent scattering signal are due solely to changes in the hydrogen content of the alloy, the incoherent scattering from hydrogen is proportional to the quantity of hydrogen present in the alloy regardless of whether the hydrogen is dissolved in the matrix, or is incorporated in the hydride phase. A sample-dependent calibration is necessary to convert from neutron counts in the tail section of a diffraction pattern to hydrogen concentration. Such a calibration was obtained by measuring the total hydrogen concentration in the material at the beginning and end of the neutron scattering experiment by Hot-Vacuum Extraction Mass Spectroscopy (HVEMS). These data were combined with the corresponding neutron counts (tail section) to establish a simple calibration relation.

To determine the hydrogen solubility, the average neutron counts per detector channel in the tail and peak sections for each pattern were first obtained by summing the counts on all the channels in each section and dividing by the corresponding number of channels. The values obtained for the tail section of each pattern were then converted into the equivalent hydrogen concentrations using the calibration relation. The excess counts in the peak section compared with the tail section, due solely to diffraction from the hydride phase, were then determined by simple subtraction. The excess counts in the peak section are plotted as a function of hydrogen concentration in Fig. 8.16. The excess counts are zero within uncertainty for the first six patterns, after which they increase linearly with hydrogen concentration. This linear increase with hydrogen concentration is consistent with the Lever Rule (Eq. 8.4). The critical concentration obtained from the x-intercept of the best-fit line to the linearly increasing segment is the TSS, determined as 67 ± 7 wt. ppm for this experiment. This uncertainty is determined from the standard uncertainty in the slope obtained from the least-squares fitting process.

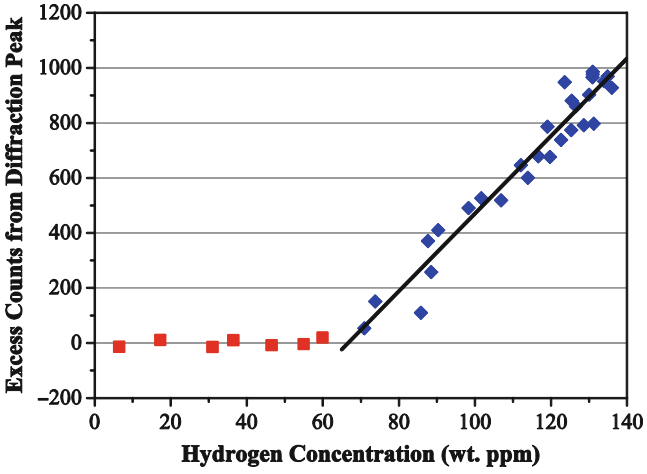

Fig. 8.16 Excess counts in the peak section compared with the tail section as a function of hydrogen concentration

This technique constitutes an elegant and robust means to accurately determine the solubility of hydrogen in metals because (1) it relies on multiple robust experimental measurements, which represent averages over a macroscopic volume, (2) the straightforward calculations are not subject to user interpretation, (3) all the required measurements, including those required for calibration of the hydrogen concentration, are performed on a single specimen. The solid solubility result is not critically dependent on the ability to very sensitively detect the first formation of the hydride phase—it is only necessary to have sufficient measurements before and after the hydrogen concentration exceeds the solid solubility (i.e. to the right and left of the blue dot in Fig. 8.11) to perform the analysis.

8.5 Conclusion

Neutron scattering is a powerful tool for studying hydrogen in engineering materials. Though the techniques described here have been applied to critical materials for the nuclear power-generation industry, they apply equally well to important structural materials such as steels, aluminium alloys, and ceramics. The main strengths of the techniques include:

1. The ability to sample over a representative macroscopic volume, thanks to the high penetrating power of neutrons in a wide variety of materials, which yields robust and reproducible measurements.
2. The high sensitivity of neutron scattering to the presence of hydrogen, thanks to the strong incoherent scattering of neutrons by hydrogen.

References

1. M.P. Squires, *Introduction to the Theory of Thermal Neutron Scattering*, 3rd edn. (Cambridge University Press, New York, 2012)
2. V.F. Sears, Neutron News **3**, 29 (1992)
3. J.H. Root, P. Wanjara, S. Yue, R. Drew, A. Oddy, M. McDill, F. Marsiglio, R.W.L. Fong, Physica B **1181**, 241–243 (1998)
4. M.P. Puls, *The Effect of Hydrogen and Hydrides on the Integrity of Zirconium Alloy Components: Delayed Hydride Cracking* (Springer, New York, 2012)
5. K.E. Moore, J. Nucl. Mater. **32**, 46 (1969). (Figure generated using the Pauling Binaries File software)

Chapter 9
Inelastic and Quasi-Elastic Neutron Scattering

D. Keith Ross and Daniel L. Roach

Abstract This chapter describes the basic principles of inelastic and quasi-elastic neutron scattering as applied to hydrogen storage systems—in particular to provide an understanding of the vibrations and diffusion of hydrogen and deuterium in the host lattice. The techniques are then illustrated using typical hydrogen storage materials. Incoherent inelastic scattering can be applied to isolated hydrogens—where the protons can be modelled as in an isolated potential well formed by the surrounding atoms. At higher concentrations, the effect of H–H interactions and the role of hydrogen vibrational density of states are described. Ab initio theory becomes important in this case. The advantages of modelling the dynamics of a deuteride by simulation of the polycrystalline coherent inelastic neutron scattering in comparison with ab initio modelling are then described. The final area of application of inelastic scattering is to the case of adsorbed H_2 molecules where particular spin transitions are observed. Here the results provide important information on the geometry of the potential energy surface around the adsorbing site. Quasi-elastic neutron scattering is then described. In particular the Chudley–Elliott model is derived for a Bravais lattice and it is indicated how this approach can be extended to more general cases where there are multiple sublattices which may have differing energies of adsorption. Here the important case of intermetallic Laves phases is described.

Keywords Neutron inelastic scattering • Quasi-elastic scattering • Incoherent and coherent scattering • Quantum states of H • Scattering function • Inelastic incoherent scattering • Q-dependence of coherent inelastic scattering • Dynamics of H in hydrogen storage systems • Anharmonic potentials • Pd/H • $NaAlH_4$ • Lattice dynamics • Laves phase hydrides • polyCINS • DFT simulations • Ortho-/para-hydrogen scattering from H_2 • H_2 in MOFs • Clathrates • Quasi-elastic scattering • Chudley–Elliott model • Diffusion on lattices with traps

---

Editor's note: it is with deep regret that we learned about the passing of D. Keith Ross in February 2016.

D.K. Ross • D.L. Roach (✉)
Centre for Materials Physics, School of Computing, Science and Engineering,
University of Salford, Manchester M5 4WT, UK
e-mail: d.roach@salford.ac.uk

H. Fritzsche et al. (eds.), *Neutron Scattering and Other Nuclear Techniques for Hydrogen in Materials*, Neutron Scattering Applications and Techniques,
DOI 10.1007/978-3-319-22792-4_9

9.1 Introduction: The Advantages of These Methods

In the search for useful hydrogen storage materials, whether the H atoms are incorporated into a solid state compound or are in the form of H_2 molecules adsorbed on surfaces, the most immediately relevant data are, of course, the macroscopic thermodynamics, the kinetics of the ab(ad)sorption/desorption processes and the macroscopic hydrogen diffusion within the bulk. However, if we need to understand the binding of H within the solid and its related quantum states, and also the atomic diffusion rate within the lattice, inelastic and quasi-elastic neutron scattering are ideal techniques, particularly in view of the extremely large incoherent neutron scattering cross section of H. Also, inelastic scattering from the spin states of ortho-/para-H_2 gives enormous advantages in understanding the binding of H_2 molecules onto large surface area substrates. It is in these contexts that thermal neutron scattering (both inelastic and quasi-elastic) has made crucial contributions, particularly when linked to ab initio modelling results. The basic theory of neutron scattering is described in the well-known text books, e.g. Squires [1]. A full discussion of neutron scattering from metal-hydrogen systems was given in Hydrogen in Metals III [2]. The theory of inelastic scattering from H_2 molecules was first given by Young and Koppel [3] and quasi-elastic neutron scattering is very fully described in the book by Bee [4]. In the present chapter, we will summarise the theory behind the technique and illustrate it with some recent examples.

As mentioned in Sect. 2.5.2, inelastic neutron scattering can be used to measure the energies of the quantum states of hydrogen in a solid via the transfer of one or more quanta of energy ($\hbar\omega$) between the proton and the neutron—in either neutron energy loss or energy gain—because we can either select the incident neutron energy and measure the final neutron energy with sufficient accuracy to define the energy transfer with some precision (direct geometry), or vice versa (indirect geometry). Moreover, by measuring the associated angle of scatter (φ), we can also determine the associated momentum transfer, $\hbar Q$. The situation for quasi-elastic scattering (Sect. 2.5.3) is rather different in that here the atomic motion is diffusional and this gives rise to a continuous range of energy transfers, centred on the incident energy. This process is called quasi-elastic broadening [4]. The extent of the broadening of the elastic line depends on the jump-rate of the hydrogen atom and its angular dependence on the mechanism of the diffusive process.

The particular advantage of neutron scattering from hydrogen is that the proton (H^1) scattering cross section is significantly larger than that of other nuclear isotopes and it is almost completely incoherent (see Sect. 2.4.1). Thus it contains information about the behaviour of a single H^1 nucleus averaged over all the H^1 nuclei present. On the other hand, the cross section for deuterium (with a more typical value of the cross section) is mainly coherent and so contains information about the pairwise motions of the deuterons, i.e. the scattering is influenced by the relative motion of two adjacent D nuclei.

In the present chapter, we will first describe the use of incoherent inelastic neutron scattering (IINS) to measure the vibrational density of states of hydrogen

in solids. Here, for a parabolic potential in the absence of H–H interactions, the H^1 scatters as if it were an Einstein (harmonic) oscillator with equally spaced energy levels where the nth level has an energy of $E_n = (n + ½)\,\hbar\omega$ relative to the bottom of the potential. For more complex structures, e.g. covalently bound hydrides, such as $NaAlH_4$, the vibrational density of states is more complicated as there are also rotational and bond-bending modes and theoretical simulations using density functional theory (DFT) are usually necessary to identify the various experimental features [5].

The situation of scattering from H_2 molecules adsorbed on surfaces is rather different because the molecule is in either the ortho-state (total spin = 1) or the para-state (total spin = 0) [3]. As these states are coupled to the angular momentum of the molecule (the total wave function being anti-symmetric), the para-state must have odd values of angular momentum, J, and the ortho-state must have even values (i.e. the $J = 0$, the ground state, is ortho). The energy difference between the $J = 0$ (ortho) and the $J = 1$ (para) state in an isolated molecule is thus 14.7 meV. At low temperature, if there is a suitable catalyst present, the molecules of H_2 will mainly occupy the $J = 0$ ground state and a neutron can therefore excite the molecule to the para-state by neutron energy loss. In the liquid state, the energy levels are precisely defined but for the case of the molecule adsorbed on an inhomogeneous surface, the energy level of the $J = 1$ state is split [6, 7] by the reduced symmetry of the site. This splitting gives unique information on the nature of the interaction of the H_2 molecule with the surface in question.

9.2 Theory

9.2.1 The Basic Theory of Neutron Scattering

The neutron is an uncharged nucleon with a mass essentially the same as that of a proton, with a spin of ½ and a magnetic moment of −1.913 nuclear Bohr magnetons. As we can neglect consideration of magnetic interactions, being only interested here in the behaviour of hydrogen, we can confine our attention to the neutron–nucleus interaction. Full discussion of the theory for this case can be found in Chap. 2 and in standard text books [1–4] so the present treatment is considerably simplified with emphasis on physical principles rather than on mathematical rigour.

The inelastic cross section can be defined [as in Eqs. (2.12)–(2.15)] in terms of the incident and scattered energies and of the scattering angle (φ). Van Hove [8] showed that this function of three variables could be reduced to one of two variables (namely energy transfer, $E_0 - E' = \hbar\omega$, and momentum transfer, $\hbar(\boldsymbol{k_f} - \boldsymbol{k_0}) = \hbar\boldsymbol{Q}$), i.e. to the van Hove scattering function, $S(Q, \omega)$, by using the equation:

$$\frac{d^2\sigma(\varphi)}{dE' d\Omega} = {}^{k_f}/_{k_0}\left(\frac{\sigma_s}{4\pi}\right)S(Q,\omega) \tag{9.1}$$

where $\boldsymbol{k_0}$ and $\boldsymbol{k_f}$ are the incident and scattered neutron wave vector. There are two versions of this equation, one for incoherent scattering and one for coherent scattering (see below). For a fixed nucleus at the origin, the scattering function is easily derived in quantum mechanical terms. If we represent the incident neutron flux as a plane wave, we can write the neutron wave function $\psi(\boldsymbol{r}) = \exp(i\boldsymbol{k_0}\cdot\boldsymbol{r})$, where $\boldsymbol{k_0}$ is the wave vector of the incident neutron so that $\hbar\boldsymbol{k_0} = m\boldsymbol{v_0}$ is the momentum of the incident neutron (with $m =$ neutron mass and $\boldsymbol{v_0} =$ incident neutron velocity) (see Fig. 2.2). On this basis, the neutron probability density in the incident beam, $\psi\psi^*$, is unity so that the incident flux is $|v|$ neutrons/unit area/sec. We can now represent the scattered wave as an expanding spherical wave centred on the origin which can be written $\psi'(\boldsymbol{r}) = (-b/r)\exp(i\boldsymbol{k}'\cdot\boldsymbol{r})$. Here, $\boldsymbol{k}'$ is the scattered wave vector and b is known as the neutron scattering length. The $-$ sign is conventionally inserted here because, for most isotopes, the "compound nucleus" is formed from the neutron and the target nucleus is remote from a nuclear energy level of the target nucleus and so we get only "potential scattering" which produces a 180° phase change in the scattered wave function.

Now we can introduce the coherent and incoherent scattering as defined in Eqs. (2.10) and (2.11). Here, the scattering length, b, depends on the nuclear properties of a given nucleus (and hence is different for every isotope). In particular, if the nucleus has a finite spin, I, the neutron–nucleus interaction is spin-dependent and so we need to define b^+ and b^- for parallel and anti-parallel orientations of the neutron spin relative to the nuclear spin. Here the total spin of the compound nucleus, $J^+ = (I + ½)$ *or* $J^- = (I - ½)$, needs to be defined because it determines the statistical weight of the b^+ and b^- states. It should be noted that if the compound nucleus has an energy level somewhere near the energy of a stable state, the values of b can vary quite widely and indeed can be either +ve, −ve or complex as there is strong coupling between the incident neutron wave function and the potential well of the target nucleus. The proton is a good example of this situation because, in the anti-parallel state, the compound nucleus formed is very close to the ground state of the deuteron (spin zero!). This is why b^- is negative and is so much larger than for any other nucleus. It also follows that the scattering cross section for an isolated fixed nucleus will be $d\sigma/d\Omega = b^2 = \sigma/4\pi$.

We can now consider the scattering from a set of N nuclei rigidly fixed at positions $\boldsymbol{r_i}$ (so that the neutron does not exchange energy with the target nuclei). If we observe the scattered waves a long way from the scattering nuclei, we can sum their amplitudes and then define the scattered flux by multiplying the summed wave function by its complex conjugate and hence we obtain [1], an expression for the angular cross section, defined/nucleon:

$$d\sigma/d\Omega = \left(1/N\right)\left|\sum_i b_i \exp(i\boldsymbol{Q}\cdot\boldsymbol{r_i})\right|^2 = \left(1/N\right)\sum_{i,j} b_i b_j \exp\left[i\boldsymbol{Q}\cdot\left(\boldsymbol{r_i} - \boldsymbol{r_j}\right)\right] \quad (9.2)$$

Here, $\boldsymbol{Q}$ can be thought of as the wave vector transport because $\hbar\boldsymbol{Q}$ is the momentum transferred in the collision. The matrix on the right-hand side of the equation can be simplified by first averaging over the diagonal terms, yielding $<b^2>$ and then over the non-diagonal terms, where, remembering that the values of b_i and b_j are completely uncorrelated and are separated by the vector, $\boldsymbol{r_{ij}}$, we get terms $<b>^2$ $\Sigma_{ij(i\neq j)}\exp(i\boldsymbol{Q}\cdot(\boldsymbol{r_i}-\boldsymbol{r}))$. Now, by inserting terms, $<b>^2$, into the diagonal positions in the summation and subtracting the same quantity from the leading term, we can write:

$$d\sigma/d\Omega = [<b^2> - <b>^2] + (1/N)\,<b>^2\sum_{i,j}\exp(i\boldsymbol{Q}\cdot(\boldsymbol{r}_i - \boldsymbol{r}_j)\Big) \quad (9.3)$$

Here the first term, $[<b^2> - <b>^2]$, is independent of the angle of scattering (φ). It is called the differential incoherent scattering cross section. Note that it is zero if b has the same value for all nuclei. If we integrate over solid angle, we get an expression for the incoherent scattering cross section, $\sigma_{\text{inc}} = 4\pi[<b^2> - <b>^2]$. Also, the second term, $(1/N)<b>^2\Sigma_{ij}\exp(i\boldsymbol{Q}\cdot(\boldsymbol{r_i}-\boldsymbol{r_j}))$ is the differential coherent scattering and we can similarly write $\sigma^{\text{coh}} = 4\pi<b>^2$ to simplify this expression. This term depends on the positions of all the atoms present, taken in pairs, and it defines the neutron diffraction pattern for the solid. It is analogous to the expression obtained for X-ray diffraction except that, because the scattering is from the nucleus, there is no atomic form factor.

This last expression, (9.3), has been derived for a set of fixed nuclei but the process of separating it into incoherent and coherent terms carries over into all other kinds of neutron scattering. Moreover, it is particularly important for hydrogen. Remembering that the number of quantum states associated with a compound nuclear spin of J will be $2J+1$, we find that the average scattering length taken over all H nuclei is:

$$<b> = \left\{(2J^+ + 1)b^+ + (2J^- + 1)b^-\right\} \Big/ \left\{(2J^+ + 1) + (2J^- + 1)\right\} \quad (9.4)$$

Substituting $J^+ = (I + ½)$ and $J^- = (I - ½)$, for the case of the proton with $I = ½$, we find that $<b> = ¾b^+ + ¼b^-$. As mentioned above, b^- is large and negative while b^+ positive and close to $^1/_3$ of the value of b^- so that $<b>$ is very small—and is just negative. Numerically, this means that the incoherent cross section, σ^{inc}, is 79.7 barns while the coherent cross section, σ^{coh} ($=4\pi<b>^2$), is only 1.8 barns and so the proton is a strongly incoherent scatterer. On the other hand, the deuteron turns out to have $\sigma^{\text{coh}} = 5.6$ barns and $\sigma^{\text{inc}} = 2.0$ barns. Hence, if we wish to use neutron diffraction to identify the position of hydrogen in a crystal structure, it is virtually essential to prepare the deuterated version of the material, because the incoherent

scattering from H just gives an intense flat background in addition to any diffraction pattern. Also, as $<b>$ is negative for hydrogen and positive for deuterium, it is possible to make an isotopic mixture such that $<b>$ is exactly zero. Scattering from tritium is also of interest in some cases. It has a total scattering cross section of 3.1 barns ($\sigma^{\mathrm{coh}} = 2.89$ barns, $\sigma^{\mathrm{inc}} = 0.14$ barns). Tabulations of the values of cross sections and scattering lengths of all elements can be found, e.g. on the NIST web site [9].

9.2.2 Quantum Treatment of Inelastic Neutron Scattering

To complete our discussion of these general features of neutron scattering, we will formally extend the quantum mechanical treatment introduced above to include energy transfers, i.e. by assuming that the atoms in our sample are held together by a quantised set of mutual interaction energies. The initial state of the system is therefore described by a particular set of quantum numbers which define the Hamiltonian or its total energy. As a result of an inelastic collision, any of these quantum numbers can be changed by an integer—so long as they remain positive. In each case, an equal amount of energy will be transferred to or from the neutron. This process is described by Fermi's golden rule [1] which may be written:

$$d^2\sigma^{(E_0-E',\ \varphi)}\Big/_{dE'\,d\Omega} = \sum_i\sum_j\sum_n p_n \sum_{n'}\left(k'\Big/_{k_0}\right)\int_0^\infty \psi_n(\boldsymbol{r_i}) b_i b_j \delta\big(\boldsymbol{r} - (\boldsymbol{r_i} - \boldsymbol{r_j})\big) \times \psi^*_{n'}(\boldsymbol{r_j})\exp(i\boldsymbol{Q}\cdot\boldsymbol{r})d\boldsymbol{r}\ \delta\big(E_0 - E' - E_{n'} + E_n\big) \tag{9.5}$$

In this expression, the scattering system is assumed to be in thermal equilibrium with its surroundings and so the cross section has to be averaged over each possible initial state of the system, n, weighted by the appropriate Bose–Einstein thermal occupation number, p_n and then summed over all final states, n'. The delta function in $\boldsymbol{r}$ defines the positions of the nuclei and the one in energy ensures energy conservation. Here, the wave function for the nth quantum state is $\boldsymbol{\psi_n}(\boldsymbol{r})$. As before, $\boldsymbol{Q} = \boldsymbol{k_f} - \boldsymbol{k_0}$. For incoherent scattering, the same expression holds except that because $<b> = 0$ only terms in $i = j$ remain so the term in $\delta(\boldsymbol{r} - (\boldsymbol{r_i} - \boldsymbol{r_j}))$ is always unity. The full usefulness of this equation may be found in the standard textbooks, e.g. [1].

In Eq. (9.5), it will be seen that, if we separate out the parts of the equation that involve the neutron scattering lengths and the wave vectors before and after scattering, the rest of the equation is only a function of $\boldsymbol{Q}$ and ω. Van Hove [8] pointed out that this was a general property of neutron scattering cross sections. Thus the equation can be reduced to a term involving the neutron scattering lengths and wave vectors multiplied by the scattering functions, $-S^{\mathrm{coh}}(Q,\omega)$ or $S^{\mathrm{inc}}(Q,\omega)$ for coherent and incoherent cases, respectively—which only depend on the

interatomic interactions and are a function of only two variables. This relationship can be written:

$$d^2\sigma^{\mathrm{coh,\,inc}}\left(E_0-E',\ \varphi\right)_{dE'\,d\Omega} = \left(\frac{\sigma_{\mathrm{coh,\ inc}}}{4\pi}\right)\left(k_{\mathrm{f}}/k_0\right)S^{\mathrm{coh,\,inc}}(\boldsymbol{Q},\omega) \tag{9.6}$$

Note that Eq. (9.6) exists in both coherent and incoherent versions.

9.2.3 *Theory of Inelastic Neutron Scattering from Crystals*

As described above, inelastic neutron scattering measures the probability that the system can exchange a given amount of energy with the neutron (see Eq. (9.5)). Given that we are only interested in hydrogen, we can initially restrict ourselves to incoherent scattering, i.e. those terms in Eq. (9.5) for which $i = j$. We should now also distinguish between one-phonon transitions—where $n' = n \pm 1$ and the more general multi-phonon terms where more than one phonon is transferred. Clearly, the most direct information comes from the 1-phonon terms as here each energy transfer is associated with a particular phonon whereas, in the multi-phonon terms, a given energy transfer can arise in many different ways. Fortunately at low Q, the one-phonon term dominates but at larger energy transfers—usually accompanied by larger Q values—the multi-phonon terms will generally dominate.

When it comes to predicting the phonon spectrum, we can set the problem up in two different ways—either as the wave function of an individual proton in a potential well created by the surrounding (usually metal) atoms—where the scattering cross section consists of a set of delta functions in energy transfer—or, alternatively, in terms of phonons in a periodic lattice where the incoherent cross section is related to the phonon density-of-states. The first approach works best for protons that do not interact significantly with neighbouring protons. It is most directly applicable when the proton is in a harmonic potential but the method is fairly easily adapted to the case where the potential is anharmonic [10–12]. It also works for protons in intermetallic compounds such as Laves phases [13]. The second approach works well if the material has a periodic stoichiometric structure involving H–H interactions. This model yields a vibrational energy density-of-states curve but going beyond harmonic interactions is difficult. The experimental measurements, of either category, are now generally compared with ab initio calculations of the phonon spectrum, obtained using DFT. In general the agreement is not bad but the comparison of experiment and theory generally throws some light on the deficiencies of either method. The example of Ti activated $NaAlH_4$ [5] will be discussed below.

For more complicated structures, where dispersion effects are strong, a convincing comparison with experiment requires the application of an experimental method capable of determining the phonon dispersion curves. This clearly involves the use of a deuterated sample so that coherent effects due to near-neighbour pairwise

interactions can be measured. Here, we would normally use a single crystal sample and a triple axis spectrometer on a steady-state (reactor) source—the method pioneered by Brockhouse [14]—but there are few deuterides other than Pd/H [12] that are available in a single crystal form. An alternative approach is to analyse the coherent inelastic neutron scattering from polycrystalline samples (polyCINS) [15]. Because of the complexity of the coherent inelastic scattering after it has been averaged over crystallite orientation, this approach only works if combined with the simulation of the coherent inelastic scattering (using a suitable force constant model) and then by adjusting the model parameters to match the experimental data. This approach becomes possible through exploitation of the extensive modelling software and computer power now available. The parameters of the force constant model, constructed from initial DFT calculations, can then be adjusted to make the simulations match the experimental data using a least-squares method. The advantage of this more detailed approach is that it can model the interatomic interactions less ambiguously than can the simpler approach of fitting incoherent scattering to the measured density of state spectrum.

9.2.4 *Incoherent Inelastic Scattering from a Proton in a Harmonic Potential Well: The Einstein Oscillator Model*

The simplest analytic model for an isolated proton in a lattice assumes that it is situated in a harmonic potential well centred at an interstitial site such that the energy levels are given by $E_i = (n_i + ½)\hbar\omega_i$ in a particular Cartesian direction, i. This model is particularly appropriate for protons in transition metal lattices, where the electrons from the hydrogen atoms can be accommodated in the d-band of the metal, but is also applicable to many other cases—e.g. to molecular hydrogen trapped in clathrates (see Sect. 9.2.10). The model assumes that there are no interactions between neighbouring hydrogen atoms and that there is little coupling between the hydrogen atom and the lattice modes. This implies that $m_p/m_l \ll 1$ where m_p is the mass of the proton and m_l is the mass of the lattice atom. In transition metals, with f.c.c, b.c.c. or h.c.p lattices, the proton normally sits on either an octahedral or tetrahedral site. In more complex intermetallic lattices, such as AB_2 Laves phases [13] or AB_5 intermetallics [16], the site geometries can be much more complex. However, even in these more complex cases, the shape of the potential well can be expanded in Cartesian directions using a Taylor's expansion. In this case, the first term in the expansion of the potential energy will be a constant, the second will be zero (if the origin is taken at the centre of the well) and the third term will be the harmonic (parabolic) term. The resulting H wave functions can be separated into three independent oscillators in the x, y and z directions (i.e. putting the Cartesian directions along the orthogonal axes of the potential so that $V(r) = ½ m_p(\omega_x x^2 + \omega_y y^2 + \omega_z z^2)$. If the higher order terms in the expansion can be neglected,

the wave function of the proton can be represented as the product of three independent one-dimensional Hermite polynomials, for each of which the corresponding energy levels are equally spaced with energies, $E_{nx} = (n_x + ½)\hbar\omega_x$. Here, n_x is the number of quanta in the wave function in the x direction. Fermi's golden rule (9.5) can now be used to calculate the cross sections explicitly (see [10]). The result is:

$$S(Q,\omega) = \exp(-2W(Q))\exp\left(\frac{\hbar\omega}{2kT}\right)\sum_{k,l,m=0}^{\infty} I_k(s_x)I_l(s_y)I_m(s_z) \times \delta(\hbar\omega - k\hbar\omega_x - l\hbar\omega_y - m\hbar\omega_z) \tag{9.7}$$

where k, l and m represent the change in the existing quantum numbers in each of the Cartesian directions, subject to the condition that the initial and final quantum numbers must be positive and $I_n(s_x)$ are the modified Bessel functions for k quanta change in the Cartesian directions x, where

$$s_x = \left\{\hbar {Q_x}^2/2m_p\omega_x\right\}\mathrm{cosech}(\hbar\omega_x/2kT) \tag{9.8}$$

and Q_x is the component of $\boldsymbol{Q}$ in the x direction—and likewise for y and z. Here, $\exp(-2W(Q_x))$ is the Debye–Waller factor in the direction, $\boldsymbol{Q_x}$, which in turn can be written for the harmonic case:

$$2W(\boldsymbol{Q_x}) = (<n_x> + ½)\left(\hbar/m_p\omega_x\right){Q_x}^2 = \Sigma_i <{u_i}^2> {Q_i}^2 \tag{9.9}$$

Here $<n_x>$ is the thermal-averaged phonon occupation number in the x direction and $<{u_x}^2>$ is the mean square displacement of the proton from its mean position in this direction. The Debye–Waller factor describes the reduction in scattering intensity with increasing Q due to the displacement probability distribution of the H nuclei from their mean position caused by thermal motion. These equations imply that if the wave vector, $\boldsymbol{Q}$, has a component in a particular Cartesian direction, x, then there is a finite probability that the proton can be transferred to any energy level in this direction so long as the process satisfies energy conservation. Consideration of the modified Bessel functions shows that a term involving n quanta transferred will vary as Q^{2n} times a form factor which is the Fourier transform of the product of the initial and the complex conjugate of the final wave function of the proton in this level. It will be noted that if the parabolic potential is known, then the cross sections can be calculated explicitly with no selection rules depending on the electronic structure as would be the case for IR and Raman measurements. This approach can, for instance, be used to fit Born–Mayer potentials to the M-H potentials to describe interstitial H sites in Laves phase hydrides for different pairs of metals [17].

9.2.5 *Perturbation Analysis of Anharmonic and Anisotropic Effects in Inelastic Incoherent Neutron Scattering from H in Solids*

Because the proton wave function is not localised, it samples the potential energy surface over a volume around the centre of the interstitial site. Hydrogen, being the lightest nucleus, samples this potential further from the centre of the site than does any other nucleon (with the exception of the μ^+ meson). Its wave function is therefore more subject to the effects of the higher terms of the Taylor's expansion of the M-H potential than is that of any other scatterer. The allowed set of such terms depends on the symmetry of the interstitial site. For octahedral sites in an f.c.c. system, the potential can be written—for terms up to the quartic—as

$$V(x,y,z) = c_0 + c_2\left(x^2+y^2+z^2\right) + c_4\left(x^4+y^4+z^4\right) + c_{22}\left(x^2y^2+y^2z^2+z^2x^2\right) \tag{9.10}$$

From this equation, we can obtain a reasonable estimate of the wave functions and energy levels to be expected for this potential using perturbation theory [11]. The energy levels are given by the expression

$$E_{klm} = \left\{(\hbar\omega_0/2) + \beta\left(j^2 + j + \tfrac{1}{2}\right) + \gamma[(2k+1)(2l+1) + (2l+1)(2m+1) + (2m+1)(2k+1)\}\right] \tag{9.11}$$

with $j = k + l + m$. From this, we can derive a set of energy transfers:

$$\begin{aligned} &\varepsilon_{100} = \varepsilon_{010} = \varepsilon_{001} = \hbar\omega_0 + 2\beta + 4\gamma && \text{(fundamental terms)} \\ &\varepsilon_{200} = \varepsilon_{020} = \varepsilon_{002} + \hbar\omega_0 + 6\beta + 8\gamma && \text{(first harmonic)} \\ &\varepsilon_{110} = \varepsilon_{011} = \varepsilon_{101} = 2\hbar\omega_0 + 4\beta + 12\gamma && \text{(combination vibration)} \end{aligned} \tag{9.12}$$

where these parameters are related to the parameters defining the potential by:

$$\omega_0 = \sqrt{2}c_2/m_\mathrm{p} \quad \beta = 3\hbar c_4/4m_\mathrm{p}c_2, \quad \gamma = \hbar^2 c_{22}/c_2 m_\mathrm{p} \tag{9.13}$$

Here, the notation, ε_{110}, implies that the Cartesian operators have been raised by unity in the x and y directions (but not in the z direction) and this implies that $\boldsymbol{Q}$ has to have finite components in both the x and y directions.

These results show that the energy levels are no longer evenly spaced and that the intensity of the corresponding inelastic peak will vary strongly with the direction of $\boldsymbol{Q}$ relative to the crystal axes. This model works well for α-Pd/H [11]. Here the respective energy levels were observed at 69, 138 and 156 meV, yielding the following values for the parameters: $\hbar\omega_0 = 50$ meV, $\beta = 9.5$ meV and

$\gamma = 0$. It should be noted that these parameters imply rather too much perturbation of the potential for us to expect that perturbation theory should work well.

9.2.6 Comparison with Ab Initio Calculations

Over the last decade or so, ab initio calculations of the lattice dynamics using DFT have become increasingly accurate. In these calculations, the total energy of an assembly of atoms is calculated using DFT to represent the effects of electron–electron correlations. The nuclear coordinates can then be relaxed so as to minimise the total energy. As long as the initial configuration of the atomic positions was sufficiently accurate, the relaxed structure should coincide quite closely with the real system. Once the process of relaxing the atomic positions to the minimum energy has been accomplished, force constant data for a dynamical calculation can be readily extracted to provide a direct comparison with neutron scattering data, e.g. [18]. The situation is somewhat more complicated when we consider proton dynamics because the quantum properties of the proton have to be allowed for. If there are anharmonic effects present, the proton wave function is no longer a hermite polynomial but its actual form can be derived using the Born–Oppenheimer approximation, namely that motions on different time scales (i.e. protons and electrons) can be quantised separately. Specifically, this means that we can solve the Schrödinger equation for the electrons using an array of different proton positions so that the variation of the total energy of the system with proton position yields a potential energy surface within which we can calculate the wave functions and energy levels of the proton. This method, sometimes referred to as the "Frozen Phonon" method, was pioneered by Ho et al. for the $NbH_{1.0}$ system [19]. The calculation was done for a periodic lattice and the protons were all moved in phase with each other but in anti-phase with the metal atoms (the zone centre phonons). The various excited states of the proton were calculated and these agreed well with experiment. The approach was extended to the Pd-H system by Elsässer [20] and for a single crystal Pd-$H_{0.85}$, by Kemali et al. [12] where the full ab initio calculations of the inelastic scattering cross section were compared with experimental neutron scattering measurements for a single crystal sample as a function of crystal orientation (Fig. 9.1). Having determined the three-dimensional wave functions of the proton for each energy level, the full inelastic cross section was calculated explicitly as a function of Q, using Eq. (9.5). For a harmonic spherically symmetric wave function, the energy levels would be fully degenerate and the scattering would be spherically symmetric. However, for an anharmonic system like Pd-H, the (1,1,0) level is split from the (2,0,0) level which is itself split into one singly degenerate state, $|C\rangle$ and two doubly degenerate states, $|A\rangle$ and $|B\rangle$. These energy levels can be easily separated in the experiment using their directional dependence: the (1,1,0) level gives maximum scattering in the (110) and (111) directions and is zero in the (100) direction while the (2,0,0) level gives a maximum in the (100) direction (because here Q lies entirely in one Cartesian direction, so that only one

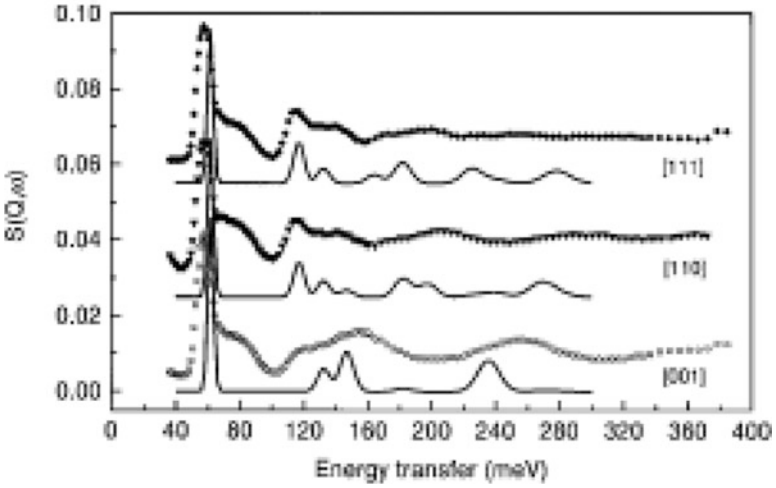

Fig. 9.1 The experimental and calculated incoherent scattering functions $S(Q, \omega)$, plotted against the energy transfer (*points* represent the data, *lines* represent the theory). For clarity, the spectra for the [110] and the [111] directions have been shifted vertically. The calculated spectra have been convoluted with the experimental resolution function [12]

Cartesian wave function can change its energy level). Similarly, the (111) level has its maximum in the (111) direction. The energy levels and the directional dependence of the associated scattering agreed remarkably well with the calculated values [12].

9.2.7 Incoherent Scattering from Systems Analysed Using Lattice Dynamics

The discussion above has been concerned with systems in which the protons do not significantly interact with each other so that we can analyse the scattering on the basis of scattering from individual protons in a fixed potential energy well. However, for crystalline systems in which there is significant interaction, we have to analyse the scattering in terms of the phonon dispersion curves. In this approach, which is so far limited to harmonic potentials, we describe the motion of the atoms in terms of their periodic displacements in the crystal, i.e. plane waves with wave vectors $\boldsymbol{q}$. The full theory can be found in the standard text books [1]. By using the periodicity of the lattice, the equations of motion for a given phonon yield the "dynamical matrix". This matrix is of dimension $3n$, where n is the number of atoms in the unit cell and the 3 represents the number of Cartesian axes. Each element, i, j, in this matrix is determined by the force constant relating the relative displacements of two atoms, each in a particular orthogonal direction. This solution can be solved, yielding $3n$ eigenvalues, $\omega_s(\boldsymbol{q})$, which are the frequencies of the $3n$ solutions for the

particular $\boldsymbol{q}$ used. For each $\omega_s(\boldsymbol{q})$, there is an eigenvector, representing the corresponding displacements of the n atoms in the unit cell which is resolved into each orthogonal direction. These displacements are, in general, complex numbers, implying that the phase of the displacements of a given atom may differ from the phase of the phonon solution being assumed at lattice points.

However, here we are mainly interested in samples where the scattering will be dominated by hydrogen and, as we have seen, the coherent scattering of hydrogen is very small compared to the incoherent cross section. Hence the inelastic scattering will be dominated by the self (diagonal) term in the full cross section. All the information about the conservation of momentum disappears and what we are left with is a hydrogen vibrational amplitude-weighted contribution from each phonon mode in the unit cell.

$$\left.d^2\sigma^{\text{inc}}\right/_{dQd\omega} = \left(\left.k_f\right/_{4\pi k_0}\right)[< n(\omega)+1 >]\left(Q^2/2\omega\right)\Theta(\omega) \tag{9.14}$$

Here we have replaced $|(\boldsymbol{k_f}-\boldsymbol{k_o})|$ by Q and $(E'-E_o)$ by $\hbar\omega$, $<n(\omega)>$ is the thermal population of modes of frequency, ω, and $\Theta(\omega)$ is the amplitude-weighted vibrational density of states given by:

$$\Theta(\omega) = f(\omega)\Sigma(\sigma_\rho^{\text{inc}}/M_p)\exp(-Q^2 < u_\rho^2 >)\Sigma_j|e_{s,\rho}(\omega)|^2 \tag{9.15}$$

Here $f(\omega)$ is the normalised number of phonon modes/unit frequency summed over all phonon modes, s, and wave vectors, $\boldsymbol{q}$, in the Brillouin zone of the crystal, $\boldsymbol{e_{s,\rho}}(\omega)$ is the displacement of the ρth hydrogen atom, of mass, M_p, in the sth mode summed over all the phonons of frequency, ω, and $<u_\rho^2>$ is the mean square amplitude of displacement of the ρth hydrogen averaged over $f(\omega)$ for all modes.

For the case of a binary hydride with two atoms/unit cell, there are six modes. The first three of these are "acoustic", that is to say the metal atom and the hydrogen atom are roughly in phase with each other and both have about the same amplitude of vibration. The other three modes are "optical", i.e. the lattice and hydrogen atoms are roughly in anti-phase but keeping the centre of gravity immobile. This means that the relative H vibration amplitude squared increases in proportion to the mass of the metal atom. Thus, the scattering from the optical modes will normally outweigh that from the acoustic modes by more than an order of magnitude. Further, if there are no interactions between adjacent H atoms, the frequency range within a given dispersion curve will vary as m_p/m_l where m_l is the mass of the lattice atom. For heavy metals, this range is small and so the scattering appears as a rather narrow intense peak. However, for lighter metals, particularly where H–H interactions can be significant, the spectral shape can become much more complex. However, with the development of ab initio calculations, and software packages designed to interface directly with DFT outputs, e.g. [18], it has become possible to calculate the inelastic scattering cross section directly for comparison with neutron scattering data. Examples of such measurements will be given below.

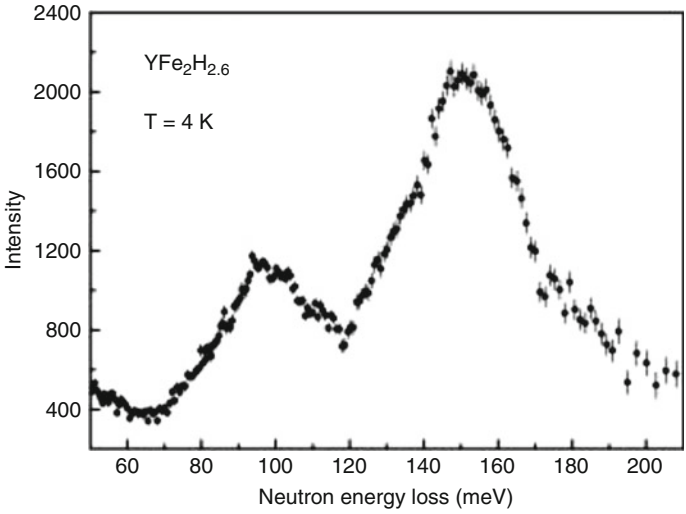

Fig. 9.2 Inelastic neutron scattering from $YFe_2H_{2.6}$ showing that the two higher energy modes are close to being degenerate [13]

In many metal hydrogen compounds, the IINS spectra can be interpreted in terms of Einstein oscillators in sites with non-cubic symmetries. A good example is scattering from H in distorted tetrahedral sites, for instance, in a Laves phase such as $YFe_2H_{2.6}$ [13] where the hydrogen occupies *g* sites which are tetrahedral with Y2-Fe_2 coordination (Fig. 9.2). The inelastic scattering shows peaks with close to 1:2 intensity ratio. It is clear that the point symmetry of the site is such that two of the modes are close to being degenerate, i.e. the potential energy surface is roughly cigar-shaped.

As shown by Fernandez et al. [17], it is possible to empirically construct the shape of the different *g* site potential energy surfaces using Born–Mayer potentials for Zr-H, Ti-H and Cr-H that are self-consistent, predicting vibration frequencies for all six Laves phases formed from the three Born–Mayer expressions that describe the six different M-H compounds. This demonstrates that for a pair of metal atoms, the potential seen by the proton is a sum of the repulsive parts of the nearest-neighbour M-H potentials.

9.2.8 Neutron Scattering from Systems with Interacting Hydrogen Atoms: Comparison with DFT Simulations

The discussion above was concerned with systems in which protons do not interact significantly with each other so that we can analyse the scattering on the basis of incoherent scattering from individual protons having rather flat optical dispersion curves. However, for crystalline systems in which there is significant interaction

between hydrogen atoms, we have to analyse the scattering in terms of overlapping phonon dispersion curves where features in the scattering are difficult to relate to particular motions in the solid. In this approach, which is limited to harmonic potentials, we describe the motion of the atoms in terms of their periodic displacements in the crystal, i.e. as plane waves with wave vectors $\boldsymbol{q}$. The full theory can be found in the standard text books [1]. As outlined above using the periodicity of the lattice, the equations of motion of the atoms in the crystal, for a given phonon wave vector $\boldsymbol{q}$, yield the "dynamical matrix". This matrix is of dimension $3n$, where n is the number of atoms in the unit cell and the 3 represents the number of Cartesian axes. Each element, i, j, in this matrix is determined by the force constant relating the relative displacements of two atoms, each in a particular orthogonal direction. This matrix can in principle be solved, yielding $3n$ eigenvalues, $\omega_s(\boldsymbol{q})$, which are the frequencies of the $3n$ solutions for the particular $\boldsymbol{q}$ used. For each $\omega_s(\boldsymbol{q})$, there is an eigenvector, representing the corresponding displacements of an atom in the sth mode in each Cartesian direction. These displacements are, in general, complex numbers, implying that the phase of the displacements of a given atom may differ from the phase of the phonon solution assumed.

Now we can plot out the $3n$ "dispersion curves", $\omega_s(\boldsymbol{q})$, as a function of $\boldsymbol{q}$. We will first describe the case of incoherent scattering from hydrogen which now depends on the distribution of phonon frequencies sampled over the whole Brillouin zone. Each frequency is weighted with the square of the amplitude of vibration of that mode, yielding a function known as the amplitude-weighted density of states which can be compared with the measured inelastic incoherent scattering cross section after careful normalisation, correcting for multiple phonon and multiple scattering, detector efficiency, etc. This technique, particularly as applied using the instrument TOSCA at ISIS [21], is very fully described in the book by Mitchell et al. [22]. This book contains a very full description of the scope of the IINS technique, particularly as applied to hydrogen storage systems.

9.2.9 *Measurement of Amplitude-Weighted Phonon Density of States Curves for Hydrogen for Comparison with the Simulated Data*

As described above, the classical method of using coherent scattering to measure phonon dispersion curves involves the use of single crystal samples. However, we are mainly interested in samples where the scattering will be dominated by hydrogen and here, as we have seen, the coherent scattering of hydrogen is small compared to the incoherent cross section. Hence the inelastic scattering will be dominated by the self (diagonal) term in the full cross section expression. All the information about the conservation of momentum thus disappear and we are left with a hydrogen vibrational amplitude-weighted contribution from each phonon

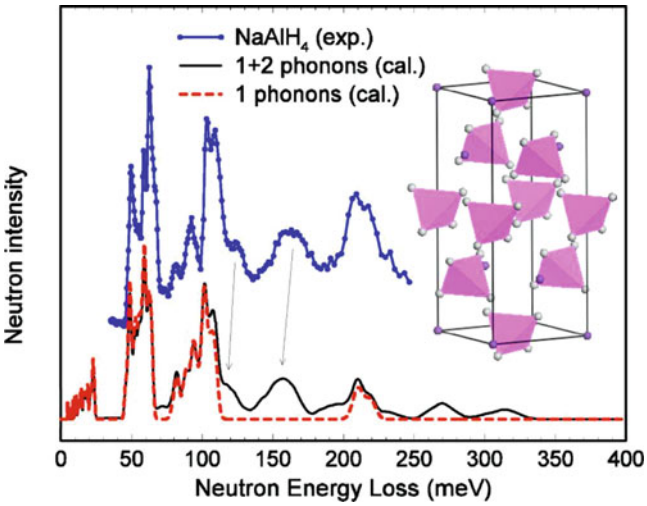

Fig. 9.3 The measured inelastic neutron scattering spectrum from $NaAlH_4$ (*top*) and the calculated 1 and 1 + 2 phonon cross sections (*below*). The *inset* shows the unit cell arrangement emphasising the AlH_4 tetrahedra [5]

mode in the unit cell. This quantity can be determined experimentally and compared with the same quantity derived from the density functional calculations.

As an example of this approach, we can consider the case of the prototype hydrogen storage material, $NaAlH_4$, which, when activated using $TiCl_3$, reversibly releases and absorbs hydrogen [23]. This compound has been measured using the FANS spectrometer at the NIST Centre for Neutron Research by Iniguez et al. [5].

In Fig. 9.3, the inelastic neutron scattering for the $NaAlH_4$ sample—here without Ti—is compared with the DFT calculations of the 1-phonon modes. These calculations were performed using a plane wave implementation of the generalised gradient approximation (GGA) to DFT using the ABINIT package [24]. Both the experiment and the theory show little interaction between the H atoms in different tetrahedra. The modes up to 25 meV are translational modes of the tetrahedra. The peak above 200 meV consists of the first harmonic of the Al-H stretching modes. The complex modes, in the energy transfer range 40–115 meV, are single phonons due to rotations and stretches and show reasonable agreement between theory and experiment. The intervening peaks in the experimental data—in the energy range between 120 and 200 meV—are multi-phonon peaks—features which are often strong in metal hydrides. This case is a little unusual because there are 2-phonon peaks lying below the energy of the fundamental Al-H stretch mode and above the other 1-phonon peaks. This is a clear demonstration of how important it is to be able to simulate the spectrum from DFT as these features would be difficult to identify without a realistic simulation.

9.2.10 Coherent Inelastic Neutron Scattering from Polycrystals

Using DFT, we can now calculate the $3n$ "dispersion curves", $\omega_s(\boldsymbol{q})$, as a function of $\boldsymbol{q}$. We can also derive the corresponding coherent neutron scattering cross section for the creation or annihilation of a phonon which depends on satisfying both energy and momentum conservation, where the phonon has an energy $\hbar\omega$ and a momentum $\hbar\boldsymbol{q}$:

$$\hbar\omega = E^{'} - E_0 \quad \text{and} \quad \boldsymbol{Q} = \boldsymbol{k}^{'} - \boldsymbol{k}_0 = \boldsymbol{\tau} + \boldsymbol{q} \tag{9.16}$$

Here $\boldsymbol{\tau}$ is a reciprocal lattice vector. The intensity of the scattering at a particular value of $\boldsymbol{q}$ is determined from the relative vibration amplitudes of all the atoms taken in pairs over the unit cell and weighted by the scattering lengths of each atom in the pair.

The classical method of using neutrons to measure these dispersion curves involves the use of coherently scattering single crystal samples and a triple axis spectrometer, as first developed by Brockhouse and Stewart [14]. We can thus measure phonon dispersion curves using deuterated samples but to do so we would need to have single crystals. As most hydrides are formed in the solid state via a first order transition involving significant lattice parameter changes (with the notable exception of palladium [12] and a couple of other systems), it is generally impossible to get adequate single crystals.

Recently, however, significant progress has been made with methods for identifying the coherent inelastic scattering features from polycrystalline samples and extracting the interatomic force constants from this powder data—the polyCINS method. The method employed is similar to the Ewald sphere approach to predicting elastic diffraction from polycrystals. If the force constants are known, e.g. from DFT or lattice dynamics calculations, the dynamical matrix can be solved for a particular orientation of $\boldsymbol{Q}$ relative to the reciprocal lattice vectors (thus defining the value of $\boldsymbol{q}$) and the contribution to the coherent inelastic scattering can be calculated from (9.5). As it now has to be summed over the different reciprocal lattice vectors it can be written in full as:

$$\begin{aligned} S^{'}_{\mathrm{coh}}(\mathbf{Q},\omega) = \frac{1}{2N}\sum_s \sum_\tau \frac{1}{\omega_s}\left|\sum_d \frac{\overline{b_d}}{\sqrt{M_d}}\exp(-W_d)\exp(i2\pi t\cdot \mathbf{r}_d)(\mathbf{Q}\cdot\xi_{ds})\right|^2 \\ \times \left\langle n_s + \frac{1}{2} \mp \frac{1}{2}\right\rangle \delta(\omega \mp \omega_s)\delta(\mathbf{Q} \mp \mathbf{q} - \tau) \end{aligned} \tag{9.17}$$

where here the scattering function describes both neutron energy gain (proportional to n_s, the thermal occupation factor) and neutron energy loss—proportional to $(n_s + 1)$.

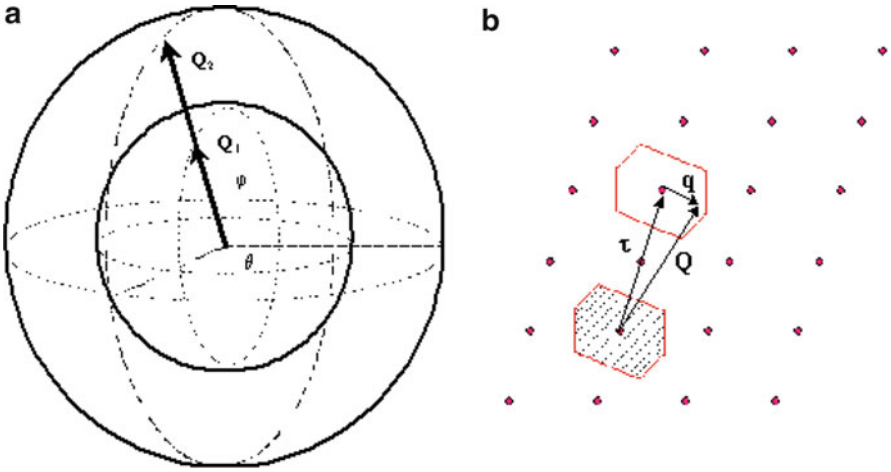

Fig. 9.4 (**a**) Diagram indicating the sampling process over surfaces of spheres in **Q**. (**b**) Sketch of a specific **Q** vector relative to a given orientation of the reciprocal lattice and the corresponding value of **q** in the corresponding Brillouin zone [25]

The calculation then has to be repeated for all directions of the $\boldsymbol{Q}$ vector, suitably distributed over the surface of a sphere as indicated in Fig. 9.4. This yields a prediction of the 1-phonon term in the polycrystalline scattering function which can be compared with experiment. The characteristic of this 1-phonon coherent scattering is that it shows step changes in intensity where the scattering sphere in Q touches a dispersion surface in Q, ω. In general, this 1-phonon cross section obtained from the DFT force constants can differ significantly from the measured 1-phonon term. The important question now is how can we adjust the calculated force constants to produce a model that matches the experimental measurements. In one approach, the force constants obtained from DFT are used to calculate the initial 1-phonon scattering term. The total cross section is then modelled by adding estimates for the additional multi-phonon and multiple scattering terms. The force constants are then allowed to vary in a least-squares refinement to fit all the experimental data yielding improved estimates of the force constants [25].

In the second approach [15, 26, 27], advantage is taken of the fact that the 1-phonon term, as mentioned above, includes many sharp discontinuities in the polycrystalline cross section, described as coherence edges as they occur due to the coherence condition $\delta(\boldsymbol{Q} \pm \boldsymbol{q} - \boldsymbol{\tau})$ from Eq. (9.17) at specific points in (Q, ω) space where the sphere in Q touches the scattering surface in Q, ω for at least one crystal orientation. The fitting process, therefore, only needs to adjust the calculated force constants so as to shift the calculated discontinuities to match the corresponding edge features in the experimental data and has the added advantage of enabling one to resolve and track sections of individual dispersion curves along high symmetry directions in reciprocal space, as illustrated in Fig. 9.5. This is possible because there are no such discontinuities in the multi-phonon or multiple scattering terms. It appears that most of these discontinuities occur along high

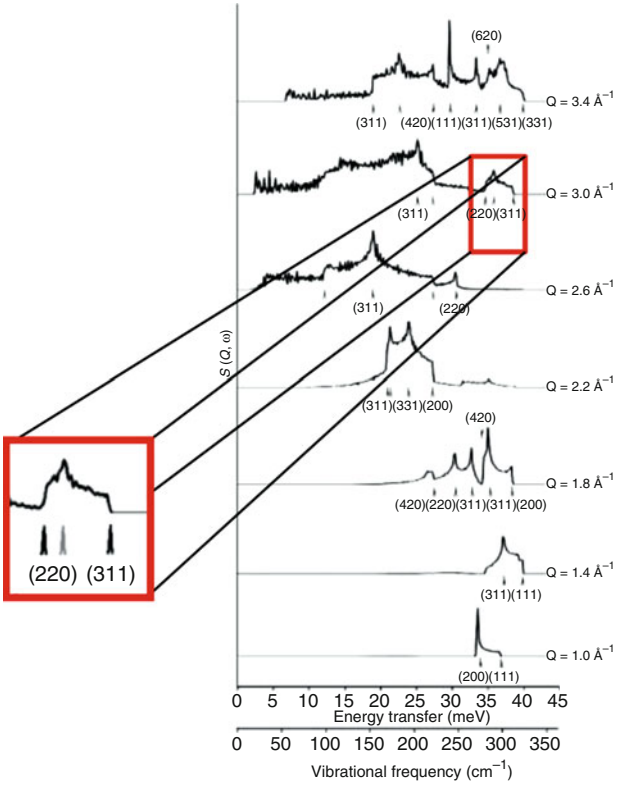

Fig. 9.5 Coherence edges corresponding to specific dispersion curves in (Q, ω) space identified from cuts through theoretical scattering data (in this case for polycrystalline aluminium [25])

symmetry directions so that the method allows the experimentalist to trace out dispersive features directly.

This method has recently been applied to the cases of aluminium [26] and magnesium deuteride [27]. In Fig. 9.6, we show a contour plot of the coherent inelastic scattering function for MgD_2 measured on the MARI instrument at ISIS, compared with the equivalent range in ($\boldsymbol{Q}$, ω) space produced by force constants generated from a large ($3 \times 3 \times 4$) DFT supercell calculation, using the Wu–Cohen (GGA) functional [28]. It is clear from this plot that the energy dependence of the scattering varies as a function of Q so that a full coherent analysis has to be applied for comparison with the polyCINS simulation. Furthermore, it is also clear that, whilst the DFT calculation is very close to the experiment for the highest and lowest frequency modes, it differs significantly from experiment in its prediction of the mid-range (optic) frequencies, suggesting that the functional used needs to be refined.

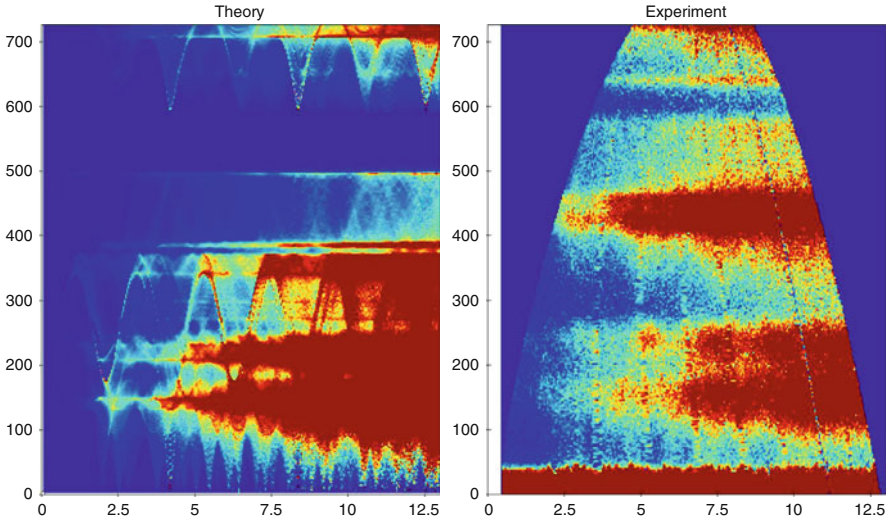

Fig. 9.6 Contour plot of the coherent inelastic scattering function for MgD_2 in ($\boldsymbol{Q}$, ω) space as measured on the MARI spectrometer at ISIS [21], compared with that calculated from DFT. Note: x-axis is Q (in $Å^{-1}$) and y-axis is frequency (in cm^{-1}) with colours denoting scattering intensity

9.2.11 *Inelastic Neutron Scattering from Molecular Hydrogen*

An exception to the above analysis of the incoherent scattering from hydrogen comes for the case where the hydrogen exists as a molecule. Deuterium, not considered here, differs significantly because of its different spin statistics. Here, due to the light mass of the atoms and the weak interaction with the surroundings, the overall wave function of the molecule has to be anti-symmetric. Thus, if the nuclear spins are anti-parallel (para-hydrogen), the angular momentum, J, must be even—whereas, for parallel spins (ortho-hydrogen), it must be odd. The energies of the rotational states for a free hydrogen molecule are given by:

$$E_{Jm} = E_J = BJ(J+1) \tag{9.18}$$

where $B = \hbar^2/2m_r{d_e}^2$ is the rotational constant, =7.35 meV for H_2. Here, m_r is the reduced mass of the molecule, d_e is the equilibrium separation of the H nuclei (0.0741 nm) and $m\hbar$ is the component of the angular momentum, $\hbar J$, parallel to the quantisation axis where $m = -1,0,1$ for the $J = 1$ level. It is obvious that this association of the relative nuclear spin states with the angular momentum state is contrary to our assumption above that the spin direction (and hence the scattering length) of a given proton is independent of its surroundings. This has a profound effect on the neutron scattering from molecular hydrogen. The full theory of this process has been given by Young and Koppel [3]. These authors showed that the

scattering can be divided up into terms corresponding to transitions between different J states—if $J' - J$ is even, then the neutron spin stays unchanged but if $J' - J$ is odd, then the neutron has to exchange a spin with one of the nuclei and the nuclear spin of the molecule is thus changed from odd to even (ortho to para) or vice versa. Also, of course, if J changes, the double differential equation can be written:

$$\left.{}^{d^2\sigma_{JJ'}}\right/_{d\Omega dE'} = \left(\left.{}^{k'}\right/_{k_o}\right) F_{J,J'}(\boldsymbol{Q})\exp\left((-2W(\boldsymbol{Q}))\delta\left(E_0 - E' + E_j - E_{j'}\right)\right) * S_{\mathrm{mol}}(Q,\omega) \tag{9.19}$$

where * represents a convolution. Here, the $F_{J-J'}(\boldsymbol{Q})$ functions are the form factors for the rotational transitions and $S_{\mathrm{mol}}(\boldsymbol{Q}, \omega)$ is the scattering function for the molecule centre-of-mass. Explicitly, the first few rotational transition form factors can be written:

$$\begin{aligned} F_{0-0}(Q) &= 4(\sigma_{\mathrm{c}}/4\pi){j_0}^2(Qd_e/2) \\ F_{0-1}(Q) &= 12(\sigma_{\mathrm{i}}/4\pi){j_1}^2(Qd_e/2) \\ F_{1-0}(Q) &= (4/3)(\sigma_{\mathrm{i}}/4\pi){j_1}^2(Qd_e/2) \\ F_{1-1}(Q) &= 4[(\sigma_{\mathrm{c}}/4\pi) + (2/3)(\sigma_{\mathrm{i}}/4\pi)][2{j_2}^2(Qd_e/2) + {j_0}^2(Qd_e/2)] \end{aligned} \tag{9.20}$$

Here σ_{c} and σ_{i} are as defined above for the hydrogen nucleus and j_0, j_1 and j_2 are the zero, first and second spherical Bessel functions with arguments $(Qd_e/2)$. Remembering that $\sigma_{\mathrm{i}} = 80.3$ barn and $\sigma_{\mathrm{c}} = 1.8$ barnit is clear that for para-hydrogen in its ground state, the scattering will be dominated by the $J = 0$ to $J' = 1$ (or $J = 0$ to $J' = 3, 5\ldots$) neutron energy loss transition. As the $J = 0$ state has zero rotational energy and the $J = 1$ has an energy $J(J + 1)B = 14.7$ meV, the neutron energy loss cross section will be dominated by a delta function at 14.7 meV.

The above expressions for the rotational form factors are based on the assumption that the molecule is situated in a spherical potential so that the different m states are degenerated. However, if the molecule is trapped in a perturbed potential well, the degeneracy of the m levels will be lifted. Thus, for ellipsoidal perturbation of the $J = 1$ state, we expect to find the $m = \pm 1$ levels split from the $m = 0$ state. The energy level diagram for this situation can be found in, for instance, [6]. Simple perturbation theory would suggest that the mean energy should remain fixed at 14.7 meV—so long as d_e remains fixed. Thus, if the mean energy decreases from the normal H_2 value, we can interpret this to mean that the H–H distance $(2d_e)$ has increased due to interaction with the trapping medium.

As can be seen in Eq. (9.19), this rotational transition part of the cross section has to be convoluted with the scattering function for the molecule centre of mass. If the molecule is rigidly bound, $S_{\mathrm{mol}}(Q, \omega) = \delta(\omega)$. If it is free to recoil, its cross section will be as for scattering from a perfect gas. The assumption here is that the initial state of the molecule has a defined momentum from a Maxwell–Boltzmann distribution at the sample temperature and that all final states are available for the recoiling molecule. In this case, the molecular scattering function can be written:

$$S_{\mathrm{PG}}(Q,\omega) = \left(M/\pi\hbar^2Q^2k_{\mathrm{B}}T\right)^{1/2}\exp\left[-\left(\hbar\omega - \hbar^2Q^2/4M\right)^2/\left(\hbar^2Q^2k_{\mathrm{B}}T/M\right)\right] \quad (9.21)$$

where M is the mass of the molecule, k_{B} is Boltzmann's constant and T is an effective gas temperature. It will be noted that this function has a Gaussian shape, with its mean value displaced to the average recoil energy, $\hbar^2Q^2/4M$ [6, 7].

If, on the other hand, the molecule is trapped in a harmonic potential well, the simple harmonic oscillator scattering function $S_{\mathrm{SHO}}(Q, \omega)$ will take the usual form [1] and the neutron will scatter the molecule into one of a series of equally spaced energy levels, the spacing being proportional to the steepness of the parabolic well. At low temperatures there will be a probability that it starts and finishes in its ground state. Here, the cross section for elastic scattering will vary as $\exp(-<u^2>Q^2)\delta(\omega)$ where $<u^2>$ is the mean square displacement of the molecule in the potential at temperature T. However, if the molecule is trapped in a sufficiently shallow potential well, it ends up in one of a number of closely spaced energy levels. Summing the scattering over these closely spaced states will give a continuous distribution that will approximate to the perfect gas distribution. The total scattering function for this system can be well represented by:

$$S_{\mathrm{SHO}}(Q,\omega) = \exp\left(-<u^2>Q^2\right)\delta(\omega) + \left(1-\exp\left(-<u^2>Q^2\right)\right)S_{\mathrm{PG}}(Q,\omega) \quad (9.22)$$

Now, this expression can be substituted into Eq. (9.19) to yield the full expression for the scattering including both a rotational transition combined with the molecular centre of gravity response. In particular, if the molecule starts in the para-ground state ($J=0$), the scattering will be dominated by the transition to the $J'=1$ (ortho) state (i.e. proportional to the incoherent cross section). Now, performing the convolution integral, the scattering will consist of a peak at $J(J+1)B$ (=14.7 meV) due to elastic scattering from the molecule and a broad Gaussian peak centred on $J(J+1)B+\hbar^2Q^2/4M$. Similar terms will appear at larger energy transfers for $J'=3, 5, \ldots$, etc.

Because the conversion rate between the ortho- and para-states is low except in the presence of magnetic catalysts, we have to equilibrate the gas at a given temperature in the presence of such a catalyst before adsorbing on the sample. In this case, for low temperatures, the system will become almost entirely para—while for high temperatures it will tend to 25 % para and 75 % ortho. We can therefore perform neutron scattering experiments with different predetermined ratios of the two forms so that both cross sections can be extracted.

An early example of this technique was for the case of H_2 adsorbed on bundles of single-walled carbon nanotubes [6, 7]. In Fig. 9.7 we show the inelastic scattering spectra covering the scattering from the $J=0$ to $J=1$ peak in the vicinity of 14.7 meV neutron energy loss for the forward (a) and backward (b) detector banks on the TOSCA spectrometer at ISIS. Data were obtained for a series of surface coverages. The figure shows data for 35 % coverage. For this coverage, the scattering has three components. The central component is assumed to originate

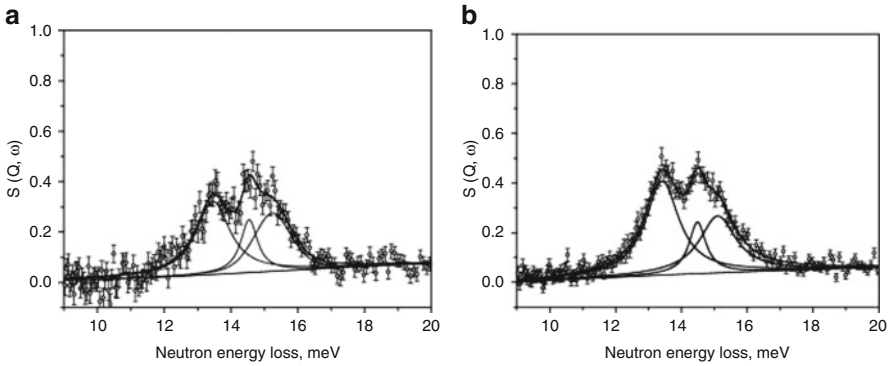

Fig. 9.7 (**a**) Forward and (**b**) back scattering spectra measured on TOSCA for H_2 on SWNT at 17 K and 30 % average surface coverage [6, 7]

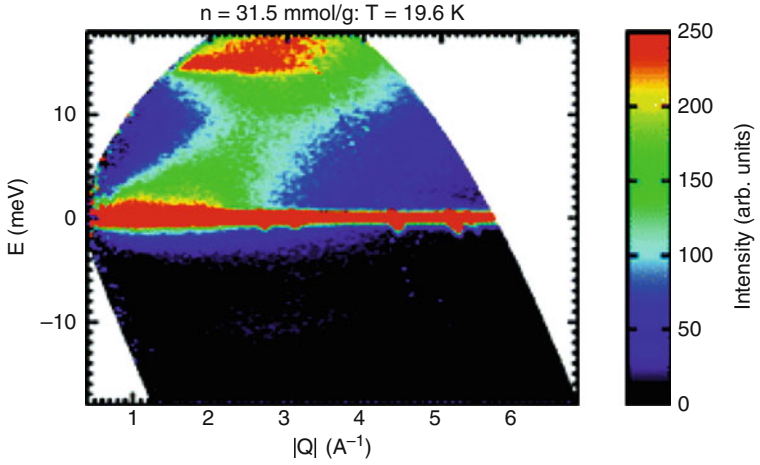

Fig. 9.8 Colour contour plots of the dynamic structure factor, $S(Q, \omega)$, of a partial loading of H_2 in MCM-41 in the liquid phase (19.6 K). The rotational level is centred on 15 meV but shows considerable Q-dependent broadening [30]

from molecules on the external convex surface of the nanotubes while the higher and lower energy peaks originate from H_2 molecules trapped along the groove sites where two nanotubes touch tangentially. In this situation, the molecule is attracted to both nanotubes giving a tetragonal distortion of the field, in which case the degeneracy is broken into a 2:1 intensity ratio.

When this measurement was repeated for activated carbons [29] the detailed structure was smeared out, presumably because the surface was much more heterogeneous.

This technique has yielded useful data for other H_2 adsorbing systems. For instance, Prisk et al. [30] have studied H_2 adsorbed in MCM-41—a high surface

area mesoporous silica glass with a narrow pore size distribution centred on 3.5 nm. In this case, the detail in the para–ortho peak is also not well defined (see Fig. 9.8), presumably because, as in the case of activated carbon, the surfaces of the silica pores were rather heterogeneous.

A major advantage of this technique arises where there are different adsorption sites in the material examined. Thus, if the sample is cooled below $\Delta E/k$ where ΔE is the energy of a given site relative to the lowest energy state, then the different types of site will progressively fill as hydrogen molecules are added. Thus the spectrum of site energies and the associated energy splittings for each site can be established. If the sample is crystalline, measurements can then be repeated using neutron diffraction but now dosing the sample with D2 for the same fillings as used previously. By fitting each diffraction pattern as a function of gas dosage, each site can be located. This technique has been particularly useful for MOF structures see Fig. 9.9 [31]. A final interesting example of this technique involves the investigation of H_2 in clathrates. This work nicely illustrates the consequences of the molecular scattering function that appears convoluted with the rotational level change scattering. There has been some interest in storing H_2 in ice clathrates. Unfortunately forming them using only H_2 requires an impractical hydrogen pressure of 2 kbar. However, if the larger of the two cavities is filled with TFH (tetrahydrofurane), the smaller cavity

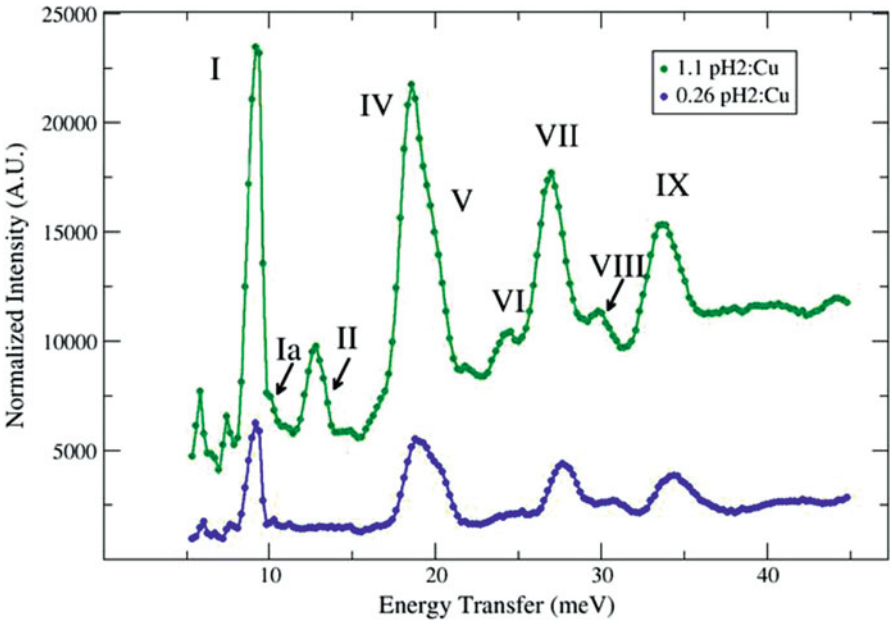

Fig. 9.9 Inelastic neutron scattering difference spectra for p-H_2 loaded HKUST-1 and the bare substrate measured on FANS at NIST. The displayed spectra result from p-H_2 scattering only and peaks of significant intensity are labelled I through IX. Ratios of p-H_2 to Cu are 0.26 (*dark grey* (*blue* online) *circles*) and 1.1 (*light grey* (*green* online) *circles*). Error bars are of similar size as the symbols [31]

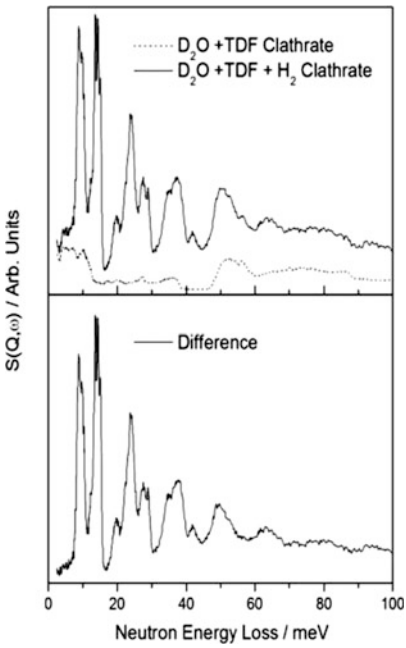

Fig. 9.10 IINS spectra from a D_2O clathrate having molecules of tetradeuterofurane (TDF) in the larger cavity to stabilise the clathrate structure and with H_2 molecules in the smaller cavity. The *upper panel* shows spectra measured both with and without H_2 and the *lower panel* shows the difference [32]

can adsorb a useful amount of H_2 at a much lower pressure. Ulivi et al. [32] have examined the scattering from one molecule of H_2 in the smaller cavity by measuring the scattering with and without the H_2. In this case it is difficult to convert all the hydrogen to the para-form in situ so measurements were made at different o/p ratios and the individual ortho and para spectra were extracted, see Fig. 9.10. The resultant spectra have been analysed showing conclusively that H_2 molecules are in a rather harmonic potential with a fundamental rattling transition at about 10 meV with its first overtone at about 21 meV. The rotational para–ortho transition at 14.7 meV shows little structure, suggesting that the rotational potential in the cavity, as seen by the molecule, is nearly spherically symmetric.

9.3 Quasi-Elastic Neutron Scattering

9.3.1 The Theory of Quasi-Elastic Neutron Scattering

In the description of inelastic neutron scattering above, the cross sections—measured or derived—describe the probability that the neutron causes a transition of the scattering system from one fixed quantum state to another. In contrast to this, "quasi-elastic" scattering describes a situation where the scattering nucleus is free to diffuse around in space and time and this causes a form of Doppler broadening, the final neutron velocity (energy) acquiring a continuous range of

values symmetrically around the original velocity. Quasi-elastic scattering therefore provides us with a very direct technique for studying the diffusion of an atomic species in either the liquid or solid phase. Given that hydrogen has a large incoherent cross section, it is easy to identify incoherent QENS due to the self-diffusion of hydrogen and hence the mechanisms giving rise to the hydrogen diffusion through a hydrogen storage system. The basic formulation of this problem was given by Van Hove [8] in the form of his space–time correlation functions, $G_s(r,\ t)$ and $G(r,\ t)$. He showed that the scattering functions, as defined below, are given, for a diffusing system, by the Fourier transformation of these correlation functions in space and time. As noted above, incoherent scattering is linked to the self-correlation function, $G_s(\boldsymbol{r},\ t)$—which provides a full definition of tracer diffusive motions—while coherent scattering is the double Fourier transform of the full correlation function, $G(\boldsymbol{r},\ t)$, which is similarly related to chemical or Fick's law diffusion processes. Formally the equations can be written:

$$\begin{aligned} S_{\mathrm{inc}}(\boldsymbol{Q},\omega) &= (1/2\pi)\int\int G_s(\boldsymbol{r},t)\exp[i(\boldsymbol{Q}\cdot\boldsymbol{r}+\omega t)]d\boldsymbol{r}dt \\ S_{\mathrm{coh}}(\boldsymbol{Q},\omega) &= (1/2\pi)\int\int G(\boldsymbol{r},t)\exp[i(\boldsymbol{Q}\cdot\boldsymbol{r}+\omega t)]d\boldsymbol{r}dt \end{aligned} \tag{9.23}$$

Here, $G_s(\boldsymbol{r},\ t)$, the self-correlation function, is defined to be the probability of finding a nucleus at position $\boldsymbol{r}$ at time t if that same nucleus was at the origin at $t=0$. Similarly, $G(\boldsymbol{r},\ t)$, the pair correlation function, is the probability of finding any atom at position $\boldsymbol{r}$, at time t, if a particular atom was at the origin at $t=0$. Strictly speaking, the scattering functions are not symmetric in ω because the probability of neutron energy gain is related to that of energy loss by the Boltzmann (detailed balance) factor, $exp(\hbar\omega/kT)$, but so long as $\hbar\omega \ll kT$, the scattering functions will be symmetric and the correlation functions will be real and so do not need to be treated as operators. It should be noted that, in practice, we have to construct models for the diffusion process and then calculate the corresponding scattering function and hence compare the resulting function with experiment. The simplest such model is that due to Vinyard [33] who noted that in Einstein or tracer diffusion (i.e. self-diffusion measured using incoherent QE scattering) for times significantly longer than the mean time between individual diffusive jumps (assumed to be uncorrelated with each other) the self-correlation function will be a Gaussian of mean square deviation $<r^2> = 6D_t t$, where D_t is the tracer diffusion coefficient. On substituting this expression into (10.20) above, we obtain:

$$S_{\mathrm{inc}}(Q,\omega) = (1/\pi)\left(D_t Q^2\right) \Big/ \left[\left(D_t Q^2\right)^2 + \omega^2\right] \tag{9.24}$$

This expression is a normalised Lorentzian in ω, of half width at half maximum, $D_t Q^2$. Thus, by measuring the quasi-elastic width as a function of Q^2, we can extract D_t. Now, in practice, when we plot data of this kind, we get a curve which at low Q can be perfectly fitted to a straight line starting from the origin but which always

flattens out at higher Q. This is due to the fact that at higher Q, the effective observation time becomes shorter and the details of the individual jumps become important.

9.3.2 The Chudley–Elliott Model

There are a variety of models in the literature to describe self-diffusion of atoms in a liquid or some other disordered solid in terms of the short-time behaviour. Full details of these models can be found in the book by Bee [3]. As we are mainly interested in diffusion in a periodic lattice, we shall move directly to consideration of the Chudley–Elliott model [34]. Here the basic model is that the diffusing species is able to hop between equivalent sites on a regular Bravais lattice where the probability of a given atom jumping from a given site occupied at $t = 0$ to a nearest-neighbour site is given by a Poisson distribution. The original derivation due to Chudley and Elliott was given in terms of a set of differential equations but a more transparent approach is that due to Gissler and Rother [35]. The latter derivation is based on the fact that a Markovian random walk on the lattice can be related to the van Hove correlation function by the expression

$$G_s(r,t) = \sum_{n=1}^{\infty} R_n\left(\boldsymbol{r}_{i,j,k}\right) T_n(t) \tag{9.25}$$

where n is the number of random jumps on the Bravais lattice and $\boldsymbol{r}_{i,j,k}$ is the vector to the lattice site displaced by i, j, k lattice vectors from the origin. Thus $R_n(\boldsymbol{r}_{i,j,k})$ is the probability function describing the probability of displacement of the proton from the origin to the lattice point i, j, k after n jumps and $T_n(t)$ is the Poisson function describing the probability of the diffusing atom having had n jumps at time t.

The important point here is that $G_s(\boldsymbol{r}, t)$ is only separable in time and space so long as there is no correlation between the nth and $(n+1)$th jump. This is precisely true for a small proton concentration. At higher concentrations, however, correct allowance for correlations, obtained using the powerful general method of Monte Carlo simulation, shows that for f.c.c. lattices, correlations make relatively little difference to the correlation function [36]. Now, for cases where $G_s(r, t)$ is separable into separate functions in $\boldsymbol{r}$ and t, it is easy to calculate the incoherent scattering function from Eq. (10.22). First, we calculate $I(\boldsymbol{Q}, t)$ the "Intermediate Scattering Function", by Fourier transforming the self-correlation function over $\boldsymbol{r}$:

$$I_{\text{inc}}(\boldsymbol{Q},t) = \int_0^{\infty} \sum_{n=1}^{\infty} R_n(\boldsymbol{r}) T_n(t) \exp(i\boldsymbol{Q}\cdot\boldsymbol{r}) d\boldsymbol{r} \tag{9.26}$$

Now $R_n(\boldsymbol{r})$ is just the n-fold convolution of the single jump probability distribution with itself n times, i.e. a Markov chain, where $R_1(\boldsymbol{r}) = \left({}^{1}/_{m}\right)\sum_{l}\delta(\boldsymbol{r}-\boldsymbol{r}_l)$ is the probability of the atom jumping to the lth site of a set of m nearest-neighbour sites around the origin and $T_n(t) = \frac{(\Gamma t)^n}{n!}e^{-\Gamma t}$ is the probability of the atom having taken n jumps at time t, i.e. the nth Poisson function, Γ being the probability of jumping/unit time. The "separability" property of the function implies that the probability of occupation of all sites $\boldsymbol{r}_{i,j,k}$ follows the same time dependence. Now a well-known property of convolution functions is that the F.T. of a convolution of two functions is the product of the FT of each function. Hence

$$\int_0^\infty R_n(r)\exp(iQ\cdot r)dr = F_n(Q) = (F(Q))^n \tag{9.27}$$

where $F(\boldsymbol{Q}) = \int_0^\infty \exp(i\boldsymbol{Q}\cdot\boldsymbol{r})\left[(1/m)\sum_l \delta(\boldsymbol{r}-\boldsymbol{r}_l)\right]d\boldsymbol{r}$ is the FT of the first jump probability distribution.

Hence $I(\boldsymbol{Q},t) = \sum_n F(Q)^n T_n(t) = \sum_n F(Q)^n \frac{(\Gamma t)^n}{n!}e^{-\Gamma t}$

The expression for $I(\boldsymbol{Q}, T)$ is thus an exponential expansion which can be summed to give

$$I(\boldsymbol{Q},t) = \exp(-\Gamma t)\exp[F(\boldsymbol{Q})\Gamma t) = \exp\left[-(1-F(\boldsymbol{Q}))\Gamma t\right). \tag{9.28}$$

We can now derive the incoherent scattering function by doing an F.T. in t. In doing so, we have to remember that $G_s(r, t)$ is symmetric about $t=0$ ($G_s(\boldsymbol{r}, t)=\delta(\boldsymbol{r})$ at $t=0$) so that, to integrate over both + and − time, we have to use |t|. This amounts to doing the F.T. in positive time and then adding to this term its complex conjugate.

$$S_{\text{inc}}(Q,\omega)_{C-E} = \int_{-\infty}^{\infty}\exp\left[i\omega t-(1-F(Q)\,\Gamma|t|\right]dt = \frac{1}{\pi}\left[\frac{\Gamma(1-F(Q))}{i\omega-1-F(Q)|}\right] + \text{its}$$

complex conjugate. i.e.

$$S_{\text{inc}}(Q,\omega)_{C.E} = \left({}^{1}/_{\pi}\right)\frac{\Gamma\left(1-F(Q)\right)}{\omega^2+[(1-F(Q))\Gamma]^2} \tag{9.29}$$

This expression is a Lorentzian in ω with a width that varies in Q as $\Gamma[1-F(Q)]$.

Let us, as an example, derive the form of $(1-F(Q))$ for diffusion on an f.c.c. lattice. If the lattice parameter is a, the jumps are $(a/2(\boldsymbol{i}+\boldsymbol{j}))$ and equivalent, where $\boldsymbol{i}, \boldsymbol{j}, \boldsymbol{k}$ are unit vectors in the x, y, z directions. Thus, by resolving $\boldsymbol{Q}$ into the respective components, Q_x, Q_y and Q_z, we can write the broadening $L(Q)$ as

$$L(Q) = \Gamma(1 - F(\boldsymbol{Q})) = \Gamma\{1 - 1/3[\cos(Q_x a/2)\cos(Q_y a/2) + \cos(Q_y a/2)\cos(Q_z a/) + \cos(Q_z a/2)\cos(Q_x a/2)\}] \quad (9.30)$$

We can see from this equation that the broadening at small Q is $L(Q) = \Gamma Q^2 a^2/12$ and this yields $D_t = \Gamma < r^2 > /6$ where $< r^2 >$ is the mean square jump length ($a^2/2$). As expected at higher Q, the broadening flattens off and then reduces to zero at the reciprocal lattice points of the defect lattice. Similar behaviour is found for the broadening function on b.c.c. and h.c.p. lattices.

9.3.3 Diffusion of H in the α Pd/H System

The classic example of the Chudley–Elliott model may be seen in the α-phase of the Pd/H system in which the hydrogen occupies the octahedral interstitial sites on the f.c.c. lattice these sites themselves forming an f.c.c. lattice. Here the hydrogen concentration is sufficiently low for successive jumps to be uncorrelated. By introducing hydrogen into a single crystal of palladium without crossing into the β-phase, which would disrupt the lattice, it was possible to show that the Chudley–Elliott model for nearest-neighbour jumps reproduced the measured broadening as a function of both the magnitude and direction of Q [37, 38]. It was subsequently shown to also describe, to a good approximation, the broadening in a single crystal of Pd maintained in the beta phase by keeping the crystal hot when under hydrogen pressure [39]. This experiment demonstrated that the Chudley–Elliott model can be used at higher concentrations, allowing for the fact that the diffusion is reduced by the site blocking factor $(1 - c)$, the chance that a neighbouring site is empty and, to a lesser extent, by correlation effects [36]. It is interesting to note that the first attempts to predict this process theoretically suggested that, once a proton escaped from its site, it moved through several sites before re-trapping [40]. However, when the interaction with conduction electrons was included, the jump was found to be limited to the nearest-neighbour site so the agreement with experiment was excellent [41].

9.3.4 Lattices with More Than One Atom/Unit Cell

The original formulation of the Chudley–Elliott Model is only valid for a Bravais lattice. However, it has been extended to the case of hydrogen absorbed in the transition metals with b.c.c. lattices (Nb, Ta and V) having non-Bravais lattices by Rowe et al. [42]. In these systems, the H atoms are located on distorted tetrahedral sites (6/metal atom). The solution of the multi-site Chudley–Elliott for this case involves a set of 6 coupled differential equations which yield a solution consisting of a set of 6 Lorentzians having different Q-dependent widths and intensities. For the polycrystalline samples of V/H investigated by these authors in an early

experiment, after polycrystalline averaging, it was found that the broadening could be fitted with a single Lorentzian which yielded good values for D_t, the tracer diffusion temperature as a function of temperature. The real situation, however, is rather more complicated because the trapped H atom causes local distortion. A full description of the diffusion in this system has recently been given by Blomqvist et al. [43] using ab initio molecular dynamics which fully describes the process. At low temperatures the hydrogen is strongly trapped in a local strain field but at higher temperature the proton escapes before the strain field is fully developed and the activation energy for diffusion is reduced. The other familiar example of a non-Bravais lattice is the hexagonal lattice where the hydrogen can be trapped on both tetrahedral and octahedral sites. Here again the full theory gives rise to a set of Lorentzian broadenings [44].

9.3.5 QENS from an Atom Diffusing in a Lattice with Traps

There are a variety of cases where the diffusing atom is initially trapped on one or more localised sites between which it jumps rapidly. The crucial point here is that when there is localised diffusion, $G_s(\mathbf{r}, t) \rightarrow G_s(\boldsymbol{r}, \infty)$ as $t \rightarrow \infty$. Thus, for most of the relevant time scale, $G_s(r, t)$ is independent of time so that the corresponding scattering function is elastic, i.e. a delta function at $\omega = 0$ while the remaining part, $[G_s(\boldsymbol{r}, \mathrm{t}) - G_s(\boldsymbol{r}, \infty)]$ is quasi-elastic. Here we are using the fact that

$$S_{\mathrm{inc}}(Q, \omega = 0) = (1/2\pi) \int G_s(r, \infty) \exp(i\boldsymbol{Q} \cdot \boldsymbol{r}) d\boldsymbol{r} \tag{9.31}$$

The Q-dependence of the elastic scattering is known as the incoherent elastic scattering function which is normalised to unity at low Q and reduces gradually to zero at high Q. The wider the self-correlation function in $\boldsymbol{r}$, the narrower is the elastic scattering function in Q. The quasi-elastic terms increase from zero with increasing Q so as to keep the total scattering normalised to unity. Now, if the trapping process has a finite lifetime and alternates with a slower lattice diffusion process, the elastic peak becomes quasi-elastic with a small broadening that increases with Q and is superimposed on the broad QE term due to the rapid jumps between the localised trapping sites.

The most fully investigated case of localised H jumping combined with longer range lattice diffusion arises for the case of hydrogen diffusion in C15 Laves phase hydrides which have been fully investigated by Skripov et al. [13 and references cited there]. The scattering function is fitted with a model for a localised jump process:

$$S_{\mathrm{inc}}(Q, \omega) = A_0(Q)\delta(\omega) + A_1(Q)L(\omega, \Gamma) \tag{9.32}$$

Here it is assumed that the lifetime of the proton on the local trapping sites is too long for there to be significant QE broadening of the elastic peak due to long-range diffusion. The measured scattering function is obtained by convoluting this expression with the resolution function of the instrument and fitting the observed data to the resulting peaks for each value of Q (angle of scatter)—where it is assumed that $A_0(Q) + A_1(Q) = 1$. This model assumes that the broadening, L, due to the localised jumping is independent of Q, as expected for such a process. The fitted form of the function, $A_0(Q)$, in this case [13] is consistent with a 2-site jump model rather than a 6-site model which might have been expected. It is also concluded that a fraction of the protons, p, which do not participate in the jumping process—presumably due to H–H interactions or trapping on defects—increases as the temperature is lowered.

Another situation in which two Lorentzian functions have been observed is for the case of H diffusing in nanoscale Pd in comparison with coarse-grained palladium [45]. In this experiment, the nanoscale Pd/H showed one elastic and two quasi-elastic components. It was also observed that the measured fractional intensity of each component appears to be Q-independent, suggesting that separate site populations may be responsible for the broadening rather than two types of motion for a single site population. The authors' conclusion was that the elastic component was due to hydrogen trapped at lattice defects and the broad Lorentzian (faster diffuser) was due to surface diffusion as this component is not present in microcrystalline palladium measured at the same time.

9.4 Conclusions

Neutron scattering techniques have proved to be a powerful way of understanding the detailed behaviour of hydrogen in hydrogen storage materials. The use of the latest generation of high powered neutron sources, e.g. the SNS at Oak Ridge and the ESS in Sweden will undoubtedly continue this tradition.

References

1. G.L. Squires, *Introduction to the Theory of Thermal Neutron Scattering* (Cambridge University Press, Cambridge, 1978)
2. D.K. Ross, Neutron scattering studies of metal hydrogen systems, in *Hydrogen in Metals III: Properties and Applications*, ed. by H. Wipf (Springer, New York, 1997), pp. 153–210
3. J.A. Young, J.A. Koppel, Phys. Rev. **135**, A603–A611 (1964)
4. M. Bee, *Quasi-Elastic Neutron Scattering* (Institute of Physics, Bristol, 1988)
5. J. Iniguez, T. Yildrum, T.J. Udovic, M. Sulic, C.M. Jensen, Phys. Rev. B **70**, 060101(R) (2004)
6. P.A. Georgiev, D.K. Ross, A. De Monte, U. Montoaretto-Marullo, R.A.H. Edwards, A.J. Ramirez-Cuesta, D. Colognesi, J. Phys. Condens. Matter **16**, L 73–78 (2004)
7. P.A. Georgiev, D.K. Ross, A. De Monte, U. Montoaretto-Marullo, R.A.H. Edwards, A.J. Ramirez-Cuesta, M.A. Adams, D. Colognesi, Carbon **43**, 895–906 (2005)
8. L. Van Hove, Phys. Rev. **95**, 249 (1954)

9. National Centre for Neutron Research, National Institute for Science and Technology USA. See web site: http://www.ncnr.nist.gov/resources/n-lengths
10. J. Eckert, J.A. Goldstone, D. Tonks, D. Richter, Phys. Rev. **B27**, 1980 (1983)
11. J.J. Rush, J.M. Rowe, D. Richter, Z. Phys. B **55**, 283 (1984)
12. M. Kemali, J.E. Totolici, D.K. Ross, I. Morrison, Phys. Rev. Letts. **84**, 1531 (2000)
13. A.V. Skripov, V. Paul-Bancour, T.J. Udovic, J.J. Rush, J. Alloys Compd. **595**, 28 (2014)
14. B.N. Brockhouse, A.T. Stewart, Phys. Rev. **100**, 756 (1955)
15. D.L. Roach, J.D. Gale, D.K. Ross, Neutron News **18**, 21 (2007)
16. M.J. Benham, D.K. Ross, C. Lartigue, A. Percheron-Guegan, Zes. Physik. Chemie NF **147**, S219–S229 (1985)
17. J.F. Fernandez, M. Kemali, D.K. Ross, C. Sanchez, J. Phys. Condens. Matter **11**, 10353–10373 (1999)
18. A.J. Ramirez-Cuesta, Comput. Phys. Commun. **157**, 226–238 (2004)
19. K.-M. Ho, H.-J. Tao, X.-Y. Zhu, Phys. Rev. Lett. **53**, 1586 (1984)
20. C. Elsässer, K.M. Ho, C.T. Chan, M. Fähnle, J. Phys. Condens. Matter **4**, 5189 (1992); ibid **4**, 5207 (1992)
21. Neutron instrumentation at ISIS, http://www.isis.stfc.ac.uk/instruments/instruments2105.html
22. P.C.H. Mitchell, S.F. Parker, A.J. Ramirez-Cuesta, J. Tomkinson, *Vibrational Spectroscopy with Neutrons with Applications in Chemistry, Biology and Materials Science* (World Scientific Publishing and Imperial College Press, Singapore and London, 2005)
23. B. Bogdanovic, M. Schwickardi, J. Alloys Compd. **253–254**, 1 (1997)
24. ABINIT. See http://www.abinit.org
25. M. Koza, A. Leithe-Jasper, H. Rosner, W. Schnelle, H. Mukta, M.R. Johnston, Y. Grin, PRB **89**, 014306 (2014)
26. D.L. Roach, D.K. Ross, J.D. Gale, J.W. Taylor, J. Appl. Crystallogr. **46**, 1755–1770 (2013)
27. A.C. Buckley, D.L. Roach, J.D. Gale, M.T. Garba, C.E. Buckley, D.K. Ross, D.A. Sheppard, D. Carter, J.W. Taylor, A Q-dependent model for the vibrational modes in MgD2 using poly-CINS (in preparation)
28. Z. Wu, R.E. Cohen, Phys. Rev. B **73**, 235116 (2006)
29. P.A. Georgiev, D.K. Ross, P. Albers, A.J. Ramirez-Cuesta, Carbon **44**, 2724 (2006)
30. T.R. Prisk, M.S. Bryan, P.E. Sokol, Phys. Chem. Chem. Phys. **16**, 17960 (2014)
31. C.M. Brown, Y. Liu, T. Yildrim, V.K. Peterson, C.J. Kepert, Nanotechnology **20**, 204025 (2009)
32. L. Ulivi, M. Celli, A. Giannasi, A.J. Ramirez-Cuesta, M. Zoppi, J. Phys. Condens. Matter **20**, 104242 (2008) (5 pages)
33. G.H. Vinyard, Phys. Rev. **110**, 999 (1958)
34. C.T. Chudley, R.J. Elliott, Proc. Phys. Soc. **77**, 353 (1960)
35. W. Gissler, H. Rother, Physica **50**, 380 (1070)
36. D.K. Ross, D.L.T. Wilson, *Neutron Inelastic Scattering Vienna 1977*, vol. 1 (IAEA, Vienna, 1978), p. 383
37. J.M. Rowe, K. Sköld, L.A. de Graaf, G.A. Ferguson, Phys. Rev. Lett. **29**, 1250 (1972)
38. C.J. Carlile, D.K. Ross, Solid State Commun. **15**, 1923 (1974)
39. I.S. Anderson, D.K. Ross, C.J. Carlile, *Neutron Inelastic Scattering Vienna 1977*, vol. 2 (IAEA, Vienna, 1978), p. 229
40. M. Gillen, J. Phys. Chem. **19**, 6169 (1986)
41. Y. Li, G. Wahnstrom, Phys. Rev. B **46**, 14528 (1992)
42. M.J. Rowe, K. Sköld, H.E. Flotow, J.J. Rush, J. Phys. Chem. Solids **32**, 41 (1971)
43. A. Blomqvist, G.K. Palsson, C.M. Araujo, R. Ahuja, B. Hjörvarsson, Phys. Rev. Lett. **105**, 185901 (2010)
44. I.S. Anderson, J.E. Bonnet, A. Heidemann, D.K. Ross, S.K.P. Wilson, J. Less-Common. Met. **101**, 405 (1984)
45. S. Janssen, H. Natter, R. Hempelmann, T. Striffler, U. Stuhr, H. Hahn, J.C. Cook, Nanostruct. Mater. **9**, 579–582 (1997)

Chapter 10
Elastic Recoil Detection Analysis

Pascal Berger, Caroline Raepsaet, and Hicham Khodja

Abstract Among the family of Ion Beam Analysis techniques for material characterization, Elastic Recoil Detection Analysis (ERDA) exploits the spectroscopy of recoil nuclei moving under the impact of the ions of the beam. This technique is well suited to light elements profiling, especially for hydrogen measurements which can be performed with usual helium-4 beams available in most facilities. This chapter presents an overview of ERDA main features and focuses on a selection of recent papers dealing with hydrogen measurements in materials for miscellaneous applications, divided into four sections: metals, ceramics, minerals, and thin films.

Keywords Ion Beam Analysis • Elastic Recoil • Hydrogen • Hydrides • Zircaloy • Proton Conductors • Anhydrous Minerals • DLC films • SiGe multilayers

10.1 Introduction

Ion Beam Analysis (IBA) had grown from a branch of nuclear physics devoted to the study of the structure of the nuclei and of the related mechanisms of the interaction of MeV ions with matter. As early as in the 1950s, data acquired on elastic scattering or nuclear reaction cross sections have been identified as a novel means to access to materials elemental analysis [1]. Questions arising at this pioneering time were to find suitable data in the mass of nuclear experiments, especially for light elements [2]. Whereas Nuclear Reaction Analysis (NRA) and Rutherford Back-Scattering (RBS) became rapidly reference techniques for a large range of elemental characterizations, specific methods for hydrogen analysis appeared later, in the 1970s only.

Hydrogen quantification and profiling had been developed from both nuclear reactions and elastic scattering. Merely, nuclear reactions used were already known proton induced reactions on heavier elements, but with the heavy element used as

P. Berger (✉) • C. Raepsaet • H. Khodja
Laboratory for the Study of Light Elements (LEEL), NIMBE, CEA, CNRS, Université Paris-Saclay, CEA-SACLAY, F-91191, Gif sur Yvette, France
e-mail: pascal.berger@cea.fr; caroline.raepsaet@cea.fr; hicham.khodja@cea.fr

H. Fritzsche et al. (eds.), *Neutron Scattering and Other Nuclear Techniques for Hydrogen in Materials*, Neutron Scattering Applications and Techniques,
DOI 10.1007/978-3-319-22792-4_10

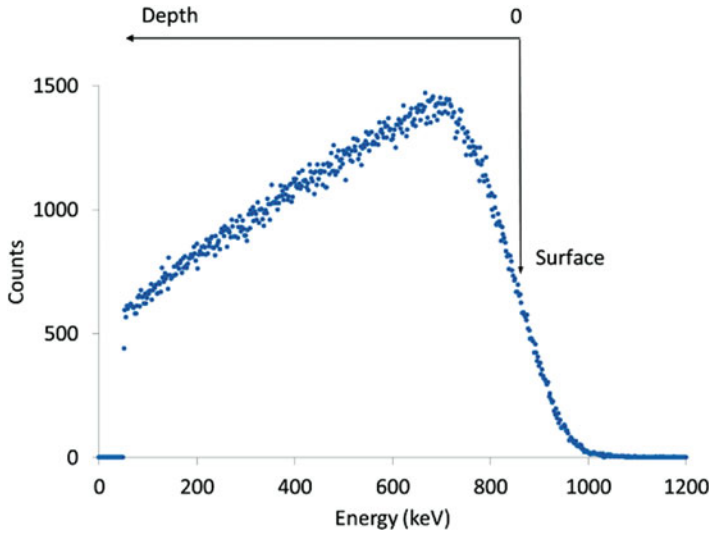

Fig. 10.1 ERDA spectrum of a Kapton® film bombarded with 3 MeV $^{4}He^{+}$ beam

the projectile and the hydrogen as the target. Optimum analytic characteristics and availability of heavy ions beams have led to a use of ^{19}F induced reactions [3], ^{7}Li induced reactions [4], ^{11}B induced reactions [5], and above all ^{15}N induced reactions [6]. Detection of recoil protons has also been developed during the same period. Indeed spectrometry of elastically scattered recoil protons or Elastic Recoil Detection Analysis (ERDA) is possible, provided, a particle detector is placed at backward angles, which requires specific geometry, grazing incidence, or forward transmission [7, 8].

Although mostly less sensitive than NRA for hydrogen measurement, ERDA has reached a predominant position for quantitative hydrogen profiling, thanks to its easy implementation. Figure 10.1 presents an example of a basic ERDA spectrum obtained for homogeneous hydrogen depth distribution (here in a Kapton® foil). This spectrum records the number of recoil protons detected as a function of their energy.

The position of the step at higher energy corresponds to the protons arising from the surface of the sample whereas lower energy counts correspond to deeper hydrogen atoms, which opens up the possibility of hydrogen concentration depth profiling by converting the energy shift from the surface into a depth scale. The intensity of the signal is related to hydrogen concentration, but the yield depends on beam energy and depth. Absolute hydrogen concentrations may be obtained either with the use of standards or with the help of simulation codes which integrate fundamental parameters of particle–matter interaction. Basics of ERDA spectrum formation are detailed in the next sections.

10.2 Principles of Elastic Recoil

10.2.1 Kinematics of Scattering Events

In their principles, fundamentals of ERDA are very similar to those governing RBS. Since valuable and exhaustive presentations of those techniques are found in dedicated books [9–11], only basics will be reported in this section.

When a sample is exposed to a high energy ion beam, ions undergo both elastic and inelastic processes. Elastic processes are mere collisions with nuclei of the sample with conservation of the total kinetic energy. Inelastic processes mainly consist in interactions with electrons which induce excitations and ionizations. Figure 10.2 illustrates a schematic representation of elastic impact where M_1 represents the incident ion (scattered) and M_2 the impacted nucleus (recoil). RBS is based on the spectroscopy of scattered particles, whereas ERDA measurement concerns recoil nuclei, but they share the same kinematics.

By applying the principles of energy conservation for elastic impact (momentum and kinetic energy), energy transfer and scattering angles of the nuclei are strictly determined, such as for the following relation:

$$\tan\theta = \frac{\sin(2\phi)}{(M_1/M_2) - \cos(2\phi)} \tag{10.1}$$

In the case of hydrogen measurement by ERDA, the projectile is heavier than the recoil ($M_1 > M_2$). A consequence of this is a limitation of the incident beam deflection angle up to θ_{max} with $\sin(\theta_{max}) = M_2/M_1$ and the existence of two solutions (θ, ϕ) for relation (10.1). In usual ERDA experiments (^{4}He beam, ^{1}H detection), θ_{max} value is 14.47° and the measurement setup detects recoil protons at angles ϕ near 30° (cf. Sect. 10.3.2).

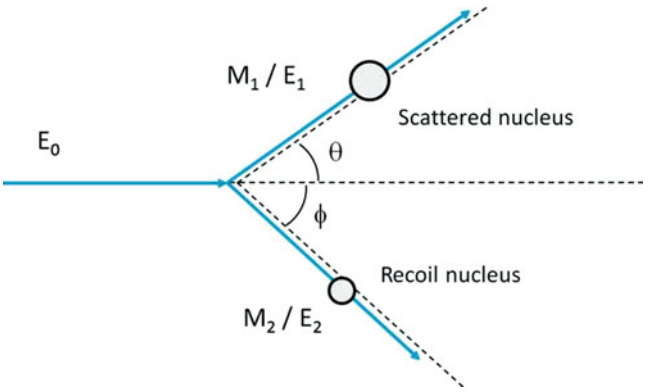

Fig. 10.2 Kinematics of elastic scattering

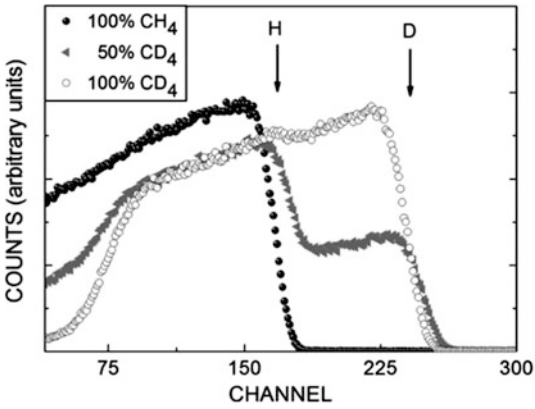

Fig. 10.3 ERDA spectra of deuterated a-CH films (from [12])

Like for RBS, a kinematic factor relating projectile and recoil energies applies for ERDA:

$$E_2 = KE_0 \quad \text{with} \quad K = \frac{M_1 M_2 \cos^2 \phi}{(M_1 + M_2)^2} \tag{10.2}$$

For a ^{4}He beam on a hydrogen-containing target, the K variation with M_2 is rapid enough to distinguish ^{1}H and ^{2}H recoil atoms, at least at the sample surface (see section below for depth information). Figure 10.3 illustrates this feature with ERDA spectra acquired on amorphous hydrogenated carbon thin films, grown by plasma-enhanced chemical vapor deposition from a deuterated methane precursor [12]. Steps related to hydrogen and deuterium are clearly separated and enable to measure H/D concentration ratios according to the CH_4/CD_4 proportion in the inlet mixture (0–100 %).

10.2.2 Energy Loss and Depth Resolution

When entering matter, ions slow down progressively, mainly by interaction with the electrons, and, at low energies, by nuclear interaction. This energy loss depends on the nature of the incident ion, its energy, and on the composition of the target. Hence, a nuclear scattering event localized below the surface occurs at lower energy than the nominal energy of the beam and scattered particles undergo additional slowing down to get out of the sample. So, the deeper the nuclear impact occurs, the lower is the energy of the recoil nucleus.

This process is the basis of depth resolution offered by ERDA spectra. The conversion of the energy shift from the surface signal into a depth scale is based on the knowledge of stopping power, S, of the probed material, which is defined as the energy loss dE of particles deposited through interaction processes in a thickness dx

of the material. The total energy loss ΔE into a thickness x, between energies E_{in} and E_{out} may be then expressed as:

$$\Delta E = \int_0^x \frac{dE}{dx} dx = \int_{E_{\text{in}}}^{E_{\text{out}}} S(E) dE \tag{10.3}$$

Since beam energies in use for common IBA are relatively high, stopping power $S(E)$ comes from electronic interaction only and is well described theoretically in this range by the Bethe–Bloch formula [13] which predicts variations of $S(E)$ proportional to $1/E$. However, best estimations are obtained from compilations of large sets of experimental data to get analytical equations of $S(E)$ [14, 15]. Although empirical, these models are included in most simulation codes.

Depth resolution should be theoretically limited by the minimum detectable energy loss (energy resolution of usual particle detectors is typically 15 keV). In practice, depth resolution degrades under *straggling* effects. Since statistical in nature, interaction of particles with matter leads to energy loss fluctuations which broaden energy distribution and angular dispersion of ion beams [16]. Thus, best depth resolutions are achieved only close to the sample's surface.

Energy straggling is still difficult to take into account in simulation codes and is mostly evaluated from Bohr's simple model which assumes that the amount of energy straggling is Gaussian and related to the areal density of electrons traversed by the beam. As a consequence of multiple scattering, angular distribution broadening also occurs and contributes to depth resolution broadening in ERDA spectra [17].

10.2.3 Hydrogen Concentration Determination

As already indicated in the introduction section, hydrogen concentrations can be deduced from ERDA spectra in two ways, measurement of a known standard or spectrum simulation.

The use of standards is relatively easy to implement as it is based on a comparison of ERDA yield between a reference and the unknown sample. For a given number of incident ions, the amount of recoil protons detected is related to the number of hydrogen atoms present in the analyzed thickness (H atoms/cm^2). Quantification requires then the assessment of this thickness from stopping power data (cf. Sect. 10.2.2), since it varies with the composition of the matrix. Accuracies within 4–5 % are currently achieved. The most used hydrogen standard in the IBA community is polymer films of Kapton®, known to be resistant enough to ion irradiation, at least within the typical time needed for spectrum acquisition (a few minutes to a few ten of minutes). Accurately characterized metallic hydrides can also be used. Depending on the matrix material, detection limits in the 100–300 at. ppm (a few tens of wt. ppm) can be achieved.

Since ERDA spectra contain depth-resolved information, selection of an appropriate energy region of interest (ROI) in the spectrum enables to determine

hydrogen concentration at a given depth. This feature is at first used to avoid bias due to surface hydrolysis or atmosphere contamination (presence of a surface peak) by selecting a ROI related to deeper hydrogen, but may also be used for depth profiling within the full analyzed depth.

Although spectra can be treated manually to extract depth profile from successive selection of ROIs, data reduction is more conveniently obtained with the help of a simulation code, by fitting calculated spectra to experimental data. ERDA dedicated codes had been at first developed in the 1980s, such as GABY [18], but use of general purpose RBS-ERDA-NRA simulation codes is preferred now, such as SIMNRA [19] and IBA Data Furnace [20]. All these codes are based on physical models which describe ion–matter interaction, without adjustable scaling parameters.

10.3 Instrumentation

10.3.1 Accelerators and Beam Lines

A facility dedicated to IBA is usually based on a high voltage electrostatic accelerator, one or several beam lines, including focusing lenses if used in microbeam mode, and analysis chambers equipped with detectors for particles, X-rays and gamma rays. An analyzing magnet, placed at the exit of the accelerator, deflects the beam and distributes ions in beam lines. Its major role is to limit ion energy spread around nominal energy. High vacuum is maintained in the beam lines, in the 10^{-4}–10^{-5} Pa range.

There exist two designs of electrostatic accelerators: Van de Graaff (single stage) or Tandem (double stage). In a single stage, the ion source is internal to the tank of the accelerator, whereas it is external in a tandem, which enables a large flexibility in the choice of the ions to be accelerated, especially for medium and heavy ions. However, since negative ions are required, beam brightness is lower with a tandem which limits the available intensity especially for helium microbeams. Single stage accelerators are then preferred when μ-ERDA is in the suite of analytical techniques of the facility.

10.3.2 Conventional Detection Setup. Reflection and Transmission Geometry

A conventional ERDA setup consists of a ^{4}He beam directed onto the target surface at a grazing incidence so that recoil hydrogen atoms can leave from the sample surface, also at a grazing incidence and be detected by means of a silicon surface barrier detector. Since forward scattered ^{4}He from the elements of the matrix are also emitted in the same direction, an absorber foil (usually aluminum) of adequate thickness is

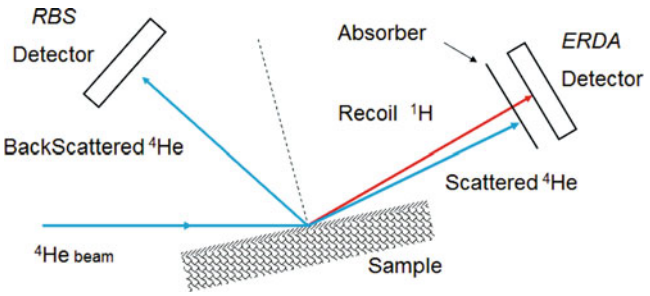

Fig. 10.4 Geometry of conventional ERDA setup

placed before the detector so that ^{4}He are stopped in the foil, whereas protons slow down only and remain detected. A second particle detector is often placed at a backward angle to monitor the RBS signal (Fig. 10.4). This geometry can be extended to the measurement of others light elements by the use of heavier incident ions [21].

Whereas a grazing incidence is required to perform ERDA on thick targets, normal incidence is possible with thin samples provided material thickness is low enough—typically up to a few tens of micrometers—for recoil protons to be collected at the rear side through the sample [22]. The main advantage of transmission ERDA is the increase of analyzed thickness and lateral resolution due to absence of sample tilt and a higher sensitivity resulting of the possibility to use larger solid angles of detection without significant variation of interaction parameters (cross sections, kinematics).

10.3.3 Less-Conventional Detection Setups

An attractive variant of transmission ERDA is Elastic Recoil Coincidence Spectroscopy (ERCS) based on the use of a proton beam. Each proton–proton collision leads to a simultaneous forward emission of both protons at 90° with respect to each other's trajectory. By detecting them in coincidence, as seen on Fig. 10.5, hydrogen events can be sorted from the huge background of simple forward scattering events on heavier elements.

The improvement of sensitivity comes from high cross sections of scattering events at forward angles. Very high sensitivities, up to the at. ppm, can be reached when using high energy protons (10–20 MeV) and very large solid angle detectors [23]. Since proton–proton scattering cross sections became recently available [24], ERCS can be performed without any reference standards. However, the drawback of ERCS is a quantification process no longer straightforward for the lower proton energy range (up to 5 MeV) because of multiple scattering effects which induces attenuation of the signal as a function of depth. Novel detectors are now proposed to

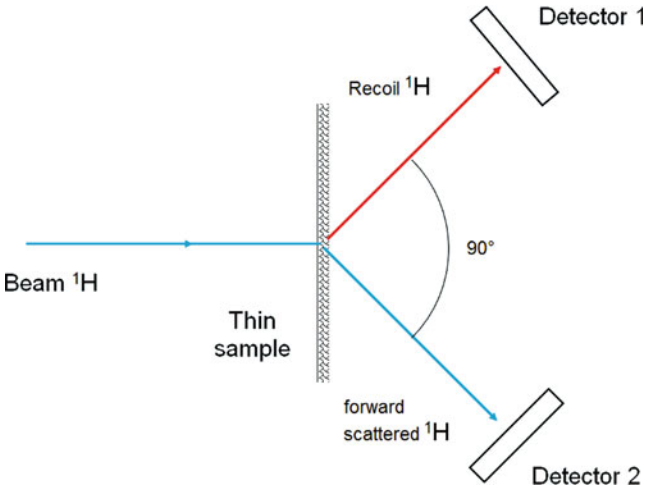

Fig. 10.5 Geometry of ERCS setup

enhance energy resolution with position sensitive detection to reduce effects of angular spread of large detectors used for ERCS [25].

In conventional ERDA, the absorber foil intends to separate forward scattered incident ions from recoil atoms. Its presence limits depth resolution in the near surface region and imposes the use of incident ions heavier than the analyzed ones. Alternatives solutions exist such as telescope detection where the role of the foil is played by a thin particle detector placed before a thick one. Ions are then identified according to their energy loss ΔE in the thin detector whereas the residual energy E_r is measured by the thick one. Scattered particles may also be removed by a ExB filter, but solid angles of such detectors are small. On the other hand, Time of Flight ERDA, largely in use with heavy ions beams, is not suitable for hydrogen detection because of a very low efficiency (~30 %).

10.4 Hydrogen Measurements in Metals

Mastering hydrogen concentration in metals is a crucial question which covers several domains such as steel embrittlement, where hydrogen is considered as unwanted, or hydrogen storage, where concentration levels are wished to be as high as possible. Apart from the intrinsic analytical difficulty of hydrogen measurement, easy mobility of hydrogen in metals and its influence on mechanical properties, starting from very low concentrations, tend to favor the use of indirect determination, such as thermal outgassing, a reference technique in steel industry. However, provided concentrations remain above the sensitivity limits, ERDA can be used to study hydrogen mobility at a more local scale.

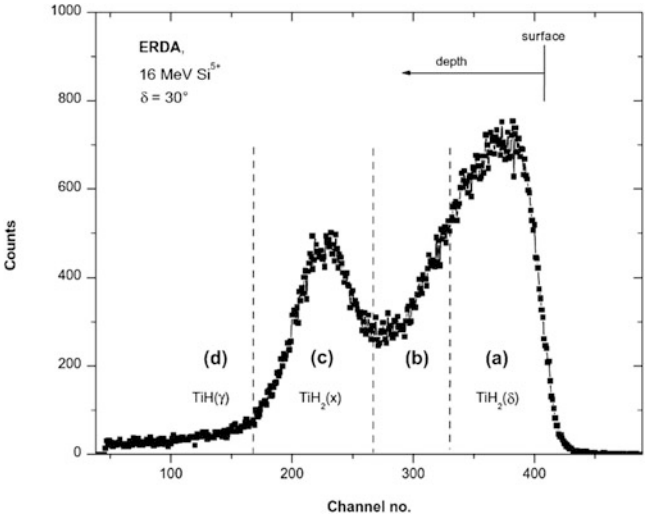

Fig. 10.6 ERDA spectrum of a polished titanium sample, hydrogen implanted with a fluence of 6×10^{17} H/cm^2 (from [27])

Owing to their exceptional physical and chemical properties and to their hydrogen absorption and storage capabilities, titanium alloys have been very early investigated by ion beam-based hydrogen characterization. Experiments conducted on hydrogen implanted samples, combining the use of resonant NRA with ^{15}N beams and ERDA mapping have evidenced the presence of several forms of hydrogen, one quasi-mobile and the others chemically bonded in hydrides [26]. Figure 10.6 shows an ERDA spectrum of a polished titanium sample, hydrogen implanted with a fluence of 6×10^{17} H/cm^2 [27].

The observed large hydrogen concentration in the surface region (a), known as Beilby layer, results from polishing. It has been identified by X-ray diffraction as normal titanium-dihydride phase ($TiH_2(\delta)$). The region of the hydrogen implantation peak (c) corresponds to a relatively unknown titanium-dihydride phase ($TiH_2(x)$) whereas the deeper region (d) corresponds to a titanium-monohydride γ-phase ($TiH(\gamma)$) with a tetragonal structure generated by the implantation. By mechanical bending of the samples, an increase of the hydrogen inhomogeneity is observed, but also surface forward hydrogen diffusion as a consequence of the dehydrogenation of the less stable phases. More recently, an identical experiment on titanium samples has evidenced by ERDA mapping evolution under stress of the inhomogeneity of the deeper hydrogen distribution [28].

Hydrogen absorption in metals causes volume expansion of the host lattice. In metal–hydrogen thin films, lateral film expansion is hampered by adhesion to the substrate. Compressive in-plane stresses increase and may exceed the work of adhesion, leading to peeling, or buckle formation. The stress dependency on the chemical potential strongly affects the thermodynamic properties of metal–hydrogen

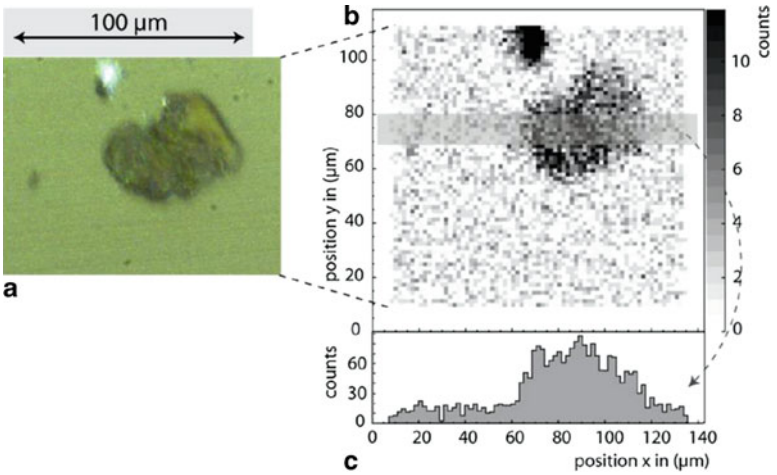

Fig. 10.7 (**a**) Isolated buckle in 640 nm NbH thin film. (**b**) pp-Scattering events in the investigated area in (**a**). (**c**) Line-profile of the hydrogen events detected in the *grayed area* in (**b**) (from [29])

systems. Due to the presence of compressive stress the hydrogen solubility is reduced and hydride phases, precipitating at the solid solution limit, are destabilized.

Attractivity of ERCS performed with high energy protons (20 MeV) had been demonstrated for the study of hydrogen-induced buckling in niobium thin films (600–800 nm) deposited on a silicon substrate (65 µm) [29]. Figure 10.7 shows a 2D hydrogen concentration map measured on an isolated buckle. Film buckling is accompanied by local stress release, which strongly enhances the local hydrogen solubility, while the hydrogen solubility in clamped film fractions is depleted.

The buckles have been shown to form hydride phases, whereas the clamped parts of the film remained in the solid solution, with hydrogen concentration at the solid solution limit. In addition the measured local hydrogen concentrations are in fair agreement with those calculated from simple models that take into account the impact of mechanical stress on the hydrogen chemical potential.

When hydrogen is stabilized in the form of hydrides, inclusions may be observed within microstructure and quantities are estimated from image analysis (from SEM pictures for instance). However for relatively large concentrations inclusions overlap and direct concentration measurement is needed. Since sensitivity is no longer an issue, ERDA is the right tool for this purpose.

Studies on nuclear materials aim at the improvement of safety of nuclear reactors. Mechanical behavior and corrosion resistance of in-core structural materials are strongly influenced by the presence of hydrogen and its localization in the microstructure of the considered materials. Nuclear fuel cladding tubes of pressurized water reactors (PWR) represent the first confinement barrier, preventing the release of radioactive elements in the water of the primary circuit. Under normal working conditions, cladding tubes (Zircaloy-4) are submitted to corrosion by water of the primary coolant (150 bars/330 °C). Due to the oxidation reaction between

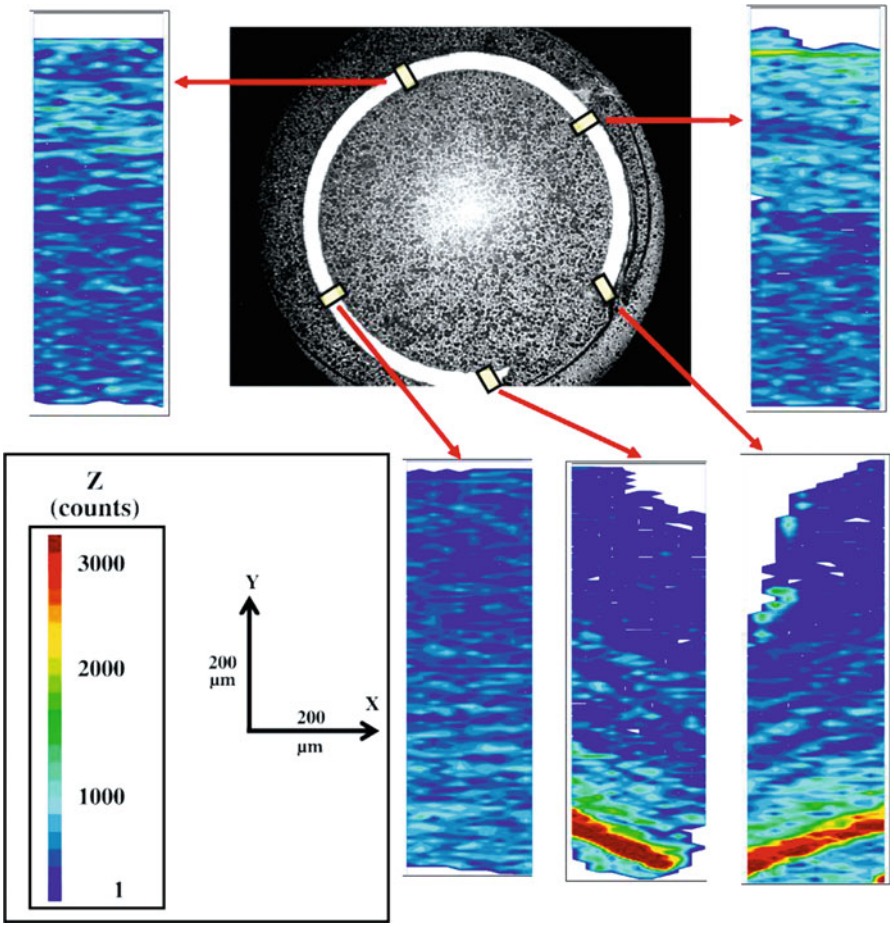

Fig. 10.8 Hydrogen content mapping on a 5 PWR cycles irradiated Zircaloy-4 burst sample (from [32])

zirconium and water ($Zr + 2H_2O \rightarrow ZrO_2 + 2H_2$), a part of the hydrogen atoms diffuses within the thickness of the cladding and, passing beyond the solubility limit, can form secondary phases (hydrides such as ZrH_2) in the metal. These investigations can be performed both on test experiments, but also on real cladding tubes after a long exposure in normal working conditions [30], thanks to the availability of a dedicated beam line for the study of radioactive materials at the CEA-Saclay nuclear microprobe facility [31].

Figure 10.8 represents a cross section of a cladding tube, used up to five cycles in a French PWR (Pressurized Water Reactor), with an average burn-up of 56 GWd/tU, after a burst test (high internal pressure set inside the tube) to reveal brittle zones [32]. Hydrogen profiling by means of ERDA confirms both the presence of a hydride rim at the interface metal/oxide (very high concentrations of H, reaching 4000–5000 wt ppm), and the correlation between rim and crack site.

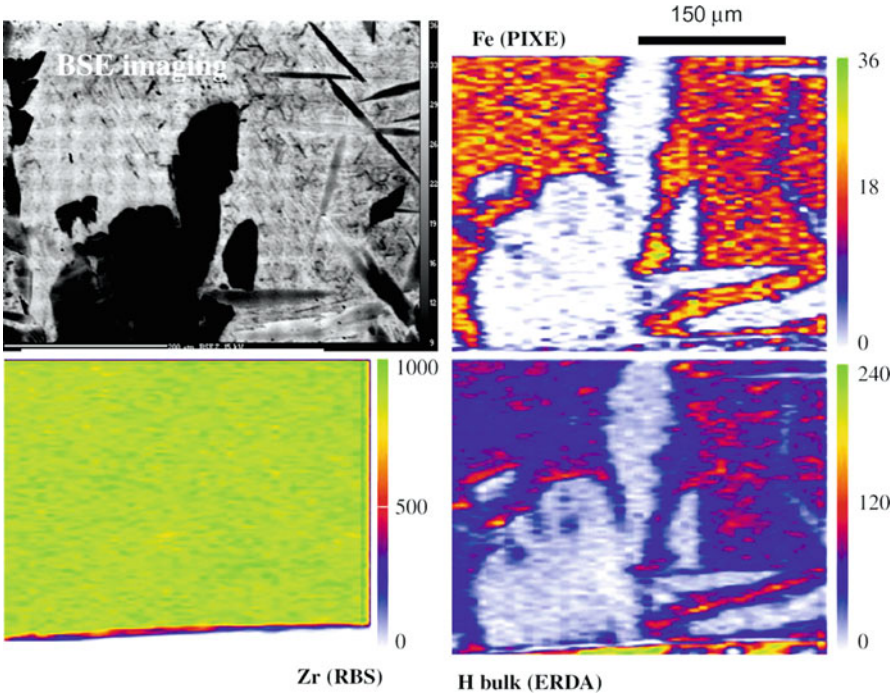

Fig. 10.9 Zircaloy-4 sample, prehydrided at 600 ppm H, oxidized 50 s at 1200 °C, quenched at 800 °C. BSE (Back Scattered Electrons) imaging, Fe mapping from PIXE (Particle-induced X-ray Emission), Zr mapping by RBS, ERDA hydrogen mapping in the bulk (from [32])

A second example, taken from the same paper [32], illustrates evolution of a non-irradiated cladding related to simulated conditions of a hypothetical Loss of Coolant Accident (LOCA) scenario. The LOCA corresponds to the rupture of a section of the primary circuit of the reactor. Water is therefore drained off the core, leading to a brutal accidental temperature transient of the cladding which undergoes heavy steam oxidation and deep metallurgical transformations. The reactor is then reflooded, after a few minutes to half an hour, depending of the type of accident. Microstructure evolution during the quenching step is mainly governed by the β–α allotropic phase transformation (at the end of the oxidation phase, Zy-4 is totally transformed into β-phase) and depends on the quenching temperature. Figure 10.9 shows resulting elemental maps (hydrogen map obtained by ERDA) for a quenching at 800 °C. During the cooling, a progressive growing of α-phase laths begins, enriched in O and depleted in Fe, Cr, and H. These three elements are rejected in the remaining non-transformed β-phase where they finally precipitate when the cooling goes down to room temperature.

Without considering such drastic conditions, hydrogen diffuses easily in zirconium alloys under a thermal gradient towards the coldest regions to accumulate into localized high hydrogen concentration zones [33]. On cladding tubes, such

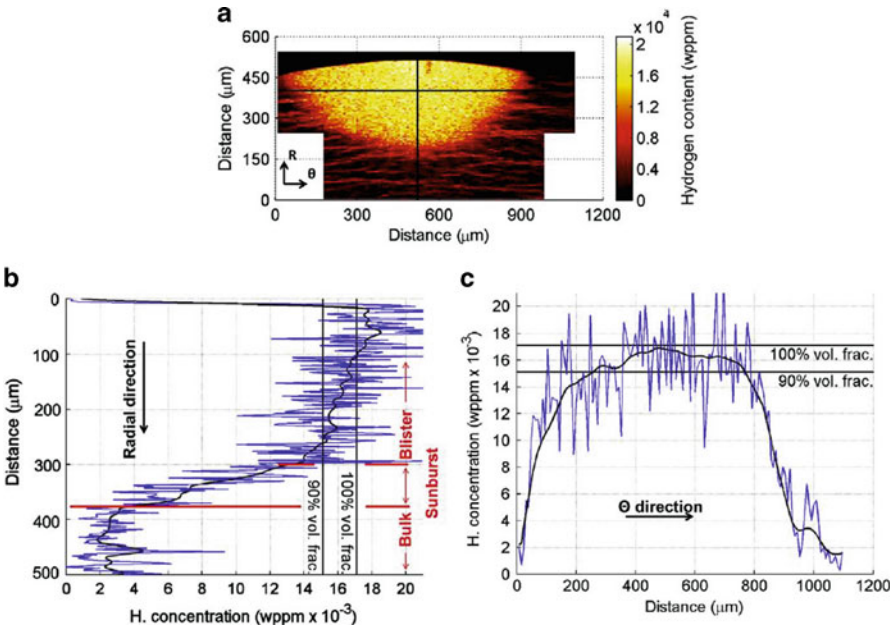

Fig. 10.10 (**a**) Hydrogen cartography of a blister in wt. ppm hydrogen cartography of a blister and distribution along the (**b**) *horizontal* and (**c**) *vertical line* (from [34])

mechanisms induce formation of rims, layers of uniform depth which cover the outer diameter and can reach up to 50–60 μm in thickness. But in the presence of cold spots, hydrogen accumulates more locally, in the form of blisters of elliptic shape, with concentrations higher than in rims [34]. A transition zone referred to as sunburst is located between the blister and the zirconium matrix and consists of a mix of thin and large radial and circumferential hydrides.

Whereas single hydrides can still be distinguished inside a rim using high magnification SEM pictures, this is no longer possible in blisters to evaluate hydrogen concentration. As seen in Fig. 10.10, ERDA microanalysis enables a quantitative mapping of hydrogen, enhancing both core and sun burst zones. 100 % volumetric lines refer to δ-hydride composition $ZrH_{1.557}$, as suggested in recent publication [35]. The non-saturation of the blister at this composition confirms that hydrogen can still diffuse in δ-hydrides, in agreement with Korn and Goren [36].

To quantify the accuracy of ERDA at high hydrogen content, the hydrogen concentration of highly hydrided Zircaloy-4 and unalloyed zirconium coupons were determined by fusion of bulk samples (measurement of evolved hydrogen) and by ERDA. The highest discrepancy in the hydrogen quantification between the two techniques was only 2.5 %.

Materials research for fusion is also an active field for ERDA use. Needs for characterization have stimulated design of novel setups to perform ERDA in situ, at first developed for studying interactions of metallic membranes with hydrogen or

deuterium [37]. Plasma facing components, whatever their nature, share the same questions of erosion and hydrogen retention rates since it may result in a significant impact on the tritium inventory. Moreover, high fluxes of neutrons generate light species (hydrogen, helium) via transmutation reactions with a predicted amount at least one order of magnitude higher in fusion than in fission reactors.

The generic approach consists in implanting hydrogen in materials at increasing doses and looking for evolutions upon annealing. This has been applied for instance to irradiation resistant ferritic/martensitic steels, such as Eurofer and oxide dispersion strengthened Eurofer (ODS-Eurofer) considered as good candidates to be located in fusion reactors [38].

Figure 10.11 shows raw ERDA spectra of ODS steels, as implanted and annealed (numbers used in legend refer to annealing temperature (°C) and duration (hours)) [39]. Hydrogen is easily released from all studied steels from room temperature, but heating at temperatures as low as 300 °C (below operation temperature) strongly accelerates the hydrogen depletion up to 90 % of hydrogen of the total amount, which is highly desirable to prevent swelling effects.

Hydrogen interaction with tungsten has been also widely investigated since tungsten target plates are found in the divertors of tokamaks. As already stated, prediction of hydrogen retention in W is an important issue especially due to tritium-

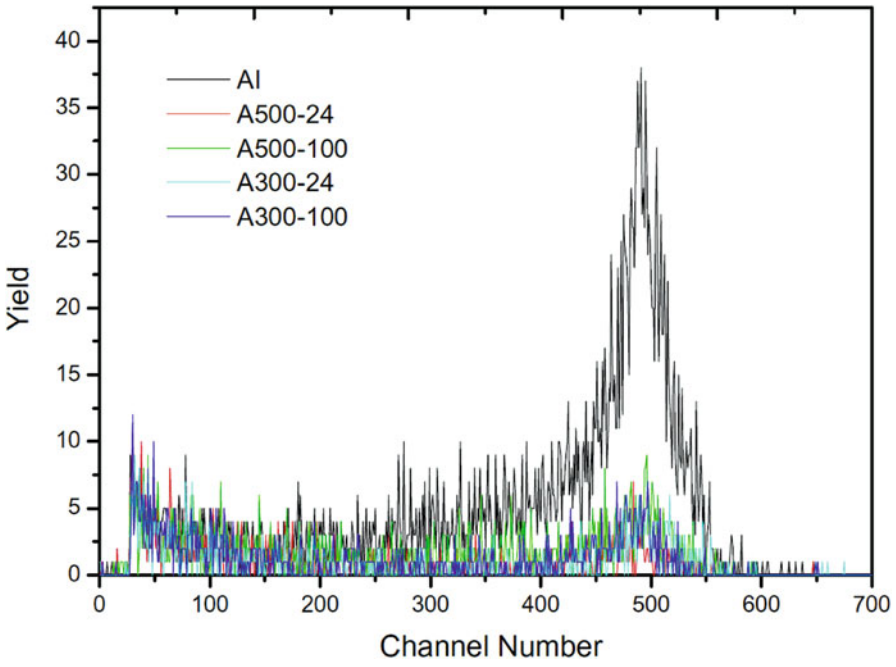

Fig. 10.11 ERDA spectra for ODS-Eurofer samples after H implantation and after different annealing treatments; the black solid line represents the as-implanted sample, without annealing (from [39])

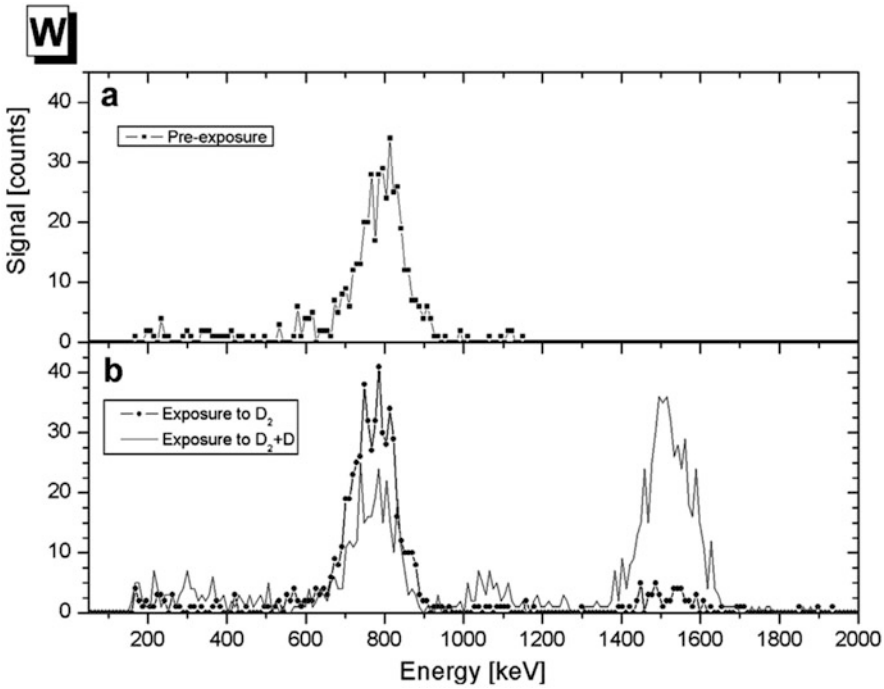

Fig. 10.12 ERDA spectra of hydrogen and deuterium in a tungsten sample. The signal at around 800 keV is from hydrogen on the surface and the signal at around 1500 keV is from deuterium on the surface. (**a**) Before any gas exposure. (**b**) After exposure to deuterium gas: exposure to molecules only (*black line* with *circles*) and exposure to partly dissociated deuterium (*gray line*) (from [40])

related safety limitations. ERDA, performed in situ and in real time, is an adequate diagnostic tool which can give simultaneously absolute concentrations for both isotopes, H and D. The example shown below deals with studies on adsorption, desorption, abstraction, recombination, and diffusion on tungsten surface and near surface.

Figure 10.12 illustrates effect of surface exposure to deuterium gas, in molecular or atomic form [40]. ERDA spectra are recorded in a dedicated chamber using 4.2 MeV Li^{2+} beam enabling sample exposure to a controlled atmosphere and simultaneous in situ measurements of hydrogen concentration depth profiles. A heating tungsten filament is mounted on the top of the cell in order to dissociate hydrogen molecules. The upper spectrum of the example shows a single peak related to H presence before exposure, whereas the lower one shows an additional signal at higher energy related to D (the impact of Li ions transfers more energy to D than to H). Although ERDA provides the depth profile of the hydrogen concentration up to 400 nm in tungsten, the surface part of this profile is dominant since hydrogen diffusion from surface to bulk is small allowing clear study of surface processes.

It has been shown later that exposure to molecular deuterium enables to monitor physisorption of D_2 molecules whereas presence of atomic deuterium promotes

isotopic exchange [41]. Time evolution of hydrogen and deuterium ERDA peaks can be modelled taking into account a set of elementary reactions as trapping of the incoming atoms on the surface or recombination with previously adsorbed atoms. For instance the Langmuir–Hinshelwood recombination process considers adsorbed atoms diffusion on the surface and recombination if they come close to each other to produce hydrogen molecules which leave the surface.

Still in the frame of fusion research, liquid metals, mostly lithium and gallium, have been acknowledged as a suitable solution to solve the erosion problems encountered by solid plasma facing components. Once again, high retention rates may result in a significant impact on the tritium inventory. It is imperative to evaluate hydrogen solubility in those liquid metals. It has been shown from *post mortem* ERDA measurements on plasma-exposed gallium targets that retained fractions rise around 1 at.%, for an average ion flux of 4×10^{22} ion/m^2 s (plasma exposure time around 3 s). However, it should be noticed that all the changes in composition occurred near the samples surface, as observed from ERDA. In particular, experimental data points towards the existence of a saturation retention level. As a consequence, lower retained fraction could be observed at higher ion fluencies.

An impressive demonstration of ERCS use with high energy protons (ranging from 17 to 22 MeV) has been recently demonstrated with a study of tungsten foils

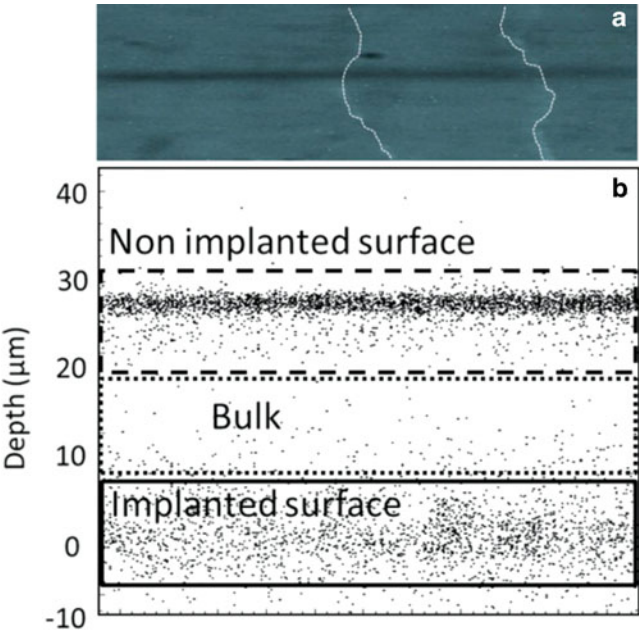

Fig. 10.13 Line scan along two grain boundaries measured with a 17 MeV proton beam: (**a**) optical micrograph of the scanned area under viewing angle of 0° of the implantation side of the front side; (**b**) 2D plot of filtered coincident proton–proton events calibrated as two dimensional cross section of hydrogen distribution (from [42])

implanted at low energy (200 eV) representative of the divertor wall conditions [42]. Figure 10.13 shows a transverse profile of hydrogen after implantation in a 25 μm thick foil. The beam is scanned along to cross two grain boundaries. It has been observed that only a small fraction of the implanted hydrogen remained in the tungsten, with an upper limit of less than 0.1 % in the foil at the surface while no additional hydrogen found in the bulk within the detection limit (about 5 atom.ppm in such heavy matrix). In addition, surface scans have shown that the surface hydrogen is inhomogeneously distributed within the microstructure of the implanted surface. At the opposite, high energy implantation (1.8 MeV) shows that all the implanted hydrogen is retained in the bulk. This approach has been extended to ERCS measurements of deuterium with the use of deuterium beams (17 MeV) to obtain a background-free deuterium distribution [43].

Metal hydrides used for hydrogen storage accommodate an extremely high density of hydrogen in their structures. Studies of absorption/desorption processes may be investigated by a combination of ion beam-based analysis methods, RBS for medium and heavy elements, and ERDA specifically for hydrogen or deuterium. A typical example is the study of hydrogen absorption–desorption properties of bulk materials, without preliminary enhancement of storage capacity by a prior treatment, such as simple disk-shaped titanium–aluminum alloys [44]. On such samples, when hydrogenated, oxygen atoms present in the near surface zone can migrate to the bulk and may occupy interstitial sites in the metal lattice. ERDA and RBS can be then used to assess the effect of surface oxidation and roughness on the hydrogen uptake rate. It was observed that the amount of absorbed hydrogen decreases with increasing roughness during the first hydrogenation cycles. However, the embrittlement of the alloy structure during the first cycle activates the hydrogen uptake during the following cycles.

Among candidate metals, magnesium has also been widely investigated, but still encounters stability and kinetic issues (for instance when the envisioned use is transport applications) originating from slow diffusion of hydrogen atoms through the formed hydride layer, from the presence of MgO and $Mg(OH)_2$ at the surface and from the large potential barrier to decompose the H_2 molecule on Mg/MgH_2 surfaces. Nanostructuration or thin films patterning seems a way to solve these drawbacks. The following example considers palladium capped magnesium layers deposited on aluminum substrate [45]. Palladium acts indeed as a catalyst for H_2 dissociation or for H–H recombination during absorption/desorption process on MgH_2 and Mg surfaces. Besides, it protects the surface against massive formation of magnesium oxide and hydroxide without hindering hydrogen diffusion process (the hydrogen diffusion coefficient has a high value in Pd). However, formation of Mg–Pd interlayers could be detrimental to catalytic effects.

Figure 10.14 presents elemental depth profiles obtained on hydrogenated Pd capped Mg films, submitted to thermal desorption. Before hydrogenation, nominal thicknesses of Mg and Pd films were about 300 nm and 10 nm, respectively. Using a 2.6 MeV $^4He^+$ beam for a combination of RBS (Pd, Mg, Al, and O profiling) and ERDA (H profiling), evolution of profiles as a function of thermal treatment can be monitored. Figure 10.14a refers to the initial state whereas Fig. 10.14b corresponds to desorption completion.

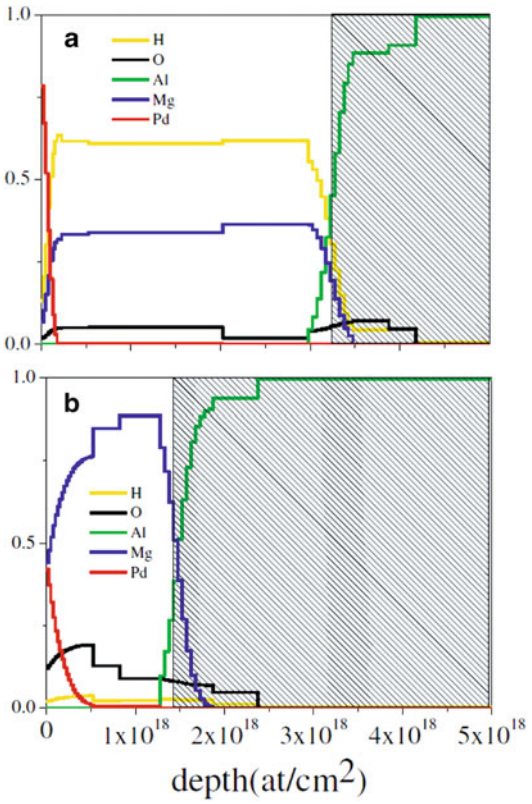

Fig. 10.14 Evolution of concentration profiles obtained from RBS-ERDA measurements in Pd-capped MgH_2 films: (**a**) sample treated at 125 °C before hydrogen desorption and (**b**) hydrogen desorption up to 180 °C (from [45])

Before desorption starts, the concentration profile clearly shows the hydrogen inside the film (Fig. 10.14a). H-concentration is practically constant along the film depth with a ratio of H/Mg = 1.7 ± 0.1 indicating that the film is practically hydrided and stable up to this temperature (125 °C). Formation of MgH_2 does not involve a meaningful variation of the intermixed Mg–Pd region thickness whereas profilometer measurements show that film thickness has increased up to ~380 nm confirming a practically total hydrogenation of the initial film. Increasing temperature up to ~180 °C induces complete hydrogen desorption accompanied by a film thickness diminution, recovering its initial value (~300 nm) (Fig. 10.14d). While H/Mg ratio is decreasing, the hydrogen profile in the film remains practically constant along the Mg layer. No formation of a Mg/MgH_2 interface along the whole sample is observed. This indicates that the control mechanism, based on migration of Mg/MgH_2 interface, occurs inside each MgH_2-nanocrystal in the film, thus confirming the importance of the MgH_2 nanocrystallite size on desorption kinetics.

Similar studies have been conducted by ERDA on Pd/Mg/Pd trilayers (total thickness ~800 nm) deposited on silicon wafers [46], but by means of high energy heavy ions (120 MeV $^{107}Ag^{+}$) which enables measurement of heavier elements than hydrogen.

Besides those studies on more or less complex samples, the need for knowledge of elementary interaction processes of hydrogen with simple metallic surfaces has also induced the use of ERDA, for hydrogen or deuterium implantation in pure metal and diluted alloys [47, 48], but also, when highly energetic light ions are available, in situ measurements at atmospheric pressure. One advantage is the relatively large analyzed depth, a few microns, compared to conventional ERDA implemented with a few MeV ^{4}He. Ishigami reports use of 15 MeV $^4He^{++}$ beam to investigate thermal stability of PdH and PdD under air, after exposure to hydrogen atmosphere [49]. Hydrogen desorption had been found to start from 120 °C under vacuum whereas under air hydrogen content falls down from 85 °C. This latter behavior is interpreted as a promotion of the reaction of adsorbed hydrogen with H_2O present in air, with no isotopic effect when considering deuterium absorption.

10.5 Hydrogen Measurements in Ceramics

Ceramics are facing very similar questions of ageing under hydrogen exposure. Like for metals, hydrogen is well known to induce ceramic compatibility issues, such as embrittlement or swelling, which have to be mastered for the use of next-generation "green" fuels. The example below (Fig. 10.15) shows hydrogen-induced degradation of piezoelectric materials used as actuators for direct hydrogen injection (high pressure up to 35 MPa) in internal combustion engines [50]. Barium titanate (BTO) and lead zirconate titanate (PZT) films (thickness ~50 nm) have been deposited onto silicon wafers and capped with a palladium layer (~25 nm). The Pd coating was applied to test the impact of a metal layer to promote absorption of high-pressure hydrogen. After hydrogen exposure, surface degradation in the form of blistering (diameter ≤ 1 μm for PZT and in the range 1–5 μm for BTO) was observed. For PZT films, Pd/Pb intermixing also occurred, whereas Pd/Ba profiles in Pd/BTO films remained unchanged. This hydrogen-induced mixing is explained by the role of atomic hydrogen increasing the electronegativity of Pb, reducing the electronegativity difference relative to Pd, and thus the alloy heat of formation.

Figure 10.15 shows ERDA spectra and related hydrogen concentration depth profiles after exposure. Compared to uncapped layers, hydrogen absorption is up to 20 at. % higher, thanks to the catalytic H_2 dissociation at the Pd layer which increases the H absorption. A general trend is observed with hydrogen concentration decrease at the interface Pd/Layer, possibly due to interface strain increasing the energetic cost of forming a hydride which usually results in a slight lattice expansion.

Similar ERDA experiments had been conducted on bilayered metal/ceramic hydrogen storage material to be used in conjunction with a hydrogen fuel cell [51]. Hydrogen is absorbed at the metal surface and stored in the ceramic. $Pt/Li_2ZrO_3/Pt$ sandwiches absorb hydrogen gas at room temperature and re-emit it by heating at temperatures lower than 150 °C. Hydrogen absorption kinetics was estimated to be three times lower than on $BaCe_{0.9}Y_{0.1}O_{3-\delta}$ ceramics.

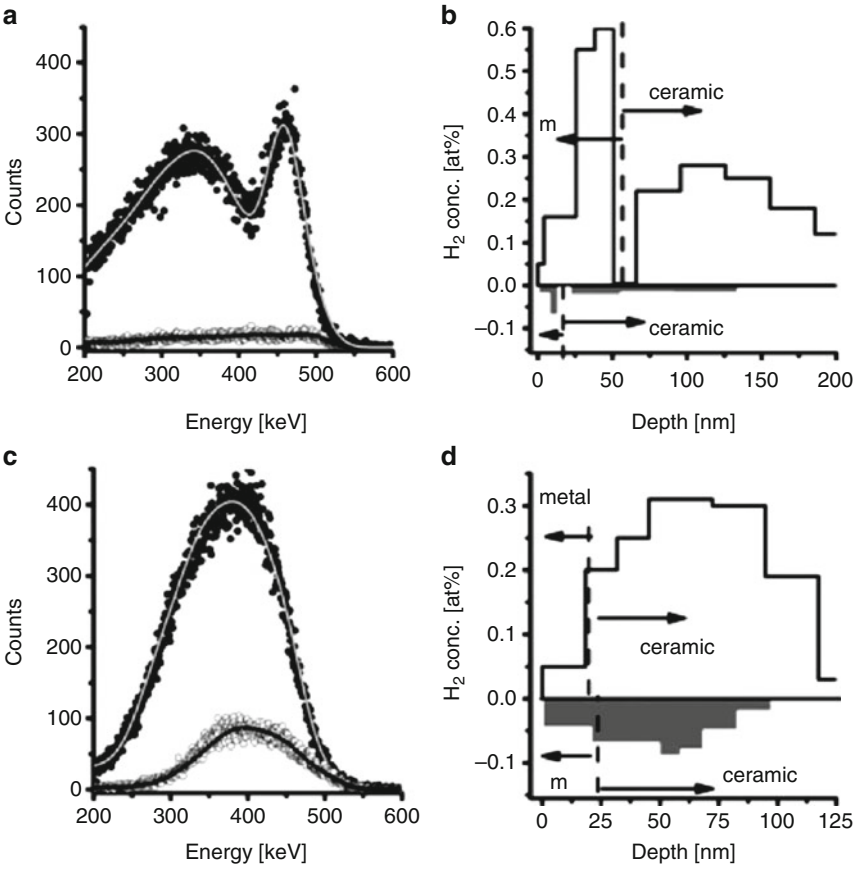

Fig. 10.15 (**a**) ERDA spectra for PZT/Pd H_2 exposed (*filled circles*) and control (*open circles*) with fits (*solid lines*). (**b**) Associated depth profiles for PZT/Pd H_2 exposed (positive axis) and control (negative axis). (**c**) Same as (**a**) with BTO/Pd (**d**) Same as (**b**) with BTO/Pd (from [50])

Whereas hydrogen is easily solubilized in metals, incorporation of hydrogen in ceramics may change crystal structure. A combination of ERDA and RBS in channeling mode (sample oriented along given crystalline directions to investigate modifications of RBS yield) provides a direct overview of hydrogen-induced modifications. Mackova had studied hydrogen interaction with lithium tantalates, $LiTaO_3$ wafers, intended to be used as optical waveguides [52]. Compared to more investigated lithium niobates, $LiTaO_3$ is less susceptible to optical damage, more transparent in the near ultraviolet spectral region and has even better mechanical properties. The basic condition to fabricate optical waveguides is to increase the pertinent refractive index in the desired area. This is done by a two-step process, proton exchange and annealing (APE) where the surface is exposed to a melt of buffered adipic acid (adipic acid with addition of 0.5 mol.% of lithium carbonate) and then stabilized by thermal annealing.

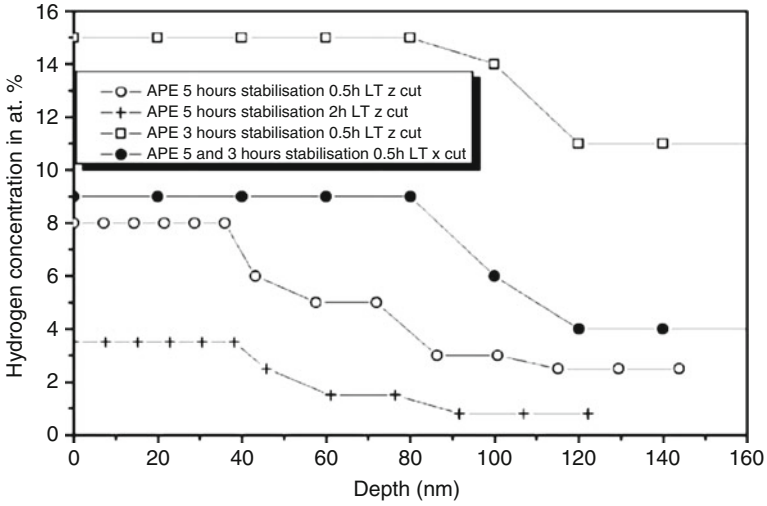

Fig. 10.16 Hydrogen depth profiles determined from ERDA measurements in proton exchanged and annealed $LiTaO_3$ wafers (from [52])

$LiTaO_3$ single crystals grown by the Czochralski method, were cut into wafers with several different surface orientation. Figure 10.16 shows hydrogen depth profiles obtained on Z-(⟨0001⟩) and X-(⟨11—20⟩) cuts after full treatment. In comparison with 5 h proton exchange, 3 h of the APE treatment result in a higher amount of hydrogen incorporated in the surface layers of the $LiTaO_3$. These samples exhibited also the largest structural modification as deduced from the RBS-channeling (higher minimal yield) and XRD measurements. In the Z-(⟨0001⟩) cut samples, the minimal yield after a short period (0.5 h) of annealing is relatively high (19 % of random), while after 2 h of annealing the minimal yield was comparable with the pristine crystal (~5 %). These effects are assigned to redistribution of the as-exchanged ions (H^+ and Li^+) and indicate that the original structure of the $LiTaO_3$ can be restored.

The ability of some ceramics to promote hydrogen mobility benefits electrochemical devices requiring solid state electrolytes, such as high temperature fuel cells or electrolyzers. Electrolyte materials have to display both high proton conductivity, high chemical stability facing their working environment (such as low sensitivity to carbonate formation), and lack of reactivity against electrode materials. Transport properties are worldwide studied by impedance spectroscopy. This approach gives an overall answer but diagram interpretation remains sometimes speculative, especially about charge carriers when ionic conduction is only minority. Among oxides with proton conduction, the most studied are alkaline earth cerates and zirconates-based perovskites. Their conduction mechanism had been described according to a proton hopping mechanism from an oxide ion to an adjacent one, assisted by lattice vibrations [53], but this mechanism can be revisited to put forward interstitial proton diffusion, free from any covalent bonding [54].

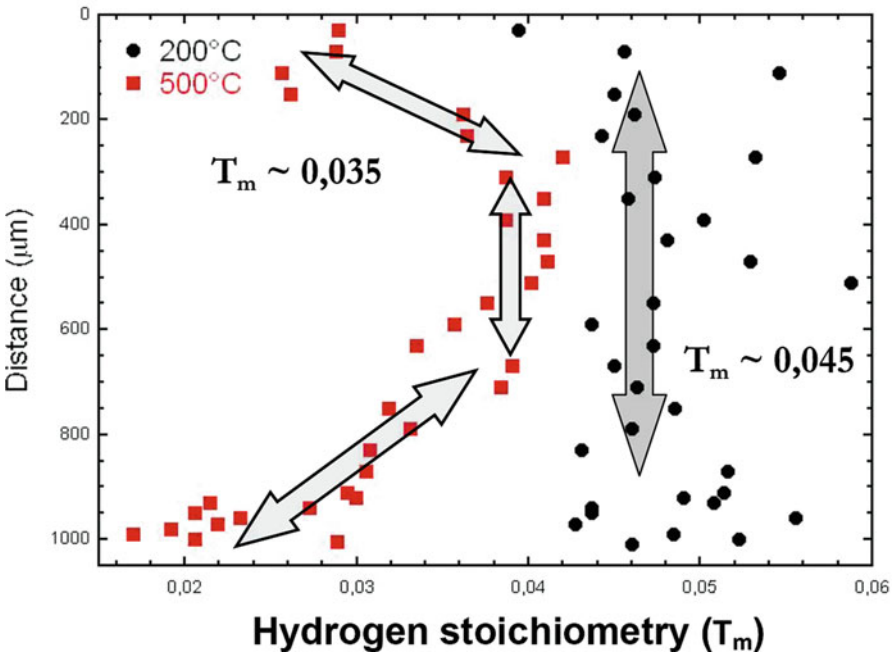

Fig. 10.17 Hydrogen profiles on cross sections of hydrogenated $BaCe_{0.9}Y_{0.1}O_{3-\delta}$ pellets annealed for a few minutes at 200 and 500 °C (from [55])

Direct measurements within ceramic microstructure aim at visualizing hydrogen transport, detecting barriers, or short-circuits and, when possible, measuring formal diffusion coefficients. Various diffusion and transport models can be directly assessed from knowledge of long distance hydrogen concentration gradients.

Figure 10.17 shows an example of hydrogen profiles measured on $BaCe_{0.9}Y_{0.1}O_{3-\delta}$ perovskites [55]. Ceramics were initially fully hydrated under wet atmosphere and then annealed in vacuum for about 15 minutes, followed by ERDA profiling on cut samples to get hydrogen concentration profiles on the whole cross section from one edge to the other.

As expected, the shape of hydrogen concentration profiles is a combination of a central plateau and near surface concentration gradients. With the help of a simple Fick law model, formal hydrogen diffusion coefficients can be deduced. Unexpectedly, the concentration of the plateau decreases rapidly with ageing which means that only a fraction of hydrogen contained in these perovskites is strongly bonded, the other having a much larger mobility.

The quantity of proton charge carriers depends on the number of oxygen vacancies and thus on the dopant concentration (yttrium in the above mentioned example) which is set typically between 5 and 10 %, rarely more. Compared to undoped materials, the gain in protonic conductivity can be enhanced up to 4 orders of magnitude. So, attempts have been achieved to enhance the number of vacancies

in the oxygen sub-lattice by irradiation damage. For instance, argon irradiation of $BaCe_{0.9}Y_{0.1}O_{3-\delta}$ ceramics with increasing fluences (10^{16}–10^{18} Ar^{+} ions/cm^2) has been investigated using ERDA, SEM/EDS, XPS analysis, and AC impedance measurements [56, 57]. It was observed from ERDA measurements that surface hydrogen concentration increased with the fluence of the ion beam, interpreted with the help of XPS results as an increase of oxygen vacancies.

When the preparation of thin samples is possible, such as in the case of dense ceramics, ERDA can be implemented in forward geometry (cf. Sect. 10.3.3). The following example shows coincident detection, ERCS, applied with a micron size proton beam to study grain boundary hydrogen mobility in large grained melt-textured $SrCe_{0.9}Y_{0.1}O_{3-\delta}$ ceramics synthesized by laser assisted oriented growth [58]. Figure 10.18a (top) shows a map of the microstructure obtained by scanning the sample in STIM mode (Scanning Transmission Ion Microscopy) which images energy loss contrast across the thin sample. Due to the presence of an intergranular secondary phase, black lines are an image of grain boundaries. Figure 10.18b (bottom) presents the corresponding ERCS image which shows that hydrogen is mainly localized in grain boundaries. As suspected from impedance measurements, grain boundaries trap hydrogen and lower their overall mobility. Since ERCS is depth-resolved, microbeam ERCS has a potential to offer a full 3D microcopy of this kind of materials at the micron scale.

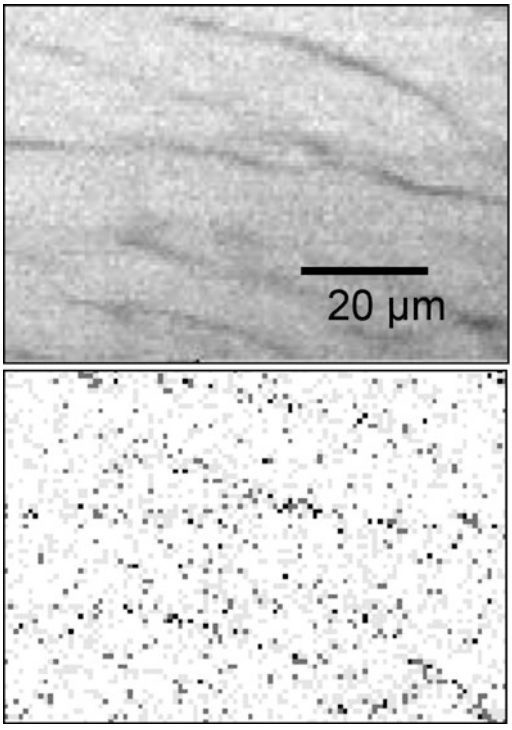

Fig. 10.18 (**a**) STIM image of a large grain $SrCe_{0.9}Y_{0.1}O_{3-\delta}$ ceramic synthesized by laser assisted oriented growth. *Dark lines* reveal grain boundaries. (**b**) Corresponding ERCS hydrogen map (from [58])

10.6 Hydrogen Measurement in Minerals

Presence of low concentrations of hydrogen in deep earth, mostly in oxidized forms OH or H_2O, has a tremendous impact on mantle properties, since it affects its rheology, the propagation of seismic waves, modifies conditions for partial fusion of mantle material and finally controls volcanos eruptions [59]. Hydrogen is indeed present in the minerals of the upper mantle, such as in olivine, a constitutive phase (about 80 %), but also in orthopyroxenes, clinopyroxenes, and garnets. Considering that these olivines can typically store about 100 wt. ppm hydrogen, one can calculate that there is more hydrogen stored in deep earth than in near surface, oceans included. A lot of efforts have been then devoted to the precise measurement of hydrogen in natural geological samples with low hydrogen content, nominally anhydrous natural minerals (NAM). Accurate determination of hydrogen content in NAM is then a crucial challenge in Earth Sciences since it enables to set mass balances and to identify the deep reservoirs of our planet. In this context, ERDA is used both as direct probe for hydrogen mapping [60] but also as a method of absolute calibration of IR spectroscopy [61].

The examples presented in Figs. 10.19 and 10.20 show that both hydrous and nominally anhydrous phases (glasses and minerals) can be characterized together by ERDA, during the same analysis.

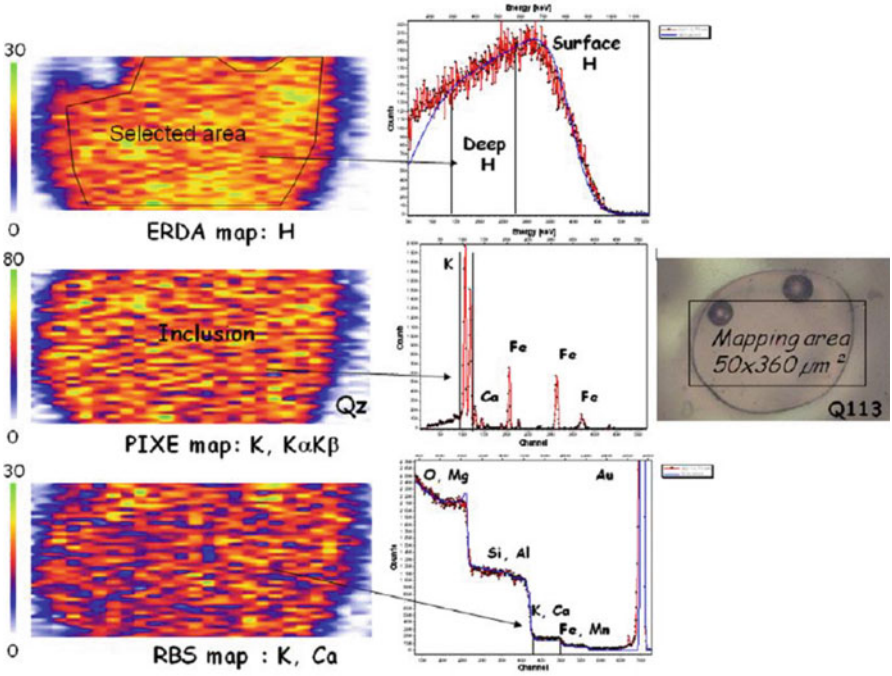

Fig. 10.19 Mappings and spectra for ERDA, PIXE, and RBS characterization of a rhyolitic melt inclusion trapped in magmatic quartz from Guadeloupe Island (from [60])

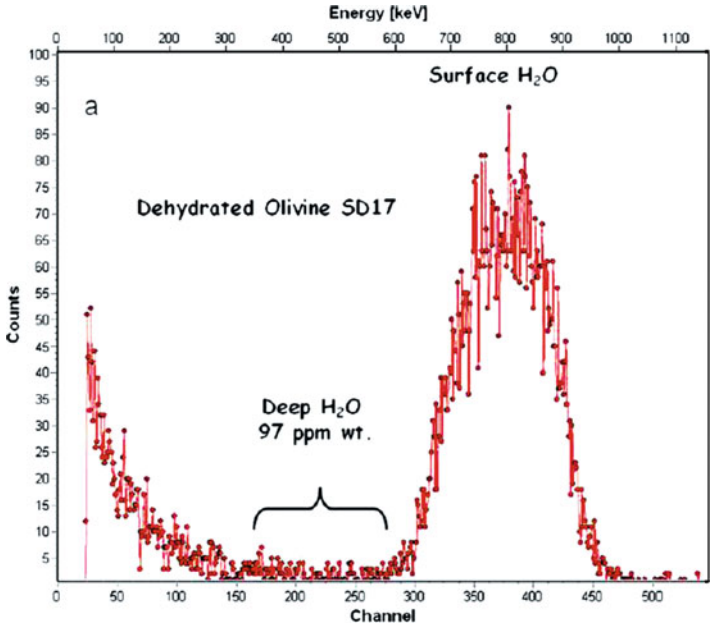

Fig. 10.20 ERDA spectrum of a synthetic olivine dehydrated in a rapid quench pressure vessel. Deep hydrogen analysis gives a water content of 97 wt ppm (from [60])

Figure 10.19 shows the characterization of a rhyolitic melt inclusion trapped in magmatic quartz from Guadeloupe Island (sample Q113) [60]. In addition to ERDA, combination of RBS and PIXE maps of relevant elements offsets the chemical contrast between the phases present in the investigated samples, such as Ca, Fe, or K which are good markers to differentiate rhyolitic glassy inclusions (Ca, Fe, K-bearing) from their host quartz crystals (approximately free of Ca, K, Fe).

The example shown in Fig. 10.20 presents ERDA characterization of a clinopyroxene [60]. The surface H contribution appears as a large peak at high energy whereas deep H, which is interpreted to be the intrinsic H content of the sample, appears as a plateau at lower energy which is evaluated here to correspond to 97 wt ppm.

Figure 10.21 shows FTIR-ERDA intercalibration curve obtained with synthetic and natural volcanic glass samples, already used for SIMS-FTIR intercalibration [62]. The offset at the origin, 140 ppm, may be attributed to ERDA background, but deviation from the 1:1 slope may come from FTIR calibration. Another possibility for this deviation could be that all of the hydrogen present in the NAM samples was not bonded to oxygen atoms, hence invisible from FTIR measurements.

FTIR calibration from ERDA confirms the accuracy of phase-specific calibrations which provide better estimates of H_2O contents in NAMs than the generalized methods formerly in use in the geochemists community, such as the Paterson calibration [63] which systematically underestimates the H content in olivine by at least a factor of 1.7 for polarized measurements.

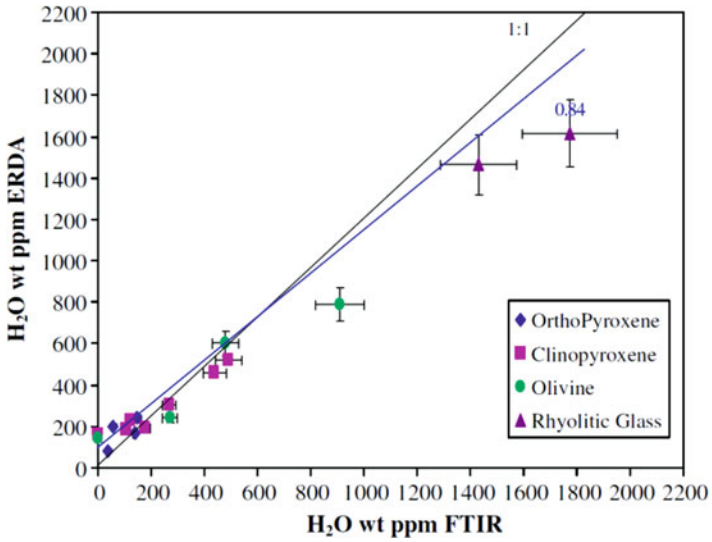

Fig. 10.21 Comparison between ERDA and FTIR results of H_2O content for mantle nominally anhydrous minerals and hydrous glasses (from [62])

As an extension of ERDA use in geochemistry, measurements on heritage artifact, and gemstones is worth to be mentioned, especially for the efforts devoted to implement ERDA at atmospheric pressure [64, 65].

10.7 Hydrogen Measurements in Thin Films

Characterization of thin films is by far the most common use of ERDA, for hydrogen content measurements in as-deposited layers or for profiling after exposure to various atmospheres or treatments. This review will focus on the most recent investigations. Although investigated films are often thicker than the analysis depth, many interesting questions can be addressed by absolute hydrogen content measurements and/or concentration profiling at the near-surface region. ERDA is used both for ageing or growth mechanisms related studies, sometimes to help extracting quantitative information from others spectroscopies such as XPS, FTIR, RAMAN, and XANES [66, 67].

Investigations in diamond-like (DLC) or amorphous carbon films have been for a long time a typical use of ERDA [68, 69]. This field is still active thanks to a renewed interest in their tribological properties. Most recent papers focus on (1) correlations between hydrogen content, carbon speciation, deposition parameters, and possibly a given physical property, for instance on relationships between hardness, structure and composition [70–72], deposition by Plasma Jet CVD [73], fabrication of carbon 3-D nanostructures by FIB-CVD [74], (2) on the introduction

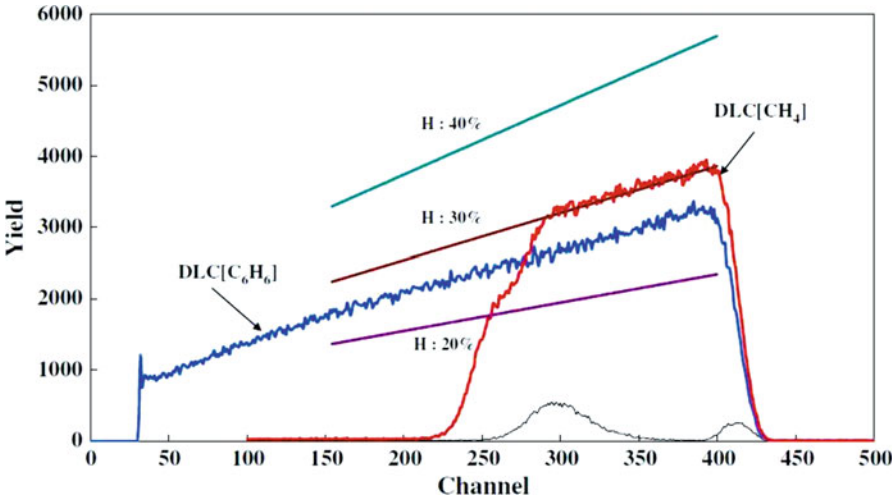

Fig. 10.22 ERDA spectra of DLC layers obtained from CH_4 and C_6H_6 precursors (from [82])

of nitrogen, argon, or hydrogen injection in the plasma [75–78], (3) on the implantation of nitrogen [79], for tailoring superlubricity properties [80], (4) or even for hydrogen storage [81].

The following example is taken from a recent paper [82] dealing with ball-on-disk friction tests and characterization of DLCs films produced by rf-plasma chemical vapor deposition on silicon or tungsten carbides using methane or benzene as source gas. Tribological parameters (friction coefficient, wear losses,. . .) were correlated to XPS data (carbon sp2/sp3 ratios), Raman spectra (structural integrity), and hydrogen content. The figure reproduced below (Fig. 10.22) shows ERDA spectra measured on films obtained from CH_4 or C_6H_6 precursors and indicates the calculated levels that should be observed according to various hydrogen contents.

Whereas hydrogen is much more concentrated in methane than in benzene, hydrogen eventually trapped in the DLC[CH_4] and DLC[C_6H_6] differs by a few percents only. According to the authors, better tribological properties of DLC[CH_4] films may be partially attributed to this higher hydrogen content.

Hydrogen content may be even the only parameter to interpret differences in DLC films properties.

Research on organic materials as magnetic materials has attracted considerable interest since it had been found that amorphous-like carbon prepared by pyrolysis possesses ferromagnetic properties [83]. Recent studies have suggested that the origin of the magnetic moment in carbon materials is related to the presence of hydrogen in those materials, which has been evidenced by ERDA measurements [84]. Depending on PECVD deposition parameters, both ferromagnetic and diamagnetic DLC films were obtained. Raman studies confirmed that the ratio of sp3 to sp2 bonded carbon was not significantly different. However, ERDA studies revealed that the hydrogen content of the ferromagnetic DLC films was much higher than that of the diamagnetic films.

Stability of films is also a major concern since usage properties might be debased in ageing conditions. Hence, carbon films are submitted to various treatments and environments to investigate composition and structure evolution. Thermal stability of a-CH, DLC, and Polymer-like (PLCH) is expected to be very different due to their relative percentage of *sp3*-C and *sp2*-C bonds. Buijnsters, for instance, has compared thermal stability under high vacuum conditions (1 h at temperatures ranging from 150 to 450 °C) of PLCH and DLC films from ERDA measurements of hydrogen release [85]. The results indicate that H bonding differs in both structures, with weaker C–H bonds in PLCH. In principle, such investigations can be applied to any variant of hydrogenated films such as W-incorporated DLC films [86] or SiC_x:H films which hardness is related to the $sp2/(sp2 + sp3)$ ratio and the hydrogen content [87].

Behavior of thin films under environmental exposure is also a usual question. For instance, soft X-ray exposure is known to lead to hydrogen desorption and etching of highly hydrogenated DLC films (H-DLC films, containing up to 40 % hydrogen). For use in outer space vacuum, DLC films are expected to be used as lubrication substitution for oil. Using IR-Soft X-ray synchrotron radiation source, it has been recently shown that the exposure excites the 300 eV inner shell of carbon K edge to break chemical bonds of DLC films [88]. This modification caused both flattening and etching of the surface. Increasing irradiation dose, a sharp decrease of hydrogen content, measured by ERDA, have been observed and directly correlated to hardness increase.

Semiconductors can be treated according to a similar approach. Hydrogen treatment is used to passivate dangling bonds in semiconductors, either crystalline or amorphous, like Si, Ge, Si-Ge, and more or less complex variants. The incorporation of hydrogen in the network is a way for reducing the density of defect states in the midgap, to gain better electro-optical characteristics. ERDA can be at first used to measure hydrogen content in as-deposited layers [89, 90].

Si-Ge thin films are mostly deposited in the form of multilayers which are not in an equilibrium state. They have high interfacial density gradients and sufficient atomic mobility, even at moderate temperatures, so that changes in the composition profiles are expected to occur. Knowledge of environmental, thermal stability, and understanding of the factors controlling the structural changes of these multilayers is required for the interpretation of operation and prediction of lifetime.

As a first example, hydrogenation of mercury cadmium telluride (MCT) wafers, a key material for advanced infrared detector systems, provides both electrical and compositional stability. When used in military and space applications, MCT are exposed to heavy ions irradiation. ERDA experiments with heavy ions enable to perform simultaneously exposure and characterization. Figure 10.23 presents evolution of hydrogen content of MCT wafers under 80 MeV Ni^{9+} ions as a function of nickel ions fluence [91]. The shape of the curve is interpreted to origin in the latent tracks, of nanometer dimensions, generated along the paths of the ions. The change in slope after a given fluence could be due to overlapping of ion-damaged zones, which also changes the hydrogen loss behavior.

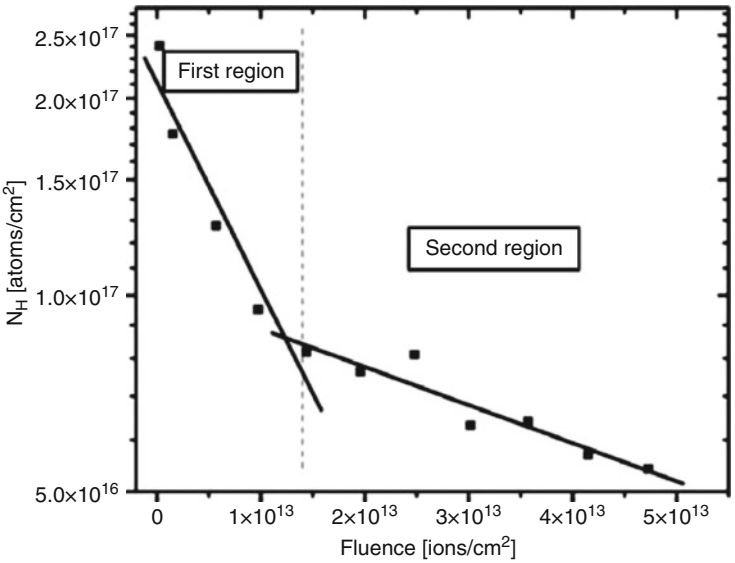

Fig. 10.23 N_H, total areal concentration of hydrogen (atoms/cm^2) versus incident ion fluence (ions/cm^2) (from [91])

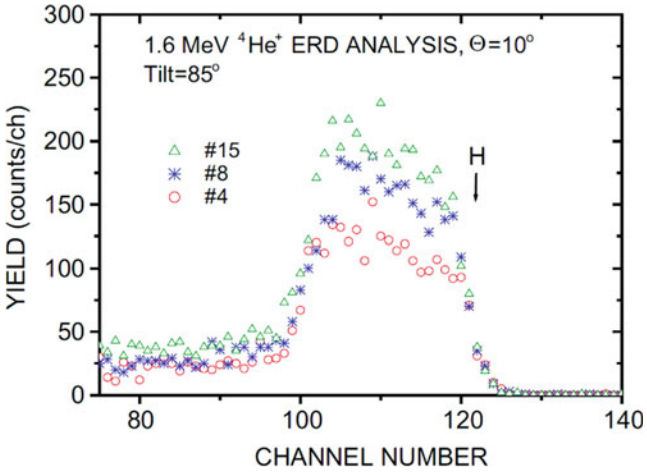

Fig. 10.24 1.6 MeV ^{4}He$^+$ ERDA spectra of hydrogen in as-deposited a-Si samples exposed to hydrogen flow rates of 0.4 (#4), 0.8 (#8), and 1.5 ml/min (#15) (from [92])

Next example is related to characterization by ERDA of hydrogenated a-Si and a-Ge monolayers deposited on silicon wafers by RF sputtering. Measurements were achieved after exposure to hydrogen flow, both on as-deposited layers and following a thermal treatment at 350 °C [92, 93]. Thickness of these single layers, 40 nm, was low enough to easily measure the whole hydrogen profile by ERDA (cf. Fig. 10.24).

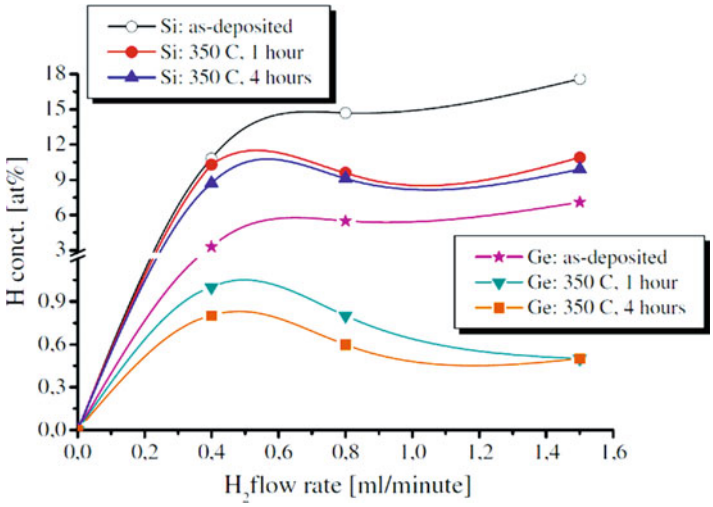

Fig. 10.25 Hydrogen concentration as a function of the hydrogen flow rate in the deposition chamber in a-Si and a-Ge single layers, as-deposited, before and after annealing at 350 °C for 1 and 4 h (from [93])

During thermal annealing, hydrogen can diffuse out faster from the Ge film than from the Si one (cf. Fig. 10.25). The residual hydrogen remaining in the layers is nearly 15 % and 55–65 % of the incorporated one for Ge and Si, respectively [92].

With Si-Ge nanostructures (multilayers, alternating Si and Ge layers, 3 nm thick each), surface bubbles, i.e. blistering, form with a density and size that increase with time and temperature of annealing [93, 94]. Depassivation of the dangling bonds first starts in the Ge layers since hydrogen is released earlier and more efficiently from Ge than from Si, but also of the smaller mechanical strength of Ge. The liberated hydrogen is partially lost through open craters.

Formation of hydrogen bubbles and blistering during treatment of as-deposited layers is indeed a general concern. This next example is related to recrystallization of amorphous silicon layers intended to be used in photovoltaic devices [95]. Amorphous layers are treated by laser irradiation by a moving Continuous Wave (CW) which promotes the melting of the a-Si to produce polycrystalline silicon films with large grains. Since grain boundaries are detrimental to the density of charge carriers, large grain silicon microstructures tend to increase photovoltaic performances of the solar cell.

As already mentioned, as-deposited silicon layers may contain a high amount of hydrogen resulting from deposition processes. Unfortunately, hydrogen-rich amorphous silicon cannot sustain CW laser treatment. Bubbles and dewetting are observed due to explosive effusion of hydrogen at very high temperature induced by the laser radiation. Prior to laser treatment, thermal annealing is required for hydrogen effusion.

To compare standard PECVD to EBE (Electron Beam Evaporation, a technique working under high quality vacuum), hydrogen profiles have been measured by ERDA on samples annealed under different conditions. Figure 10.26 shows

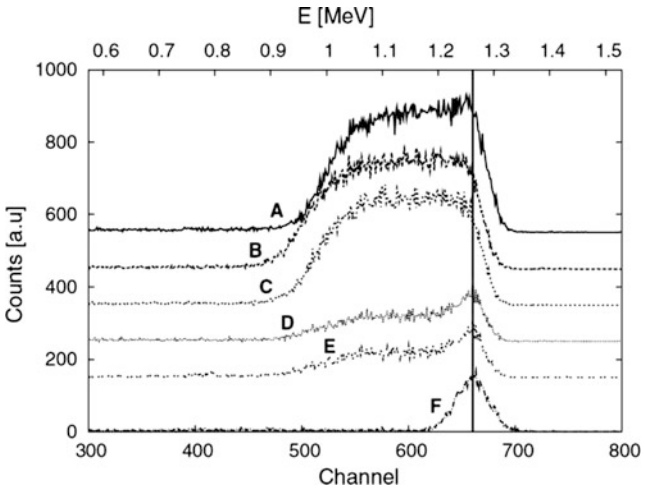

Fig. 10.26 ERDA spectra of a-SiH samples (refer to text for letter assignment) on c-Si. The *vertical line* indicates the surface of the a-Si film (from [95])

the ERDA spectra of PECVD layers (samples A–E) and EBE layer (sample F). Sample A corresponds to as-deposited a-SiH, whereas B–E are thermally annealed in different conditions, with a double annealing for D and E to induce a strong effusion of hydrogen.

These ERDA measurements were coupled to FTIR spectroscopy to evaluate the hydrogen content and the bonding configurations of hydrogen in the a-Si network. The bonded hydrogen proportion in the as-deposited layer (the only hydrogen type seen by FTIR) is equal to 6.5 at.% while the total hydrogen is 11.5 % according to the ERDA analysis, which means that nearly 5 at.% of hydrogen is free. After thermal annealing, the amount of bonded hydrogen is reduced drastically below 2 at.% but ERDA analysis shows a more moderate reduction of the total hydrogen. This means that some dissociated hydrogen did not exodiffuse upon thermal annealing, and stays in the layer as free hydrogen. After more pronounced thermal annealing, a residual of 2.3 at.% H content still remains in the a-Si film. In sample F, indicated for comparison only, the analysis reveals the presence of hydrogen near surface only, without trace detected in the volume.

At the opposite of the preceding example, hydrogen may be introduced on purpose to tailor physical properties. Quantum dots (QDs) embedded in silicon nitride films are being considered for third generation solar cells and spectral converters. They can be obtained from silicon-rich silicon nitride (SRSN) precursor material by PECVD deposition of a-SiN_x. Recent investigations on luminescence of a-SiN_x:H layers deposited by PECVD have focused on treatment by low temperature hydrogen plasma annealing (HPA) [96]. Whatever the stoichiometry from a-$SiN_{0.3}$ to a-Si_3N_4, an overall enhancement of hydrogen concentration post HPA is observed by ERDA (implemented with heavy ions, 100 MeV Ag^+) in conjunction with an enhancement in the photoluminescence (PL) for all the films.

Modifications observed in the shape of PL spectra are considered as only be due to hydrogen passivation of defects, without quenching of luminescence. It should be noticed that even if large variations of hydrogen contents in a-SiN_x:H layers and information on growth mechanisms can be evidenced by spectroscopies based on synchrotron radiation such as resonant soft X-ray reflectivity (R-SoXR) in conjunction with measurements of optical constants, ERDA calibration is still required [97].

Since the behavior of hydrogen has a profound impact on the electronic and structural properties of a-Si and related layers, understanding of hydrogen diffusion mechanisms is of primary importance, thought to be mediated by dangling bond type defects. Hydrogen diffusion in a-Si is indeed relatively complex. At low concentration, it is independent of the concentration, but shows at higher levels both immobile and mobile components [98, 99]. Real-time and in situ ERDA measurements enable to approach kinetic parameters from a single ramped thermal annealing [100].

Figure 10.27a shows ERDA hydrogen profile measured before annealing in a buried a-Si layer (2 μm thick), obtained by Si implantation in a (100) oriented silicon wafer, and hydrogen implanted. Figure 10.27b is the related thermal evolution during the temperature ramp. Assuming the implanted hydrogen concentration is described by a Gaussian distribution, time and temperature evolutions of diffusion coefficient can be derived from the full width at half maximum. The parameters found for hydrogen diffusion ($E_a = 1.82 \pm 0.09$ eV and $D_0 = 1.1 \pm 0.9 \times 10^{-1}$ cm^2/s) are in excellent agreement with previous studies on hydrogenated a-Si containing hydrogen at similar concentrations (~7 at.%).

Besides characterization of the films, elucidation of the hydrogen transport and incorporation process during deposition is crucial for synthesis parameters control. For diamond films grown by chemical vapor deposition, a high concentration of H_2 is required in the gas mixture to generate a large amount of atomic hydrogen in order to promote diamond nucleation and growth instead of graphite. These films exhibit grained microstructure and papers report contradictory conclusions about hydrogen location, either in grain boundaries or trapped at in grain defects. The effects of synthesis conditions on hydrogen incorporation has been investigated by ERDA in diamond thin films [76, 101]. By using the same input gas ratios for all the samples but with adopting conditions to obtain different grain sizes (50 nm to 1 μm), it has been shown that the concentration of hydrogen increases with decreasing grain size and that the high hydrogen concentration is related with the increase in non-diamond phase at grain boundaries [101].

Although supported by Raman and XPS experiments, the above-mentioned conclusions remain partly speculative. Use of deuterium isotope labelling is another way to unravel the origin of hydrogen incorporated in the film. Mixtures of a hydrogenated precursor and molecular hydrogen are often used to control carbon hybridation and hydrogen content. The example shown Fig. 10.28 is related to the use of a combination of CH_4 and D_2 for a-C:H deposition by reactive RF magnetron sputtering [102]. Raising partial pressure of D_2, it was found that the total amount of H + D concentration remains constant (~22.7 %) whereas the D concentration in

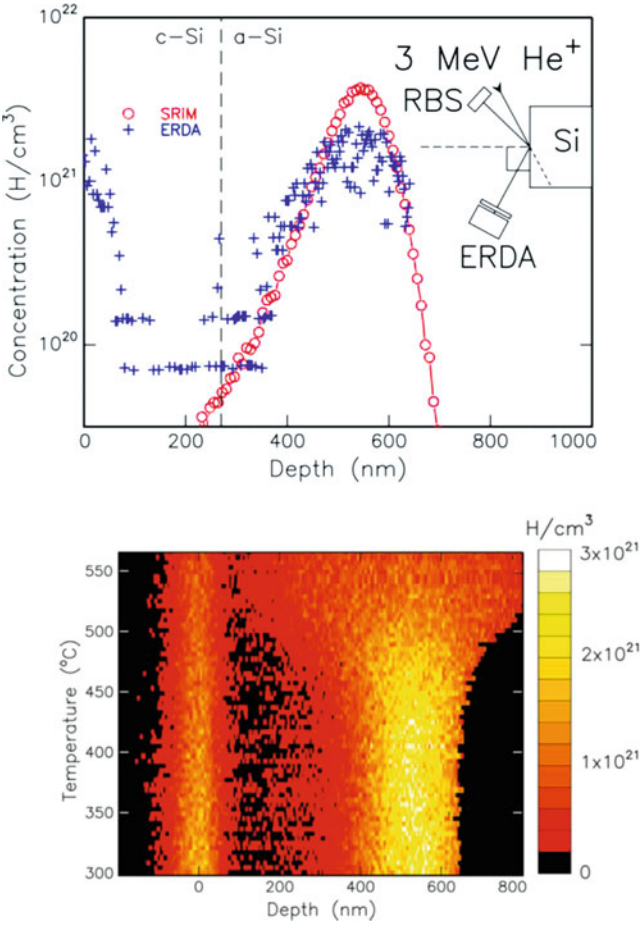

Fig. 10.27 ERDA characterization of hydrogen profile in a buried a-Si layer obtained by Si implantation. (**a**) Hydrogen concentration profile measured on as-implanted sample (*blue*) and SRIM code theoretical profile. (**b**) Map of the hydrogen concentration as a function of temperature and depth. The *color bar* on the *right* shows the hydrogen concentration scale (from [100])

the films linearly increases with the relative partial pressure $P_{D_2}/(P_{D_2} + P_{CH_4})$. XPS results show that all the samples have the same structure, mostly *sp3* bonding. This suggests that the activated CH_4 and D_2 molecules stick to the growing films and release the excess H and D atoms.

Modelization of hydrogen incorporation in carbon films is also considered in fusion research field. Diamond has been recognized as a candidate Plasma Facing Material (PFM) when it was anticipated less dust could be produced than with graphite. A primary concern of applying carbon-based material for PFM is their plasma induced etching and their ability to introduce impurities into the plasma. To develop diamond coatings for application in a fusion environment, it is necessary to have a good understanding of the paths by which the films may lose integrity. In a

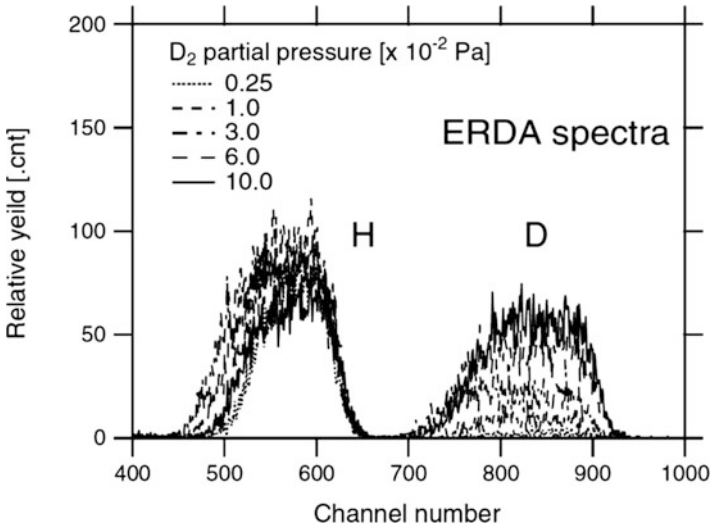

Fig. 10.28 ERDA spectra on the a-C:H + D films prepared with different D_2 partial pressure by reactive RF magnetron sputtering (from [102])

recent paper, CVD diamond films were exposed to moderate density hydrogen plasma, followed by ERDA characterization of as-treated films [103]. No significant hydrogen retention was observed under these conditions, indicating hydrogen is either not incorporated at all into the diamond structure or is initially retained and then removed if the top layers of the film are etched away. This conclusion however differs in the case of extended re-deposition of materials present in the plasma. Characterization by PIXE, RBS, and ERDA of Carbon Fiber Composite JET tiles exposed to deuterium plasma has shown that the tiles have incorporated metallic impurities at their surface, resulting from the erosion and re-deposition of structural material (Inconel and tungsten use as a marker) at the beginning of the plasma pulse. A significant amount of deuterium and hydrogen was so incorporated within the re-deposited layer [104].

In comparison to the above-mentioned studies, others uses of ERDA for thin film characterization remains at the margin, mainly dealing with irradiation effects in polymers, consecutive to ion implantation [105–107].

10.8 Conclusion

From this review of recent uses of ERDA, a conclusion emerges that this technique, rather than elderly, remains central for quantitative hydrogen characterization. Several reasons can be put forward:

– Need for hydrogen characterization is still growing, notably in the frame of researches on hydrogen storage materials. This benefits to any kind of technique provided it offers attractive analytical performance.

- Since very light elements, such as hydrogen, cannot be detected from their electron cloud, information used for quantification comes either from the nucleus or from bonding and/or close environment. Nuclear techniques, such as ERDA, have then kept their attractiveness.
- Vibrational spectroscopies can conveniently detect and quantify the amount of bonded hydrogen in most materials. However, a frequent question arises about "free" hydrogen atoms which remain almost invisible. At the opposite, ERDA probes any kind of hydrogen atoms, whatever their speciation.
- Quantification of hydrogen concentration from ERDA is absolute and reliable since accuracy rests on straight proportionality rules between the number of incident ions and the amount of recoil atoms detected.
- Depth resolution of ERDA enables to distinguish surface contamination from deeper hydrogen content. Measurements are then more representative of bulk material.

On the other hand, it is well known that characterization with IBA techniques requires accessing to dedicated facilities, which restrains frequent uses. Most facilities however allocate beam time after evaluation of experiment proposals.

ERDA has the role of a reference technique, used in combination with more common laboratory equipment. To illustrate this point, this is for instance the case for hydrogen embrittlement studies, often tackled in industrial laboratories with the help of Glow Discharge Optical Emission Spectroscopy. GDOES needs standards, difficult to prepare at low hydrogen content, but does not require sample preparation and provides in a few minutes concentration profiles of several elements, including hydrogen, with very low detection limits.

To maintain this favorable position, performances of ERDA technique must continue to be improved, at least in terms of sensitivity, such as atom.ppm detection limits obtained for hydrogen measurement in ERCS mode, but also to be adapted to novel approaches such as in situ/in operando devices.

References

1. S. Rubin, T.O. Passel, L.E. Bailey, Anal. Chem. **29**(5), 736 (1957)
2. R.F. Sipple, E.D. Glover, Nucl. Instrum. Methods **9**, 37 (1960)
3. D. Leich, T.A. Tombrello, Nucl. Instrum. Methods **108**, 67 (1973)
4. M.C. Stauber, G.M. Padawer, W. Brandt, M.D. D'Agostino, E.A. Kamykowski, D.A. Young, Proc Fourth lunar Sci. Conf. Geochim. Cosmochim. Acta Sup 4 Vol 2 2189, Pergamon (1973)
5. E. Ligeon, A. Guivarch, Radiat. Eff. **22**(2), 10 (1974)
6. W.A. Lanford, H.P. Trautvetter, J.F. Ziegler, J. Keller, Appl. Phys. Lett. **28**, 566 (1976)
7. B.L. Cohen, C.L. Fink, J.H. Degnan, J. Appl. Phys. **43**, 19 (1972)
8. J. L'Ecuyer, C. Brassard, C. Cardinal, J. Chabbal, L. Deschênes, J.P. Labrie, B. Terreault, J.G. Martel, R. St. Jacques, J. Appl. Phys. **47**, 381 (1976)
9. J. Tirira, Y. Serruys, P. Trocellier, *Forward Recoil Spectroscopy* (Plenum Press, New York, 1996)
10. W.-K. Chu, J. Mayer, M. Nicolet, *Backscattering Spectrometry* (Academic, New York, 1978)

11. J. Tesmer, M. Nastasi, *Handbook of Modern Ion Beam Materials Analysis* (Materials Research Society, Pittsburgh, 1995)
12. M. Da Costa, F.L. Freire, Surf. Coat. Technol. **204**, 1993 (2010)
13. H. Bethe, W. Heitler, Proc. R. Soc. Lond. A **146**, 83 (1934)
14. H. Andersen, J. Ziegler, *Hydrogen Stopping Powers and Range in All Elements*, vol. 3 (Pergamon, New York, 1977)
15. F. Ziegler, J. Biersack, U. Littmark, *Stopping Powers and Range of Ions in Solids* (Pergamon, New York, 1985)
16. E. Szilàgyi, F. Pàszti, G. Amsel, Nucl. Instrum. Methods B **100**, 103 (1995)
17. E. Szilàgyi, Nucl. Instrum. Methods B **268**, 1731 (2010)
18. J. Tirira Contribution à l'étude de la collision ^{4}He- proton et à la spectrométrie de recul élastique. Rapport CEA-R-5529 (1990)
19. M. Mayer, SIMNRA user's guide, Tech. Rep. IPP 9/113, Max–Planck–Institut für Plasmaphysik, Garching (1997)
20. C. Jeynes, N. Barradas, P. Marriott, G. Boudreault, M. Jenkin, E. Wendler, R. Webb, J. Phys. D Appl. Phys. **36**, R97 (2003)
21. F.H. Habraken, Nucl. Instrum. Methods **68**(1–4), 181 (1992)
22. J. Tirira, P. Trocellier, J.-P. Frontier, Nucl. Instrum. Methods B **45**, 147 (1990)
23. G. Dollinger, P. Reichart, G. Datzmann, A. Hauptner, H.J. Körner Appl, Phys. Lett. **82**, 148 (2003)
24. M. Moser, P. Reichart, C. Greubel, G. Dollinger, Nucl. Instrum. Methods B **269**, 2217 (2011)
25. M. Borysiuk, L. Ros, P. Kristiansson, H. Skogby, N. Abdel, M. Elfman, P. Golubev, E.J.C. Nilsson, J. Pallon, Nucl. Instrum. Methods B **306**, 49 (2013)
26. T. Wang, D. Grambole, R. Grötzschel, F. Herrmann, U. Kreißig, F. Eichhorn, G. Brauer, W. Möller, Surf. Coat. Technol. **158–159**, 139 (2002)
27. D. Grambole, T. Wang, F. Herrmann, F. Eichhorn, Nucl. Instrum. Methods B **210**, 526 (2003)
28. T.S. Wang, H.Y. Lv, D. Grambole, Z. Yang, H.B. Peng, Y.C. Han, J. Nucl. Mater. **386–388**, 214 (2009)
29. S. Wagner, M. Moser, C. Greubel, K. Peeper, P. Reichart, A. Pundt, G. Dollinger, Int. J. Hydrog. Energy **38**, 13822 (2013)
30. J.C. Brachet, C. Toffolon-Masclet, D. Hamon, C. Raepsaet, J.-L. Bechade, Diffusion and defects data Part B (solid state phenomena). **172–174**, 753 (2011)
31. C. Raepsaet, H. Khodja, P. Bossis, Y. Pipon, D. Roudil, Nucl. Instrum. Methods B **267**, 2245 (2009)
32. C. Raepsaet, P. Bossis, D. Hamon, J.-L. Bechade, J.C. Brachet, Nucl. Instrum. Methods B **266**, 2424–2428 (2008)
33. A. Sawatzky, J. Nucl. Mater. **2**(4), 321 (1960)
34. A. Hellouin de Menibus, Q. Auzoux, O. Dieye, P. Berger, S. Bosonnet, E. Foy, V. Macdonald, J. Besson, J. Crépin, J. Nucl. Mater. **449**, 132 (2014)
35. M. Puls, J. Nucl. Mater. **393**, 350 (2009)
36. C. Korn, S. Goren, Phys. Rev. B **33**(1), 68 (1986)
37. S. Markelj, I. Čadež, P. Pelicon, Z. Rupnik, Nucl. Instrum. Methods B **259**, 989 (2007)
38. A. Tavassoli, A. Alamo, L. Bedel, L. Forest, J.-M. Gentzbittel, J.-W. Rensman, E. Diegele, R. Lindau, M. Schirra, R. Schmitt, H.C. Schneider, C. Petersen, A.-M. Lancha, P. Fernandez, G. Filacchioni, M.F. Maday, K. Mergia, N. Boukos, I. Baluc, P. Spatig, E. Alves, E. Lucon, J. Nucl. Mater. **329–333**, 257 (2004)
39. R. Gonzalez-Arrabal, F. Munnik, M. González, P. Romero, R. Heller, F. Leardini, J.M. Perlado, Nucl. Instrum. Methods B **270**, 27 (2012)
40. S. Markelj, P. Pelicon, J. Simčič, Z. Rupnik, I. Čadež, Nucl. Instrum. Methods B **261**, 498 (2007)
41. S. Markelj, O. Ogorodnikovab, P. Pelicon, T. Schwarz-Selingerb, I. Čadež, Appl. Surf. Sci. **282**, 478 (2013)

42. K. Peeper, M. Moser, P. Reichart, E. Markina, M. Mayer, S. Lindig, M. Balden, G. Dollinger, J. Nucl. Mater. **438**, S887 (2013)
43. K. Peeper, M. Moser, P. Reichart, E. Markina, S. Elgeti, M. Balden, T. Schwarz-Selinger, M. Mayer, G. Dollinger, Phys. Scr. **T159** 014070
44. A. Lòpez-Suàrez, Int. J. Hydrog. Energy **35**, 10404 (2010)
45. J.R. Ares, F. Leardini, P. Diaz-Chao, I.J. Ferrer, J.F. Fernàndez, C. Sànche, Int. J. Nucl. Energy **39**, 2587 (2014)
46. Y.K. Gautam, M. Kumar, R. Chandra, Surf. Coat. Technol. **237**, 450 (2013)
47. A. Didyk, V. Kulikauskas, R. Winiewski, T. Wilczynska, K. Kitowski, Phys. Part. Nucl. Lett. **9**(1), 96 (2012)
48. A. Didyk, V. Kulikauskas, R. Winiewski, T. Wilczynska, K. Kitowski, A. Hofman, A. Shiryaev, Y. Zubavichus, Phys. Part. Nucl. Lett. **9**(1), 86 (2012)
49. R. Ishigami, Y. Ito, K. Yasuda, Nucl. Instrum. Methods B **266**, 1319 (2008)
50. K.J. Alvine, V. Shutthanandan, W.D. Bennett, C.C. Bonham, D. Skorski, S.G. Pitman, M.E. Dahl, C.H. Henager, Appl. Phys. Lett. **97**, 221911 (2010)
51. B. Tsuchiya, S. Nagata, K. Morita, Solid State Ion. **192**, 30 (2011)
52. A. Mackova, L. Salavcova, J. Špirkova, R. Groetzschel, F. Eichhorn, Nucl. Instrum. Methods B **249**, 339 (2006)
53. K.D. Kreuer, S. Paddison, E. Spohr, M. Schuster, Chem. Rev. **104**, 4637 (2004)
54. P. Colomban, Fuel Cells **13**(1), 6 (2013)
55. S. Sorieul, S. Miro, M. Taillades-Jacquin, J. Dailly, F. Mauvy, M.-H. Berger, P. Berger, Nucl. Instrum. Methods B **266**, 1430 (2008)
56. J.-H. Kim, B. Tsuchiya, S. Nagata, T. Shikama, Solid State Ion. **180**, 271 (2009)
57. J.-H. Kim, H. Choi, T. Shikama, Appl. Surf. Sci. **257**, 8876 (2011)
58. P. Berger, J.-P. Gallien, H. Khodja, L. Daudin, M.-H. Berger, A. Sayir, Solid State Ion. **177**, 1655 (2006)
59. T. Diedrich, T.G. Sharp, K. Leinenweber, J.R. Holloway, Chem. Geol. **262**, 87 (2009)
60. H. Bureau, C. Raepsaet, H. Khodja, A. Carraro, C. Aubaud, Geochim. Cosmochim. Acta **73** (11), 3111 (2009)
61. C. Aubaud, H. Bureau, C. Raepsaet, H. Khodja, A.C. Withers, M. Hirschmann, D.R. Bell, Chem. Geol. **262**, 78 (2009)
62. C. Raepsaet, H. Bureau, H. Khodja, C. Aubaud, A. Carraro, Nucl. Instrum. Methods B **266**, 1333 (2008)
63. M.S. Paterson, Bull. Mineral. **105**, 20 (1982)
64. I. Reiche, J. Castaing, T. Calligaro, J. Salomon, M. Aucouturier, U. Reinholz, H.-P. Weise, Nucl. Instrum. Methods B **249**, 608 (2006)
65. T. Calligaro, Y. Coquinot, I. Reiche, J. Castaing, J. Salomon, G. Ferrand, Y. Le Fur, Appl. Phys. A **94**, 871 (2009)
66. S. Takabayashi, K. Okamoto, T. Nakatani, H. Sakaue, T. Takahagi, Jpn. J. Appl. Phys. **48**, 092304-1 (2009)
67. J.G. Buijnsters, R. Gago, I. Jiménez, M. Camero, F. Agulló-Rueda, C. Gómez-Aleixandre, Jpn. J. Appl. Phys. **105**, 093510-1 (2009)
68. D. Boutard, B. Scherzer, W. Möller, J. Appl. Phys. **65**, 3833 (1989)
69. W. Jacob, W. Möller, Appl. Phys. Lett. **63**, 1771 (1993)
70. F. Černý, V. Jech, I. Štěpănek, A. Mackovă, S. Konvičkovà, Appl. Surf. Sci. **256S**, S77 (2009)
71. S. Miyai, T. Kobayashi, T. Terai, Jpn. J. Appl. Phys. **48**, 05EC05-1 (2009)
72. M. Kahn, S. Paskvale, M. Čekada, T. Schöberl, W. Waldhauser, C. Mitterer, P. Pelicon, E. Brandstätter, Diam. Relat. Mater. **19**, 1245 (2010)
73. L. Marcinauskas, V. Valinčius, A. Grigonis, Surf. Coat. Technol. **205**, S71 (2011)
74. R. Kometani, S. Ishihara, Sci. Technol. Adv. Mater. **10**, 034501-1 (2009)
75. M. Čekada, M. Kahn, P. Pelicon, Z. Siketić, I. Bogdanović Radović, W. Waldhauser, S. Paskvale, Surf. Coat. Technol. **211**, 72 (2012)

76. S.A. Rakha, G. Yu, J. Cao, J. Exp. Nanosci. **7**(4), 378 (2012)
77. S. Nakao, A. Matsumoto, T. Soga, N. Kishi, Nucl. Instrum. Methods B **308**, 328 (2013)
78. S. Nakao, K. Yukimura, H. Ogiso, S. Nakano, T. Sonoda, Vacuum **89**, 261 (2013)
79. S. Nakao, A. Kinomura, T. Sonoda, Nucl. Instrum. Methods B **307**, 333 (2013)
80. X. Chen, T. Kato, J. Appl. Phys. **115**, 044908 (2014)
81. K. Yokota, M. Tagawa, A. Kitamura, K. Matsumoto, A. Yoshigoe, Y. Teraoka, Appl. Surf. Sci. **255**, 6710 (2009)
82. S. Yamamoto, A. Kawana, C. Masuda, Surf. Coat. Technol. **236**, 457 (2013)
83. K. Murata, H. Ushijima, H. Ueda, K. Kawaguchi, J. Chem. Soc. Chem. Commun. 567 (1992)
84. T. Saito, K. Terashima, Y. Utsushikawa, J. Appl. Phys. **107**, 073522-1 (2010)
85. J.G. Buijnsters, R. Gago, A. Redondo-Cubero, I. Jiménez, J. Appl. Phys. **112**, 093502 (2012)
86. A. Wada, T. Suzuki, M. Niibe, F. Ito, K. Kanda, Jpn. J. Appl. Phys. **50**, 06GG05 (2011)
87. A. Wada, T. Ogaki, M. Niibe, M. Tagawa, H. Saitoh, K. Kanda, H. Ito, Diam. Relat. Mater. **20**, 364 (2011)
88. R. Imai, A. Fujimoto, M. Okada, S. Matsui, T. Yokogawa, E. Miura, T. Yamasaki, T. Suzuki, K. Kanda, Diam. Relat. Mater. **44**, 8 (2014)
89. A. Focsa, A. Slaoui, H. Charifi, J.P. Stoquert, S. Roques, Mater. Sci. Eng. B **159–160**, 242 (2009)
90. F. Ehrhardt, G. Ferblantier, D. Muller, C. Ulhaq-Bouillet, H. Rinnert, A. Slaoui, J. Appl. Phys. **114**, 033528 (2013)
91. Anjali, S. Ghosh, P. Srivastava, S.A. Khan, A.P. Pathak, Nucl. Instrum. Methods B **267**, 1797 (2009)
92. N.Q. Khánh, M. Serényi, A. Csik, C. Frigeri, Vacuum **86**, 711 (2012)
93. C. Frigeri, M. Serényi, N.Q. Khánh, A. Csik, L. Nasi, Z. Erdélyi, D.L. Beke, H.G. Boyen, Appl. Surf. Sci. **267**, 30 (2013)
94. A. Csik, M. Serényi, Z. Erdélyi, A. Nemcsics, C. Cserhati, G.A. Langer, D.L. Beke, C. Frigeri, A. Simon, Vacuum **84**, 137 (2010)
95. Z. Said-Bacar, P. Prathap, C. Cayron, F. Mermet, Y. Leroy, F. Antoni, A. Slaoui, E. Fogarassy, Appl. Surf. Sci. **258**, 9359 (2012)
96. R.K. Bommali, S. Ghosh, G. Vijaya Prakash, K. Gao, S. Zhou, S.A. Khan, P. Srivastava, J. Appl. Phys. **115**, 053525 (2014)
97. R.K. Bommali, M.H. Modi, S. Zhou, S. Ghosh, P. Srivastava, Appl. Surf. Sci. **305**, 173 (2014)
98. B.C. Johnson, J.C. McCallum, A.J. Atanacio, K.E. Prince, J. Appl. Phys. **95**(10), 101911 (2009)
99. S. Acco, D.J. Williamson, P.A. Stolk, F.W. Saris, M.J. Van den Boogaard, W.C. Sinke, W.F. Van der Weg, S. Roorda, P.C. Zalm, Phys. Rev. B **53**(8), 4415 (1996)
100. D. Smeets, B.C. Johnson, J.C. McCallum, C.M. Comrie, Nucl. Instrum. Methods B **269**, 2657 (2011)
101. S.A. Rakha, C. Jianqing, X. Huihao, Y. Guojun, D. Zhu, J. Gong, Diamond Relat. Mater. **18**, 1247 (2009)
102. D. Sekiba, N. Takemoto, M. Okada, S. Ishii, T. Sakurai, K. Akimoto, Diamond Relat. Mater. **27–28**, 60 (2012)
103. A. Deslandes, M.C. Guenette, C.M. Samuell, I. Karatchevtseva, M. Ionescu, D.D. Cohen, B. Blackwell, C. Corr, D.P. Riley, Fusion Eng. Des. **88**, 3101 (2013)
104. L.C. Alves, E. Alves, N.P. Barradas, R. Mateus, P. Carvalho, J.P. Coad, A.M. Widdowson, J. Likonen, S. Koivuranta, Nucl. Instrum. Methods B **268**, 1991 (2010)
105. A. Mackova, J. Bocan, R.I. Khaibullin, V.F. Valeev, P. Slepicka, P. Sajdl, V. Svorcik, Nucl. Instrum. Methods B **267**, 1549 (2009)
106. A. Mackova, P. Malinskya, R. Miksova, R.I. Khaibullin, V.F. Valeev, V. Svorcik, P. Slepicka, M. Slouf, Appl. Surf. Sci. **275**, 311 (2013)
107. A. Mackova, P. Malinsky, R. Miksova, H. Pupikova, R.I. Khaibullin, P. Slepicka, A. Gombitová, L. Kovacik, V. Svorcik, J. Matousek, Nucl. Instrum. Methods B **325**, 89 (2014)

Chapter 11
Nuclear Reaction Analysis

Hans-Werner Becker and Detlef Rogalla

Abstract Nuclear reaction analysis (NRA) is a method utilizing an ion beam from an accelerator to determine the hydrogen content in materials. The hydrogen concentration can be quantified absolute and the method can provide depth profiles in the range up to 2–3 μm with a depth resolution in the range of a few nm. Concentrations of 500 at. ppm are easily measurable and with special efforts sensitivities down to 1 ppm have been achieved. The chapter describes the basic principles of the measurements and data analyses and discusses special cases and complications arising with particular samples or when very low concentrations are to be measured.

Keywords Absolute hydrogen concentration • Accelerator • Background • Beam current • Beam intensity • Beam resolution • Borehole detector • Calibration • Chemical binding • Cross section • Depth information • Depth profiling • Depth resolution • Detector • Deterioration • Doppler broadening • Efficiency • Fluence • Hydrogen concentration • Hydrogen loss • Hydrogen storage material • Low concentration detection • Nuclear reaction analysis • Nuclear resonance reaction • resolution • Resonance • Resonance energy • Stability of samples • Stability of samples • Stopping power • Straggling • Surface • Surface cleaning • Surface peak • Yield • γ-ray detection

11.1 Introduction

The study of hydrogen in materials with a resonance in a nuclear reaction induced by an ion beam from an accelerator is possible because the products of such a reaction (usually α-particles and/or γ-rays) give a unique and quantitative signature of hydrogen present in the sample. Although being a nuclear method, nowadays this technique is so mature and straightforward that in order to be used by the material scientist to analyze his samples and to understand and interpret the results, only little knowledge of nuclear physics is necessary.

H.-W. Becker (✉)
RUBION, Central Unit for Ion Beams and Radioisotopes, Ruhr-University Bochum, Universitätsstraße. 150, Bochum 44801, Germany
e-mail: hans-werner.becker@rub.de

H. Fritzsche et al. (eds.), *Neutron Scattering and Other Nuclear Techniques for Hydrogen in Materials*, Neutron Scattering Applications and Techniques,
DOI 10.1007/978-3-319-22792-4_11

Nuclear resonance reactions have been used for hydrogen detection in materials already since the 1970s, for example by Leich and Tombrello for the investigation of lunar samples [1]. In this work they used a ^{19}F beam and the resonance at a beam energy of 16.6 MeV. The method became more spread and common in material analysis, when Lanford and coworkers established the resonance at the energy of 6.4 MeV in the reaction induced by a ^{15}N beam [2]. This reaction is nowadays the one mostly used due to the excellent properties of the resonance leading to favorable sensitivity and depth resolution. Therefore in this chapter this reaction is discussed mainly, the principle considerations apply however for other reactions [3–5] as well.

In the case of the ^{15}N method the absolute hydrogen concentration in a sample can be detected down to 500 at. ppm easily with standard techniques and for more sophisticated experimental approaches concentrations down to the 1 at. ppm level have been measured [6]. The hydrogen content is determined depth resolved with a resolution of about 10 nm decreasing somewhat with depth. The maximal probing depth is 2–3 μm. An excellent and very detailed review about the method has been published recently [7].

11.2 The Principle of the Method

11.2.1 Interaction of Ions with Matter

For an understanding of the Nuclear Resonance Reaction Analysis it is necessary to bear in mind the processes that occur when fast ions penetrate into matter. The by far most probable process is the interaction of the ions with the electronic cloud of the atoms mostly with electrons with the smallest binding energies (such as conduction electrons). Each interaction leads to an energy loss of the ion, which reduces the energy successively and brings the ion eventually to a stop within a maximal range. Since the mass difference of ions and electrons is large the energy loss in each collision is small such that this statistical process can be considered in most cases as quasi-continuous. (The Coulomb interaction with the nuclei can be neglected for the ions and energies relevant here.) The energy loss per atomic layer, the stopping cross section ε, is dependent on the element in a sample (i.e. the number of electrons or the atomic numbers Z) and it is given in units of eV/(atoms/cm^2). For compounds the stopping cross section is just the linear combination of the components (Bragg's rule), which is sufficient accurate in most cases, but in some circumstances corrections for the chemical binding need to be applied [8].

Alternatively, the stopping of ions in matter is often described by the so-called stopping power, which is defined as the energy loss per length unit and sometimes there is confusion about these quantities in literature. Though both values describe the same phenomenon, the difference is that the stopping cross section is dependent on the density of the material, which can vary much from element to element and moreover might not be well defined for thin layers or specific sample preparations. There is a vast amount of measured data in literature about the stopping cross

section or the stopping power of many ions in various elements and compounds for a large range of ion energies. These data have been collected in data bases, the most famous and mostly used being SRIM [9], a program which calculates the stopping power of any ion in any sample on a semi-emperical approach taking into account experimental data. Thus, for practical purposes of material analysis stopping cross sections can be considered as something available in the toolbox of the analyst and known with an accuracy of 5–10.

To get a feeling for the stopping cross section one can obtain for example for ^{15}N ions with an energy of 7 MeV in silicon or gold a penetration depth of 5.88 µm and 2.32 µm, a stopping power of 1.38 keV/nm and 3.91 keV/nm and a stopping cross section of 277 eV/(10^{15} atoms/cm^2) and 663 eV/(10^{15} atoms/cm^2) respectively.

11.2.2 Basic Principle of Depth Profiling

Compared to the energy loss process described above, there is a low probability for an ion beam to interact with hydrogen in a sample via the nuclear forces. This nuclear reaction leads to the formation of the intermediate nucleus ^{16}O which in turn decays to an α-particle and an excited ^{12}C which emits a γ-ray of 4.4 MeV. This γ-ray is a unique signature of hydrogen present in the sample and can be used for analysis.

The probability of the reaction as a function of the beam energy is plotted in Fig. 11.1 as a nuclear cross section. This cross section has an isolated and narrow resonance at the beam energy of 6.4 MeV because the energy of the oxygen formed at this beam energy corresponds to an excitation energy state of the oxygen nucleus. This state has a certain lifetime and therefore an energy width associated with it. Several authors [4, 12] have measured this width to be some 1.8 keV or smaller, which is ideal for material analysis purposes and the reason for the high depth resolution of the technique.

The data points in Fig. 11.1 show in the vicinity of the resonance only one point at the maximum because the energy resolution in an accelerator experiment is not good enough for a measurement of such a narrow resonance, which has a Breit-Wigner (i.e. a Lorentzian) shape. Experimentally one observes reactions from the integral over the resonance, from which the cross section at the maximum can be calculated when the width of the resonance is known. The Breit-Wigner curve given in Fig. 11.1 is therefore calculated [10] from measurements integrated over the resonance and the known width. In addition to the resonance at 6.4 MeV there is a small off resonance cross section, which will become important in measurements of very low hydrogen concentrations (see Sect. 11.3.4).

It should be noted that Fig. 11.1 has a logarithmic scale; the cross section at the resonance is more than four orders of magnitude larger than off resonance. Simplifying for a moment the essence of Fig. 11.1 one can say that the resonance occurs at the resonance energy of 6.4 MeV in an energy window of 1.8 keV only. This opens up the possibility for depth profiling.

The principle of the procedure is sketched in Fig. 11.2. If a ^{15}N beam with the energy of the resonance energy enters a sample, the reaction can occur at the

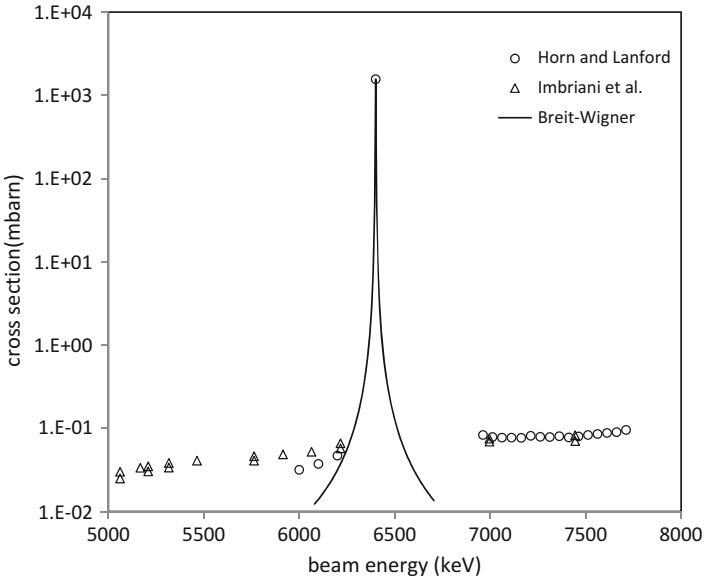

Fig. 11.1 Non-resonant cross section of the ^{1}H(^{15}N,$\alpha\,\gamma$)^{12}C reaction [10, 11]. The *solid line* gives the shape of the resonance with the resonance parameters used in [10]

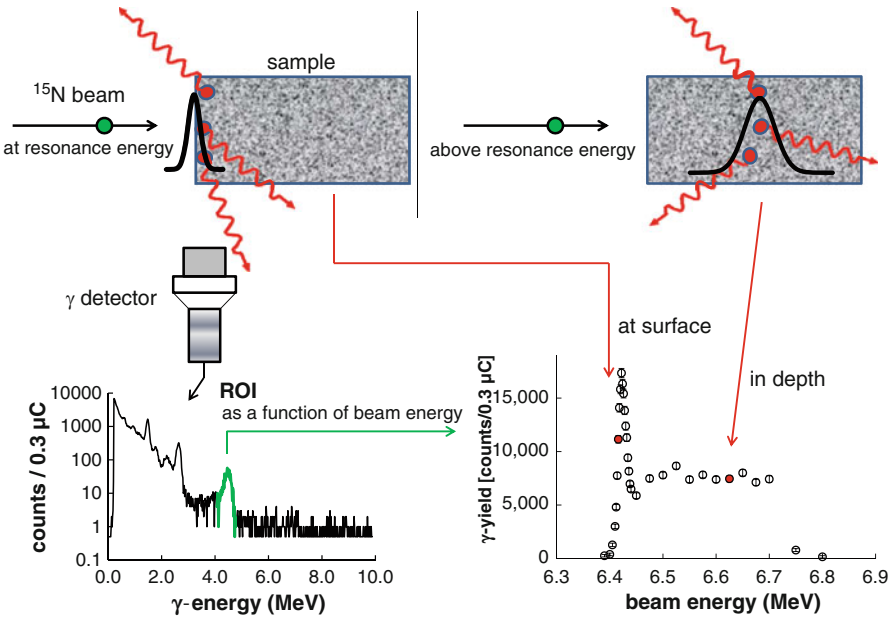

Fig. 11.2 Schematic sketch of depth profiling (see text). The γ-spectrum has been accumulated for a beam charge of 0.3 µC. ROI (region of interest) are the integrated counts over the hydrogen signal (*green peak*). For more details see Sect. 11.3.3

surface. After penetrating a few nm into the sample (depending on the stopping power), the beam has lost more energy than the resonance window and therefore hydrogen cannot be detected. If the beam energy is now increased above the resonance energy, the reaction cannot occur at the surface but after a certain penetration depth, when the ions have lost just enough energy to get into the resonance window. Thus by increasing the beam energy the resonance is visually speaking "shifted" through the sample and probes layers at different depth. The thickness of this layer i.e. the depth resolution is limited by the resonance width and can be estimated from the stopping power (see examples above) to be some 2 nm. However, in reality the depth resolution is poorer, which will be discussed below (Sect. 11.2.5).

The detector in this procedure is for counting the emitted γ-rays only, its resolution is necessary to identify and discriminate the reaction γ-rays against background, but, other than in ERDA (see Chap. 10) or Rutherford-Backscattering-Spectrometry measurements, has no influence on the depth resolution. In most experimental setups today NaI(Tl) detectors or Bithmut Germanate (BGO) detectors are employed because of their high detection efficiency. For a detailed explanation of the spectrum in Fig. 11.2 see Sect. 11.2.5.

The yield Y, i.e. the intensity in the 4.4 MeV γ-line normalized to the number of incident beam particles, is a direct measure for the hydrogen concentration in a sample at a certain depth. The number of beam particles in one measurement is preferably determined by electrical integration of the beam current; the number of particles is then obtained by dividing the accumulated charge by the charge state of the ion beam and the elementary charge. In literature yields are often displayed in units of counts/μC; in comparing different data in this unit one has to consider, which charge state of the ions was used for an experiment. In the following yields are always given in counts per particle μC, where "particle" indicates that the charge is always normalized to the charge state of the ions.

Since the energy of the beam ions is much larger than chemical binding energies the detection process is independent from chemical binding. In this sense the method is "just counting nuclei". This is sometimes advantageous, but on the other hand NRA is not able to give information about the chemical binding.

11.2.3 Determining a Hydrogen Concentration

The total γ-ray yield Y_T from a narrow hydrogen detecting resonance which is defined as the emitted γ-rays per ion beam particles is first of all dependent on the hydrogen concentration of the sample material as well as on the probability of the reaction. Y_T at a certain depth can be written then as:

$$Y_T = R_H \cdot S \cdot \frac{1}{\varepsilon} \tag{11.1}$$

R_H is the ratio of hydrogen atoms to total atoms of the sample material and corresponds to the hydrogen concentration c_H as defined throughout this book via the relation:

$$R_H = \frac{c_H}{c_H + 1} \tag{11.2}$$

S is a constant representing the probability of the reaction which is here the integral over the resonance cross-section characterized by its height and width sometimes called the strength of the resonance. The third term $1/\varepsilon$ of Eq. (11.1) accounts for the effect of the stopping cross section ε of the sample material. The depth window in which the resonant reaction takes place depends on the energy loss of the ion beam. For a small ε this depth range is larger compared to a case with high stopping cross section and thus containing a larger amount of hydrogen. In other words, the stopping cross section determines the number of hydrogen atoms which are passed by the ions at energies in the small region of the resonance during their deceleration in the sample material.

According to Eq. (11.1) the hydrogen concentration of a sample in a certain depth can be calculated as a function of a measured yield Y and the stopping cross section ε of the sample material. Since γ-detectors in principle detect only a fraction of γ-rays with detection efficiency η the measured yield Y is given by $Y = Y_T \cdot \eta$. A factor $K = 1/(S \cdot \eta)$ can be defined including the strength of the resonance and the detector efficiency. K is a constant for an experimental set up and independent from the sample. Now R_H can be expressed as

$$R_H = Y \cdot K \cdot \varepsilon \tag{11.3}$$

In case of an unknown sample, the determination of the stopping cross section ε requires the knowledge of the hydrogen concentration, which is not known a priori. For small H concentrations the influence of the hydrogen to ε can be neglected, but for higher concentration it becomes significant. One option for calculating R_H is to initially assume a concentration for calculating ε and iteratively recalculate Eq. (11.3) until a consistent result is achieved. Alternatively, a formalism described by Rudolph et al. [13] can be applied. This approach is based on the separation of the total stopping cross section ε of the sample material into the contribution of the hydrogen and the contribution of all other atoms denoted as matrix atoms. It is simply done by adding the stopping cross section of pure hydrogen ε_H and the stopping cross sections of a hydrogen-free matrix ε_M weighted with the individual abundances.

$$\varepsilon = R_H \cdot \varepsilon_H + (1 - R_H)\varepsilon_M \tag{11.4}$$

Combining Eqs. (11.3) and (11.4) one derives to an expression for R_H which does not need an a priori knowledge of the hydrogen concentration.

$$R_H = K \cdot Y \cdot \varepsilon_M \cdot \frac{1}{1 + K \cdot Y \cdot (\varepsilon_M - \varepsilon_H)} \tag{11.5}$$

In order to calculate H concentrations from Eq. (11.5) the stopping cross section ε_M of the sample matrix at the probing depth can be obtained for example using SRIM (Chap. 11.2.1). It should be noted that for many compounds the stopping cross section is not very sensitive to details of the stoichiometry and the influence of uncertainties to the determination R_H is often small.

Though the constant K can be calculated from the resonance parameters and the detector efficiency it is in practice much easier and more reliable to obtain it from a measurement of a standard material with the known parameters $R_{H,s}$ and ε_s. Using Eq. (11.3) K is then

$$K = \frac{R_{H,s}}{Y_s \cdot \varepsilon_s} \tag{11.6}$$

This determination of K includes the calibration of the individual setup and it is good practice to check it from time to time. It should be emphasized however that nuclear reaction analysis is a method that needs a calibration only once because this calibration is valid for all types of samples and no standard is needed for an individual sample. This is a striking advantage of NRA compared to other analytical techniques such as for example Secondary Ion Mass Spectrometry (SIMS), where chemical and structural similar samples with known concentrations are needed for each sample type.

A numerical example for the calculation of a hydrogen concentration in a sample is given below in Sect. 11.2.7.

11.2.4 Depth Information

The depth information in a profile originates from the energy difference between the energy of the incident beam and the resonance energy. Since long the resonance is denoted as "the resonance at 6385 keV" though later measurements indicate a slightly higher value. A very precise measurement of the inverse reaction (i.e. the reaction of a proton beam with an ^{15}N sample) result in a value for an ^{15}N beam of (6393.6 ± 1.3) keV [14], another work reports the value of (6399.1 ± 2.9) keV [4]. In order to be independent from the absolute value of the resonance energy as well as from the absolute energy calibration of the accelerator one uses in practice a surface energy found in a measurement from a sample known to have surface hydrogen. The difference between surface energy and the energy at depth can then be converted by the stopping cross section into an areal atomic density (in units of atoms/cm^2) or an areal mass density. It is important to note that nuclear reaction analysis does not give the depth in length units (nm). To calculate this, the density of the sample has to be known which is not necessarily the density of bulk

material, in particular for thin layers or layered structures. Therefore, care has to be taken when thickness measurements of NRA are compared to analytical methods measuring the thickness of a sample layer directly in nm such as profilometric methods. In fact combining such results offers the option to determine densities. Nevertheless the description of layers in length units is often preferred in spite of uncertainties in the density since this is more vivid and ostensive.

For layered structures with significant different stopping cross sections the depth information over the entire system has to be calculated stepwise from the surface into the depth.

11.2.5 Depth Resolution

The depth resolution is ultimately limited by the width of the resonance used for depth profiling but for the narrow resonance at 6.4 MeV in the $^{15}N + H$ reaction other factors determining the depth resolution are dominant. One major contribution is the beam energy resolution ΔE_B, which is caused mainly by the high voltage ripple of the accelerator and the charge state of the ion beam used. It is determined eventually by the energy defining elements of the accelerator such as slits at the analyzing magnet. Detailed studies can be found in [15, 16]. At a tandem accelerator the beam resolution is usually between 5 and 10 keV for a 6.4 MeV nitrogen beam but for many accelerators it is not known exactly. It is not worthwhile to investigate and improve the beam resolution much further unless sophisticated cryogenic techniques for the sample are employed because another factor determining the depth resolution is the Doppler broadening [15, 17] which is due to thermal motion of the sample atoms. Though thermal energies are much smaller than the energy of the ion, the effective energy for the hydrogen atom is given by

$$E_{eff} = \frac{1}{2} M(\mathbf{v}_N + \mathbf{v}_H)^2 \tag{11.7}$$

where M is the mass of the projectile (here ^{15}N) and $\mathbf{v}_N$ and $\mathbf{v}_H$ the velocity vectors of the beam and the hydrogen atom respectively. Though $\mathbf{v}_H$ is negligible compared to $\mathbf{v}_N$ the mixed term of this quadratic addition is not and—since $\mathbf{v}_H$ is randomly distributed in space—gives rise to a distribution which is well approximated by a Gaussian with a FWHM of

$$\Delta E_D = 4\sqrt{\frac{\ln 2\, ME\, k_B T}{m}} \tag{11.8}$$

Here E is the energy of the beam, k_B the Boltzmann constant, T the temperature and m the mass of the sample atom (here hydrogen). This formula is in principle correct for free hydrogen atoms (or noble gases) only, in cases of molecules and/or lattices corrections have to be applied, which can be complicated [18, 19] and give

rise to significant larger values than obtained by Eq. (11.8). In fact several groups [20, 21] used the Doppler broadening to study the hydrogen bonding in gases or at solid surfaces. The width of the Doppler broadening depends on the sample material and is around 10 keV.

Like the Doppler broadening the beam resolution can be approximated by a Gaussian as well. Both influences add quadratically to the experimental resolution

$$\Delta E_{exp} = \sqrt{\Delta E_D^2 + \Delta E_B^2} \tag{11.9}$$

To get the total resolution this Gaussian needs to be convoluted with the resonance shape, which is a Breit-Wigner curve (i.e. a Lorentzian) resulting in a Voigt profile. This distribution is centered around the resonance energy, its width cannot be calculated analytically and is between a linear and quadratic summation of the Gaussian and Lorentzian components. Details can be found in [15].

For the case of an ^{15}N beam and the resonance at 6.4 MeV the total resolution is dominated by the experimental resolution since the resonance is so narrow. From the discussion above one can estimate an achievable energy resolution between 10 and 20 keV. Such values are found in practice in many laboratories and correspond to a depth resolution e.g., in silicon between 7 and 14 nm and in tungsten between 2.5 and 5 nm. This information is sufficient for many applications where structures with much larger thicknesses are investigated.

In cases where the exact resolution needs to be known, e.g. when layer thicknesses are in the range of the resolution one has to study experimentally the so-called instrument function. This is essentially the shape of the yield curve for a monatomic or very thin hydrogen layer. For this, a sample with low hydrogen concentration in the bulk but a defined surface layer is needed. There are several materials possible such as silicon wafers, W samples or even standard Al household foil [6], which is known to have very low hydrogen content. The main experimental challenge is here to maintain a defined surface layer during the measurement, which requires a very good vacuum in the UHV regime to avoid hydrogen build up by adsorption from the vacuum or beam induced deposition of Carbon on the surface. The experimental details will be discussed in Sect. 11.3.5.

Figure 11.3 shows a yield curve of a thin hydrogen layer on a silicon wafer measured with the set up employed at present at the tandem accelerator of the University of Bochum. The data points have been fitted with a Gaussian distribution only since the influence of the resonance width is negligible. The fit leads to a full width at half max of (13.9 ± 0.3) keV. If the layer is thinner than the width of the instrument function the hydrogen concentration and depth cannot be calculated anymore, as discussed above. Here the yield curve has to be analyzed differently, details of which are beyond the scope of this book and can be found in [22]. With this somewhat more complicated analysis one can determine the areal density of a thin hydrogen layer, which is for the data in Fig. 11.3 $1.9 \cdot 10^{15}$ atoms/cm^2 and therefore in the monolayer range only.

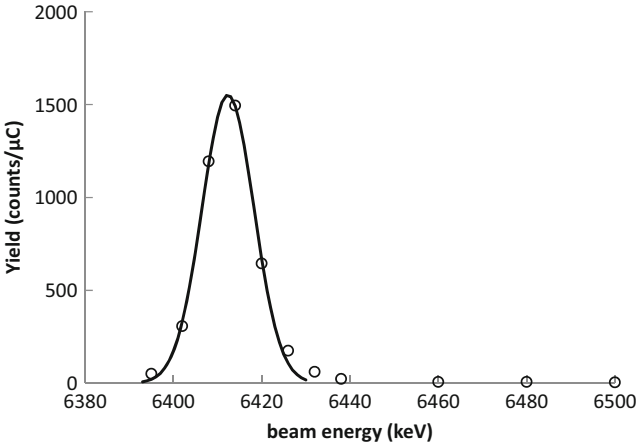

Fig. 11.3 Yield curve of a layer of hydrogen in the monolayer range on Si as an example for an instrument function

11.2.6 Straggling

The depth resolution discussed so far is valid in near surface regions only. In larger depth the energetic beam width deteriorates due to the statistical nature of the energy loss process. This effect is called the energy straggling ΔE_S and needs to be taken into account for larger energy losses e.g. when interfaces in larger depth are studied. It can be estimated qualitatively by Bohr's formula [23], which is a good approximation for a ^{15}N beam at the energies of relevance here.

$$\Delta E_S = 2\sqrt{2 \cdot \ln 2} \cdot \sqrt{4\pi\, e^2\, Z_1^2\, Z_2\, N} \tag{11.10}$$

with e being the elementary charge, Z_1 and Z_2 the atomic number of the projectile and the sample atoms, respectively and N the thickness of the layer the beam has penetrated. It is noteworthy that this approximation is independent of the energy of the projectile. In numerical values one gets $E_S = 1.2 \cdot \sqrt{Z_1^2\, Z_2\, N}$ in keV, when the layer thickness is given in 10^{18} atoms/cm^2. So, for a 100 nm thick Si layer which is $0.5 \cdot 10^{18}$ atoms/cm^2 one gets $\Delta E_S = 22.2$ keV (i.e. 16 nm), a 1 µm layer would result in a straggling of 70 keV (i.e. 50 nm). These values have to be added quadratically to the energy resolution discussed above. For compounds the straggling of each component has to be added quadratically [5]

A summary of more refined theoretical descriptions of the straggling can be found e.g. in [5]. A very practical way (e.g. for layers containing compounds or layered structures) to calculate the straggling is to use the SRIM program, which is not only a source for tabulated stopping power values but can also do a sophisticated Monte Carlo simulation of the energy loss process. After entering thickness,

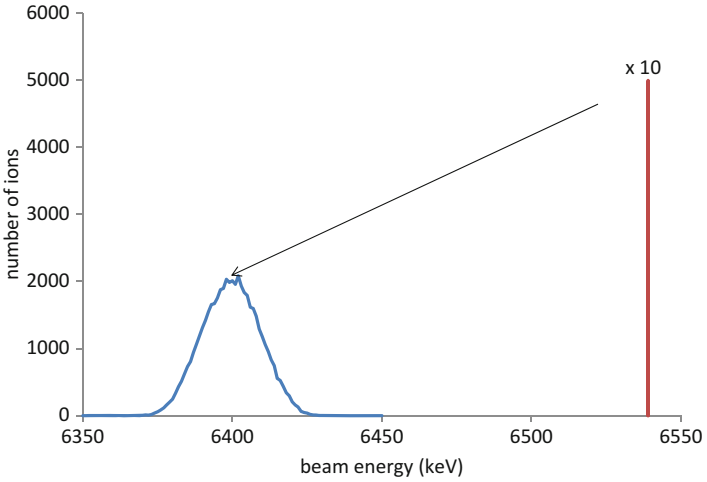

Fig. 11.4 Monte Carlo SRIM simulation of the energy broadening of a monoenergetic ^{15}N beam of 6.54 MeV after penetrating 100 nm of silicon

stoichiometry and density of one or more layers penetrated by the beam the program has the option to calculate the energies of the transmitted ions. If these values are binned appropriately one gets a distribution such as displayed in Fig. 11.4. The initial energy has been chosen such that the distribution of the transmitted ions is centered around the resonance energy of 6.4 MeV after passing 100 nm of silicon. The width of this distribution is 23.6 keV, which is in good agreement with the value of 22.2 keV from Bohrs approximation.

Finally it should be mentioned that a broadening of a slope of a hydrogen concentration can be caused not only by straggling but also by cases when a layer thickness is inhomogeneous within the area of the beamspot which will have a similar effect on the hydrogen concentration profile.

11.2.7 A Simple and Straightforward Example

As an example for the measurement of a depth profile we discuss here a study carried out in the course of a research program dealing with hydrogen storage materials [24, 25]. This example is simple and straightforward in the sense that the samples proved to be stable during the measurements (see discussion below) and the hydrogen concentrations are high.

The depth profiling has been performed with a setup used at present at the Ruhr-University of Bochum (Fig. 11.5) and described in more detail in [22]. It is designed for the measurement of low hydrogen concentrations, which will be discussed in Sect. 11.3.5. In brief, the beam enters the main chamber via a pipe with 2 mm in

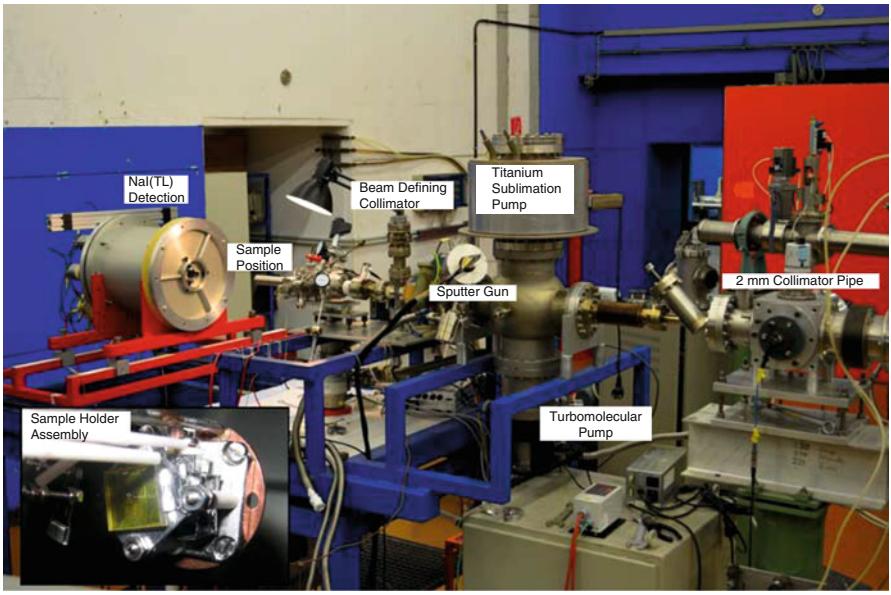

Fig. 11.5 Photograph of the setup at the Ruhr-University Bochum and (*inset*) details of the sample holder assembly with a ZnO-crystal mounted (see text)

diameter and a length of 10 mm, which serves also to separate the UHV in the chamber from the standard vacuum in the accelerator beam line ($\approx 10^{-6}$ mbar). The beam is then defined by a collimator of 1 mm or 3 mm in diameter, 60 cm in front of the sample position to avoid contributions from possible hydrogen contaminations in the collimator material. The sample is placed at the end of a pipe, which can be entirely surrounded by a 30 cm $\times$ 30 cm NaI(TL) borehole detector, which has a photopeak detection efficiency of 48 % for the 4.4 MeV γ-ray. The K factor for this arrangement as defined in Sect. 11.2.3, Eq. (11.6) has been determined in various measurements from standard samples with known hydrogen concentrations to be $7.10 \cdot 10^7$ μC/(eV cm^2).

Sample layers of Yttrium were produced by magnetron sputtering onto a SiO_2/Si substrate. These samples were loaded with hydrogen inside the sputter chamber with forming gas (95 % Ar/5 % H_2) for 1 h. This was done either in-situ at room-temperature directly after the deposition or after exposure to air and at a temperature of 500° C. Depth profiles for the two types of samples are shown in Fig. 11.6. In the upper part of Fig. 11.6 the raw data are plotted as the γ-yield per particle μC and in the lower part the hydrogen concentration is calculated according to the formalism given in Sect. 11.2.3. One can clearly see that the slopes between Fig. 11.6a, b are different because the varying stopping power due to the changing hydrogen concentration has been taken into account. The measurements have been carried out with a beam intensity of 10–20 nA, the total time needed for one depth profile was about 2 h.

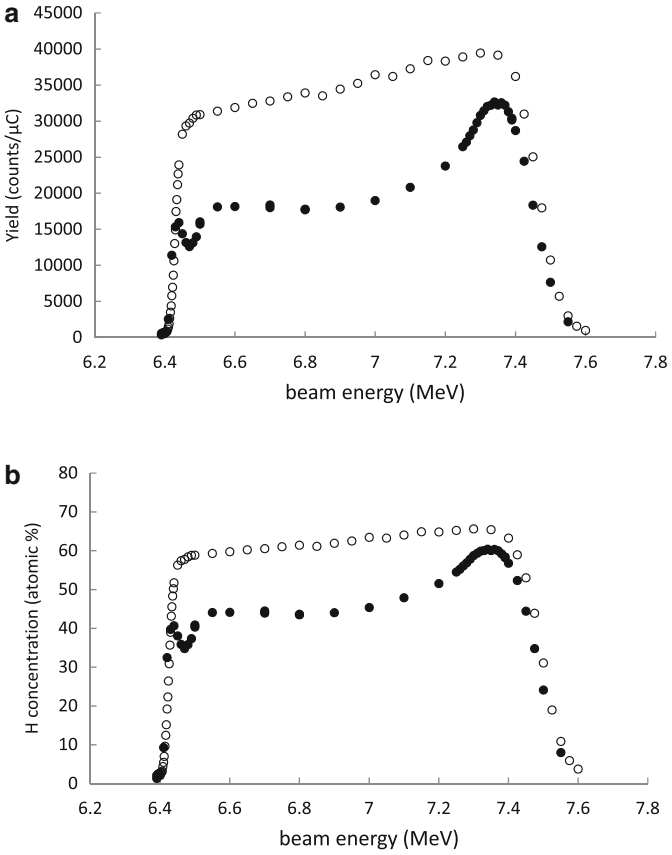

Fig. 11.6 Yield (**a**) and hydrogen concentration R (**b**) of Y layers loaded in-situ after deposition (*open circles*) and loaded after exposure to air (*solid points*)

In order to give a numeric example for the calculation of a hydrogen concentration outlined in Sect. 11.2.3 we select the point measured at 7 MeV for the sample exposed to air. Here 11290 γ-rays have been measured with a particle beam charge of 0.6 μC. The yield is therefore $1.88 \cdot 10^4$ counts/μC. The stopping cross sections of yttrium and hydrogen at 6.4 MeV are $566 \cdot 10^{-15}$ and $60.9 \cdot 10^{-15}$ eV$\cdot$ cm^2, respectively. Note that even though the beam energy is 7 MeV the stopping power at the resonance energy is relevant because the γ-rays are produced in the depth, where the ions have 6.4 MeV.

With these numbers and the K-factor given above Eq. (11.3) leads to R = 76 %, while Eq. (11.5) yields R = 45 %. This shows exemplarily the necessity to include the hydrogen in the calculation of the stopping power, when measuring high hydrogen concentrations.

For the sample loaded in-situ one gets an almost homogeneous hydrogen concentration over the entire thickness of the layer while for the sample loaded after exposure to air the hydrogen storage capacity is significantly reduced. In

addition one can identify a surface peak, which arises from a layer adsorbed from the ambient air.

The energy difference of the 50 % points of the rising and falling edge of the depth profile for the in-situ loaded layer is here 1074 keV. Assuming an average hydrogen concentration of 60 % and therefore a stopping power of 263 eV/(10^{15} atoms/cm^2) throughout the layer, the thickness is then $4.09 \cdot 10^{18}$ atoms/cm^2 of Y and H atoms together. In this case it is very uncertain to convert this into length units, because the density of the layer after loading is very uncertain. Additionally the layer is partly oxidized (as found by RBS measurements), which would have to be included in the stopping power calculation. Assuming the literature value for the density of yttrium the thickness would be 1.35 µm but most probably it is significantly smaller.

11.3 More Special Cases and Complications

While the example discussed above illustrates the simplicity of the measurement and the analysis of the data one has to be aware that complications and difficulties come along with certain samples, which require additional efforts for the experimental set up and the analysis of the data. One crucial point in each measurement is the stability of the samples under beam irradiation. Another important issue is the detection of low hydrogen concentrations which requires a closer look at the γ-ray detection, a discussion of background and the problems arising when measuring low concentrations in a certain depth while high concentrations are present at other depths or at the surface.

Measuring low hydrogen concentrations is important since hydrogen can change the properties of materials significantly even at low concentrations. Many efforts have been undertaken in the past to measure small traces of hydrogen. A prominent example is the determination of hydrogen in minerals of the Earth's crust and mantle such as olivine. Here, concentrations in the range of a few at. ppm have strong impacts on the mechanical properties such as viscosity and melting point behavior of rocks containing these minerals, which are crucial for an understanding of geodynamics [26]. Moreover, the hydrogen content in the so-called nominal anhydrous minerals (NAMs) may be an important contribution in the water balance of the earth mantle and could exceed the water stored in the oceans [27].

Although there are analytical techniques to measure low hydrogen concentrations such as IR spectroscopy (FTIR), these techniques need to be calibrated for the determination of absolute quantities. Remarkable work in the field of geoscience on the calibration of hydrogen concentrations down to a level of 10 at. ppm has been done in the past [28, 29]. A setup dedicated for the measurement of concentrations in the at. ppm region with NRA is described in [6]. In the following the experimental challenges and requirements to be fulfilled for such analyses are discussed in more detail.

11.3.1 Stability of Samples Under Irradiation

Sometimes the question arises about the change of the hydrogen concentration in a sample by the detecting nuclear reaction, which converts the hydrogen with the beam ion into a ^{12}C atom and an alpha particle. It is easily understood, however, that with atomic densities of materials in the order of 10^{22} atoms/cm^3 a layer of about 10 nm thickness as probed by the resonance has still 10^9 hydrogen atoms/cm^2 at a hydrogen concentration of 1 at. ppm. If a beam has a diameter of 1 mm^2 there are 10^7 hydrogen atoms available for the detection. Considering a detection efficiency of some 50 % the conversion of 10^3 hydrogen atoms by the nuclear reaction, i.e. four orders of magnitude less, would lead to an excellent counting statistics in the γ-peak, disregarding whether this can be accomplished in reasonable time for such a low concentration. Therefore the "consumption" of hydrogen by the detecting reaction is always negligible.

Nevertheless the stability of samples under irradiation is an important issue and it is mandatory in each study to prove that samples are stable or that the deterioration of the hydrogen concentration is understood and corrected for. Changes in the concentration can be caused by various effects of the beam such as structural or chemical changes by the ions or just by warming up the samples due to the power deposited by the beam. This power can be easily calculated by multiplying the energy of the ions with the number of ions per time, which is the electrical beam current divided by the charge state of the ions (in units of the elementary charge e). For example a nitrogen beam of ions with charge state 3 e and a beam intensity of 30 nA at an energy of 6.4 MeV results in a power of 64 mW, which needs to be dissipated by the sample.

Therefore, the deterioration of the hydrogen concentration can be dependent on both, the fluence, which is the number of ions per cm^2 accumulated during a measurement ("how long and how many points have been measured?") and on the beam intensity i.e. number of ions per seconds ("how fast has been measured?"). Sometimes samples reach a stable level after an initial degradation, which can be an indication that hydrogen is present in different phases. For specific applications detailed studies can be found in literature such as the early work of Thomas et al. [30].

Fortunately many layers are stable or change only little under beam irradiation in particular when a detector with high detection efficiency is employed or the beam can probe a larger area on the sample. Both approaches lead to a smaller beam load per sample area and thus to smaller deterioration effects. However, some samples are very sensitive to the beam and a detailed study of the effect of hydrogen loss is needed to be able to gain at least some information about depth profiles.

We present here an example related to cosmochemistry studies. Hydrothermal serpentinization experiments of amorphous silicates ($FeMgSiO_4$) are performed to constrain the conditions of alteration (temperature, timescale) of such silicates in asteroids, where they reacted with water at the time of the solar system formation. In these experiments, amorphous silicates react with water at a temperature

between 50 and 150° C and amorphous hydrated silicates are formed. This leads to a hydrogen (water) containing layer structure at the minerals surface in the depth range of μm and NRA is used to obtain hydrogen depth profiles. Details and results of these studies can be found in [31, 32].

These samples are very sensitive to beam damage and a reference material (natural serpentine; water content ≈ 14 mol%) was used to determine empirically a law for the hydrogen loss behavior and ultimately apply this law to real experimental samples. To probe the hydrogen loss at a certain depth the beam energy was set to 6.7 MeV. First the hydrogen content was measured with a low beam current of 0.8 nA for a time of about 1 min. This was repeated several times. The loss of hydrogen as a function of the total beam charge accumulated on the sample is shown in Fig. 11.7a. Then the beam current was progressively increased. One finds that the hydrogen loss (i.e. the difference between the measured and the initial concentration) follows a steady trend, which can be fitted with a logarithmic function of the fluence i.e. the accumulated charge. Above beam currents of 100 nA, the hydrogen loss rate increases indicating that further mechanisms such as warming-up by the beam intensity come into play.

The data from Fig. 11.7a corrected with the obtained loss function are shown in Fig. 11.7b. The hydrogen concentration is converted into a water concentration assuming that hydrogen is present in the layer in form of water only. One can see that the logarithmic correction works well within the statistical errors up to a beam current of 12 nA; under this condition depth profiles can be gained.

11.3.2 High Efficiency γ-Ray Detection

In order to measure low hydrogen concentrations it is crucial to detect the γ-rays with high efficiency. As pointed out above this is not only necessary for a high sensitivity but also advantageous for sensitive samples, which can then be measured with low beam current. Hence, a large detector is needed which is ideally a borehole detector with the sample in its center thus covering a large solid angle. Since the detector resolution is of minor importance, scintillation detectors are favorable. Typical detectors are sodium iodide (see Fig. 11.5) or bismuth germanate (BGO) detectors [6]. Barium fluoride as detector material has the disadvantage of an intrinsic background. While NaI(Tl) detectors have a slightly better energy resolution, BGO detectors are smaller in size for the same efficiency, which can be important for the design of a background shielding. Another issue in the design of a high efficiency setup is that the constructive elements of the sample holder assembly and vacuum chamber should be designed such that absorption of γ-rays on their path from the sample to the detector is minimal.

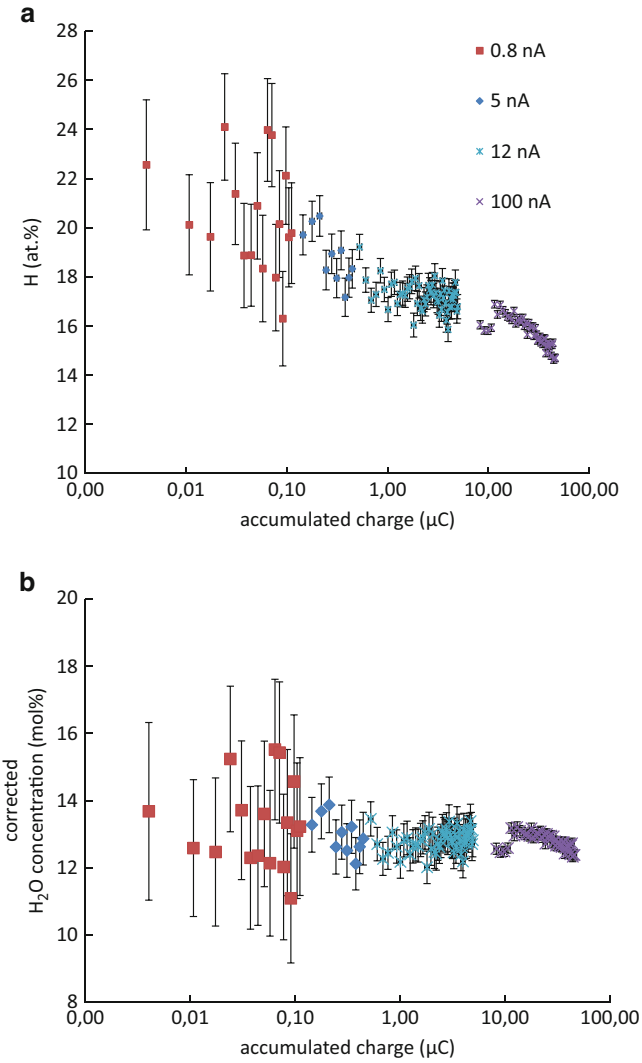

Fig. 11.7 (**a**) Hydrogen loss in serpentine induced by the beam measured with increasing intensities (**b**) water content deduced from (**a**) after correction for the loss

11.3.3 Background

When measuring the γ-yield of the 4.4 MeV line one has to consider background counts in the region of interest (see spectrum in Fig. 11.2), in particular for low hydrogen concentrations. Background can arise from the room, cosmic rays, the accelerator, and in the beam transport system as well as from contributions produced in the sample itself.

The room background is due to natural radio nuclides in ambient materials, mainly the γ-activity of ^{40}K and ^{208}Tl of building materials like concrete or bricks. The corresponding γ-ray lines of 1461 and 2614 keV can clearly be seen in the spectrum in Fig. 11.2. Although these lines are below the region of interest of the hydrogen signal their intensity can be high in environments with a high amount of concrete, which is typical for accelerator buildings. Then a summing of two simultaneously occurring events (pile up) leads to counts in the region of 4.4 MeV. This effect can be reduced only by a lead shielding of the detector with a thickness of at least 5 cm.

Cosmic rays, mainly muons, cause a smoothly sloping background level all over the spectrum and are the dominant contribution at energies higher than the room background. Unfortunately a lead shielding against the room background increases the height of the cosmic background by secondary rays from the shielding material. Muons and their secondary γ-rays can be suppressed by an active shielding. This is usually a scintillator surrounding the detector, which detects the muons and can veto the erroneous event in the γ-detector. Both shieldings together allow background suppressions roughly in the order of one magnitude.

Since the intensity of the room background and the muons is dependent on the acquisition time only, its influence is smaller when the measurements can be done with high beam intensity. In practice accelerators can provide beam currents from below 1 nA to several hundreds nA or even more. This corresponds to a change in the signal to background ratio over more than two orders of magnitude. The limiting factor is here the stability of the sample as discussed in Sect. 11.3.1. Therefore in general, the sensitivity to low concentrations is not attributed to the experimental setup only, but also depends strongly on the sample stability.

Background induced by the beam hitting the constructive elements of the setup is another source for a spurious contribution to the γ-spectra. This is in particular true for the beam defining collimators, which must be manufactured out of low hydrogen containing material. However, most surfaces even under UHV conditions will adsorb over time a hydrogen bearing layer, which are a source of unwanted signals. There are several technical solutions to overcome this problem such as heating the collimators [6]. Another approach is to mount the last beam defining collimator that far in front of the detector position (see for example Fig. 11.5) that the efficiency for detecting γ-rays from there is small. In practice, that is half a meter or more which, however, makes the size and position of the beam on the sample less defined and puts some constrains on the minimal sample size. For the setup in Fig. 11.5 for example the minimum sample size is 3 mm in diameter.

Beside these sources of background the accelerator and beam transport system can be a source of neutrons. If those neutrons reach the detector, neutron capture reactions with the detector material will produce interfering detector signals.

Another source of background coming from the sample itself can arise from nuclear reactions of ^{15}N ions with other nuclides than hydrogen. One relevant case is the reaction with deuterium, which produces several γ-ray lines possibly interfering with the region of interest around 4.4 MeV. Therefore, care has to be taken when deuterated materials are studied and a subtraction of background induced by deuterium has to be applied.

11.3.4 Samples with Hydrogen Concentrations Strongly Varying with Depth

When samples have a hydrogen concentration depth profile which changes over several orders of magnitude the assumption of a detection window only at the resonance energy is not valid any more. Then the non-resonant cross section (Fig. 11.1) will contribute to the reaction yield. For example if a layer with a higher hydrogen concentration is deposited on a substrate with very low concentration and the hydrogen in the substrate is probed, the non-resonant yield from the layer might be equivalent to the yield at the resonance window in the substrate. In those cases one has to measure the hydrogen concentration in the layer and calculate from the total (integrated) hydrogen present in the layer the non-resonant yield in measurements of the substrate. This is the product of the hydrogen areal density of the layer multiplied by the non-resonant cross section and the detector efficiency. For example, if the thickness of the layer is measured to be 10^{17} atoms/cm2 and the mean hydrogen concentration is 10 at. %, then the number of hydrogen atoms is 10^{16} atoms/cm^2. The cross section for a non-resonant contribution at a beam energy of e.g. 7 MeV is about 0.1 mbarn (Fig. 11.1) . This leads to a probability of $5 \cdot 10^{-13}$ counts per incident particle or about 3 counts per particle μC beam charge, assuming a detector efficiency of 50 %.

The problem of the non-resonant yield becomes important also when hydrogen concentrations in the at. ppm range are to be measured. Then hydrogen containing surface layers, almost always found on sample surfaces, will contribute to the yield. As an example, the influence of a surface layer containing 10^{16} hydrogen atoms/cm^2 (about 10 monatomic layers only) is simulated for a measurement of hydrogen-free silicon with the set-up at Bochum (Fig. 11.8). It can be seen that already at

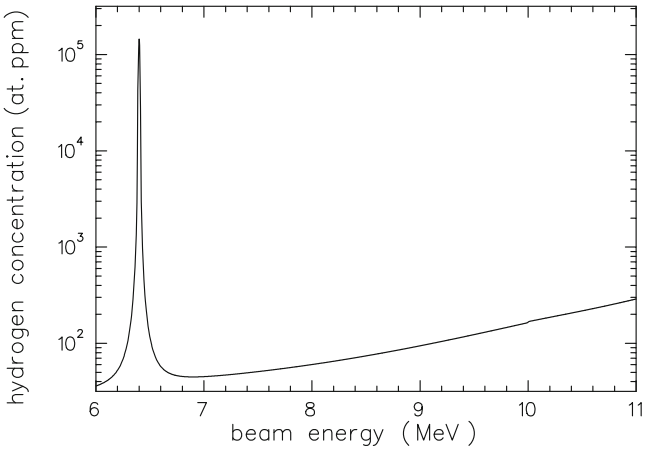

Fig. 11.8 Influence of a hydrogen surface layer of 10^{16} atoms/cm^2 on measurements at greater depth for a hydrogen free material (Si) due to non-resonant contribution

7 MeV the surface layer feigns some 30 at. ppm hydrogen and at greater depth the effect exceeds 100 ppm.

As a consequence, investigating such low concentrations requires an ultra-high vacuum in the region of 10^{-9} mbar or better and measures such as surface cleaning. Surface cleaning can be done by e.g. conventional low energy ion sputtering and/or heating the sample [22, 33]. A commercial sputter gun for surface cleaning installed at the setup in Bochum can be seen in Fig. 11.5. Sometimes surface cleaning is done for simplicity with the analyzing ^{15}N beam at higher beam currents. However, cleaning with a high energy beam comes along with a damage of the sample at greater depth.

11.3.5 Example of Low Concentration Detection

To illustrate the results and limits for a measurement of hydrogen concentrations we present here measurements on ZnO single crystals [22]. ZnO is an interesting material in a number of applications, like in the fields of optoelectronics and semiconductors as well as in heterogeneous catalysis. In this framework an understanding of hydrogen adsorption on single crystal surfaces as well as the determination of the native hydrogen bulk concentration is important.

It turned out, that unprepared ZnO surfaces have a surface coverage of unspecified hydrogen compounds and a well-defined preparation of the sample is an essential requirement for these studies. A clean single crystal surface can be prepared in-situ by several cycles of low energy ion sputtering and subsequent heating and annealing of the surface. With this procedure a H surface coverage in the order of 10^{14} at/cm^2 can be achieved which was slowly increasing to $6 \cdot 10^{14}$ at/cm^2 (one atomic monolayer of ZnO) due to hydroxylation from the residual gas ($\approx 10^{-9}$ mbar). Under this condition studies of H adsorption and hydroxylation at the ZnO surface in the range of one atomic layer are feasible. Additionally, these conditions minimize the spurious non-resonant contribution when measuring the low concentration of the crystal bulk. It should be noted that for this type of measurements sample preparation takes several days and therefore much more time than the measurements with the ion beam itself.

The results for the surface studies can be found in [22]; we show here the result of bulk measurements. As an example, a γ-spectrum taken at a depth of 160 nm in ZnO is displayed in Fig. 11.9. Extensive studies before showed that the bulk hydrogen concentration did not change due to beam deterioration even at beam intensities up to 100 nA particle current. The spectrum in Fig. 11.9 has been obtained with this beam intensity in about 5 min (red curve). A typical bulk concentration of ZnO was determined from such a spectrum to be 300 at. ppm with a variation of $+/-$ 100 at. ppm for different crystals. In order to explore background contributions from the collimators a background spectrum has been taken with the same beam charge but with Al household foil as a sample (black curve). This spectrum illustrates the sensitivity for this measurement and allows estimating the detection limit in this case to less than 100 at. ppm.

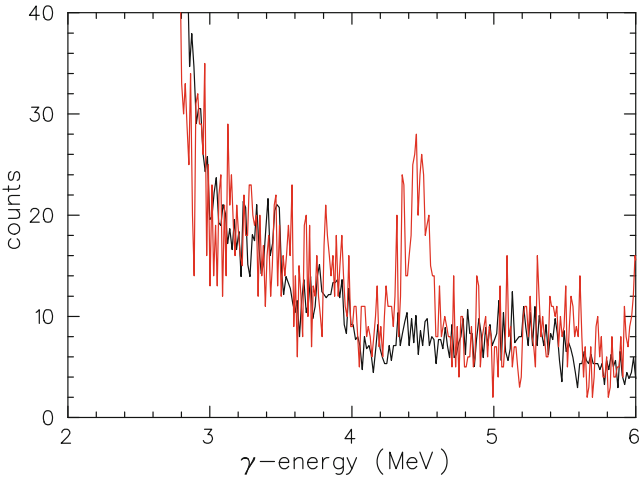

Fig. 11.9 The gamma spectrum of the ZnO bulk concentration shows a clear signal of hydrogen in a depth of 160 nm (*red*). The signal intensity corresponds to a H concentration of 300 at. ppm. The background level (*black*) is represented by a blank measurement of aluminum, which is known to have a hydrogen content of few at. ppm only [6]

Acknowledgements We would like to thank F. Traeger, S. Chakraborty and C. Le Guillou for fruitful discussions and comments on the manuscript. We are also thankful to M. Kieschnick and A. Ludwig for providing data not yet published.

References

1. D.A. Leich, T.A. Tombrello, Nucl. Instrum. Methods **108**, 67 (1973)
2. W.A. Lanford, H.P. Trautvetter, J.F. Ziegler, J. Keller, Appl. Phys. Lett. **28**, 566 (1976)
3. W.A. Lanford, Nucl. Instrum. Methods **B66**, 65 (1992)
4. H.W. Becker, M. Bahr, M. Berheide, L. Borucki, M. Buschmann, C. Rolfs, G. Roters, S. Schmidt, W.H. Schulte, G.E. Mitchell, J.S. Schweitzer, Z. Phys. A **351**, 453 (1995)
5. Y. Wang, M. Nastasi (eds.), Handbook of Modern Ion Beam Materials Analysis, 2nd edn. (Materials Research Society, Pittsburgh, 2009). ISBN 978-1-60511-215-2
6. D. Endisch, H. Sturm, F. Rauch, Nucl. Instrum. Methods **B84**, 380 (1994)
7. M. Wilde, K. Fukutani, Surf. Sci. Rep. **69**, 196 (2014)
8. J.F. Ziegler, SRIM, The Stopping and Range of Ions in Matter (2013), http://www.srim.org/SRIM/Compounds.htm
9. J.F. Ziegler, M.D. Ziegler, J.P. Biersack, Nucl. Instrum Methods **B268**, 818 (2010) http://www.srim.org
10. K.M Horn, W.A. Lanford, Nucl. Instrum Methods **B34**, 1 (1988)
11. G. Imbriani, R.J. deBoer, A. Best, M. Couder, G. Gervino, J. Görres, P.J. LeBlanc, H. Leiste, A. Lemut, E. Stech, F. Strieder, E. Uberseder, M. Wiescher, Phys. Rev. C **85**, 065810 (2012)
12. B. Maurel, G. Amsel, Nucl. Instrum Methods **218**, 159 (1983)
13. W. Rudolph, C. Bauer, K. Brankhoff, D. Grambole, R. Grötzschel, C. Heiser, F. Herrmann, Nucl. Instrum Methods **B15**, 508 (1986)

14. T. Osipowiez, K.P. Lieb, S. Brüssermann, Nucl. Instrum Methods **BI8**, 232 (1987)
15. G. Amsel, B. Maurel, Nucl. Instrum Methods **218**, 183 (1983)
16. L. Borucki, H.W. Becker, F. Gorris, S. Kubsky, W.H. Schulte, C. Rolfs, Eur. Phys. J. A **5**, 327 (1999)
17. W.H. Schulte, H. Ebbing, S. Wüstenbecker, H.W. Becker, M. Berheide, M. Buschmann, C. Rolfs, G.E Mitchell, J.S. Schweitzer, Nucl. Instrum Methods **B71**, 291 (1992)
18. W.E. Lamb, Phys. Rev. **55**, 190 (1939)
19. J.M. Donhowe, J.A. Ferry, W.G. Monrad, R.G. Herb, Nucl. Phys. **A102**, 383 (1967)
20. M. Zinke-Allmang, O. Kruse, Nucl. Instrum Methods **B90**, 579 (1994)
21. K.M Horn, W.A. Lanford, Nucl. Instrum Methods **B29**, 609 (1988)
22. F. Traeger, M. Kauer, Ch. Wöll, D. Rogalla, H.W. Becker, Phys. Rev. B **84**, 075462 (2011)
23. N. Bohr, K. Dan Viden, Selsk. Math. Fys. Medd. **18**, 1 (1948)
24. A. Ludwig, J. Cao, B. Dam, R. Gremaud, Appl. Surf. Sci. **254**, 682 (2007)
25. A. Ludwig, J. Cao, A. Savan, M. Ehmann, J. Alloys Compd. **446–447**, 516 (2007)
26. G. Hirth, D.L. Kohlstedt, Earth Planet. Sci. Lett. **144**, 93 (1996)
27. M. Murakami, K. Hirose, H. Yurimoto, S. Nakashima, N. Takafuji, Science **295**, 1885 (2002)
28. D.R. Bell, G.R. Rossmann, J. Maldner, D. Endisch, F. Rauch, J. Geophys. Res. **108**(B2), 2105 (2003)
29. J. Gose, P. Reichart, G. Dollinger, E. Schmädicke, Am. Mineral. **93**, 1613 (2008)
30. J.-P. Thomas, M. Fallavier, J. Tousset, Nucl. Instrum. Methods **187**, 573 (1981)
31. C. Le Guillou, H.G. Changela, R. Dohmen, T. Müller, A.J. Brearley, C. Vollmer, D. Rogalla, H.W. Becker, Contribution to the 45th Lunar and Planetary Science Conference, The Woodlands
32. C. Le Guillou, R. Dohmen, D. Rogalla, T. Müller, C. Vollmer, H.-W. Becker, Chem. Geol. Chem. Geol. **412** (2015) 179
33. J. Maldner, F. Rauch, AIP Conf. Proc. **392**, 689 (1997)

Chapter 12
Nuclear Magnetic Resonance

Alexander V. Skripov and Marina G. Shelyapina

Abstract Nuclear magnetic resonance (NMR) is one of the most versatile methods for studies of the behavior of hydrogen in materials. For metal – hydrogen systems and complex hydrides, this technique provides microscopic information of diverse nature, including the electronic properties, local structural features, and hydrogen dynamics. The present survey discusses the basic principles that make NMR useful for investigations of hydrogen in materials. Such a discussion is complemented by recent examples of application of this technique to studies of metal – hydrogen systems and complex hydrides. The emphasis is put on applications related to hydrogen mobility. The complementarity between NMR and quasielastic neutron scattering is also addressed.

Keywords Metal hydrides • Complex Hydrides • Hydrogen mobility • Nuclear spin relaxation • Knight shifts • Chemical shifts

12.1 Introduction

The phenomenon of nuclear magnetic resonance (NMR) discovered in 1946 [1, 2] was originally considered as an important contribution to the field of nuclear physics. The key point of this phenomenon is that a system of nuclear spins in an external magnetic field can absorb electromagnetic energy at a well-defined frequency, which is proportional to the external magnetic field and to the nuclear gyromagnetic ratio γ. Since the value of γ is the intrinsic property of a particular nuclear isotope, NMR exhibits element and isotope selectivity. Soon after the discovery of NMR, it was realized that nuclear spins are involved in a number of interactions with their

A.V. Skripov (✉)
Institute of Metal Physics, Ural Branch of the Russian Academy of Sciences,
S. Kovalevskoi 18, Ekaterinburg 620990, Russia
e-mail: skripov@imp.uran.ru

M.G. Shelyapina
Department of Nuclear Physics Research Methods, Faculty of Physics,
St. Petersburg State University, 7/9 Universitetskaya nab.,
199034 Saint Petersburg, Russia
e-mail: marina.shelyapina@spbu.ru

H. Fritzsche et al. (eds.), *Neutron Scattering and Other Nuclear Techniques for Hydrogen in Materials*, Neutron Scattering Applications and Techniques,
DOI 10.1007/978-3-319-22792-4_12

environment; therefore, they can be used as natural probes to yield information about processes at the atomic level. This gave rise to the rapid development of NMR from an interesting phenomenon to the powerful experimental technique widely used in condensed matter physics, chemistry, biology, and medicine.

For hydrogen in materials, NMR appears to be one of the most versatile experimental methods, allowing one to obtain microscopic information of diverse nature. In a broad outline, there are three basic "channels" of extracting microscopic information from NMR measurements. The first "channel" uses the local nature of NMR data; this gives an opportunity to detect small changes in the environment of the resonance nuclei and the presence of structurally inequivalent atoms. The second "channel" employs the direct relation between the density of electron states at the Fermi level and such NMR parameters as the Knight shift and the spin-lattice relaxation time in metals. And, finally, the third "channel" is related to sensitivity of NMR parameters to fluctuations of local magnetic and electric fields at nuclear sites; this can yield information on atomic motion. The range of atomic jump rates that can be probed by the standard NMR techniques is of the order of 10^4–10^{11} s^{-1}. The use of such special NMR techniques as measurements of the decay of dipolar spin order [3] and spin-alignment echo NMR spectroscopy [4] allows one to study ultraslow atomic motion with characteristic jump rates of the order of 10^{-1}–10^3 s^{-1}. Thus, by combining different NMR techniques, it is in principle possible to probe an extremely wide dynamic range of atomic jumps. Besides NMR techniques giving information on the atomic jump rates, there is also the unique NMR method—spin-echo with static or pulsed field gradient (PFG)—that allows one to measure the diffusion coefficients directly. This method provides a bridge between microscopic and macroscopic measurements of atomic mobility. It should be noted that NMR parameters are generally not sensitive to atomic *vibrations*, since the vibrational frequencies are much higher than the resonance frequencies of NMR.

An important feature of NMR approach to studies of hydrogen in materials is that different nuclear isotopes can be used as natural probes of the local structure and dynamics. Only isotopes consisting of an even number of protons *and* an even number of neutrons (such as ^{12}C or ^{16}O) have zero nuclear spin. All other isotopes can be used in NMR studies. In particular, all three hydrogen isotopes (^1H, ^2D, and ^3T) have non-zero nuclear spins. Generally, an isotope is considered "good" for NMR if it has both high natural abundance and high nuclear gyromagnetic ratio. The examples of such "good" NMR isotopes are ^1H, ^7Li, ^{11}B, ^{19}F, ^{23}Na, ^{27}Al, ^{31}P, ^{45}Sc, ^{51}V, ^{55}Mn, ^{59}Co, ^{63}Cu, ^{69}Ga, and ^{93}Nb. Certainly, this list does not exhaust all the isotopes on which NMR measurements are practicable. The limitations related to low natural abundance and/or low gyromagnetic ratios can often be lifted by experiments in high magnetic fields. In many cases, it is advantageous to perform NMR measurements on a number of different nuclei in the same compound, since such measurements are expected to yield complementary information.

Excellent reviews devoted to applications of NMR to studies of metal–hydrogen systems were published by Cotts [5] in 1978 and Barnes [6] in 1997. However, these reviews did not address non-metallic complex hydrides which are of great current interest. The primary aim of the present survey is to discuss the basic features which

make NMR useful for investigations of hydrogen in materials. Such a discussion will be complemented by recent examples of application of this technique to studies of metal–hydrogen systems and complex hydrides. We hope that the present review will help non-NMR experts working in the field of hydrogen storage materials to understand NMR papers in more detail and to use NMR measurements in their future studies. In Sect. 12.2, we discuss the basic interactions of nuclear spins which are responsible for the observed shape of NMR spectra in solids. The experimental arrangements and methods of NMR measurements are considered in Sect. 12.3. The structural information that can be obtained from NMR experiments on hydrides is discussed in Sect. 12.4. Section 12.5 addresses the relevance of NMR for investigations of the electronic properties of metal–hydrogen systems. And, finally, Sect. 12.6 is devoted to hydrogen mobility probed by NMR measurements.

12.2 Basic Interactions of Nuclear Spins

In condensed matter, nuclear spins interact with their environment; therefore, the observed shape of the NMR spectrum usually differs from that expected for isolated nuclear spins. The most universal type of interaction is the magnetic dipole–dipole interaction between nuclear spins. The Hamiltonian of the dipole–dipole interaction is written as:

$$\hat{H}_{\mathrm{d}} = \tfrac{1}{2}\sum_{j}\sum_{k}\left[\frac{\boldsymbol{\mu}_j\boldsymbol{\mu}_k}{r_{jk}^3} - \frac{3\left(\mu_j\mathbf{r}_{jk}\right)\left(\mu_k\mathbf{r}_{jk}\right)}{r_{jk}^5}\right], \tag{12.1}$$

where the subscripts j and k refer to different nuclear spins, $\mathbf{r}_{jk}$ is the vector connecting spins j and k, $\boldsymbol{\mu}_j$ is the operator of the nuclear magnetic moment, $\boldsymbol{\mu}_j = \gamma_j\hbar\mathbf{I}_j$, γ_j is the nuclear gyromagnetic ratio, and $\mathbf{I}_j$ is the dimensionless operator of the nuclear angular moment. The dipole–dipole interaction in the "rigid" lattice leads to a broadening of the NMR spectrum. The actual shape $f(\omega)$ of the NMR line for a multi-spin system usually cannot be calculated in analytic form. However, for a known lattice structure, it is possible to calculate the *second moment* M_2 of the $f(\omega)$ line using the Van Vleck formula [7]. For example, for ^{1}H nuclei (protons) in a metal–hydrogen system, it is necessary to take into account the dipole–dipole interactions between different protons (H–H) and between protons and host-metal nuclei (H–M). For protons occupying the equivalent sites in the crystalline lattice, the second moment due to dipole–dipole interactions in a powder sample can be expressed as a sum of the H–H and H–M contributions, $M_{2\mathrm{HH}} + M_{2\mathrm{HM}}$, where

$$M_{2\mathrm{HH}} = \tfrac{3}{5}\gamma_{\mathrm{H}}^4\hbar^2 I_{\mathrm{H}}(I_{\mathrm{H}}+1)\sum_{j} r_{ij}^{-6}, \tag{12.2}$$

$$M_{2\mathrm{HM}} = \frac{4}{15}\gamma_{\mathrm{H}}^2\gamma_{\mathrm{M}}^2\hbar^2 I_{\mathrm{M}}(I_{\mathrm{M}}+1)\sum_k r_{ik}^{-6}. \tag{12.3}$$

Here γ_{H} and γ_{M} are the gyromagnetic ratios of H and M nuclei, and $I_{\mathrm{H}} = 1/2$ and I_{M} are the corresponding nuclear spins. The sum in (12.2) is over all hydrogen sites, j, from a generic hydrogen site i, and the sum in (12.3) is over all metal sites k from a generic proton site i. Since the dipole–dipole interaction is *pairwise*, the expressions (12.2) and (12.3) can be easily generalized to the cases of several inequivalent proton sites in the lattice and several types of host-metal nuclei. Comparison of the experimental values of M_2 with those calculated for different models of hydrogen distribution over interstitial sites may sometimes be helpful for choosing the correct structural model of a metal–hydrogen system.

Nuclei with $I > 1/2$ have a non-zero electric quadrupole moment eQ (where e is the electron charge) that interacts with the local electric field gradient (EFG). Components of the EFG tensor are defined as:

$$V_{ij} = \frac{\partial^2 V}{\partial x_i \partial x_j}, \tag{12.4}$$

where V is the potential of the electric field at the nuclear site, and x_i are the coordinates (x, y, z). Since the tensor V_{ij} is symmetric, it is always possible to choose such a system of principal axes, where only diagonal elements V_{ii} are non-zero. If the potential V is created by charges located outside the nucleus, it should satisfy the Laplace equation, $\nabla^2 V = 0$. Therefore, only two of three V_{ii} components are independent, and the EFG tensor can be fully characterized by two parameters that are chosen in the following way:

$$eq \equiv V_{zz}, \tag{12.5}$$

$$\eta \equiv \frac{V_{xx} - V_{yy}}{V_{zz}}. \tag{12.6}$$

By convention, the axes are chosen so that the inequality $|V_{zz}| \geq |V_{yy}| \geq |V_{xx}|$ is fulfilled; in this case, the asymmetry parameter η can vary between 0 and 1. For the case of an axially symmetric environment of a nucleus, $\eta = 0$. If the symmetry of the environment is cubic, then $V_{xx} = V_{yy} = V_{zz} = 0$ (the latter equality is written using the Laplace equation).

The Hamiltonian of the quadrupole interaction in the system of principal axes is written as [8]

$$\hat{H}_Q = \frac{e^2 qQ}{4I(2I-1)}\left[3I_z^2 - I(I+1) + \eta\left(I_x^2 - I_y^2\right)\right] \tag{12.7}$$

For strong magnetic fields H_0 (when $e^2 qQ/\gamma\hbar H_0 \ll 1$), the effects of the quadrupole interaction on NMR spectrum can be described in terms of the perturbation theory.

The main effect is that the Zeeman spectrum of nuclear spin levels, $E_m = m\gamma\hbar H_0$ ($m = -I, -I+1, \ldots I$), becomes non-equidistant, which leads to the splitting of the NMR line into $2I$ lines. It should be emphasized that the quadrupole splitting depends on the angles between the external magnetic field and the principal axes of the EFG tensor (which are determined by the crystallographic axes). In powder samples, these angles are distributed over all possible values. Therefore, the intensities of the resonance lines corresponding to each $m \leftrightarrow m-1$ transition may be distributed over wide frequency ranges. Detailed calculations of the shape of NMR spectra in powders taking into account the quadrupole interaction (up to the second order of the perturbation theory) and the anisotropic hyperfine interaction can be found in [9, 10]. On the basis of these calculations, it is possible to determine the EFG parameters (eq and η) from the experimental NMR spectra.

The theoretical expression for the EFG at nuclear sites in metals is usually written in the form

$$q = (1 - \gamma_\infty) q_\mathrm{l} + q_\mathrm{e}, \tag{12.8}$$

where q_l is the lattice contribution to the EFG resulting from the atomic core shells which are considered as point charges,

$$q_\mathrm{l} = \sum_i Z_i \frac{3\cos^2\theta_i - 1}{r_i^3}, \tag{12.9}$$

Z_i is the charge of the ith core, r_i and θ_i are the length and the polar angle of the vector $\mathbf{r}_i$ connecting the considered nuclear site with the ith core, q_e is the contribution to the EFG due to conduction electrons, and γ_∞ is the antishielding factor [11]. This factor takes into account that the EFG at a nuclear site is enhanced due to deformation of its own electronic shells in the electric field produced by outer charges. The calculation of q_e requires the knowledge of the electron wave functions in the system. It should be noted that the EFG at nuclear sites is a very sensitive indicator of changes in the local environment. Even small displacements of atoms surrounding the considered nucleus may lead to strong changes in the EFG, and thus, to strong changes in the NMR spectrum.

Hyperfine interactions of nuclear spins with orbital and spin magnetic moments of electrons are responsible for the sensitivity of NMR parameters to electronic properties of solids. In metals, the main effect of magnetic hyperfine interactions is the shift of the resonance frequency of a nucleus with respect to its value for the same nucleus in a diamagnetic substance. This shift (known as the Knight shift) originates from an additional magnetic field, $\Delta\mathbf{H} = \hat{K}\,\mathbf{H}_0$, produced by conduction electrons at a nuclear site in the presence of the external magnetic field $\mathbf{H}_0$, where $\hat{K}$ is the Knight shift tensor. In the system of principal axes, the Knight shift tensor is characterized by three components, K_x, K_y, and K_z. Depending on the point symmetry of a nuclear site, two or all three of these components may be degenerate. For example, for the axial point symmetry, only two components are required to describe the Knight shift tensor; these are usually chosen in the form of the isotropic

and axial components, $K^{iso} = (K_x + K_y + K_z)/3$ and $K^{ax} = (2K_z - K_x - K_y)/6$. Since the additional field is proportional to the external magnetic field, the values of the Knight shift components are expressed in percent or parts per million (ppm). For transition-metal nuclei, the main contributions to the Knight shift are usually related to the Fermi contact interaction of nuclear spins with the spin density of unpaired s electrons (K_s) and the Fermi contact interaction of nuclear spins with the core-polarization spin density resulting from polarization of the inner s shells due to exchange with d electrons (K_d). Because of the isotropic nature of the Fermi contact interaction, both K_s and K_d contribute only to the isotropic component of the Knight shift. Each of these contributions is proportional to the corresponding Pauli (spin) magnetic susceptibilities of s- and d-electrons, and therefore, they are determined by the densities of electron states at the Fermi level, $N_s(E_F)$ and $N_d(E_F)$. For transition-metal nuclei, an important anisotropic contribution to the Knight shift can result from the interaction between nuclear spins and orbital magnetic moments of electrons (K_{orb}) [12]. Although formally this contribution represents a second-order effect, for transition metals it can be significant since the d-electron band is very narrow. Generally, the Knight shifts increase with increasing number of electron shells and can reach values of a few percent. In non-metallic solids, the observed shifts of the resonance frequency are usually much smaller; they are called the chemical shifts being determined by the orbital magnetic moments of electrons. As in the case of the Knight shifts, chemical shifts are proportional to the external magnetic field. The detailed theory of chemical shifts is presented in Slichter's book [13]. Since chemical shifts are usually smaller than the NMR line broadening due to dipole–dipole interactions between nuclear spins in solids, accurate measurements of chemical shifts require line narrowing techniques, such as magic-angle spinning (MAS) or special multi-pulse sequences (see Sect. 12.3).

An important property of the nuclear spin system in condensed matter is the nuclear spin-lattice (longitudinal) relaxation time T_1. This time characterizes the process of recovery of the longitudinal nuclear magnetization in the external magnetic field $\mathbf{H}_0$ after deviations of the nuclear spin system from the equilibrium. In quantum mechanical terms, this process corresponds to recovery of the equilibrium populations of the Zeeman-split energy levels. Since such a process is related to a change in the energy of the nuclear spin system in the magnetic field, the relaxation requires an energy transfer between the nuclear spin system and some other degrees of freedom (which, in this case, are generally called "lattice"). The mechanisms of the spin-lattice relaxation may be diverse. Depending on the physical nature of a substance, the role of "lattice" may be played by phonons, conduction electrons, thermal fluctuations, etc. A number of spin-lattice relaxation mechanisms will be discussed in the following sections. If several relaxation mechanisms are operative, their corresponding contributions to the spin-lattice relaxation *rate* T_1^{-1} are additive. Another time parameter describing the behavior of the nuclear spin system is the spin–spin (transverse) relaxation time T_2. This time characterizes the decay of transverse (with respect to the magnetic field $\mathbf{H}_0$) components of the nuclear magnetization. In contrast to the longitudinal relaxation, the transverse relaxation is not related to the energy transfer between the nuclear spin system and other degrees of freedom.

12.3 Experimental Arrangements and Basic Methods

To observe NMR phenomena, one needs an external static magnetic field $\mathbf{H}_0$ which leads to the Zeeman splitting of energy levels of the nuclear spin system. An alternating rf field $\mathbf{H}_1$ with the frequency close to the splitting between nuclear energy levels excites transitions between these levels. Hence, for an NMR experiment the following equipment is necessary [14]:

- a source of a static magnetic field;
- a source of an rf field;
- a device to convert the energy of quantum transitions into rf signals;
- a device to record these signals.

There are two fundamentally different methods to observe NMR signals: under continuous irradiation by an rf field (this is the so-called *continuous-wave* or cw method), or between rf pulses (pulse method). At present, almost all NMR measurements are carried out using pulse methods. However, the cw-NMR merits to be mentioned not only for methodology reasons, but also because in pulse methods a rather long *dead time* of the receiver may lead to a partial loss of useful information. Modern commercial NMR spectrometers (especially those for biomolecular research) employ superconducting magnets creating extremely high magnetic fields (up to 21.1 T that is 900 MHz in the proton resonance frequency, or even higher). On the other hand, the optimal frequency range to observe ^{1}H NMR in metallic hydrides is 10–100 MHz.

12.3.1 Typical Experimental Setup

CW NMR Setup A description of hardware for cw-NMR can be found elsewhere, see for example [14]. Here we only consider the basic principles of recording the NMR spectra by the stationary (cw) method. The simplest functional diagram of any cw-NMR spectrometer is shown in Fig. 12.1. The main functional parts are the magnet, rf transmitter, rf sensor coil with the sample, modulator and sweep generator, spin detector, rf receiver and amplifier, control console, and recorder. The operating principle is that the induction coil with the sample is placed into the magnet gap in such a manner that the coil axis (and hence the vector of the alternating field $\mathbf{H}_1$) is perpendicular to the direction of the static field $\mathbf{H}_0$. To observe NMR, the static magnetic field is modulated (with modulation frequency $f_m = 20$–100 Hz). The NMR spectrum is recorded either by sweeping the magnetic field $\mathbf{H}_0$ over a small range, at the constant frequency of $\mathbf{H}_1$, or by varying the frequency of the rf field while holding the external field constant. The spin detector transforms the energy of quantum transitions between the Zeeman levels into rf signals, which are amplified and finally detected.

Pulse NMR Setup A description of typical hardware for pulse NMR can be found in a number of references (see, for example, [14, 15]). The simplest functional

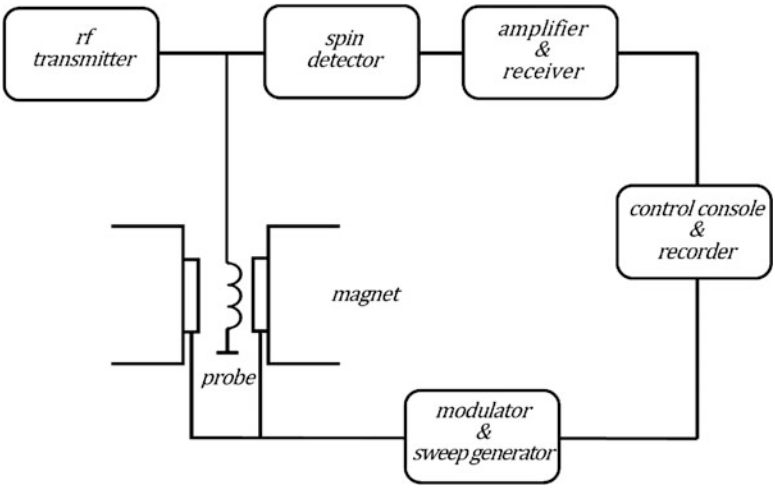

Fig. 12.1 Block diagram of a typical cw NMR spectrometer

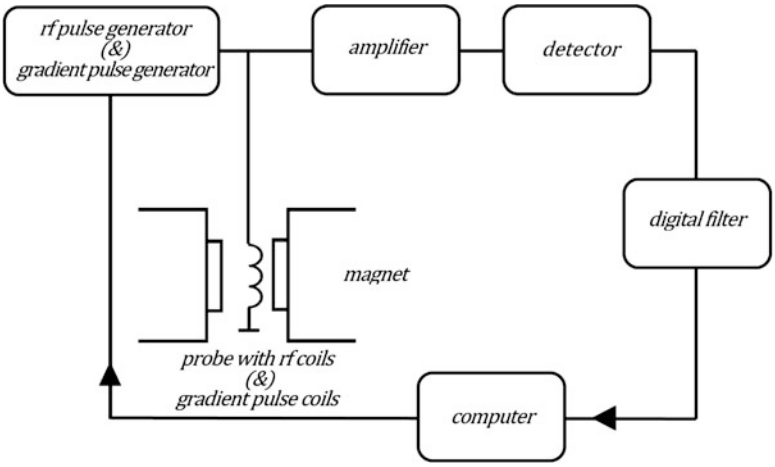

Fig. 12.2 Block diagram of a typical pulse NMR spectrometer

diagram of a pulse spectrometer is shown in Fig. 12.2. The main functional parts of any pulse NMR spectrometer are the magnet, rf pulse generator (transmitter), rf sensor coil with the sample, amplifier, and quadrature detector. The electromagnet or superconducting magnet produces the field $\mathbf{H}_0$ that is necessary to split the nuclear levels. The rf sensor coil is placed in the field $\mathbf{H}_0$ and has two functions: first, to produce rf magnetic field $\mathbf{H}_1$ that rotates nuclear spins by the angle $\alpha = \omega_1 t_p$ ($\omega_1 = \gamma H_1$, and H_1 and t_p are the pulse amplitude and duration, respectively), and second, to probe the induction signal from the spins of the sample. The quadrature detector is used to separate the x- and y-components of

the nuclear magnetization probed by the rf coil. For some special applications, such as diffusion measurements or magnetic resonance imaging (MRI), the NMR spectrometer can also be equipped with gradient coils producing gradients of the static magnetic field $\mathbf{H}_0$.

12.3.2 Methods of Spectral Measurements

As noted in Sect. 12.2, NMR spectra contain information on internuclear and nuclear–electron interactions. Depending on the method of detection of NMR signals, there are two fundamentally different methods of spectral measurements: direct recording by the continuous-wave NMR and the Fourier transform of the free induction decay (FID) signal after rf pulses.

For the continuous-wave NMR approach, it is important to discuss the speed of the passage through the resonance, dH_0/dt. Analysis of the Bloch equations describing the behavior of the nuclear magnetization vector in a magnetic field leads to the following condition for dH_0/dt [16]:

$$\frac{dH_0}{dt} \leq \frac{1}{4\gamma T_2^{*2}} \tag{12.10}$$

Here $1/T_2^*$ characterizes the observed width of the spectrum. If the line width is small (long T_2^*), one has to choose a very slow sweep rate dH_0/dt to meet the condition (12.10). This makes a cw-NMR experiment very time-consuming. If the condition (12.10) is not met, the recorded shape of the spectrum would be distorted. For solids, typical NMR lines are broad (short T_2^*), and the condition (12.10) is relatively easy to meet. In this case, the method of *differential passage through resonance* is often used. This method illustrated in Fig. 12.3 employs a low-frequency modulation (H_m) of the static magnetic field H_0. The first derivative of the NMR resonance line is recorded in this method. It should be noted, however, that for accurate recording of NMR spectra, the modulation field should be small ($H_\mathrm{m} \to 0$), and in this case the signal amplitude U also becomes small.

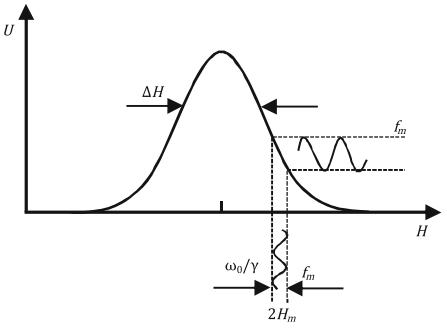

Fig. 12.3 Differential passage through resonance

In pulse NMR, the signal that is detected after a pulse or a pulse sequence is the FID. The NMR spectrum in the frequency domain is related to the FID signal in the time domain by the Fourier transformation (FT). After the rf pulse with the amplitude H_1 and duration t_p, the nuclear magnetization vector is turned from the direction of the $\mathbf{H}_0$ field (z-axis) by the angle $\alpha = \gamma H_1 t_p$. For the case of exponentially decaying behavior of FID,

$$f(t) = f_0 \sin\alpha \exp\left[i\Delta\omega t - \frac{t}{T_2^*}\right], \tag{12.11}$$

where $\Delta\omega$ is the frequency detuning, its Fourier transform

$$f(\omega) = \int_0^\infty f(t)\exp(i\omega t)dt \tag{12.12}$$

results in the complex spectrum

$$f(\omega) = f_0 \sin\alpha \left[\frac{1}{T_2^*}\frac{T_2^{*2}}{1 + \left(\Delta\omega T_2^*\right)^2} - i\Delta\omega\frac{T_2^{*2}}{1 + \left(\Delta\omega T_2^*\right)^2}\right] \tag{12.13}$$

(the two components correspond to adsorption and dispersion signals). It follows from Eq. (12.13) that $f(\omega)$ reaches its maximum at $\alpha = \pi/2$ (so-called 90°-pulse).

Evidently, each of the functions $f(t)$ and $f(\omega)$ contains the same information on the nuclear spin system. However, for a multi-line NMR spectrum, the frequency representation is more convenient. It should be noted that the Lorentzian shape of the NMR spectrum described by Eq. (12.13) is typical of liquids. In solids, FID signals often deviate from the exponential behavior, so that the shape of the NMR spectrum is no longer Lorentzian. The principal limitation of the FT approach is related to the fact that in experiments the $f(t)$ function is available only in the time range from the receiver *dead time* to the acquisition time (not from 0 to ∞). Another limitation is related to the width of the observed NMR spectrum. If the width of the spectrum exceeds the spectral width of the rf pulse (this often occurs in cases of non-zero quadrupole interaction), the pulse cannot excite the whole spectrum. In such situations, the Clark method of recording NMR spectra [17, 18] may be useful. This method combines the Fourier transform with the sweep of the magnetic field. In modern NMR experiments, the pulse methods are almost exclusively used. They are generally much faster than the cw-NMR measurements. Moreover, high-resolution solid NMR techniques developed on the basis of pulse methods (MAS, multi-pulse sequences, 2D NMR, multiple-quantum experiments, etc.) often provide opportunities to separate contributions of different interactions and hence to extract more detailed information on the properties of solids. For more details see [15].

12.3.3 Magic-Angle Spinning

Most of the basic interactions of nuclear spins considered in Sect. 12.2 are anisotropic. In liquids, the anisotropy of these interactions is averaged out. However, in solids such an anisotropy is not averaged out; this leads to considerable broadening of NMR spectra. Furthermore, most of solid state NMR experiments are performed on polycrystalline samples (powders), and a distribution of the angles between the magnetic field direction and the crystallographic axes leads to the additional broadening. The line shape taking into account such a broadening due to the powder averaging of the dipole–dipole and quadrupole interactions can be described by the equation:

$$f(x) = \int_{-\infty}^{\infty} \sqrt{\frac{1}{3(2x' + 1)}}\, g\left(x - x'\right) dx', \tag{12.14}$$

where $x = (\omega - \omega_0)/C$, with $C = 3e^2qQ(2m - 1)/4I(2I - 1)\hbar$ for the quadrupole interaction and $C = 3\gamma^2\hbar/2r^3$ for the dipolar interaction, and $g\left(x - x'\right)$ is the line shape of an individual single crystal. Because of the line broadening, small chemical shifts (for example, resulting from non-equivalent nuclear sites) usually cannot be resolved from the standard NMR spectra in solids.

The MAS technique is widely used in solid state NMR experiments to remove (completely or partly) the chemical shift anisotropy, quadrupolar interactions, and dipolar interactions. This method employs the mechanical rotation of the sample around an axis which makes the angle $\theta_R = 54.74^\circ$ with the direction of magnetic field $\mathbf{H}_0$ (for this "magic" angle, $3\cos^2\theta_R - 1 = 0$). More detailed discussion of the nature of line narrowing in MAS-NMR experiments can be found in [15]. The rotation speed ω_R should be higher than the strength of interactions (in frequency units) one intends to suppress. For example, for the dipolar interaction, the rotation speed should exceed the line width resulting from this interaction. For standard NMR spectrometers, the maximum rotation speed is about 24 kHz, which is often not sufficient for ^{1}H homonuclear dipolar coupling. Slow spinning produces a set of sidebands in addition to the central line, and for the chemical shift the central line corresponding to the isotropic shift, is not the most intensive. The presence of the sidebands complicates the analysis of MAS-NMR spectra. The effects of the spinning rate on the NMR spectrum for the cases of chemical shift anisotropy and homonuclear dipolar interaction are illustrated in Fig. 12.4. For more details about MAS-NMR, see [15].

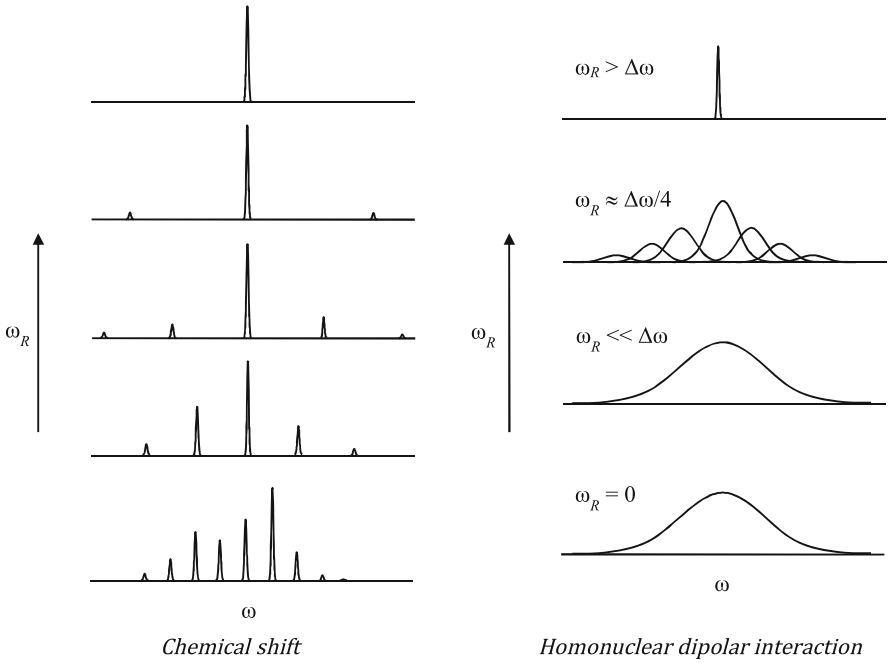

Fig. 12.4 Effects of the spinning rate on NMR spectra

12.3.4 Methods of Relaxation Time Measurements and Pulse Sequences

All methods of nuclear relaxation time measurements are based on application of certain combinations of rf pulses with the frequency ω close to $\omega_0 = \gamma H_0$. Each of these pulses rotates the nuclear magnetization vector **M** by a certain angle α. One of the most popular methods of measuring the spin-lattice (longitudinal) relaxation time T_1 is the inversion-recovery method (180°–τ–90°). In this method, the first 180° pulse is applied to invert the nuclear magnetization. The reading 90° pulse is applied after a variable delay time τ to measure the partially recovered nuclear magnetization at the moment $t = \tau$. The inversion-recovery method is illustrated in Fig. 12.5. For this method, the evolution of the longitudinal nuclear magnetization is written as:

$$M_z(\tau) = M_0\left[1 - 2\exp\left(-\frac{\tau}{T_1}\right)\right]. \tag{12.15}$$

Another common method of T_1 measurements applicable to systems with $T_1 \gg T_2$ is the saturation-recovery method (90°–τ–90°). In this case, after the first (saturating) pulse the z-component of **M** is zero. For broad NMR lines, it is often preferable to use a train of saturating 90° pulses instead of a single saturating pulse.

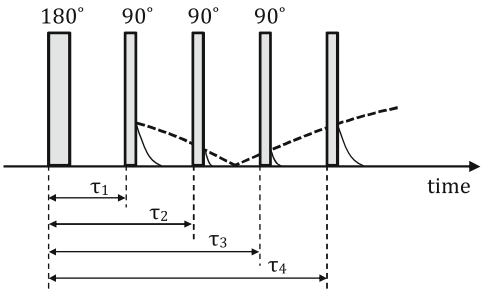

Fig. 12.5 Inversion-recovery pulse sequence for T_1 measurements

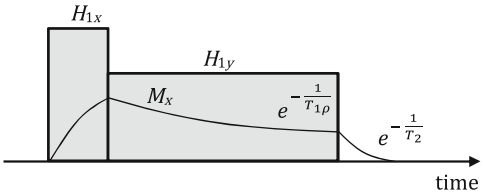

Fig. 12.6 Spin-locking pulse sequence for $T_{1\rho}$ measurements

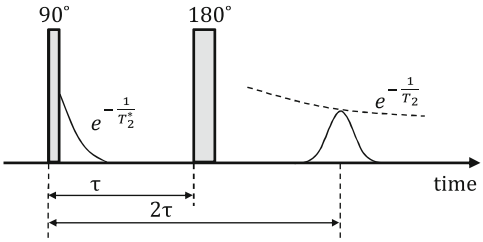

Fig. 12.7 Hahn spin-echo pulse sequence for T_2 measurements

For systems with slow hydrogen jump motion, in addition to T_1 measurements, it is useful to measure the so-called rotating-frame spin-lattice relaxation time $T_{1\rho}$ (see Sect. 12.6.1). This time refers to the relaxation of the transverse nuclear magnetization being aligned along the rotating component of the rf magnetic field. The corresponding *spin locking* experiment is illustrated in Fig. 12.6. The first 90° pulse rotates the nuclear magnetization vector to the *xy* plane. Immediately after this pulse, a second (long) rf pulse with the 90°-shifted phase is applied, so that the nuclear magnetization remains aligned along the rotating component of the rf field. The value of $T_{1\rho}$ can be measured by changing the second pulse duration.

As noted in Sect. 12.2, the spin–spin relaxation time T_2 characterizes the decay of the transverse components of the nuclear magnetization. However, to measure T_2, it is generally not sufficient just to record the FID signal after a single pulse. The reason is that this decay may be affected by the inhomogeneity of the static magnetic field. To exclude the effects of field inhomogeneity, the two-pulse Hahn spin-echo method [19] is often used. This method is illustrated in Fig. 12.7. The first 90° pulse rotates the nuclear magnetization to the *xy* plane creating the transverse magnetization, which starts to dephase due to the field inhomogeneity.

The application of the second 180° pulse at time τ after the first 90° pulse is equivalent to the time reversal for the nuclear spin system, so that the transverse magnetization starts to rephase, forming an echo signal at time 2τ. In this case, the decay of the echo amplitude is determined by T_2:

$$M(2\tau) = M_0 \exp\left(-\frac{2\tau}{T_2}\right). \tag{12.16}$$

In order to measure T_2, it is necessary to perform a series of these two-pulse experiments with varying delays τ. It should be noted, however, that this two-pulse approach can give reliable values of T_2 only for systems where the resonance nuclei remain static, at least during the measurement time 2τ. If species with the resonance nuclei participate in diffusive motion, an additional contribution to the echo decay is expected (see Sect. 12.3.5). In order to eliminate the effects of diffusion and to measure the true values of T_2, multi-pulse sequences using trains of closely spaced 180° pulses (instead of a single 180° pulse) have been suggested [20, 21].

More specialized solid state NMR techniques, such as decoupling sequences, multi-nuclear, multi-quantum, and multi-dimensional NMR experiments are out of the scope of the present chapter, since they are rarely applied to metal–hydrogen systems. A comprehensive description of these NMR techniques and a number of their practical applications can be found in [15].

12.3.5 Diffusion Measurements by NMR

NMR methods for measuring the tracer diffusion coefficient are based on observation of an additional attenuation of the spin-echo signal due to displacement of nuclear spins in an external magnetic field gradient. The application of the field gradient serves to set a spatial scale in a certain direction. If the magnetic field changes linearly along the z axis with the gradient $G = \partial H_z/\partial z$, the spin-echo amplitude formed by the two-pulse Hahn sequence ($\pi/2$–t–π) at the moment $2t$ is expressed as:

$$M(2t) = M(0) \exp\left(-\frac{2t}{T_2} - \frac{2}{3}\gamma^2 G^2 D t^3\right), \tag{12.17}$$

where D is the tracer diffusion coefficient. In order to exclude the contribution to the echo decay due to the spin–spin interaction, the interval t between the rf pulses is usually fixed, and the echo amplitude is studied as a function of the applied gradient G. In most of the modern experiments, the magnetic field gradient is not static; it is applied in the form of two or more gradient pulses between the rf pulses and between the rf pulse and the echo [22]. The fundamental aspects of this PFG technique are discussed in reviews [5, 23]. The echo attenuation is simply related to

the displacement of nuclear spins along the direction of the gradient during the time interval between the gradient pulses. Therefore, the PFG technique provides a *direct* way of measuring the tracer diffusion coefficient D.

The range of hydrogen diffusion coefficients that can be measured by the PFG technique in metal–hydrogen systems is typically 10^{-8}–10^{-4} cm^2/s. To measure small values of D with sufficient accuracy, large gradient pulses and/or long time intervals between the gradient pulses (i.e., long diffusion times) are needed. Thus, the lower limit of the measurable D range is determined mainly by the maximum values of the gradient available from the pulse circuitry and by the spin–spin (transverse) relaxation responsible for the characteristic time of the echo decay. Modern PFG-NMR spectrometers can generate pulsed gradients up to 0.3 T/cm [23]. For systems with short T_2 values, instead of the two-pulse Hahn sequence, it is often preferable to use the three-pulse sequence forming the stimulated echo signal; the corresponding PFG experiment was proposed by Tanner [24]. In the case of stimulated echo, the echo decay not related to the applied field gradient is determined mainly by T_1 ($T_1 > T_2$); this allows one to use longer time intervals between the gradient pulses. The most serious difficulty in applying the PFG technique to metal–hydrogen systems is the presence of "background" field gradients associated with non-uniform sample magnetization in a static magnetic field. This problem is especially severe for powders with large magnetic susceptibility χ, where the demagnetizing fields of the order of $3\chi H_0$ change strongly over the size of a particle. Ideally, the applied field gradient should be much larger than the "background" gradients; however, this is not always experimentally feasible. In order to reduce the problems related to "background" gradients, several approaches can be used. One possibility is to use foil samples instead of powders. For homogeneous foils with the plane parallel to z (the static magnetic field direction), the internal fields are expected to be nearly homogeneous. Another possibility is to decrease the static magnetic field H_0, which would also lead to poorer signal-to-noise ratio for the echo. It was also demonstrated that the effects of "background" gradients can be strongly reduced by using special multi-pulse sequences with alternating polarity of the gradient pulses [5, 23, 25]. However, such sequences are experimentally very demanding.

For measurements of hydrogen diffusion coefficients in metal–hydrogen systems, typical intervals between the gradient pulses (diffusion times) are of the order of 10 ms. If the tracer diffusion coefficient is 10^{-6} cm^2/s, the displacement of a proton during this time is about 10^{-4} cm. Thus, the PFG technique can probe the diffusivity over macroscopic distances. This fact should be taken into account for systems where the diffusive motion is restricted by certain boundaries. In such cases, the diffusion coefficients measured by the PFG technique may start to depend on the diffusion times [23]. The spatial scale of the diffusive motion is also important for comparison of the results obtained by the PFG technique with those derived by quasielastic neutron scattering (QENS) experiments (see Sect. 12.6.3).

12.4 Structural Information from NMR Measurements

NMR measurements may help to solve a number of structural problems in metal–hydrogen systems. In particular, NMR measurements may be used to determine the location of hydrogen atoms in the metal lattice. Static NMR can provide structural information on metal–hydrogen systems through dipole–dipole interactions between nuclear spins (protons–protons and protons–metallic nuclei) and through interactions of nuclear quadrupole moments with EFG at nuclear sites [6]. In high-resolution NMR, valuable information can be obtained from the chemical shifts. As noted in Sect. 12.2, by comparing the experimental value of the second moment of the proton NMR line with the calculated values for different structural models, it is sometimes possible to determine which interstitial sites are occupied by H atoms [5]. The same approach can also be used to study partial hydrogen ordering.

As a recent example of such an analysis, we consider the results for the alloy hydride $TiV_{0.8}Cr_{1.2}H_{5.25}$ [26, 27]. This hydride has a face-centered cubic structure, where Ti, V, and Cr atoms are randomly distributed over 4*a* sites. It was predicted theoretically [28] that hydrogen atoms preferably occupy tetrahedral (T) sites. Neutron diffraction experiment on the deuterium-substituted compound [29] confirmed it. However, it should be noted that the preferred interstitial sites for D atoms may differ from those for H atoms. The ^{1}H cw-NMR spectrum recorded at room temperature at the frequency of 42 MHz represents a superposition of broad and narrow components (see Fig. 12.8a). The presence of the narrow line is related to fast hydrogen motion; this component disappears at low temperatures. The experimental value of the second moment (in field units) for the broad line is 35 G^2. The theoretical value of the second moment can be calculated using the Van Vleck formula (Eqs. (12.2) and (12.3)). In the present case, only ^{1}H–^{1}H and ^{1}H–^{51}V dipolar interactions should be taken into account, since the other metallic nuclei with non-zero spin have low natural abundance and/or low gyromagnetic ratio. The calculated second moment as a function of the radius of summation R (assuming that all H atoms are distributed over T-sites) is shown in Fig. 12.8b. It can be seen from this figure that only the first vanadium neighbors give a significant contribution to M_2, whereas the ^{1}H–^{1}H interactions are important up to about 10 Å. Figure 12.8c represents the M_{2HH} value calculated within $R = 50$ Å assuming that H atoms randomly occupy both tetrahedral and octahedral (O) sites. As can be seen from this figure, the calculated second moment increases with increasing fraction of occupied O-sites, C_{oct}, and exceeds the experimental second moment even at small values of C_{oct}. Therefore, it can be concluded that hydrogen atoms in $TiV_{0.8}Cr_{1.2}H_{5.25}$ preferably occupy T-sites, in agreement with both the neutron diffraction data [29] and ab initio calculations [28].

It is known that deuterium and hydrogen site occupancies may depend on both D/H and D/M (or H/M) ratios. An example of the applicability of ^{1}H and ^{2}H NMR to study proton and deuterium site occupancies can be found in works of Bandyopadhaya and Hayashi [30, 31]. In particular, it was found that in body-centered tetragonal phases of $VH_{0.82}$ and $VH_{0.6}D_{0.2}$ the preferential site occupancy

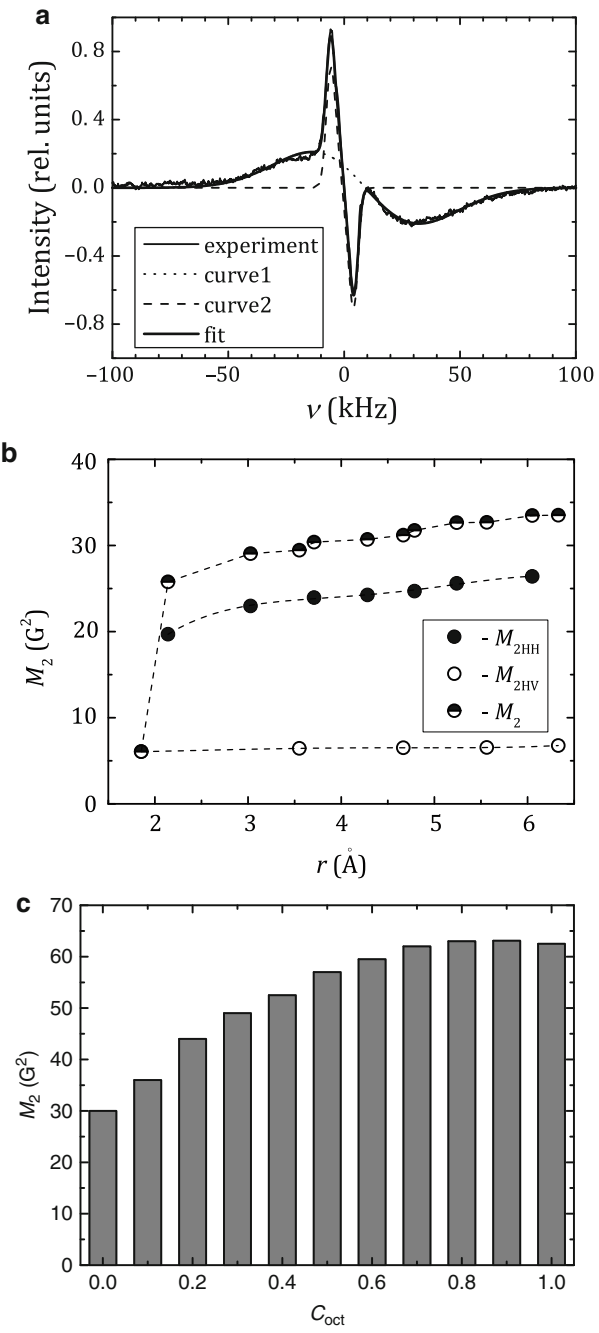

Fig. 12.8 Proton NMR spectrum of the $TiV_{0.8}Cr_{1.2}H_{5.25}$ hydride as a function of $\nu = \omega/2\pi$ (**a**); the total second moment (M_2) and contributions from ^1H–^1H and ^1H–^{51}V interactions (M_{2HH} and M_{2HV}, respectively) calculated as a function of the radius of summation (hydrogen atoms occupy only T-sites) (**b**); M_{2HH} calculated as a function of O-site occupancy (**c**). Adapted with permission from [26]. Copyrighted by Pleiades Publishing Ltd

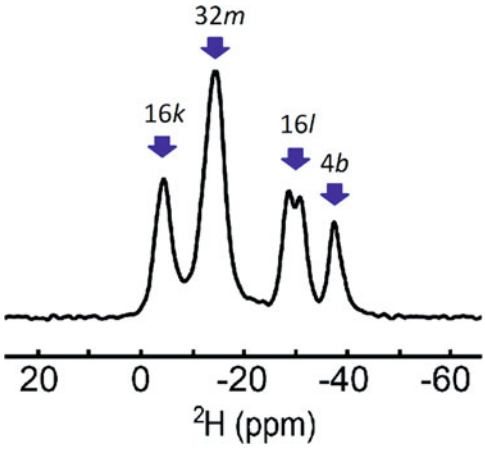

Fig. 12.9 The ^{2}H MAS-NMR spectrum of $Zr_2NiD_{4.8}$ at 76.79 MHz recorded at 193 K. Reproduced with permission from [32]. Copyrighted by Elsevier Science Ltd

strongly depends on the D/H ratio: in $VH_{0.82}$ hydrogen atoms occupy O-sites, and H diffusion occurs between the ordered O sites, whereas in $VH_{0.6}D_{0.2}$ hydrogen and deuterium atoms occupy both O- and T-sites, and H and D atoms at T-sites diffuse faster than those at O-sites. In body-centered cubic $VH_{0.2}D_{0.6}$ and $VD_{0.81}$, both H and D atoms occupy T-sites [30]. A careful study of deuterium site occupancy in VD_x with different D/V ratio ($x = 0.4$, 0.5 and 0.57) was made by Hayashi using static ^{2}D NMR at the frequencies of 30.7 and 61.4 MHz [31]. The spectra recorded at low temperatures (where the deuterium diffusion is frozen) exhibit features of both quadrupole and Knight shift interactions. By fitting the spectra in the framework of the model proposed in [30], it was found that for $x = 0.4$ deuterium atoms predominantly occupy O-sites (β-phase). For $x = 0.5$, a small part of D atoms (about 9 %) was found to occupy T-sites, and for $x = 0.57$, D atoms were found to occupy O-sites in the δ and α′ phases.

There are only a few works in which high-resolution NMR methods have been applied to studies of transition-metal hydrides showing metallic behavior. One of the recent examples is the ^{2}D MAS-NMR study of the intermetallic deuteride $Zr_2NiD_{4.8}$ [32]. The ^{2}D MAS-NMR spectra were measured at the resonance frequency of 76.79 MHz with the relatively low rotation frequency (7 kHz). The authors [32] were able to resolve different interstitial sites occupied by D atoms from the low-temperature spectra (see Fig. 12.9). Moreover, the occupancies of four different deuterium sites (4*b*, 16*k*, 16*l*, and 32*m*) obtained from the MAS-NMR spectra were in satisfactory agreement with neutron diffraction measurements.

Mg-Ni hydrides form another class of materials, for which even low resolution NMR may provide valuable structural information. For example, by applying the standard ^{1}H NMR line width analysis, it has been found that hydrogen atoms in α-Mg_2NiH_x are randomly distributed over the metallic lattice [33]. The ^{1}H MAS-NMR study of nanostructured Mg_2Ni-H composites has revealed the presence of four phases in these materials: α-Mg_2NiH_x, β-Mg_2NiH_4, α-MgH_x, and β-MgH_2 [34]. The separation was based on the chemical shift analysis. However,

it is worth noting that when one deals with nanostructured materials, such an assignment is rather relative and only means that local structures around the hydrogen atoms are close to those in the corresponding crystalline materials.

Light metal hydrides, such as MgH_2 or AlH_3 with ionic-covalent bonding exhibit non-metallic properties, and for their study it is easier to apply high-resolution NMR spectroscopy (including MAS, multi-pulse, multi-dimensional, and other NMR techniques). Magusin et al. [35, 36] have applied various high-resolution NMR techniques to study $Mg_{0.65}Sc_{0.35}H_2$ with fluorite-type structure. Comparison of the ^{1}H MAS-NMR spectra for MgH_2, ScH_2 and $Mg_{0.65}Sc_{0.35}H_2$ has shown that the latter compound is not phase separated. The ^{1}H NMR spectra suggest that hydrogen atoms are located in tetrahedral sites with different metal coordination. Since the ^{2}D–^{2}D dipole–dipole interaction is considerably weaker than that between protons, the ^{2}D NMR lines should be narrower, and the study of the deuteride seems to be more promising. Nevertheless, even the study of $Mg_{0.65}Sc_{0.35}D_2$ did not enable the authors to resolve the ^{2}H MAS-NMR line (that is, to identify which components correspond to a certain metal coordination). To solve this problem, the double-quantum NMR method with the ^{45}Sc decoupling has been applied. The ^{2}D Hahn-echo MAS-NMR spectra recorded with and without the ^{45}Sc irradiation during the evaluation time (so-called TRAPDOR experiment) have helped to assign the spectral components to deuterium atoms with different numbers of Sc neighbors. Further analysis has revealed that in magnesium–scandium hydride there is a non-statistical Mg and Sc distribution over the crystal lattice: the material is segregated into Mg-rich and Sc-rich nanodomains (the size of these domains is a few unit cells). It is worth noting that for X-ray and neutron diffraction the material looks homogeneous [36].

Alane (AlH_3) is a metastable hydride with a large hydrogen storage capacity (about 10 wt.%), however, after hydrogen release it cannot be regenerated simply by applying a hydrogen gas overpressure, as in the case of Mg or transition-metal alloys. Nevertheless, it is still attractive for hydrogen storage research. From this perspective, the structural information, especially concerning structural changes in the course of thermal decomposition, is of considerable interest. There are several polymorphic modifications of AlH_3 (α, β, γ-phases), which differ by the arrangement of AlH_6 octahedra in space. It has been shown [37] that ^{27}Al MAS-NMR is sensitive enough to distinguish subtle differences in the local environment of aluminum nuclei. The chemical shift is a kind of a fingerprint that allows one to identify different phases of AlH_3 [38] and to follow its decomposition kinetics [37]. It is well known that hydrogen sorption processes are inhomogeneous; however, most of the experiments are not spatially resolved. Recently Setthanan et al. [39] have suggested applying MRI to visualize the thermal decomposition of AlH_3 in situ in real time. Besides MAS-NMR, static NMR and relaxation measurements can also be applied to study the structural properties of AlH_3. The proton relaxation measurements in AlH_3 at low resonance frequency have revealed two components in both T_1 and T_2^*: the dominant one with long T_1 and short T_2^* and a minor one with short T_1 and long T_2^* [40]. The former component can be readily

attributed to hydrogen rigidly bonded to the AlH_3 crystal lattice, whereas the attribution of the latter (mobile) component was rather controversial. Senadheera et al. [41] have studied the proton NMR spectra and spin-lattice relaxation in AlH_3 in the temperature range from 11 to 423 K and found that this minor component remains mobile even at very low temperatures. This suggests that the minor component corresponds to molecular H_2 which is physically trapped in cavities of the material, in agreement with the ortho-para conversion observed by both NMR and neutron scattering.

12.5 Electronic Properties of Metal–Hydrogen Systems

For metallic hydrides, hyperfine interactions of nuclear spins with conduction electrons are responsible for the Knight shifts (see Sect. 12.2). A detailed description of the nature of the Knight shift tensor can be found in the review [42]. Important information on electronic properties can also be obtained from the conduction-electron (Korringa) contribution to the spin-lattice relaxation rate, T_{1e}^{-1}. This contribution is generally proportional to the temperature and to the square of the density of electron states at the Fermi level, $N^2(E_F)$. For most metallic hydrides, T_{1e}^{-1} is the dominant contribution to the measured spin-lattice relaxation rate at low temperatures. It should be noted that the relation between the measured NMR parameters and the electronic structure is very complex, and should be adapted for the particular systems under study. In practice, the data analysis is based on simplified approaches described in the reviews [5, 43]. As discussed in Sect. 12.2, each of the main contributions to the Knight shift in transition metals should be proportional to the corresponding contribution to the magnetic susceptibility χ [43]:

$$K = K_s + K_d + K_{orb} = \frac{1}{A\mu_B}\left[H_{hf}^{(s)}\chi_s + H_{hf}^{(d)}\chi_d + H_{hf}^{(orb)}\chi_{orb}\right], \tag{12.18}$$

where A is the Avogadro's number, μ_B is the Bohr magneton, and $H_{hf}^{(i)}$ is the hyperfine field associated with ith contribution. The electronic contribution to the nuclear spin-lattice relaxation rate can be written as [43]:

$$T_{1e}^{-1} = 4\pi\mu_0^2\gamma^2\hbar k_B T\left\{\left[H_{hf}^{(s)}N_s(E_F)\right]^2 + p\left[H_{hf}^{(d)}N_d(E_F)\right]^2 + q\left[H_{hf}^{(orb)}N_d(E_F)\right]^2\right\}, \tag{12.19}$$

where p and q are the dimensionless factors depending on the electron orbital degeneracy at the Fermi level. It should be noted that, while the spin contributions to the Knight shift, K_s and K_d, are proportional to the corresponding densities of electron states at the Fermi level, $N_s(E_F)$ and $N_d(E_F)$, the orbital contribution K_{orb} is not directly related to $N(E_F)$. In contrast, all the contributions to the spin-lattice

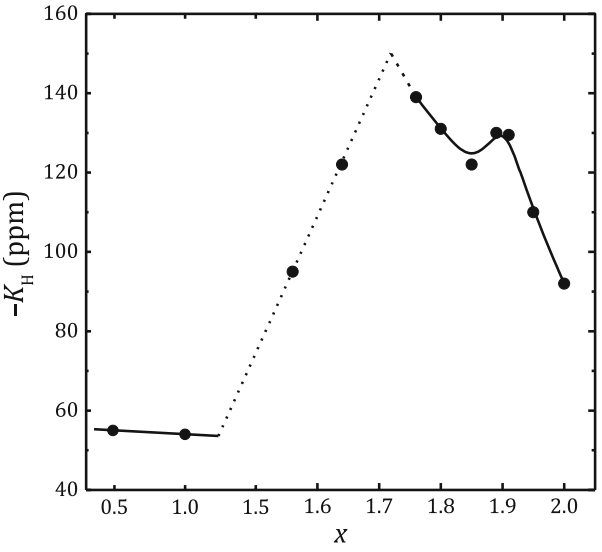

Fig. 12.10 Hydrogen concentration dependence of the proton Knight shift in TiH_x at $T = 4.2$ K. Reproduced with permission from [44]. Copyrighted by the Institute of Physics

relaxation rate (12.19) are proportional to the squares of the corresponding densities of electron states at the Fermi level. The isotropic contribution of s-electrons to the Knight shift, K_s, is always positive (i.e., the shift occurs towards higher resonance frequencies with respect to diamagnetic substances). For most of transition-metal nuclei, the core-polarization contribution K_d (resulting from polarization of the inner s shells due to exchange with d electrons) is negative. In some cases, when detailed measurements of the magnetic susceptibility, Knight shift and T_{1e}^{-1} are available over a wide temperature range, it is possible to separate different contributions on the basis of Eqs. (12.18) and (12.19), and to estimate the hyperfine fields and the values of $N_s(E_F)$ and $N_d(E_F)$ [12, 43].

As an example of the data, Fig. 12.10 shows the H concentration dependence of the proton Knight shift at $T = 4.2$ K for TiH_x [44]. It can be seen that the measured Knight shift is negative and exhibits strong variations as a function of hydrogen content. Measurements of the proton NMR parameters were also found to be sensitive to the $N(E_F)$ change at the fcc–fct lattice distortion in ZrH_x [45] associated with a Jahn–Teller effect in the d-band. NMR measurements on host-metal nuclei in YH_x [46] and LaH_x [47] have been used to trace the metal-insulator transition that occurs in both hydrides when the hydrogen concentration becomes nearly equal to $x = 3$. Since in the insulating state the density of electron states at the Fermi level is zero, the metal-insulator transition is accompanied by strong changes in the Knight shift and the spin-lattice relaxation rate.

Theoretical ab initio calculations can give the density of electron states in solids. Therefore, a combination of the results of NMR measurements with calculations of the electronic structure may provide a promising approach to studies of the electronic properties of metal–hydrogen systems. For lanthanum hydrides LaH_x, a

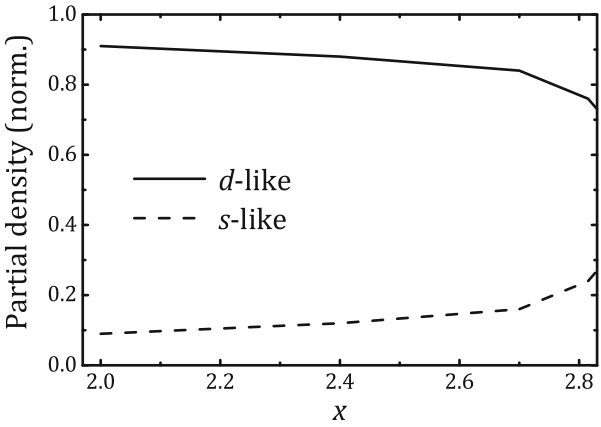

Fig. 12.11 Partial s- and d-like conduction-electron density of states at the La site in LaH_x, derived from quantitative modeling of the spin-lattice relaxation rate. Adapted with permission from [44]. Copyrighted by the American Physical Society

detailed investigation of the electronic structure based primarily on the low-temperature ^{139}La NMR measurements has been reported by Leyer et al. [47]. The combined analysis of the ^{1}H and ^{139}La spin-lattice relaxation rates and the x-dependent total density of electron states has revealed the predominant d-like character of conduction electrons at La sites (see Fig. 12.11). The present status, achievements, and limitations of the electronic band structure calculations for metal–hydrogen systems were reported in the review articles [48–50]. Modern density functional theory (DFT) methods can describe the key properties of materials, such as binding energies and heats of formation, with sufficient accuracy [50]. Therefore, they can be particularly effective for screening large series of hydrides, in order to find those with potential for various applications.

12.6 Hydrogen Mobility

12.6.1 Hydrogen Jump Rates: Localized Motion and Long-Range Diffusion

NMR studies of hydrogen jump motion are based on the sensitivity of NMR parameters to fluctuations of the local magnetic and electric fields. These fluctuations originate from jump motion of hydrogen atoms. For NMR on protons (^{1}H) having nuclear spin $I = 1/2$, the key role is played by fluctuations of the dipole–dipole interaction between nuclear spins. At low temperatures, the ^{1}H NMR line width $\Delta\omega_R$ is usually determined by static dipole–dipole interactions. With increasing temperature, this "rigid-lattice" line width starts to decrease when the H jump rate τ^{-1} becomes nearly equal to $\Delta\omega_R$. For typical metal–hydrogen systems this occurs at the temperature at which τ^{-1} reaches about 10^5 s^{-1}. However, the motional narrowing of the ^{1}H NMR line is limited by the magnetic field

inhomogeneity over the sample volume; for powder samples, such an inhomogeneity is determined by a distribution of demagnetizing fields. Because of this limitation, measurements of the NMR line width usually allow one to trace changes in H mobility over a rather narrow range of τ^{-1} values, not exceeding two orders of magnitude. Measurements of the spin-lattice relaxation rates T_1^{-1} and the rotating-frame spin-lattice relaxation rates $T_{1\rho}^{-1}$ can give information on changes in the H jump rates over much broader ranges. However, the measured values of T_1^{-1} may contain additive contributions not related to hydrogen motion. For proton T_1^{-1} in metal–hydrogen systems, such contributions are usually related to the hyperfine interaction between nuclear spins and conduction electrons (see Sect. 12.5) and to the dipole–dipole interaction between nuclear spins and localized electron spins at paramagnetic impurities [51]. The motional contribution to the spin-lattice relaxation rate, T_{1d}^{-1}, can be extracted using the difference in the temperature and frequency dependences of different contributions to T_1^{-1} [6]. Such a procedure may be effective, if the T_1^{-1} measurements are performed over wide ranges of temperature and resonance frequency. The motional contribution is described by a sum of several terms, each of the general form [6]:

$$T_{1d}^{-1} = \langle M^2 \rangle J(\omega_I, \omega_S, \tau_c), \tag{12.20}$$

where $\langle M^2 \rangle$ is the part of the interaction (dipole–dipole for ^{1}H) of the nuclear spin with its environment that fluctuates due to the motion, and $J(\omega_I, \omega_S, \tau_c)$ is the spectral density function that describes the dependence of fluctuations in M on the resonance frequencies ω_I and ω_S of the resonant and nonresonant nuclei, respectively, and on the correlation time τ_c of the fluctuations. For hydrogen diffusion in metals, τ_c is approximately equal to the mean residence time τ of a hydrogen atom in an interstitial site. The characteristic feature of the temperature dependence of T_{1d}^{-1} is the maximum that occurs when $\omega_I \tau \approx 1$. In other words, the T_{1d}^{-1} maximum is observed at the temperature at which the H jump rate τ^{-1} becomes nearly equal to the (circular) resonance frequency ω_I. In the limit of slow motion ($\omega_I \tau \gg 1$), T_{1d}^{-1} is proportional to $\omega_I^{-2}\tau^{-1}$, and in the limit of fast motion ($\omega_I \tau \ll 1$), T_{1d}^{-1} is proportional to τ, being frequency independent. If the temperature dependence of τ follows the usual Arrhenius relation,

$$\tau = \tau_0 \exp(E_a / k_B T), \tag{12.21}$$

a plot of ln T_{1d}^{-1} vs. T^{-1} should be linear in the limits of both slow and fast motion with the slopes of $-E_a/k_B$ and E_a/k_B, respectively. Thus, the activation energy E_a for hydrogen jump motion can be obtained directly from these slopes. The typical behavior of T_{1d}^{-1} at two different resonance frequencies as a function of the inverse temperature is shown in Fig. 12.12. Included in Fig. 12.12 is also the behavior of the rotating-frame spin-lattice relaxation rate $T_{1\rho}^{-1}$ for a system with the same motional parameters. It should be noted that the motional contribution to $T_{1\rho}^{-1}$ is usually much

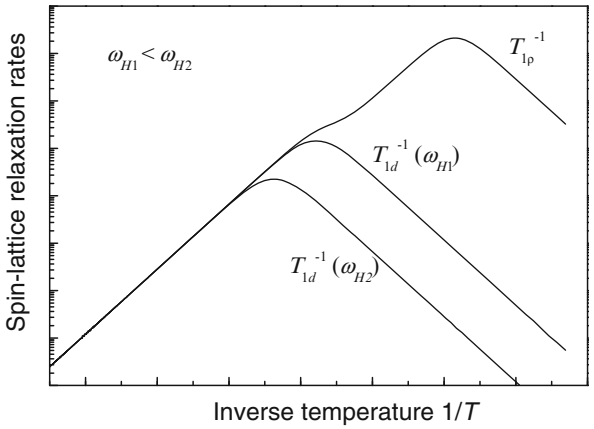

Fig. 12.12 Typical behavior of the motional contributions to the proton spin-lattice relaxation rate, T_{1d}^{-1}, at two resonance frequencies, ω_{H_1} and ω_{H_2}, and the rotating-frame spin-lattice relaxation rate, $T_{1\rho}^{-1}$, as functions of the inverse temperature. The vertical scale is logarithmic

higher than all other contributions, at least, in the region where $T_{1\rho}^{-1}$ measurements are technically feasible (not far away from its maximum). General features of the temperature dependence of $T_{1\rho}^{-1}$ resemble those of T_{1d}^{-1}; however, the $T_{1\rho}^{-1}$ maximum is determined by the condition $\omega_1\tau \approx 1$, where $\omega_1 = \gamma H_1$ is the circular frequency of nuclear spin precession in a (weak) rf magnetic field H_1. Since ω_1 is several orders of magnitude lower than the resonance frequency ω_I, the $T_{1\rho}^{-1}$ maximum is observed at much lower jump rates than the T_{1d}^{-1} maximum.

For long-range diffusion of hydrogen, the appropriate spectral densities $J(\omega_I, \omega_S, \tau_c)$ in Eq. (12.20) cannot be calculated in the analytic form. Therefore, in order to extract $\tau^{-1}(T)$ from the T_{1d}^{-1} or $T_{1\rho}^{-1}$ data, one has to rely either on the results of numerical (Monte Carlo) calculations [52–54] or on the model spectral densities [55–57]. The most widely used model is that based on the Lorentzian form of the spectral densities, as introduced by Bloembergen, Purcell, and Pound (BPP) [55]. The BPP model correctly describes the main features of the T_{1d}^{-1} and $T_{1\rho}^{-1}$ data (including the asymptotic behavior in the limits of slow and fast motion) and provides rather simple expressions relating the relaxation rates and τ. Comparison of the BPP results with those of more sophisticated calculations shows that, although the absolute τ values derived from the BPP model analysis may be in error by as much as a factor of 2, their relative temperature-dependent behavior is usually far more reliable, resulting in diffusion activation energies that agree to within ~10 % with those obtained by other techniques [5].

For a metal–hydrogen system, the BPP expression for the proton spin-lattice relaxation rate due to H–H and H-metal (H–M) dipole–dipole interactions modulated by diffusive motion of hydrogen can be written as

$$T_{1d}^{-1} = \left(T_{1d}^{-1}\right)_{HH} + \left(T_{1d}^{-1}\right)_{HM} = \frac{2M_{2HH}}{3}\left[\frac{\tau_c}{1+\omega_H^2\tau_c^2} + \frac{4\tau_c}{1+4\omega_H^2\tau_c^2}\right] + \frac{M_{2HM}}{2}\left[\frac{\tau_c}{1+(\omega_H-\omega_M)^2\tau_c^2} + \frac{3\tau_c}{1+\omega_H^2\tau_c^2} + \frac{6\tau_c}{1+(\omega_H+\omega_M)^2\tau_c^2}\right] \quad (12.22)$$

Here ω_H and ω_M are the resonance frequencies of protons and metal nuclei, respectively, and M_{2HH} and M_{2HM} are the contributions of H–H and H–M dipole–dipole interactions to the "rigid lattice" second moment of the ^{1}H NMR spectrum. For the H–M term in Eq. (12.22), the value of τ_c is equal to the mean residence time τ of a hydrogen atom in an interstitial site, and for the H–H term, $\tau_c = \tau/2$, since in a pair of interacting protons, a jump of each of them leads to strong changes in the dipole–dipole interaction. Both the H–H and H–M terms in Eq. (12.22) yield the relaxation rate maximum at $\omega_H\tau \approx 1$, the amplitude of the peak being determined by the strength of the corresponding dipole–dipole interaction. Equation (12.22) can be easily generalized for the case of several metal nuclei in the system. The BPP expression for the rotating-frame spin-lattice relaxation rate $T_{1\rho}^{-1}$ has a similar structure to that of Eq. (12.22); however, it contains additional terms depending on the nutation frequency ω_1. For example, the BPP expression for the H–H dipolar contribution to the proton rotating-frame relaxation rate is given by:

$$\left(T_{1\rho}^{-1}\right)_{HH} = \frac{M_{2HH}}{3}\left[\frac{3\tau_c}{1+4\omega_1^2\tau_c^2} + \frac{5\tau_c}{1+\omega_H^2\tau_c^2} + \frac{2\tau_c}{1+4\omega_H^2\tau_c^2}\right] \tag{12.23}$$

This expression predicts the rotating-frame relaxation rate maximum at $\omega_1\tau = 1$.

Hydrogen jump motion can also be *localized*. This means that at a time scale of a certain experiment, a hydrogen atom jumps only within a small group of sites. In metal–hydrogen systems, this can occur for specific sublattices of interstitial sites consisting of groups (such as pairs or hexagons) of sites well separated from each other. In complex hydrides, the localized H motion corresponds to reorientations of anion groups (such as BH_4 or AlH_4). For localized motion, the appropriate spectral densities can often be calculated analytically (see, for example, [58, 59]). In many cases, the corresponding expressions for T_{1d}^{-1} are analogous to Eq. (12.22); however, instead of the full "rigid lattice" contributions of the H–H and H–M interactions to the second moment, one should use only their parts ΔM_{2HH} and ΔM_{2HM} that are averaged out by a particular type of motion. This feature originates from the fact that, in contrast to the case of long-range diffusion, a localized motion does not fully average out the dipole–dipole interactions for protons. Because of this feature, the amplitude of the T_{1d}^{-1} peak due to localized H motion is smaller than that for the long-range diffusion. Usually, the localized H motion occurring at a short time scale can coexist with long-range diffusion at a much longer time scale. In this case, the temperature dependence of T_{1d}^{-1} exhibits two well-separated peaks: the low-temperature one corresponds to fast localized H jumps, and the high-temperature one is associated with slower H jumps leading to long-range diffusion.

For NMR on nuclei with $I > 1/2$ (i.e., nuclei with non-zero electric quadrupole moments), the important contribution to the measured spin-lattice relaxation rate may originate from the electric quadrupole interaction modulated by atomic jump motion. Spin-lattice relaxation due to the quadrupole interaction is generally not described by a single-exponential function. Single-exponential relaxation is expected for $I = 1$ and for nuclear spin systems which are characterized by the

spin temperature [60]. The temperature dependence of the spin-lattice relaxation rate due to motionally modulated quadrupole interaction also exhibits a peak corresponding to the condition $\omega_I\tau \approx 1$. For metal–hydrogen systems, the quadrupole relaxation of deuterium nuclei ($I_D = 1$) is of special interest. Since the gyromagnetic ratio of ^{2}D is rather small ($\gamma_D/\gamma_H = 0.154$), the electronic and dipolar contributions to the ^{2}D spin-lattice relaxation rate in metal deuterides are usually much smaller than the quadrupole contribution T_{1Q}^{-1}, especially near the relaxation rate peak. The EFG at moving ^{2}D nuclei may be produced by static charges (host-metal atoms) or mobile charges (other D atoms). If the screening of EFG by conduction electrons is neglected, the corresponding quadrupole contributions to the spin-lattice relaxation rate should be proportional to the dipole–dipole contributions D–M and D–D [61]. Taking the screening into account leads to the difference between the radial dependences for the quadrupole and dipole–dipole interactions; however, the frequency dependence of the spectral density functions for the quadrupole interaction should be analogous to that for the dipole–dipole interaction. Therefore, it can be expected that the temperature and frequency dependences of T_{1Q}^{-1} are similar to the corresponding dependences for the dipolar contributions to the spin-lattice relaxation rate. This is fully applicable to the case of deuterides having non-zero EFG values at interstitial sites due to the host-metal neighbors. In this case, fluctuations of the quadrupole interaction for ^{2}D are dominated by changes in the orientation of the principal EFG axis due to D jumps from one site to another. The corresponding correlation time is equal to the mean residence time τ, and the behavior of T_{1Q}^{-1} should be similar to that of the dipole–dipole contribution $\left(T_{1d}^{-1}\right)_{DM}$.

In some deuterides, the host-metal contribution to EFG at the centers of interstitial sites may be equal to zero because of the high local symmetry of these sites. The examples are the octahedral and tetrahedral interstitial sites in face-centered cubic lattices. In this case, the fluctuating EFG at ^{2}D nuclei is produced only by other moving D atoms. However, in contrast to the dipole–dipole ^{2}D–^{2}D interaction, the correlation time for the quadrupole interaction in this case may differ from $\tau/2$ [61]. The difference is related to the fact that, while the dipole–dipole interaction can be represented as pairwise, the quadrupole moment interacts with the total EFG produced by all surrounding charges. Therefore, a description of the quadrupole relaxation due to interaction with moving charges may require taking into account three-particle correlation functions [61]. As a result, the T_{1Q}^{-1} maximum is shifted to higher $\omega_I\tau$ values with respect to the $\left(T_{1d}^{-1}\right)_{DD}$ maximum.

The jump rates of H(D) atoms in metal–hydrogen systems can also be studied using spin-lattice relaxation measurements on host-metal nuclei. In this case, the relaxation is caused by fluctuating magnetic or electric fields at host-metal sites due to H(D) jumps. For nuclei with $I > 1/2$, the relaxation is usually dominated by the quadrupole mechanism. Relaxation measurements on such host-metal nuclei may be especially useful for studies of isotope effects on H(D) motion [62]. Indeed, a comparison of the ^{1}H and ^{2}D relaxation rates in a hydride and the corresponding

deuteride may fail to yield reliable information on the ratio of τ values for H and D, since the main relaxation mechanisms for ^{1}H and ^{2}D may differ (the dipolar and quadrupole one, respectively). On the other hand, for quadrupole relaxation of host-metal nuclei, the relaxation mechanism in a hydride and the corresponding deuteride is the same, and the moving H and D atoms act as the same charge sources. Therefore, the shift of the host-metal relaxation rate maximum for a hydride with respect to that for the corresponding deuteride allows one to compare the values of τ for H and D quite reliably.

We shall start our discussion of recent experimental results with those related to atomic motion in complex hydrides. In this class of materials, there are two basic types of atomic motion: the reorientational motion of complex anions (such as $[BH_4]^-$, $[NH_2]^-$, $[AlH_4]^-$, $[SiH_3]^-$, $[B_{12}H_{12}]^{2-}$) and the translational diffusion of cations and anions. Usually, the reorientational motion is much faster than the translational diffusion. Therefore, at low temperatures, the NMR data should be dominated by the effects of reorientational motion. Among the complex hydrides, the reorientational motion has been studied most extensively in borohydrides, where the tetrahedral BH_4 groups can rotate around twofold and threefold symmetry axes. Such a motion provides a strong mechanism of the ^{1}H spin-lattice relaxation due to modulation of the dipole–dipole interactions, since the H–B and H–H distances within a BH_4 group are rather short. For pure borohydrides, the measured proton spin-lattice relaxation rates usually do not contain any significant contributions not related to atomic motion (such as the conduction-electron contribution in metallic systems). This allows one to trace the atomic jump rates in some borohydrides over the range of eight orders of magnitude (10^4–10^{12} s^{-1}) [63]. The simplest picture of the reorientational motion of BH_4 groups was observed for cubic alkali-metal borohydrides ABH_4 (A = Na, K, Rb, Cs). Figure 12.13 shows the ^{1}H spin-lattice relaxation rates measured at three resonance frequencies as functions of the inverse temperature for KBH_4 [63] and $CsBH_4$ [64]. These results provide a textbook example of the behavior of T_{1d}^{-1} governed by a single thermally activated jump process (see Fig. 12.12). Motional parameters (the activation energy E_a and

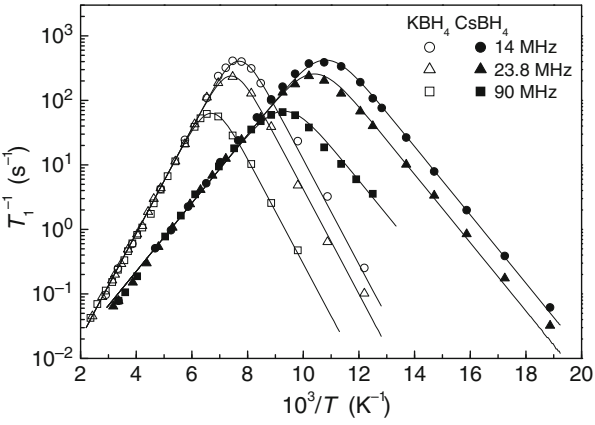

Fig. 12.13 Proton spin-lattice relaxation rates at three resonance frequencies for KBH_4 [63] and $CsBH_4$ [64] as functions of the inverse temperature. The *solid curves* show the results of simultaneous fits of the standard model [60] to the experimental data

the pre-exponential factor τ_0) of this process can be obtained from fits of the standard model [60] with the Lorentzian spectral densities to the experimental data. The solid curves in Fig. 12.13 show the results of the *simultaneous* fit at three resonance frequencies. Among the alkali-metal borohydrides, the fastest BH_4 reorientations are observed for $CsBH_4$. The position of the T_1^{-1} maximum for $CsBH_4$ in Fig. 12.13 indicates that the reorientational jump rate τ^{-1} in this compound reaches the value of ~10^8 s^{-1} at 93 K. It is interesting to note that, in a series of isomorphous cubic alkali-metal borohydrides ABH_4, the dependence of the activation energy E_a for BH_4 reorientations on the cation size is non-monotonic, showing a maximum for A = K [64]. For this group of compounds, a close correlation has been found [64] between the value of E_a and the relative deviation of the actual A–B distance from the sum of the ionic radii of A and BH_4. The phase transition from the low-temperature ordered to the high-temperature disordered phase of ABH_4 is accompanied by an abrupt increase in τ^{-1}. Such a behavior is well documented for $NaBH_4$ where the transition from the ordered tetragonal phase to the disordered cubic phase occurs near 190 K. It has been found [63, 65] that this transition in $NaBH_4$ is accompanied by a sharp change in the proton T_1^{-1} corresponding to nearly an order of magnitude increase in the jump rate τ^{-1}.

A more complex picture of the reorientational motion has been observed for the low-temperature orthorhombic phase of $LiBH_4$. For this compound, the temperature dependence of the proton T_1^{-1} looks like a superposition of two partially overlapping peaks [65, 66]. This suggests a coexistence of two reorientational processes with different jump rates. Since all BH_4 groups in the orthorhombic $LiBH_4$ are structurally equivalent, the two jump processes can be attributed to rotations around different symmetry axes. Another interesting example of reorientational motion has been found for the ammonium borohydride NH_4BH_4 [67] where both NH_4^+ and BH_4^- ions exhibit fast reorientations.

For the alkaline-earth borohydrides $Ae(BH_4)_2$ (Ae = Mg, Ca), the existence of distributions of reorientational jump rates appears to be quite common. Both $Mg(BH_4)_2$ and $Ca(BH_4)_2$ are known to have several crystalline modifications, and the structures of some of them are very complex. For example, the unit cell of the α-phase of $Mg(BH_4)_2$ contains 330 atoms. The presence of several crystallographically inequivalent BH_4 groups should lead to jump rate distributions. Another structural feature contributing to the complex picture of the reorientational motion is related to the coordination of BH_4 groups. In all known phases of $Mg(BH_4)_2$, the BH_4 tetrahedra are nearly linearly coordinated by two Mg atoms via the H–H edges. As discussed in [68], such a coordination is expected to lead to inequivalence of reorientations around different twofold symmetry axes of the same BH_4 tetrahedron. Indeed, the reorientation around the twofold axis nearly parallel to the Mg–B–Mg direction should be characterized by a small activation energy, since this motion does not break any of the four Mg–H bonds [68]. The reorientations around other twofold axes (perpendicular to this "easy" one) break all four Mg–H bonds; therefore, the corresponding activation energy is expected to be larger. The most obvious sign of the presence of a two-peak distribution of the jump rates is the

temperature dependence of the proton T_{1d}^{-1} with two maxima. This type of behavior was observed for α-$Mg(BH_4)_2$ [68]. One-peak distribution of the jump rates also changes the standard behavior of the proton T_{1d}^{-1} shown in Fig. 12.12. First, the low-temperature slope of the log T_{1d}^{-1} vs. T^{-1} plot becomes less steep than the high-temperature slope. Second, the frequency dependence of T_{1d}^{-1} at the low-temperature slope becomes weaker than the standard ω^{-2} dependence [69]. These features can be considered as signs of the presence of one-peak distribution of the jump rates. The corresponding behavior of the proton T_1^{-1} was found for β-$Mg(BH_4)_2$ [70, 71]. For parametrization of jump rate distributions at different temperatures, it is often convenient to use the model with a distribution of activation energies $G(E_a)$. This model assumes a single value of the pre-exponential factor τ_0, and the distribution of τ values at a given temperature is obtained by combining the Arrhenius relation (Eq. (12.21)) and $G(E_a)$. The resulting relaxation rate is expressed as [69]:

$$T_{1d}^{-1} = \int T_{1d}^{-1}(E_a) G(E_a) dE_a, \tag{12.24}$$

where $T_{1d}^{-1}(E_a)$ is determined by Eqs. (12.22) and (12.21). For disordered solids, a Gaussian shape of $G(E_a)$ is often used. In this case, the distribution is defined by the average activation energy $\bar{E}_a$ and the dispersion ΔE_a. Such a description satisfactorily reproduces all features of both the temperature and frequency dependences of T_{1d}^{-1} in β-$Mg(BH_4)_2$ over wide ranges of T and ω [70].

While the volumetric and gravimetric hydrogen densities in borohydrides of light alkali and alkaline-earth metals are quite high, the stability of these compounds with respect to thermal decomposition and poor reversibility of H desorption/absorption remain the major obstacles on the way to their practical use as hydrogen storage materials. In order to overcome these drawbacks, many new borohydride-based systems with mixed anions and/or cations have been synthesized over recent years. Some of these systems exhibit very fast reorientational motion even at low temperatures. The examples of such systems are $LiBH_4$-LiI solid solutions [72], $LiLa(BH_4)_3Cl$ [73], and $Na_2(BH_4)(NH_2)$ [74]. For the 1:1 solid solution $Li(BH_4)_{0.5}I_{0.5}$, the proton spin-lattice relaxation rate maximum at $\omega/2\pi = 14$ MHz is observed near $T = 40$ K [72]. This means that the reorientational jump rate in $Li(BH_4)_{0.5}I_{0.5}$ reaches the value of ~10^8 s^{-1} already at 40 K. It should be noted that a number of borohydride-based systems with fast reorientational motion of BH_4 groups also exhibit rather fast translational diffusion of cations (Li^+, Na^+). The particularly interesting relation between the BH_4 reorientations and the diffusion of Li^+ ions has been found for the cubic borohydride-chloride $LiLa(BH_4)_3Cl$ [73]. Figure 12.14 shows the temperature dependences of the proton spin-lattice relaxation rates in this compound at three resonance frequencies. The measured relaxation rate exhibits two frequency-dependent peaks. The low-temperature peak corresponds to the fast reorientational motion of BH_4 groups, presumably around the threefold axis along the La–B direction [73]. The nature of

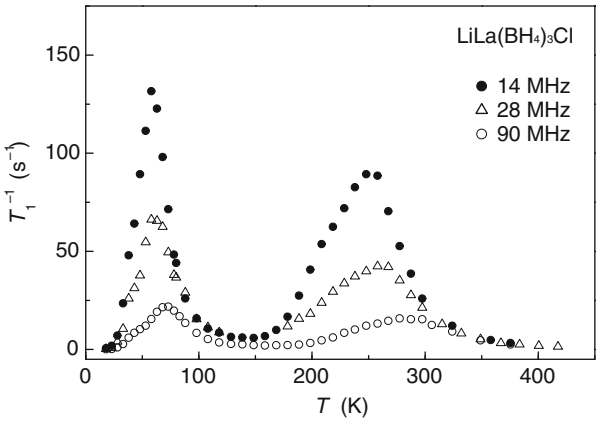

Fig. 12.14 Temperature dependences of the proton spin-lattice relaxation rates for $LiLa(BH_4)_3Cl$ [73] at three resonance frequencies

the high-temperature peak corresponding to some slower type of motion requires a special consideration. In principle, the high-T peak in the proton T_1^{-1} may result from Li^+ jump motion (as in the case of $LiBH_4$ [75] and $Li(BH_4)_{1-y}I_y$ [72]). Moreover, measurements of the ^{7}Li NMR spectra and ^{7}Li spin-lattice relaxation rate in $LiLa(BH_4)_3Cl$ [73] indicate that the *position* of the high-T proton T_1^{-1} peak is consistent with that expected for diffusive Li^+ jumps. However, the *amplitude* of the high-T proton T_1^{-1} peak appears to be too large to result solely from Li^+ diffusion. Therefore, the high-T peak originates from a combined effect of two motional processes occurring *at the same frequency scale*: Li ion diffusion and another (slower) type of BH_4 reorientations. This suggests a possibility of dynamic coupling between the anion rotation and cation diffusion, as discussed in terms of the "paddle-wheel" mechanism [76].

Interesting NMR studies of hydrogen dynamics have been performed in solid ammonia borane NH_3BH_3 using the ^{11}B T_1^{-1} and the proton spectroscopic, T_1^{-1} and $T_{1\rho}^{-1}$ measurements [77], as well as the ^{2}D spectroscopic and T_1^{-1} measurements for the partially deuterated compound [78]. It has been found that in the low-temperature orthorhombic phase of NH_3BH_3 ($T < 225$ K), the NH_3 and BH_3 groups exhibit independent reorientations with different jump rates and activation energies. On the other hand, in the high-temperature tetragonal phase, the jump rates of NH_3 and BH_3 groups are close to each other, which suggests reorientations of the whole NH_3BH_3 molecule about the B–N bond [78]. These results were complemented by the ^{15}N NMR data [79] that revealed a strong drop in the jump rate at the transition from the high-temperature to the low-temperature phase of NH_3BH_3.

Another group of complex hydrides with intriguing dynamical properties is represented by alkali-metal dodecahydro-*closo*-dodecaborates $A_2B_{12}H_{12}$. These ionically bonded salts consisting of alkali-metal A^+ cations and icosahedral $[B_{12}H_{12}]^{2-}$ anions have attracted recent attention, since they appear to be

energetically favorable intermediate compounds in the decomposition of the corresponding borohydrides ABH_4 [80]. The formation of these highly stable compounds is believed to be partly responsible for the poor hydrogen cycling performance of the borohydrides. The relatively large anion/cation size ratios and the reorientational mobility of the anions lead to interesting physical properties of $A_2B_{12}H_{12}$, including high-temperature order–disorder phase transitions [81, 82]. For the isomorphous cubic compounds $A_2B_{12}H_{12}$ (A = K, Rb, Cs), the results of ^{11}B and ^{1}H NMR experiments [83, 84] indicate that the rate of $[B_{12}H_{12}]^{2-}$ reorientations increases with increasing cation radius. The monoclinic compound $Na_2B_{12}H_{12}$ undergoes a first-order transition to the high-temperature disordered cubic phase [85] near 520 K. This phase transition is accompanied by a two-orders-of-magnitude drop of the proton spin-lattice relaxation rate [84]. Since such a drop is found to occur at the high-temperature slope of the relaxation rate peak, it corresponds to the two-orders-of-magnitude *increase* in the reorientational jump rate τ^{-1} in the cubic disordered phase. The ^{23}Na spin-lattice relaxation rate measurements [84] have shown that the transition to the high-temperature disordered phase of $Na_2B_{12}H_{12}$ is also accompanied by the onset of fast translational diffusion of Na^+ cations. Thus, $Na_2B_{12}H_{12}$ represents another example of correlations between the anion reorientations and the cation diffusion.

NMR was also applied to study the reorientational motion of $[AlH_4]^-$ [86] and $[NH_2]^-$ groups [87] in complex hydrides. As for translational diffusion of H-containing species in complex hydrides, the corresponding experimental observations are relatively rare. Recent well-documented cases include the diffusion of intact $[BH_4]^-$ groups in $LiBH_4$ embedded into nanoporous carbon [88], in the high-temperature phase of bulk $LiBH_4$ [75, 89], and the diffusion of intact $[AlH_4]^-$ groups in $KAlH_4$ [86]. In the temperature ranges studied, the diffusive jumps of the anion groups remain too slow to be probed by the spin-lattice relaxation experiments; therefore, these results rely mostly on the NMR line width measurements.

Recent investigations of H jump motion in metal hydrides were focused on hydrogen in alloys and intermetallic compounds. Among intermetallics, H diffusion was most extensively studied in Laves phases AB_2 which can have either the cubic (C15-type) or the hexagonal (C14-type or C36-type) structures. For many of the Laves-phase hydrides, a coexistence of two hydrogen jump processes with different characteristic rates has been found. The most pronounced evidence for such a coexistence has been obtained in the series of NMR measurements on the C15-type system TaV_2–H(D) [62, 90, 91]; these measurements have revealed the temperature dependences of both ^{1}H and ^{51}V spin-lattice relaxation rates with two well-separated peaks. The two frequency scales of H jump motion in Laves-phase hydrides have been found to originate from the structural features of the sublattice of interstitial sites. In cubic Laves phases, H atoms usually occupy only 96*g* sites (coordinated by A_2B_2 tetrahedra) at low and intermediate hydrogen concentrations (up to ~2.5 H atoms per formula unit). In particular, only 96*g* sites are occupied by H(D) atoms in $TaV_2H_x(D_x)$ over the entire range of attainable H(D) concentrations ($x \leq 1.7$). The sublattice of *g* sites consists of regular hexagons lying in the planes

perpendicular to the <111> directions. Each g site has three nearest neighbors: two g sites (on the same hexagon) at a distance r_1 and one g site (on the adjacent hexagon) at a distance r_2. The ratio r_2/r_1 is determined by the positional parameters (x_g and z_g) of hydrogen atoms at g sites. Examination of the available neutron diffraction data for cubic Laves-phase deuterides reveals strong changes in the ratio r_2/r_1 from one compound to another; these changes are related to the changes in the ratio of metallic radii of elements A and B forming an AB_2 compound [92, 93]. For example, the value of r_2/r_1 is 1.45 for TaV_2D_x, 1.07 for $ZrCr_2D_x$ and 0.53 for $YFe_2D_{2.6}$ [94]. For $TaV_2H_x(D_x)$, the g-site hexagons are well separated from each other. Therefore, a hydrogen atom performs many jumps within a hexagon before jumping to another hexagon. In this case, the faster jump process can be attributed to the localized H motion within g-site hexagons, and the slower process can be associated with H jumps from one g-site hexagon to another.

Two-peak behavior of the nuclear spin-lattice relaxation rates was observed for a number of Laves-phase hydrides with $r_2/r_1 > 1$. As an example of the data, Fig. 12.15 shows the temperature dependence of the ^{51}V spin-lattice relaxation rate in the ternary cubic Laves-phase deuteride $NbVCrD_{0.38}$ with $r_2/r_1 = 1.36$ [95]. This figure demonstrates that the H(D) jump motion can be probed by spin-lattice relaxation measurements on host-metal nuclei. The low-T peak here corresponds to fast localized motion of D atoms within g-sites hexagons, and the high-T peak is associated with D jumps between the hexagons leading to long-range diffusion. At high H content ($x > 2.5$), hydrogen atoms start to occupy $32e$ sites (coordinated by AB_3 tetrahedra) in C15-type hydrides, the relative occupancy of e sites increasing with x. The partial e-site filling makes the microscopic picture of H motion less tractable. However, one may generally expect that the partial occupation of e sites leads to an increase in the long-range H mobility due to the opening of new diffusion paths. This effect is well documented for ZrV_2H_x [96, 97].

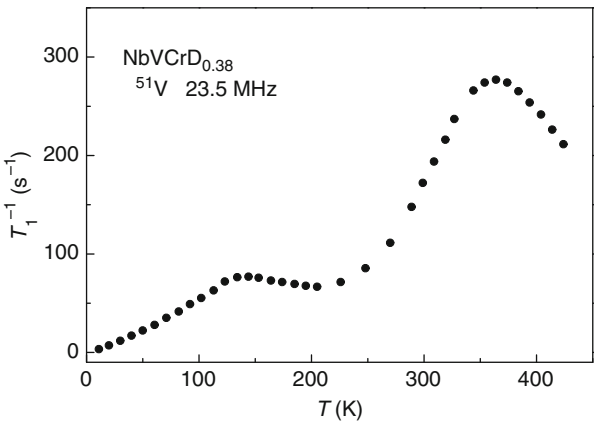

Fig. 12.15 Temperature dependence of the ^{51}V spin-lattice relaxation rate for Laves-phase $NbVCrD_{0.38}$ [95] at 23.5 MHz

Apart from the cubic Laves-phase hydrides, two coexisting frequency scales of H jump motion were observed for some hexagonal (C14-type) Laves-phase hydrides [98–100], hexagonal $CaCu_5$-type $LaNi_5H_x$ compounds [101], cubic Ti_2Ni-type Ti_2CoH_x [102], cubic A15-type hydrides Nb_3AlH_x [103], and the rhombohedral Th_2Zn_{17}-type compounds $Pr_2Fe_{17}H_5$ [104] and $Ce_2Fe_{17}H_5$ [105]. In all these cases, two frequency scales of H motion can be related to structural features of the sublattices of interstitial sites. The motion of hydrogen dissolved in disordered alloys is usually described in terms of continuous distributions of H jump rates [106, 107].

Another interesting class of hydrogen-containing solids is represented by clathrate hydrates, where H_2 *molecules* are enclosed in cages formed by hydrogen-bonded water molecules. Proton NMR line shape measurements in H_2–D_2O clathrate hydrate [108] have revealed the complex dynamics of H_2 guest molecules. Below 120 K, the observed line shape of *ortho*-H_2 in this compound is governed by the reorientational motion, and above 120 K, an additional line narrowing is attributed to diffusion of H_2 from one cage to another [108]. Recently, ^{1}H and ^{2}D NMR measurements have also been performed in H_2- and D_2-filled ice Ic framework [109].

12.6.2 Direct Measurements of Hydrogen Diffusion Coefficients

As discussed in Sect. 12.3.5, hydrogen diffusion coefficients can be directly measured using the spin-echo technique with static or PFG. However, the corresponding experimental studies for metal hydrides are still relatively rare. One of the reasons for this is the presence of large background field gradients in powder samples with high magnetic susceptibility (see Sect. 12.3.5). For complex hydrides, the limiting factor is related to low values of the diffusion coefficients for hydrogen-containing species. While in a number of complex hydrides the long-range diffusion of intact BH_4 groups [75, 89] and AlH_4 groups [86] has been observed by NMR line width measurements, the diffusive motion up to the melting or decomposition temperatures remains too slow to be probed by direct NMR methods of diffusivity measurements.

For binary metal–hydrogen systems, comprehensive compilations of experimental data on hydrogen diffusion coefficients measured by different methods have been published by Völkl and Alefeld [110] and Wipf [111]. For hydrides of alloys and intermetallic compounds, the experimental data on hydrogen diffusivity are scarce. Among the hydrides of intermetallic compounds, hydrogen diffusion has been most extensively studied in Laves-phase hydrides [92], since in many of these compounds hydrogen exhibits very high mobility. The pulsed-field-gradient NMR technique was used to measure the hydrogen diffusivity in $ZrCr_2H_x$ [112, 113], ZrV_2H_x [97, 113], HfV_2H_x [113], $ZrTi_2H_x$ [114], $HfTi_2H_x$ [115], $ZrMo_2H_x$ [116], $TaV_2H_{1.24}$ [113], and $HfCr_2H_x$ [117]. Recent examples of NMR diffusivity measurements for hydrogen in disordered alloys include H in V–Ta alloys [118] and Ti–V–Cr alloys [119]. For most of the studied Laves-phase hydrides, the temperature dependence of the measured hydrogen diffusion coefficient follows the Arrhenius

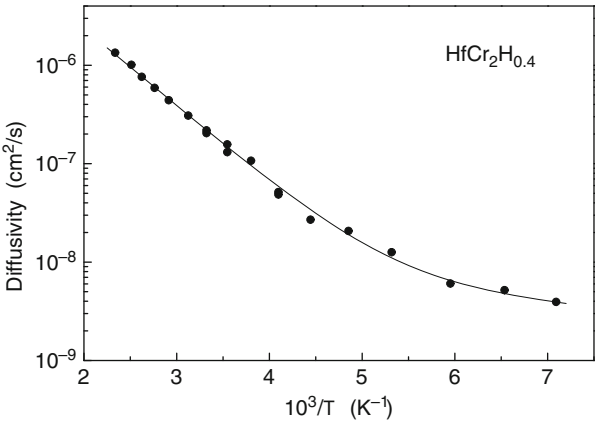

Fig. 12.16 The measured hydrogen diffusion coefficient for Laves-phase $HfCr_2H_{0.4}$ as a function of the inverse temperature. The *solid curve* shows the data fit by a sum of two Arrhenius terms. Reproduced with permission from [117]. Copyrighted by Elsevier Science Ltd

law, and the activation energy E_a for H diffusion tends to increase with increasing hydrogen concentration. This can be attributed (at least, partially) to the increase in the intersite distances due to the expansion of the lattice. However, this effect is not very strong. On the other hand, if the increase in H concentration is accompanied by filling of an additional type of interstitial sites by H atoms, the effects on E_a may be more pronounced. The appropriate example is the behavior of E_a in ZrV_2H_x system [113], where the value of the activation energy first increases with increasing x (from 179 meV for $x = 0.5$ to 217 meV for $x = 1.5$), but starts to decrease for $x > 2$ (down to 188 meV for $x = 4.1$). Since H atoms in ZrV_2H_x are known to occupy only interstitial g sites at low hydrogen content, but start to fill e sites (in addition to g sites) for $x > 2$, it is natural to assume that the observed decrease in E_a at high x is related to opening of new diffusion paths due to g–e jumps.

For two Laves-phase systems, $ZrCr_2H_x$ and $HfCr_2H_x$ with $x \leq 0.5$, strong deviations from the Arrhenius-type temperature dependence of the hydrogen diffusion coefficient have been revealed [112, 117] at low temperatures. As an example of the data, Fig. 12.16 shows the behavior of the H diffusion coefficient measured by the pulsed-field-gradient NMR technique for the hexagonal (C14-type) $HfCr_2H_{0.4}$ [117]. Because of the high long-range mobility of hydrogen in this system, the diffusion coefficient D could be measured by PFG-NMR down to 140 K. Below 200 K, the temperature dependence of D deviates markedly from the Arrhenius behavior. Similar deviations from the Arrhenius law have been reported for b.c.c. solid solutions α-NbH_x and α-TaH_x [120, 121]. It should be noted that for all these systems, no phase transitions have been found in the range of the observed change in the slope of the Arrhenius plot. The behavior of $D(T)$ for $HfCr_2H_{0.4}$ can be described well by a sum of two Arrhenius terms with different pre-exponential factors and different activation energies (157 meV and 19 meV [117]). This

suggests that different jump mechanisms dominate at high and low temperatures. As discussed in [112], the incoherent H tunneling transitions between the *excited* vibrational states [122] are likely to determine the hydrogen diffusion at $T > 200$ K, whereas at lower temperatures one may expect a significant contribution due to the phonon-assisted H tunneling between the *ground* states [123].

12.6.3 Complementarity Between NMR and Quasielastic Neutron Scattering

NMR and incoherent QENS are known to give complementary microscopic information on hydrogen jump motion in materials. In this section, we shall consider the relation between these two methods, for details on QENS see Chap. 9. It is interesting to note that nuclear spins play the crucial role for both methods. While for NMR this is quite evident, one should also keep in mind that the *incoherent* part of neutron scattering by nuclei of the same isotope is determined by the difference between the scattering lengths for different mutual spin orientations of a neutron and a nucleus. For isotopes with a zero nuclear spin, the incoherent neutron scattering cross-section is also zero. Both methods yield information on the jump rates of H atoms. Standard NMR measurements of the spectra and spin relaxation can probe the atomic jump rates over the dynamic range of ~10^4–10^{11} s^{-1}. Using some special NMR techniques, such as measurements of the decay of dipolar spin order [3] and the spin-alignment NMR spectroscopy [4], it is possible to push the lower limit of the dynamic range to jump rate values of the order of 0.1 s^{-1}. Incoherent QENS measurements can probe the H jump rates over the dynamic range of ~10^8–10^{12} s^{-1}. The lower limit of this range is determined by the energy resolution of the available neutron spectrometers. Thus, the atomic jump ranges probed by NMR and QENS are overlapping, and NMR has evident advantages in terms of the width of the dynamic range, being sensitive to much slower motion than QENS. However, standard NMR measurements usually cannot give direct information on the spatial aspects of atomic motion. Indeed, because of their local nature, the measured NMR parameters appear to be integrated over the entire q-space. In contrast, incoherent QENS measurements can probe the q dependences of the autocorrelation functions [124, 125] giving information on the paths of the moving atoms. Thus, the q dependence of QENS spectra is determined by the geometry of the atomic jump motion.

As an example of the complementarity between NMR and QENS, we can consider recent studies of BH_4 reorientations in $LiBH_4$-LiI solid solutions [72, 126]. The partial iodine substitution for BH_4 groups in this system stabilizes the structure of the hexagonal $LiBH_4$ phase down to low temperatures. NMR measurements of the ^1H and ^{11}B spin-lattice relaxation rates in $Li(BH_4)_{1-y}I_y$ [72] have revealed extremely fast BH_4 reorientations in this system. Indeed, for $Li(BH_4)_{0.5}I_{0.5}$ the proton spin-lattice relaxation rate measured at $\omega/2\pi = 14$ MHz exhibits a maximum near $T = 40$ K [72]. This means that the reorientational jump rate reaches the value of ~10^8 s^{-1}

already at 40 K. However, the temperature dependence of T_{1d}^{-1} cannot be described in terms of a single frequency scale of the reorientational motion. In fact, the high-temperature slope of the $T_{1d}^{-1}(T)$ peak in this system exhibits a pronounced "shoulder" near 100 K; this suggests the presence of an additional (slower) type of BH_4 reorientation. The nature of the two reorientational processes in $Li(BH_4)_{0.5}I_{0.5}$ has been clarified by subsequent QENS measurements [126]. The observed q dependence of the elastic incoherent structure factor (EISF) indicates that the faster jump process corresponds to BH_4 reorientations around the threefold symmetry axis parallel to the crystallographic c axis, while the slower process is associated with exchange between the apical (static) H atom on this axis and one of the three moving H atoms at the perpendicular plane.

The tracer diffusion coefficients of hydrogen can be directly measured by QENS at small momentum transfer (small q). In the limit of small q ($2\pi/q \gg L$, where L is the length of the elementary H jump), the details of the jump motion mechanism are not important, and the dynamic structure factor measured by QENS should be Lorentzian with the half-width at half-maximum equal to Dq^2 [124, 125]. In QENS experiments, the value of D is usually measured over the distances of 20–50 Å. The upper limit of this spatial range is determined by the lower q limit accessible for a neutron spectrometer. As in the case of the pulsed-field-gradient NMR technique (see Sect. 12.3.5), QENS experiments at low q provide a model-independent way of measuring the diffusion coefficients. However, the pulsed-field-gradient NMR technique probes the diffusivity over much longer distances (up to micrometer range). This should be taken into account while comparing the values of D obtained by the low-q QENS and the pulsed-field-gradient NMR. In particular, one may expect considerable differences between these values for nanostructured materials or materials with significant concentrations of defects acting as traps for diffusive motion.

References

1. E.M. Purcell, H.C. Torrey, R.V. Pound, Phys. Rev. **69**, 37 (1946)
2. F. Bloch, W.W. Hansen, M. Packard, Phys. Rev. **69**, 127 (1946)
3. J. Jeener, P. Broekaert, Phys. Rev. **157**, 232 (1967)
4. H.W. Spiess, J. Chem. Phys. **72**, 6755 (1980)
5. R.M. Cotts, in *Hydrogen in Metals I*, ed. by G. Alefeld, J. Völkl (Springer, Berlin, 1978), p. 227
6. R.G. Barnes, in *Hydrogen in Metals III*, ed. by H. Wipf (Springer, Berlin, 1997), p. 93
7. J.H. Van Vleck, Phys. Rev. **74**, 1168 (1948)
8. M.H. Cohen, F. Reif, in *Solid State Physics*, ed. by F. Seitz, D. Turnbull, vol. 5 (Academic Press, New York, 1957), p. 321
9. W.H. Jones, T.P. Graham, R.G. Barnes, Phys. Rev. **132**, 1898 (1963)
10. R.B. Creel, S.L. Segel, R.J. Schoenberger, R.G. Barnes, D.R. Torgeson, J. Chem. Phys. **60**, 2310 (1974)
11. R.M. Sternheimer, Phys. Rev. **95**, 736 (1954)

12. G.C. Carter, L.H. Bennett, D.J. Kahan, *Metallic Shifts in NMR* (Pergamon Press, Oxford, 1977)
13. C.P. Slichter, *Principles of Magnetic Resonance* (Springer, Berlin, 1992)
14. V.I. Chizhik, Y.S. Chernyshev, A.V. Donets, V.V. Frolov, A.V. Komolkin, M.G. Shelyapina, *Magnetic Resonance and Its Applications* (Springer, Cham Heidelberg New York Dordrecht London, 2014)
15. M.J. Duer (ed.), *Solid-State NMR Spectroscopy. Principles and Applications* (Blackwell Science, Oxford, 2002)
16. A. Lösche, *Kerninduktion* (Deutscher Verlag der Wissenschaften, Berlin, 1957)
17. W.G. Clark, Rev. Sci. Instrum. **35**, 316 (1964)
18. A. Avogadro, G. Bonera, M. Villa, J. Magn. Reson. **35**, 387 (1979)
19. E.L. Hahn, Phys. Rev. **80**, 580 (1950)
20. H.Y. Carr, E.M. Purcell, Phys. Rev. **94**, 630 (1954)
21. S. Meiboom, D. Gill, Rev. Sci. Instrum. **29**, 688 (1958)
22. O.E. Stejskal, J.E. Tanner, J. Chem. Phys. **42**, 288 (1965)
23. F. Stallmach, P. Galvosas, Annu. Rep. NMR Spectrosc. **61**, 51 (2007)
24. J.E. Tanner, J. Chem. Phys. **52**, 2523 (1970)
25. R.F. Karlicek, I.J. Lowe, J. Magn. Reson. **37**, 75 (1980)
26. V.S. Kasperovich, B.B. Khar'kov, I.A. Rykov, S.A. Lavrov, M.G. Shelyapina, Y.S. Chernyshev, V.I. Chizhik, N.E. Skryabina, D. Fruchart, S. Miraglia, Phys. Solid State **53**, 234 (2011)
27. V.I. Chizhik, V.S. Kasperovich, M.G. Shelyapina, Y.S. Chernyshev, Int. J. Hydrog. Energy **36**, 1601 (2011)
28. M.G. Shelyapina, V.S. Kasperovich, N.E. Skryabina, D. Fruchart, Phys. Solid State **49**, 399 (2007)
29. S. Miraglia, D. Fruchart, N. Skryabina, M. Shelyapina, B. Ouladiaf, E. Hlil, J. Alloys Compd. **442**, 49 (2007)
30. B. Bandyopadhaya, S. Hayashi, Phys. Rev. B **60**, 10302 (1999)
31. S. Hayashi, J. Solid State Chem. **177**, 824 (2004)
32. C. Kim, S.-J. Hwang, R.C. Bowman Jr., M.H. Sørby, B. Hauback, J. Alloys Compd. **645**, S361 (2015)
33. S. Hayashi, K. Hayamizu, O. Yamamoto, J. Phys. Chem. Solid **45**, 555 (1984)
34. S. Hayashi, S. Orimo, H. Fujii, J. Alloys Compd. **261**, 145 (1997)
35. P.C.M.M. Magusin, W.P. Kalisvaart, P.H.L. Notten, R.A. van Santen, Chem. Phys. Lett. **456**, 55 (2008)
36. S. Srinivasan, P.C.M.M. Magusin, Solid State Nucl. Magn. Reson. **39**, 88 (2011)
37. S.-J. Hwang, R.C. Bowman Jr., J. Graetz, J.J. Reilly, W. Langley, C.M. Jensen, J. Alloys Compd. **446–447**, 290 (2007)
38. T.D. Humphries, K.T. Munroe, T.M. DeWinter, C.M. Jensen, G.S. McGrady, Int. J. Hydrog. Energy **38**, 4577 (2013)
39. U. Setthanan, B. MacMillan, G.S. McGrady, Int. J. Hydrog. Energy **34**, 8067 (2009)
40. O.J. Zogal, B. Stalinski, S. Idziak, Z. Phys. Chem. **145**, 167 (1985)
41. L. Senadheera, E.M. Carl, T.M. Ivancic, M.S. Conradi, R.C. Bowman Jr., S.-J. Hwang, T.J. Udovic, J. Alloys Compd. **463**, 1 (2008)
42. J.J. van der Klink, H.B. Brom, Prog. Nucl. Magn. Reson. Spectrosc. **36**, 89 (2000)
43. A. Narath, in *Hyperfine Interactions*, ed. by A.J. Freeman, R.B. Frankel (Academic, New York, 1967), p. 287
44. R. Göring, R. Lukas, K. Bohmhammel, J. Phys. C Solid State Phys. **14**, 5675 (1981)
45. R.C. Bowman Jr., E.L. Venturini, B.D. Craft, A. Attalla, D.B. Sullenger, Phys. Rev. B **27**, 1474 (1983)
46. A.H. Vuorimäki, E.E. Ylinen, B. Nowak, O.J. Żogał, Solid State Commun. **122**, 469 (2002)
47. S. Leyer, S. Heck, A. Kaiser, E. Dormann, R.G. Barnes, Phys. Rev. B **72**, 125115 (2005)

48. M. Gupta, in *Encyclopedia of Materials: Science and Technology*, 2nd edn., ed. by K.H.J. Buschow, R.W. Cahn, M.C. Flemings, B. Ilschner, E.J. Kramer, S. Mahajan, P. Veyssière (Elsevier, Oxford, 2002) p. 1
49. M.G. Shelyapina, D. Fruchart, Solid State Phenom. **170**, 227 (2011)
50. K.M. Nicholson, N. Chandrasekhar, D.S. Sholl, Acc. Chem. Res. **47**, 3275 (2014)
51. T.T. Phua, B.J. Baudry, D.T. Peterson, D.R. Torgeson, R.G. Barnes, M. Belhoul, G.A. Styles, E.F.W. Seymour, Phys. Rev. B **28**, 6227 (1983)
52. L.D. Bustard, Phys. Rev. B **22**, 1 (1980)
53. D.A. Faux, D.K. Ross, C.A. Sholl, J. Phys. Chem. **19**, 4115 (1986)
54. D.A. Faux, C.K. Hall, Z. Phys. Chem. N. F. **164**, 855 (1989)
55. N. Bloembergen, E.M. Purcell, R.M. Pound, Phys. Rev. **73**, 679 (1948)
56. H.C. Torrey, Phys. Rev. **92**, 962 (1953)
57. C.A. Sholl, J. Phys. Chem. **21**, 319 (1988)
58. D.C. Look, I.J. Lowe, J. Chem. Phys. **44**, 3437 (1966)
59. J.E. Anderson, J. Magn. Reson. **11**, 398 (1973)
60. A. Abragam, *The Principles of Nuclear Magnetism* (Clarendon, Oxford, 1961)
61. E.F.W. Seymour, J. Less-Common Met. **88**, 323 (1982)
62. A.V. Skripov, S.V. Rychkova, M.Y. Belyaev, A.P. Stepanov, J. Phys. Condens. Matter **2**, 7195 (1990)
63. O.A. Babanova, A.V. Soloninin, A.P. Stepanov, A.V. Skripov, Y. Filinchuk, J. Phys. Chem. C **114**, 3712 (2010)
64. O.A. Babanova, A.V. Soloninin, A.V. Skripov, D.B. Ravnsbæk, T.R. Jensen, Y. Filinchuk, J. Phys. Chem. C **115**, 10305 (2011)
65. T. Tsang, T.C. Farrar, J. Chem. Phys. **50**, 3498 (1969)
66. A.V. Skripov, A.V. Soloninin, Y. Filinchuk, D. Chernyshov, J. Phys. Chem. C **112**, 18701 (2008)
67. R. Flacau, C.R. Ratcliffe, S. Desgreniers, Y. Yao, D.D. Clug, P. Pallister, I.L. Moudrakovski, J.A. Ripmeester, Chem. Commun. **46**, 9164 (2010)
68. A.V. Skripov, A.V. Soloninin, O.A. Babanova, H. Hagemann, Y. Filinchuk, J. Phys. Chem. C **114**, 12370 (2010)
69. J.T. Markert, E.J. Cotts, R.M. Cotts, Phys. Rev. B **37**, 6446 (1988)
70. A.V. Soloninin, O.A. Babanova, A.V. Skripov, H. Hagemann, B. Richter, T.R. Jensen, Y. Filinchuk, J. Phys. Chem. C **116**, 4913 (2012)
71. D.T. Shane, L.H. Rayhel, Z. Huang, J.C. Zhao, X. Tang, V. Stavila, M.S. Conradi, J. Phys. Chem. C **115**, 3172 (2011)
72. A.V. Skripov, A.V. Soloninin, L.H. Rude, T.R. Jensen, Y. Filinchuk, J. Phys. Chem. C **116**, 26177 (2012)
73. A.V. Skripov, A.V. Soloninin, M.B. Ley, T.R. Jensen, Y. Filinchuk, J. Phys. Chem. C **117**, 14965 (2013)
74. A.V. Soloninin, O.A. Babanova, E.Y. Medvedev, A.V. Skripov, M. Matsuo, S. Orimo, J. Phys. Chem. C **118**, 14805 (2014)
75. A.V. Soloninin, A.V. Skripov, A.L. Buzlukov, A.P. Stepanov, J. Solid State Chem. **182**, 2357 (2009)
76. M. Witschas, H. Eckert, D. Wilmer, R.D. Banhatti, K. Funke, J. Fitter, R.E. Lechner, G. Korus, M. Jansen, Z. Phys. Chem. **214**, 643 (2000)
77. E.C. Reynhardt, C.F. Hoon, J. Phys. Condens. Matter **16**, 6137 (1983)
78. G.H. Penner, Y.C.P. Chang, J. Hutzal, Inorg. Chem. **38**, 2868 (1999)
79. O. Gunaydin-Sen, R. Achey, N.S. Dalal, A. Stowe, T. Autrey, J. Phys. Chem. B **111**, 677 (2007)
80. S.-J. Hwang, R.C. Bowman, J.W. Reiter, J. Rijssenbeek, G.L. Soloveichik, J.-C. Zhao, H. Kabbour, C.C. Ahn, J. Phys. Chem. C **112**, 3164 (2008)
81. N. Verdal, H. Wu, T.J. Udovic, V. Stavila, W. Zhou, J.J. Rush, J. Solid State Chem. **184**, 3110 (2011)

82. M. Paskevicius, M.P. Pitt, D.H. Brown, D.A. Sheppard, S. Chumphongphan, C.E. Buckley, Phys. Chem. Chem. Phys. **15**, 15825 (2013)
83. I. Tiritiris, T. Schleid, K. Müller, Appl. Magn. Reson. **32**, 459 (2007)
84. A.V. Skripov, O.A. Babanova, A.V. Soloninin, V. Stavila, N. Verdal, T.J. Udovic, J.J. Rush, J. Phys. Chem. C **117**, 25961 (2013)
85. N. Verdal, J.-H. Her, V. Stavila, A.V. Soloninin, O.A. Babanova, A.V. Skripov, T.J. Udovic, J.J. Rush, J. Solid State Chem. **212**, 81 (2014)
86. E.G. Sorte, S.B. Emery, E.H. Majzoub, T. Ellis-Caleo, Z.L. Ma, B.A. Hammann, S.E. Hayes, R.C. Bowman, M.S. Conradi, J. Phys. Chem. C **118**, 5725 (2014)
87. J. Senker, Solid State Nucl. Magn. Reson. **26**, 22 (2004)
88. D.T. Shane, R.L. Corey, C. McIntosh, L.H. Rayhel, R.C. Bowman, J.J. Vajo, A.F. Gross, M.S. Conradi, J. Phys. Chem. C **114**, 4008 (2010)
89. R.L. Corey, D.T. Shane, R.C. Bowman, M.S. Conradi, J. Phys. Chem. C **112**, 18706 (2008)
90. A.V. Skripov, M.Y. Belyaev, S.V. Rychkova, A.P. Stepanov, J. Phys. Condens. Matter **1**, 2121 (1989)
91. A.L. Buzlukov, A.V. Skripov, J. Alloys Compd. **366**, 61 (2004)
92. A.V. Skripov, Defect Diffus. Forum **224–225**, 75 (2003)
93. A.V. Skripov, J. Alloys Compd. **404–406**, 224 (2005)
94. A.V. Skripov, V. Paul-Boncour, T.J. Udovic, J.J. Rush, J. Alloys Compd. **595**, 28 (2014)
95. A.V. Skripov, A.L. Buzlukov, V.N. Kozhanov, T.J. Udovic, Q. Huang, J. Alloys Compd. **359**, 27 (2003)
96. A.V. Skripov, M.Y. Belyaev, S.V. Rychkova, A.P. Stepanov, J. Phys. Condens. Matter **3**, 6277 (1991)
97. G. Majer, U. Kaess, M. Stoll, R.G. Barnes, J. Shinar, Defect Diffus. Forum **143–147**, 957 (1997)
98. R. Hempelmann, D. Richter, A. Heidemann, J. Less-Common Met. **88**, 343 (1982)
99. A.V. Skripov, M. Pionke, O. Randl, R. Hempelmann, J. Phys. Condens. Matter **11**, 1489 (1999)
100. A.V. Skripov, A.V. Soloninin, A.L. Buzlukov, L.S. Voyevodina, J.C. Cook, T.J. Udovic, R. Hempelmann, J. Phys. Condens. Matter **17**, 5011 (2005)
101. C. Schönfeld, R. Hempelmann, D. Richter, T. Springer, A.J. Dianoux, J.J. Rush, T.J. Udovic, S.M. Bennington, Phys. Rev. B **50**, 853 (1994)
102. A.L. Buzlukov, A.V. Soloninin, A.V. Skripov, Solid State Commun. **129**, 315 (2004)
103. A.V. Skripov, A.V. Soloninin, A.P. Stepanov, V.N. Kozhanov, J. Phys. Condens. Matter **12**, 9607 (2000)
104. E. Mamontov, T.J. Udovic, O. Isnard, J.J. Rush, Phys. Rev. B **70**, 214305 (2004)
105. A.V. Skripov, N.V. Mushnikov, P.B. Terent'ev, V.S. Gaviko, T.J. Udovic, J.J. Rush, J. Phys. Condens. Matter **23**, 405402 (2011)
106. L. Lichty, J. Shinar, R.G. Barnes, D.R. Torgeson, D.T. Peterson, Phys. Rev. Lett. **55**, 2895 (1985)
107. D.S. Sibirtsev, Y.G. Cherepanov, A.V. Skripov, J. Alloys Compd. **278**, 21 (1998)
108. L. Senadheera, M.S. Conradi, J. Phys. Chem. B **111**, 12097 (2007)
109. R. Kumar, D.D. Klug, C.I. Ratcliffe, C.A. Tulk, J.A. Ripmeester, Angew. Chem. Int. Ed. **52**, 1531 (2013)
110. J. Völkl, G. Alefeld, in *Hydrogen in Metals I*, ed. by G. Alefeld, J. Völkl (Springer, Berlin, 1978), p. 321
111. H. Wipf, in *Hydrogen in Metals III*, ed. by H. Wipf (Springer, Berlin, 1997), p. 51
112. W. Renz, G. Majer, A.V. Skripov, A. Seeger, J. Phys. Condens. Matter **6**, 6367 (1994)
113. G. Majer, W. Renz, A. Seeger, R.G. Barnes, J. Shinar, A.V. Skripov, J. Alloys Compd. **231**, 220 (1995)
114. W. Renz, G. Majer, A.V. Skripov, J. Alloys Compd. **224**, 127 (1995)
115. U. Eberle, G. Majer, A.V. Skripov, V.N. Kozhanov, J. Phys. Condens. Matter **14**, 153 (2002)
116. G. Majer, Mater. Res. Soc. Symp. Proc. **513**, 109 (1998)

117. A.V. Skripov, K. Ulrich, F. Grinberg, A.V. Soloninin, A.L. Buzlukov, J. Alloys Compd. **475**, 16 (2009)
118. F. Grinberg, G. Majer, A.V. Skripov, J. Alloys Compd. **425**, 24 (2006)
119. A.V. Vyvodtceva, M.G. Shelyapina, A.F. Privalov, D. Fruchart, J. Alloys Compd. **614**, 364 (2014)
120. R. Messer, A. Blessing, S. Dais, D. Höpfel, G. Majer, C. Schmidt, A. Seeger, W. Zag, R. Lässer, Z. Phys. Chem. N. F. H2 (Suppl.), 61 (1986)
121. M. Hampele, G. Majer, R. Messer, A. Seeger, J. Less-Common Met. **172–174**, 631 (1991)
122. D. Emin, M.I. Baskes, W.D. Wilson, Z. Phys, Chem. N. F. **114**, 231 (1979)
123. C.P. Flynn, A.M. Stoneham, Phys. Rev. B **1**, 3966 (1970)
124. M. Bée, *Quasielastic Neutron Scattering* (Hilger, Bristol, 1988)
125. R. Hempelmann, *Quasielastic Neutron Scattering and Solid State Diffusion* (Clarendon, Oxford, 2000)
126. N. Verdal, T.J. Udovic, J.J. Rush, H. Wu, A.V. Skripov, J. Phys. Chem. C **117**, 12010 (2013)

Chapter 13
Positron Annihilation Spectroscopy (PAS)

Kouji Sakaki

Abstract A positron is an anti-particle of an electron and is annihilated with the electron in a sample. When lattice defects with open-volume exist in the samples, positrons are trapped there. Therefore, positron annihilation spectroscopy (PAS) is used to investigate lattice defects in samples. In this chapter, we will introduce the principles of the PAS technique and show some examples of how PAS was applied to studies on hydrogen storage materials. The topics are the formation mechanism of lattice defects by the initial hydrogenation in $LaNi_5$-based alloys and the effect of hydrogen charging on the formation of lattice defects by tensile strain (hydrogen embrittlement). PAS showed that both vacancies and dislocations are introduced by the initial hydrogenation in $LaNi_{4.5}M_{0.5}$ and by plastic deformation in pure Fe. The presence of hydrogen enhanced the increase in the concentration of vacancies rather than the dislocation density in pure Fe.

Keywords Positron annihilation • Lattice defects • Vacancies • Dislocations • Hydrogen storage • $LaNi_5$ • $LaNi_5Cu$ • $LaNi_5$-based alloys

13.1 Introduction

Positron annihilation spectroscopy (PAS) is a technique to investigate lattice defects in samples. By using this method, the lattice defects associated with open-volume such as vacancies, vacancy clusters (voids), and dislocations can be observed. We have applied this method for understanding the formation mechanisms of lattice defects during the hydrogenation in hydrogen storage materials. In this chapter, we will introduce the principles of the PAS technique and show some examples of how PAS was applied to studies on hydrogen storage materials. How PAS can be applied in other scientific fields of solid-state physics is described in detail elsewhere [1–4].

K. Sakaki (✉)
National Institute of Advanced Industrial Science and Technology, Research Institute of Energy Frontier, Hydrogen Industrial Use and Storage Group, AIST Tsukuba Central 5, 1-1-1 Higashi, Tsukuba 305-8565, Ibaraki, Japan
e-mail: kouji.sakaki@aist.go.jp

H. Fritzsche et al. (eds.), *Neutron Scattering and Other Nuclear Techniques for Hydrogen in Materials*, Neutron Scattering Applications and Techniques,
DOI 10.1007/978-3-319-22792-4_13

The positron, the anti-particle of the electron, was predicted by Dirac [5] and was discovered by Anderson [6, 7]. The rest mass of the positron ($9.10938188 \times 10^{-28}$ g) is the same as the electron but its charge is opposite ($+1.602176462 \times 10^{-19}$ C). There are two ways to create positrons. One is to use radioisotopes which undergo β^+ decay such as ^{22}Na, ^{68}Ge, etc. Among them, ^{22}Na is the most popular radioisotope for the positron annihilation studies, especially the positron lifetime measurement. This is because the half-life of ^{22}Na is long (2.6 years) and a γ ray with 1.275 MeV is emitted almost simultaneously with the positron production by the following reaction:

$$^{22}\mathrm{Na} \rightarrow {}^{22}\mathrm{Ne} + \beta^+ + \gamma$$

For the positron lifetime measurement, this γ ray acts as the start signal indicating the positron birth. The other method of creating positrons is by irradiating metals with high energy (>1.022 MeV) photons or electrons. This so-called pair production creates a positron and an electron.

When the positrons are implanted into a sample, they lose their kinetic energy within a few ps and possess only thermal energy after this short time period. The implantation depth of the positrons generated by the β^+ decay of ^{22}Na is in the range of 0.1–1 mm, depending on the density of the samples. The thermalized positrons diffuse in the sample's lattice and their diffusion length is generally around 100 nm in the perfect crystal without lattice defects. When the positron collides with an electron during the diffusion, both the positron and the electron are annihilated. During the annihilation process, two γ rays are emitted in almost opposite directions. The energy of each γ ray is 0.511 ($\pm\Delta E$) MeV because of the conservation of the total energy and momentum of a positron–electron pair. This γ ray is taken as the stop signal for the positron lifetime measurement or to evaluate the electron momentum distribution. In a perfect lattice, the positrons are delocalized at interstitial sites during diffusion because of the repulsive force from an ion core as shown in Fig. 13.1a and then are annihilated there. When

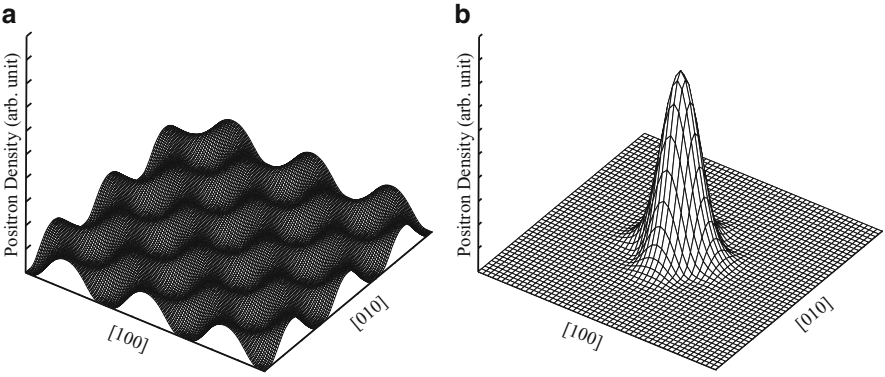

Fig. 13.1 Calculated positron density in Pd; (**a**) a perfect crystal and (**b**) a crystal with a vacancy [8]

there are the lattice defects in the sample, the positrons are trapped there. This is because the lattice defects have a negative charge compared to the positive charge of the positron. Therefore, the positrons are localized at the lattice defects as shown in Fig. 13.1b. In addition, because of this affinity of the positron to lattice defects, vacancy concentrations down to the ppm level can be detected. The positron annihilation spectrum depends on the type and the concentration of lattice defects and the local electronic structure at the positron annihilation sites. The PAS technique consists of positron lifetime measurement, (coincidence) Doppler broadening measurement, and angular correlation of the annihilation radiation. The positron lifetime is sensitive to the electron density at positron annihilation sites and the others are sensitive to the momentum of the electron taking part in the annihilation. The details will be explained in the following paragraphs.

13.2 Principles and Setup of the PAS

13.2.1 Positron Lifetime Measurement

Figures 13.2 and 13.3 show the instrumental setup for the positron lifetime measurement. When ^{22}Na is used as the positron source, a positron and a γ ray with 1.275 MeV are generated by β^+ decay. This γ ray is detected by one of the detectors as a positron birth signal. The detector consists of a scintillator (BaF_2) and a photomultiplier tube (PMT). Usually the ^{22}Na sealed by kapton films is placed between two identical samples as shown in Fig. 13.3. Therefore, most of the generated positrons penetrate into the samples and approximately 10–20 % of the positrons are annihilated in the kapton films. The implanted positrons diffuse in the samples and annihilate with electrons at the interstitial site or the lattice defects. Then two γ rays with 0.511 ($\pm\Delta E$) MeV are emitted in almost opposite directions. One of these γ rays is detected by the other detector as a positron annihilation signal. The positron lifetime is obtained by measuring the time difference between

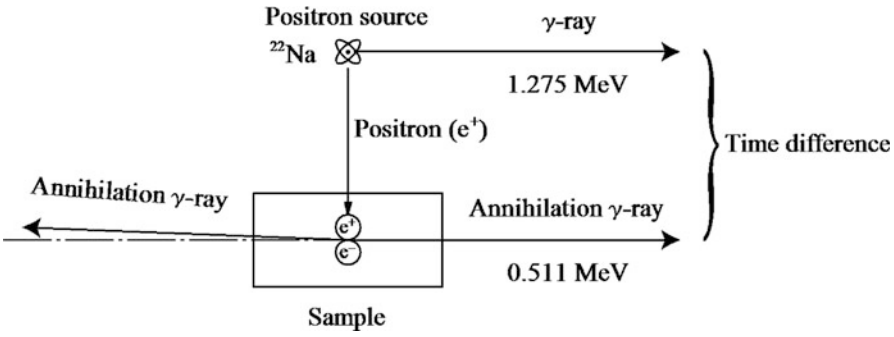

Fig. 13.2 Experimental setup for a positron lifetime measurement

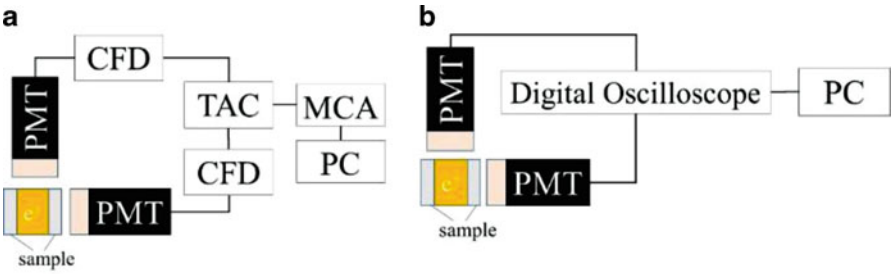

Fig. 13.3 Electronic setup of a positron lifetime measurement with an analog-type system (**a**) and a digital-type system (**b**); PMT, CFD, TAC, and MCA stand for photomultiplier tube, constant fraction discriminator, time-to-amplitude converter, and multi-channel analyzer

the γ rays with 1.275 and 0.511 MeV. Using an analog-type system, the γ ray energy is selected by a constant fraction discriminator (CFD) and the time difference between the positron creation and annihilation signals is converted into an amplitude using a time-to-amplitude converter (TAC). The histogram is generated by a multi-channel analyzer (MCA). Recently the performance of analog–digital converters of digital oscilloscopes has been improved significantly. Therefore, the system comprised of CFD, TAC, and MCA can be replaced by a digital oscilloscope [9]. This digital-type system shows better time resolution and signal-to-noise ratios than the analog system. It is also crucial for the positron lifetime measurement to use a detector with excellent time resolution such as a scintillator in combination with a PMT.

The positron lifetime is in good approximation described with the following equation [10]:

$$\tau = \frac{1}{2 \times 134 n_0} \times 10^3 \,(\mathrm{ps}) \tag{13.1}$$

with n_0 (a.u.; atomic unit) being the electron density. Therefore, the positron lifetime shows a characteristic dependence on the atomic number in completely defect-free metals as can be seen in Fig. 13.4 [11]. If there are lattice defects in samples, the positron annihilation probability decreases because the electron density at the lattice defects is much lower than at the interstitial sites and then the positron lifetime increases depending on the size of open-volume of lattice defects. Therefore, the positron lifetimes in samples with lattice defects are much longer than in perfect lattices. Figure 13.5 shows the calculated positron lifetimes in vacancy clusters as a function of the number of vacancies [12]. The positron lifetime increases with increasing number of vacancies in the vacancy cluster. Figure 13.6 shows the positron annihilation rate, which is inverse proportional to the positron lifetimes, of dislocations with different Burgers vectors [13]. The positron annihilation rate changes with Burgers vectors because of the different free volumes at their dislocation cores. These figures show that each lattice defect

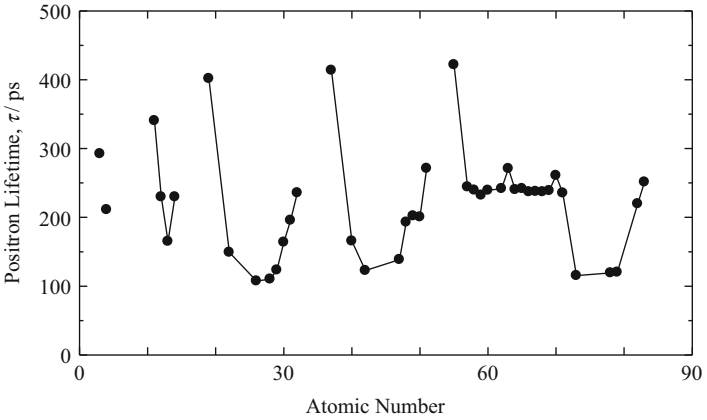

Fig. 13.4 Positron lifetimes in metals [11]

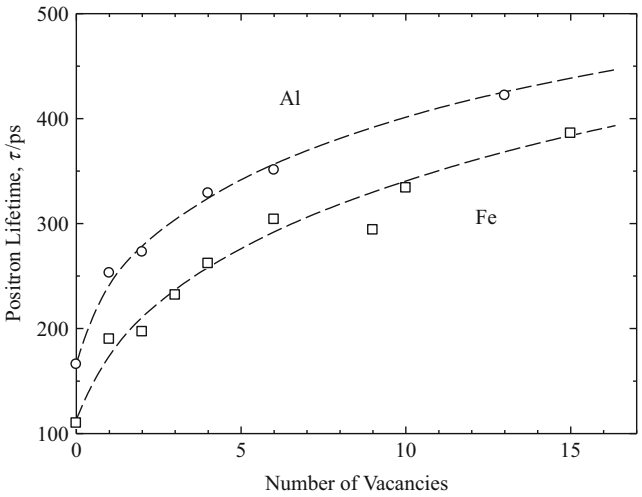

Fig. 13.5 Calculated positron lifetimes in vacancy clusters as a function of the number of vacancies [12]

corresponds to a different positron lifetime. Therefore, the type of the lattice defects can be identified by the analysis of the positron lifetime spectrum.

In order to ensure good statistics and measurement reproducibility, more than 10^6 positron annihilation events are collected to make a positron lifetime spectrum (Fig. 13.7) and several spectra are obtained at the same conditions. A part of the generated positrons (10–20 %) are annihilated in kapton films because ^{22}Na is sealed by kapton films. Therefore, it is important to evaluate the contribution of the positron annihilation in kapton films accurately. It is recommended that the positron lifetime spectrum of the completely defect-free target sample is measured before

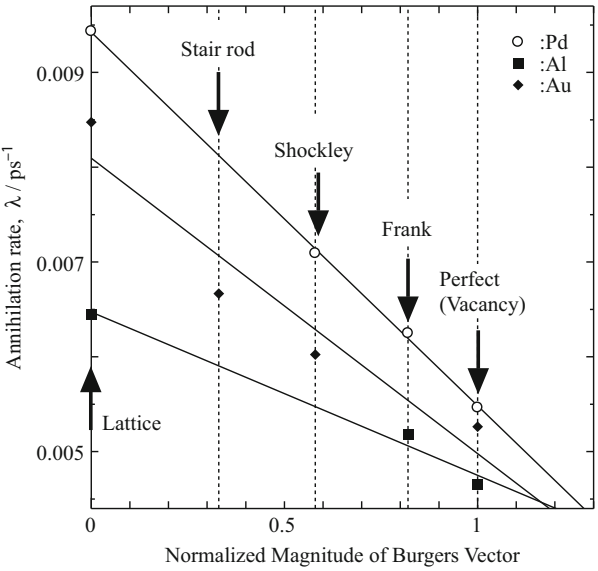

Fig. 13.6 Positron lifetimes of dislocations with different Burgers vectors [13]

Fig. 13.7 Positron lifetime spectra in $LaNi_5$ before and after hydrogenation

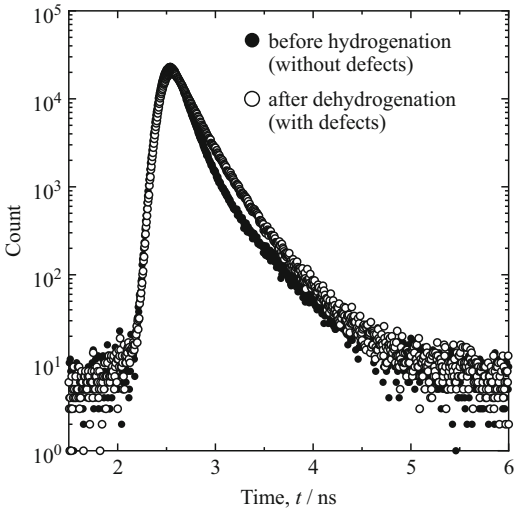

doing the experiments. This is the easiest way to evaluate the contribution of the positron annihilation because positrons annihilate only in kapton films and at the interstitial site in samples. In addition, the resolution function is also determined from this spectrum using the code Resolution [14]. The positron lifetime spectra are analyzed using the Positronfit Extended program [15, 16]. Information about another software for the analysis of positron lifetime spectra can be found in [4].

If all positrons annihilate in a perfect lattice, the positron lifetime spectrum, $I(t)$ exhibits a simple exponential form:

$$I(t) = (1/\tau_f)\exp(-t/\tau_f) \qquad \tau_f = \frac{1}{\lambda_f} \tag{13.2}$$

where τ_f and λ_f are the lifetime of positrons annihilating at interstitial sites of the perfect lattice and its annihilation rate, respectively. When lattice defects with lower concentration exist in the samples, some positrons annihilate in these lattice defects and the others annihilate at interstitial sites. In this case, the positron lifetime spectrum consists of discrete multiple components.

$$I(t) = (I_0/\tau_0)\exp(-t/\tau_0) + (I_d/\tau_d)\exp(-t/\tau_d) \qquad \tau_0 = \frac{1}{\lambda_f + \kappa_d} \qquad \tau_d = \frac{1}{\lambda_d} \tag{13.3}$$

where I and κ are the relative intensity and the positron-trapping rate, respectively. τ_0 and τ_d are positron lifetimes for un-trapped positron and at the defects, respectively. According to these equations, τ_0 is shorter than τ_f because of the effect of positron trapping at the lattice defects. Taking into account a two-state trapping model [17], the obtained τ_0, τ_d, and I_0, I_d must satisfy the following equation:

$$\frac{1}{\tau_f} = \frac{I_0}{\tau_0} + \frac{I_d}{\tau_d} \tag{13.4}$$

If the positron lifetime spectrum cannot be decomposed into discrete multiple components, the mean positron lifetime can be used to monitor the change in the defect structure. The mean positron lifetime can be approximately expressed by the following equation:

$$I(t) = (1/\tau_m)\exp(-t/\tau_m) \qquad \tau_m = \sum_{i=1}^{N} I_i \tau_i \tag{13.5}$$

where I_i denotes the relative intensity of the τ_i component.

When the concentration of a certain type of lattice defect dominates, all the positrons are always trapped there and then the positron lifetime spectrum exhibits a single exponential form because no positrons annihilate at the interstitial sites.

$$I(t) = (1/\tau_d)\exp(-t/\tau_d) \tag{13.6}$$

As shown in Fig. 13.7, the slope of the positron lifetime spectrum changed after dehydrogenation compared with that before hydrogenation. This indicates that the longer positron lifetime component was caused by hydrogenation. The details will be described later.

13.2.2 (Coincidence) Doppler Broadening Measurement

Here, the principle of (coincidence) Doppler broadening measurement will be explained. As described above, two γ rays with 0.511 MeV are immediately emitted in opposite directions when the positron annihilates with the electron. The energy of γ rays are slightly shifted by $\pm\Delta E$ ($=p_z c/2$) from 0.511 MeV because of the momentum of the electron taking part in the annihilation process. The p_z is the electron momentum in the propagation direction. In a Doppler broadening measurement, the energy distribution of the γ rays is recorded with a detector with excellent energy resolution, e.g., a Ge detector with a liquid-nitrogen cooling system. Figure 13.8 shows the instrumental setup for a Doppler broadening measurement. One of the γ rays with 0.511 MeV is detected by a Ge detector. The detected γ ray causes a charge separation, which with the help of a preamplifier and an amplifier, is converted into an electric pulse height that corresponds to the energies of the γ rays. The histogram is generated by an analog-to-digital converter (ADC) and a MCA. The coincidence Doppler broadening (CDB) technique with two Ge detectors was also proposed [18, 19]. In this method, both γ rays with 0.511 MeV are detected simultaneously. The advantage of this method is that the background level is dramatically reduced at higher momentum region compared with the conventional Doppler broadening measurement as shown in Fig. 13.9 and the information in this high-momentum region can be extracted. The high-momentum region of the Doppler broadening spectrum contains information on the core electrons, which are characteristic for each element. Therefore, the elements, to which the annihilated electron belongs, can be identified experimentally using the CDB technique.

Figure 13.10 shows an example of a change in the Doppler broadening spectrum by the formation of lattice defects after hydrogenation of $LaNi_5$. The Doppler broadening spectrum became narrower after hydrogenation. The shape of the Doppler broadening spectrum depends on the momentum of the electrons being annihilated together with the positrons. Valence electrons contribute to the central part of the Doppler broadening spectrum because of their lower momentum (small ΔE) while core electrons contribute to the tail of the spectrum because the core electrons have higher momentum (larger ΔE) than the valence electrons. When the

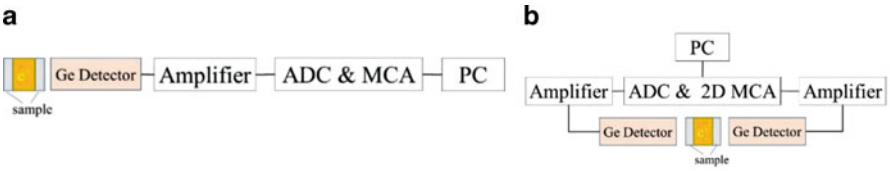

Fig. 13.8 Schematic setup for (**a**) 1D and (**b**) 2D Doppler broadening measurements. ADC and MCA stand for analog-to-digital converter and multi-channel analyzer

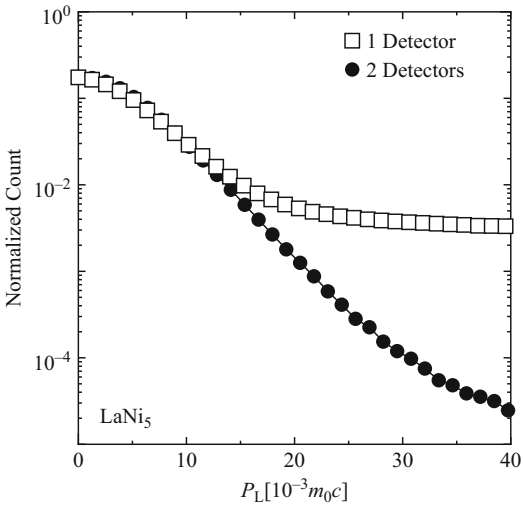

Fig. 13.9 Comparison of Doppler broadening spectra with 1 detector and 2 detectors

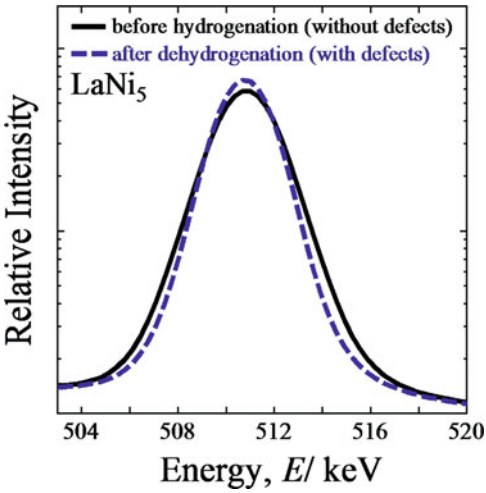

Fig. 13.10 Change in Doppler broadening spectra by the lattice defects

lattice defects are introduced, the positron annihilation probability with the valence electrons becomes high compared with a perfect lattice because of the positron trapping at the lattice defects. Therefore, the Doppler broadening spectrum becomes narrower by introducing the lattice defects. In fact, as shown in Fig. 13.10, the Doppler broadening spectrum of $LaNi_5$ became narrower by hydrogenation. This indicates that the lattice defects are introduced in $LaNi_5$ by hydrogenation. This is consistent with the positron lifetime measurement shown in Fig. 13.7.

For the quantitative analysis of the Doppler broadening spectrum, two specific parameters, S and W are used. They are defined as follows:

$$S = \frac{\text{Central part of spectrum}}{\text{whole spectrum}}, \quad \text{Central part of spectrum} = \int_{E_0-E_s}^{E_0+E_s} N_D dE$$
$$W = \frac{\text{tail part of spectrum}}{\text{whole spectrum}}, \quad \text{tail part of spectrum} = \int_{E_1}^{E_2} N_D dE \tag{13.7}$$

where N_D is the intensity of the Doppler broadening spectrum in each energy channel. S represents the contribution of valence electrons to the Doppler broadening spectrum while W represents the contribution of the core electrons. When the lattice defects are introduced, the fraction of the positron annihilation with the valence electrons increases and that with core electron decreases. This leads to an increase of S and a decrease of W.

13.3 Examples of Positron Annihilation Studies on Lattice Defects

13.3.1 Formation of Lattice Defects Upon Hydrogenation in $LaNi_5$-Based Alloys [20]

It is important to identify the types of lattice defects introduced by the initial hydrogenation and to understand the effect of substitution on the formation of the lattice defects. Therefore, positron lifetime measurement was applied in $LaNi_{4.5}M_{0.5}$ (M = Al, Co, Ni) after the initial hydrogenation and dehydrogenation. Here, the types of lattice defects introduced in $LaNi_{4.5}M_{0.5}$ and substitution effect on the formation of the lattice defects will be shown.

For positron annihilation experiments, it is strongly recommended to prepare a fully annealed and defect-free sample. It is because it becomes easy to accurately evaluate the contribution of positron annihilation in kapton films and to determine the resolution function of the positron lifetime equipment. For this purpose, $LaNi_5$, $LaNi_{4.5}Co_{0.5}$, and $LaNi_{4.5}Al_{0.5}$ were annealed at 1223 K. After this annealing the positron lifetimes in $LaNi_5$, $LaNi_{4.5}Co_{0.5}$, and $LaNi_{4.5}Al_{0.5}$ were 126, 121, and 129 ps, respectively. These values are close to the positron lifetime in a perfect crystal of $LaNi_5$ (125 ps) calculated by the DV-Xα cluster method [21] using the program code SCAT [22, 23]. It indicates that the fully annealed $LaNi_5$-based alloys had no lattice defects where the positrons are trapped. After the initial hydrogenation at 7 MPa and then dehydrogenation at 296 K, the mean positron

lifetimes which were obtained by one-component analysis increased by more than 50 ps and were 198, 193, and 181 ps in $LaNi_5$, $LaNi_{4.5}Co_{0.5}$, and $LaNi_{4.5}Al_{0.5}$, respectively. As described above, the positron lifetimes of the lattice defects are much higher than that in the perfect lattice. In addition, these mean positron lifetimes after the dehydrogenation were higher than the calculated positron lifetimes of Ni vacancies in $LaNi_5$ (166–177 ps) [21]. Therefore, this suggests that vacancy clusters such as di- or tri-vacancies were introduced by the initial hydrogenation and dehydrogenation.

In general, the lattice defects are recovered by annealing and the recovery temperature depends on the type of the lattice defects and samples. This recovery behavior is also an important information to identify the type of the lattice defects. Therefore, the isochronal annealing (temperature increase at a constant rate) with the positron lifetime measurement is often carried out. Figure 13.11 shows the mean positron lifetime changes during the isochronal annealing in $LaNi_{4.5}M_{0.5}$ after the initial hydrogenation. In $LaNi_5$ the mean positron lifetime increased up to 240 ps with increasing of the annealing temperature to 623 K and then decreased to 170 ps at 723 K. In these temperature ranges, additional lattice defects are not introduced by the annealing in $LaNi_5$. Therefore, this increase of the mean positron lifetime cannot be explained by the formation of lattice defects but can be explained only by vacancy clustering. It is because that if the vacancy concentration is high enough excess vacancies form larger vacancy clusters during the recovery process and then these vacancy clusters are annealed out at higher temperature leading to the increase and decrease of the mean positron lifetime with increasing the annealing temperature. In fact, the positron lifetime in vacancy clusters in $LaNi_5$ increased with their dimensions as shown in Fig. 13.12. Therefore, these clearly indicate that vacancies were introduced by the initial hydrogenation.

Above 773 K, the mean positron lifetimes in $LaNi_5$ gradually decreased with increasing the annealing temperature. Even after annealing at 1273 K, however, the

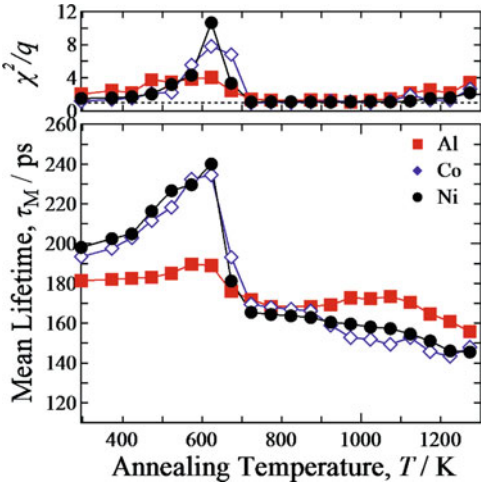

Fig. 13.11 Change in mean positron lifetime of $LaNi_{4.5}M_{0.5}$ after hydrogenation during isochronal annealing, reprinted from Sakaki et al. [20] with permission from Elsevier Ltd.

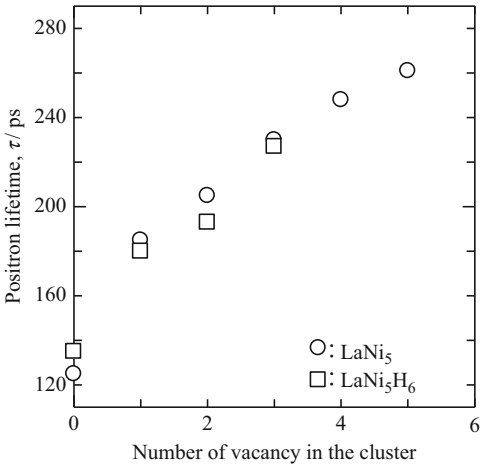

Fig. 13.12 Calculated positron lifetimes of vacancy clusters in $LaNi_5$, reprinted from Sakaki et al. [20], with permission from Elsevier Ltd.

mean positron lifetime did not go back to the lifetime in fully annealed $LaNi_5$. It means that another type of lattice defect with higher migration temperature than vacancies exists after the initial hydrogenation.

The change in the mean positron lifetime as a function of the annealing temperature in $LaNi_{4.5}Co_{0.5}$ was identical to that in $LaNi_5$. That means that $LaNi_{4.5}Co_{0.5}$ after the initial hydrogenation had a similar defect structure to $LaNi_5$. On the other hand, $LaNi_{4.5}Al_{0.5}$ showed slightly different behavior. The mean positron lifetime after the initial hydrogenation is shorter than the others and the magnitude of the mean positron lifetime change during the isochronal annealing was much smaller although it increased and decreased in the same temperature range. This suggests that vacancies were introduced in $LaNi_{4.5}Al_{0.5}$ by the initial hydrogenation, but $LaNi_{4.5}Al_{0.5}$ had a lower vacancy concentration than $LaNi_5$.

To evaluate the type of lattice defects and their concentration, the multi-component analysis for the positron lifetime spectra obtained during the isochronal annealing was performed as shown in Fig. 13.13. The positron lifetime spectra that were obtained in the temperature range below 723 K (Stage I) were decomposed into two components, larger than 200 and 160 ps. The former value is much higher than the positron lifetimes for Ni vacancies (166–177 ps) in $LaNi_5$ [21]. The positron lifetime increased up to around 400 ps with the annealing temperature and its relative intensity decreased. At 723 K, this lattice defect was completely recovered. The recovery temperature of this lattice defect agrees well with the vacancy migration temperature in $LaNi_5$ [24]. Therefore, this clearly showed that this positron lifetime component comes from the vacancy cluster (di- or tri-vacancy) introduced by hydrogenation. In this temperature range, the anomalous change of the c/a ratio of $LaNi_5$ after hydrogenation was reported suggesting the formation of finite defects such as small dislocation loops and vacancies [25]. This agrees with the result obtained by the positron lifetime measurement.

In Stage III shown in Fig. 13.13, the positron lifetime spectra were decomposed into two components, 160 and less than 125 ps. The former positron lifetime

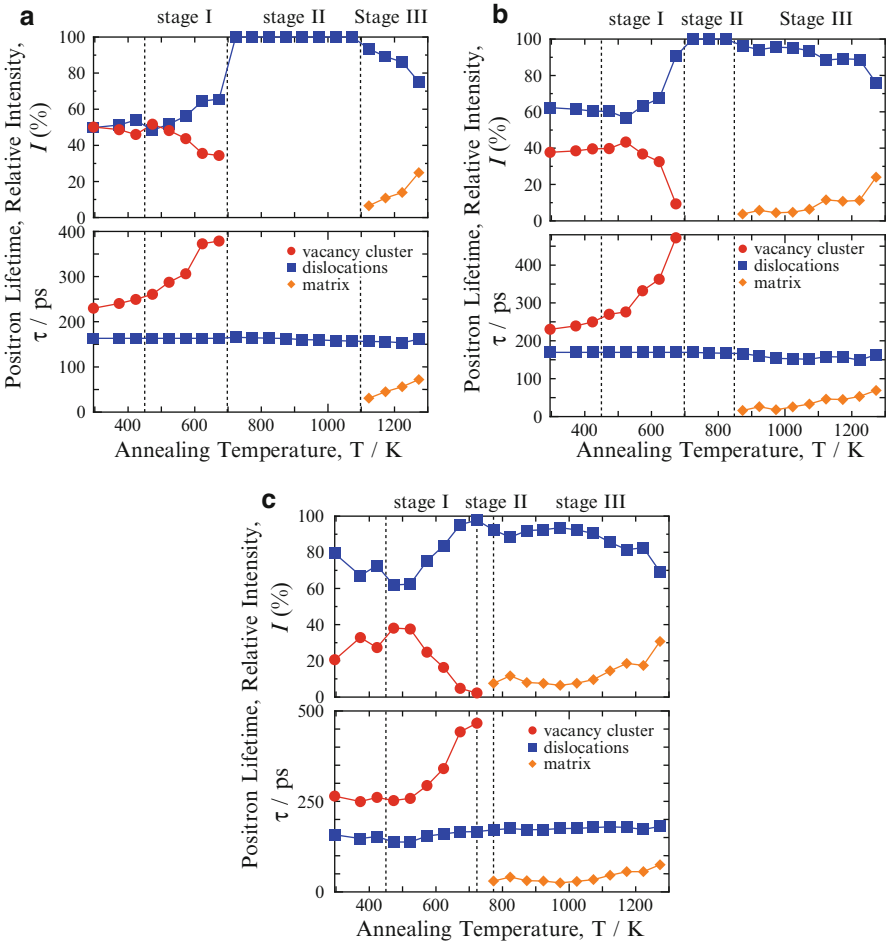

Fig. 13.13 Results of multi-component analysis of positron lifetime spectrum of $LaNi_{4.5}M_{0.5}$ after hydrogenation during isochronal annealing; (**a**) $LaNi_5$, (**b**) $LaNi_{4.5}Co_{0.5}$, and (**c**) $LaNi_{4.5}Al_{0.5}$. Reprinted from Sakaki et al. [20] with permission from Elsevier Ltd.

component was also obtained in Stage I. This positron lifetime is in between the fully annealed alloy (122–125 ps) and Ni vacancy (166–177 ps). During the whole isochronal annealing this value stayed constant and only its relative intensity decreased at higher temperatures (Stage III). In general the positron lifetimes of dislocations are shorter than that of the mono-vacancy as shown in Fig. 13.6 and the positron lifetimes of dislocations do not change during the recovery process. Therefore, this component comes from dislocations. The shorter positron lifetime obtained in Stage III was shorter than that for a fully annealed $LaNi_{4.5}M_{0.5}$. According to Eqs. (13.2) and (13.3), τ_0 is shorter than τ_f because of the effect of positron trapping at the lattice defect. Therefore, this positron lifetime component is caused by the free positrons which are annihilated at interstitial sites. Therefore,

these results clearly show that both, vacancy and dislocation, were introduced by the initial hydrogenation in $LaNi_{4.5}M_{0.5}$.

All positrons were trapped at dislocations even at 723 K in $LaNi_{4.5}M_{0.5}$. Therefore, it is impossible to estimate the dislocation density directly by means of the positron lifetime technique. Assuming that the substitution element does not influence the recovery temperature of dislocations, the positron lifetime component for the free positrons appears at lower annealing temperature in the sample with lower dislocation density compared to samples with a higher dislocation density. Therefore, the onset temperature which the positron lifetime component for the free positrons is observed, can be used as an indicator of the dislocation density. These temperatures were 1073, 873, and 773 K for $LaNi_5$, $LaNi_{4.5}Co_{0.5}$, and $LaNi_{4.5}Al_{0.5}$, respectively. This suggests that Al substitution prevented the formation of dislocations as well as vacancy formation. The result for dislocation agrees with TEM observation and synchrotron powder diffraction [26, 27].

By using the trapping model [28–30], the concentrations for vacancies introduced by the initial hydrogenation were estimated [31]. When all the positrons are trapped at either dislocations or vacancies, the positron lifetimes and the relative intensities can be described with the following equations:

$$\begin{aligned} \tau_d &= \frac{1}{\lambda_d}, \quad I_d = \frac{\kappa_d}{\kappa_d + \kappa_v} \\ \tau_v &= \frac{1}{\lambda_v}, \quad I_v = \frac{\kappa_v}{\kappa_d + \kappa_v} \end{aligned} \tag{13.8}$$

where the subscripts "v" and "d" mean vacancy and dislocation, respectively. Each positron-trapping rate is proportional to the concentration of each lattice defect according to the following equation:

$$\kappa_i = \mu_i \rho_i \tag{13.9}$$

where μ is the specific positron-trapping rate; and ρ, the concentration of the lattice defect. From these equations, the vacancy concentration can be determined using the following equation:

$$\rho_v = (I_v/(1 - I_v)) \times (\mu_d/\mu_v) \times \rho_d \tag{13.10}$$

The general specific trapping rates for vacancy and dislocation in metals, $\mu_v = 10^{14}\ s^{-1}$ and $\mu_d = 1\ cm^2\ s^{-1}$, respectively were adopted here [32–34] because these specific trapping rates for $LaNi_5$-based alloys have not been reported. The dislocation densities in $LaNi_5$, $LaNi_{4.25}Co_{0.75}$, and $LaNi_{4.7}Al_{0.3}$ reported using the synchrotron X-ray powder diffraction are 2.5×10^{11}, 2.0×10^{11}, and $0.29 \times 10^{11}\ cm^{-2}$, respectively [26]. Assuming that the dislocation densities of $LaNi_{4.5}M_{0.5}$ are the same as their values because the composition of these alloys are similar, the vacancy concentrations for $LaNi_5$, $LaNi_{4.5}Co_{0.5}$, and $LaNi_{4.5}Al_{0.5}$ were 0.25, 0.13, and 0.01 atomic%, respectively. This indicates that the vacancy formation upon hydrogenation was suppressed by Al substitution.

13.3.1.1 Summary

The types of lattice defects introduced by the initial hydrogenation in $LaNi_{4.5}M_{0.5}$ (M = Al, Co, Ni) were identified by the positron lifetime technique and the effect of substitution on the formation of the lattice defects was investigated. The multicomponent analysis of positron lifetime spectra indicates that both, vacancies and dislocations, were introduced by the initial hydrogenation in $LaNi_{4.5}M_{0.5}$. In addition, Al substitution significantly suppressed the formation of vacancies and dislocations and Co substitution did not.

13.3.2 Vacancy Formation and Recovery During Hydrogenation of $LaNi_5Cu$ [35]

In order to understand the formation mechanism of the lattice defects during hydrogenation, in situ measurements under hydrogen pressure are essential. The PAS technique is based on γ ray detection. Since the γ rays have a large penetration length, they can be easily detected outside a high pressure vessel containing the samples and the positron source. The in situ positron annihilation equipment developed to simultaneously measure *P–C* isotherms is shown in Fig. 13.14. This setup is capable to measure the positron lifetime using a digital oscilloscope and the CDB.

The positron lifetimes for the fully annealed $LaNi_5$, $LaNi_{4.5}Al_{0.5}$, $LaNi_4Al$, and $LaNi_5Cu$ were 119, 127, 130, and 120 ps, respectively. These were close to the positron lifetimes of the $LaNi_5$-based alloys without any lattice defects [20, 24]. It was confirmed that the lattice defects were completely removed by the annealing. In addition, the time resolution of this in situ positron lifetime measurement was 172–180 ps. This was considerably better than that obtained by the analog-type

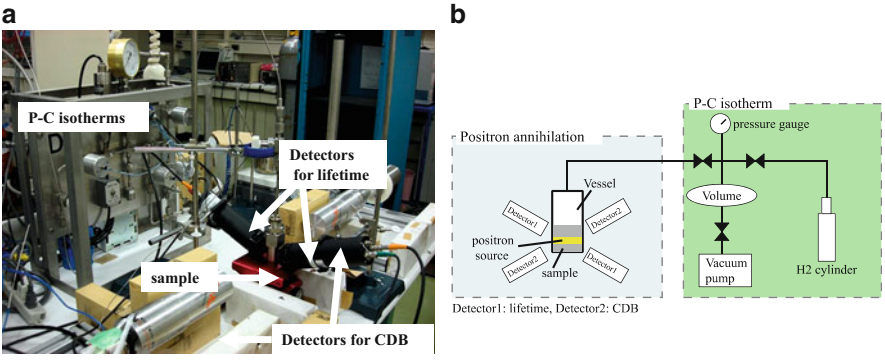

Fig. 13.14 In situ positron annihilation setup capable of simultaneously measuring *P–C* isotherms, reprinted from Sakaki et al. [35], with permission from the American Chemical Society

system (209 ps) which we used previously [36] because a digital oscilloscope was installed to collect the data.

The Doppler broadening spectra of $LaNi_5$ measured with the in situ CDB equipment in the coincidence mode (two detectors) and non-coincidence mode (one detector) were shown in Fig. 13.9. Measurements in the coincidence mode reduced the background in the high-momentum region by more than two orders of magnitude.

Figure 13.15 shows the ratio curves for the $LaNi_5$-based alloys, which have been all normalized by the CDB spectrum of $LaNi_5$. The ratio curves are defined by the following equation:

$$f_{\text{sample}}(p_{\text{L}}) = \frac{N_{\text{sample}}(p_{\text{L}})}{N_{\text{reference}}(p_{\text{L}})} \tag{13.11}$$

where $f_{\text{sample}}(p_{\text{L}})$ is the ratio curve and $N_{\text{reference}}(p_{\text{L}})$ and $N_{\text{sample}}(p_{\text{L}})$ are the (coincidence) Doppler broadening spectra of the reference and target samples, respectively. As seen in Eq. (13.11), the ratio curve is equal to unity, if the positron annihilation behavior in the target sample is the same as that in the reference sample. In $LaNi_5Cu$, the ratio curve starts to decrease below 1 above $5 \times 10^{-3} m_0 c$ and then increases for $p_{\text{L}} > 10 \times 10^{-3} m_0 c$ as shown in Fig. 13.15. This tendency is similar to that observed in pure Cu except for the magnitude of change. In $LaNi_{5-x}Al_x$, the ratio curves start to decrease at $3 \times 10^{-3} m_0 c$ and then gradually increase for $p_{\text{L}} > 15 \times 10^{-3} m_0 c$. The shape of these curves was similar to that observed in pure Al except for the magnitude of the change. These indicate that some positrons were annihilated with the electrons belonging to Cu in $LaNi_5Cu$ and Al in $LaNi_{5-x}Al_x$. In addition, the positron annihilation probability with the electrons belonging to Al increased with increasing Al content. These ratio curves clearly demonstrate that the effect of substitution elements on the positron annihilation behavior was successfully detected.

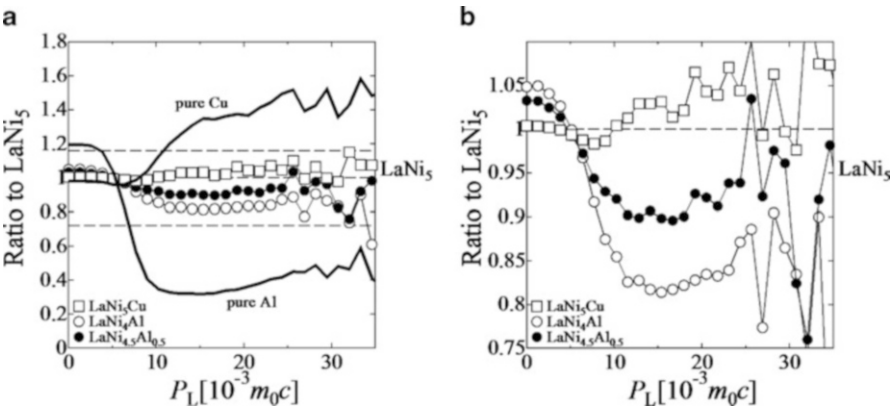

Fig. 13.15 Curves of the CDB spectra of $LaNi_5$-based alloys normalized by the CDB spectrum for $LaNi_5$ represented in (**a**) normal scale and (**b**) zoomed in. Reprinted from Sakaki et al. [35] with permission from the American Chemical Society

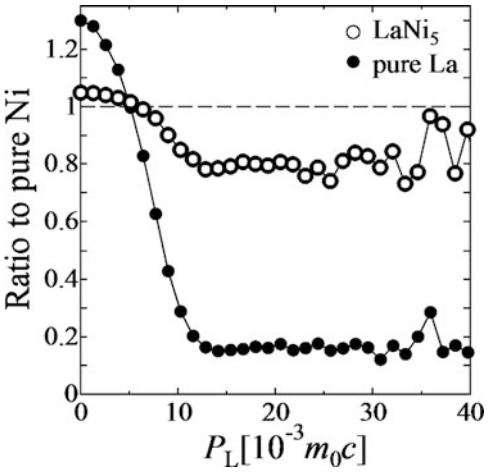

Fig. 13.16 CDB spectra of annealed $LaNi_5$ (along with that of pure La) normalized by the CDB spectrum of Ni. Reprinted from Sakaki et al. [35] with permission from the American Chemical Society

The ratio curve of the CDB spectrum of $LaNi_5$ normalized by the CDB spectrum of pure Ni is shown in Fig. 13.16 along with the ratio curve of pure La. As described above, the ratio curve must change between a constant value of unity and the ratio curve of pure La depending on the fraction of positron annihilation with each element. The ratio curve of $LaNi_5$ decreases with increasing p_L and becomes constant above $p_L = 12 \times 10^{-3} m_0 c$. This tendency is similar to that observed for pure La except for the magnitude of the change. This indicates that the positrons are annihilated with electrons belonging to both, La and Ni. In binary compounds, the Doppler broadening spectrum can be expressed to approximation by the following equation [37]:

$$N_{LaNi_5}(p_L) \propto x \times N_{La}(p_L) + (1 - x) \times N_{Ni}(p_L) \tag{13.12}$$

The parameter x is the fraction of positrons annihilating with electrons belonging to La. Therefore, the ratio curve can be expressed by the following equation:

$$\begin{aligned} f_{LaNi_5}(p_L) &\propto \frac{x \times N_{La}(p_L) + (1 - x) \times N_{Ni}(p_L)}{N_{Ni}(p_L)} \\ &\propto (1 - x) + x \times f_{La/Ni}(p_L) \end{aligned} \tag{13.13}$$

where $f_{La/Ni}(p_L)$ is the curve of pure La normalized by the CDB spectrum of pure Ni. Therefore, the fraction of positron annihilation can be roughly estimated. In $LaNi_5$, the fraction of positron annihilation with La, x, was determined as approximately 22 %. This was slightly larger than the atomic composition but indicates that information on elements relating to the positron annihilation can be obtained at least qualitatively. If positron affinities of the constituent elements [38] are considered, more accurate analysis can be done.

In the following, the in situ measurements of positron lifetimes and CDB in $LaNi_5Cu$ during hydrogenation and dehydrogenation will be discussed. $LaNi_5Cu$

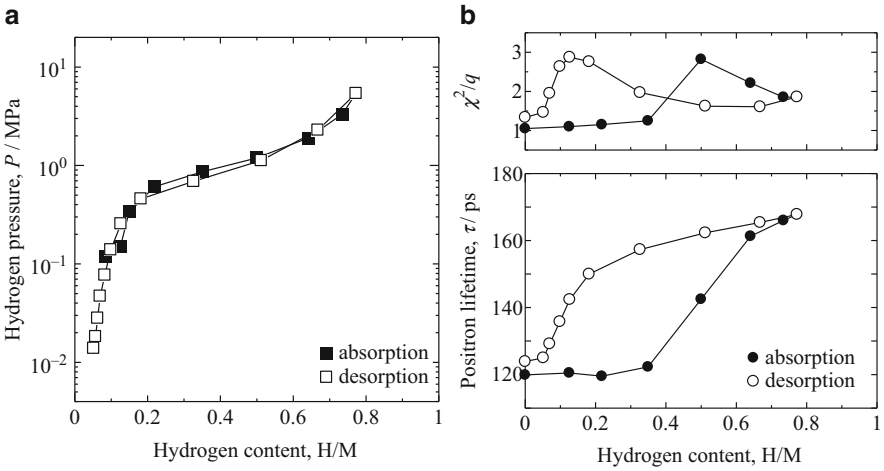

Fig. 13.17 (**a**) *P–C* isotherms and (**b**) variation in positron lifetime and variance of fit (χ^2/q) during hydrogenation and dehydrogenation of $LaNi_5Cu$. Reprinted from Sakaki et al. [35] with permission from the American Chemical Society

absorbs hydrogen up to 0.77 H/M and has a sloping plateau as shown in Fig. 13.17a. Previous reports on in situ X-ray and neutron diffraction showed similar *P–C* isotherms and indicated that $LaNi_5Cu$ absorbed hydrogen without any phase transformation to its hydride [39, 40]. Figure 13.17b shows the change in the positron lifetime and χ^2/q which indicates the accuracy of the one-component analysis as a function of the hydrogen content. The positron lifetime of $LaNi_5Cu$ was 120 ps before hydrogenation and remained unchanged until the hydrogen content reached 0.35 H/M. Then the mean positron lifetime increased to 168 ps with increasing the hydrogen content to 0.77 H/M. In this region, χ^2/q initially increased and then decreased. This increase of χ^2/q indicates that a single exponential approximation for the positron lifetime spectrum is not adequate and lattice defects were introduced. The decrease of χ^2/q indicates that the concentration of the lattice defects increased with hydrogen content and most of the positrons were trapped at the lattice defects (saturation positron trapping). The mean positron lifetime at 0.77 H/M was higher than the positron lifetime of dislocations (150–160 ps) and close to that of Ni vacancies [20, 24]. These findings indicate that lattice defects were not introduced below H/M = 0.35 and vacancies were created above H/M = 0.35.

During dehydrogenation, the mean positron lifetime slowly decreases from 0.77 H/M to 0.33 H/M and then it drastically decreases to 124 ps below 0.33 H/M, accompanied by a rapid change of χ^2/q. The mean positron lifetime after dehydrogenation was close to that of the fully annealed alloy before hydrogenation. This shows that the introduced vacancies started to be recovered below 0.33 H/M during dehydrogenation.

From the Doppler broadening spectra of $LaNi_5Cu$, the parameters *S* and *W* were determined. As described above, an increase in *S* indicates the formation of the

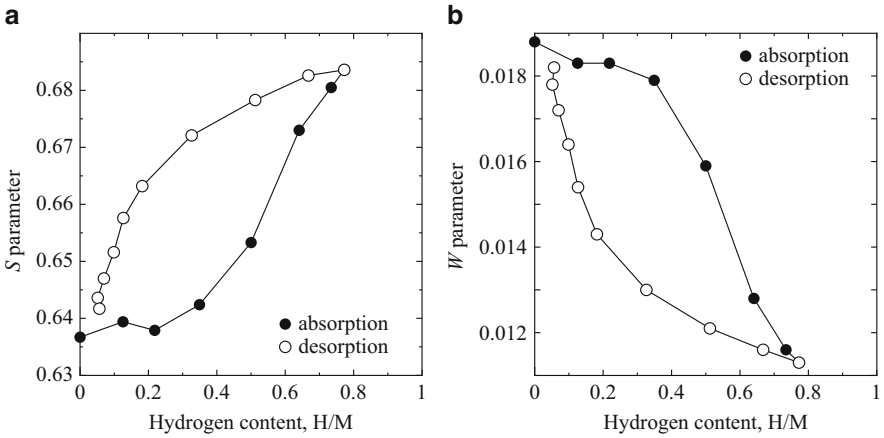

Fig. 13.18 Change in the parameters S and W during hydrogenation and dehydrogenation of $LaNi_5Cu$. Reprinted from Sakaki et al. [35] with permission from the American Chemical Society

lattice defects and a decrease in S indicates the recovery of the lattice defects because the probability of positron annihilation with valence electrons increases when positrons are trapped at the lattice defects. Conversely, the formation of the lattice defects causes a decrease of W and the recovery of the lattice defects leads to an increase of W. During hydrogenation, S remained unchanged below 0.35 H/M and then increased with hydrogen content as shown in Fig. 13.18a. During dehydrogenation, S gradually decreased in the range of above 0.33 H/M and then significantly decreased to the initial value. The variation in S was similar to the positron lifetime shown in Fig. 13.17b. In Fig. 13.18b, on the other hand, W decreased with increasing hydrogen content above 0.35 H/M during hydrogenation and increased significantly below 0.33 H/M during dehydrogenation. Therefore, the variation in S and W indicates that vacancies were introduced during hydrogenation and that the introduced vacancies were recovered during dehydrogenation.

Figure 13.19 shows the relationship between S and W (S–W plot) of $LaNi_5Cu$ during hydrogenation and dehydrogenation. In order to understand the type of the lattice defect, a new parameter, R is defined [41]:

$$R = \frac{S - S_b}{W - W_b} = \frac{S_d - S_b}{W_d - W_b} \tag{13.14}$$

R is determined from the slope of the S–W plot and is independent from the concentration of the lattice defects. If only the concentration of a certain lattice defect increases, R must be constant and the S–W plot is a straight line. If a new type of lattice defect is introduced, R and the slope of the S–W plot will change. The obtained S–W plot in $LaNi_5Cu$ shows a linear relationship during hydrogenation and dehydrogenation. It indicates that the type of the lattice defect did not change and only their concentration changed during hydrogenation and dehydrogenation.

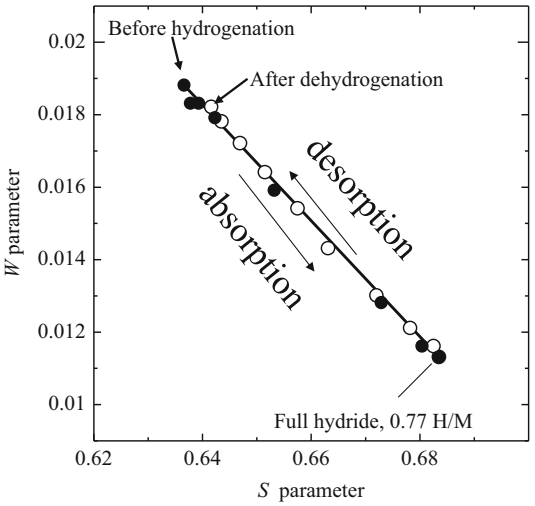

Fig. 13.19 Variation in W with S (S–W plot) during hydrogenation and dehydrogenation of $LaNi_5Cu$. Reprinted from Sakaki et al. [35] with permission from the American Chemical Society

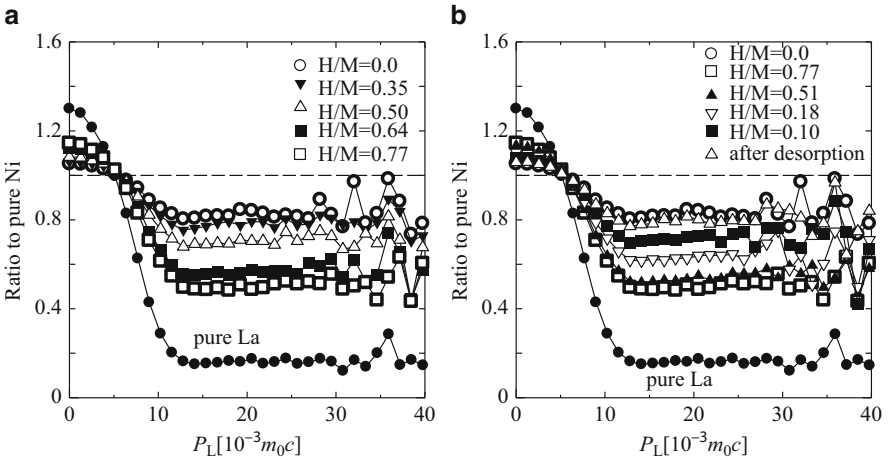

Fig. 13.20 Variation in the ratio curves of the CDB spectra of $LaNi_5Cu$ during (**a**) hydrogenation and (**b**) dehydrogenation, normalized by the CDB spectrum of Ni. Reprinted from Sakaki et al. [35] with permission from the American Chemical Society

Figure 13.20 shows the changes in the ratio curves of $LaNi_5Cu$ during hydrogenation and dehydrogenation. The ratio curves were unchanged below 0.35 H/M and subsequently they shifted toward the curve of pure La with increasing hydrogen content. The changes in the ratio curves indicate that the probability of positron annihilation with electrons belonging to La increased with the increase in hydrogen content. Using Eq. (13.13), the fraction of positrons annihilating with electrons in La did not change below 0.35 H/M but increased with hydrogen content above 0.35 H/M with a value of around 60 % at 0.77 H/M. During dehydrogenation, the

curves were approaching that of fully annealed $LaNi_5Cu$ with decreasing hydrogen content. This suggests that the introduced vacancies were recovered during dehydrogenation, which is consistent with the results obtained from the positron lifetime measurements as well as *S* and *W* parameters.

As shown in Fig. 13.17, vacancies were introduced with increasing hydrogen content during hydrogenation. If vacancies are created at the La sites, the probability of annihilation of positrons with electrons in Ni increases because La is surrounded by only Ni in $LaNi_5$. When Ni vacancies are introduced, the signal from the La atom increases because Ni atoms at both 2*c* and 3*g* sites are surrounded by Ni and La atoms. Therefore, the variations in the ratio curves indicate that the vacancies were formed at Ni sites and not at La sites. To identify the detailed vacancy sites (i.e., Ni 2*c* site or 3*g* site), further quantitative analysis of the Doppler broadening spectrum combined with theoretical calculations is required.

From our previous calculations using the DV-Xα method, the positron lifetime in $LaNi_5$ was found to be 241 ps at an La vacancy, 166 ps at the 2*c* site of the Ni vacancy, and 177 ps at the 3*g* site of the Ni vacancy, respectively [21]. The experimentally observed positron lifetime in the hydrogenated $LaNi_5Cu$ was around 168 ps. This is significantly lower than the calculated positron lifetime at an La vacancy and is closer to that calculated at Ni vacancies (in particular, the value is close to the lifetime at the 2*c* site). In addition, the reported vacancy formation energies at the 2*c* site was about 0.8 eV lower than that at the 3*g* site in $LaNi_5$ [42]. Considering these results, the 2*c* site of Ni is the most probable vacancy site introduced in $LaNi_5Cu$ by hydrogenation.

13.3.2.1 Summary

The equipment for in situ positron lifetime and CDB measurements along with the simultaneous determination of *P–C* isotherms at room temperature was successfully commissioned. This equipment clearly detected the different probabilities of positron annihilation with electrons belonging to different elements qualitatively as well as the effect of substitution on the positron annihilation. The combination of in situ positron lifetime and CDB measurements indicates that vacancies were introduced at Ni sites (probably at Ni 2*c* sites) above 0.35 H/M during hydrogenation and the introduced Ni vacancies were recovered below 0.33 H/M during dehydrogenation in $LaNi_5Cu$.

13.3.3 Hydrogen Embrittlement in Pure Fe [43]

Hydrogen embrittlement is an important phenomenon related to hydrogen and lattice defects. The effect of hydrogen charging on the formation of the lattice defects in Fe was investigated by positron lifetime measurement. First, pure Fe samples were fully annealed at 1223 K for 3 h to remove the lattice defects. The positron lifetime of the fully annealed Fe was around 100 ps and is close to the

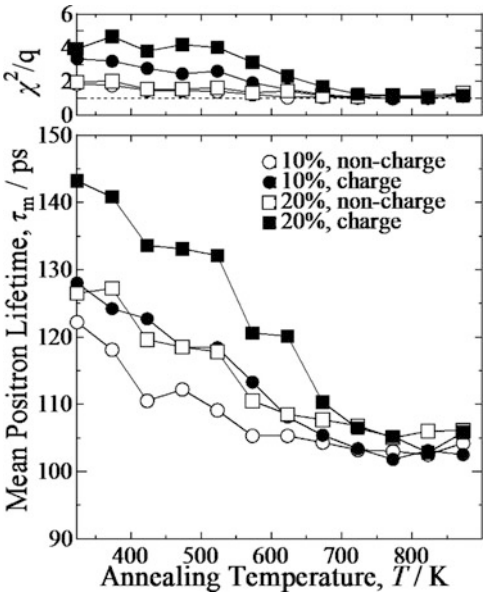

Fig. 13.21 Recovery of the mean positron lifetime during isochronal annealing of deformed iron with/without hydrogen charging. Reprinted from Sakaki et al. [43] with permission from Elsevier Ltd.

reported lifetime by Nieminen et al. (101 ps) [44]. It means that no lattice defects exist in the fully annealed sample. The hydrogen charging was performed with different current densities (0, 0.5, 2, 5 mA/cm^2) by means of cathodic electrolysis at 296 K in a 3 % NaCl aqueous solution containing 3 g/l NH_4SCN. After the hydrogen charging, the mean positron lifetime did not change. Therefore, it indicates that hydrogen charging itself did not introduce the lattice defects. It is consistent with a previous report [45].

The tensile straining to 10 % or 20 % was given with a strain rate of 1×10^{-3} s^{-1} without hydrogen charging or just after hydrogen charging. The mean positron lifetime for all samples increased by more than 20 ps indicating that the lattice defects were introduced. In order to evaluate the type and the concentration of lattice defects, positron lifetime measurements during the isochronal annealing were carried out as shown in Fig. 13.21. The higher mean positron lifetimes were obtained in more deformed and hydrogen charged samples. In addition, the hydrogen charged samples showed the larger variance of the fit, χ^2/q. These indicate that a single exponential approximation for the positron lifetime spectrum is not adequate because of the formation of lattice defects. Therefore, this increase in the mean positron lifetime indicates that the lattice defects were introduced by the tensile strain and that the presence of hydrogen enhanced the accumulation of the lattice defects, being consistent with a previous result by hydrogen TDA for martensitic steels [46]. The mean positron lifetime decreased in two steps with increasing of the annealing temperature, at around 400 and 550 K. This suggests that at least two different types of lattice defects are introduced by tensile strain. At the temperatures above 673 K, the mean positron lifetime was close to that for the

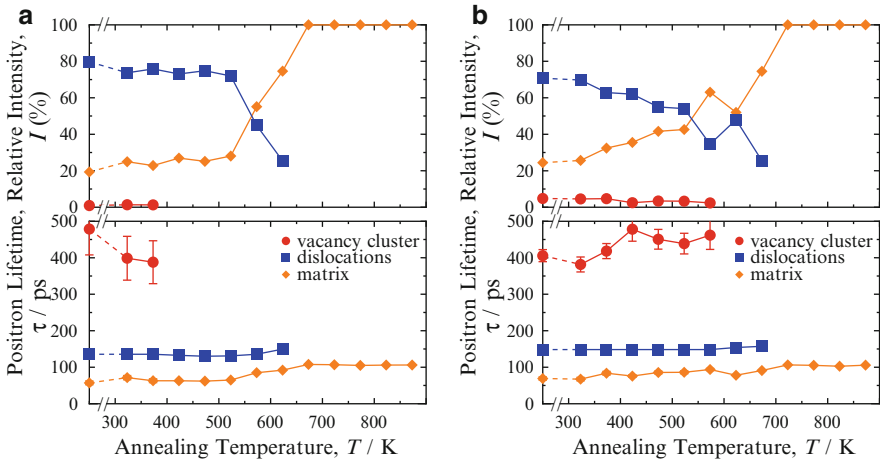

Fig. 13.22 Results of multi-components analysis of positron lifetime spectra for iron deformed by 20 %, (**a**) without and (**b**) with hydrogen charging. Reprinted from Sakaki et al. [43] with permission from Elsevier Ltd.

fully annealed samples indicating that the introduced lattice defects were completely annealed out at 673 K.

In order to identify the type of the lattice defect, multi-components analysis of positron lifetime spectra of 20 % deformed samples was employed as shown in Fig. 13.22. The analyses of the spectra obtained at high temperature annealing (the second recovery region) were firstly performed and then those at low temperature annealing were done. In the second recovery region, the values of the positron lifetimes are around 150 ps and less than 100 ps. The longer positron lifetime is identical to the reported positron lifetime for dislocations (150 ± 4 ps) [47] and the shorter positron lifetime was shorter than that of a fully annealed sample. Therefore, these components are caused by dislocations and the annihilation of un-trapped positrons in the lattice, respectively.

In the range of the annealing temperatures where more than two types of lattice defects are likely to exist, a three-component analysis was performed. For the three-component analysis, the positron lifetime for dislocations was held fixed at the value obtained by the two-component analysis because the positron lifetime at dislocations does not change during the recovery process. The data analysis led to a positron lifetime component exceeding 400 ps. It suggests that the lattice defects are vacancy-type [48, 49], but the positron lifetime was much longer than the 175 ps reported as the positron lifetime for a mono-vacancy [49]. The origin of the increase in the positron lifetime of vacancies is ascribed to micro-void formation by vacancy clustering, as calculated by Puska and Nieminen as a function of the number of vacancies [12]. An increase in the long positron lifetime component up to 400 ps on isochronal annealing of plastically deformed samples was also reported and ascribed to the increase in the number of clustered vacancies [49]. Therefore, this long positron lifetime component is caused by vacancy clusters.

Table 13.1 Dislocation density and vacancy concentration in deformed iron with/without hydrogen charging

Strain (%)	Hydrogen	ρ_d ($\times 10^{10}$/cm^2)	ρ_v ($\times 10^{-7}$)
10	Non-charged	1.0	–
	Charged	0.9	1.7
20	Non-charged	2.2	1.7
	Charged	1.9	8.2

When two types of lattice defects, micro-void and dislocations, are present, $\kappa_{microvoid}$ and κ_d are expressed as follows [49]:

$$\kappa_{microvoid} = \frac{\lambda_f - \lambda_d I_d - \lambda_{microvoid}(1 - I_d)}{1 - (I_d + I_{microvoid})} \cdot I_v = \mu_{microvoid}\rho_{microvoid} = N\mu_v \frac{\rho_v}{N}$$
$$\kappa_d = \frac{\lambda_f - \lambda_{microvoid} I_{microvoid} - \lambda_d(1 - I_{microvoid})}{1 - (I_d + I_{microvoid})} \cdot I_d = \mu_d \rho_d. \tag{13.15}$$

N is the average number of vacancies in a micro-void. The specific trapping rates for mono-vacancy, μ_v, and for dislocations, μ_d, are given in the literature as 1.1×10^{15} s^{-1} [49, 50] and 0.51 cm^2 s^{-1} [34], respectively. The defect concentrations evaluated by Eq. (13.15) are shown in Table 13.1 for the as-deformed samples. ρ_v is represented in the unit of mono-vacancy, not in the unit of micro-void. Since hydrogen charging itself did not create the lattice defects in samples as described above, these results indicate that the presence of hydrogen substantially enhanced the accumulation of vacancies introduced by straining. The result is consistent with a previous interpretation for TDA results [46].

The present result is also consistent with previous results by TDA [51, 52] that showed an increase in the hydrogen absorption capacity by straining. The TDA results, however, ascribed most increase to an enhanced vacancy accumulation from an annealing experiment, while the present positron annihilation experiment showed the accumulation of dislocations as well. The difference might suggest that interactions between hydrogen and dislocations are not substantial.

13.3.3.1 Summary

The effect of hydrogen charging on the formation of lattice defects by tensile strain was investigated by positron lifetime measurements. The positron lifetime measurements clearly showed the creation of vacancies and dislocations by plastic deformation. The presence of hydrogen enhanced the increase in the concentration of vacancies rather than the dislocation density.

References

1. P. Hautojaervi (ed.), *Positrons in Solids* (Springer, Heidelberg, 1979)
2. W. Brandt, A. Dupasquier (eds.), *Positron Solid-State Physics* (North-Holland Publishing Company, New York, 1983)
3. A. Dupasquier, A.P. Mills Jr. (eds.), *Positron Spectroscopy of Solids* (IOS Press, Amsterdam, 1995)
4. http://positronannihilation.net/
5. P.A.M. Dirac, Proc. Camb. Phil. Soc. **26**, 361 (1930)
6. C.D. Anderson, Science. New Series **76**, 238 (1932)
7. C.D. Anderson, Phys. Rev. **43**, 491–494 (1933)
8. K. Sakaki, T. Yamada, M. Mizuno, H. Araki, Y. Shirai, Mater. Trans. **43**, 2652–2655 (2002)
9. H. Saito, Y. Nagashima, T. Kurihara, T. Hyodo, Nucl. Instrum. Methods Phys. Res. Sect. A. **487**, 612–617 (2002)
10. W. Brandt, J. Reinheimer, Phys. Lett. **35A**, 109–110 (1971)
11. K. MacKenzie, *Positron Solid-State Physics*, ed. by W. Brandt (North-Holland, Amsterdam, 1983), pp. 196–260
12. M.J. Puska, R.M. Nieminen, J. Phys. F: Met. Phys. **13**, 333–346 (1983)
13. Y. Shirai, K. Matsumoto, G. Kawaguchi, M. Yamaguchi, Mater. Sci. Forum **105–110**, 1225–1228 (1992)
14. P. Kirkegaard, M. Erldrup, O.E. Morgensen, N. Pedersen, Comput. Phys. Commun. **23**, 307–335 (1981)
15. P. Kirkegaard, M. Eldrup, Comput. Phys. Commun. **3**, 240–255 (1972)
16. P. Kirkegaard, M. Eldrup, Comput. Phys. Commun. **7**, 401–409 (1974)
17. W. Brandt, *Positron Annihilation*, ed. by A.T. Stewart, L.O. Roeling (Academic, New York, 1967), pp. 155–182
18. K. Lynn, J.R. MacDonald, R.A. Boie, L.C. Feldman, J.D. Gabbe, M.F. Robbins, E. Bonderup, J. Golovchenko, Phys. Rev. Lett. **38**, 241–244 (1977)
19. P. Asoka-Kumar, M. Alatalo, V.J. Ghosh, A.C. Kruseman, B. Nielsen, K.G. Lynn, Phys. Rev. Lett. **77**, 2097–2100 (1996)
20. K. Sakaki, E. Akiba, M. Mizuno, H. Araki, Y. Shirai, J. Alloy. Compd. **473**, 87–93 (2009)
21. M. Mizuno, K. Sakaki, H. Araki, Y. Shirai, J. Alloy. Compd. **356–357**, 186–190 (2003)
22. H. Adachi, M. Tsukada, C. Satoko, J. Phys. Soc. Jpn. **45**, 875–883 (1978)
23. D.E. Ellis, G.S. Painter, Phys. Rev. B **2**, 2887–2898 (1970)
24. Y. Shirai, H. Araki, T. Mori, W. Nakamura, K. Sakaki, J. Alloy. Compd. **330–332**, 125–131 (2001)
25. E.H. Kisi, E. Wu, M. Kemali, J. Alloy. Compd. **330–332**, 202–207 (2002)
26. R. Cerny, J.-M. Joubert, M. Latroche, A. Percheron-Guegan, K. Yvon, J. Appl. Cryst. **33**, 997–1005 (2000)
27. H. Inui, H. Sakamoto, T. Yamamoto, M. Yamaguchi, Mat. Res. Soc. Symp. Proc. **753**, 469–474 (2003)
28. W. Brandt, in *Positron Annihilation*, ed. by A.T. Stewart, L.O. Roeling (Academic, New York, 1967), pp. 155–182
29. B. Bergersen, M.J. Stott, Solid State Commun. **7**, 1203–1205 (1969)
30. D.C. Connors, R.N. West, Phys. Lett. A. **30**, 24–25 (1969)
31. M. Doyama, R.R. Hasiguti, Crystal Lattice Defects **4**, 139–163 (1973)
32. R.W. Siegel, in *Positron Annihilation*, ed. by P.G. Coleman, S.C. Sharma, L.M. Diana (North-Holland, Amsterdam, 1982), pp. 351–368
33. R.W. Siegel, in *Positron Annihilation*, ed. by P.G. Coleman, S.C. Sharma, L. M. Diana (North-Holland, Amsterdam, 1982), pp. 369–380
34. Yong-Ki Park, J.T. Waber, M. Meshii, C.L. Snead Jr., C.G. Park, Phys. Rev. B. **34**, 823–836 (1986)
35. K. Sakaki, Y. Nakamura, E. Akiba, J. Phys. Chem. C **116**, 22238–22244 (2012)

36. K. Sakaki, R. Date, M. Mizuno, H. Araki, Y. Nakamura, Y. Shirai, R.C. Bowman, Jr., E. Akiba, J. Alloy. Compd. **477**, 205–211 (2009)
37. Y. Nagai, T. Nonaka, M. Hasegawa, Y. Kobayashi, C.L. Wang, W. Zheng, C. Zhang, Phys. Rev. B **60**, 11863–11866 (1999)
38. M.J. Puska, P. Lanki, R.M. Nieminen, J. Phys. Condens. Matter **1**, 6081 (1989)
39. M. Latroche, P.H.L. Notten, A. Percheron-Guegan, J. Alloy. Compd. **253**, 295–297 (1997)
40. P.H.L. Notten, R.E.F. Einerhand, J.L.C. Daams, J. Alloy. Compd. **210**, 221–232 (1994)
41. S. Mantl, W. Triftshauser, Phys. Rev. B **17**, 1645–1652 (1978)
42. M. Mizuno, H. Araki, Y. Shirai, J. Phys. Condens. Matter **20**, 275232 (2008)
43. K. Sakaki, T. Kawase, M. Hirato, M. Mizuno, H. Araki, Y. Shirai, M. Nagumo, Scr. Mater. **55**, 1031–1034 (2006)
44. M.J. Puska, R.M. Nieminen, Rev. Mod. Phys. **66**, 841 (1994)
45. H. Ohkubo, S. Sugiyama, K. Fukuzato, M. Takenaka, N. Tsukuda, E. Kuramoto, J. Nucl. Mater. **283–287**, 858–862 (2000)
46. M. Nagumo, M. Nakamura, K. Takai, Metallur. Mater. Trans. A **32A**, 339–347 (2001)
47. C. Hidalgo, G. Gonzalez-Doncel, S. Linderoth, J. San Juan, Phys. Rev. B **45**, 7017–7021 (1992)
48. J. Takamura, I. Takahashi, M. Amano, Trans. JISI **9**, 216–221 (1969)
49. A. Vehanen, P. Hautojärvi, J. Johanson, J. Yli-Kauppila, Phys. Rev. B **25**, 762–780 (1982)
50. H.E. Schaefer, P. Valenta, K. Maier, in *Positron Annihilation*, ed. by R.R. Hasiguti, K. Fujiwara (Japan Institute of Metals, Sendai, 1979), p. 509
51. S. Suzuki, N. Ishii, Y. Tsuchida, Tétsu-to-Hagané **80**, 855–859 (1994)
52. M. Nagumo, K. Ohta, K. Takai, Scr. Mater. **40**, 313–319 (1999)

Index

H. Fritzsche et al. (eds.), *Neutron Scattering and Other Nuclear Techniques for Hydrogen in Materials*, Neutron Scattering Applications and Techniques,
DOI 10.1007/978-3-319-22792-4

D